



University
of Glasgow

Vasiev, Iskandar (2015) *3D self-folding tissue engineering scaffold origami*. PhD thesis.

<http://theses.gla.ac.uk/7071/>

Copyright and moral rights for this thesis are retained by the author

A copy can be downloaded for personal non-commercial research or study

This thesis cannot be reproduced or quoted extensively from without first obtaining permission in writing from the Author

The content must not be changed in any way or sold commercially in any format or medium without the formal permission of the Author

When referring to this work, full bibliographic details including the author, title, awarding institution and date of the thesis must be given

3D SELF-FOLDING TISSUE ENGINEERING SCAFFOLD ORIGAMI

by Iskandar Vasiev

Submitted in fulfilment of the requirements
for the degree of Doctor of Philosophy in
Biomedical Engineering

School of Engineering
College of Science and Engineering
University of Glasgow

October 2015

ACKNOWLEDGEMENTS

This work would be nothing without the support and guidance of the people around me during this sometimes stressful and ultimately rewarding chapter of my life. First and foremost I have to thank my supervisors Professors Nikolaj Gadegaard and Elizabeth Tanner who through their patience, creativity and wisdom helped guide me over the years.

My parents, my sister Sofia and my partner Kristyn, I want to thank you all for putting up with me, whether it was during the write up, or being far away from home, day dreaming or having to work late, feed cells on weekends and all the other inconveniences I may have brought to your lives. Your motivating words and optimism during the most difficult periods are what ultimately made a huge difference.

The technicians, administrators and staff of the University of Glasgow deserve much more than this simple mention, for the hard work they put into providing the comprehensive and most dedicated infrastructure that a researcher could ask for. The JWNC remains in my mind one of the best run and efficient labs that one could have the privilege to work in.

I would additionally like to thank the Sullivan group at the University of Oslo, School of Medicine, for their hospitality and invaluable education in stem cell culture and regenerative medicine.

Finally, a special thank you to all the people of our 'BIG' and Tanner research groups at the University of Glasgow who have been not only fantastic friends but also an immeasurable bank of knowledge and expertise. I will miss our research meetings in the local watering hole. Your creativity, attention to detail and scientific curiosity are second to none.

Author's Declaration

I declare that this thesis embodies the results of my own special work, that it has been composed by myself and that it does not include work forming part of a thesis presented successfully for a degree in this or another University.

TABLE OF CONTENTS

Nomenclature	7
1 Introduction	39
1.1 3D constructs, their occurrence in nature, relevance to tissue engineering, and man-made recreation.....	39
1.1.1 3D architecture in nature	39
1.1.2 Simulated 3D constructs	43
1.2 Actuation and the spontaneous formation of engineered 3D structures	44
1.3 Hydrogels as tissue engineering scaffolds and actuators	46
1.3.1 Neutral or structural hydrogels.....	49
1.3.2 Stimuli responsive hydrogels	50
1.3.3 Hydrogel synthesis	52
1.3.4 Hydrogel performance	56
1.3.5 Hydrogel bilayer actuators.....	58
1.4 Nanopatterning, methods and applications.....	59
1.4.1 NIL with flexible media.....	60
1.4.2 Hierarchical patterning	62
1.4.3 3D surface patterning.....	64
1.5 Cell-scaffold interaction or the ‘biointerface’	65
1.5.1 Contact guidance.....	65
1.5.2 Surface chemistry.....	66
1.5.3 ECM and protein self-organization.	69
1.5.4 Surface stiffness	70
1.6 The use of hESCs for tissue engineering	72
2 Nanopatterning techniques	76
2.1 Introduction	76
2.2 Materials and methods.....	77
2.2.1 Materials	77
2.2.2 Instrumentation	77
2.2.3 Methods	80
2.3 Results.....	87
2.3.1 The benefits of using FEP as a stamp material.....	87
2.3.2 FEP imprint stamps	88
2.3.3 Master replication.....	93
2.3.4 Hierarchical patterning	95
2.3.5 Curved surface patterning.....	100
2.3.6 Modular mastering process	101
2.3.7 Transferring patterns from higher throughput methods.....	103
2.3.8 Hydrogel patterning	104
2.3.9 UV-NIL as a means of manufacturing patterned hydrogel films.....	106

2.4	Discussion	113
2.4.1	Fluoropolymer thin film stamps.....	113
2.5	Conclusions	118
3	Hydrogels and hydrogel actuators.....	119
3.1	Introduction	119
3.2	Materials and methods.....	120
3.2.1	Materials	120
3.2.2	AFM and metrology for feature depth measurement	120
3.2.3	SEM imaging of nanostructures	120
3.2.4	O ₂ plasma ashing.....	120
3.2.5	Spin coating.....	121
3.2.6	Micro- and nanopattern formation on quartz and silicon	121
3.2.7	Release coating for stamps and photomasks.....	121
3.2.8	PDMS replica stamps for NIL and UV-NIL.....	122
3.2.9	Sacrificial layer for lift-off of patterned devices.....	122
3.2.10	Thermal nanoimprint lithography (Thermal NIL).....	123
3.2.11	Photolithography	123
3.2.12	Hydrogel synthesis	125
3.2.13	Hydrogel bilayers.....	128
3.2.14	Hydrogel actuator triggering.....	128
3.2.15	Hydrogel analysis	129
3.3	Results.....	135
3.3.1	Photo initiator efficiency and suitability	135
3.3.2	Hydrogel properties	136
3.3.3	Fourier transform infrared spectroscopy.....	153
3.3.4	Bilayer actuation and predicted ideal conditions	158
3.4	Conclusions	161
4	Design and manufacture of 3D structures.....	164
4.1	Introduction	164
4.2	Materials and methods.....	165
4.2.1	Materials	166
4.2.2	Software	166
4.2.3	Methods	166
4.3	Design of containers	172
4.3.1	Hinge design.....	172
4.3.2	Box design	174
4.4	Results.....	187
4.4.1	Roughness of PAA	187
4.4.2	Patterning of SU8 surfaces.....	190
4.4.3	Patterning of PLLA surfaces.....	191
4.4.4	Manufacture of all-hydrogel 3D microcontainers.....	193

4.4.5	Manufacture of hybrid containers	197
4.4.6	Boundary layers.....	200
4.4.7	Lotus structures.....	205
4.4.8	Device immobilization.....	209
4.5	Conclusions	211
5	Cell culture in 2D and 3D	213
5.1	Introduction	213
5.2	Materials and methods.....	215
5.2.1	Materials	215
5.2.2	Cell freezing and defrosting	215
5.2.3	Nano patterned insert preparation.....	215
5.2.4	Contact angle	216
5.2.5	Matrigel coating	216
5.2.6	Vitronectin coating.....	217
5.2.7	Sulfo-SANPAH modification of hydrogel rolls	219
5.2.8	Anchoring inserts in 6-well trays with a cell repelling hydrogel	219
5.2.9	Cell seeding procedure.....	220
5.2.10	Initial screening with hTERT immortalized cell lines.....	221
5.2.11	hESC small molecules initiated differentiation into hepatocytes	222
5.2.12	cDNA preparation for Real Time - qPCR.....	223
5.2.13	Real-time quantitative PCR	224
5.2.14	Estimating substrate stiffness of tall pillar arrays	225
5.2.15	Quantifying cell colony size and area coverage with Cell profiler™	228
5.3	Results.....	231
5.3.1	Contact angle	231
5.3.2	Fibroblast attachment to hydrogel surfaces.....	232
5.3.3	Fibroblast attachment to SU8 epoxy surfaces	234
5.3.4	hESC proliferation on patterned surfaces	235
5.3.5	hESC colony formation on Pillar Gradient Array	260
5.4	Conclusions	264
6	Overall discussion and conclusions.....	267
7	Future work.....	271
	References	272
	Appendix A – Simulation of oxygen concentration in cell culture microcontainers.....	284
	Appendix B – Output from this work	291

Abstract

In the field of tissue engineering complex 3D architecture has become increasingly relevant in the pursuit of precisely engineered control over living tissue. It is needed to recreate the heterogeneous and complex arrangements of cells seen in nature, and to be able to influence their proliferation, differentiation and fate. A method for the 3D structuring of cells is therefore desired and is something standard lithographic methods cannot provide - the precision engineered 3D cellular niche. This work transfers traditional 2D lithographic techniques used in MEMS (E-beam lithography, photolithography, soft lithography and nanoimprint lithography) to the construction of 3D as well as complex hierarchical structures compatible with cell culture. To address this, hydrogel bilayers act as biocompatible, flexible and environmentally responsive hinges to fold the 2D structure into a 3D conformation. To achieve this, a rapid method of producing nanopatterns with the potential for large area patterning was developed. These were fluorinated ethylene propylene (FEP) and polydimethylsiloxane (PDMS) replica stamps with 2D and 2.5D hierarchical patterns. They were capable of bending and conforming to uneven and curved surfaces. These were used in a novel combinational lithography approach to construct complex hierarchical structures by photolithography through photomasks with nanopatterned transparent FEP inlays to create unfolded 3D cellular niches by a 2D method. Several different hydrogels were synthesised and patterned by photolithography to be used as bilayer hinges. Actuation mechanisms included thermoresponsive N-isopropylacrylamide (NIPAAm), and anionic acrylic acid (AA) monomers. Successful bilayers were formed using acrylate based photochemistry with poly(ethylene glycol) dimethacrylate (PEGDMA) and pH responsive polyacrylic acid (PAA) in a novel sacrificial layer functionalisation method. These structures would bend and roll due to differential swelling in neutral pH and when acting as a hinge would result in self-folding of photolithographically defined 2D structures into 3D containers. To test the compatibility of this method of manufacture with cell culture hESCs were trialled on the container materials, and showed excellent adhesion on the SU8 structures. More ambitiously to see if they could in the future be used for the directed differentiation of stem-cells, hESCs were cultured on nanopatterned injection moulded polymer substrates with varying nanofeature type. It was found that hESCs had improved adhesion on vitronectin coated nanotopographies even at extremely low vitronectin concentrations, and showed an increased 3D colony structure leading to the enhanced expression of certain lineage markers. It was found that hESC attachment could be mediated by feature height and substrate elasticity. This work has demonstrated as a proof-of-principle, a rapid and simple method of producing nanopatterned 3D self-folding containers, compatible with cell culture which could in the future serve as 3D self-folding nanopatterned cellular niches for tissue engineering.

NOMENCLATURE

List of Abbreviations

AFM	<i>Atomic force microscopy</i>
ATR-FTIR	<i>Attenuated total reflectance-FTIR</i>
AAc	<i>Acrylic acid</i>
DEAEMA	<i>N,N-Diethylaminoethyl methacrylate</i>
DMEM	<i>Dulbecco's Modified Eagle Medium</i>
DMSO	<i>Dimethyl sulfoxide</i>
EBL	<i>Electron beam lithography</i>
ECM	<i>Extracellular matrix</i>
EDTA	<i>Ethylenediaminetetraacetic Acid</i>
EGDMA	<i>Ethyleneglycol dimethacrylate</i>
EtOH	<i>Ethanol</i>
FEP	<i>Fluorinated ethylene propylene</i>
FTIR	<i>Fourier transform infrared spectroscopy</i>
HEMA	<i>2-Hydroxyethyl methacrylate</i>
hTERT	<i>Human telomerase reverse transcriptase</i>
hESCs	<i>Human embryonic stem cells</i>
ICP	<i>Inductively coupled plasma</i>
IPA	<i>Isopropanol</i>
MeOH	<i>Methanol</i>
MIBK	<i>Methyl isobutyl ketone</i>
NiCr	<i>Nickel-chrome also known as 'nichrome'</i>
NIL	<i>Nanoimprint lithography</i>
NIPAAm	<i>N-isopropyl acrylamide</i>
PAAc	<i>Poly(acrylic acid)</i>
PC	<i>Polycarbonate</i>
PCL	<i>Polycaprolactone</i>
PEG	<i>Poly(ethylene glycol)</i>

PEGDMA	<i>Poly(ethylene glycol) dimethacrylate</i>
PEGDA	<i>Poly(ethylene glycol) diacrylate</i>
PHEMA	<i>Poly(hydroxyethyl methacrylate)</i>
PLLA	<i>Poly-L-lactide</i>
PLGA	<i>Poly(lactic-co-glycolic acid)</i>
PMAA	<i>Poly(methacrylic acid)</i>
PMMA	<i>Poly(methyl methacrylate)</i>
PNIPAAm	<i>Poly(N-isopropyl acrylamide)</i>
PS	<i>Polystyrene</i>
RT-qPCR	<i>Real time - Quantitative polymerase chain reaction</i>
qz	<i>Quartz</i>
RIE	<i>Reactive-ion etching</i>
ROCK-i	<i>Rho kinase (ROCK) inhibitor</i>
RO water	<i>Reverse osmosis purified water</i>
RPMI-B27	<i>Cell culture media with low FBS supplementation</i>
SEM	<i>Scanning electron microscopy</i>
Si	<i>Silicon</i>
SiN	<i>Silicon nitride</i>
Sulfo-SANPAH	<i>Sulfosuccinimidyl 6-(4'-azido-2'-nitrophenylamino)hexanoate</i>
TCP	<i>Tissue culture plastic</i>
TEA	<i>Triethylamine</i>
TEMED	<i>Tetramethylethylenediamine</i>
TMPTMA	<i>Trimethylolpropane trimethacrylate</i>
TPM	<i>3-(Trimethoxysilyl)propyl methacrylate</i>
UV-NIL	<i>Ultraviolet nanoimprint lithography</i>
Vtn	<i>Vitronectin</i>

Glossary of terms

Ashing	<i>The process of exposing sample to oxidising O₂ plasma to remove any fine residual layers</i>
Accutase®	<i>A cell detachment solution</i>
Baking	<i>The process of removal of moisture and solvent from a resist</i>
Degassing	<i>The removal of gas from a liquid or polymer, epoxy melt</i>
Deposition	<i>The immobilization of a substance onto a surface, such as the evaporation of metal to form a conductive coating</i>
Descum	<i>The removal of residues deposited during processing of a substrate</i>
Etching	<i>A chemical process of removing material, can be dry or wet, depending on the use of a liquid etchant, dry etching often more anisotropic</i>
Emboss	<i>A thermal imprinting process</i>
Mask	<i>A pattern on a transparent material used to mask areas during photolithography, thus defining a pattern.</i>
Matrigel®	<i>A blend of ECM proteins used for coating surfaces for stem cell attachment</i>
MA6	<i>SÜSS MA6 photolithographic mask aligner</i>
MF319	<i>Micro resist developer based on Tetramethylammonium hydroxide</i>
Plating	<i>The process of coating the substrate with ECM constituent proteins or ligands for cell attachment</i>
Resist	<i>A polymeric substance used to resist chemical etches of the substrate.</i>
Residual layer	<i>Thin film of material left after imprinting between imprint stamp features and substrate</i>
Seeding	<i>The process of dispensing cells in suspension with the intent of them adhering to the substrate surface</i>
Selectivity	<i>The rate at which one substance etches in relation to another</i>
SU8	<i>A negative photoresist consisting of bisphenol-A novolac epoxy, gamma-butyrolactone and a blend of triarylsulfonium and hexafluoroantimonate salt.</i>
S1818	<i>Shibley 1818 positive photoresist consisting of electronic grade propylene glycol monomethyl ether acetate, Mixed cresol novolak resin and a diazo photoactive compound.</i>
Spinning	<i>A method of applying thin films by spinning of the substrate at high speed, thickness is controlled by varying fluid viscosity, spin speed and duration.</i>

List of Symbols

a	Fitting parameter
A	Area
χ	A solvent/polymer interaction parameter. the materials used in synthesis can be correlated to the swelling ratio of the
C_n	Flory characteristic ratio
D	Diffusion coefficient
D_0	Diffusivity of solute
E	Young's modulus
ϕ	Quantum yield
$\varphi_{2/s}$	Specific volume of the polymer
G	Shear modulus
h	Layer thickness
I	Area moment of inertia
k_B	Boltzmann constant
k	Material stiffness
K	Bilayer curvature
n	Integer value, number of bonds, number of values
ν	Poisson's ratio
η	Viscosity
M_c	Molecular weight of polymer crosslinking chain
M_n	Molecular number averaged molecular weight
M_r	Average molar mass of the repeat unit of the polymer
M_w	Weight averaged molecular weight
ρ	Density
pK_a	Acid dissociation constant
Q	Equilibrium volume swelling ratio
q	Equilibrium mass swelling ratio
r	Surface roughness
r_s	Stokes-Einstein hydrodynamic radius of solute
R	Radius of curvature
σ	Stress
T	Temperature
T_{tilt}	Pillar deflection tilt correction factor
θ	Angle

θ_c	Contact angle
θ'_c	Contact angle on patterned surface (reduced wetted area)
V_d	Gel dry volume
V_s	Gel swollen volume
$V_{sp,2}$	Specific volume of the solvent
V_1	Molar volume of solvent
ζ	Damping factor
γ_{LS}	Liquid-solid interfacial energy
γ_{LG}	Liquid-gas interfacial energy
γ_{SG}	Solid-gas interfacial energy
γ	Ratio of critical volume required for successful translational movement of the solute molecule to the average free volume per molecule of liquid.

List of figures

Figure 1-1 - The 3D architecture in cyanobacterium exoskeletons. A-C: SEM image of cells of *B. bigelowii*. D-E: Optical micrographs of *B. bigelowii* cells showing dodecahedron shaped constructs of the exoskeleton composed of pentagonal sections. All scale bars: 1 μm . Reproduced from Hagino et al. [2]. 39

Figure 1-2 - Architecture and self-folding of pollen grains. (A) Mechanism of folding response to changes in humidity, allows a partial dehydration of the wall material while preventing complete desiccation of the internal genetic information and death. (B) A three aperture pollen grain with wall construction. (C)–(F) SEM images of pollen grains in hydrated states. (C) The single aperture pollen grain of *Lilium longiflorum*. D) The three aperture pollen grain of *Euphorbia milii*. (E) The single aperture pollen of *Aristolochia gigantea*. (F) The single aperture pollen grain of maize (*Zea mays*). Scale bars: 20 μm . Reproduced form Katifori et al. [3]. 40

Figure 1-3 – Depiction of liver metabolism, showing the processes of the lobule to lobule interaction, nutrient and waste transport and chemical gradients including the chemical gradients and metabolic zones (1 to 3) resulting in nutrient and oxygen uptake as it transits the hepatic lobule. This image highlights the importance of geometric order in hepatic tissue constructs. Reproduced from Mohty et al. [7] 41

Figure 1-4 – Pathways for bile regurgitation in cellular hepatic junction. In numbered order of: 1. escape through leaky junction, 2. vesicle mediated transport, 3. Transport to the sinusoid endothelial cell membrane. Scale bar: 20 μm . Reproduced from Desmet [12]. 42

Figure 1-5 – Various actuating micro systems. A: Hemisphere of a dodecahedron formed by capillary force. Scale bar: 50 μm . Reproduced with permission from Legrain et al. [22] B-C: A tetrahedron before and after folding made of differentially exposed hydrogel, among other geometric shapes,

the structure is formed by acidic and hot environment reproduced from Yoon et al. [23], scale bars 300 μm . D-E: A Venus flytrap mimicking device composed of rigid SU8 segments with a NIPAm-AAc/PEODA bilayer hinge folding with low pH and high temperature,. scale bars: 3mm. reproduced with permission from Bassik et al. [24]. F: A jellyfish like hydrogel container formed by differential swelling of a NIPAAm based bilayer in cold water, scale bar: 100 μm . Reproduced with permission from Guan et al.[25]..... 44

Figure 1-6 – Hydrogel formation and actuation based on steady state equilibrium swelling and actuation between hydrophilic and hydrophobic states..... 47

Figure 1-7- Phase-contrast photomicrographs of (a) fibroblast and (b) HUVEC cell proliferated on a PNIPAAm hydrogel film. (1–3): Fibroblast sheet detachment upon decreasing the temperature to 10–20 °C when the gel falls below its LCST and begins to swell. Scale bars: 200 μm . Reproduced with permission from Haraguchi [78]. 49

Figure 1-8 –A: shows the advancing (open square) and receding (closed square) contact angle of PNIPAAm gels. B: The swelling ratio of PNIPAAm gels in pH 7 buffered solutions of increasing ionic strength over a range of 0.005mol/dm³ (open circle) – 0.154 mol/dm³ (closed triangle) intermediate concentrations (closed circle, open triangle). Reproduced from Makino [103]..... 52

Figure 1-9 – Spontaneous hierarchical structure formation and evolution of hierarchical surface pattern in13nm gold films on pre-strained elastomer substrates. In the top panel the biaxially strained substrates have a prestrain of $\epsilon_{f1}= 67\%$ and $\epsilon_{f2}= 3\%$ (a), 20 % (b), 50 % (c) and 67 % (d). In the top panel the prestrain is $\epsilon_{f1} = \epsilon_{f2} = 5\%$ (e), 30 % (f), 50 % (g) and 67 % (h). Scale bars are 10 μm in top panels and 2 μm in bottom panels of all images. Reproduced with permission from Cao et al. [149]. 63

Figure 1-10 - Optical micrographs of cells on the four types of substrate textures. The arrows show the direction of textural features to which the cells may align. A similar grating of 500 nm width and pitch is utilized and converted into a FEP stamp later in this chapter. Reproduced with permission from Seunarine et al. [148]. © 2009 IEEE 64

Figure 1-11 – The spontaneous differentiation of MSCs into osteoblasts on ‘near-square’ nanopatterned surfaces. Surface patterned with pits arranged in increasingly disordered configurations, with osteoblasts labelled green, MSCs labelled red. Pattern with preferential bone formation is NSQ50 (d and j), with 150 nm diameter pits arranged on a 2:1 pitch, with a 50 nm degree of disorder. Reproduced from McMurray et al. [159]..... 66

Figure 1-12 –An illustration of chemical interactions between human pluripotent stem cells (hPSCs) and culture surfaces. Specific ligands and cell adhesion molecules (CAMs) are included if they have been reported in hPSC attachment and/or culture studies. CAMs involved in hPSC adhesion include

integrin subtypes $\alpha 5\beta 1$ (green), $\alpha v\beta 5$ (red), $\alpha v\beta 3$ (purple), $\alpha 6\beta 1$ (blue) and $\alpha 2\beta 1$ (navy blue), E-cadherin (black blocks), heparan sulphate proteoglycans (HSPGs; dashed blue lines) and unidentified CAMs (orange). Ligands are portrayed as coloured ovals and include the SMB domain of vitronectin (yellow/red), GKKQFRHRNRKG (orange/red), KGGPQVTRGDVFTMP (red/dark red), AG-10 (CGGNRWHSIYITRFG; blue/dark blue), C-16 (CGGKAFDITYVRLKF; purple/navy blue), AG-73 (CGGRKRLQVQLSIRT; yellow/orange), GRGDSP (green) and laminin E8 fragments (light blue/blue). The ligands are presented by ECMPs [represented by curved coloured lines: laminin-511 or -322 (blue), laminin-111 (navy blue), vitronectin (red), fibronectin (green) collagen (yellow)] or synthetic surfaces (thick black lines) including SynthemaxTM, StemAdhereTM and PMEDSAH. On the left of the image complex extracellular matrix extracts (e.g. MatrigelTM and GeltrexTM) are illustrated as combinations of ECMPs, and on the right cell-cell adhesion is simplified in the extreme to illustrate homophilic E-cadherin binding. Where specific ECMP ligands are poorly-defined, CAMs are shown to interact with the ECMP line. Where specific CAMs have not been identified the orange CAM is used, and undefined, adsorbed ligands are represented by orange ovals with a white question mark.

Reproduced from Lambshead et al. [161] 68

Figure 1-13 - Self organization of fibronectin on different polymeric substrates shows the potential for geometrically mediated signalling by the tendency for the fibronectin to organise based on surface concentration. FN organisation and distribution on the surface then depends, for each substrate, on the concentration of the initial protein solution from which the protein is adsorbed.

Reproduced with permission from Guerrero et al. [173] 69

Figure 1-14 – The relationship between focal adhesion area (FA) and transduced force, and the correlated force to pillar stiffness and effective modulus of the substrate of pillars if it were represented by an infinite flat surface. A decrease in pillar stiffness is equivalent to a material of lower stiffness, such as a transition from a plastic to a rubber like hyperelastic material which will accommodate larger displacements due to loading. Scale bars: 10 μm . Reproduced from Trichet et al. [158]. 71

Figure 1-15 – Changes in MSC gene expression with varying substrate stiffness. Correlation was seen between reduced cell proliferation on softer substrates. Gene expression shown in C.) shows the genes which are down regulated in (red) and genes which are up regulated in (green), showing lineage specific signalling depending on substrate stiffness. Scale bars 20 μm . Reproduced from Trichet et al. [158]. 72

Figure 1-16 - The process of differentiating hESCs into hepatocytes by the small molecules process demonstrated by the Sullivan group at the University of Oslo. Illustration, showing the stages between seeding hESCs and obtaining hepatocyte like cells. A.) Three phase process transitioning

from a definitive endoderm to hepatic specification and hepatocyte maturation. B.) The chemical changes made in the media to move the cells through the specific stage. C.) Changes in gene up regulation during this stage of differentiation D.) Morphological changes in cell clustering during the specific stage. Reproduced from Siller et al. [172]. 74

Figure 2-1 - Contact angle measurement of an FEP film by optical densitometry. Droplets were dispensed on surface and imaged in silhouette illumination mode..... 78

Figure 2-2 - Diagram of surface energy interactions at solid, liquid and gas interfaces, and their effect on contact angle of liquid droplets on planar and patterned surfaces in the Young (left) and Cassie-Baxter state (right). The presence of a nanopattern creating a higher contact angle as the droplet sits in a suspended higher energy state..... 79

Figure 2-3 – Left to right: contact angle measurement, with water droplet before and after contact with a untreated silicon surface. Bottom: trace of contact angle over time shows the droplet reaching a steady state contact angle at roughly 300 seconds. 80

Figure 2-4 - Process for the nanopatterning of quartz master stamps by electron beam lithography (EBL), undercut development of PMMA resist layer aids lift-off without removing NiCr features during the lift-off step. The NiCr etch mask is applied by sputtering and then acts as to increase selectivity for the reactive ion etching (RIE) of the qz surface. 81

Figure 2-5 – Illustration of the material yield strength, and the equivalent conversion to applied pressure at a given temperature. Trend is used to identify the necessary NIL pressure to transfer a pattern and reflow the FEP film. DuPont aggregate data for commercial FEP films. [137]. 83

Figure 2-6- Process flow for the manufacture of patterned fluoropolymer stamps. A.) qz master stamp is applied to a preheated FEP film attached to a glass backing plate. B.) Stack of quartz, FEP and glass is then held under pressure and elevated temperature. C.) After cooling the master is delaminated, and leaves behind a replica FEP stamp. Thermal expansion differences between FEP, glass, qz/Si master are not observed to damage the replica pattern quality..... 84

Figure 2-7- Process flow showing the use of modular stamps for UVNIL applications. A.) patterned FEP film placed onto a photoresist spun on a substrate with acetate photomask applied above to define the dimensions of the pattern. B.) Photolithography is carried out. C.) Stack is separated and photoresist developed producing defined micro- or nanoscale features. 85

Figure 2-8- Diagram of 3D tube moulding rig, manufactured from stainless steel. A central guide pin is wrapped in FEP patterned film, with wall of main chamber lined with alternate patterned film, a polymer melt is then introduced, and chamber is held at pressure. Central rod is optional (green) and can be removed all together to pattern cylinders externally. 87

Figure 2-9 – Contact angles of materials used (PLLA, SU8), and those of the available stamp materials (silicon, PDMS, glass, FEP). The contact angle of FEP is significantly higher than the alternatives being considered. Error bars: 1SD over n=5 measurements. 88

Figure 2-10 – (A) FEP film stamp replicating a silicon master during removal from master stamp. Scale bar 5 mm. (B) SEM of 500 nm holes in the FEP film replicated from a silicon pillar surface. (C) SEM of 150 nm holes replicated in FEP film from a silicon master stamp. (D) 500 nm pillars on 500 nm square pitch replicated from pitted silicon master stamp. Scale bars = 5 mm, 3 μ m, 2 μ m and 5 μ m for A, B, C, D respectively. 89

Figure 2-11 - Figure 1.4. AFM microscopy of FEP stamps post embossing by a quartz master stamp. (A) The quartz master with low aspect ratio pits. (B) FEP replica low aspect pillars (C) FEP replica 200 nm high aspect ratio pillars. Scale bars = 2 μ m, 2 μ m and 1 μ m respectively. 90

Figure 2-12 - Profile scan of those patterns seen in Figure 10 (centre). A: Average pillar height formed in FEP replica is 420 nm close to the original 450 nm depth of features in the Quartz master stamp. B: profile scan across master stamp (n=5). 90

Figure 2-13 – (A) Original silicon grating master stamp and FEP replica stamp produced by embossing at 275 °C. (B) Demonstrated ease of multiple stamp manufacture in FEP within a short periods of time frame. (C) Graph of contact angle measurements of flat FEP film originally (Series 1), and after nanopatterning of 500 nm gratings at Orientation 1 (Series 2 - parallel to plane of view) Orientation 2 (Series 3 - perpendicular to view plane). Error bars 1SD (n=5). Scale bars = 10 mm. 91

Figure 2-14 - AFM scans of FEP replica stamps of a 500 nm grating, produced in a varied series of imprint temperatures. Left to right (A) 205°C, (B) 240°C, (C) 280°C respectively, imprint temperature maintained for a 3 minutes duration at 10 bar. Some stretching is seen causing wavy lines to form. Scale bars = 4 μ m, 4 μ m and 5 μ m respectively. 91

Figure 2-15 - AFM scans of FEP replica stamps of a 500 nm grating, showing improving feature height replication as melting point of FEP is reached. Left: 240 °C, Right: 280 °C respectively, imprint temperature maintained for a 3 minutes duration at 10 bar. (n=3). 92

Figure 2-16 - Imprint feature height after imprinting a 500 nm pitch and width grating for 3 minutes at 10 bar imprint pressure at different temperatures. Flow of FEP drastically improves above its melt temperature. Error bars are 1SD (n=6). 92

Figure 2-17 – Measured spin thickness of 84,000 Da PMMA dissolved to 8 v/v % dilution in o-xylene after a 1 minute spin duration. Error bars are 1SD (n=3). 93

Figure 2-18 - Ash rates of spun PMMA film A in oxygen plasma with varying RF power, and AFM of imprinted PMMA film post 2 min ash. 84,000 Da PMMA dissolved to 8 v/v % dilution in o-xylene.

Measurements were taken by Dektak profilometer at the end of each ash cycle. Error bars are 1SD (n=3)..... 94

Figure 2-19 – (A) AFM scan of PMMA imprinted by FEP stamp prior to metal sputtering. AFM scan of a Ti stamp produced by sputtering, an attempted inversion of the original master, which was a silicon (Si) pillar array of 500 nm diameter pits on a 500 nm square pitch. (B) Magnified scan of same stamp. (C) A macro photo of the resulting pattern on silicon, like with many imprint processes, areas of pattern damage can be seen where the stamp failed to fully imprint the PMMA lift-off layer. (D) The FEP replica stamp produced from the original Si master. Scale bars: A) 2 μm , B) 3 μm , C) 5 mm and D) 3 μm respectively. 94

Figure 2-20 – Example SEMs of hierarchical patterning in FEP films by novel combinational replica moulding. Initial micro pattern A can be combined with either B or D to produce C or E respectively. Scale bars are 30 μm , 5 μm and 10 μm respectively. Reproduced from Greer and Vasiev et al. [188]. 95

Figure 2-21 – A.) SEM images of hierarchical patterns showing 20 μm hexagonal islands with 500 nm pillars. B.) A magnified SEM image showing the hexagonal structure of the islands. C.) The nanopattern which was applied during the second emboss step. D.) The micropatterned hexagonal islands before the application of the secondary nanopattern. Scale bars: 5 μm , 10 μm , 20 μm and 30 μm respectively..... 96

Figure 2-22- A) Hierarchical fluoropolymer stamp structure under AFM, in a 50 x 50 μm scan. B)magnified 5 x 5 μm scan. C) AFM of hexagonal islands with 2.7 μm height and a 400 nm grating pattern on top surface. Selection of different micro and nanopattern configurations allows for a mix and match approach to potentially cell confining patterns with selected topographical interaction. D) Section profile across topography with hierarchical grating. Scale bars: A) 20 μm , B) 2 μm , and C) 20 μm respectively..... 97

Figure 2-23 –SEM images of FEP hierarchical structures showing a combined hexagonal microstructure (A,B,D) with a 500 nm grating surface nanopatterns (C), produced by sequential embossing of the FEP layer. Illustrating the flexibility of the process and the customization of possible patterns. Scale bars: A) 10 μm , B) 20 μm , C) 5 μm and D) 50 μm 98

Figure 2-25 –SEM images of SU8 Imprinted with a FEP hierarchical stamp. Imprinting done with combinational method through 1 cm square aperture above the FEP film. Scale bars: A) 50 μm , B) 10 μm , C) 10 μm and D) 50 μm 99

Figure 2-24 - Feature heights of hierarchical patterns showing an aggregate from 8 measurements. Error bars = 1SD (n=8 samples)..... 99

Figure 2-26 – A) Optical image of a half cylinder cut from a PCL rod which had its circumference imprinted by a flexible FEP stamp at 80°C. B) AFM scan of imprinted cylinder surface showing the nanopits formed on the cylinder surface. C) Optical CMM image of cylinder surface, showing the 200 μm gaps in the nanopatterned array on the cylinder surface. D) AFM of the FEP replica stamp used, same as that used for evaporation of Ti mastering process. Scale bars: A) 2 mm, B) 5 μm, C) 1 mm, D) 4 μm. 100

Figure 2-27 - SEM image of A) micro star shapes and B) spirals produced by the combinational mastering approach utilizing FEP replica stamps and printed acetate photomasks. Scale bars: 1 mm. 101

Figure 2-28 - A) Image of 'lotus' micro containers produced by combinational mastering and printing in SU8. B) Image of the FEP replica stamp used in the processing, attached to a glass backing slide just after manufacture. C) AFM scan of the FEP film surface showing 250 nm pits on a 1 μm square pitch. D) Demonstrating the flexibility of imprinted FEP stamps when removed from the glass backing plate. Scale bars: 2 mm, 5 mm, 5 μm and 5 mm respectively..... 102

Figure 2-29- AFM scans of polycarbonate injection moulded topographies reproduced as negative replicas in PDMS by casting. A) PDMS replica produced from non-ashed original NSQ surface with resulting lower feature fill. B) PDMS replica with good fill from an ashed original NSQ surface with much better feature replication. C) PDMS replica produced from ashed SQ surface showing good feature fil, showing orange profile trace. D) The profile trace of PDMS replica of SQ surface. Scale bars: 2 μm. 103

Figure 2-30 - Top: feature fill diagram for the original master depth and the expected fill profile of the PDMS replica features. Bottom: Feature height of PDMS replicas taken from injection moulded polycarbonate (PC) masters. Error bars: 1SD from 5 measurements..... 104

Figure 2-31 – Film thickness for a range of spin speeds for different molecular weights and concentrations of commercial PAA. Average values from 3 profile scans. 105

Figure 2-32 - Fabrication process for creation of nanopatterned and micropatterned PEGDMA hydrogel films by PAA sacrificial layer embossing. A) PAA is spun onto Si wafer. B) PAA film is embossed using the master stamp. C) Hydrogel is applied to PAA surface. D) Master stamp or mask is applied and assembly is exposed to UV and developed in IPA. E) Wafer placed in RO water allowing for dissolution of PAA layer and subsequent lift-off of hydrogel patterned film [1]..... 106

Figure 2-33 – Hydrogel bilayer fabrication and actuation by pH modulation. Gel sheets patterned by photolithography leading to shape and active carboxyl group transfer to the gel film from below and patterning from the stamp above. This patterned film then undergoes a deprotonation of the –COOH terminus of its pendant carboxyl groups in elevated pH (pH>pKa). Subsequently rolled sheet

can be unrolled if pH is lowered past the pKa value again, this process is notable slower. Reproduced from Vasiev et al. [1]..... 107

Figure 2-34 – SEM imaging of Embossed PAA. 2µm wide and 500nm tall pillars and B: 200nm wide and 250nm deep holes with 200nm square pitch. Both produced from FEP imprinting of PAA at 90°C and 15bar. Scale bars: 5µm..... 107

Figure 2-35 – A) AFM scan of PAA surface with HEX pit array. B) A section showing the profile of 500 nm pits on a 1 µm HEX pitch 500 nm deep reproduced in PAA by embossing with a Quartz (Qz) master. Scale bar 4 µm. 108

Figure 2-36 – A) AFM scan of hydrogel nanopatterned film reproduced from an embossed PAA surface with 300 nm wide pillar distribution on a 300 nm pitch. B) Fourier plot showing feature size and frequency with the main peak in the sub µm range. C) Section profile of pillars showing 300 nm feature height. Scale bar: 4 µm..... 108

Figure 2-37 A) Rolled micropatterned PEGDMA hydrogel film after exposure to pH 7 buffer and air drying, scale bar: 500 µm. B) Unrolled micropatterned PEGDMA hydrogel film after unrolling in pH 4 buffer and air drying, scale bar: 200 µm. C) bottom surface of roll showing 1 µm pits replica from the nanopatterned PAA sacrificial under-layer, scale bar: 50 µm D) Top surface micropattern created as replica of top PDMS stamp. Scale bar: 50 µm. Reproduced from Vasiev et al. [1]..... 109

Figure 2-38 - A, B: SEM image of 250 nm wide and 270 nm tall pillars remaining on PEGDMA film after pattern transfer from PAA sacrificial layer, scale bar: 1µm and 4µm. C: PEGDMA film nanopatterned edge, scale bar: 10 µm. D: Cross-section view of rolled PEGDMA scaffold, scale bar: 200 µm. Reproduced from Vasiev et al. [1]. 110

Figure 2-39 - AFM trace of PEGDMA roll topography. A periodic pattern 250 nm high was recorded, the features also show reasonably square shoulders, suggesting the hydrophilic PAA layer has excellent filling properties, drawing the resist well into the right angled corner of the pit..... 110

Figure 2-40- A) Hydrogel hierarchical pattern of 400 µm long 80 µm tall spacers made with PDMS mould. B) Two level topography for manufacture of PDMS moulds. 10 µm circular pattern with 30x20µm hexagonal pillars 100 µm tall above. 111

Figure 2-41 - Spacer on hydrogel film when the film is rolled up. Rolls actuated by DMEM cell media (buffered), the process discussed in Chapter 5. Scale bars 100 µm and 250 µm..... 112

Figure 2-42- (A, B) Patterning of hydrogel rolls with high aspect spacer features. (C, D) Rolls patterned with 500 nm lines of 500 nm depth and 500 nm pitch. The spacer pillars measure 400 µm long 50 µm wide and 80 µm tall. Scale bars: 300 µm, 500 µm, 200 µm and 500 µm respectively. 112

Figure 2-43 - Dragging of nanopillars through FEP during imprinting, wither by stamp rotation or early peeling from the master, can result in the ditches created here. Scale bar: 4 µm. 114

Figure 2-44 – An SEM image of the 'flowers' formed by PMMA climbing up the hydrophobic FEP pillars during imprinting at 180 °C. The thickness of the PMMA layer being less than the height of the FEP can cause this problem. Scale bar: 10 μm..... 115

Figure 2-45- An AFM scan of the 'flower' surface illustrates the PMM bridging between individual FEP pillars. This is particularly noticeable when the PMMA film is roughly half the thickness or less than the height of the FEP features. Scale bar: 20 μm. 115

Figure 2-46 – A) 3D plot of Image of 'flower' morphology resulting from low viscosity of molten PMMA imprint layer, and a hydrophobic FEP stamp. B) The features are roughly twice as high as the spun film of PMMA, causing it to fill up the voids in the stamp by wicking up the stamp pillar features. C) A thin residual layer in the PMMA is still visible at the base of the features. 116

Figure 2-47 – SEM image of PMMA imprinted with a FEP pillar stamp, produced by spinning a thicker PMMA layer roughly 90 % of the height of the FEP features (500 nm). Non-uniformity can still be seen in the imprinted surface due to gas traps and the PMMA climbing up the FEP features. Marker bar: 20 μm..... 117

Figure 2-48 –A) SEM images of damage caused to master stamp and FEP film due to catching o the replica on the high aspect ratio (4:1 aspect 250 nm wide) pillars. The high aspect prevented the successful peeling of the FEP replica stamp. B) Peeling caused permanent damage by breaking the pillars free from the substrate on the master. Scale bars: 4 μm and 1 μm respectively. 118

Figure 3-1 – Optical microscopy images of demonstrated lift-off of photopatterned components from a PAA sacrificial layer. One edge submerged in water causing gradual washing away of the water-soluble polymer. A) Hydrogel features on PAA being approached by a wetting front (B-C). Scale bars: 200 μm 123

Figure 3-2 - NiCr photomasks on glass slides, scale bar 10 mm. 124

Figure 3-3 - Mask alignment process. A) MA6 mask aligner during lithography. B) Process of 'alignment' where features are positioned using microscope and x-y stage. C) Process of photolithography, and D) photolithography with lift-off process. 124

Figure 3-4 – A) Illustration of a parallel plate rheometer setup, the application of load and rotation rate used by the rheometer when the gel specimen is in a petri dish. B) The correction necessary to remove the thickness of the petri dish from the shear modulus calculation and obtain the true modulus of the material being tested. 131

Figure 3-5 – A) Gel tensile specimen after rupture, B) The standard ASTM D412 type A sample schematic. C) The expected relationship from a perfectly linear sample as a force-displacement or stress-strain plot. It should be noted that with hydrogels a perfectly elastic response is highly unlikely given the multi-phase porous structure. 133

Figure 3-6- Absorption with concentration at various absorption peaks for LTPO photoinitiator. Distances in mm are the working distance of the UV-Vis spectrophotometer. Outside of the 380 nm peak for LTPO, curves show molar absorption coefficient decreases nonlinearly with concentration at the other prominent absorption peaks. 135

Figure 3-7 - Swelling ratios of PEGDMA based hydrogels with exposure dose and monomer concentration. Values measured by weighing swollen samples incubated for 24 hours in RO H₂O for 24 hours after synthesis, and after dehydration by drying in a 120 °C oven, followed by placing in a 100 mTorr vacuum for 12 hours. 136

Figure 3-8 - Mesh size correlation to monomer volume fraction for PEGDMA hydrogels synthesized in EtOH solvent. 137

Figure 3-9- Adapted values for Stokes radii and baseline diffusion coefficients (D_0) at tissue culture temperatures for dissolved species in water at in vitro temperature (37 °C, $\nu=0.682$) [199, 200] . 138

Figure 3-10 - Diffusion correlation to hydrogel mesh size for PEGDMA gels synthesized at various exposure doses and monomer concentrations as illustrated in Figure 3-7. 138

Figure 3-11 - Swelling ratio with recipe for NIPAAm based gels, Correlation of levels at each swelling ratio used to interpret effect on gel network. Error bars: 1SD from 2 measurements..... 140

Figure 3-12 - Taguchi plot of mean value and associated variance for up and down regulation of certain synthesis parameters. (Red): variable at low level 1, (Blue) variable at high level 2. Error bars: 1SD from n=4 values. 141

Figure 3-13 – Conversion ratio with exposure dose of MBAAm crosslinked PNIPAAm gels with LTPO as initiator, cast weight prior to development against fully swollen state, shows correlation between overexposure and loss of swelling potential as gel network is so rigid it barely accommodates any liquid other than that replacing unreacted monomer and solvent used in synthesis (n=1). 142

Figure 3-14- Swelling ratio of MBAAm crosslinked PNIPAAm gels compared with PNIPAAm-co-PEGDMA gels (n=1). 142

Figure 3-15 – PNIPAAm gel actuation ratios (weight fraction of water displaced above the hydrogel LCST) of the two thermo-responsive PNIPAAm hydrogel recipes (n=1)..... 143

Figure 3-16- N,N-Diethylaminoethyl methacrylate (DEAEMA) cationic gel swelling as it varies with exposure dose (n=1). 144

Figure 3-17 - Transition in Cationic gel homogeneity. Left to right: doses of exposure varying from A) 15 seconds, B) 30 seconds, C) 45 seconds, D) 60 seconds and E) 75 seconds at 7.2 mW/cm², scale bar 10 mm. 144

Figure 3-18 - The swelling ratios of DEAEMA and 1-butanol solvent gel, as a result of changes in exposure dose under the MA6 mask aligner. Error bars 1 SD from (n=3) measurements..... 145

Figure 3-19 - Torque sweep of PEGDMA (90 % monomer concentration in EtOH with added 0.01 % TEA synergist) hydrogel thin film at angular frequency 10 rad/s. Storage and loss moduli corrected for the extra thickness of the sample holding plate. (T = 21 °C)..... 145

Figure 3-20 - Effect of drying as seen in the storage and loss moduli of the same gel sample- PEGDMA (90 % monomer concentration in EtOH) at 108 mJ/cm² exposure. (T = 21 °C) 146

Figure 3-21 - Averaged storage and loss moduli of polymerized 90 v/v % PEGDMA films, a drop off in storage modulus is seen with reducing exposure dose, with an inverse relationship seen for the loss modulus (T = 21 °C, 1-100 rad/s). This was a short investigation, with repeat experiments were not conducted due to time constraints and limited access. 146

Figure 3-22 - Comparison of PEGDMA 90 v/v % with (red) and without 0.01 v/v % TEA (blue) polymerization chain transfer agent..... 147

Figure 3-23 - Changes in PNIPAAm based gel storage and loss moduli during a temperature sweep. As the gel passes the LCST an increase in Loss modulus is visible due to the expulsion of fluid from the gel network. Values are corrected for the sample holder thickness. Only one sample was tested due to time constraints..... 148

Figure 3-24- Complex viscosity dropping as a result of temperature sweep through PNIPAAm hydrogel LCST..... 148

Figure 3-25 - Increase in damping factor of the NIPAAm hydrogel as it passes the LCST at 32 °C..... 149

Figure 3-26 - A distinct difference can be seen between a hydrated cool NIPAAm gel sheet and one which has equilibrated at a point above the LCST. Above the LCST water is absent from the matrix, resulting in a higher modulus in the 40 °C gel. 149

Figure 3-27 - Contact angle image capture at A) 22 °C, and B) 40 °C PNIPAAm films. 150

Figure 3-28- Effect of monomer concentration on two samples of PEGDMA gel under tensile load. A lower gradient for the 50 % monomer concentration gel, shows a lower elastic modulus with a reduction in monomer concentration, possibly due to the reduced density of the gel network, longer distances between crosslinks and higher fluid portion resulting in less resistance to elastic deformation. 151

Figure 3-29 - The addition of TEA as an oxygen scavenger and copolymer even at very low concentration shows an increased elasticity of the gel (blue), with samples contracting rather than breaking and eventually sliding out from the tensometer grips, while the sample numbers are low it is assumed to give an indication of the modifications oxygen scavengers give to the gel structure, with a potentially more mature network with fewer oxygen terminated connections..... 151

Figure 3-30- Effect of TEA polymerization chain transfer agent on low monomer content gels shows a somewhat different characteristic of the oxygen scavenger. In these very soft gels the addition

appears to increase the modulus, again this is suggested to be due to a more mature network structure, with fewer oxygen terminated connections. Signal noise due to load cell sensitivity. 152

Figure 3-31 – Figure shows the effect of UV exposure dose on PEGDMA hydrogel Young's modulus, with an increase directly correlated to exposure dose. All samples were dried prior to testing to facilitate the ability to be gripped in the crosshead. 152

Figure 3-32- Figure shows the effect of exposure dose on Yield stress and elongation at failure of 90 v/v % PEGDMA hydrogels. There is a large shift from the softer weaker gels to a strong but brittle state, and a middle dose at which the network appears to have the most beneficial properties of both..... 153

Figure 3-33- FTIR spectrum of cationic gel containing N,N-diethylaminoethylmethacrylate (DEAEMA). 154

Figure 3-34- FTIR Transmittance spectrum of PNIPAAm co MBAA hydrogel when dry. 154

Figure 3-35 - FTIR Transmittance spectrum of n-isopropylacrylamide (NIPAAm) co PEGDMA hydrogel 155

Figure 3-36- FTIR absorbance spectrum of PAA modified and unmodified films. Blue- Unmodified, with the Light Blue-PAA Mw 1800, Purple PAA Mw 50,000, Red PAA Mw 100,000 all coinciding in the elevated trace. 156

Figure 3-37- FTIR spectrum of PEGDMA hydrogels (blue) with addition of 0.25 w/w % TEA (yellow) and 1 w/v % TEA (red)..... 157

Figure 3-38 - Polymerization extent with exposure dose A) W shift in C=O peak in methacrylated PEG polymer (red = 6 s, purple = 8 s, blue = 40 s, green = 80 s). B) The shift in peak is thought to occur due to increasing crosslink density changing local conditions and thus harmonics of the pendant group by the proximity of local chains. 157

Figure 3-39 - PEGDMA 550 hydrogel film roll radius of curvature after scaffold lift-off from PAA 50,000 Da spun at 4000 rpm for 30 s and buffered at pH 7 at different UV exposure doses. Error bars = 1SD from n=5 measurements of minimum curvature radius in the centre of SEM cross-section of gel rolls. Reproduced from Vasiev et al. [1]. 158

Figure 3-40 – Effect of bilayer thickness ratio (active/passive) as well as active gel actuation ratio on relative curvature. Young's modulus and base swelling kept constant (8 kPa, 0.3 ε respectively), only actuator thickness and actuation strain varied, resulting in most efficient curvature achieved at thickness ratio of 0.125-1, peak at 0.375..... 159

Figure 3-41 - Effect of bilayer actuation strain differential (dstrain) on the curvature (K) and modulus relationship for an idealized gel bilayer at constant thickness ratio (m=8)..... 160

Figure 3-42 - Effect of bilayer thickness (microns) on curvature $K=1/R$ (μm) for bilayers of varying Young's modulus E. 160

Figure 3-43 - SEM image of hydrogel film roll after actuation in pH7 buffer and drying at room temperature..... 161

Figure 4-1 – A) Obducat nano-imprint lithography (NIL) tool, and B) the imprinting routine for PAA patterning. Colour spectrum line shows heating cycle, blue line illustrates the variation of pressure through the imprinting cycle. 168

Figure 4-2 - Illustration of ionic hydrogel bilayer swelling in elevated pH, resulting in film rolling by an uneven swelling differential between top and bottom surfaces. Reproduced from Vasiev et al. [1].
..... 170

Figure 4-3 - Illustration of hydrogel anchoring to methacrylate groups of TPM coated surface. Attachment works for acrylic monomers and polymers, and can be used to semi-permanently bond the hydrogel photopatterns or structures to a glass slide or silicon wafer. 171

Figure 4-4 - PEGDMA plot of thickness against spin speed for 90 % PEGDMA in EtOH resist. Spin durations: 10s. Layers were exposed in proximity mode with 25 μm Teflon spacer between mask and gel surface. Thickness measured by profilometry on developed gels after development in IPA, while the gels were still adhered to the glass surface. Error bars: 1SD from 3 measurements. 172

Figure 4-5 - Gel thickness and radius of curvature for PEGDMA hydrogel films with grafted PAA from the lift off layer. Thickness was measured by profilometry immediately after development of hydrogel squares. Radius of curvature was measured from minimum cross-sectional diameter in optical microscopy images. Two exposure doses of 8s and 6s at 7.2mW/cm². Gel thickness modified by spin speed. Error bars: 1SD from 3 measurements of each representative sample. 173

Figure 4-6- Possible uses of hydrogels as hinges in folding solid structure. Solid material is indicated in this case as the photo-crosslinkable epoxy SU8. Version 1) a thermally constricting gel based on PEGDMA-Co-PNIPAAm with a PAA activated base. 2) A similar design but with elongated thermal 'pulling' actuator to give it more actuating leverage. 3) PEGDMA hinge with PAA activated base, and 4) Double hinge design where two layers of gel are separated by a rigid block. 174

Figure 4-7 - Radial plot of various container designs, shows the effect of falling versatility and complexity with rising robustness, or the susceptibility of a structure to fail when in use. 174

Figure 4-8 - Various container designs, left to right: 'Lotus' multi-symmetry containers, 'Dodecahedron' type containers and finally hydrogel rolls, showing square windows for cell movement and oxygen permeability. Scale bars: 500 μm 175

Figure 4-9 - Triangular polyhedron mask design stack. (A) The SU8 solid elements comprising the faces of the finished structure, which are non-flexible. (B) A potential all over coating with hydrogel

for improved SU8/ hydrogel interface and bonding strength. (C) The lighter hydrogel hinge alternative..... 176

Figure 4-10 Hinge dimensions - triangular polyhedral container. Plots indicate the expected hinge angle of hydrogel hinges given a set hinge size and radius of curvature (Chapter 3). 360 degree arc angle indicates full rolling (tube). 177

Figure 4-11 - Hinge dimensions - box polyhedral container. Plots indicate the expected hinge angle of hydrogel hinges given a set hinge size and radius of curvature (Chapter 3). 360 degree arc angle indicates full rolling (tube). 179

Figure 4-12 - Mask design of a single pentagonal polyhedron container. The container involves two stages, the creation of rigid elements with the first mask (left) and the addition of slightly overlapping hinges (right) for better adhesion. This is fabricated on asacrificial PAA film for lift-off. 180

Figure 4-13 - Ideal hinge dimensions for pentagonal polyhedron. Plots indicate the expected hinge angle of hydrogel hinges given a set hinge size and radius of curvature (Chapter 3). 360 degree arc angle indicates full rolling (tube). 181

Figure 4-14 - Pentagonal polyhedrons in their two stages with the design incorporating three hinge thicknesses of (left to right) 20 μm , 40 μm and 60 μm respectively. Several box dimensions were also designed, ranging from 200 μm faces up to 600 μm to cover possible future applications. 182

Figure 4-15 - Left to right: two smaller container sizes with two hinge widths of 20 and 40 μm . Far right: largest container with hinge dimension of 80 μm 182

Figure 4-16 - New 'lotus' containers with varying hinge numbers, both have six folding surfaces but one consists of the decagonal arrangement with 5 hinges per extremity while on the right is an octagonal arrangement with four hinges per extremity. The decagonal arrangement benefits from lower required hinge angles, while the octagonal structure benefits from fewer hinges and thus fewer things to fail should an alignment or exposure deviate from that required..... 183

Figure 4-17 - Comparing leaf dimensions over length from tip to median for different numbers of petals on 'lotus' form..... 185

Figure 4-18 - Comparing leaf dimensions over length from tip to median for different numbers of petals on 'lotus' form..... 185

Figure 4-19 Mask split to create negative and positive polarity hydrogel elements. (A) The full array of locking points to be patterned in magnetic resist or self-adhesive hydrogel. (B) Half of an negative to positive locking mechanism, with half the array to be made of an ionic hydrogel and the other half of a cationic one respectively. 186

Figure 4-20 - Photomask design for new 'lotus' containers. (A) faces of container to be patterned in SU8 or other 'structural' material. (B) Hydrogel hinges to be patterned during a second stage of photolithography. (C) The locking mechanism to be patterned out of another layer of structural material, or a self-adhesive hydrogel. 186

Figure 4-21 – Surface roughness plotted for increasing doses of oxygen plasma ashing of the PAA sacrificial films. It can be seen that the surface roughness increases at a non-linear rate with increasing exposure to O₂ plasma. AFM profilometry performed on three random locations on ashed samples. PAA Mw 1800 spun at 4000 rpm. Error bars: 1SD from n=5 AFM measurements of n=5 separate 20 x 20 μm square areas..... 187

Figure 4-22 - Surface roughness Ra plotted against spin speed for PAA Mw 1800 spun at increasing RPM. It can be seen that the roughness of the surface does not vary greatly with increasing spin speed. Error bars: 1SD from n=5 measurements of 20 x 20 μm AFM scans. 187

Figure 4-23 - Surface roughness of four different molecular weights of PAA. All surfaces dried on a hotplate at 90 °C for 5 minutes prior to measurement by AFM. It can be seen that while the roughness is fairly consistent between different molecular weights, it does increase dramatically when the PAA is in its neutralised state (buffered with NaOH). Error bars: 1SD of n=5 measurements of 20 x 20 μm square AFM scan..... 188

Figure 4-24 - Spin curves for SU8, PLLA 7 % w/v in CHCl₃ and PCL 8 % w/v in CHCl₃ films measured by profilometry. Error bars 1SD from 5 measurements..... 189

Figure 4-25 – Mean values for film uniformity in spun polymer films, Roughness Ra value collected from 20 x 20 μm AFM surface topography scans. Error bars: 1SD from n=5 measurements. 189

Figure 4-26 - Spun polymer films considered as an alternative to traditional SU8 photoresist. A: PLLA spun at 6000 rpm, B: PLLA spun at 2000 rpm (both solutions 8 w/v % solution in chloroform). C: PCL spun at 4000 rpm D: PCL spun at 2000 rpm (both solutions 6 w/v % in chloroform) 190

Figure 4-27 – Top left to right: 24 μm hexagonal pattern embossed into SU8 Dodecahedral container surface with a pre-embossed PAA layer creating double sided patterning. Bottom left to right: Devices with and without hinges after PAA dissolution. Scale bars: 100 μm, 50 μm. 200 μm and 300 μm respectively..... 191

Figure 4-28 – SEM images of nanopatterned PLLA film with 2500nm diameter 1:1 aspect pits on 200 nm pitch. Left to right decreasing magnification. Scale bars 500 nm and 5 μm respectively. 192

Figure 4-29 - Shown are the dry etch rates for PLLA and PAA thin films. The data shows a dry etching selectivity ratio in oxygen plasma of almost 2:1 between PLLA and PAA Mw 50,000. Point mean of n=3 profile scans. 192

Figure 4-30 - Dual exposure patterning method. The hydrogel film is exposed once to take it to the initial gelling state, it is then sequentially exposed to light through a different mask to further crosslink some sections, but leave others under-exposed. This heterogeneous exposure produces differential swelling effects across the film causing it to fold. 194

Figure 4-31 - A, Double exposure pentagonal polyhedrons prior to lift-off. B, Post lift-off but without second exposure the films roll up in a unrestricted way. Note that the second exposure was not effective at creating solid sections, as the active components Scale bars: 300 μm 194

Figure 4-32 - SU8 micro containers attempting to close by PAA immobilized SU8 epoxy at the hinges. Scale bars: 500 μm 195

Figure 4-33 - The over-exposure method for producing self-folding hydrogel containers. The exposure undercuts the mask by way of diffusion, and produces a crosslinking gradient underneath the mask feature. If correctly spaced, these under-exposed undercuts meet to produce a hinge which folds by differentia swelling. 195

Figure 4-35 – Over-folded boxes made by overexposure method for the 20 μm length hinges, faces exposed for (A) 43.2 mJ/cm^2 and (B) 57.6 mJ/cm^2 . And 40 μm length hinges exposed to: (C) 72 mJ/cm^2 and (D) 86.4 mJ/cm^2 . This folding results due to underexposure of the PEGDMA hydrogel in the container faces, making the whole structure flexible and unable to hold the shape properly. In instances where the structure is solid enough, the hinges are too rigid to attain the necessary folding angle. Scale bars: 500 μm 196

Figure 4-36 - SU8 micro-container layer before (left) and after wet etching with NMP (right) to remove the inter-facial film that had been affecting the performance of the subsequent hydrogel hinges. Excessive cracking can be seen after overdevelopment in NMP. Scale bars: 300 μm 197

Figure 4-37 - SU8 and Hydrogel hybrid containers affected by a thick boundary film, stress marks are visible after dissolution of PAA. Scale bars: 300 μm 197

Figure 4-38 - SU8 showing the effects of overdevelopment after 6 minutes in EC solvent. Scale bar: 300 μm 198

Figure 4-39 - PAA oxygen plasma dry etch depth with time, process was very time consuming with practical etch depths in the region of a micron taking approximately 15 minutes. . Depths measured by profilometry. Error bars: 1SD (n=3). 199

Figure 4-40 - Release of structures from PAA which were manufactured by this rapid processing Scale bars: 400 μm 200

Figure 4-41 - Containers made by the reverse process. A) The hinge integration into the SU8 face, and B) the closed containers in pH 7 solution. Scale bars: 50 μm and 300 μm respectively. 200

Figure 4-42 - SU8 structures patterned onto a 1 μm thick PMMA layer. The PMMA is undercut by EC solvent development, creating voids at the patterned edges, thinner layers do not suffer from the same issues, and 80 nm films spun from o-xylene proved to be a suitable candidate for this method of fabrication. Scale bar: 300 μm 201

Figure 4-43- Gold etch with time A) 10, B) 30 and C) 60 seconds with 30 nm gold barrier film a slight undercut below the SU8 features is visible. Ratio of potassium iodide to iodine is 2:1 with 4 g and 2 g in every 80 μl of MeOH:IPA 1:1 mix. Scale bars: 300 μm 201

Figure 4-44 - Containers made by the gold boundary layer process. A) etch attempt prior to cleaning with O_2 plasma. B) etch with pre-clean. C) Hinges applied. Scale bars: 500 μm 202

Figure 4-45 - Containers made by the gold boundary layer process. A,B,D) closed containers, C) container in the process of folding. Scale bars: 500 μm 203

Figure 4-46 - Lotus container made with the gold boundary layer method. (A) SU8 features of the lotus are created on a gold coated PAA surface. (B) The gold is etched in areas where it is not covered with SU8 features, exposing the PAA surface underneath, in preparation for hinge addition. Scale bars: a) 200 μm , b) 400 μm and c) 100 μm respectively. 205

Figure 4-47 – PMMA boundary layer formed 'lotus' containers manufactured from SU8 before (left) and after (right) the application of hydrogel hinges. Scale bars = 500 μm 206

Figure 4-48 - A gold covered 'lotus' container undergoing folding in pH 7 buffered solution. The position of the tips relative to the box centroid can be tracked in consecutive images to record container folding dynamics. Showing A) $t=0$, B) $t=4$ minutes C) $t=10$ minutes. Scale bars: all 500 μm 206

Figure 4-49 - Distance between the petal tip and the centroid of 'lotus' containers with time (centroid is axis in z-axis through central hexagonal face on x-y plane, where petals lie in the x-y plane), the transitional folding can be seen as the tip is folded and curled inwards to meet at the centroid of the container mask (the central hexagon to which all the petals attach). Error bars: 1SD from $n=3$ measurements. 207

Figure 4-50 - Swelling kinetics of PEDGDMA hydrogels for various monomer concentrations and exposure doses. , $n=1$ per sample. 207

Figure 4-51 - Interlocking mechanism design as applied to a 'lotus' container. The protrusions are created to overlap and thus reinforce adjoining faces, and limiting over-closure, where one face moves further inward than its neighbours, blocking them in the process. Scale bar: 300 μm 208

Figure 4-52 - Etch rate of PAA in different concentrations of methanol diluted with isopropanol. Methanol was found to dissolve PAA readily, but did so in a more controlled manner when diluted

by an unreactive solvent such as IPA or EtOH. Depths measured by profilometry. Error bars: 1SD from n=5 measurements. 209

Figure 4-53 - Lift-off of S1818 from under PAA to provide an adhesive point to anchor devices. Showing the development of S1818 with etch duration in Ethyl lactate. A) Non-etched surface, B) 45 seconds etch, C) 2 minutes etch. Scale bars: 100 μm 209

Figure 4-54- A) TPM anchoring agent evaporated to slot dissolved through PAA by a S1818 mask coating glass underneath) hydrogel roll patterned above this slot is permanently anchored to the glass surface. Scale bars: 400 μm 210

Figure 4-55 - Contact angles of Si treated with evaporated TPM. Measurements taken at discrete time points during coating in a sealed and inert container filled with N_2 heated to 150 $^\circ\text{C}$. . Error bars: 1SD from n=5 measurements. 210

Figure 5-1 - A nanopillar gradient, where pillars increase in height along one axis of the 1cmx1cm pattern area. As a result of this topographical gradient cells selectively adhere to certain areas. This topographical preference was used to distinguish different cell types that would otherwise be difficult to identify. Images were analysed with cell profiler which output cell concentration, increases in a certain fluorescence probe over a region of pattern and overall cell number on particular areas of the gradient. Reproduced from Reynolds et al. [211]. 214

Figure 5-2- Process tree for immobilizing injection moulded inserts in PEGDMA gel to limit wasted volume and create a cell repellent surface on periphery of injection moulded slides. Refer to Chapter 2 for gel formulations. 220

Figure 5-3 - PEGDMA fixated nanopatterned insert after 24 hours soaking in PBS, gel ends at edges of upper nanopatterned surface. 220

Figure 5-4 - Structure of hydrogel sheet with added dissolved collagen at three concentrations. Acetic acid solution contains 0.1 M acetic acid and collagen added to stated concentration. Gel mixtures had to be kept cool prior to photolithography to limit clumping and polymerization of collagen mixture. 222

Figure 5-5 – UHAR Pillars and insert arrangement produced by injection moulding in polystyrene (PS) using the technique of Stormonth-Darling et al. [185]. 225

Figure 5-6- Different components responsible for overall deflection of anchored pillars. Reproduced from Schoen et al. [215] 227

Figure 5-7 - Tilt correction factor with respect to substrate Poisson’s ratio. Tilt significantly reduced in rubbery materials (where ν tends to 0.5). 228

Figure 5-8 - Cell profiler pipeline tree for hESCs colony cluster analysis, and cell area coverage analysis. 229

Figure 5-9 - Area coverage output and the threshold mask image after background subtraction and the subsequent edge identification and area segregation to calculate the total area covered by hESC colonies. Field of view is 1800x2200 μm , area coverage worked out as contrast between occupied and empty pixels. 229

Figure 5-10 - Left to right: Original microscopy montage of images spanning the nanopillar gradient (bottom to top, from highest to lowest), Centre: Threshold applied to identify cell clusters, Right: Individual cell colony clusters identified. Scale in pixels, x axis distance 9mm. Scale bar: 1mm 230

Figure 5-11 - Contact angles of injection moulded (IM) nanopatterned polycarbonate substrates covered with Full Square (FSQ), Near-Square (NSQ 50) topographies and planar control. Error bars SD from 15 measurements. 231

Figure 5-12 - Cells stained with DAPI and phalloidin, attached to a collagen modified PEGDMA hydrogel sheet. (A): Cell has fallen into window of hydrogel sheet appearing more compacted, (B) Cell spreading on solid hydrogel section. Cells seeded at 10,000 cells/cm². Boxes are photolithographically defined windows in the hydrogel sheet. Scale bars 100 μm 233

Figure 5-13 - Average hTERT fibroblast count per hydrogel square on 100 square array, with various degrees of collagen modification in the pre-polymer. Fibroblasts seeded at 10,000 cells/cm² and counted manually after 24 hours of incubation in DMEM media. All hydrogel surfaces were soaked for 24 hours in PBS and 12 hours in DMEM prior to seeding of cells. Unmodified PEGDMA gel used as negative control. Only one replicate was run as a pilot study..... 233

Figure 5-14 – hTERT fibroblasts stained with DAPI (green) and phalloidin (teal) attached to (A) SU8 surfaces patterned with NSQ50 patterned nanopits, (B) SU8 simply ashed for 30 seconds at 80W in O₂ plasma, (C) SU8 patterned with FSQ nanopits and (D) SU8 patterned with a randomized series of nanopits. Untreated SU8 without patterns showed very poor cell attachment after 24 hours. Scale bars: 200 μm 234

Figure 5-15 – H2 hESCs seeded as clumps on Matrigel coated FSQ surface. Cells seeded at roughly 20,000 cells/cm² and cultured in Advanced DMEM. Phase contrast microscopy. Scale bars 600 μm 235

Figure 5-16 - H2 hESCs on NSQ patterned inserts. A) Matrigel (standard protocol – 23ml DMEM+1ml Matrigel Aliquot) 24hrs - Adherence of H2 hESCs to planar substrates was visibly reduced, perhaps due to poorer Matrigel[®] coating of the non-patterned surface. In relation to this result vitronectin coating of the polymer inserts showed significantly improved promise and greater cell attachment on all surfaces shown below. B) Vitronectin (0.5 $\mu\text{g}/\text{cm}^2$ – Standard) 24 hrs. C) Standard matrigel coatings 24hrs on three injection moulded topographies 24hrs after seeding at 40,000 cells/cm². D) Standard Vitronectin coatings on an identical set of injection moulded topographies 24hrs after

seeding shows high density layer of cells in all samples. Phase contrast microscopy. Scale bars: 300 μm 236

Figure 5-17 - A1-3: The morphology of single cell seeded H2 hESCs onto a Matrigel coated surface with rock inhibitor. B1-3 Cells seeded in 'clumps' after separation in EDTH onto Matrigel surface and shows distinct lack of cell viability In contrast to vitronectin where coverage was higher on average. C1-3: Show samples covered in vitronectin and seeded with single ROCK inhibited cells. D1-3: Clump seeded cells on vitronectin. Scale bar: 600 μm 237

Figure 5-18 - Phase contrast microscopy of H2 hESCs clustering 24 hours after seeding in clumps on vitronectin coated FSQ, NSQ and Planar injection moulded insert respectively, little change in morphology is visible at 20x magnification. Scale bars: 300 μm 238

Figure 5-19 - H2 hESC gene expression study with cells seeded as single cells from Acutase passage onto vitronectin (VTN) and Matrigel[®] coated nanopatterned inserts with NSQ50, FSQ patterned, with both planar polycarbonate and TCP controls. Cells collected after 72 hours in culture, after seeding at an initial concentration of 40,000 cells/cm². RQ is the relative quantification to Actin ACTB endogenous control, all normalized to H2 undifferentiated TCP control. Error bars: 1SD. 239

Figure 5-20 – H2 hESC gene expression study with cells seeded as clumps from EDTA passage onto vitronectin (VTN) and Matrigel[®] coated nanopatterned inserts with NSQ50, FSQ patterned, with both polycarbonate planar controls and TCP controls. Cells collected after 120 hours in culture, after seeding at an initial concentration of 40,000 cells/cm². RQ is the relative quantification to Actin ACTB endogenous control, all normalized to H2 undifferentiated TCP control. Error bars: 1SD. 240

Figure 5-21 – H2 hESCs 24 hrs after seeding. Cells cultured on TCP controls (polycarbonate) coated at progressively lower concentrations of vitronectin. A) Cells seeded at 40,000 cells/cm². B) Cells seeded at 80,000 cells/cm². Similar behaviour was seen at 0.5 and 1 $\mu\text{g}/\text{cm}^2$ rhVTN concentration. Scale bars: 500 μm 241

Figure 5-22 – H2 hESCs 24hrs after seeding on vitronectin coated NSQ substrates at various seeding densities and rhVTN concentrations. A: NSQ at 40,000 cells/cm². B: NSQ at 80,000 cells/cm². Similar behaviour was seen on FSQ substrates and at 0.5 and 1 $\mu\text{g}/\text{cm}^2$ rhVTN concentrations. Scale bars: 500 μm 241

Figure 5-23 – H2 hESCs on PS TCP controls at 48hrs after seeding: A) Seeding done at 40,000 cells/cm². B) Seeding done at 80,000 cells/cm². Scale bars: 500 μm 242

Figure 5-24 - H2 hESCs on rhVTN coated NSQ injection moulded substrates at 48hrs after seeding at various plating and seeding densities. A) NSQ 40,000 cells/cm². B) NSQ 80,000 cells/cm². Similar behaviour was seen on FSQ substrates in these conditions. Scale bars: 500 μm 242

Figure 5-25 – H2 hESC gene expression study with varying vitronectin concentration and cell seeding density. Cells collected after 96 hours in culture. 1.25, 2.5 and 5 represent plating density in $\mu\text{g}/\text{ml}$. 200 and 400 represent seeding density of 200k and 400k cells/ml. C represents TCP controls and N represents NSQ nanopatterned surfaces. Results are split by expression of Oct-4 and Sox-2 respectively which are common pluripotency markers for hESCs. RQ is the relative quantification to Actin ACTB endogenous control, all normalized to H2 undifferentiated TCP control. Error bars: 1SD.

..... 244

Figure 5-26 – H2 hESC gene expression study combining 3x96 well plates containing triplicates of cDNA from 9 culture wells and endogenous control. Substrates with varying plating concentration of vitronectin and seeding density. Cells collected after 96 hours in culture, after seeding at an initial concentration of 200,000 cells/cm². The results are showing common pluripotency and lineage markers for H2 hESCs RQ is the relative quantification to Actin ACTB endogenous control, normalized to undifferentiated H2 TCP control. Up-regulation of FoxA2 can be seen on all patterned substrates, with a down-regulation of T and MIXL1. The cells had been imaged showing nodular 3D architecture after 84 hours of incubation (a day prior). All cells kept in E8 culture medium. Error bars 1SD..... 245

Figure 5-27 - H2 hESCs 12 hours post seeding on A) NSQ B) TCP controls coated with 0.1 $\mu\text{g}/\text{cm}^2$ rhVTN and C) uncoated TCP. All seeded with 40,000 cells/ cm². Images taken using phase contrast microscopy. Similar correlation was seen in the range of 0.25 and 0.1 $\mu\text{g}/\text{cm}^2$ rhVTN in increments of 0.05. All scale bars: 300 μm 246

Figure 5-28 - H2 hESCs seeded on 0.01 $\mu\text{g}/\text{cm}^2$ rhVTN plated FSQ after 24 hrs 40,000 cells/ cm². Similar results were seen on NSQ substrates at this concentration regardless of cell seeding density. Scale bar: 300 μm 246

Figure 5-29 - Cell area coverage with vitronectin coating concentration. Error bars: 1SD from n=5 measurements 247

Figure 5-30 - Phase contrast imaging at 24 hours after start of random differentiation of H2 hESCs on FSQ at A) 0.02, B) 0.05, C) 0.1 and D) 0.25 $\mu\text{g}/\text{cm}^2$ of vitronectin respectively. NSQ showed a similar trend and 3D morphology. All scale bars: 600 μm 248

Figure 5-31- Phase contrast imaging of induced differentiation of H2 hESCs in small molecules 24 hours post media swap, 72 hours total culture duration. 0.1 $\mu\text{g}/\text{cm}^2$ rhVTN. Cells seeded at 40,000 cells/cm². Similar heterogeneous morphology was seen at concentrations of 0.02 to 0.5 $\mu\text{g}/\text{cm}^2$ rhVTN on both FSQ and NSQ. Scale bar: 600 μm 249

Figure 5-32 - Phase contrast imaging of H2 hESCs in E8 media on TCP coated with 0.5 $\mu\text{g}/\text{cm}^2$ rhVTN at 72 hours total, 24 hours after the differentiation of all sample sets started. Similar 2D flat and

homogenous morphology was seen on 1 $\mu\text{g}/\text{cm}^2$ TCP controls in the same conditions. All cells seeded at 40,000 cells/ cm^2 . Scale bar: 600 μm 249

Figure 5-33 - H2 hESCs in E8 media on: A) FSQ 0.05 $\mu\text{g}/\text{cm}^2$, B:) FSQ 0.1 $\mu\text{g}/\text{cm}^2$, C) FSQ 0.25 $\mu\text{g}/\text{cm}^2$. D) NSQ 0.05 $\mu\text{g}/\text{cm}^2$ E): NSQ 0.1 $\mu\text{g}/\text{cm}^2$, F) NSQ 0.5 $\mu\text{g}/\text{cm}^2$ rhVTN. Cells seeded at 40,000 cells/ cm^2 . All scale bars: 750 μm : 250

Figure 5-34 - Phase contrast imaging of H2 hESCs after differentiation in RPMI+B27 with small molecules, 48hrs after media swap: H2 hESCs in E8 media on: A) FSQ 0.05 $\mu\text{g}/\text{cm}^2$, B:) FSQ 0.1 $\mu\text{g}/\text{cm}^2$, C) FSQ 0.25 $\mu\text{g}/\text{cm}^2$. D) NSQ 0.05 $\mu\text{g}/\text{cm}^2$ E): NSQ 0.1 $\mu\text{g}/\text{cm}^2$, F) NSQ 0.5 $\mu\text{g}/\text{cm}^2$ rhVTN. Cells seeded at 40,000 cells/ cm^2 . All scale bars: 750 μm 250

Figure 5-35 - Phase contrast imaging of H2 hESCs on immersion in SRDMSO media after the small molecules procedure, 24 hours after this second media swap. Samples died due to contamination at 48 hours. A) Small molecules induced differentiation on NSQ with 0.1 $\mu\text{g}/\text{cm}^2$ rhVTN coating. B) Random differentiation on NSQ with 0.1 $\mu\text{g}/\text{cm}^2$ rhVTN coating. Similar results were seen on higher density rhVTN up to 0.25 $\mu\text{g}/\text{cm}^2$. All cells seeded 40,000 cells/ cm^2 . Scale bars: 600 μm 251

Figure 5-36 - Differentiation seen in H2 hESCs on nanopatterned insert substrates after 84 hours in E8 media. The pattern morphology, highly 3d structure and what appears as a changed cell phenotype is reminiscent of the behaviour seen in small molecule induced differentiation. All cells seeded at 40,000 cells/ cm^2 . Scale bars: A) 400 μm B) 300 μm 251

Figure 5-37 – Images taken of H2 hESCs 48 hours after seeding with Rock-, all cells seeded at 25,000 cells/ cm^2 . Right untreated, Left 0.1 $\mu\text{g}/\text{cm}^2$ VTN coating A, B) D100 Short, C, D) D100 Tall, E, F) D150 Short, G, H) D150 Tall. It can be seen that cells attach to the D100 short surface even without coating. All scale bars: 300 μm 252

Figure 5-38 - A-C: D150 Short at 0.05, 0.25 and 0.5 $\mu\text{g}/\text{cm}^2$ rhVTN at 24 hours. D-F: D150 Tall at 0.05, 0.25 and 0.5 $\mu\text{g}/\text{cm}^2$ rhVTN at 24 hours. G-I: D100 Short at 0.05, 0.25 and 0.5 $\mu\text{g}/\text{cm}^2$ rhVTN at 24 hours. J-L: D100 Tall at 0.05, 0.25 and 0.5 $\mu\text{g}/\text{cm}^2$ rhVTN at 24 hours. All scale bars: 300 μm 253

Figure 5-39 – hESC colony area coverage with pillar type and coating density at 24 hours. D100T, D150T, D100S and D150S refer to the Diameter 100 nm tall, 150 nm tall, 100 nm short and 150 nm short respectively. Error bars: SE. 254

Figure 5-40 - Correlation of loading plotted against deflection for the four UHAR pillar geometries as determined from calculations. D100T, D150T, D100S and D150S refer to the Diameter 100 nm tall, 150 nm tall, 100 nm short and 150 nm short respectively. 254

Figure 5-41 - Angle of inclination at pillar tip in relation to the non-deformed axis with varied tip loading compared for the four UHAR pillar geometries as determined from calculations with

decreasing accuracy above 5° pillar deflection. D100T, D150T, D100S and D150S refer to the Diameter 100 nm tall, 150 nm tall, 100 nm short and 150 nm short respectively..... 255

Figure 5-42 - Pillar stiffness's of interest between 5 and 100 nN/μm for pillars of 500 nm, 1000 nm, 1500 nm and 2000 nm in height (h), as a way of tuning substrate stiffness for cell attachment. 1000-2000 have the largest useful range for cell culture applications..... 256

Figure 5-43 - A.B.) PEGDMA-Collagen (33 %) hydrogel rolls unfolded by pinning with thin PAA layer on Glass. Scale bars 400 μm C.) Cells at 24 hours Scale bar 400 μm and D.) 48 hours forming cell colonies to escape gel sheet Scale bars 400 μm..... 258

Figure 5-44 - '6 petal octagonal Lotus' folding scaffolds with overlapping lock mechanism (see Chapter 4). Device seated on 250 nm PAA lift-off layer, slowing down release rate long enough to seed H2 hESCs. Lift-off time confirmed as 5 days post seeding. hESCs seeded as single cells after Acutase 3:1 passage in a 200,000 cell/cm² concentration. Cells were "dry-plated" onto containers immobilized on glass slide. Slide and containers previously washed in EtOH and irradiated with UV for 10 minutes, they were then soaked for 12 hours in PBS and 12 hours in E8 media. Prior to cell seeding the slide was plated with vitronectin in a 1 μl/cm² concentration for 30 minutes at room temperature. All scale bars: 250 μm..... 259

Figure 5-45 - Optical microscopy image of a closed 'lotus' container with hTERT fibroblast cells visible on the inside surface, cells visibly stressed however by lack of feeding schedule to allow container to fully detach and fold without being torn apart by frequent fluid changes. hTERTS seeded at 20,000 cells/cm². Image taken 72 hours after seeding of cells on glass slide bound tetrahedrons on 400 nm thick PAA sacrificial layer. '6 petal octagonal Lotus' containers manufactured by PMMA lift-off process from Chapter 3-4 with container design outlined in Chapter 4. Scale bars: 250 μm 260

Figure 5-46 - Compiled manual scan of the 9 x 9 mm square containing the nanopillar array. Some areas not imaged, however each strip is representative of a range of the array showing increasing colony size in each section. Scale bar: 1mm..... 260

Figure 5-47 Phase contrast microscopy 10x magnification. Images showing H2 hESC forming highly 3D colonies on pillar gradient array. These were found to occur in random differentiation conditions, with no induced differentiation (Small molecules), cells incubated in E8 media. Scale bars: 250 μm. 261

Figure 5-48 - Pillar stiffness with varying height over the nanopillar gradient array. 262

Figure 5-49 - Cell profiler labelled colonies shown as different coloured blobs, colony size and position plotted in Matlab script, correlating colony position and overall size in pixels (px) 262

Figure 5-50 – hESC cluster area histogram, showing the tally of cell colonies by their area of coverage, data post-processed from Cell Profiler® colony labelling. 263

Figure 5-51 - Plot of cluster area against maximum radius from centroid as analysed by cell profiler and post-processed in Matlab. A linear relationship can be seen between the two.	263
Figure 5-52 – Joined heat map scatter plot, where intensity (red) indicated several data points overlapping one another. The key trend to note is the average cluster area is higher where distance - > 0 with it dropping off on average moving along the x-axis. The converted location and cluster area in μm is shown in the lower plot.	264

List of tables

Table 1-1 - Previously published work on actuating micro-containers and micro-devices, showing their relevant methods of manufacture, actuation, and achieved size.....	45
Table 1-2 - pKa Values of MAA, AA and their respective polymers, the pKa value is the point at which the chain reaches its respective protonating/deprotonating threshold.	50
Table 1-3 – Photo Initiators used in this work, chosen based on frequent use in literature. The initiators have different molecular structures and thus also different excitation peaks [112]. This is useful when tuning the initiator to the light source available for curing. The most common being 365 nm UV light as that used in our mask aligner.	54
Table 1-4 – SUSS MA6 mask aligner illumination values used for calculation of exposure frequency and dose.....	54
Table 1-5 –Quantum yield conversion, data for Individual initiator quantum yield. Quantum yield is a measure of the radicals generated to produce a polymerisation reaction by the listed photoinitiators, a high value represents an efficient initiator. Data from [89], [115], [118] and [119].....	55
Table 1-6 – Structures of key monomers and polymers for hydrogel synthesis studied in this thesis	57
Table 1-7 – Commonly used soft stamp materials in NIL and UV-NIL Adapted from [136]-[137, 138]. PDMS remains the most popular choice, and is one of the most versatile and adjustable stamp materials. It does suffer from delamination when filling deep or fine features, and has too low a modulus resulting in features flopping especially in the case of higher aspect pillars.	61
Table 3-1 - Neutral hydrogel recipes investigated in this work used both HEMA and EGDMA, two commonly used monomers for contact lens manufacture[47], a consumer product with significant strength and low protein absorption. Recipes resulted out of numerous trial and error experiments to achieve a reasonably stable flexible and well defined film, the PEGDMA based gel is a modification of a structural gel used by the Gracias group at Johns Hopkins [24] a different initiator (LTPO) was also used which according to BASF is less susceptible to oxygen inhibition than I2959 [115].	126
Table 3-2 - Recipe for original PNIPAAm-co-PEGDMA hydrogel created for thermo responsive hinge manufacture.....	127

Table 3-3 - Recipe for MBAAm crosslinked PNIPAAm based gel, with the recipe adopted from the Gracias group work at Johns Hopkins Institute. Recipe for this formulation was adopted from [24].	127
Table 3-4 - Monomers and available functional and crosslinking pairs.....	128
Table 3-5 - Absorption peaks, and molar extinction coefficients of implemented photoinitiators as measured by UV-VIS spectroscopy.	135
Table 3-6 - Variable or Flory-Rehner equations for estimating hydrogel mesh size from swelling ratios. Values found from previous work by Zustiak et al. [97] and Bush et al. [198].....	137
Table 3-7 - NIPAAm with Acrylic Acid copolymerization with I2959 acting as photo Initiator. Mixtures were prepared in water with exposure of 5 minutes under a 300 W broad spectrum UV bulb.....	139
Table 3-8 – levels for Taguchi study into synthesis factors for a NIPAAm based gel prepared under a 300 W broad spectrum UV bulb.	139
Table 3-9 - Synthesis parameters for Taguchi study into synthesis factors for NIPAAm based gels. 1 and 2 indicate levels of that particular variable shown previously. When a change in level of a particular variable has a strong effect on the output variable (swelling) this is considered to have a strong effect on the overall system.	140
Table 3-10 - Contact angles on NIPAAm and PEGDMA based gels as well as hybrid with response to temperature (n=1).	150
Table 4-1 – Photolithographic processes for two low thickness SU8 formulations, the 3005 and 3010 series resists. The 10 is a more viscous formulation of the 3005, and spins a thicker film. Both resists were used as received.	168
Table 4-2- . Ideal hinge dimensions for triangular polyhedron, red indicates the ideal hinge angles, with yellow being acceptable in the case of some extra adhesive force before closing the faces. ...	176
Table 4-3 – Ideal hinge dimensions for box polyhedron. Red indicates the ideal hinge angle, with yellow being acceptable in the case of some extra adhesive force then closing the faces.	178
Table 4-4 – Ideal dimensions for pentagonal polyhedron Red indicates the ideal hinge angle, with yellow being acceptable in the case of some extra adhesive force then closing the faces	180
Table 4-5 - Petal chord widths for a 1mm diameter “lotus” container, allowing the selection of the number and arrangement of petals to optimize the folding of these containers into a sphere of relevant size.	184
Table 4-6 - Modified gold etch rates with different concentrations of potassium iodide and iodine, shown are the respective etch rates as determined by the duration necessary to strip through a 50 nm and 80 nm gold layer. Rates are measured by profilometry of etch depth at single time points over 5 discreet areas, overall etch depth then divided by etch duration.	202

Table 5-1 - Vitronectin dissolved concentration with concentration per unit area and effective dilution ratio from working stock.	218
Table 5-2 - Cells per unit area were adjusted for a standard 500ml drop of media covering an approximate area of 2.55 square centimetres based on observed average droplet diameter on injection moulded inserts.	221
Table 5-3 - UHAR pillar array dimensions from SEM imaging measurements.	226
Table 5-4 – Water contact angles on SU8 before and after plasma ashing for 20 s at 80 W (n=12)..	231
Table 5-5 - UHAR Pillar type with corresponding cantilever stiffness as linear material, corrected, linear FEA model and equivalent stiffness for a flexible flat substrate. Load applied in model 10 nN. Effective modulus determined from approximations by Trichet et al. [158].	257

Contributions

The group at the University of Oslo, School of Medicine headed by Dr. Gareth Sullivan provided the H2 ESCs used in this work, and from whom the author learned the protocols attributed to cell culture and culture of human stem cells which were performed at their lab for a month period in September 2014. While all cell seeding and culture, and QPCR was performed by the author, substantial assistance with maintenance and feeding of cell lines, and general guidance and training was received from Richard Siller and Gareth Sullivan.

Replication of nanopatterns was performed at the JWNC of the University of Glasgow by the author however Injection moulded topographies were manufactured in runs by Paul Reynolds, and John Stormonth-Darling. These included the ultra-high aspect ratio (UHAR) pillars used in this work, as well as the gradient pillar array. Nanopatterned stamps were replicated and master stamp replicas etched by the author. Nano array design were transferred from CorelDraw drawings to Layout-Beamer formats and submitted for writing by Andrew Greer, with the actual writing of the patterns with EBL performed by the JWNC staff as with all nanopatterns produced at the facility at the University of Glasgow. hTERT fibroblasts protocols were demonstrated to the author by Maranda Thompson.

Outputs from this work

Publications

1. Iskandar Vasiev, Andrew I.M. Greer, Ali Z. Khokhar, John Stormonth-Darling, K. Elizabeth Tanner, Nikolaj Gadegaard, Self-folding nano- and micropatterned hydrogel tissue engineering scaffolds by single step photolithographic process, *Microelectronic Engineering*, Volume 108, August 2013, Pages 76-81, <http://dx.doi.org/10.1016/j.mee.2013.04.003>.
2. Marta Palacios-Cuesta, Iskandar Vasiev, Nikolaj Gadegaard, Juan Rodríguez-Hernández, Olga García, Direct micrometre patterning and functionalization of polymer blend surfaces by using hot embossing, *European Polymer Journal*, Volume 59, October 2014, Pages 333-340, <http://dx.doi.org/10.1016/j.eurpolymj.2014.07.020>.
3. Andrew I. M. Greer, Iskandar Vasiev, Benoit Della-Rosa and Nikolaj Gadegaard, Fluorinated Ethylene-Propylene: The Better Alternative to PDMS for Nanoimprint Stamps (in press - nanotechnology 2015)

Conference proceedings and awards

1. Keynote speaker - Annual Stem Cell Symposium 2014 – The Norwegian Center for Stem Cell Research, University of Oslo.
2. Oral presentation The European Society for Biomaterials 25th Annual Conference 2013 – Madrid
3. Oral presentation (Life and Systems) MNE 2013 - London
4. Oral presentation The UK Society for Biomaterials Annual Conference 2012 - Nottingham
5. Poster presentation The European Society for Biomaterials 25th Annual Conference 2013 - Madrid
6. Award: Best Poster Presentation (Biomedical) Global Circus 2013 - Niigata, Japan
7. Award: Best Poster Presentation (Life and Systems) MNE 2013 – London
8. Award: Science Slam Glasgow 2014 – 3rd place
9. Award: Best Poster Presentation at Cell and Proteomic Technologies Symposium 2013 – British Society for Proteome Research, Glasgow

1 INTRODUCTION

1.1 3D CONSTRUCTS, THEIR OCCURRENCE IN NATURE, RELEVANCE TO TISSUE ENGINEERING, AND MAN-MADE RECREATION.

1.1.1 3D architecture in nature

Natural systems often depend on intrinsic 3D architectures to perform a function [1], optimise internal space or to reinforce fragile structures. These 3D architectures occur on every level of existence, from the very small micron sized structures of viruses, phytoplankton [2], the walls of pollen grains [3], bee hive honey comb [4], and more importantly for the development of embryos [5] and spatial arrangement of the cells that build our bodies (Figure 1-3). In phytoplankton 3D architecture serves the structural purpose of holding together and protecting colonies of symbiotic organelles in a protective bicarbonate sheath as shown in Figure 1-1.

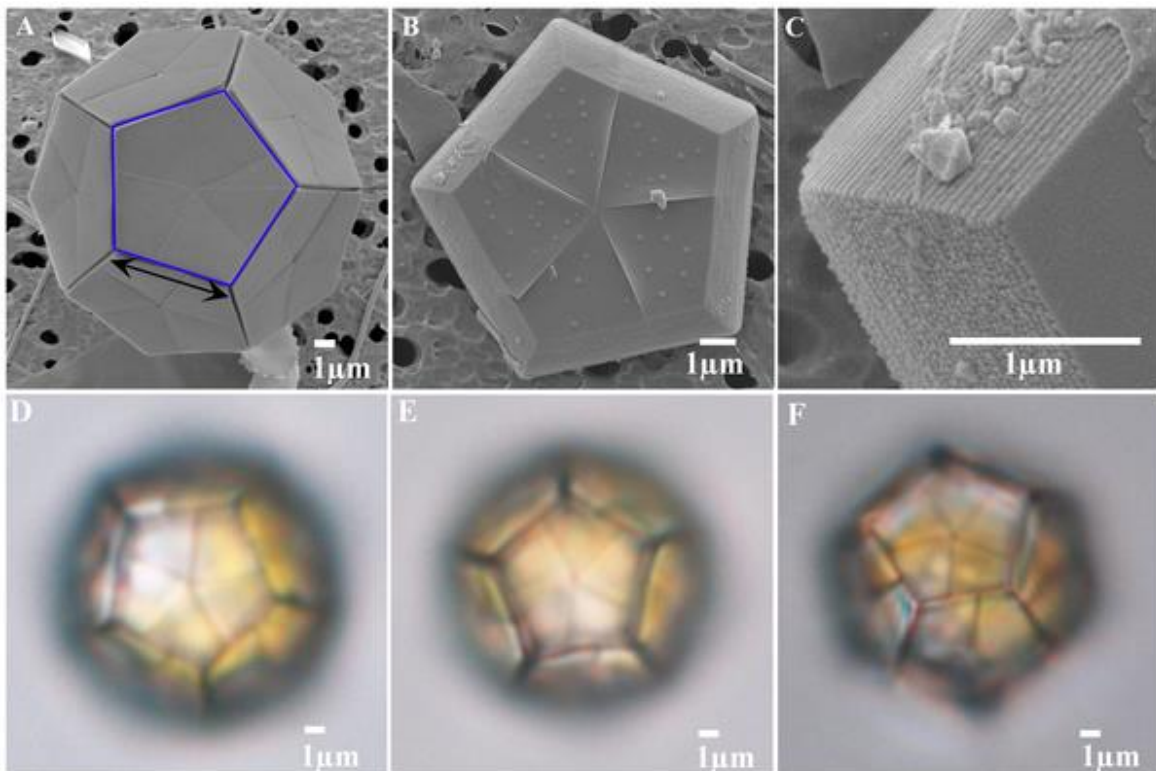


Figure 1-1 - The 3D architecture in cyanobacterium exoskeletons. A-C: SEM image of cells of *B. bigelowii*. D-E: Optical micrographs of *B. bigelowii* cells showing dodecahedron shaped constructs of the exoskeleton composed of pentagonal sections. All scale bars: 1 μm. Reproduced from Hagino et al. [2].

In pollen grains micropatterned surface structure and 3D architecture composed of swelling biopolymers facilitate a moisture dependant actuation to fold up and preserve genetic material

during times of drought, the nature of this folding and the different types of grain constructs are shown in Figure 1-2.

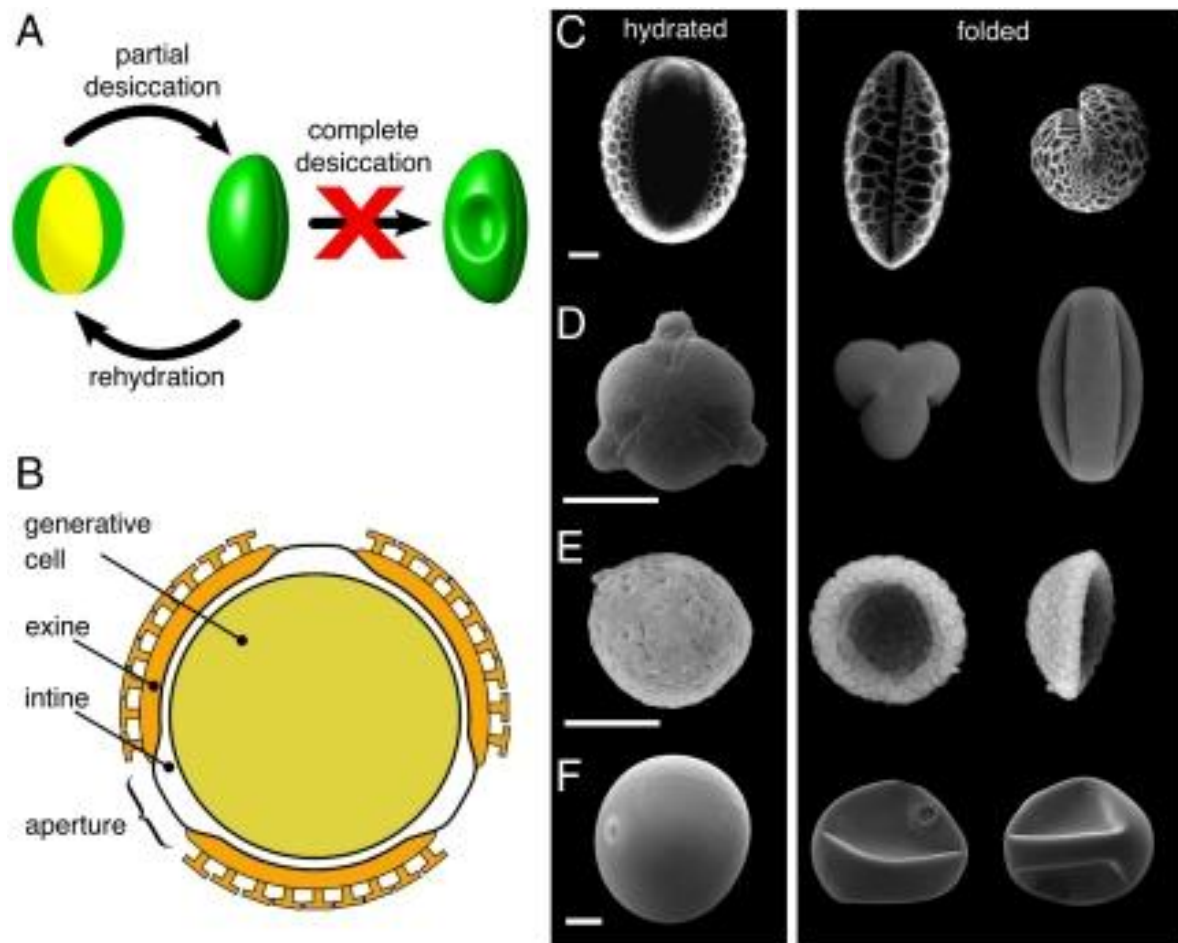


Figure 1-2 - Architecture and self-folding of pollen grains. (A) Mechanism of folding response to changes in humidity, allows a partial dehydration of the wall material while preventing complete desiccation of the internal genetic information and death. (B) A three aperture pollen grain with wall construction. (C)–(F) SEM images of pollen grains in hydrated states. (C) The single aperture pollen grain of *Lilium longiflorum*. (D) The three aperture pollen grain of *Euphorbia milii*. (E) The single aperture pollen of *Aristolochia gigantea*. (F) The single aperture pollen grain of maize (*Zea mays*). Scale bars: 20 μm . Reproduced from Katifori et al. [3].

Naturally humans have a fascination with designing 3D structures, platonic polyhedral carvings have also been found in Scotland dating back to 2000 BC and mankind has progressed to use them in art and architecture to this day [6]. This interest has slowly progressed over the last 4000 years and now, with the advent of tissue engineering and nanotechnology, the exploration has started with the application of these geometric arrangements into the construction of micro environments has started with the push to create man-made 3D architecture and hierarchy in tissue engineering.

This desire to build on the micro- and nanoscale stems from the need for sustained and precise control over cellular proliferation, function and differentiation. This task is a vital milestone in moving from materials which are observed to function, to those which are manufactured to function. This 'design' process reflects the main factors controlling cellular function *in vivo*, such as: the architecture,

chemical and mechanical stimuli, gradients and cross talk among diverse cell types. A multi-stimuli and multi-dimensional environment is therefore desirable if we are to emulate these complex systems. One area where this is quite apparent and of particular focus in this work, is hepatic tissue where there is a distinct 3D architecture (Figure 1-3).

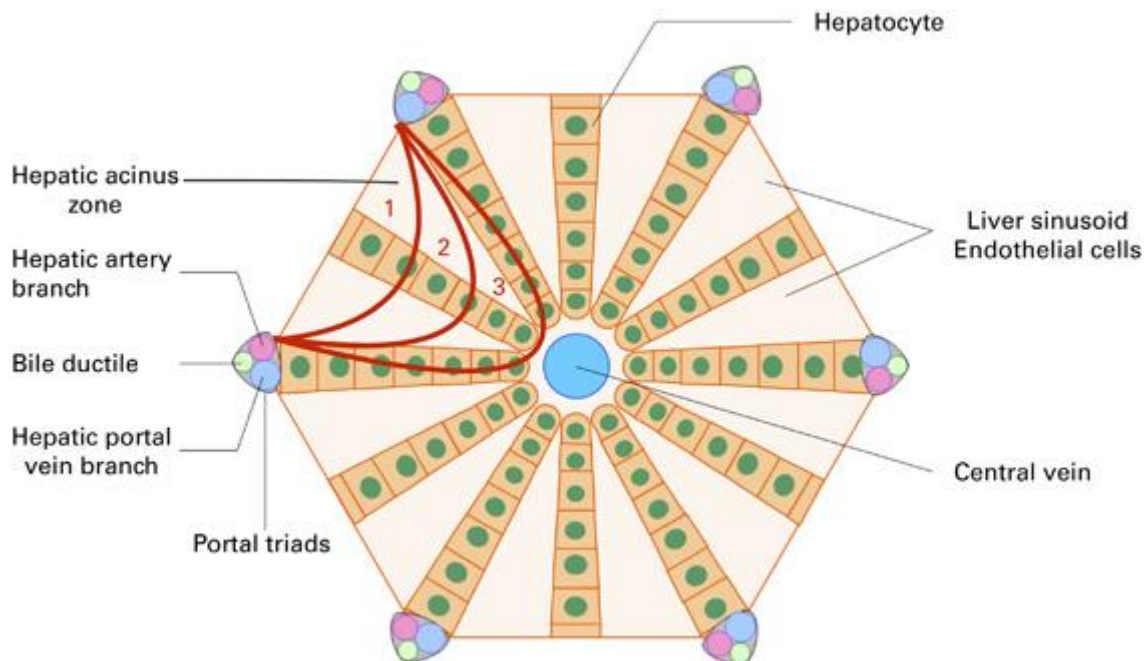


Figure 1-3 – Depiction of liver metabolism, showing the processes of the lobule to lobule interaction, nutrient and waste transport and chemical gradients including the chemical gradients and metabolic zones (1 to 3) resulting in nutrient and oxygen uptake as it transits the hepatic lobule. This image highlights the importance of geometric order in hepatic tissue constructs. Reproduced from Mohty et al. [7]

Artificially grown hepatic tissues are needed as a more sustainable and repeatable model in modern medicine and pharmaceutical research for the creation of lab grown organelles [8], repair of damaged tissues, and to be used for pharmaceutical and pathological testing [9]. The liver is one of the best examples of a complex biological structure, and one that relies on specific cellular arrangement to function at optimum efficiency and metabolism [10].

The liver consists of lobules which perform a series of metabolic functions, these are divided into individual units or hepatic acini, which can operate in heterogeneous order, independently, and can ramp up activity to meet demand. Blood flows past sheets of hepatocytes through the sinusoids and into the central vein (Figure 1-3). The first periportal zone nearest to the blood supply receives the most oxygenated blood, with the supply tapering off towards the centre of the lobule, this causes different behaviours and sensitivities in the lobule. An important aspect of this is that the oxygenated hepatocytes near the surface are specialized for oxidative functions such as gluconeogenesis, fatty-acid oxidation and production of cholesterol, while the internal cells perform glycolysis, and drug detoxification [11].

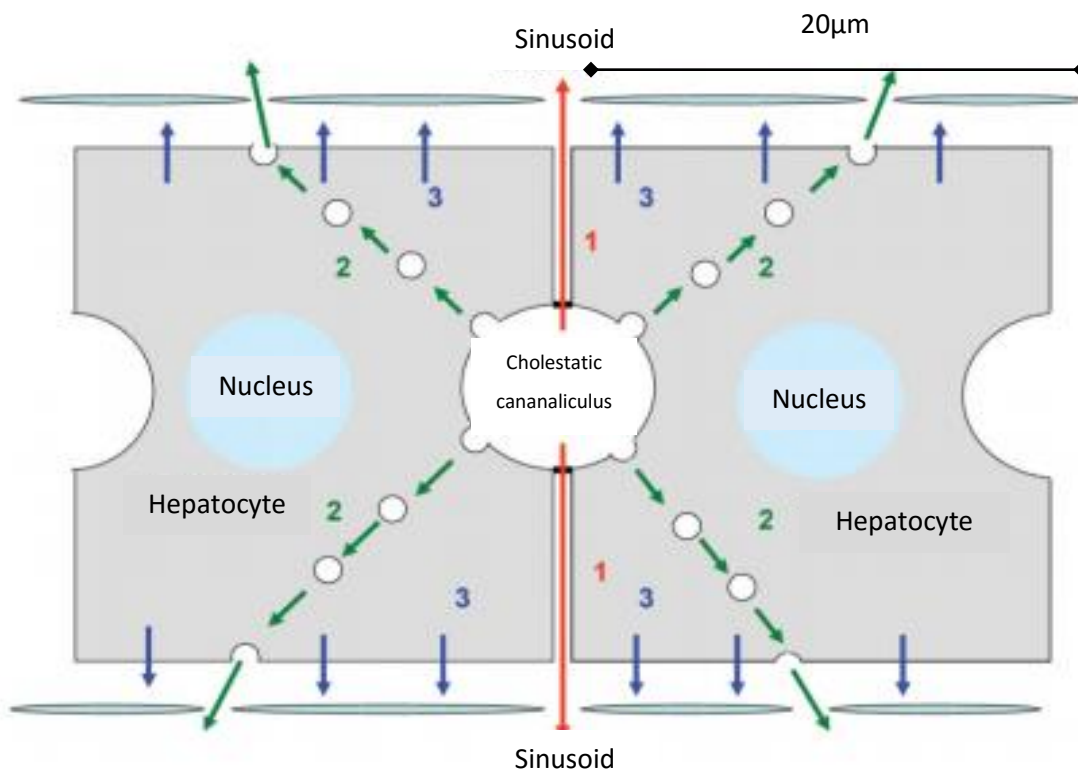


Figure 1-4 – Pathways for bile regurgitation in cellular hepatic junction. In numbered order of: 1. escape through leaky junction, 2. vesicle mediated transport, 3. Transport to the sinusoid endothelial cell membrane. Scale bar: 20 μm. Reproduced from Desmet [12].

Due to this heterogeneous and highly geometric structure, as well as the presence of multiple cell types; *in vitro* cultures of liver tissue do not show a realistic cellular metabolism, as they are not exposed to the correct ‘cross-talk’, be it due to the structural/mechanical characteristics of the substrate, lack of correct cell-to-cell contact, or lack of the correct chemical gradients seen in the native environment. Even in co-cultures with other cell types, the observed metabolism does not match that of native liver tissue [13]. The standard process of collecting biopsies for the study of drug metabolites, or doing live trials is time consuming and not as efficient as a miniature lab on a chip technique could be, evident in the number of pre-launch and post-market attrition of pharmaceuticals due to liver toxicity [13]. Animal trials are limited in their relevance to human drug metabolism, as their metabolic pathways cannot transfer to that of humans [14] this can be illustrated by the example of the drug Tirilazad which was associated with a worse outcome in patients with ischemic stroke but showed reduced infarct volume and improved neurobehavioral scores in animal models [15]. To circumvent the shortfalls of 2D hepatic cell culture, structuring is needed where cells are assembled into a 3D device, and it is hypothesized by the author that a 3D ordered configuration of hepatic tissue would lead to a boost in the liver tissue model performance and serve as a far more realistic system in a variety of clinical, pharmaceutical and research applications.

1.1.2 Simulated 3D constructs

This thesis is focused on the mechanical systems and material science in tissue engineering which combined offer potential foundations to control cell proliferation and tissue growth. The proposed importance of producing the necessary 3D architecture previously discussed in section 1.1.1.

In the literature a multitude of attempts have been made to create 3D tissue scaffolds. These have used various polymers [16], composites [17] and fabrication methods, including 3D printing [18], 2-photon lithography [19], *in situ* polymerization [20, 21] and a variety of casting methods involving heat and radiation which are discussed further in section 1.3.3. These materials can then be given a particular architectural complexity by enforced and inherent mechanisms. Inherent 3D architecture can be a product of the manufacturing method such as foaming, spinning, eroding and sintering where pores and fissures occur during the production mechanism, by solvent evaporation, phase separation or porogen addition. Enforced on the other hand refers to self-assembly and actuation, where an external system or input creates the 3D construct, it is these systems which will be investigated in greater depth within this work.

Many 3D designed structures have been attempted in the past, including various single photon lithography techniques and 3D printing. These are very slow and uneconomical to scale, something apparent in the use of 3D printing as a rapid prototyping technology, but not in commercial batch manufacture. Single photon lithography prints on a tiny scale by a femtosecond laser, this process is inherently time consuming. Actuation is then the likely solution, as every simple and high-throughput method of nano- and microfabrication available is a 2D process, any lithography is writing on a 2D surface by different means, the same applies to nanoimprint lithography (NIL) processes such as embossing, which work by 2D replication.

The problem of producing designed (enforced) 3D structures can be divided into two parts, firstly the scaffold itself has to be manufactured, and secondly is how that scaffold is then actuated and forced into forming a 3D construct. These two components need not be mutually exclusive, but creating an overlap produces a range of difficulties in handling the resulting devices which will be discussed in detail later.

1.2 ACTUATION AND THE SPONTANEOUS FORMATION OF ENGINEERED 3D STRUCTURES

As candidates for the enforced method of 3D scaffold formation a wide range of actuators have previously only been employed in biomedical engineering, these have come in the form of environmentally sensitive valves, micro-electro-mechanical systems (MEMS) and folding bilayers, a number of these actuating systems (Figure 1-5).

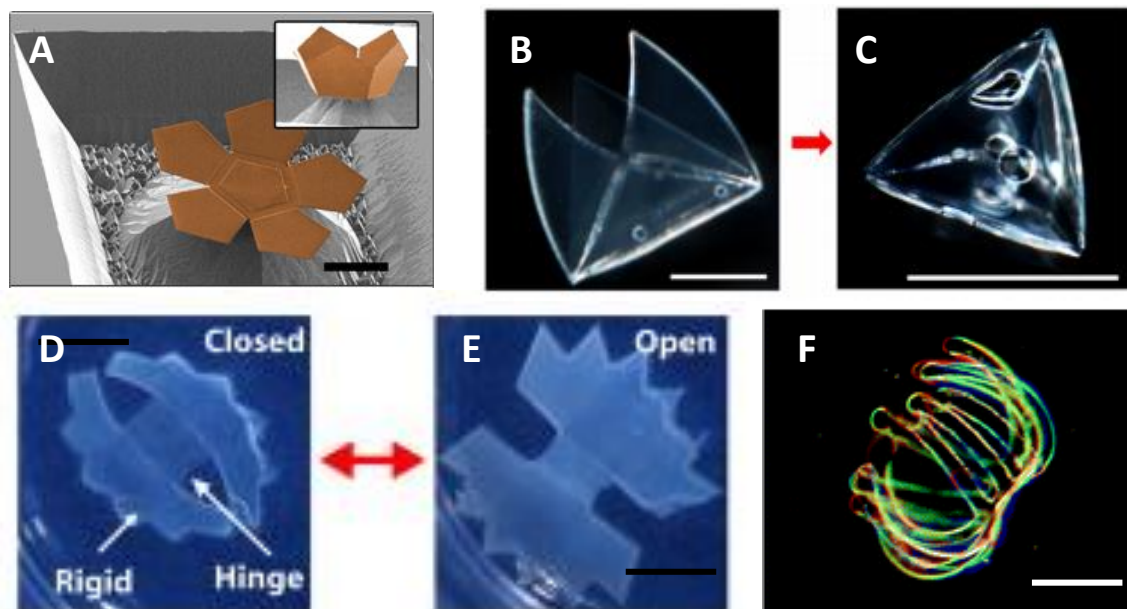


Figure 1-5 – Various actuating micro systems. A: Hemisphere of a dodecahedron formed by capillary force. Scale bar: 50 μm . Reproduced with permission from Legrain et al. [22] B-C: A tetrahedron before and after folding made of differentially exposed hydrogel, among other geometric shapes, the structure is formed by acidic and hot environment reproduced from Yoon et al. [23], scale bars 300 μm . D-E: A Venus flytrap mimicking device composed of rigid SU8 segments with a NIPAAm-AAc/PEODA bilayer hinge folding with low pH and high temperature, scale bars: 3mm. reproduced with permission from Bassik et al. [24]. F: A jellyfish like hydrogel container formed by differential swelling of a NIPAAm based bilayer in cold water, scale bar: 100 μm . Reproduced with permission from Guan et al.[25]

Various fabrication methods have been demonstrated using material and morphological approaches to produce actuating micro devices. Many of these methods have produced devices which often lack permeability, or actuate by a cytotoxic process, such as highly elevated temperature or chemical concentration as shown in Figure 1-5 and further in Table 1-1. Of these fabrication approaches a permeable and cell friendly scaffold is needed which can be modified to suit particular applications from cell transport to *in vitro* differentiation of stem cells.

Table 1-1 - Previously published work on actuating micro-containers and micro-devices, showing their relevant methods of manufacture, actuation, and achieved size.

Copolymers	Solvent	Fabrication method	Hinge material	Stimuli	Size	Nanopatter n present	Reference
P(EGDMA-co-MAA) and Chitosan	glycerin	UV-NIL with PDMS mould.	Carboxyl Deprotonation	Swell in H ₂ O	100-500 μ m	No	[25]
AAc-co-NIPAAm	1-butanol	UV Photolithography 2 step	Carboxyl swelling plus LCST transition	pH2, 60°C	350-2000 μ m	No	[23]
Nickel-Solder	N/A	Photolithography/ evaporation	Solder (Thermal shrink)	183°C	1500 μ m	No	[26]
PEGDA	PBS	Photolithography 2 step.	Swelling by Mw differential	Swell in H ₂ O	1000 μ m	No	[27]
NIPAAm-co-AAm	ethyl lactate	Photolithography 2 step.	Carboxyl swelling and LCST transition	Swell when T<22°C	400 μ m	No	[28]
(HEMA-co-NIPAAm-co-AAc) with SU8 panels	DMSO	Photolithography 3 step.	Carboxyl swelling and LCST transition	pH 2.5, 40°C	6000 μ m	No	[24]
Copper, SU8	N/A	Photolithography 4 step.	Copper oxidation and reduction	L-glutamine	0.150 μ m	No	[29]
Silicon nitride	N/A	Photolithography, undercut etching.	Surface tension	H ₂ O	100 μ m	No	[22]

The list of possible candidates for both active and passive folding includes piezo materials, magnets [30], thermal expansion, surface energy interactions, hydrogel actuators [24, 31] memory metals and polymers [32, 33] and reported in natural systems via moisture absorption [3]. The use of these materials can allow the transformation of a 2D printing or lithographic process into a method for generating 3D devices, providing a scalable toolbox for tissue engineering applications [34]. The 3D structure aims to provide an environment reminiscent of one encountered by cells *in vivo* [35] as different cell types require different chemical [36, 37], topographical [38-40] and mechanical [41, 42] stimuli as well as the presence of secondary and tertiary cell types [43] to form congruent tissue sheets or structures. This list of techniques applied and demonstrated for the manufacture of 3D containers is shown in Table 1-1. These are organized by their actuator type, method of manufacture and length scales, as well as extra features such as nano-topographical modification which they may include, although this was found to be a niche which was not present in other work. Often structures would show the ability to form a 3D architecture, but would lack nano-topographical cues, or a means of folding which was compatible with cell culture.

The list is broad and many actuators which rely on benign and biocompatible triggers were also found, the recipes used by the Gracias group at Johns Hopkins University [23] to create hydrogel bilayers played a large role in the development of my future approach, and feature prominently in the table. It should be noted that within these methods, a truly biocompatible triggering method is rare, and many of the optimum conditions for actuation in literature fall outside the envelope that cells, especially very sensitive ones such as stem cells, can survive. The strong ionic gradients or extreme temperatures are seen as necessary to achieve the full potential of the actuator being used, but this subject will be addressed later. It is believed that the devices can be improved upon in relation to biocompatibility by reducing the strength of the stimuli or increasing the amount of hinges or increasing the hinge size, reducing the actuator thickness is also a beneficial route to improving their actuation potential. Of these methods the ones which possessed the best traits for the encapsulation and sustained culture of cells were based on hydrogels due to their tenability and permeability, making a hydrogel device or hydrogel actuated device the most viable option, the merits of these materials and their synthesis methods were investigated for this purpose.

1.3 HYDROGELS AS TISSUE ENGINEERING SCAFFOLDS AND ACTUATORS

Hydrogel polymers, either synthetic or of natural origin, have a large portion of their volume taken up by absorbed water, suspending a largely interconnected matrix of crosslinked or otherwise immobilized polymer chains. Due to this structure, hydrogels are able to swell, absorbing a large amount of water without the polymer dissolving (Figure 1-6). In the case of crosslinked gels, the network can be a homopolymer [44] or contain secondary networks, copolymers, co-polymeric grafts and an array of micro-scale modifications to change the material response, cell response and mechanical behaviour of the final gel scaffold. These properties make them ideal candidates for mimicking soft tissue in tissue engineering applications, offering a range of potential chemical and mechanical modifications.

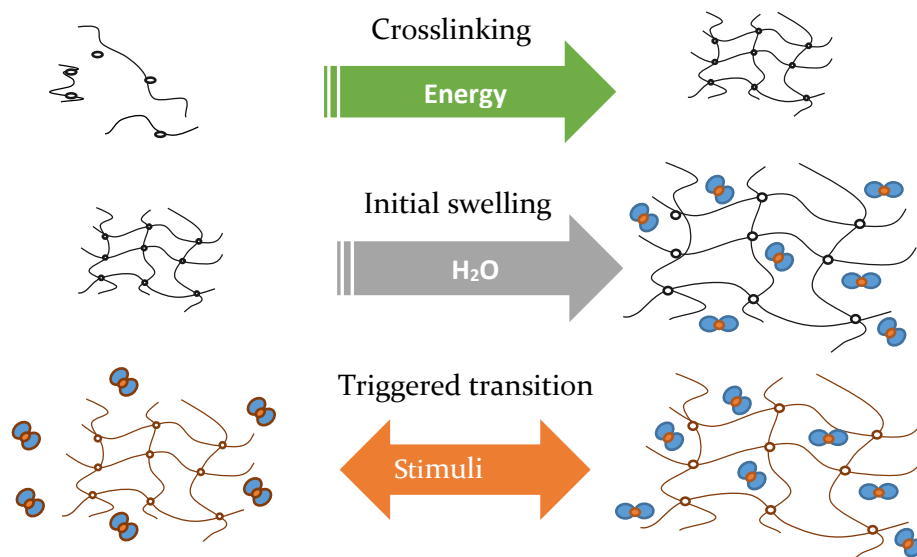


Figure 1-6 – Hydrogel formation and actuation based on steady state equilibrium swelling and actuation between hydrophilic and hydrophobic states.

In addition to their use in tissue scaffolds, hydrogels have been used as drug delivery devices [35, 45, 46], lenses [47], membranes [48], chemical sensors [31, 49] optical sensors [50], stimuli augmentable surfaces [51], capture-and-release surfaces [52], chromatographic separation media [53], actuators [54] valves [55] and bulk scaffolds for cell growth [56-59]. The wide variety of available polymers and monomers has made hydrogels extremely attractive for tissue engineering applications. They can be tuned by alteration of their crosslinking density and volume fraction, and it is due to their tuneable physical characteristics, wide range of methods of synthesis, and polymer composition, that hydrogels are the choice material for many systems in regenerative medicine [60]. They can be readily modified or treated to mimic the modulus and chemical composition of extracellular matrix proteins for improved cell proliferation and survival or strong enough to comprise the bulk of an implantable scaffold. Many hydrogel formulations are available, allowing the chemical response, mechanical properties, biocompatibility, degradation and solute transport to be carefully engineered. The relative ease with which hydrogels can be manufactured from their constituent polymers varies from heat catalysed casting [61], photo initiated free radical polymerization [62] as negative photoresists [63-65] UV-NIL [66, 67], plasma-polymerization [68], deep X-ray photolithography [69], or EBL exposure [70]. Utilizing the gel's ready conformation to solid surfaces can produce micro patterned polymeric bilayers [24, 71] which can be altered to swell and change geometry depending on their environment or due to predefined triggers [72].

They can serve as scaffolds which mimic native cell environments, provide structural integrity to tissue constructs, and in the case of many stimuli responsive gels, serve as drug and protein delivery conduits to tissues and cell cultures, or as adhesives or barriers between tissue and material surfaces on biomedical implants. However, there has not been a successful system for active cell capture

other than bulk cell encapsulation [64, 73, 74]. Some work on stimuli responsive photopatterned hydrogel structures has been done, but on a much larger macro scale [52]. This problem arises because hydrogel copolymer systems which are most responsive to external signals are often mechanically weak, while heavily crosslinked gel networks do not swell rapidly or significantly and react more slowly to external stimuli due to the high elastic force of the polymer network opposing the swelling of the gel [75]. Their ability to reversibly change can also lag when gels are too thick, both due to slow chemical reactivity, and concentration polarization where ions cannot be effectively transported in or out of the matrix [76]. Nanocomposite gels [77] polymerized with a nanoclay crosslinker have been suggested as a possible solution to many of these issues. These composite gels are also prepared by free-radical polymerization at near ambient temperature, without stirring, easily producing various shapes and surface forms. Because of their unique organic-inorganic network structure, they possess high toughness and excellent optical properties. However the biocompatibility of these still requires investigation.

Additionally no effective photoinitiated polymerization of nanocomposite smart gels currently exists [78], as the tetramethylethylenediamine (TEMED) based initiators in these systems work by actively immobilizing and absorbing on the clay particles, propagating the reaction outwards. This property does not seem to be present in photoinitiators, which usually produce weak gels. The addition of functional groups provides the basis of smart actuating hydrogels, and is achieved by attaching functional polymers to the gel network, ranging from pH [79], temperature [24, 54, 71], light [46], electrochemical [80] and enzyme sensitive polymers [81]. One final and significant advantage is their permeability to oxygen and dissolved species [82] and the adjustable level of protein immobilization [83] which make it possible to create multi-layer structures [74].

These structures can be capable of selective attachment/detachment of cells as seen in Figure 1-7 in a predefined area by minor changes to the aqueous environment [84].

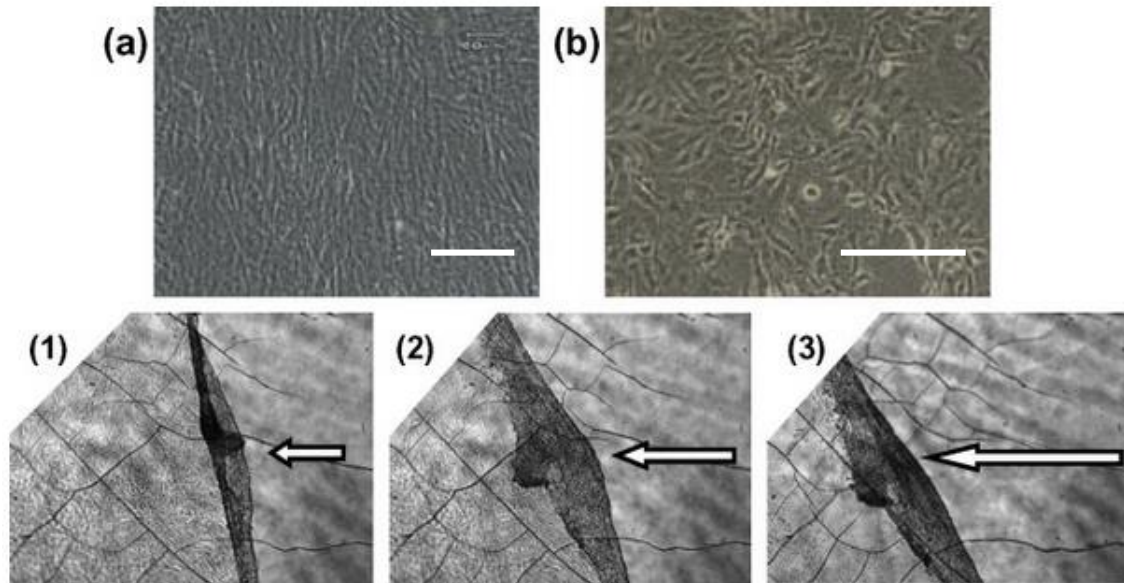


Figure 1-7- Phase-contrast photomicrographs of (a) fibroblast and (b) HUVEC cell proliferated on a PNIPAAm hydrogel film. (1–3): Fibroblast sheet detachment upon decreasing the temperature to 10–20 °C when the gel falls below its LCST and begins to swell. Scale bars: 200 μm . Reproduced with permission from Haraguchi [78].

To allow for the disposal of the scaffold, these gels can be modified to be bio [85], photo [86] and sonically [87] degradable by coupling a sensitive polymer to the network. Currently the use of gels in cell capture applications has been limited to flat surfaces [71, 72, 79]. Their porous structure also makes it tricky to nanopattern certain concentrations [66], and the process itself is often oxygen sensitive [88] requiring an inert environment, oxygen scavengers in the pre-gel, strong radiation, or an inert atmosphere [89].

1.3.1 Neutral or structural hydrogels

What can be called “neutral hydrogels” form the backbone of any hydrogel system, providing rigidity and mechanical support while remaining inactive or unchanging to ongoing chemical reactions in the local environment. This structural material for the hydrogel bilayer needs to be a material that is easily patterned and permeable to nutrients and dissolved gases to enhance cell viability and survival when the finished hydrogel scaffold, hinge or structure is operating *in vitro*. The main candidates are polyethylene glycol (PEG) [90] or hydroxyethylmethacrylate (HEMA) and its polymer polyhydroxyethylmethacrylate (PHEMA) based copolymer systems [91] which have been used in contact lenses due to their clarity, flexibility and reasonable strength [47]. PHEMA hydrogels were among the first synthesized for biomedical applications by Lim and Wichterle in 1955 [92] for use in contact lenses due to its spectacular stability in different pH, temperature and ionic conditions. PEG also known as polyethylene oxide (PEO) for high molecular weight variants [92], is one of the most

widely used hydrogels in biomedical applications. Hydrogels based on its acrylated PEGs such as PEG-dimethacrylate (PEGDMA) and PEG-diacrylate (PEGDA) are widely used due to their high biocompatibility, lack of toxic influence on surrounding tissue, lack of protein absorption and solubility [90]. These reasons have led to PEG having wide ranging applications in cell encapsulation and transport [93].

1.3.2 Stimuli responsive hydrogels

As previously mentioned, a variety of triggers can be instilled in hydrogels, from light [46] electric potential [80], temperature [24], pH and enzymes and ionic compounds[81]. This thesis will focus on stimuli which are present in culture media or are non-cytotoxic to cells and living tissue. This eliminates the use of electric potential, or very strong ionic solutions to avoid cell rupture due to high osmotic potentials. The manufacture of each actuator type requires both different hydrogel chemistry and different fabrication steps, NIPAAm [94] in particular is very sensitive to oxygen inhibition.

1.3.2.1 pH responsive gels

The pH sensitivity in hydrogels is created by the copolymerization of an acid or acidic polymer such as polyacrylic acid (PAA) or polymethacrylic acid (PMAA) into the hydrogel network. The carboxylic groups of the acid respond to changes in pH by protonating or deprotonating [95]. The extent and threshold of this change of state depends on the pK_a (acid dissociation constant) value of the acid in question. The higher the acid pK_a values the smaller its proton dissociation. A weak poly acid such as PAA has a pK_a value in the range of 4 to 6.5 in water [96] as shown in Table 1-2.

Table 1-2 - pK_a Values of MAA, AA and their respective polymers, the pK_a value is the point at which the chain reaches its respective protonating/deprotonating threshold.

Acidic polymer or monomer	pK_a value
Methacrylic acid	4.66 [97]
Acrylic acid	4.25 [96, 98]
Poly methacrylic acid	4-6 [96]
Poly acrylic acid	4.5-6.4 [96]

The values correspond to the states where the carboxyl groups exist in their COOH form and deprotonating to a COO⁻ as the pH rises [96]. The point at which this occurs can be found from the relation [98]:

$$pH - pKa = \log\left(\frac{\alpha}{1 - \alpha}\right) \quad \text{Eq. 1-1}$$

Where α is a material dependant constant related to the activity of the chemical species. The change in hydrogen dissociation at the pKa leads to changes in surface energy and in addition to changes in hydrogel swelling the surface switches between a hydrophobic and hydrophilic state. The slight charge in the carboxyl groups also leads to their attraction to positively charged surfaces or particles, which can be a problem during fabrication and testing as the structure has a great affinity for its container. An ion concentration gradient over the interfaces between the hydrogel and the surrounding solution is then developed because of the fixed negative-charged groups on the acid modified side of the hydrogel. Osmotic pressure is generated because of the ion concentration difference in the active and neutral hydrogel structures. The use of acrylic and methacrylic acids also offers improved cell adhesion [99] and can be used to attach proteins and peptides. Additionally pH sensitive copolymer, grafted and double network [100] hydrogels have also been made by a variety of combinations of acids, polyacids and neutral methacrylates, very often crosslinking acrylic acid and NIPAAm monomers by photolithography. These double network gels are very fast in response, but suffer from concentration polarization where ions cannot be transported to the core of the gel fast enough, as a result they bubble or form a hard shell if two stimuli are changed at once, for instance raising pH while raising temperature.

1.3.2.2 Thermally responsive hydrogels

While it is not the only thermoresponsive monomer, NIPAAm has seen a lot of attention due to its good processability, means of manufacture and low toxicity. Work has been on-going for several decades into ways in which the mechanical and responsive properties of these gels can be improved. The material undergoes a chemical change above 32 °C [101] at which point it contracts and becomes hydrophobic, and begins to eject the absorbed water it contains, resulting in de-swelling [55]. This property is observable at body temperature as seen in Figure 1-8. The speed of response and exact LCST temperature are tuned by changing the polymer molecular weight and type of copolymers (hydrophobic or hydrophilic) used in the hydrogel synthesis [102]. These swelling properties make this actuator type particularly useful for use *in vivo*, as it will remain curled after implantation.

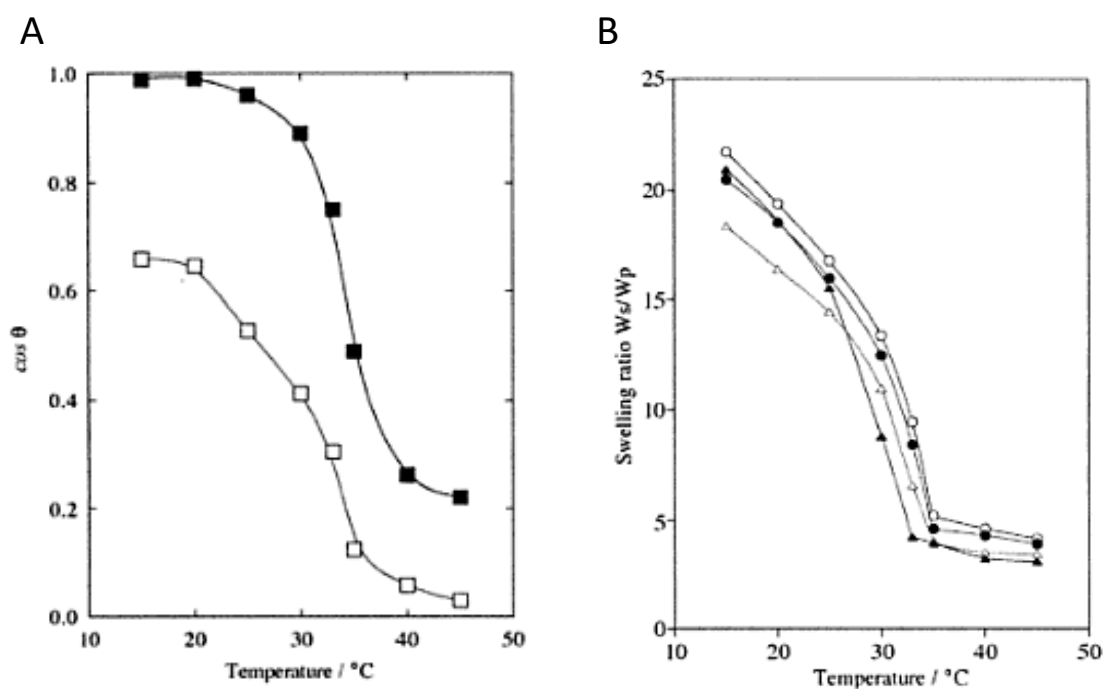


Figure 1-8 –A: shows the advancing (open square) and receding (closed square) contact angle of PNIPAAm gels. B: The swelling ratio of PNIPAAm gels in pH 7 buffered solutions of increasing ionic strength over a range of 0.005 mol/dm³ (open circle) – 0.154 mol/dm³ (closed triangle) intermediate concentrations (closed circle, open triangle). Reproduced from Makino [103].

1.3.2.3 Light responsive gels

The combination of thermo-responsive NIPAAm gels with particles such as gold nanospheres [46], fullerenes and nanotubes [104, 105] can be used to make them respond to that wavelength of light to which the selected nanoparticle reacts [17]. The heat generated by the dopant particle causes the polymer network to heat to above its transition temperature and shrink [76]. Additionally graphene sheets can be used to produce an electrically stimulated hydrogel based actuator [106].

1.3.3 Hydrogel synthesis

Hydrogels do not disintegrate during swelling due to their crosslinked structure. Crosslinking may be achieved as mentioned before, by physical or chemical immobilization of polymer chains. The crosslinking may take place in two environments: *in vitro* during the preparation of a hydrogel, or *in situ* after application in a precise location of the human body. This thesis considers device manufacture, and concerns the *in vitro* preparation of hydrogel devices, to be compatible with existing methods of manufacture, such as photolithography or solvent casting. Hydrogel actuators can be made by a variety of high throughput methods, such as photolithography, which allows for the quick creation of a network and the incorporation of certain ‘functional’ polymers, which expel the contained swelling agent when they are subjected to external stimuli [107]. Non-functional hydrogels can be made with the same method, discussed further in section 1.3.3.1, act as a permeable hydrated structure allowing for nutrient and ion transport while retaining rigidity [108].

To initiate chemical crosslinking it is necessary to introduce into the reaction mixture a low-molecular-weight crosslinking agent together with a polymer and initiator which propagates the polymerization reaction. Many factors play a role in the final properties of a gel, such as molecular weight of the constituent polymer between crosslinks, the volume fraction and type of solvent during casting, the temperature during synthesis, initiator type and crosslinker. Gels can be divided into four groups depending on the inertness, synthesis and presence of crosslinking reaction. If the crosslinking involves the creation of covalent bonds; the hydrogel could be termed a 'permanent' hydrogel [107], these include PMMA, PEGDMA and PHEMA. If the hydrogels are formed due to the physical interactions, such as van der Waals forces, ionic interaction or hydrogen bonding among the polymeric chains, then they are termed 'physical' hydrogels [107]. These hydrogen bonding groups and ionic side chains form the basis for further definition of hydrogel 'type' categorized as conventional and stimuli responsive hydrogels. The covalently bonded gels yield a polymer network resembling a chicken wire fence, where the crosslinking density depends on these factors.

1.3.3.1 Free radical polymerization

Radical polymerization is the most common means of hydrogel synthesis [90]. While other methods of producing various hydrogen bonded gels and sol-gels exist [109], these are not particularly useful for rigid structural applications. Among the free radical initiators available, thermal and photo cleavable initiators are widely used to produce gel devices [24, 48, 67, 109, 110]. Photo initiators are the more controllable choice in this instance, as they offer direct control over the shape, extent and crosslinking of the gels formed by altering the exposure dose [111], while thermal initiators are useful in instances where the shape is defined by solvent casting and moulding, as localised heating is more difficult to achieve.

1.3.3.2 UV initiated free radical polymerization.

Photoinitiation process is fast and provides spatial and temporal control of the polymerization reaction, since the radiation can be focused on a location of interest and stopped at a specified time. UV irradiation has become one of the most common way of photo-polymerization and the setup is relatively easy to prepare. Typically, the morphological properties of the final hydrogels are controlled by the type of solvent selected, as well as the amounts of crosslinking agent and initiator used (Table 1-3), as both affect the kinetics of the free-radical polymerization [109]. More pores means more space and less resistance to swelling, more crosslinking counteracts this by forming a denser network.

Table 1-3 – Photo Initiators used in this work, chosen based on frequent use in literature. The initiators have different molecular structures and thus also different excitation peaks [112]. This is useful when tuning the initiator to the light source available for curing. The most common being 365 nm UV light as that used in our mask aligner.

Photoinitiator	Chemical compound	Absorption peak wavelength (nm)
Irgacure 2959	2-Hydroxy-4'-(2-hydroxyethoxy)-2-methylpropiophenone	280,320
Irgacure 651	2,2-Dimethoxy-2-phenylacetophenone	250,340
Lucirin TPO	Diphenyl(2,4,6-trimethylbenzoyl)phosphine oxide	295,368,380,393
Irgacure 819	Phenylbis(2,4,6-trimethylbenzoyl)phosphine oxide	295,370
Darocur 1173	2-Hydroxy-2-methylpropiophenone	245,280,331

The most common method of UV photo-polymerization is using photo sensitive compounds called photoinitiators which provide the free radicals necessary to break and create new bonds within the polymer suspension creating a crosslinked polymer network [113, 114]. Carbonyl group containing photoinitiators which form free radicals by the cleaving of hydrogen atoms during hydrogen abstraction are the most widely used [115]. Several families of initiators are available of which phenones, ketals and phosphine-oxide based photoinitiators are widely used [116] and were chosen to be used in later formulations (Table 1-3). The most active are phosphine-oxide based photoinitiators, such as Lucirin TPO, which has been determined using the respective quantum yield of various photoinitiators [115] based on the MA6 exposure data shown in Table 1-4.

Table 1-4 – SUSS MA6 mask aligner illumination values used for calculation of exposure frequency and dose.

Light intensity	Emitted light wavelength
7.2mW/cm ²	365 nm

Using this and converting it into molecules decomposed per second of exposure, with the assumption that each incident photon decomposes one molecule of initiator. The energy of one photon is taken as:

$$h\nu = E * C / \lambda$$

Eq. 1-2

Where E is Planck's constant and c is the speed of light. This converts the quantum yield found for each initiator in literature to a quantifiable figure for MA6 exposure per second.

Converting the number of moles into weight decomposed will give exposure times to achieve 100 % conversion per volume of initiator so that exposure can be adjusted for the size of sample this is shown in Table 1-5. The most well established initiator system for photo encapsulation is Irgacure 2959, manufactured by Ciba and commonly used in combination with ultraviolet (UV) light. Although I2959 is tolerated by many cell types at a concentration of 0.03-0.1 % [111] it has very poor absorption in 365 nm light [111]. Initiators were first analysed by solubility, and secondly by their absorption spectra, to find the initiator most suitable for the lithography setup available using the Beer-Lambert law [117].

$$A = \varepsilon_{(L/molcm)} \cdot C_{(mol/L)} \cdot L_{(cm)} \quad \text{Eq. 1-3}$$

Where A is absorbance, c is concentration in solution, and l is the length of the path to be travelled by light. The chemical nature of the photoinitiator determines their respective curing rate, spectral sensitivity and oxygen sensitivity, the quantification of the quantum yield for several popular initiators is listed in Table 1-5. The quantum absorption coefficient was also found by varying initiator concentration under UV-VIS spectroscopy outlined in Chapter 3.

Table 1-5 –Quantum yield conversion, data for Individual initiator quantum yield. Quantum yield is a measure of the radicals generated to produce a polymerisation reaction by the listed photoinitiators, a high value represents an efficient initiator. Data from [89], [115], [118] and [119].

Initiator	Quantum yield ϕ	Moles decomposed per cm^2/s
I2959	0.05 [115]	1.099×10^{-9}
I651	0.1-0.7 [118]	2.197×10^{-9}
L-TPO	0.88 [119]	1.93×10^{-8}
I-891	0.9 [89]	1.977×10^{-8}

1.3.3.3 Oxygen Inhibition

Oxygen is a strong factor in the radical polymerisation cycle, acting as a scavenger and terminating both free radicals and radically terminated molecules or chains. For high throughput, It is desirable to carry out polymerizations in air, and therefore, methods for enhanced oxygen inhibition are of great importance [119]. Oxygen inhibition effects free radical polymerizations by slowing polymerization rates, increasing induction periods, decreasing conversion, decreasing polymer kinetic chain length and creating tacky surface properties [120]. Successful reduction of oxygen interaction with the

system would provide a significant advantage [89] in making thin films with micro- or nano-scale patterns. In films such as the gels being produced where film thickness and feature size is below 10 μm , oxygen continually diffuses across these small length scales, scavenging the initiating and propagating radicals [109].

Overcoming oxygen inhibition is done in a number of ways; purging the pre-polymer solution and mask aligner prior to exposure with an inert gas such as nitrogen or carbon dioxide, or with the addition of amine monomers such as TEA (Table 1-6) into the pre polymer solution as a synergist or oxygen scavenger[89], and/or providing more initiator or higher intensity light [120].

1.3.4 Hydrogel performance

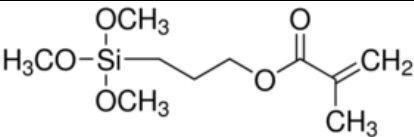
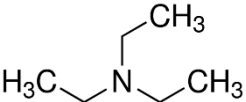
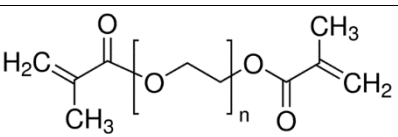
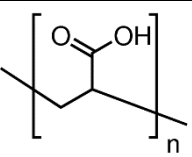
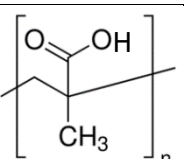
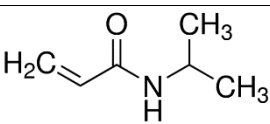
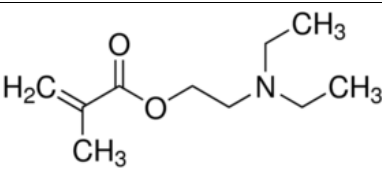
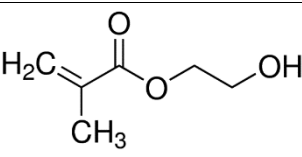
1.3.4.1 Equilibrium swelling ratio

The swelling of hydrogels is a complicated process, consisting of a number of stages. The general equation governing the network is expressed as a balance of free energy.

$$\Delta G_{\text{system}} = \Delta G_{\text{mixing}} + \Delta G_{\text{elastic}} \quad \text{Eq. 1-4}$$

Where ΔG_{system} is the total free energy of the system, ΔG_{mixing} is the Gibbs free energy of ‘mixing’ or the tendency of the polymer chains to dissolve into the aqueous solution, finally $\Delta G_{\text{elastic}}$ is the elastic retraction energy or resistance to swelling expansion by the crosslinked chains. In the first stage water molecules enter the hydrogel matrix hydrating the most polar, hydrophilic groups such as the carboxyl groups in PAA and PMAA, this hydration results in the appearance of primary bound water. In the second stage, with the hydrophilic groups bound, the hydrophobic groups begin to interact with water molecules giving secondary bound water. These two stages form what is referred to as the total bound water, or the water which remains if a pressure or osmotic gradient acts on the gel. In the final stage, as the network tries to dissolve and is resisted by the covalent or physical crosslinks, an additional amount of water is absorbed by the osmotic driving force created as ΔG_{mixing} and $\Delta G_{\text{elastic}}$ continue to grow. The water absorbed between the total bound water, and the equilibrium swelling level is called the free water; it fills the space between the network chains, but is not immobilized on the polymer network itself [92]. As equilibrium is reached, $|\Delta G_{\text{mixing}}| = |\Delta G_{\text{elastic}}|$ and $\Delta G_{\text{system}} = 0$ the driving force of the swelling is reduced and brings the gel to a steady-state balance between the mixing and elastic free energy.

Table 1-6 – Structures of key monomers and polymers for hydrogel synthesis studied in this thesis

Abbreviation	Chemical name	Molecular structure
TPM	3-(Trimethoxysilyl)propyl methacrylate	
TEA	Triethylamine	
PEGDMA	Poly(ethylene glycol) dimethacrylate	
PAA	Polyacrylic acid	
PMAA	Polymethacrylic acid	
NIPAAm	N-isopropylacrylamide	
DEAEMA	N,N-Diethylaminoethyl methacrylate	
HEMA	Hydroxyethyl methacrylate	

1.3.4.2 Hydrogel Immobilization

To aid the study of hydrogel surfaces for cell adhesion, or to monitor containers which are immobilised in one area, or to anchor specific cell type containing hydrogel niches in a particular location a method of permanent attachment of all or part of the structures to the substrate is necessary. Hydrogels based on acrylate chemistry will readily crosslink onto other acrylated polymers such as PMMA, some epoxies and, with the correct choice of crosslinkers and initiators, polystyrene surfaces. On glass and other inorganic surfaces this is not as simple. In these instances hydrogels can be immobilized using 3-(Trimethoxysilyl)propyl methacrylate (TPM) a methacrylate terminated silane (Table 1-6) which can bind to silicon and borosilicate glass surfaces [67]. This can be implemented by a similar protocol to conventional silanization to create methacrylate based anchor points on the glass, which involve it in the crosslinking process during hydrogel synthesis.

1.3.5 Hydrogel bilayer actuators

While there has been significant progress in the manufacture of precisely engineered 2D surfaces for cell interface studies, most fall short of presenting the cells with the cues which exist in the native 3D cellular environment combined with surface patterning, mechanical and chemical stimuli [121, 122], there is also a lack of self-assembly in these applications [30] which can ease manufacture and greatly increase throughput. While many engineered 3D cellular tissue scaffold constructs have been demonstrated in the past with relatively easy methods of manufacture [123], these do not offer much control over the geometry and would not serve in making a purpose designed surface topography and structure. There is therefore a need to extend the applications of defined 2D micro- and nanopatterned methods to the third dimension. Self-folding is one method of achieving this conversion of 2D patterning techniques into a viable method of manufacturing a 3D cellular environment and creating reconfigurable structures which can fold or unfold in response to specific environmental cues. An array of self-folding 3D structures [30], employing stimuli responsive materials for cell capture [124] and drug delivery have been made in the past. These have often incorporated a bilayer structure [125] with varying environmental sensitivity of the constituent layers; including heat-shrink type hinges [126], shape memory polymers [127] and hydrogel films [128]. However these devices fail to combine surface patterning on a material while remaining permeable to oxygen and nutrients. The challenge lies in the creation of permeable and patterned 2D templates composed of polymers and hydrogels so that self-folding structures can be constructed using a wider range of biocompatible and biodegradable materials. One possible solution is optical patterning using photolithography [129, 130], or soft lithographic methods such as UV-NIL [131]. Some of these methods have previously been utilized to fabricate hinge-less polymeric structures that roll up or curve spontaneously [129, 130]. Hydrogels are attractive materials for

these self-folding tissue scaffold structures because of their high water content, permittivity and mechanical properties which are comparable to non-osseous living tissues. Previous methods of manufacturing thin hydrogel scaffolds have used a two stage photolithographic process or manufacture by two-photon stereolithography. These processes are time consuming and require several stages of mask alignment or expensive equipment, as the micro-patterning of biocompatible hydrogel films is generally recognized as very difficult task [125]. The key features for a self-folding tissue engineering scaffold are patternability for cell contact guidance, nutrient permeability to avoid tissue necrosis and ease and speed of manufacture. To outline the fundamental factors affecting bilayer actuation; Timoshenko's description of a bilayer with differentially expanding materials is implemented [132, 133]. The bending is assumed to be mono directional and results in a bilayer with a uniform radius of curvature R.

$$Curvature (K) = \frac{1}{R} = \frac{6(\varepsilon_2 - \varepsilon_1)(1 + m)^2}{t \left[3(1 + m)^2 + (1 + mn) \left(m^2 + \frac{1}{mn} \right) \right]} \quad Eq. 1-5$$

Where height, m, and modulus, n, ratios are defined as:

$$m = \frac{h_1}{h_2} \quad \text{and} \quad n = \frac{E_1}{E_2}$$

Where h_1 and h_2 are the layer thicknesses, E_1 and E_2 are the Young's moduli, t is the total thickness of the bilayer, and ε_1 and ε_2 are the actuation strains of the two layers [129, 133]. The radius of curvature is inversely proportional to the film strain and is not very sensitive to the difference in stiffness between the two layers, and is mainly controlled by the actuation strain and the layer thickness. The equation idealizes beam bending in only one direction and therefore does not predict the folding direction of the bilayer [133].

1.4 NANOPATTERNING, METHODS AND APPLICATIONS.

The capacity to fabricate well-defined nanofeatures to interact selectively with biology has had tremendous implications in the field of tissue engineering. UV nanoimprint lithography (UVNIL) and soft lithography have been the key techniques to fast replication of topographical patterns, with the majority of techniques employing a siloxane based castable gel: polydimethylsiloxane (PDMS) [134]. PDMS stamps have been widely used to achieve rapid replication and repeatability, however there are many issues regarding the use of PDMS in certain applications [135]. PDMS can stick to certain surfaces, is easily fouled, absorbs certain solvents and above all is too flexible for higher loaded applications.

1.4.1 NIL with flexible media

Nanoimprint lithography (NIL) is a simple process for the reproduction of nano- and microtopographies. It utilizes a hard master stamp which drives the pattern replica into a surface or mouldable material by heat, sol-gel methods, UV polymerization or solvent casting. These stamps can be manufactured from a variety of materials, including quartz (qz), silicon (Si), silicon nitride (SiN), nickel (Ni), sapphire and diamond. The process of manufacturing these stamps often relies on commercial high resolution photolithography, electron-beam lithography, focused ion beam (FIB) and reactive ion etching (RIE) to drive the pattern created on the surface into the underlying substrate.

Thermal-NIL and NIL respectively rely on heated or non-heated imprinting of these hard stamps into much softer materials, to create localised thinning of the mouldable surface. This often forms a so called “residual layer” which is considerably thinner than the bulk and is removed by O₂ plasma ashing or etching process (depending on the material). The replica is then made by the deposition of material on the substrate through the newly created windows on the imprinted mask material surface. The deposited material can be made to act as a stamp in itself, or be used as an etch mask to drive the features into the underlying substrate with RIE, much like the aforementioned EBL and lithographic processes. Many soft material analogues for traditional solid stamps are becoming available (Table 1-7), driven both by cost and throughput, as stamp replication is relatively fast in comparison to traditional EBL methods. With stamp creation becoming more affordable it no longer requires large overheads and ceases to limit fabrication lead times as replicated stamps can be put in situations too risky for large expensive and brittle solid original stamps.

The use of flexible stamps also negates the need for a perfectly level surface, a detrimental issue in spun films due to edge bead formation, imperfections, bubbles and sometimes uneven geometries all together. In a pneumatic NIL system, pressure is applied per unit area and a soft stamp has the advantage of contouring uneven areas better than their more robust counterparts. This is a double edged sword however, as the flexibility offered by these flexible master materials also limit the pressure those pillars can withstand, how well they retain their shape, position and how well they displace the melt.

Table 1-7 – Commonly used soft stamp materials in NIL and UV-NIL Adapted from [136]-[137, 138]. PDMS remains the most popular choice, and is one of the most versatile and adjustable stamp materials. It does suffer from delamination when filling deep or fine features, and has too low a modulus resulting in features flopping especially in the case of higher aspect pillars.

Material	Description	Method of manufacture	Flexural modulus E (MPa)	Strain at break (%)
sPDMS	Soft PDMS (extra initiator) Sylgard 184	Casting	4-1.8 [136, 139]	160 [136]
hPDMS	Hard PDMS (diluted, toluene) Sylgard 184	Casting	≤8.2 [136]	7 [136]
xPDMS	Crosslinking catalysed PDMS (platinum)[140]	Casting	10-8 [138]	116 [138]
Ormostamp	Long stamp lifetime, release force optimized (FI-based modification)	UV-Polymerization [136]	unknown	unknown
FEP	Fluorinated amorphous polymer	Embossing	23 [137]	N/A

Fluoropolymers such as DuPont’s Teflon are ideal candidates to fill this niche, being previously used in various processes requiring non-stick or chemically inert properties [141]. They are well-known for their superior resistance to a wide range of chemicals and solvents which makes them almost impossible to etch, other than for surface functionalization, they also show excellent resistance to molecular adsorption and molecular leaching from the polymer into solutions [142]. Among these fluoropolymers, the semi-crystalline polymer, fluorinated ethylene-propylene (FEP), offers superior optical transparency and a mechanical strength an order of magnitude higher than PDMS. In addition it is biocompatible and differs from PTFE (polytetrafluoroethylene) in that it is compatible with conventional forming methods such as injection moulding, embossing, and extrusion [143]. The fluorine presence gives them hydrophobic behaviour due to their very low surface energy, which makes them virtually non-stick [144]. They are ideal in moulding applications, given their high melting temperatures, which can be as high as 300 °C and are resistant to a variety of harmful environments, including acids and solvents, making them compatible with a variety of photo resists and thermoplastic polymers. The material’s inherent flexibility provides the possibility of covering 3D and 2D surfaces in a manner of modular stamping systems by forming patterns on thin films of FEP ranging from 50-150 µm thick.

The FEP mastering process is considerably cheap when compared to master stamps produced in quartz (qz) or silicon (Si), and can be reproduced very quickly by embossing or direct thermal NIL. The ability to pattern large areas creates the opportunity to scale up the process for industrial applications, and roll-to-roll printing. This can be useful for biomedical and photonic applications by forming nanopatterned bio-interfaces on medical implants and a variety of culture plastics, and overcoming the limits of surface topographical engineering for applications such as high volume cell studies for cell-surface interactions. Moreover, it has already been shown in Ferchichi et al. [145] that a dual scale with a combination of micro- and nano- hierarchical structure can create super-hydrophobic behaviour on surfaces. This hierarchy is also key in the manufacture of differentially patterned zones for tissue culture substrates.

1.4.2 Hierarchical patterning

Hierarchical patterns are widely encountered in nature and create some of the most impressive properties from the lotus leaf's super-hydrophobic surface properties [146] to the feet of geckos which with their 30-130 μm long surface pillars and 200-500 nm long hierarchical 'paddles' allow them to traverse vertical and inverted surfaces [147]. Much work has been done on the formation of both randomly arranged and ordered hierarchical patterns by microstructural means, but this is fundamentally not easy to do, as it requires extra degrees of freedom in comparison to planar patterning, which many micro-fabrication techniques such as EBL [148] do not readily have without modification. One could call a hierarchical structure a 2.5D structure, being a planar surface, but with an inherent modification in the z-axis. The difficulty of producing these structures can be overcome by self-forming methods (Figure 1-9) such as residual stress and thermal shrinking [149] to produce self-organizing structures, and allow what was an initially 2D structure to buckle and arrange itself to produce a hierarchy. Others have employed consecutive direct NIL as a means of building these structures in an engineered manner [150]. Nanoimprint lithography (NIL) is a high-resolution parallel patterning method, mainly aimed towards fields in which electron beam and photolithography are costly and lack resolution at reasonable volumes of production, it has been transferred and is in the process of being applied to rolling embossing systems, and roll-to-roll UV-NIL and NIL systems capable of covering large areas.

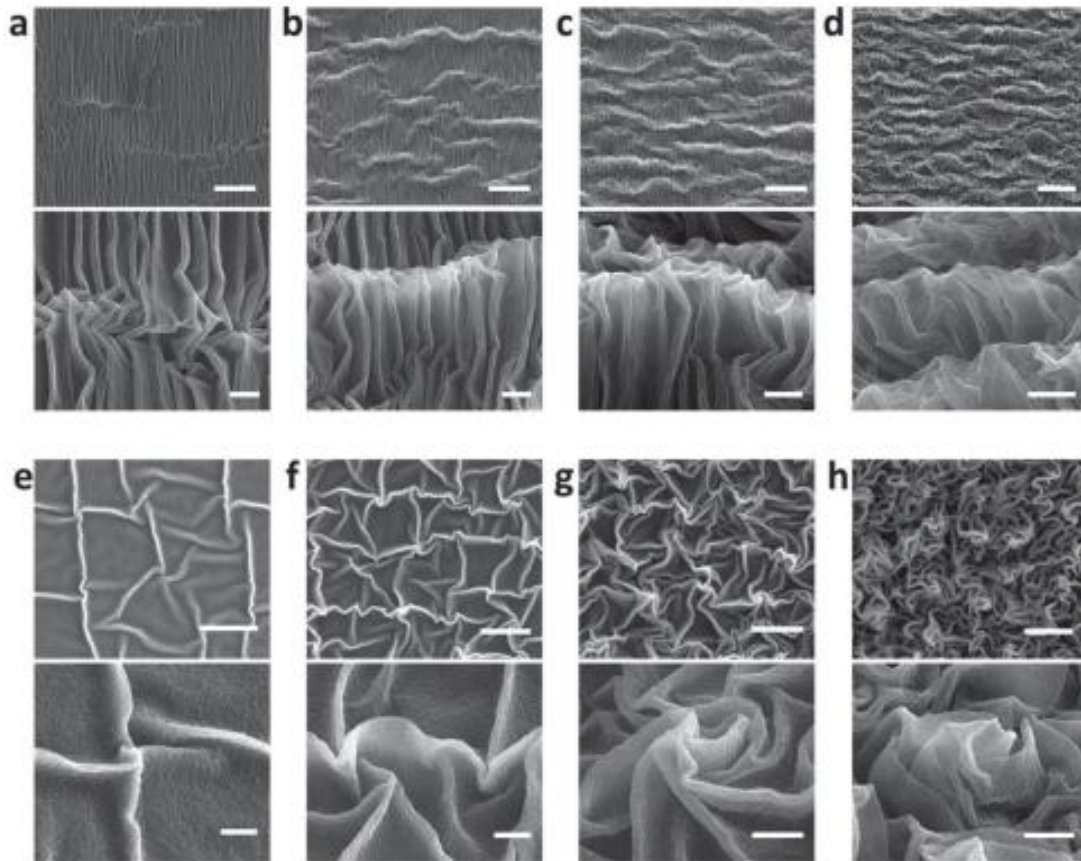


Figure 1-9 – Spontaneous hierarchical structure formation and evolution of hierarchical surface pattern in 13nm gold films on pre-strained elastomer substrates. In the top panel the biaxially strained substrates have a prestrain of $\epsilon_{f1} = 67\%$ and $\epsilon_{f2} = 3\%$ (a), 20% (b), 50% (c) and 67% (d). In the bottom panel the prestrain is $\epsilon_{f1} = \epsilon_{f2} = 5\%$ (e), 30% (f), 50% (g) and 67% (h). Scale bars are 10 μm in top panels and 2 μm in bottom panels of all images. Reproduced with permission from Cao et al. [149].

In contrast to spontaneous and naturally occurring hierarchical structures, which have limited control over the patterns that can be produced, there is significant interest in the manufacture of ordered engineered hierarchies for tissue engineering, as demonstrated by the cell behaviour in Seunarine et al. [148] in Figure 1-10, where a combination of four different hierarchies combining nano-pits and micro grooves led to selective alignment of fibroblasts *in vitro*. Others have employed the spontaneous formation of geometric pits in anodized aluminium to create PDMS stamps with a “hairy surface” topography, made by the intrusion of the PDMS into anodized aluminium surfaces [151].

While PDMS is an excellent stamp material and has also been employed in this work, it is useful in applications where permeability is key, as it will readily diffuse dissolved gases, absorb solvents and even water vapour [152]. These properties are also the same as those which make it unattractive in other more corrosive, hazardous or oxygen inhibited applications (such as many photo curing systems as discussed in Chapter 3).

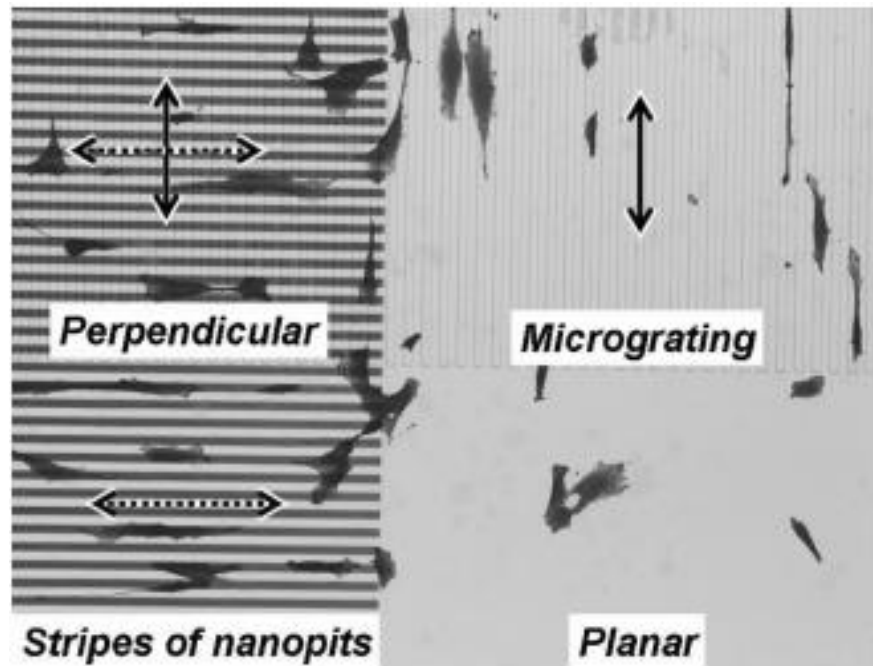


Figure 1-10 - Optical micrographs of cells on the four types of substrate textures. The arrows show the direction of textural features to which the cells may align. A similar grating of 500 nm width and pitch is utilized and converted into a FEP stamp later in this chapter. Reproduced with permission from Seunarine et al. [148]. © 2009 IEEE

Fluoropolymer films show great promise in this area due to their flexibility, relative strength (thin films resist elongation) and as to be shown in this work, their excellent patternability properties, by processes which are significantly faster and more cost effective than traditional hierarchical structure fabrication techniques. An serial embossing approach has been tried before with PMMA by Dumond et al. [153] however these were suspended structures re-flown between two surfaces and that is an issue with many polymers, the lack of any potential for sequential patterning due to high flow speeds and quick deformation of the underlying surface.

1.4.3 3D surface patterning.

The ability to pattern curved or completely non-planar surfaces with high-resolution, and in a cost-effective manner, is essential for many applications. It is the key to transferring nanofabrication technology into both consumer and complex application, such as the coating of implants, patterning of obscure surfaces and making the processability fast and accessible. Traditional methods such as EBL or most commercial lithographic tools cannot shift their basis to circumnavigate a non-planar surface in 360 degrees, and the setups which do this are expensive, and mostly non-existent for small diameter rods. This has in some cases been overcome by using nanoscale apertures in a flexible film [154]. Nickel shims often used in NIL are available in larger feature sizes on curved surfaces [155], but a large and curved nanopattern is an expensive and difficult endeavour. However, simple methods have also been shown of producing high resolution flexible moulds out of PDMS and silicon hybrid structures [155]. Nano colloidal particle deposition onto deformed polymer

microspheres [156]. FEP due to its higher modulus and chemical inertness is the perfect candidate for 3D thermal NIL applications.

1.5 CELL-SCAFFOLD INTERACTION OR THE 'BIOINTERFACE'

In the *in vivo* environment cells are subjected to various combined and time varying mechanical, topographical and chemical cues, these interactions shape embryogenesis, cell migration, differentiation, metabolic activity and generally form the fundamentals of tissue engineering as controllable factors in directing tissue formation and cell behaviour. Within this vast and relatively new area of research, the scope of this work has focused on surface topographical patterning and cell interface interaction, relying on mechanical and topographical engineered modification of substrates and devices to influence cell fate and behaviour in soft tissue engineering, with the aim of controlling stem cell behaviour before during and after differentiation. This requires a sustainable method to run large numbers of experiments to quantify gene expression and identify trends in cell and colony morphology, as indicators of any shifts in their pluripotent state or tendency to a certain line of differentiation.

Making stem cell culture accessible and affordable remains a key challenge in expanding the industry, and the modification of surfaces to aid cell adhesion and cell surface interaction is a substantial part of current tissue engineering research. A variety of available coatings, methods and linking chemicals available to anchor functional groups to polymeric, metallic and ceramic surfaces. The mechanisms of application vary depending on the area of application and cell type, and can have profoundly different effects. With a focus on soft tissue engineering for regenerative medicine, coatings which not only improve stem cell adhesion and proliferation, but also do not interfere with or at least influence cell lineage in a controllable manner are necessary.

1.5.1 Contact guidance

The concept refers to topographical cell interfaces which by their morphology and properties direct the cells to a certain position or behaviour. The variety of patterns and applications is vast, but some key aspects that have demonstrated the remarkable effectiveness of topographical cues include the alignment of epithelial cells with nanogratings [157], the affinity of fibroblasts to settle parallel with grating lines (Figure 1-10), and the ability of stem cell differentiation and multipotency to be controlled by topographical means (Figure 1-11). Contact guidance is reliant on the mechanotransduction via a cell's focal adhesions which, are shown to have a dependence of their size on the sustained force [158]. The force applied on a focal adhesion is purported to induce an elastic deformation of the contact which subsequently triggers conformational and organizational

changes in its constitutive proteins, which has the cascading effect of enhance binding with new proteins that enable the growth of the contact [158]. Contact guidance has been widely used to interface with different cell types to influence cell proliferation, differentiation and cell fate. The range of patterns varies between those which are made by self-organisation, surface roughening and precision engineered surfaces for controllable topography (Figure 1-11).

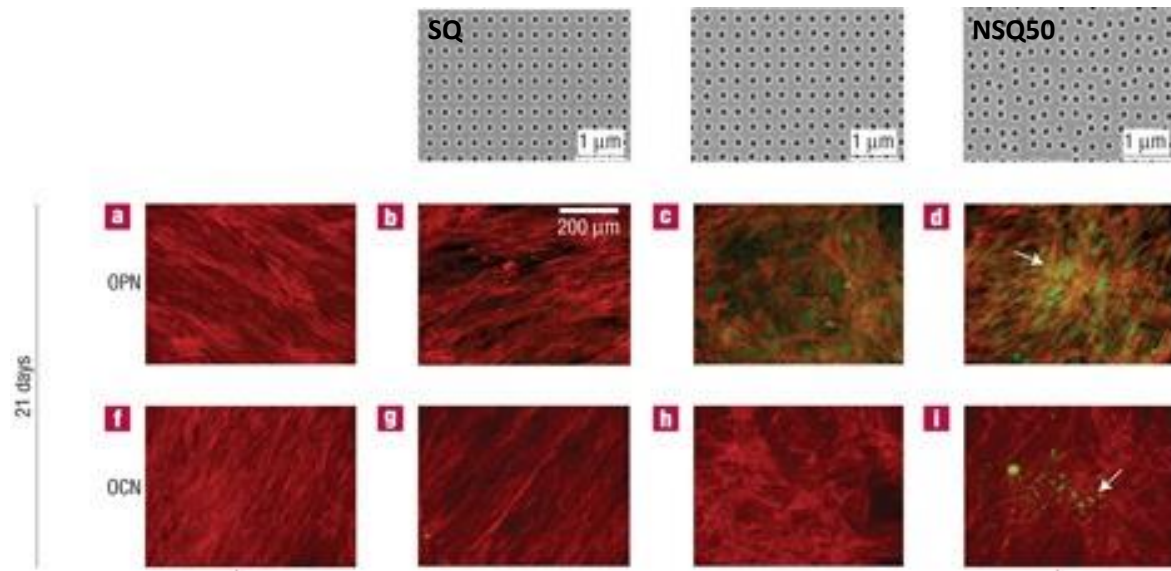


Figure 1-11 – The spontaneous differentiation of MSCs into osteoblasts on ‘near-square’ nanopatterned surfaces. Surface patterned with pits arranged in increasingly disordered configurations, with osteoblasts labelled green, MSCs labelled red. Pattern with preferential bone formation is NSQ50 (d and j), with 150 nm diameter pits arranged on a 2:1 pitch, with a 50 nm degree of disorder. Reproduced from McMurray et al. [159].

There has been significant progress with engineered nanotopographies, from those that control cell alignment and clustering behaviour, to those which sustain pluripotency in mesenchymal stem cells, or direct them into osteogenesis as seen in Figure 1-11. In this case responsive actuators will be made using high throughput methods such as photolithography [120], soft lithography [54] and UV-NIL [40,141] to achieve high throughput methods for the capture and differentiation of cells into 3D nanopatterned niches.

The topography induced differentiation seen in mesenchymal stem cells (MSCs) (Figure 1-11) demonstrates that the principle has previously been applied to stem cell differentiation. While the hESCs mentioned later in the text follow very different differentiation pathways, it is considered possible but has been noted by the author. The line of hESC differentiation is shown for the creation of hepatic tissue in Figure 1-16, albeit by chemical stimuli and not topographical cues.

1.5.2 Surface chemistry

In vitro maintenance of human pluripotent stem cells (hPSCs) requires the cells to be cultured in the correct media and a favourable microenvironment. hPSCs are routinely cultured in vessels

containing complex media and 'plated' onto non-standard culture surfaces which provide their microenvironment. The signalling pathways regulated by growth factors in the media [160] and by available ligands [161] and physical properties of the substrate [162] all contribute to downstream maintenance of pluripotency or directed lineage in pluripotent stem cells.

To achieve rapid and high volume analysis, with the relevant controls; a coating or treatment method compatible with tissue culture plastic (TCP) was also a requirement. Protocols for cell culture across laboratories the preparation of culture substrates varies, traditionally feeder layers of cells [163] were implemented to create binding sites for stem cells in this arrangement the initial feeder cells created the ECM and ligands for stem cells to plate on to. In current processes, with the advent of isolation and commercialisation of the ECM in products such as Matrigel® [164] a large variety of ECM constituent proteins and peptides [165] has been implemented as coatings [166], gels and self-assembled monolayers (SAMs). In particular collagen, integrin [167], laminin [164], fibronectin [168] and vitronectin[169] amongst others, have been the focus of many studies, with some now implemented in commercial TCP and flask products such as Synthemax® and StemAdhere®. Figure 1-12 is taken from a recent review by Lamshead et al. [161] and illustrates the binding sites of human pluripotent stem cells on various plating media and ECM constituents as well as their proposed interaction.

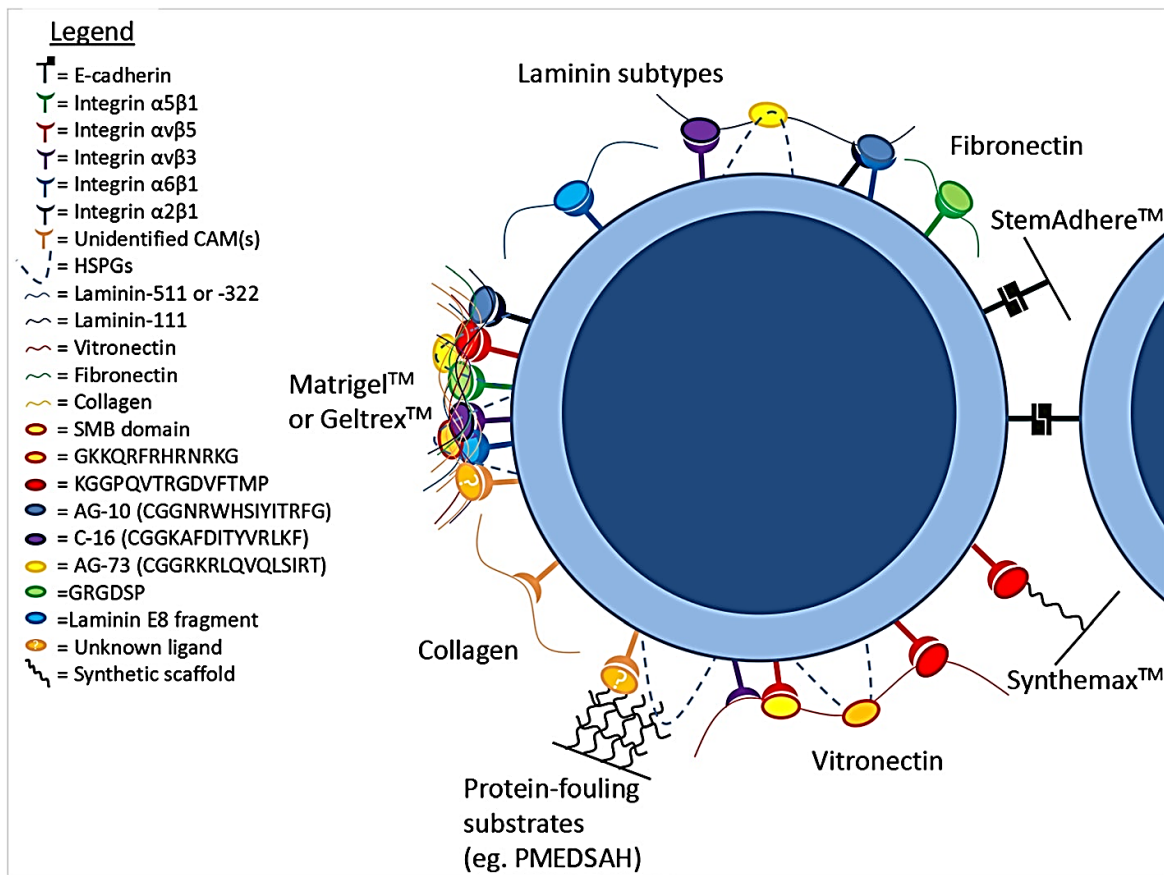


Figure 1-12 –An illustration of chemical interactions between human pluripotent stem cells (hPSCs) and culture surfaces. Specific ligands and cell adhesion molecules (CAMs) are included if they have been reported in hPSC attachment and/or culture studies. CAMs involved in hPSC adhesion include integrin subtypes $\alpha 5\beta 1$ (green), $\alpha v\beta 5$ (red), $\alpha v\beta 3$ (purple), $\alpha 6\beta 1$ (blue) and $\alpha 2\beta 1$ (navy blue), E-cadherin (black blocks), heparan sulphate proteoglycans (HSPGs; dashed blue lines) and unidentified CAMs (orange). Ligands are portrayed as coloured ovals and include the SMB domain of vitronectin (yellow/red), GKKQRFRRNRKG (orange/red), KGGPQVTRGDVFTMP (red/dark red), AG-10 (CGGNRWHSIYTRFG; blue/dark blue), C-16 (CGGKAFDITYVRLKF; purple/navy blue), AG-73 (CGGRKRLQVLSIRT; yellow/orange), GRGDSP (green) and laminin E8 fragments (light blue/blue). The ligands are presented by ECMPs [represented by curved coloured lines: laminin-511 or -322 (blue), laminin-111 (navy blue), vitronectin (red), fibronectin (green) collagen (yellow)] or synthetic surfaces (thick black lines) including Synthemax™, StemAdhere™ and PMEDSAH. On the left of the image complex extracellular matrix extracts (e.g. Matrigel™ and Geltrex™) are illustrated as combinations of ECMPs, and on the right cell-cell adhesion is simplified in the extreme to illustrate homophilic E-cadherin binding. Where specific ECMP ligands are poorly-defined, CAMs are shown to interact with the ECMP line. Where specific CAMs have not been identified the orange CAM is used, and undefined, adsorbed ligands are represented by orange ovals with a white question mark. Reproduced from Lambshead et al. [161]

The application of these ECM constituents is often done via aqueous deposition with the level and durability of the coating dependant on the surface chemistry, anchoring type and surface roughness. In addition to the well documented modification of tissue culture plastics for biology [79, 99, 166], numerous methods exist for the selective binding to gold by the use of sulphate chemistry [156], and more broadly binding to metals, plastics and hydrophilic surfaces by using DOPA ‘click’ chemistry derived from polyphenol oxidase used in anchoring of mussels to the sea floor or other structures [170].

In applications where cells can potentially stick without pre-coating with ECM such as fibroblasts and other soft structural cells [166], environmentally responsive molecules such as NIPAAm can be immobilized on surfaces, based on thermally, chemically and radiation modulated surfaces with switchable wettability [79]. The switch can cause cells to attach and release depending on the state of activation of the coating [171]. In stem cell culture pre coating with a cocktail like Matrigel®, fibronectin, vitronectin and laminin are also often used due to their susceptibility to apoptosis, or loss of pluripotency due to stress and necessity to manufacture large quantities of their own ECM [172].

1.5.3 ECM and protein self-organization.

There have been notable studies into the self-organization and ordering of extracellular matrix (ECM) constituent proteins, on various polymer surfaces [173] consisting of vinyl chains with COO⁻ (deprotonated COOH) side groups. In that recent work [173] the Salmeron-Sanches group noticed that while the absorption of fibronectin was constant across the samples, the self-organization of these proteins changed as is clearly visible in the matrix (Figure 1-13). This area of molecular assembly and geometricity at the nanoscale was modulated with changes in substrate mechanical properties to yield changes in osteoblast response. It is clear that chemical, mechanical and topographical cues regulate the differentiation and proliferation of various cell types, and it is these arrays of modulation that are of interest in building a functional 3D cellular niche.

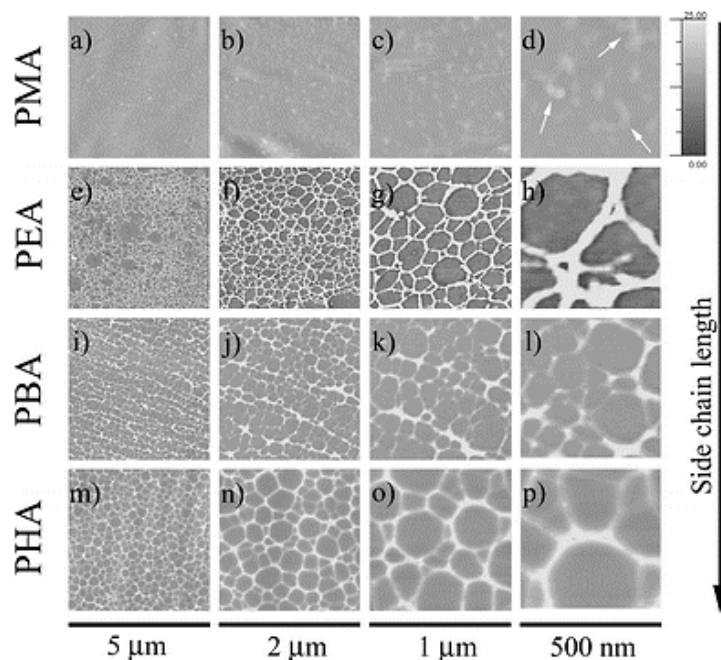


Figure 1-13 - Self organization of fibronectin on different polymeric substrates shows the potential for geometrically mediated signalling by the tendency for the fibronectin to organise based on surface concentration. FN organisation and distribution on the surface then depends, for each substrate, on the concentration of the initial protein solution from which the protein is adsorbed. Reproduced with permission from Guerrero et al. [173]

1.5.4 Surface stiffness

In addition to the modification of surface chemistry to aid cell adhesion, substrate elasticity plays a large part in the proliferation and viability of cell cultures, in particular cultures of ESCs and iPSCs which are very susceptible to apoptosis [172]. The term elasticity in this case refers to Hookean elasticity, where a material loaded in uniaxial tension shows a direct proportionality between the tensile stress (σ) in the material and the applied tensile strain (ϵ).

$$\sigma \propto \epsilon \quad \text{Eq. 1-8}$$

The constant of proportionality is the Young's Modulus (E) of the material, where:

$$E = \frac{\sigma}{\epsilon} \quad \text{Eq. 1-9}$$

While most polymeric biomaterials and certainly tissues within the body exhibit hyperelastic and or viscoelastic behaviour. These factors will be ignored in the discussion of nanofeatures and cell interaction due to the relatively small perturbations in strain, the linear elastic range of the surface is unlikely to be exceeded.

These materials are then assumed to be elastic and thus conform to Hooke's Law where the stress-strain response of a material is independent of time and the strain in the material disappears completely on removal of the applied loading. The moduli of materials range from 0.1 kPa for some hydrogels to 1000 GPa for Diamond at the extreme end of the scale. The range of proteins lies between 1 MPa and 5.4 GPa, and tissue macro elasticity of between 100 kPa and under 10 GPa [174]. The range of gels synthesised for biomedical and life science applications often lies within the range of 0.2-120 kPa [175].

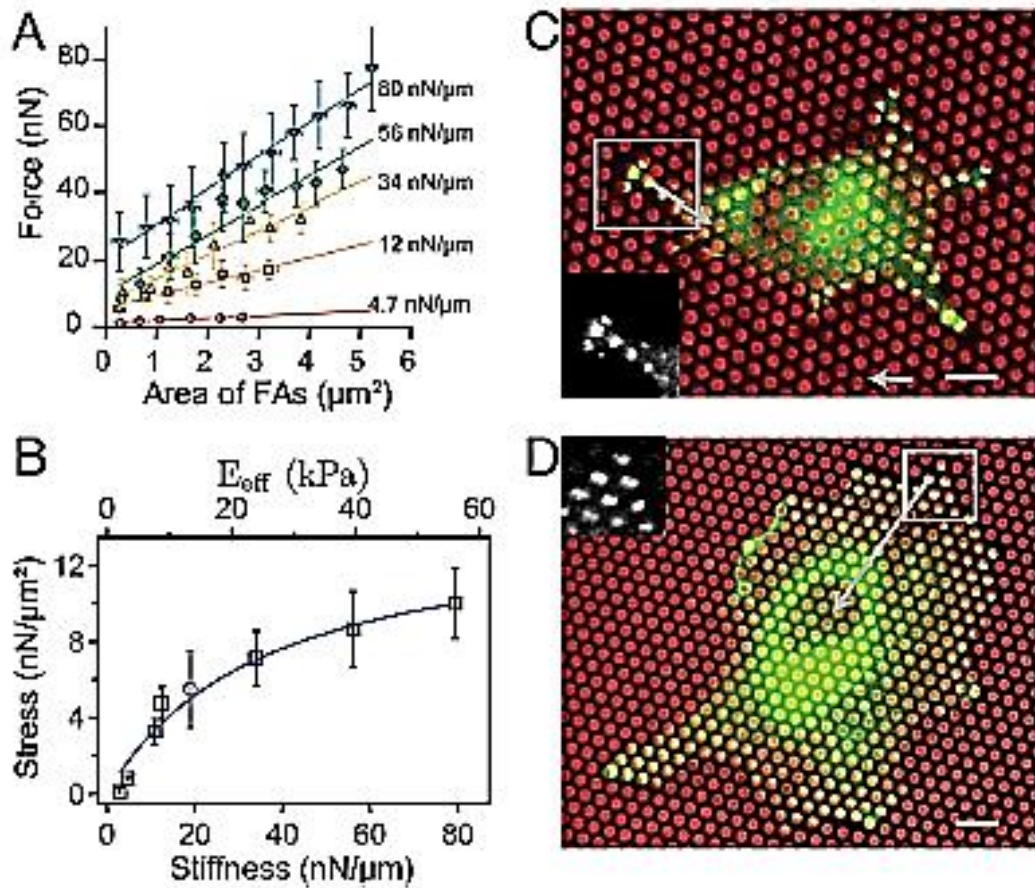


Figure 1-14 – The relationship between focal adhesion area (FA) and transduced force, and the correlated force to pillar stiffness and effective modulus of the substrate of pillars if it were represented by an infinite flat surface. A decrease in pillar stiffness is equivalent to a material of lower stiffness, such as a transition from a plastic to a rubber like hyperelastic material which will accommodate larger displacements due to loading. Scale bars: 10 μm . Reproduced from Trichet et al. [158].

In addition to the modulation of 2D patterned structures it is possible to fine tune the mechanical properties of planar substrates, and hydrogels are very useful. Hydrogels are easily adjustable by varying the extent of crosslinking. The modification of the substrate allows for a range of stiffness that can mimic or exceed the properties of natural biological tissues as illustrated in Figure 1-15.

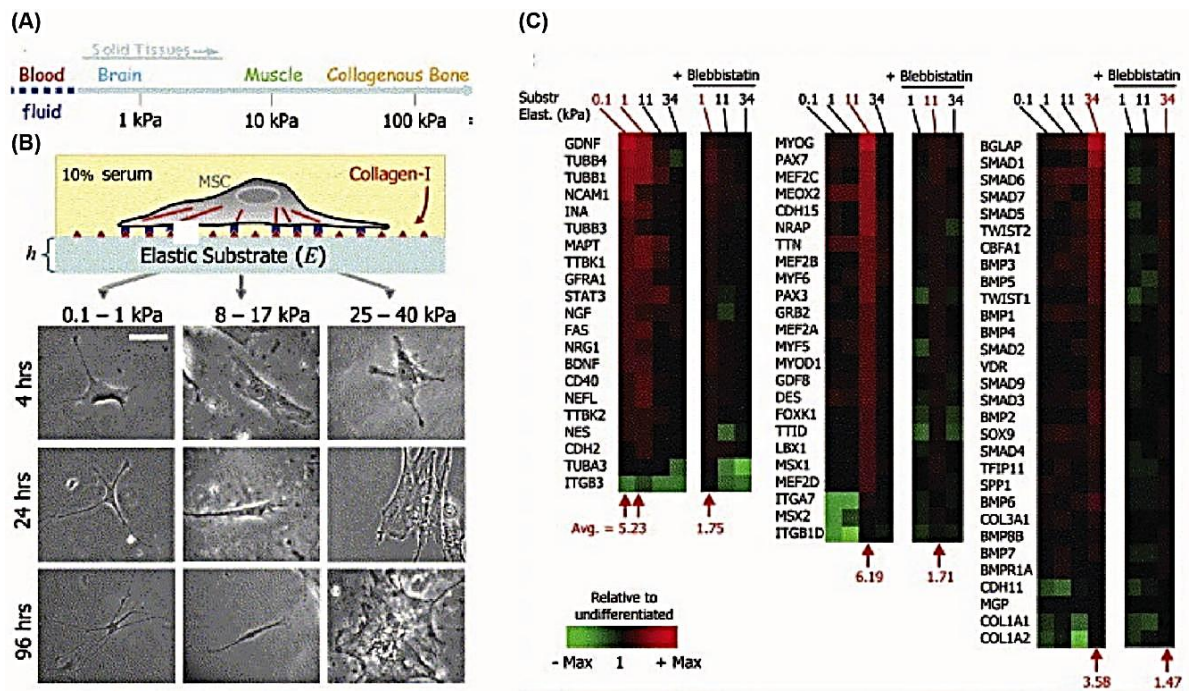


Figure 1-15 – Changes in MSC gene expression with varying substrate stiffness. Correlation was seen between reduced cell proliferation on softer substrates. Gene expression shown in C.) shows the genes which are down regulated in (red) and genes which are up regulated in (green), showing lineage specific signalling depending on substrate stiffness. Scale bars 20 μm . Reproduced from Trichet et al. [158].

1.6 THE USE OF HESCS FOR TISSUE ENGINEERING

HESCs and more recently iPSCs are capable of differentiation into a multitude of germ layers, and could be considered the ultimate starting point to engineering a variety of tissues including the liver. The control of the hESC differentiation by topographical cues has not yet been demonstrated to the same extent as bone and muscle forming MSCs. Cultures of ESCs traditionally show key morphological stages, where cells seeded as a dispersion or in very small clumps grow and form small colonies, these in turn form a web-like network and eventual confluence as the volume of cells continues to grow. The colonies are smooth with cell-to-cell proximity and interaction a key determinant in cell survival [176]. Generally it is observed that human embryonic stem cells (hESCs) display a high rate of apoptosis in culture, contributing to the problems of efficient mass culture of these cells and subsequent differentiation for organ growth [177]. The full system that regulates this high mortality is still under debate, although it has been suggested that cell-to-cell contact provides crucial signals, perhaps mediated by the NOTCH system, for the proliferation of undifferentiated human pluripotent stem cells, in the absence of Rho-associated protein kinase inhibitor (ROCK-i), contact plays a large role in this high mortality, with single cells left stranded outside the main cluster readily undergoing apoptosis. It is for these reasons that the normal protocol calls for cells to be passaged by the so called ‘clump’ method, where they are split every 4–5 days at ratios of 1:3 or even 1:2 and re-plated in small clumps with a loss of up to 90 % of cells from cultures [178]. These

losses are eventually overcome by subsequent passaging and age of the derived cell line, with those exhibiting more consistent and strong growth characteristic falling under the coined term 'adapted' or karyotypically abnormal hESCs. Both lines are sensitive to cell-to-cell proximity, and the separation and plating of cells as individuals can be overcome by treatment with ROCK-i. However, according to Barbaric et al. [177] the time from initial plating to the first passage was shorter for the normal cells (8 hr) than for the normal or adapted cells treated with ROCK-i (12hr), in subsequent passages this difference was no longer noticeable. They also demonstrated that adapted cells showed a linear increase in cell numbers in respect to the plating density, while normal cells showed a quadratic relationship between cell-plating density and population growth. The presence of ROCK-i was shown to alleviate most bottlenecks in hESCs culture in the most critical period initially after seeding. It was for these reasons that initially both clumped and single cell approaches were used in this work to investigate the effect of topographical signalling, followed by subsequent plating with inhibited hESCs to look at cell to substrate interaction and colony formation morphology. While the pathway regulation in hESCs is likely to be very different from keratinocytes, it is proposed that the failed integrin clustering on soft surfaces, or another interaction trigger, is responsible for regulation of hESC behaviour and has a knock-on effect on colony formation and the rate of cell death that leads to the formation of critical cluster sizes. The spatial organization of hESCs into clusters has been observed in Peerani et al. [179] to affect the modulation of local cell density can be used to generate directed patterns of self-renewal and differentiation.

It was found that the lowering of cell density in a cluster significantly decreased pluripotency markers in the form of an increase in pSmad1 levels which Siller et al. [172] correlated as having an inverse relationship with pluripotency which was seen with increasing colony size in hESCs. Furthermore Bauwens et al. [180] showed that controlling colony size lead to changes in hESC colonies controlled the level of pluripotency gene expression and the resulting ratio of endoderm-associated to neural-associated cells in the colony varies as a function of colony size also visible in the stages of clustering shown in Figure 1-16.

What can be drawn from all this information, and what is without exaggeration a very broad field of interest, is that cells depend on a variety of mechanisms which inform them about their environment, and provide the necessary signals for them to perform very complex and coordinated functions. So far many attempts have been made to both control cellular behaviour by the synthesis of bioactive materials, the manufacture of designed topographies and creation of fine-tuned chemical signals. Many methods of producing 3D structures out of 2D manufacturing methods by folding have also been demonstrated in the past.

The one thing which is lacking and which sets the precedent for this work is that of a nanopatterned, “smart” container which is capable of sustaining cells in a fine tuned and engineered niche, open to chemical signalling, but ordered in a controllable manner to reproduce the complex 3D structures many cell types experience in their native environment.

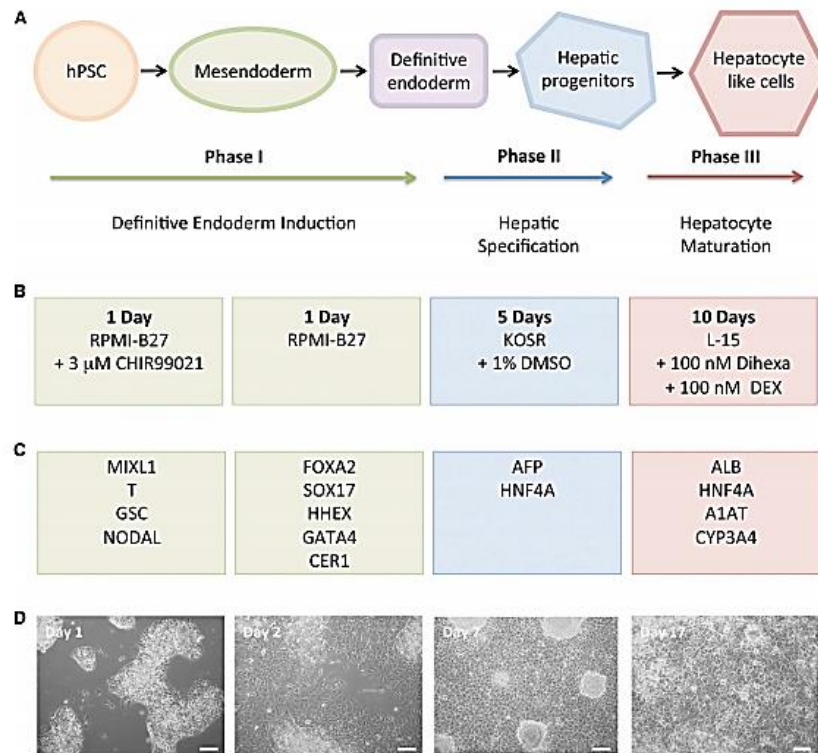


Figure 1-16 - The process of differentiating hESCs into hepatocytes by the small molecules process demonstrated by the Sullivan group at the University of Oslo. Illustration, showing the stages between seeding hESCs and obtaining hepatocyte like cells. A.) Three phase process transitioning from a definitive endoderm to hepatic specification and hepatocyte maturation. B.) The chemical changes made in the media to move the cells through the specific stage. C.) Changes in gene up regulation during this stage of differentiation D.) Morphological changes in cell clustering during the specific stage. Reproduced from Siller et al. [172].

The bulk of this work aims to create just this environment, and combines nanopatterning techniques with “smart” actuators which are not only cell culture compatible, but permeable to nutrients. The containers may then be used and tuned to specific cell culture applications by modifying the surface chemistry, topography chemical environment and cell line. While not every possible gel chemistry, cell line and pattern have been tested, this work provides a pilot platform and a proof of concept that this can be achieved using traditional MEMS and electronics manufacturing techniques.

Objectives of this work

- Produce methods for the simple and quick nanopatterning of biocompatible surfaces.
- Produce a means of translating these patterns into functional assembled 3D structures.
- Make the assembly of 3D structures or niches compatible with cell culture processes.
- Apply structures to cell culture with the ultimate aim of culturing and differentiating stem cells into functional tissue within the 3D constructs.

Strategies

The objectives of this work will be achieved using the following strategies:

- Photolithography for definition and manufacture of 3D containers.
- Nano-imprint lithography for rapid nanopatterning of surfaces of the 3D containers.
- Hydrogel thin film bilayers for assembling 2D patterned surfaces into 3D constructs.
- Cell culture with cell lines such as hTERT fibroblasts for determining the effect of patterning on walls of self-folding containers.
- hESC culture on nanopatterned surfaces as a feasibility study into the formation of organelles from undifferentiated cells within 3D cellular niches.

2 NANOPATTERNING TECHNIQUES

2.1 INTRODUCTION

To be able to pattern complex geometries it is essential to create a versatile and easy method of manufacture, which allows the rapid reproduction of nanopatterned surfaces. This is especially the case in tissue culture and anything which is intended to be used in large scale studies, or further down the line with scaling up into production. This chapter focuses on the fast methods of nanopattern mastering and transfer into more complex 2.5D hierarchical surfaces such as curved planes and hierarchical structures. These methods form a versatile foundation for the manufacture of smart nanopatterned containers and are the stepping stone towards engineered 3D environments. The available methods range from slower processes such as electron beam lithography (EBL) through to the higher throughput nanoimprint lithography and the various subdivisions of the field such as screen printing and roll-to-roll printing.

One problem with the manufacture of 3D patterned surfaces is that all manufacturing methods are inherently 2D, and all stem from some form of printing, whether it is layer by layer deposition, casting or layer by layer removal of material. Even more critical is nanopatterning, which due to the immense precision of the processes required to do it (nanoscale focusing of energy beams) is immensely slow.

A way to avoid the slow throughput and create more opportunities for these nanopatterns to be utilized is to find a method of reproducing these patterns in a more rapid fashion, by producing replicas from a master surface. This can be injection moulding against a master shim, or casting a polymer or solution on top of a master stamp and then reproducing this master in a secondary material. The currently available methods of reproduction, often have to be performed under precisely controlled pressures and temperatures, resulting in severe challenges with patterning anything that is uneven in topography or needs atmospheric control.

This chapter discusses many of the methods developed which tackle these challenges. Ways of reproducing nanopatterned master stamps quickly in materials capable of conforming to uneven and even curved and fully round surfaces will be demonstrated. Their use in the manufacture of foldable 3D geometries will then be shown as a proof of concept work, thus transferring these 2D techniques to the manufacture of so called 2.5D and 3D structures for the formation of cellular niches.

2.2 MATERIALS AND METHODS

2.2.1 Materials

Fluorinated ethylene propylene (FEP) films manufactured by DuPont were obtained from RS-Online as 304 x 200 mm films in thicknesses of 0.025 mm and 0.127 mm. Sylgard 184 (PDMS) and curing agent were obtained from Dow Corning via Farnell its UK based distributor. All reagents and commercial photolithographic resists were obtained from the distributors and used as intended without modification. Polymethylmethacrylate (PMMA) Mw 84,000 (Elvacite 2010 DuPont) was dissolved in o-xylene at a concentration of 8 %.

2.2.2 Instrumentation

2.2.2.1 AFM and surface profilometry

High resolution metrology was done using a Veeco Dimension 3100 atomic force microscope (AFM). The characterization of topographies was done via AFM in contact mode with a 10 nm diameter silicon cantilever tip. Samples were kept immobile on a stage while the tip scanned rectangular surface profiles, speed was adjusted depending on surface rigidity and size of features. This method provides accurate depth data if the tip can reach the base of a feature. For lateral dimensions there may be inaccuracy due to the conical tip geometry. Additionally surface profilometry and micro feature height were measured in scanning mode with a Veeco Dektak 6M Height Profiler, where the resolution provided by AFM was not suitable.

2.2.2.2 SEM sample preparation

Scanning electron microscopy (SEM) Imaging was done using a Hitachi S4700 SEM. Non-hydrogel samples made from SU8 epoxy or injection moulded ones were washed in isopropanol, not water followed by evaporation in a vacuum and oxygen plasma ashing to descum. Ashing duration was 6 s at 80 W RF power.

2.2.2.3 Nanoimprint lithography (NIL)

Nanoimprint lithography (NIL) was performed using an OBUCAT NIL-2.5 thermal Nano imprinter for patterning of sacrificial layers and master transfer and replication. The process is discussed for the specific imprint material in each section, these included polyacrylic acid (PAA), polymethylmethacrylate (PMMA), fluorinated ethylenepropylene (FEP) and SU8 Epoxy.

2.2.2.4 O₂ Plasma ashing

Ashing refers to the removal of thin fouling layers, or residues at the base of imprinted features with an oxygen plasma, and is the final cleaning and surface functionalising stage in many processes.

Samples and wafers were descummed and functionalized by use of an oxygen plasma asher at varied doses of 60-200 W.

2.2.2.5 Dry etching

During patterning, silicon (Si) and quartz (qz) dry etching was performed in STS ICP RIE and Oxford Instruments RIE80+ respectively. The process is discussed further in sub-section 2.2.3.1.

2.2.2.6 Sputtering

Metal deposition was done in a Plassys MEB 550S Electron Beam Evaporator for Au, Ti and NiCr deposition up to 100 nm in thickness

2.2.2.7 Contact angle measurement

Contact angle measurement was performed using a Biolin Scientific – Attension Theta Lite optical tensiometer. The data was used to identify chemical changes among various patterned surfaces. The surface wetting correlates to surface energy and roughness, key to adhesion of certain cells.

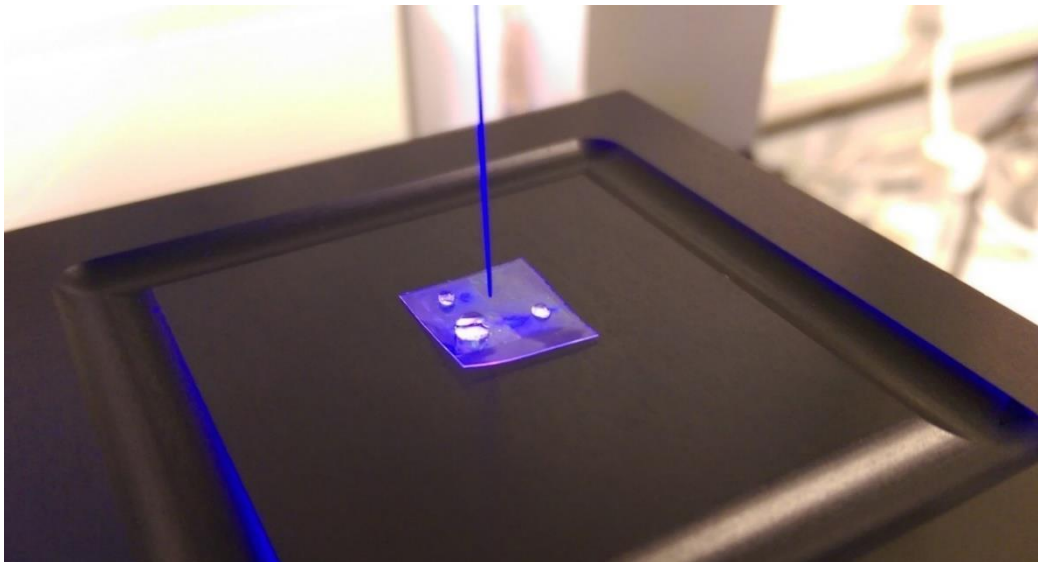


Figure 2-1 - Contact angle measurement of an FEP film by optical densitometry. Droplets were dispensed on surface and imaged in silhouette illumination mode.

The model of contact angle is shown in Figure 2-2, where γ_{SG} , γ_{SL} and γ_{LG} are the interfacial free energies per unit area of solid-gas, solid-liquid and liquid-gas boundaries respectively[181].

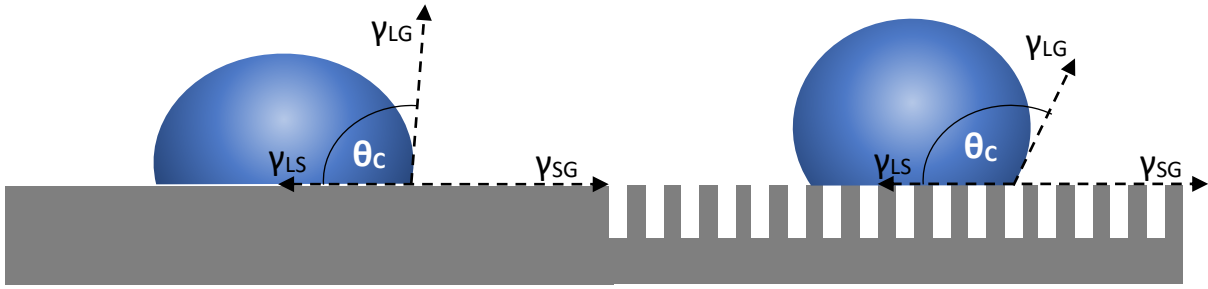


Figure 2-2 - Diagram of surface energy interactions at solid, liquid and gas interfaces, and their effect on contact angle of liquid droplets on planar and patterned surfaces in the Young (left) and Cassie-Baxter state (right). The presence of a nanopattern creating a higher contact angle as the droplet sits in a suspended higher energy state.

Wenzel's equation [182] describes the effect of surface topography on a drop in contact with a rough surface in a fully wetting state [25] and suggests that the surface roughness amplifies the surface interaction be it hydrophobic or hydrophilic resulting in a higher or lower contact angle respectively.

$$\cos \theta_C' = \frac{\gamma_{SG} - \gamma_{LS}}{\gamma_{LG}} = r \cos \theta_C \quad \text{Eq. 2 - 1}$$

The Cassie-Baxter model [183] takes into account for changes in contact angle when air trapping in the topography leads to a further amplified hydrophobicity due to increased drop free surface and thereby Gibbs free energy (Figure 2-2). This is described by the Cassie-Baxter equation:

$$\cos \theta_C' = r_f f \cos \theta_C + f - 1 \quad \text{Eq. 2 - 2}$$

Where γ_{SG} , γ_{SL} and γ_{LG} are the interfacial free energies per unit area of solid-gas, solid-liquid and liquid-gas boundaries respectively [181]. r is the roughness ratio of true area of the solid surface to the apparent area, substituted for with r_f is the roughness ratio of the wet surface area, and f the fraction of solid surface area wet by the liquid, in the Cassie-Baxter equation with ϑ_c as the contact angle, and ϑ_c' the contact angle on a nanopatterned surface [162, 183]. Wenzel's equation suggests that structuring a surface amplifies the surface effect i.e. a hydrophobic surface becomes more hydrophobic, a hydrophilic surface becomes more hydrophilic[181]. The above relation for wettability[162] lets us predict that surface patterns will amplify contact angles by increasing the surface roughness when compared to the planar material (Figure 2-3).

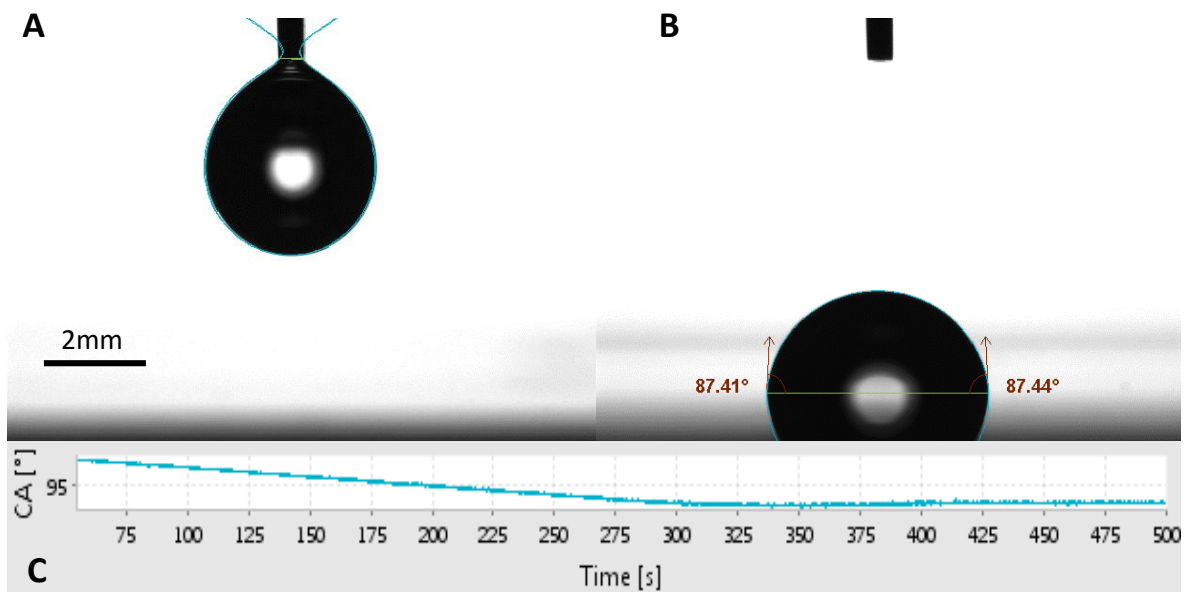


Figure 2-3 – Left to right: contact angle measurement, with water droplet before and after contact with a untreated silicon surface. Bottom: trace of contact angle over time shows the droplet reaching a steady state contact angle at roughly 300 seconds.

The purpose of measuring the contact angle is to find good surfaces for cell attachment, as wettable surfaces are conducive to cell attachment, due to the better spreading of the media drop, and to some extent correlate with the attachment of the cells themselves. It is also useful for determining good imprint materials, as those with high contact angles are less likely to stick and adsorb melted polymer or solvent cast solutions.

2.2.3 Methods

2.2.3.1 Manufacture of quartz (qz) master stamps

Nanopatterned quartz (qz) stamp utilized for patterning of the FEP film were fabricated from standard 25 × 25 mm and 1 mm thick quartz samples. Electron beam lithography, metal lift-off and reactive ion etching (RIE) were used to create the patterns. Quartz (qz) is an ideal master stamp material due to its strength and transparency, it is harder to shatter than silicon in the author's experience it is also a frequently used material in microfabrication with known etch protocols.

The process used electron sensitive poly(methylmethacrylate) (PMMA) of Mw 84,000 at 4 w/v % dilution in o-xylene. This was spun at 5000 rpm for 60 seconds followed by a 180 °C bake for 15 minutes. A second layer of PMMA at Mw 193,000 2.5 w/v % dilution in o-xylene was then spun on top of this layer at 500 rpm for 60 seconds. The purpose of the bi-layer is that larger molecular weight chains are less soluble in the developer after electron forced chain scission (process by which EBL pattern is achieved in this 'positive' lithographic resist). This difference in solubility creates an undercut in the resist. The undercut profile was to aid future metal lift-off, as it would prevent

sputtered material sticking to the walls of the pit, thereby preventing it from being ripped off during dissolution of the PMMA mask.



Figure 2-4 - Process for the nanopatterning of quartz master stamps by electron beam lithography (EBL), undercut development of PMMA resist layer aids lift-off without removing NiCr features during the lift-off step. The NiCr etch mask is applied by sputtering and then acts as to increase selectivity for the reactive ion etching (RIE) of the qz surface.

Prior to defining the desired nanopattern, using an electron beam lithography tool, a discharge surface layer is required as both the quartz (qz) and polymethylmethacrylate (PMMA) of the stack has too low electrical conductivity. A build-up of surface charge from the electron beam exposure can occur on non-conductive substrates, causing poor resolution and repeatability and thus pattern deformity. In most cases 10 nm of aluminium (Al) was evaporated onto the samples to act as a charge dissipating layer. Electron beam lithography was done by defining dosage and spot information in L-edit software and Layout Beamer software to define the regions to pattern, the process is the same as that described in the work of Vasiev et al. [1] and Greer et al. [184]. The machine used to produce the patterns was a Vistec Gaussian Vector Beam 6 (100 kV) electron beam lithography tool. The author did not produce novel pattern geometries but used well established patterns and doses created within the group which had been used in previous work on cell contact guidance [162] and [185]. The nanopattern design for the stamps varied from an ordered array of 250 nm diameter circles with a pitch of 500 nm covering a square area of 5 x 5 mm to 300 nm lines with 300 nm spacing covering four areas of 5 x 5 mm rotated 90°.

Following exposure, the Al discharge layer was removed with tetramethylammonium hydroxide and the PMMA developed in a Methyl isobutyl ketone (MIBK): Isopropanol (IPA) in a 1:1 solution. The sample was then descummed in an O₂ plasma for 1 minute at 60 W. NiCr has been shown to be an effective hard mask for RIE with qz nanofeatures [186]. To act as an etch mask 50 nm of NiCr was evaporated onto the PMMA coated qz face to produce the necessary selectivity for the nanofeature etch mask. Thereafter the PMMA resist was 'lifted-off' in acetone and a further oxygen plasma descum was performed. The penultimate step in the qz stamp fabrication was the transfer of the defined hard mask features into the qz. In order to achieve this an Oxford Instruments Plasmalab 80

plus RIE machine was used with a mixture of CHF_3 and Ar gases at flow was 25 sccm for CHF_3 and 18 sccm for Ar gas, at a process pressure 30 mTorr, the RF power was set at 200 W and temperature of 20 °C. The qz was etched to a maximum depth of 250 nm producing robust nanofeatures over 35 nm/minute etch rate. Finally any remaining NiCr on the top of the pillars was removed by giving the sample an agitated emersion in a solution of ceric ammonium nitrate and nitric acid (chrome etch) for 1 minute at a rate of 60 nm/minute.

2.2.3.2 Manufacture of silicon (Si) master stamps

Silicon (Si) stamps were fabricated for thermal nanoimprint lithography (Thermal-NIL) on Si substrates with varying size between 10 and 30 mm square. The substrates were initially cleaned with piranha solution (3:1 concentrated sulfuric acid to 30 % hydrogen peroxide solution) for 10 seconds followed by washing in H_2O , then acetone, methanol and isopropanol (IPA) in stages for 3 minutes each. After a dehydration bake the wafers were spin coated with HSQ into which the nanopattern would be written. The design was then transferred to the silicon substrate by inductively coupled plasma (ICP) dry-etching. In this process the gas used for dry-etching was $\text{SF}_6/\text{C}_4\text{F}_8$ [187] at a flow rate of 30 sccm SF_6 and 90 sccm S_4F_8 in 12 mTorr at 20 °C. The coil power of 600 W was used, with a platen power of 12 W producing an etch depth of 150 nm/min.

2.2.3.3 Manufacture of PDMS replica stamps

Polydimethylsiloxane (PDMS) micropatterned replica stamps were made by spinning SU8 3000 series resist on a silicon wafer followed by exposure through a photo mask and subsequent development. The master was coated by evaporated silane to act as a release layer to prevent adhesion. Sylgard 184 PDMS (Corning) was mixed at a ratio of 10:1 to curing agent and poured onto the master pattern in a salinized glass dish. It was then sonicated for 2 minutes and de-aerated in a vacuum for 30 minutes prior to curing in an oven for 3 hours at 70 °C. The stamps produced by this method were flexible and transparent, but thickness control and mechanical properties limit its application, as does the apparent swelling of PDMS in some solvents [138].

2.2.3.4 Manufacture of FEP stamps

Fluorinated ethylene propylene (FEP) is an excellent stamp replicating polymer, as an amorphous form of Teflon and a thermoplastic, it is easy to emboss and retains its shape readily after cooling, resulting in excellent feature reproducibility. The absence of recrystallization on cooling also limits residual stresses and limits film buckling as it cools. Nanoimprint lithography was carried out in an Obducat Nanoimprinter tool NIL-2M. The advantage of using an Obducat NIL tool is the precise control over pressure and temperature which can be carried out over a range up to, 60 bar and 300

°C. Such a high temperature is sometimes useful for fluorinated polymers whose melt temperatures are relatively high.

To find optimum imprint conditions and find a starting point an embossing temperature was found from converting the yield stress data from DuPont’s product information into units of pressure (bar) produced a range of imprint conditions that are necessary to deform the film into a new shape, these are found to be ≈15 bar at 200 °C or ≈10 bar at 270 °C shown in Figure 2-5. While this does not correlate directly to compressive strength, it gives an indication of when polymer chain mobility is great enough to allow the polymer to be deformed under pressure.

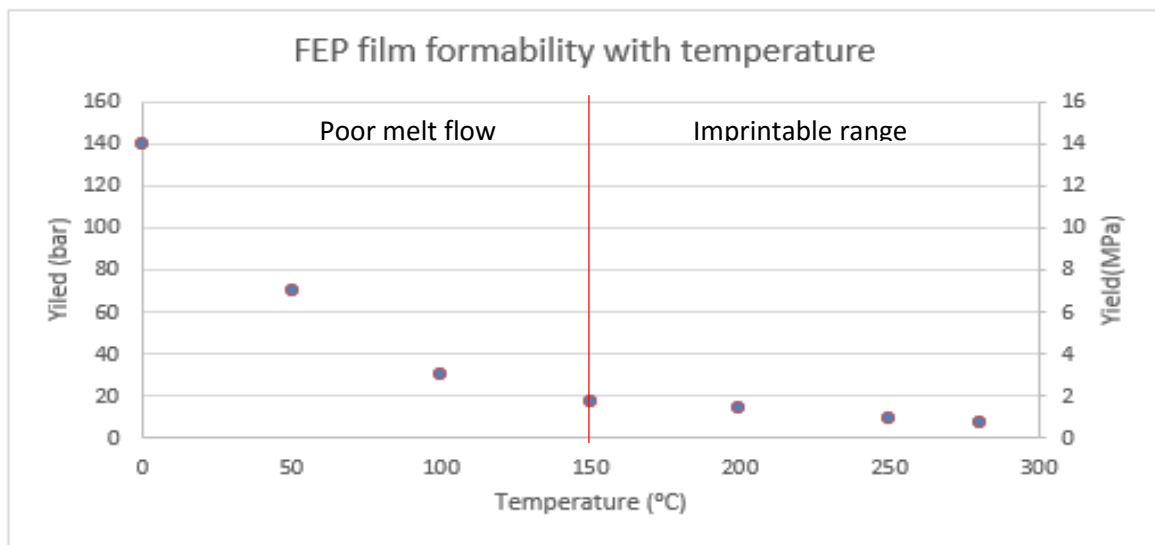


Figure 2-5 – Illustration of the material yield strength, and the equivalent conversion to applied pressure at a given temperature. Trend is used to identify the necessary NIL pressure to transfer a pattern and reflow the FEP film. DuPont aggregate data for commercial FEP films. [137].

The NIL process is schematically presented in Figure 2-6. Initially a nanopatterned qz or Si master stamp, patterned as described previously (section 2.2.3.1) is preheated to 200 °C. A FEP film of thickness ranging between 25 μm and 250 μm was positioned above the nanopatterned region of the stamp. A glass or qz backing plate was applied with a pressure of 15 bar and held at 270 °C. After a 3 minute cycle under heat and pressure the stack was cooled to 160 °C at which point pressure was removed and the stack was allowed to return to room temperature. At this point the film was separated from the master stamp by a quick flexing of the glass backing plate. This produced a free standing nanopatterned replica stamp in the FEP film, which is flexible and transparent.

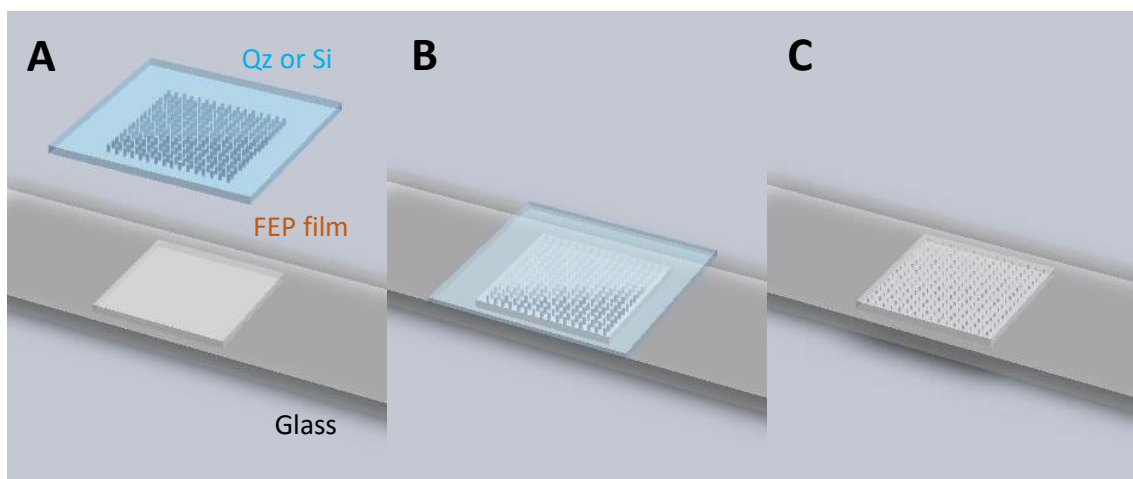


Figure 2-6- Process flow for the manufacture of patterned fluoropolymer stamps. A.) qz master stamp is applied to a preheated FEP film attached to a glass backing plate. B.) Stack of quartz, FEP and glass is then held under pressure and elevated temperature. C.) After cooling the master is delaminated, and leaves behind a replica FEP stamp. Thermal expansion differences between FEP, glass, qz/Si master are not observed to damage the replica pattern quality.

This process can be reproduced manually by hotplate and surface weight with the typical conversion of force per unit area adjusted to gravity. A 15 N load applied to an insulating film above the stamp is sufficient to drive a 1 cm² array into the FEP film.

2.2.3.5 Manufacture of novel hierarchical FEP stamps

Hierarchical FEP micro- and nanopatterned stamps were manufactured by sequential embossing of the thin film with different patterns. Initially a micropatterned PDMS stamp with 5 μm tall features in a hexagonal array was applied to the FEP film in a process outlined in section 2.2.3.4 at 10 bar and heated to 280 °C for 3 minutes while placed on a glass microscope slide. After the first embossing the glass slide was rotated and a nanopatterned Si or qz stamp was placed underneath the FEP film and embossed again at 10 bar and held for 2 minutes. This process takes advantage of the fluoropolymer melt flow creep, to reflow it into areas by applying an increased pressure, and create a nanoscale topography on top of a series of previously micropatterned islands.

2.2.3.6 Combinational mastering with FEP stamps

Combinational or modular mastering, allows combinations of macro-, micro- and nanopatterning on a variety of surfaces. Depending on the curvature of the surface a flexible acetate or rigid glass mask is used in hard contact with the material surface. Modular stamps use an exterior acetate or Ni-chrome photo-mask, and a nanopatterned transparent FEP insert. The acetate flexibility offers an opportunity for roll-to-roll printing and using UVNIL on non-planar surfaces (Figure 1-8). The UV absorption of transparent FEP stamps is also lower than that of PDMS or the qz [188], doing little to interfere with the UV doses absorbed by the underlying photosensitive material.

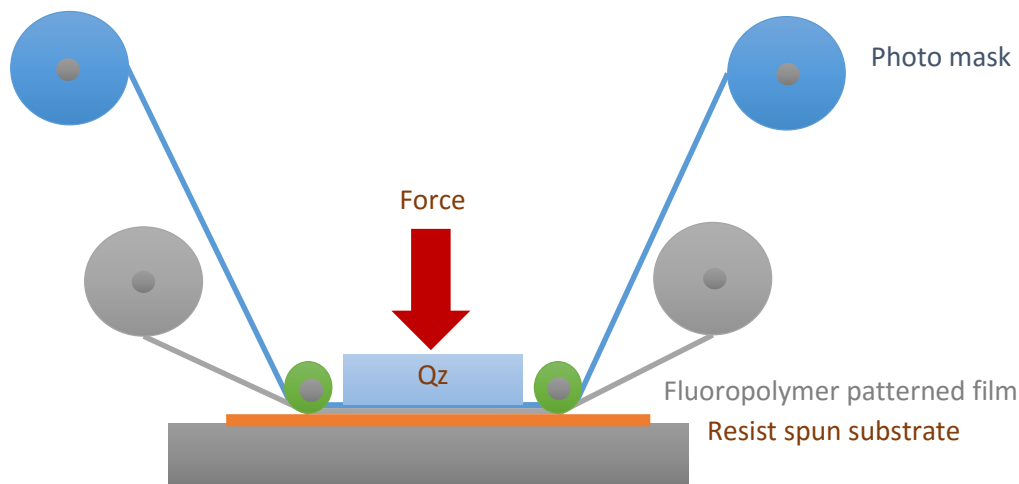


Figure 1.9. The design of a modular UVNIL printer device envisaged as a future proof of concept.

Samples were prepared using SU8 3000 series photoresist which was spun on silicon to a thickness of 5 μm and prebaked at 90 $^{\circ}\text{C}$ for 5 minutes. Exposure was carried out in a commercial SUSS MA6 photolithography tool at a dose of 150 mJ/cm^2 . After the photo exposure samples were post-baked at 90 $^{\circ}\text{C}$ for 3 minutes and developed in EC solvent for 3 minutes exposing the patterns as illustrated in Figure 2-7.

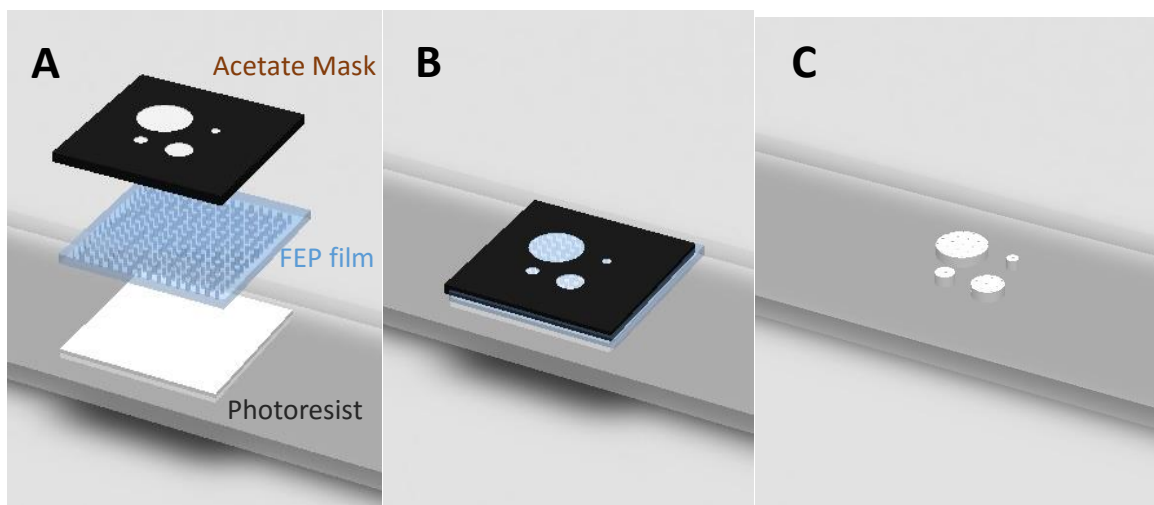


Figure 2-7- Process flow showing the use of modular stamps for UVNIL applications. A.) patterned FEP film placed onto a photoresist spun on a substrate with acetate photomask applied above to define the dimensions of the pattern. B.) Photolithography is carried out. C.) Stack is separated and photoresist developed producing defined micro- or nanoscale features.

The choice of micro and nanopattern can offer a tailored substrate for controlling cell and topographical interaction on engineered bio interfaces. The transparency of the films has the potential for serial lithography where the film is imprinted with a FEP master in serial UV flash lithography to produce a large area nanopatterned surface [188].

2.2.3.7 Master duplication from FEP replica

The fabrication process can be divided into two main steps: 1.) initially the creation of an evaporation mask using thermal NIL followed by an oxygen plasma ash to remove any residual layer on the substrate, and secondly: 2.) the subsequent metal deposition and lift-off.

Poly(methylmethacrylate) (PMMA) 2010 8 w/v % in o-xylene was spun on 500 µm thick silicon at 5000 rpm and baked at 180 °C for 15 min. The spun film was then placed on a sheet of flat aluminium wafer (Obducat specific spacer). A nanopatterned FEP film was placed above with a second layer twice the area above this, to act as a buffer for irregularities in the top die. The assembly was placed inside an Obducat NIL-2M tool. The sample was initially preloaded to 3 bar prior to the application of heat, the temperature was then ramped to 120 °C at which point the pressure was ramped up to 10 bar, and then 175 °C and 15 bar, where it was held for 5 minutes. It then ramped down to 60 °C prior to the pressure being released, allowing the melt to stabilize. The imprinted PMMA was then ashed in oxygen plasma for 2 minutes at a power of 100 W to remove any fouling at the base of the pits. Titanium was then sputtered to a depth of 100 nm followed by a 2 minute sonication in Microposit™ EC Solvent followed by a wash and sonication in acetone, methanol and IPA in that order for 1 minute each and finally a 3 minute oxygen plasma ash at 100 W power.

2.2.3.8 Novel FEP based platform for curved surface Nano imprint lithography (NIL)

The easy conformation of patterned FEP films allows for casting and NIL to be carried out on a variety of non-planar surfaces. FEP films covered with a 1 cm² nanopattern of various arrangements and pitch were inserted into a machined stainless steel casting rig (Figure 2-8), into which powdered PCL and PLLA were introduced and formed on a hot press under 5 bar at 90 °C and 160 °C respectively, flowing into the lined cavity and filling the nanofeatures. On removal from the mould and cutting with a surgical scalpel a straw like hollow cylinder with internal and external nanopattern is formed. The use of the tool without a central rod allows the casting of solid cylinders with exterior curvature nanopattern.

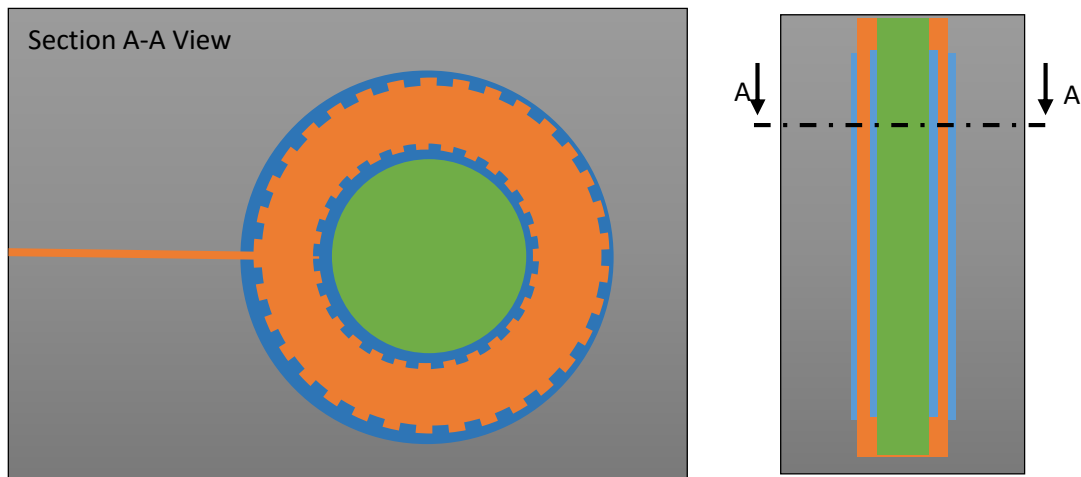


Figure 2-8- Diagram of 3D tube moulding rig, manufactured from stainless steel. A central guide pin is wrapped in FEP patterned film, with wall of main chamber lined with alternate patterned film, a polymer melt is then introduced, and chamber is held at pressure. Central rod is optional (green) and can be removed all together to pattern cylinders externally.

2.3 RESULTS

The use of fluorinated ethylene propylene (FEP) films was shown to make the mastering process considerably quicker, and less risky when applying patterns to SU8 with silicon stamps, a process that can be costly if a brittle silicon or quartz were to shatter. They are additionally shown to be far more hydrophobic in their natural state (without post treatment by salinization), a good property for de-moulding from an imprinted surface, without imprint and stamp damage. The results of various stamp manufacturing processes and successful applications thereof are shown in the following section.

2.3.1 The benefits of using FEP as a stamp material

Compared in Figure 2-9 are the measured contact angles of the imprinting materials and imprintable materials used in this work, FEP was shown to have an exceptionally high contact angle

of $(119 \pm 3.2^\circ)$ compared to that measured for PDMS of $(107.5 \pm 2.67^\circ)$.

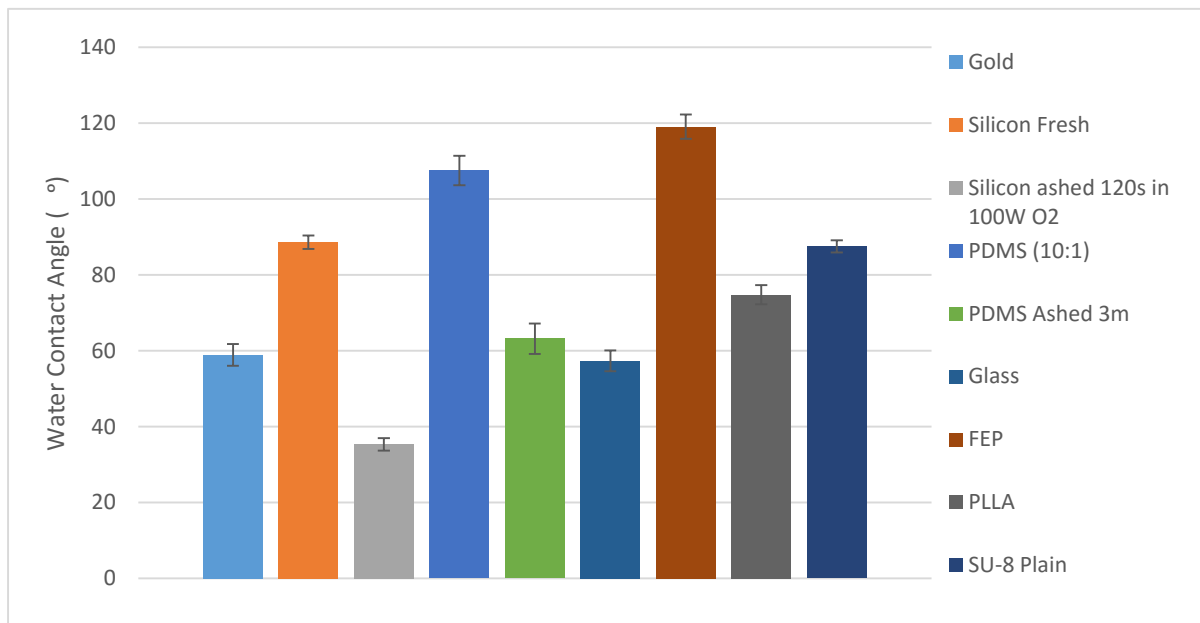


Figure 2-9 – Contact angles of materials used (PLLA, SU8), and those of the available stamp materials (silicon, PDMS, glass, FEP). The contact angle of FEP is significantly higher than the alternatives being considered. Error bars: 1SD over $n=5$ measurements.

This allows for relatively easy de-moulding, along with improved mechanical properties compared to PDMS, and better transparency at 365 nm light used in UV photolithography, and the synthesis undertaken in earlier chapters of this work.

2.3.2 FEP imprint stamps

FEP stamps showed excellent uniformity and transparency (Figure 2-10), combined with very easy release due to their fluorinated nature, not requiring a release coating on the original Si master stamp, although it is recommended, some residue was noticed in the master after 15-20 replicates were made, particularly noticeable on cold de-moulding, warming the stamp to 100-120 °C made the release considerably easier for large patterns with deep features such as the gratings.

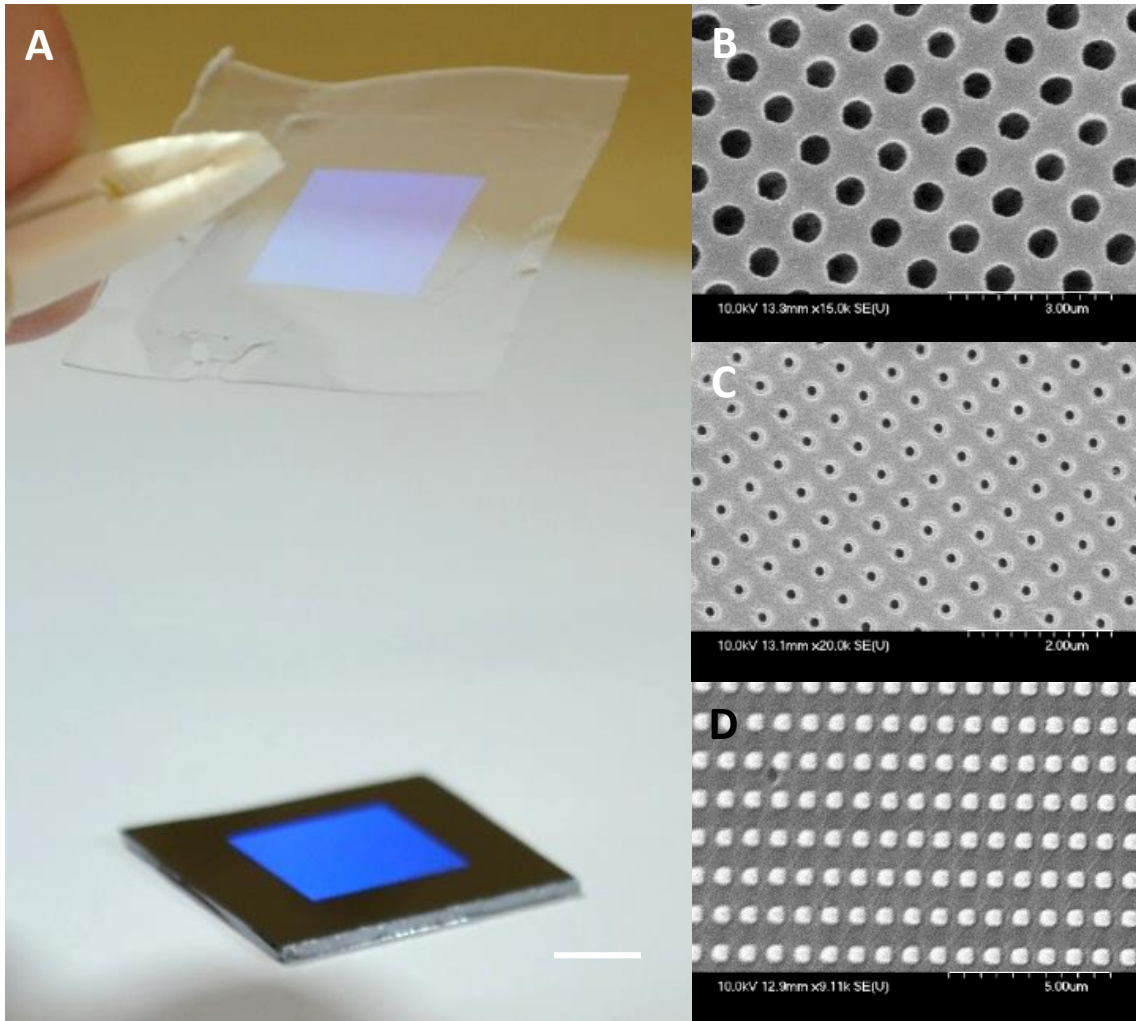


Figure 2-10 – (A) FEP film stamp replicating a silicon master during removal from master stamp. Scale bar 5 mm. (B) SEM of 500 nm holes in the FEP film replicated from a silicon pillar surface. (C) SEM of 150 nm holes replicated in FEP film from a silicon master stamp. (D) 500 nm pillars on 500 nm square pitch replicated from pitted silicon master stamp. Scale bars = 5 mm, 3 μm , 2 μm and 5 μm for A, B, C, D respectively.

Nanopatterns within a variety of pitches and feature sizes were tested, the range rising from 150 nm features with 250 nm pitch to 1000 nm in diameter features with 50 nm pitch. Release problems were encountered on narrowly spaced pillars with aspect ratios greater than 4:1, where the FEP became stuck and did not de-mould from the silicon, or extracted pillars from the original stamp.

FEP was well suited to filling Pillars between 150 nm and 2000 nm in diameter and holes down to 150 nm in diameter (Figure 2-10). The limiting factor was found to be the release process, due to the FEP film being very thin relative to its area; pure vertical removal was difficult, and resulted in tearing and hazing under excessive force. AFM scans of the low aspect (0.25) and medium aspect (1.5) pillars reproduced in FEP from a quartz (qz) master stamp are shown in Figure 2-11 (B and C).

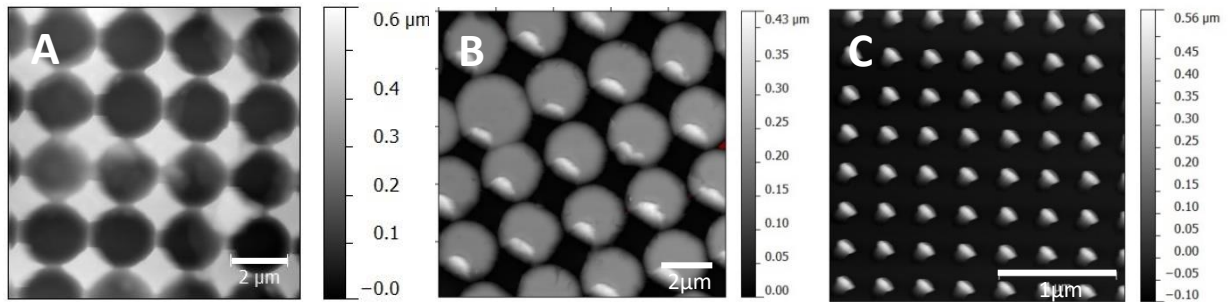


Figure 2-11 - Figure 1.4. AFM microscopy of FEP stamps post embossing by a quartz master stamp. (A) The quartz master with low aspect ratio pits. (B) FEP replica low aspect pillars (C) FEP replica 200 nm high aspect ratio pillars. Scale bars = 2 μm , 2 μm and 1 μm respectively.

The self-repelling qualities of FEP that are so attractive in imprinting, also serve to facilitate thin gaps between features, as visible in Figure 2-11. In addition to pillars, reproduction of grating replicas has been demonstrated using an original silicon (Si) master with grating of 500 nm depth and pitch.

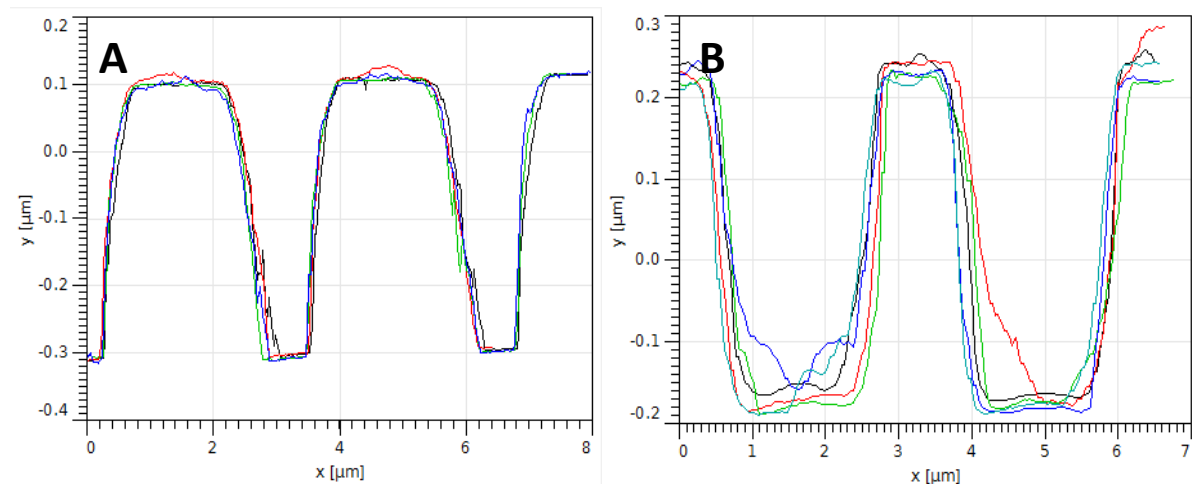


Figure 2-12 - Profile scan of those patterns seen in Figure 10 (centre). A: Average pillar height formed in FEP replica is 420 nm close to the original 450 nm depth of features in the Quartz master stamp. B: profile scan across master stamp ($n=5$).

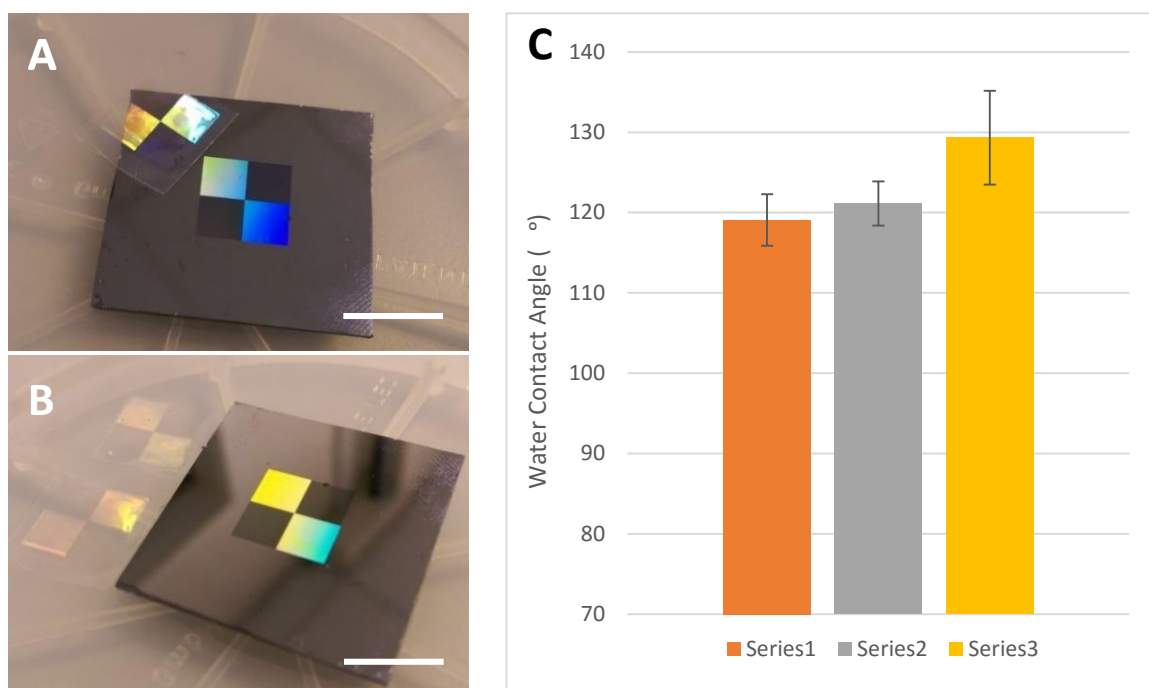


Figure 2-13 – (A) Original silicon grating master stamp and FEP replica stamp produced by embossing at 275 °C. (B) Demonstrated ease of multiple stamp manufacture in FEP within a short periods of time frame. (C) Graph of contact angle measurements of flat FEP film originally (Series 1), and after nanopatterning of 500 nm gratings at Orientation 1 (Series 2 - parallel to plane of view) Orientation 2 (Series 3 - perpendicular to view plane). Error bars 1SD (n=5). Scale bars = 10 mm.

2.3.2.1 Formability

Data on FEP from the manufacturer (DuPont) was used to determine the nano imprint (NIL) conditions for the manufacture of FEP replica stamps. Although this is similar to the process of fluoro polymer imprinting demonstrated in Palacios-Cuesta and Vasiev [189], the process of imprinting uniform thin films proved to be easier than handling powdered polymers or monomers. The manufacturer’s data on temperature effect on polymer properties shown in Figure 2-5 cite a T_g of 200 °C and a melting temperature in the region of 280 °C.

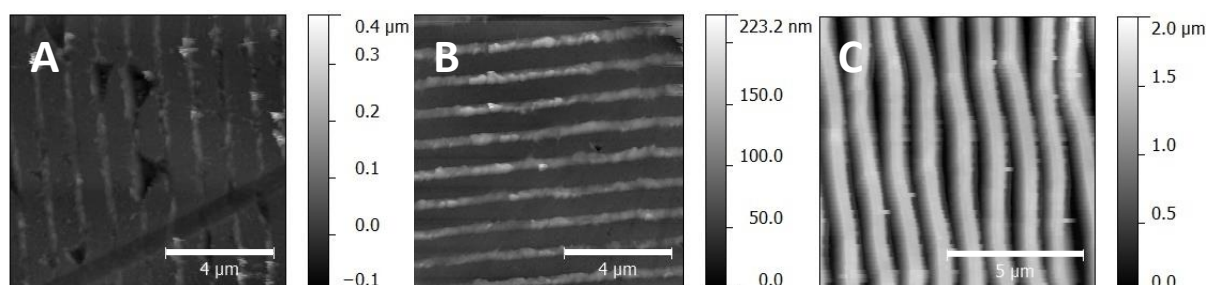


Figure 2-14 - AFM scans of FEP replica stamps of a 500 nm grating, produced in a varied series of imprint temperatures. Left to right (A) 205°C, (B) 240°C, (C) 280°C respectively, imprint temperature maintained for a 3 minutes duration at 10 bar. Some stretching is seen causing wavy lines to form. Scale bars = 4 μm, 4 μm and 5 μm respectively.

This was compared to imprints made into FEP films with a grooved master stamp at three temperatures and constant pressure and cycle duration. The process mentioned previously was used adjusting holding time from 200 °C to 240 °C and 280 °C for 3 minute durations.

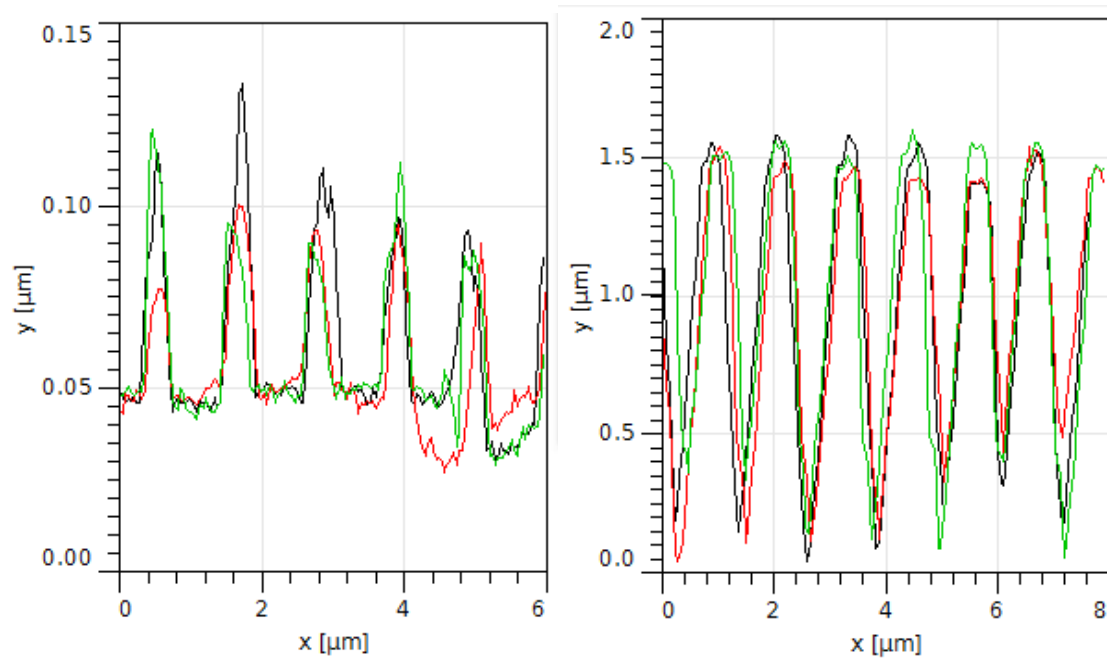


Figure 2-15 - AFM scans of FEP replica stamps of a 500 nm grating, showing improving feature height replication as melting point of FEP is reached. Left: 240 °C, Right: 280 °C respectively, imprint temperature maintained for a 3 minutes duration at 10 bar. (n=3).

The samples when imaged with AFM showed an increasing flow tendency with an under-fill visible at that duration near the glass transition temperature T_g and improving flow characteristics as the material neared melting.

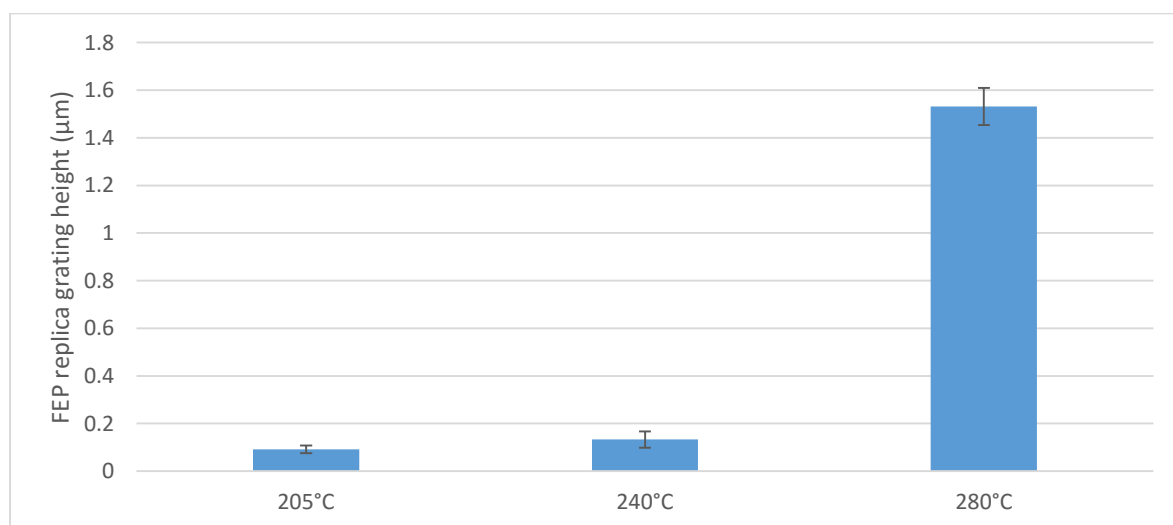


Figure 2-16 - Imprint feature height after imprinting a 500 nm pitch and width grating for 3 minutes at 10 bar imprint pressure at different temperatures. Flow of FEP drastically improves above its melt temperature. Error bars are 1SD (n=6).

Although it was seen that the release of tall grating features underwent slight waving due to the long length scales this could be due to catching and slight plastic deformation of the grating section.

2.3.3 Master replication

Master stamps were attempted to be recreated by imprinting a resist with the FEP replica stamp, thus being able to loop the process back and allow a more economical creation of solid qz and Si master stamps without the use of EBL. The resulting calibration of the three stages to replicating masters in titanium are outlined in section 2.3.3.1 using profilometry, AFM and SEM imaging. As mentioned this is a three stage process to reproduce solid features using evaporation of a metal through pores created by FEP-NIL.

2.3.3.1 Master replication by PMMA imprinting

PMMA imprinting was done on layers slightly thinner than the pillar height to make sure the residual layer was as thin as possible. The spin thickness curves for 84,000 Da PMMA indicate an average thickness of between 200-325 nm.

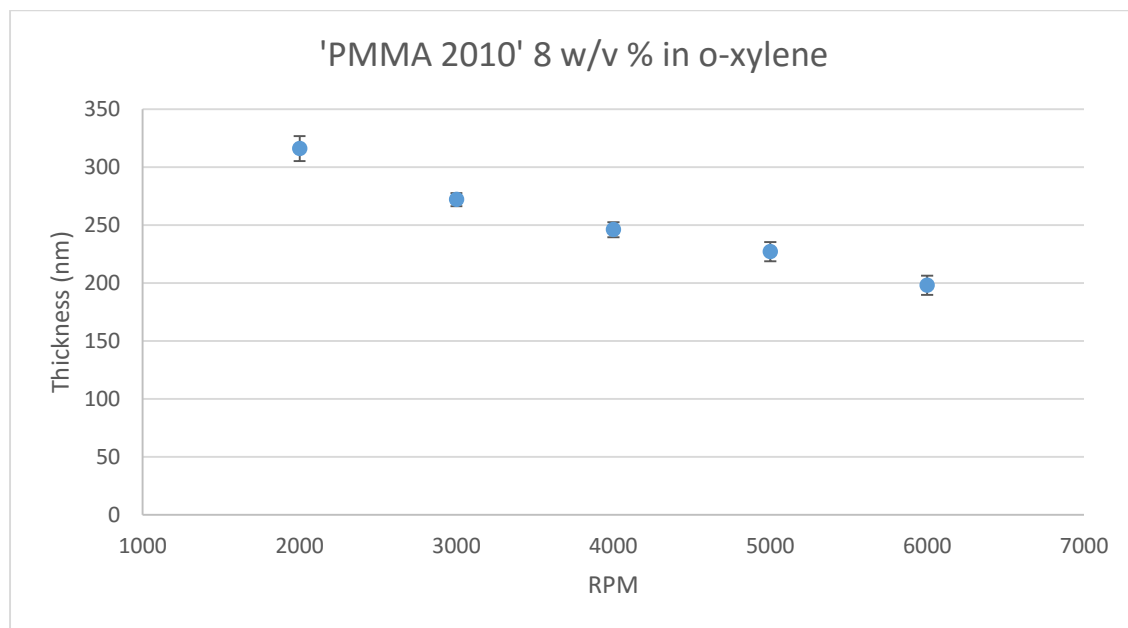


Figure 2-17 – Measured spin thickness of 84,000 Da PMMA dissolved to 8 v/v % dilution in o-xylene after a 1 minute spin duration. Error bars are 1SD (n=3).

This layer was imprinted by FEP features of over 300 nm in height, and ashed with O₂ plasma to remove any residual layer. The imprint was followed by deposition of a 100 nm thick layer of titanium onto the imprinted and ashed PMMA pits. Subsequent lift-off yielded bound titanium nanofeatures replicated on silicon.

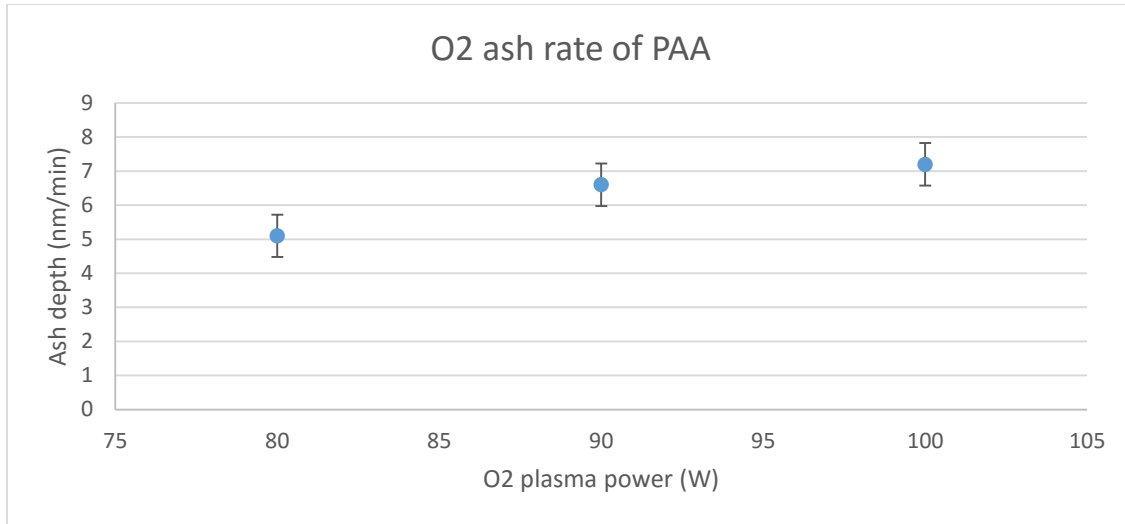


Figure 2-18 - Ash rates of spun PMMA film A in oxygen plasma with varying RF power, and AFM of imprinted PMMA film post 2 min ash. 84,000 Da PMMA dissolved to 8 v/v % dilution in *o*-xylene. Measurements were taken by Dektak profilometer at the end of each ash cycle. Error bars are 1SD (n=3).

Pillars of 500 nm 1:1 aspect ratio pillars with 500 nm pitch were replicated from a silicon master.

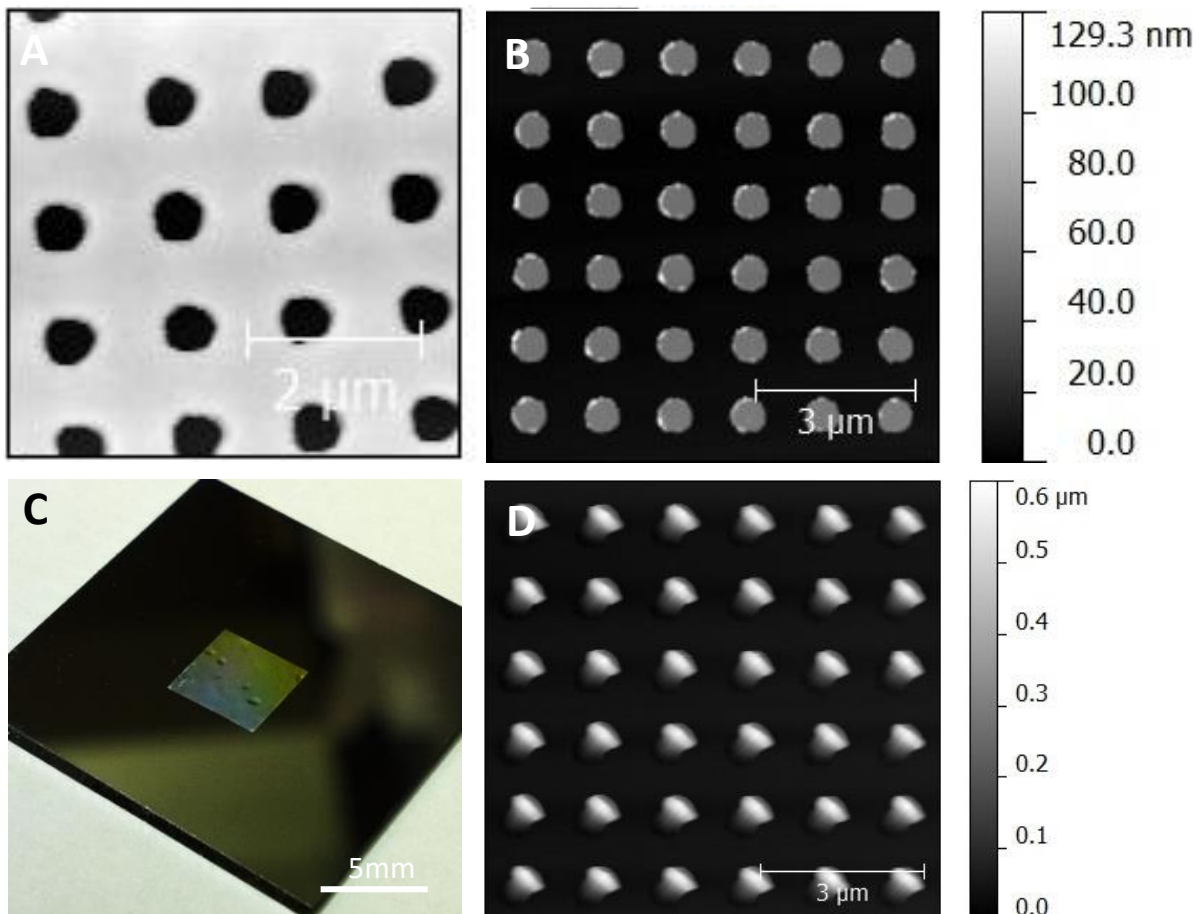


Figure 2-19 – (A) AFM scan of PMMA imprinted by FEP stamp prior to metal sputtering. AFM scan of a Ti stamp produced by sputtering, an attempted inversion of the original master, which was a silicon (Si) pillar array of 500 nm diameter pits on a 500 nm square pitch. (B) Magnified scan of same stamp. (C) A macro photo of the resulting pattern on silicon, like with many imprint processes, areas of pattern damage can be seen where the stamp failed to fully imprint the PMMA lift-off layer. (D) The FEP replica stamp produced from the original Si master. Scale bars: A) 2 μm, B) 3 μm, C) 5 mm and D) 3 μm respectively.

It should be noted that the resulting evaporated stamp inverse is of a low aspect ratio, thus the original stamp was taller than the master produced (500 nm stamp against roughly 100 nm evaporated metal) the process yields a fast approach to producing hard material stamps. The titanium can then be used as an etch mask for deep silicon etching to reproduce the original height.

2.3.4 Hierarchical patterning

Hierarchical patterns can be produced by sequential imprinting of the FEP features, with micropatterns defined initially, followed by nanopatterning of the feature surfaces as illustrated in Figure 2-20.

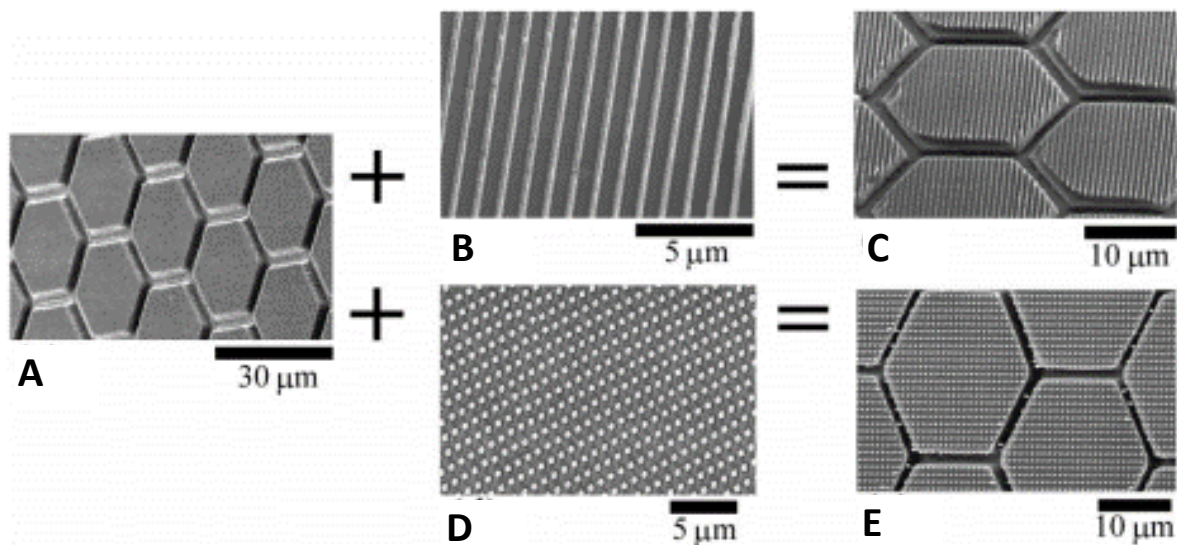


Figure 2-20 – Example SEMs of hierarchical patterning in FEP films by novel combinational replica moulding. Initial micro pattern A can be combined with either B or D to produce C or E respectively. Scale bars are 30 μm , 5 μm and 10 μm respectively. Reproduced from Greer and Vasiev et al. [188].

Hierarchical patterns were produced by serial imprinting as illustrated in Figure 2-20. Initially the micropattern was created in the form of 20 μm hexagonal microarrays with a 4 μm deep PDMS stamp. The islands were then imprinted with a qz stamp containing 5 nm 1:1 aspect ratio pits on a 500 nm pitch, and also 500 nm deep and 500 nm wide gratings with a 1:2 pitch. The patterning could be adjusted depending on micro and nanopattern selection, for a combinational approach shown in Figure 2-21.

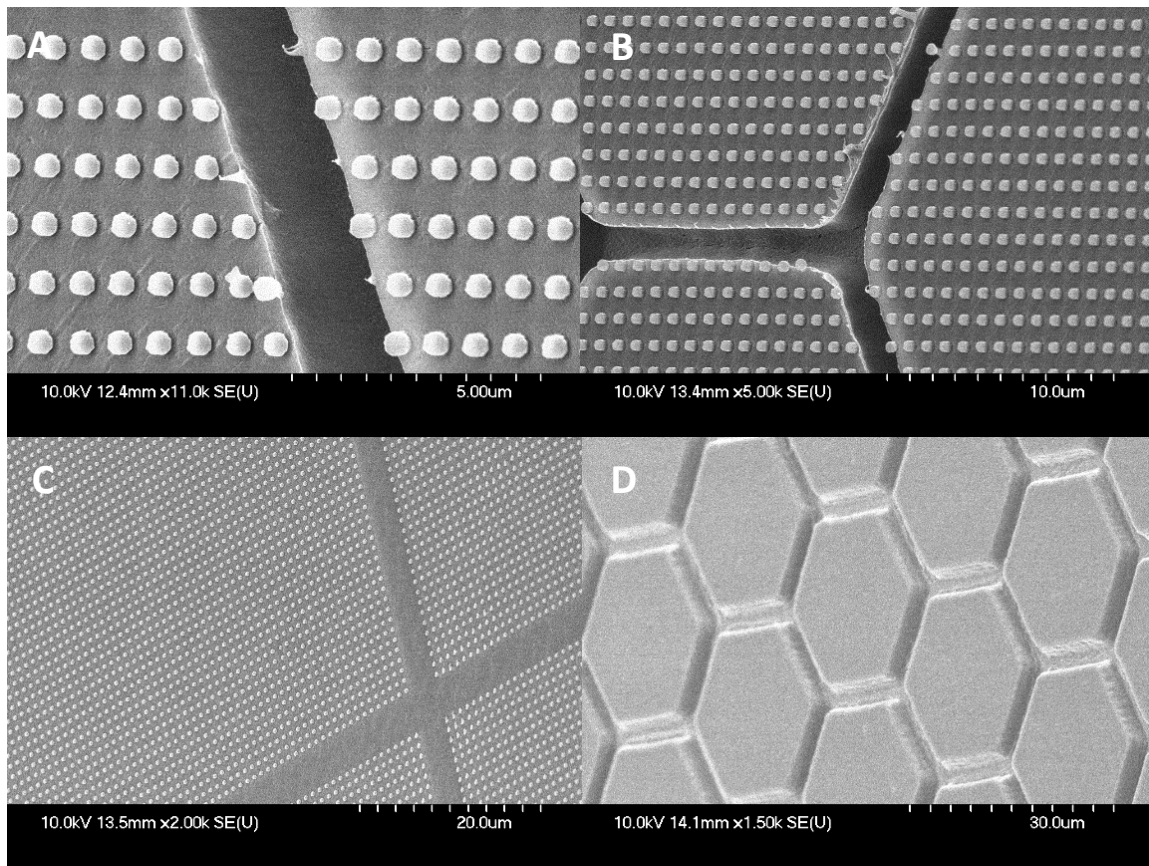


Figure 2-21 – A.) SEM images of hierarchical patterns showing 20 μm hexagonal islands with 500 nm pillars. B.) A magnified SEM image showing the hexagonal structure of the islands. C.) The nanopattern which was applied during the second emboss step. D.) The micropatterned hexagonal islands before the application of the secondary nanopattern. Scale bars: 5 μm , 10 μm , 20 μm and 30 μm respectively.

AFM imaging of the stamp confirmed feature heights in the range of 500 nm as seen in Figure 2-22. The combination of topographies can be adjusted for a particular use but the initial micro feature loss is minimal given initial PDMS feature size of 4 μm , a 75 % under fill occurs between PDMS replication and transfer into FEP for the large features, this could be due to trapped gas pockets, or insufficient melt time as larger features have to displace more flowing polymer melt. Combining different nanotopographically patterned stamps during the second stage allows selection and combinational use of a primary and secondary pattern:

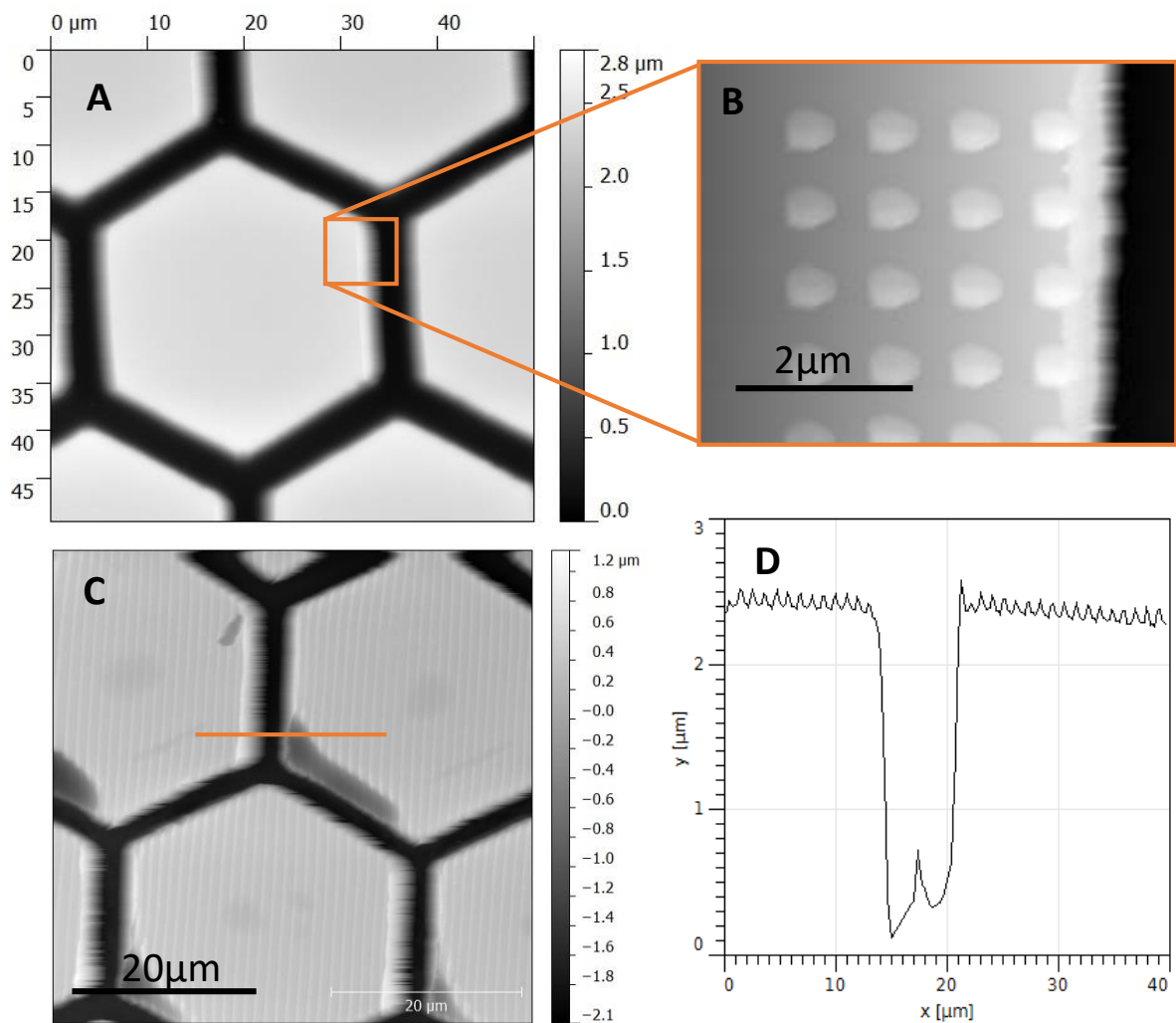


Figure 2-22- A) Hierarchical fluoropolymer stamp structure under AFM, in a 50 x 50 μm scan. B) magnified 5 x 5 μm scan. C) AFM of hexagonal islands with 2.7 μm height and a 400 nm grating pattern on top surface. Selection of different micro and nanopattern configurations allows for a mix and match approach to potentially cell confining patterns with selected topographical interaction. D) Section profile across topography with hierarchical grating. Scale bars: A) 20 μm , B) 2 μm , and C) 20 μm respectively.

The top pattern morphology was not tested on high aspect pillars, for fear of the pressure required liquefying the underlying micro-pattern, but appears to work well on a variety of topographies especially gratings as seen in Figure 2-23.

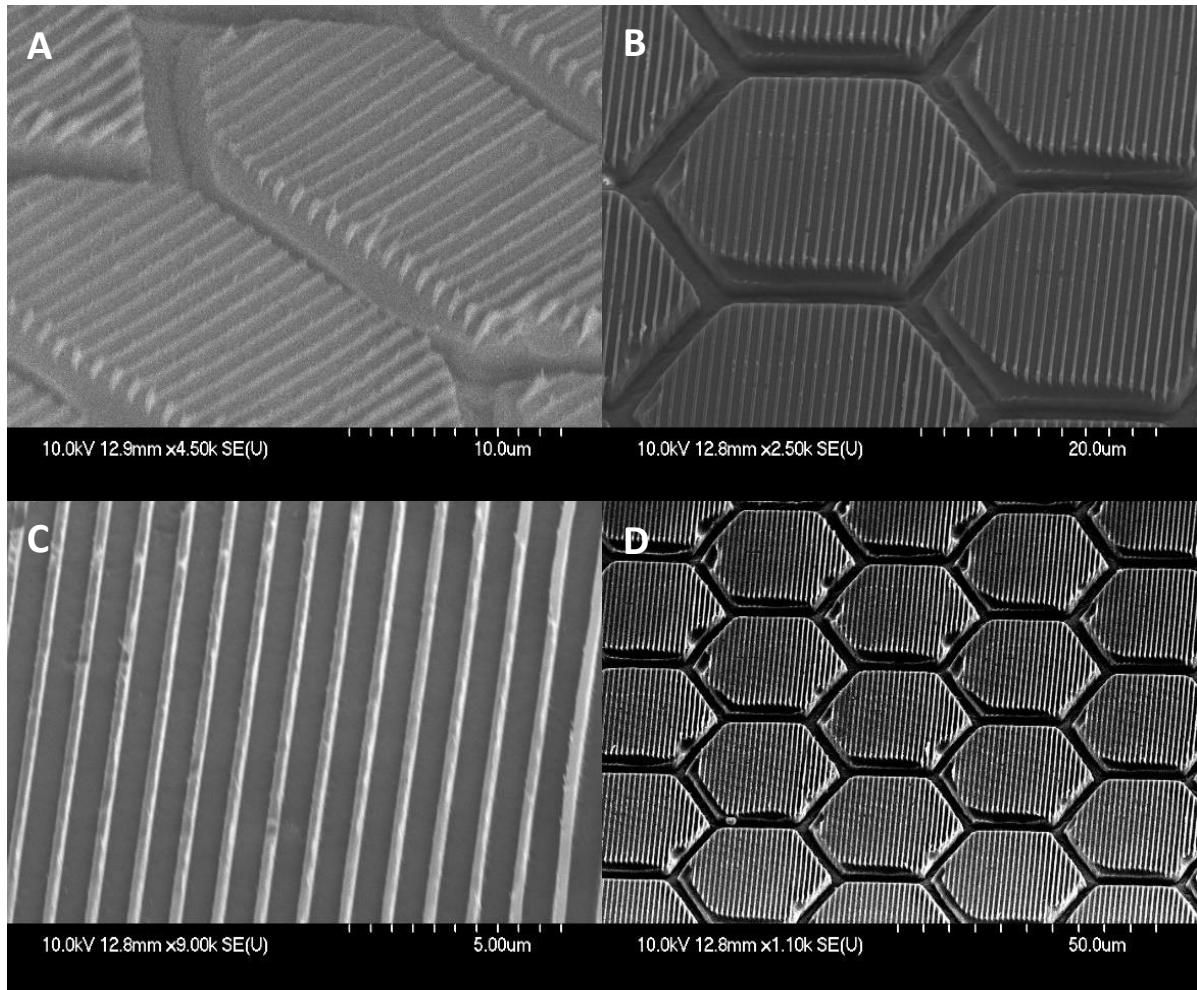


Figure 2-23 –SEM images of FEP hierarchical structures showing a combined hexagonal microstructure (A,B,D) with a 500 nm grating surface nanopatterns (C), produced by sequential embossing of the FEP layer. Illustrating the flexibility of the process and the customization of possible patterns. Scale bars: A) 10 μm , B) 20 μm , C) 5 μm and D) 50 μm .

The maximum height of features obtained was 2443 ± 73 nm for the micro islands themselves, and 424 ± 64 nm for the hierarchical nanopattern covering the islands (Figure 2-25).

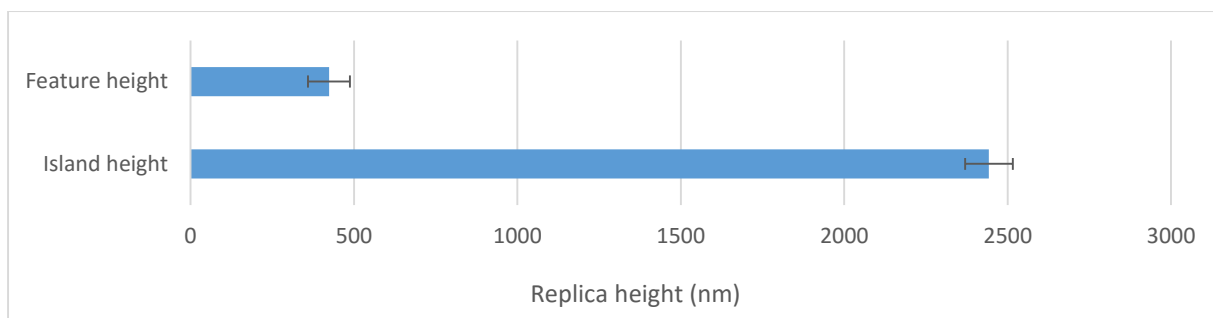


Figure 2-25 - Feature heights of hierarchical patterns showing an aggregate from 8 measurements. Error bars = 1SD (n=8 samples).

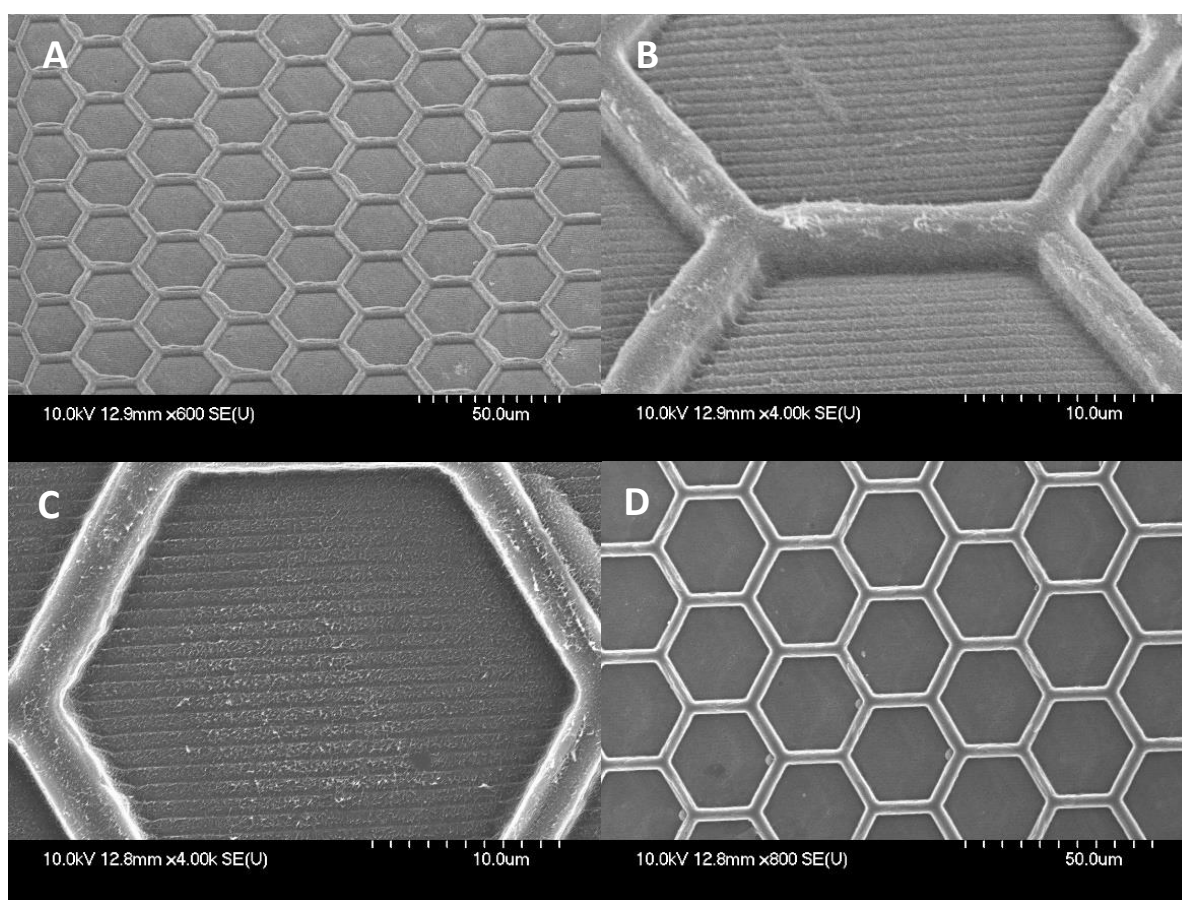


Figure 2-24 –SEM images of SU8 Imprinted with a FEP hierarchical stamp. Imprinting done with combinational method through 1 cm square aperture above the FEP film. Scale bars: A) 50 μ m, B) 10 μ m, C) 10 μ m and D) 50 μ m.

These patterns can then be transferred to SU8 for container patterning or any other thermoplastic with a lower melt temperature than the T_g of FEP (205 °C). The reproduction of FEP patterns in SU8 easily accommodates the hierarchical structure during its liquid phase prior to exposure during the pre-bake or after exposure during the post-bake. The resulting transfer into SU8 by imprinting during the post exposure bake can be seen in Figure 2-25. This type of hierarchy can be useful in tissue culture by adjusting micro borders to cell size and can be used for cell segregation studies with alternating topographies to test cell-topography triggers for array studies eliminating cell-to-cell interaction without using low cell volumes.

2.3.5 Curved surface patterning

Curved surfaces were patterned and produced through utilising an FEP casting inlay method whereby PCL and PLLA pellets were melted in a mould lined with a nanopatterned FEP film at 80 °C and 200 °C respectively. This has application in traditional forming as it can be applied to the interiors of other forming moulds.

If patterning a transparent curved surface it could be applied to the production of large area patterns for roll-to-roll printing, and 3D nanopatterning applications such as screws, cranial plates and other non planar implants. The pattern quality showed oscillations as seen in Figure 2-26, possibly caused by mould non uniformity or buckling of the FEP film inside the forming space. In addition to patterned cylinders, this interior and exterior patterning could be performed on cast hollow tubes and PDMS channels and is shown as a proof-of-principle.

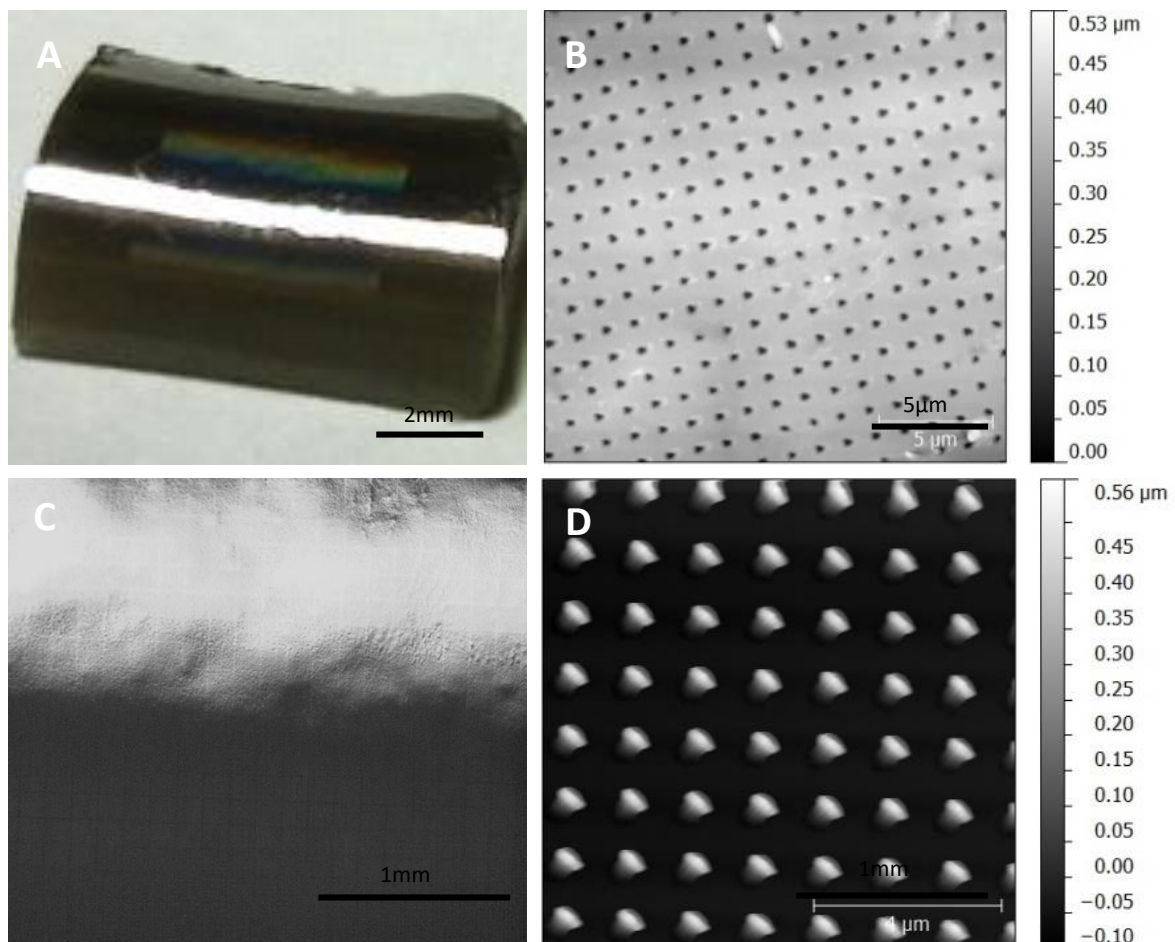


Figure 2-26 – A) Optical image of a half cylinder cut from a PCL rod which had its circumference imprinted by a flexible FEP stamp at 80°C. B) AFM scan of imprinted cylinder surface showing the nanopits formed on the cylinder surface. C) Optical CMM image of cylinder surface, showing the 200 µm gaps in the nanopatterned array on the cylinder surface. D) AFM of the FEP replica stamp used, same as that used for evaporation of Ti mastering process. Scale bars: A) 2 mm, B) 5 µm, C) 1 mm, D) 4 µm.

2.3.6 Modular mastering process

Subsequent imprinting and lithography by this method was shown to allow the structuring of a combinational pattern, with modular micro- and nanopatterned arrays for conducting cell-surface interaction analyses. There are numerous ways to create a 3D patterned box, or other patterned surfaces, but to be able to pattern multiple materials at relatively high throughput with a variable selection of nanotopographical and micropattern geometries (Figure 2-27) produced by combinational mastering and photolithography through FEP is not as easily achieved. This approach, to the author's knowledge, has not been demonstrated before.

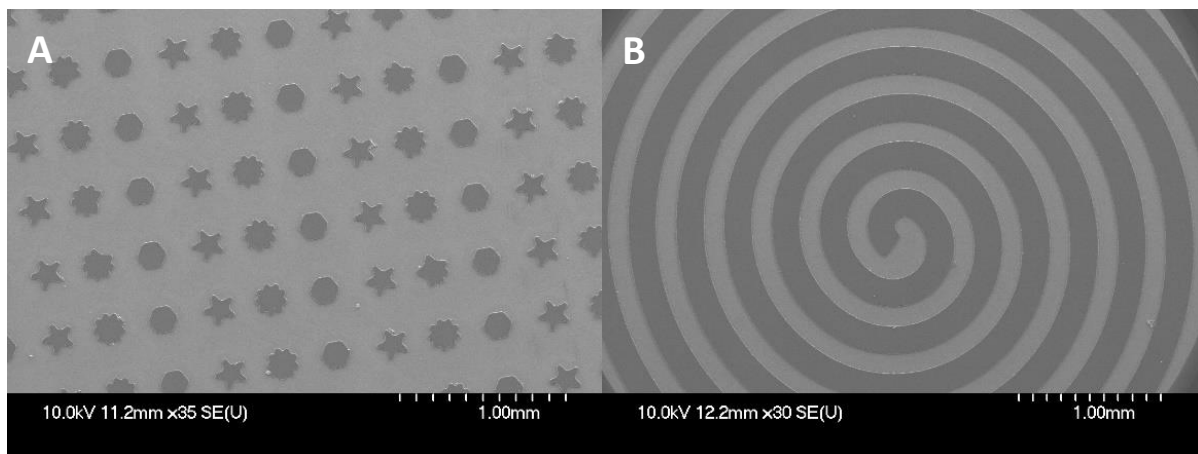


Figure 2-27 - SEM image of A) micro star shapes and B) spirals produced by the combinational mastering approach utilizing FEP replica stamps and printed acetate photomasks. Scale bars: 1 mm.

The use of FEP film as a non-stick easy to clean nanopatterned inlay can be used with NIL to reduce wafer damage on fragile substrates without causing fracture. As the material is considerably lower modulus than silicon, and as a ductile material it accommodates machine surface irregularities and absorbs harder inclusion or dust particles that would normally cause stress concentrations on the wafer surface, and result in cracks in an expensive master stamp. This method allows for significantly faster design prototyping and simple manufacture of a variety of 3D micro containers, with different internal nanopatterns shown in Figure 2-28 being applied to the manufacture of 3D origami containers discussed later in Chapter 4 section 4.3.

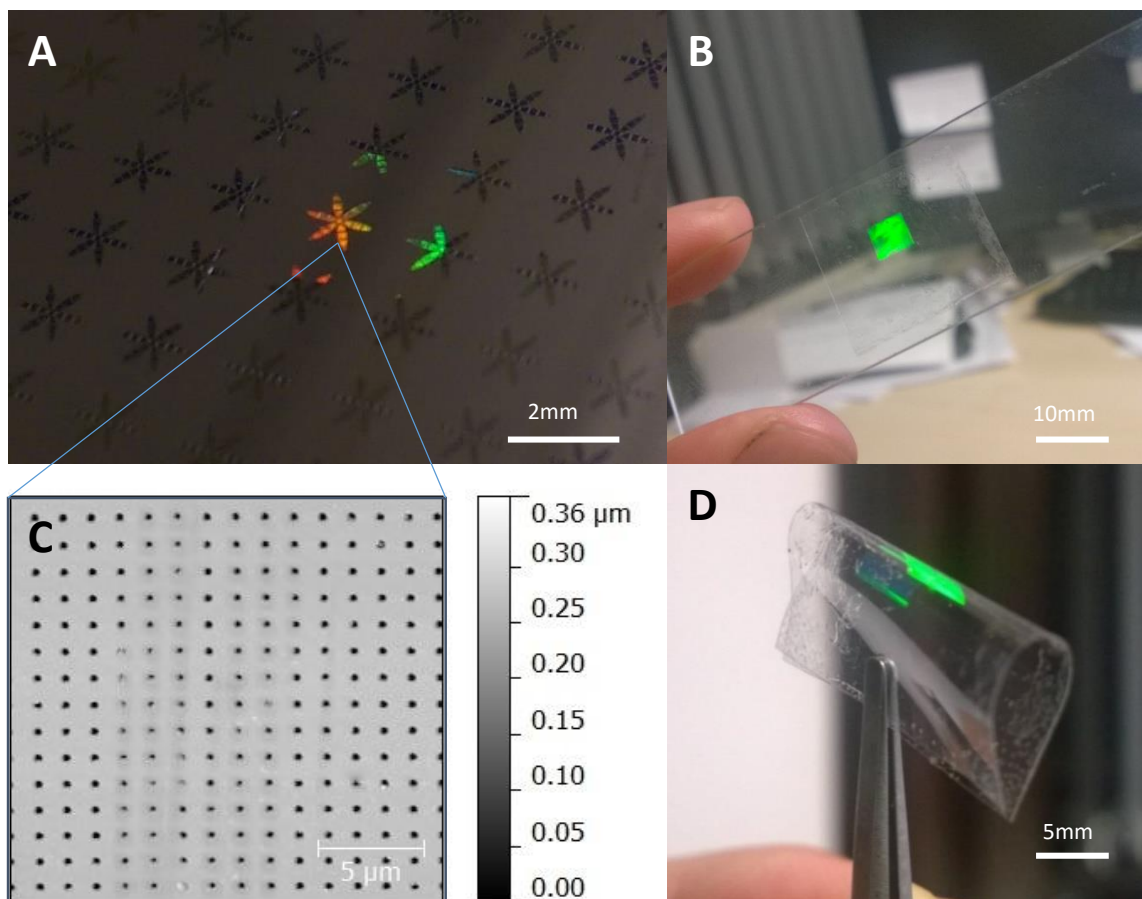


Figure 2-28 - A) Image of 'lotus' micro containers produced by combinational mastering and printing in SU8. B) Image of the FEP replica stamp used in the processing, attached to a glass backing slide just after manufacture. C) AFM scan of the FEP film surface showing 250 nm pits on a 1 µm square pitch. D) Demonstrating the flexibility of imprinted FEP stamps when removed from the glass backing plate. Scale bars: 2 mm, 5 mm, 5 µm and 5 mm respectively.

To increase and sustain the supply of available nanopatterns, a method of transferring injection moulded topographies produced by the group and utilized in the work of Dalby et al. [39] into FEP stamps is beneficial, combining an established process of manufacturing nanotopographies for cell culture with a material that is compatible with the aforementioned fabrication methods.

2.3.7 Transferring patterns from higher throughput methods

Feature replication for contact guidance can be done from injection moulded topographies using a PDMS replica pattern. The process of stamp fill by PDMS is assisted by ashing as demonstrated by the AFM profiles of cast PDMS surfaces in Figure 2-29. The replica surfaces were compared with profilometry to compare the replica pillar heights with the original mould as shown in the aggregate feature fill profiles and data in Figure 2-30. The original feature depth on the master mould is compared to replica PDMS features produced before and after ashing in O₂ plasma for 1 minute at 80 W RF power.

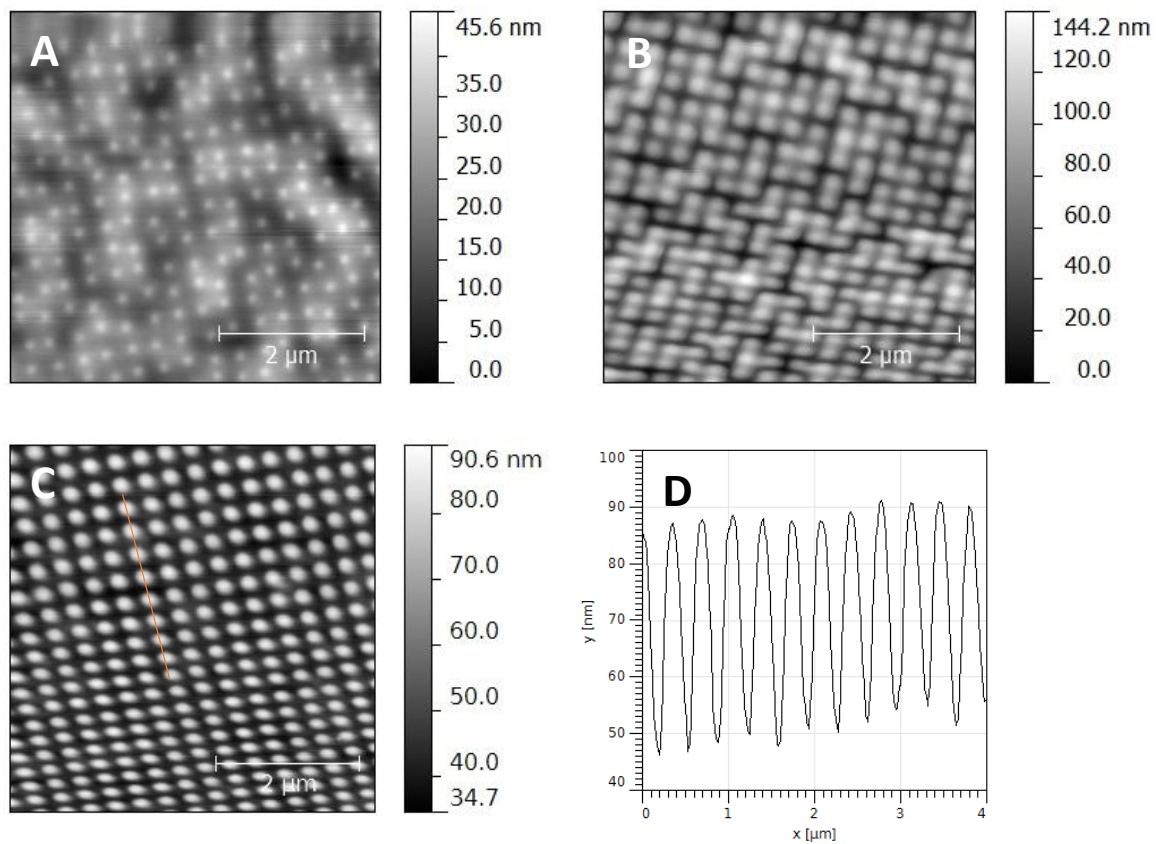


Figure 2-29- AFM scans of polycarbonate injection moulded topographies reproduced as negative replicas in PDMS by casting. A) PDMS replica produced from non-ashed original NSQ surface with resulting lower feature fill. B) PDMS replica with good fill from an ashed original NSQ surface with much better feature replication. C) PDMS replica produced from ashed SQ surface showing good feature fill, showing orange profile trace. D) The profile trace of PDMS replica of SQ surface. Scale bars: 2 μm .

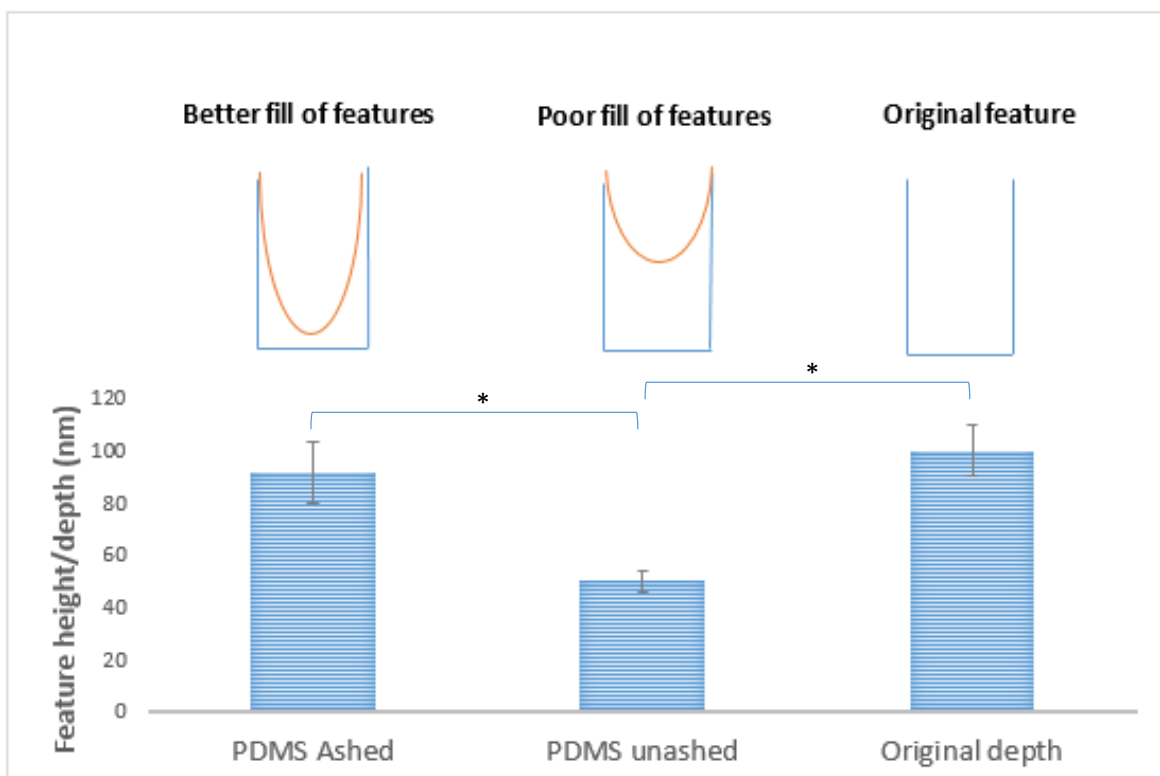


Figure 2-30 - Top: feature fill diagram for the original master depth and the expected fill profile of the PDMS replica features. Bottom: Feature height of PDMS replicas taken from injection moulded polycarbonate (PC) masters. Error bars: 1SD from 5 measurements.

Ashing is thought to improve the wetting of the surface by slight roughening and immobilization of transient functional groups, yielding better feature fill than non-ashed samples. The resulting depth profiles of the replica stamps are compared with the injection moulded master and show the scale of the improvement (Figure 2-30). The resulting PDMS stamp can then be used to recreate the pattern in photopatterned SU8 surfaces, for application on the self-folding 3D containers discussed in Chapter 4.

2.3.8 Hydrogel patterning

Patterns were transferred into the PAA sacrificial layer by thermal NIL, followed by replication into the subsequent hydrogel to be patterned after spinning above (described in section 2.3.8). This method of surface patterning also yields functionalization as the carboxyl group containing PAA chains are transferred to the gel underside by free radical polymerization. The sacrificial layer [190] can be embossed at approximately 100 °C or imprinted at room temperature [190] using a silanised Si stamp. In addition to NIL methods this layer can be wet etched in EDTA [191]. To optimize the preparation and application of the PAA sacrificial film, and allow the release layer to be finely controlled, different molecular weights (1800, 50000 and 100000 Da) and aqueous concentrations were spun between 1000 and 6000 rpm to determine the resulting film thicknesses. By varying the

viscosity of the PAA sacrificial layer, the spin thickness and thus possible feature size can be adjusted as shown in Figure 2-31.

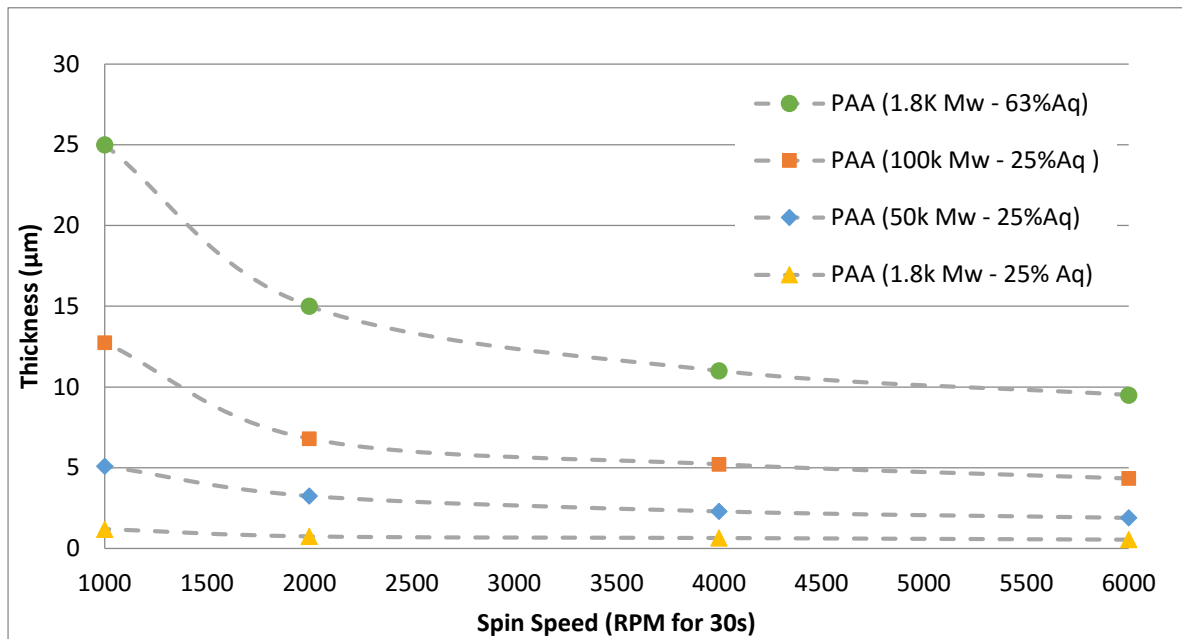


Figure 2-31 – Film thickness for a range of spin speeds for different molecular weights and concentrations of commercial PAA. Average values from 3 profile scans.

The PAA embossing method allows ingress of the pre-polymer and subsequent patterning by UV exposure. The process resolution is limited by pre-polymer surface energy and viscosity. However the ability to control sacrificial layer thickness allowed for a wide range of depths and aspect ratios to be imprinted ranging from 5000 to 50 nm diameter pits and pillars of 2000 to 200 nm, to a maximum aspect ratio of 2 to 1. PAA is soluble in water [190], but not in IPA which is used to develop PEG, this allows for selective layering and two-sided patterning as the PAA is not affected by the PEG hydrogel developer in this process.

2.3.9 UV-NIL as a means of manufacturing patterned hydrogel films

The fabrication of nanofeatures on the hydrogel top layer was carried out with a transparent nanopatterned master stamp (Figure 2-32) where a procedure similar to photolithography was used. The process flow consisted of either a transparent quartz (qz) or polydimethylsiloxane (PDMS) stamp which was applied under slight pressure to the polyethyleneglycoldimethacrylate (PEGDMA) solution in a Suss MA6 mask aligner and exposed to UV light at 7.2 mW/cm^2 as before. For samples made in bulk, following exposure, the samples were developed in isopropanol and sliced into individual sheets of required size prior to rehydration overnight in RO H_2O .

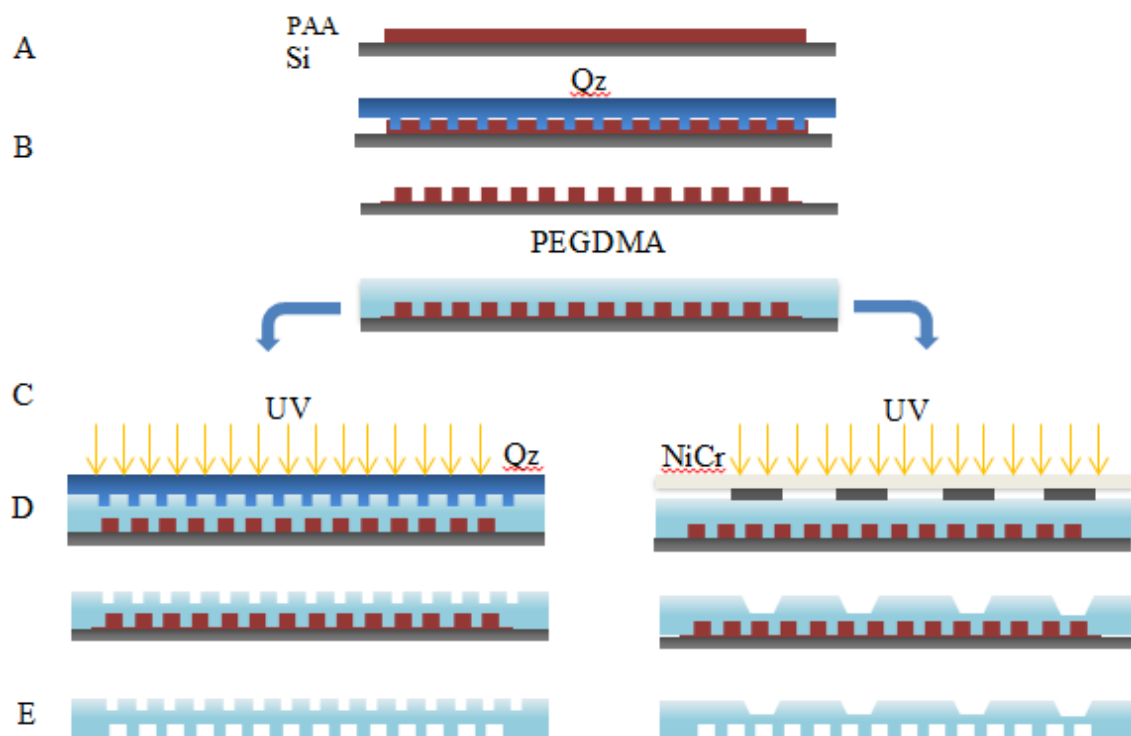


Figure 2-32 - Fabrication process for creation of nanopatterned and micropatterned PEGDMA hydrogel films by PAA sacrificial layer embossing. A) PAA is spun onto Si wafer. B) PAA film is embossed using the master stamp. C) Hydrogel is applied to PAA surface. D) Master stamp or mask is applied and assembly is exposed to UV and developed in IPA. E) Wafer placed in RO water allowing for dissolution of PAA layer and subsequent lift-off of hydrogel patterned film [1].

Sheets of gel photolithographically patterned through the PDMS mould were developed in IPA and then allowed to soak in RO H_2O . Device lift-off occurred between several seconds and several days depending on the thickness of lift-off layer with the process shown in Figure 2-33. The PDMS procedure was replaced by a novel FEP imprinting technique discussed in Chapter 2. The micro- and nanopatterned hydrogel device were created through a series of stages to create the foundation for a high throughput one-step lithographic method. For each pattern, a mastering process was required in which quartz (qz), silicon (Si) or PDMS stamps were prepared, to be used in subsequent hot embossing and photolithography steps of the sacrificial polyacrylicacid (PAA) base layer to facilitate lift-off and functionalization of the PEGDMA hydrogel layer.

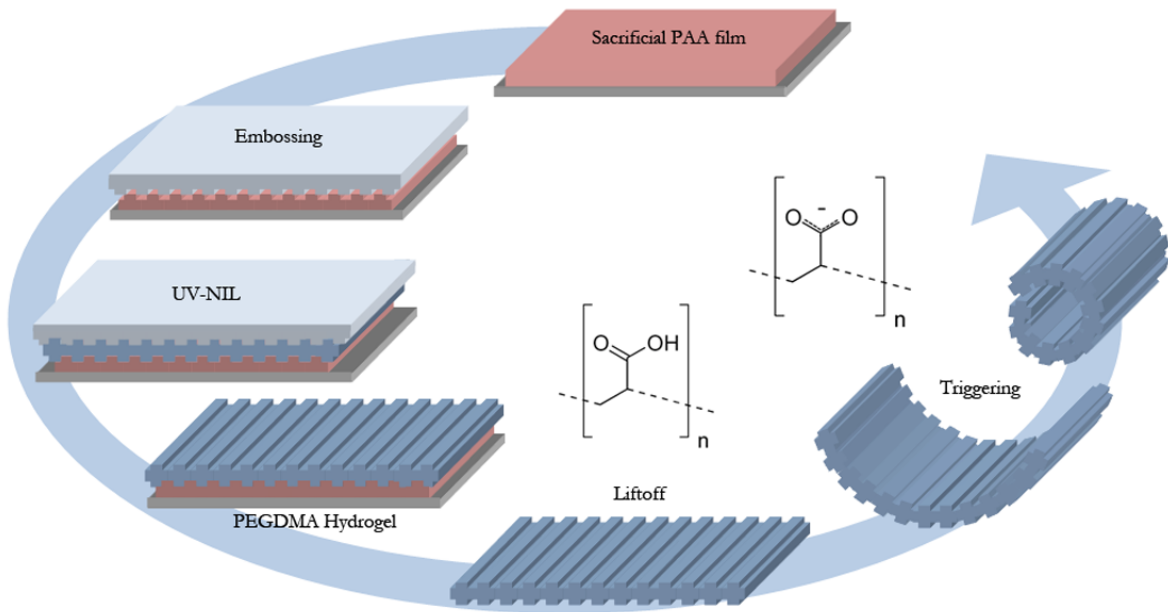


Figure 2-33 – Hydrogel bilayer fabrication and actuation by pH modulation. Gel sheets patterned by photolithography leading to shape and active carboxyl group transfer to the gel film from below and patterning from the stamp above. This patterned film then undergoes a deprotonation of the $-COOH$ terminus of its pendant carboxyl groups in elevated pH ($pH > pK_a$). Subsequently rolled sheet can be unrolled if pH is lowered past the pK_a value again, this process is notable slower. Reproduced from Vasiev et al. [1].

The range of imprints can then be transferred into the hydrogel film above to create a patterned hydrogel surfaces with added carboxyl group functionality. To achieve this, and double sided patterning a range of patterns in PAA are required. The hydrophilic nature of the PAA film allows for good transport of hydrogel resist into the feature cavities, allowing for the replication of sharp details.

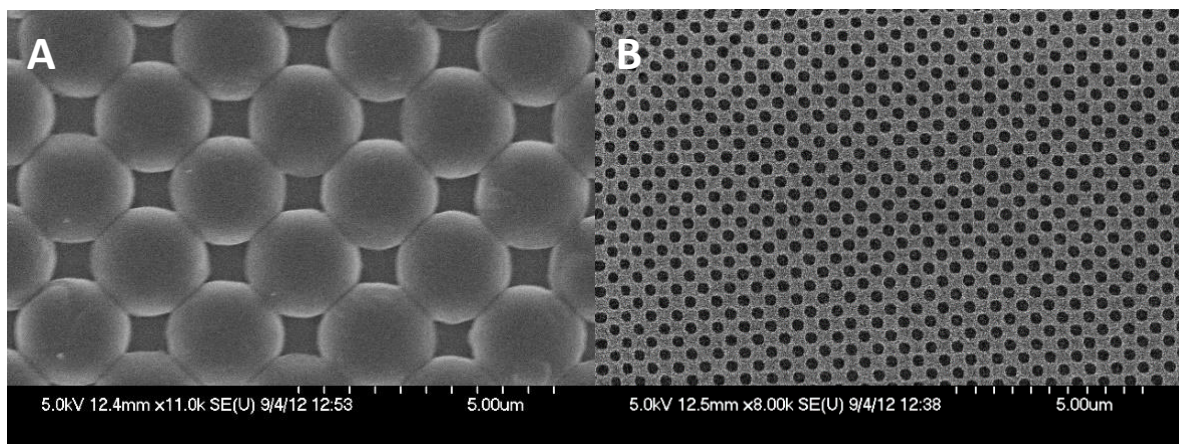


Figure 2-34 – SEM imaging of Embossed PAA. 2µm wide and 500nm tall pillars and B: 200nm wide and 250nm deep holes with 200nm square pitch. Both produced from FEP imprinting of PAA at 90°C and 15bar. Scale bars: 5µm.

The diverse range of pattern morphologies obtained by embossing PAA shown in Figure 2-34 where PAA has been embossed with a FEP stamp.

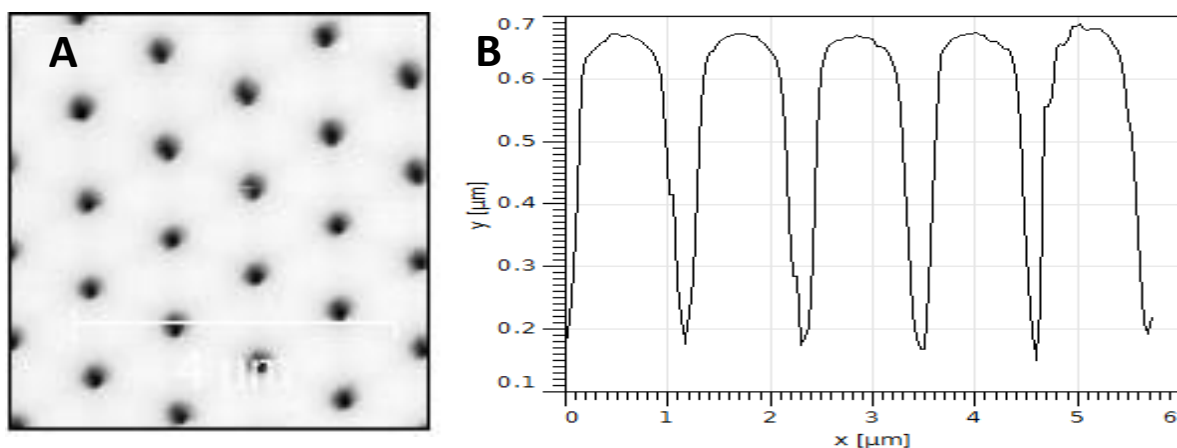


Figure 2-35 – A) AFM scan of PAA surface with HEX pit array. B) A section showing the profile of 500 nm pits on a 1 μm HEX pitch 500 nm deep reproduced in PAA by embossing with a Quartz (Qz) master. Scale bar 4 μm .

The patternability of PAA itself improves when using a hard stamp such as quartz (Figure 2-35).

These embossed PAA surfaces can be used to cast and lift-off hydrogel features, transferring the underlying nanopatterns into the hydrogel layer above. AFM profiling of the hydrogel films patterns shows the ability to create hydrogel pillar features as a replica of the underlying embossed PAA surface (Figure 2-36).

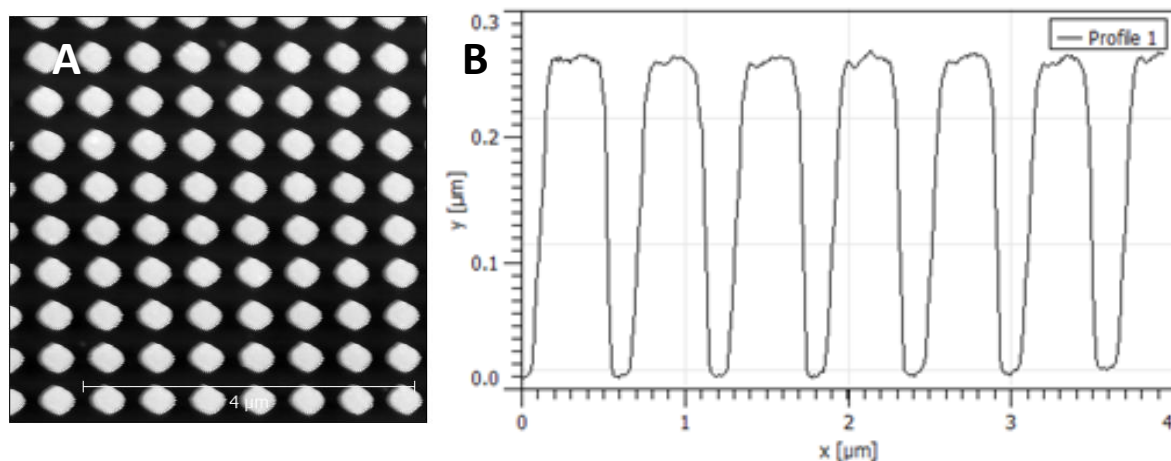


Figure 2-36 – A) AFM scan of hydrogel nanopatterned film reproduced from an embossed PAA surface with 300 nm wide pillar distribution on a 300 nm pitch. B) Fourier plot showing feature size and frequency with the main peak in the sub μm range. C) Section profile of pillars showing 300 nm feature height. Scale bar: 4 μm .

The incorporation of PAA onto the PEGDMA gel network likely arises from diffusion of initiating radicals to the sacrificial PAA layer causing it to tangle with the many methacrylate groups above to form a semi inter penetrating network with the PEGDMA gel even though no initiator was present in the PAA when spun. The pH response was observed to be reduced or elevated, with lower Mw PAA providing a quicker swelling response, this may be caused by the increased difficulty of long chains to migrate into the PEGDMA network.

The resulting hydrogel rolling patterned films are shown in Figure 2-37, with the spacer pillars clearly visible on the surface. This method of embossed sacrificial UV-NIL is based on hydrogel technology using simple wet chemical methods, a highly flexible and controllable patterned tissue scaffold has been fabricated that can be switched and controlled by external media. The fabrication technology is inexpensive, scalable, and rapid, reducing fabrication stages and reducing the use of expensive photo initiators to create the bilayer structure.

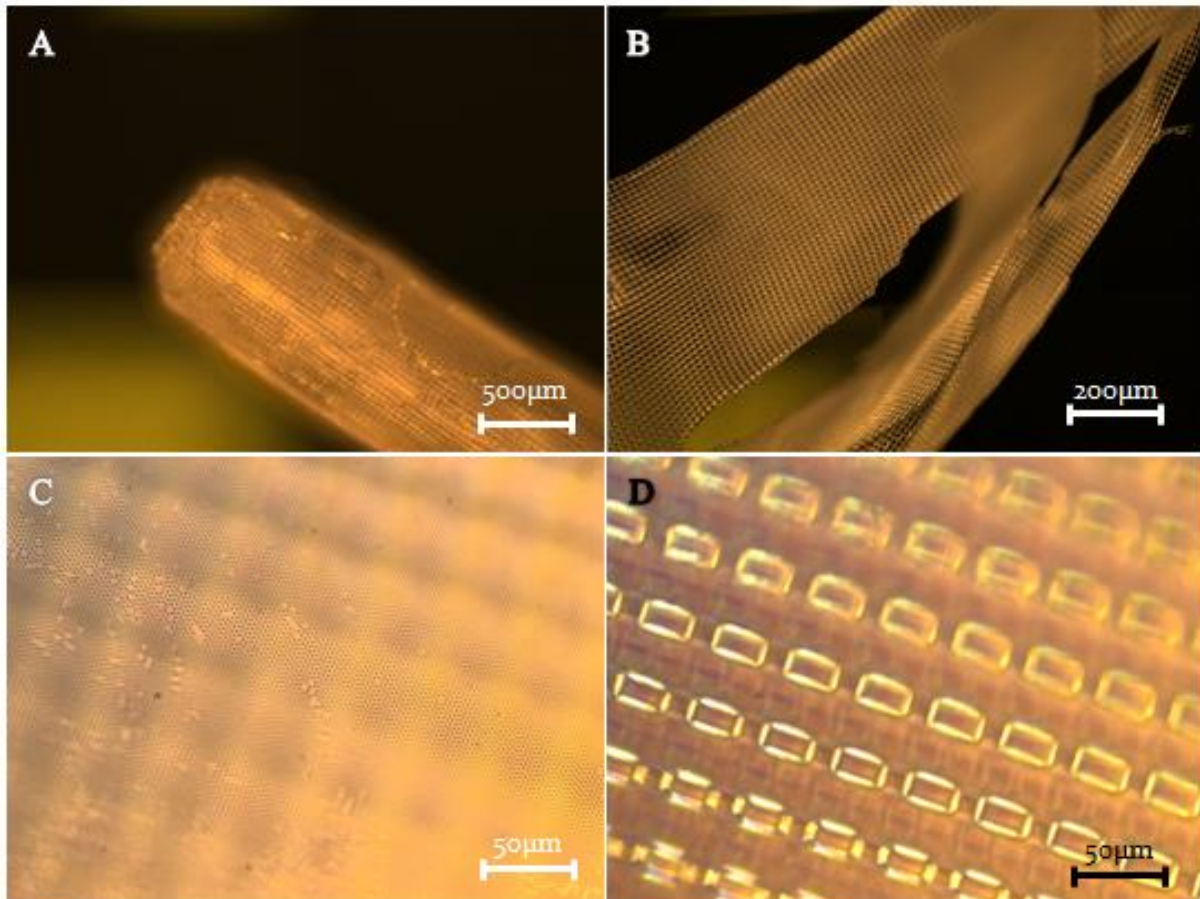


Figure 2-37 A) Rolled micropatterned PEGDMA hydrogel film after exposure to pH 7 buffer and air drying, scale bar: 500 μm . B) Unrolled micropatterned PEGDMA hydrogel film after unrolling in pH 4 buffer and air drying, scale bar: 200 μm . C) bottom surface of roll showing 1 μm pits replica from the nanopatterned PAA sacrificial under-layer, scale bar: 50 μm D) Top surface micropattern created as replica of top PDMS stamp. Scale bar: 50 μm . Reproduced from Vasiev et al. [1].

While some diffusion occurs which creates the bilayer structure, PAA remains relatively insoluble in IPA and EtOH the two main solvents used in the PEGDMA pre-solution. As a result the predefined pattern in the sacrificial layer remains intact long enough to force the above solution into a replicated shape during crosslinking, and does not inhibit subsequent lift-off of the patterned structure. The definition of these features is good, with slight squaring of feature edges due to the inherently good wetting of the PAA, resist appears to be drawn further into the embossed features. These rolls can include photolithographically defined nanofeatures as seen in Figure 2-38. After sputtering with a gold conductive layer, SEM imaging does show some slight dissolution at pillar

bases, this is due to being exposed to the larger surface area of free solvent in comparison to the base of the pit or the flat PAA surface. Some partial dissolution of the sacrificial master must occur.

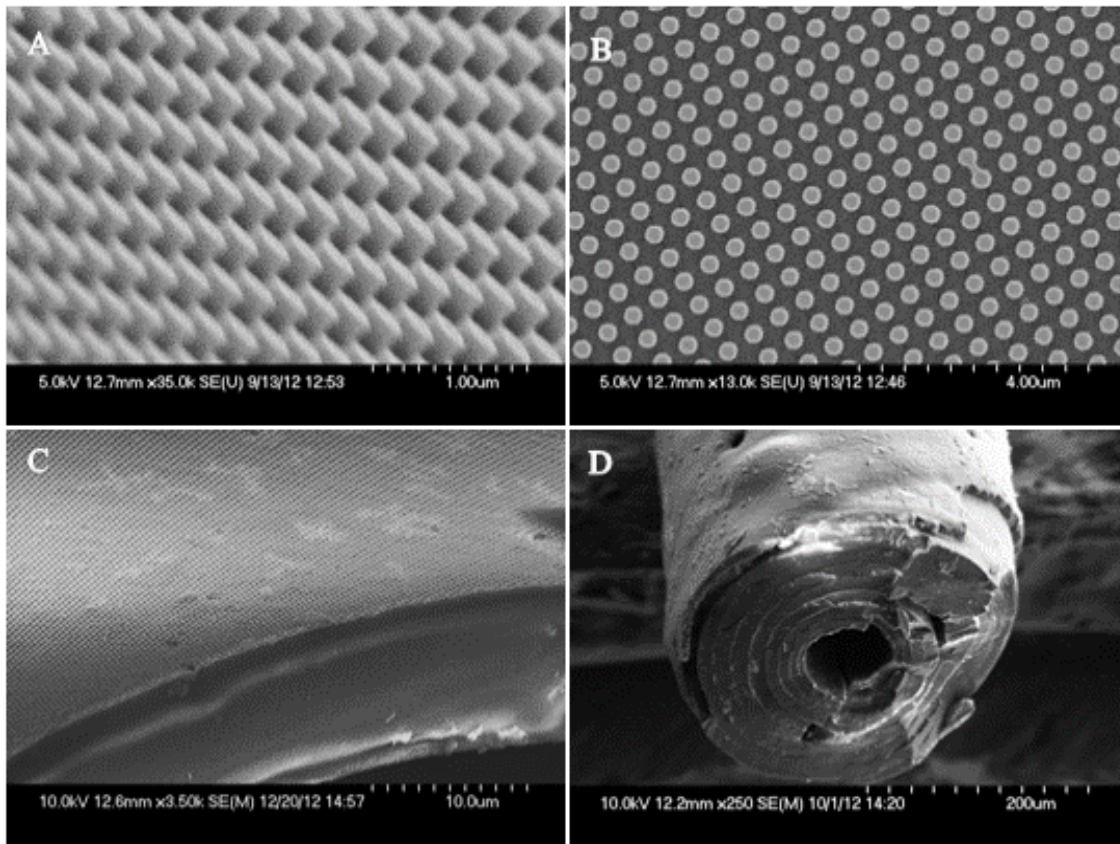


Figure 2-38 - A, B: SEM image of 250 nm wide and 270 nm tall pillars remaining on PEGDMA film after pattern transfer from PAA sacrificial layer, scale bar: 1 μm and 4 μm. C: PEGDMA film nanopatterned edge, scale bar: 10 μm. D: Cross-section view of rolled PEGDMA scaffold, scale bar: 200 μm. Reproduced from Vasiev et al. [1].

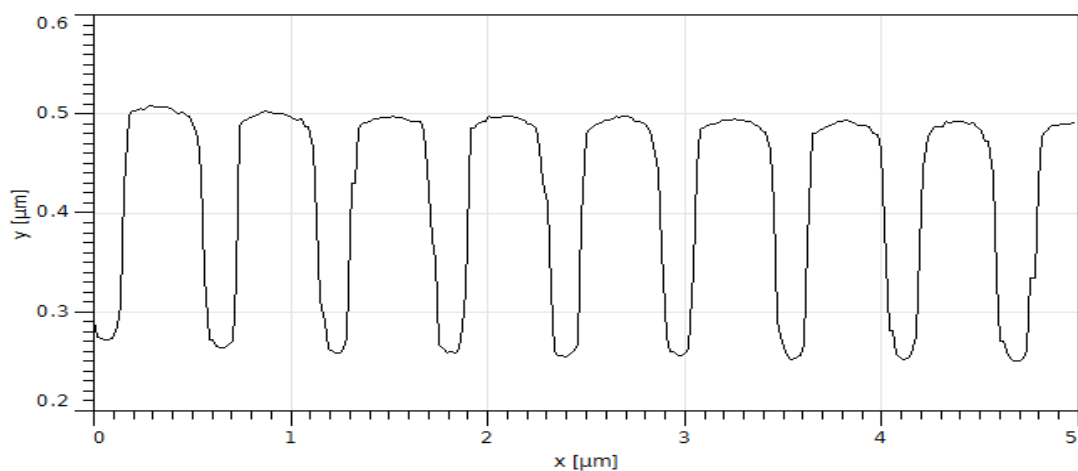


Figure 2-39 - AFM trace of PEGDMA roll topography. A periodic pattern 250 nm high was recorded, the features also show reasonably square shoulders, suggesting the hydrophilic PAA layer has excellent filling properties, drawing the resist well into the right angled corner of the pit.

2.3.9.1 Incorporation of macro-pores in hydrogel films

While hydrogels offer some porosity, to produce enhanced flow and potentially to allow cells to migrate between the layers, windows were created in the photomask to leave non-patterned regions in the hydrogel sheet. These varying diameter holes allow better nutrient and gas diffusion between the hydrogel sheets. The size of pores was varied with gel sheet size pore dimensions kept at 10 % of the edge length with square sheets in the dimension of 2.5, 5 and 10 mm thus ranging from 200 μm to 1 mm.

2.3.9.2 Fabrication of spacers in hydrogel films

Hydrogel films are flexible, and will readily stack and collapse on one another when they are rolled into a tube. To avoid this and create room for cells proliferation and nutrient transport, spacers were introduced by performing UVNIL through a hierarchical PDMS stamp. The use of high aspect PDMS stamps in UV-NIL allows for the incorporation of tall spacers into the hydrogel roll as shown in Figure 2-40. These spacers are intended to act as inter-sheet supports allowing for better cell proliferation and nutrient permeability. The stamp was made by serial lithography of shallow and deep SU8 features. The full procedure is mentioned previously in section 3.2.8 on PDMS, with the different versions of spacer including elongated and hexagonal pillar designs.

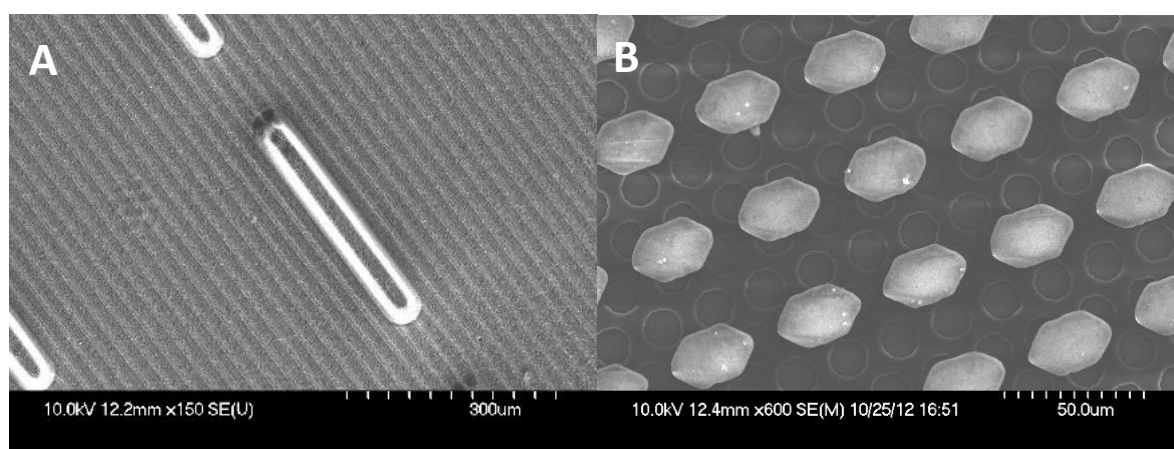


Figure 2-40- A) Hydrogel hierarchical pattern of 400 μm long 80 μm tall spacers made with PDMS mould. B) Two level topography for manufacture of PDMS moulds. 10 μm circular pattern with 30x20 μm hexagonal pillars 100 μm tall above.

A hydrogel pre-mixture was then applied drop-wise onto a glass slide and compressed by the PDMS deep feature replica mould and a NiCr photomask glass plate or acetate. After exposure the hydrogel was rinsed in IPA and detached in RO H_2O to produce spacer features of up to 80 μm tall. The lower structure can be lithographically or thermal NIL patterned SU8 or by etching silicon first and applying SU8 micro features on top, but this is more risky due to the costly process of producing nanofeatures by etching.

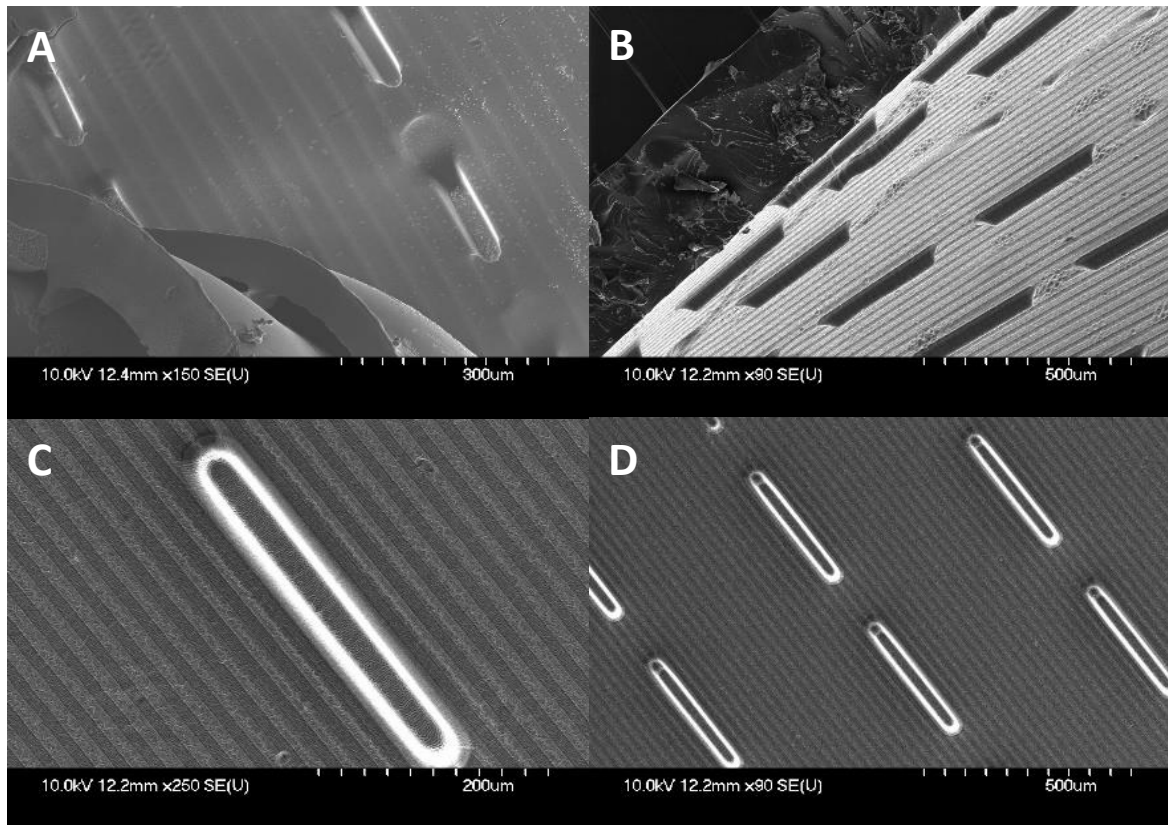


Figure 2-42- (A, B) Patterning of hydrogel rolls with high aspect spacer features. (C, D) Rolls patterned with 500 nm lines of 500 nm depth and 500 nm pitch. The spacer pillars measure 400 μm long 50 μm wide and 80 μm tall. Scale bars: 300 μm , 500 μm , 200 μm and 500 μm respectively.

The spacers produced in the PEGDMA roll surface by these spacer stamps is shown in Figure 2-42. The elongated spacer was chosen as it added anisotropy to the roll and could be used to control rolling direction as well as providing structural support. While the features were too high to measure by AFM successfully, they were measured by profilometry (see Dektak) and measured to be 63 ± 4 μm tall (1σ where $n=8$), reproduced from SU8 3050 features originally 70 ± 1 μm tall.

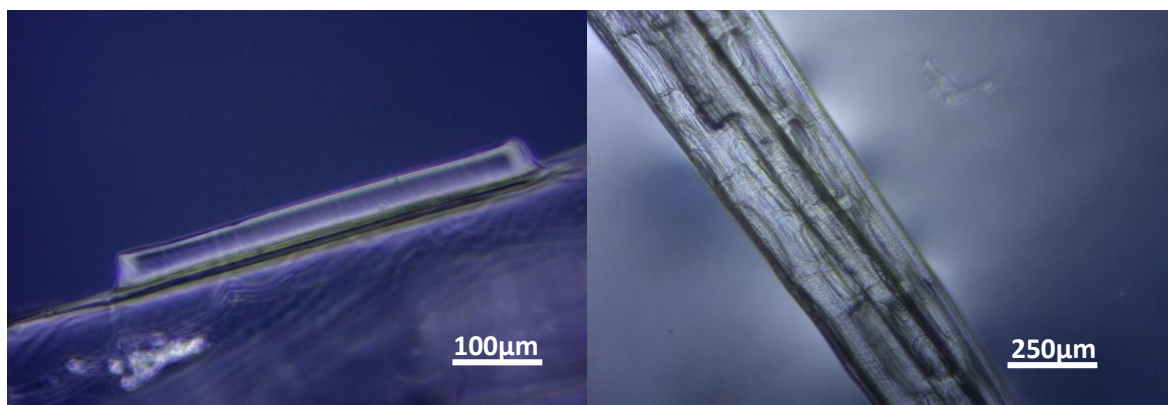


Figure 2-41 - Spacer on hydrogel film when the film is rolled up. Rolls actuated by DMEM cell media (buffered), the process discussed in Chapter 5. Scale bars 100 μm and 250 μm .

Because of the high stamp contact and thickness of resist in the mould during spacer formation, the spacer zone appears to be slightly more rigid than the surrounding film, which works to the

advantage of strengthening the roll lengthways and making sure the spacer does not collapse or buckle under subsequent layers. The addition of spacers is assumed to improve flow between the rolled scaffold layers, and allow space in which cells can migrate and proliferate.

2.4 DISCUSSION

This process provides an effective means of producing self-folding, patterned hydrogel scaffolds. The scaffold incorporates a dual surface micro- and nanopatterned structure with controlled topography for scaffold-cell mechanical interaction and enhanced nutrient permeability. Some fabrication issues do occur when creating replica stamps.

2.4.1 Fluoropolymer thin film stamps

2.4.1.1 Positive attributes of method

A substantial improvement has been made in the manufacturing process of hydrogel and hybrid containers by the incorporation of fluoropolymer stamps to replace quartz and silicon mastering processes, which are now replacing the aforementioned PDMS hierarchical method with numerous advantages:

- Can be injection moulded or thumb embossed
- More flexible and easier to use than PDMS
- Does not stick to PDMS, or glass unless it is pre-treated
- Much stiffer than PDMS (Young's modulus of 23 MPa vs. 2.2 MPa respectively)
- Results in flexible nanopatterned films 25um thick

The use of fluoropolymer films in master fabrication offers substantial increases in throughput due to the ease of embossing, de-moulding and subsequent NIL use of the non-adhesive films. Feature fill has been investigated for low to high aspect ratio patterns with excellent de-moulding. The flow properties of these polymers near their T_g allows for a staggered double patterning procedure, cutting the processing time for structures such as the one shown in section 1.2. Patterning of pillars is a huge advantage as gas entrapment in impermeable stamps often leads to loss of feature depth and quality. This ability to retain stamped nanofeatures is what makes fluoropolymers an ideal candidate for a modular lithographic system.

2.4.1.2 Artefacts and flaws affecting product quality

However some short falls remain. Whereas PDMS can be cast and left to cure, the softness of FEP during the replication process means that it will continue to flow under even minute deformations. Figure 2-43 shows the effect of a 3 μm slip of the imprinting stamp due to chuck rotation. The resulting shear easily moves the pillars through the melt creating an array of lines, while this could be advantageous for certain applications, (saving EBL exposure time in the writing of lines by rather writing dots) it adds an element of uncertainty, and requires correct cooling of the melt prior to de-moulding.

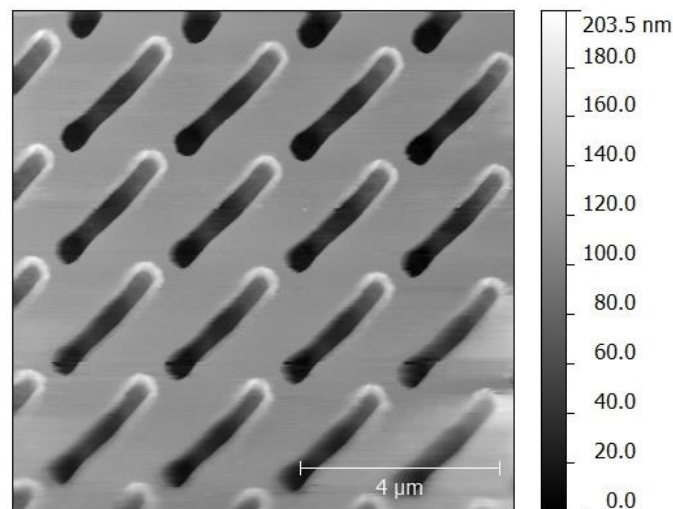


Figure 2-43 - Dragging of nanopillars through FEP during imprinting, wither by stamp rotation or early peeling from the master, can result in the ditches created here. Scale bar: 4 μm .

When FEP features are too high in relation to the PMMA being imprinted and the imprint temperature is above the melt temperature of the PMMA the melt is drawn up by capillary force into the mould to form these geometric patterns nicknamed ‘flowers’ a stilted cloister like 2.5D structure. In this case 200 °C, with a spun layer 200 nm thick and imprinting pillars of 200 nm high and 400 nm tall.

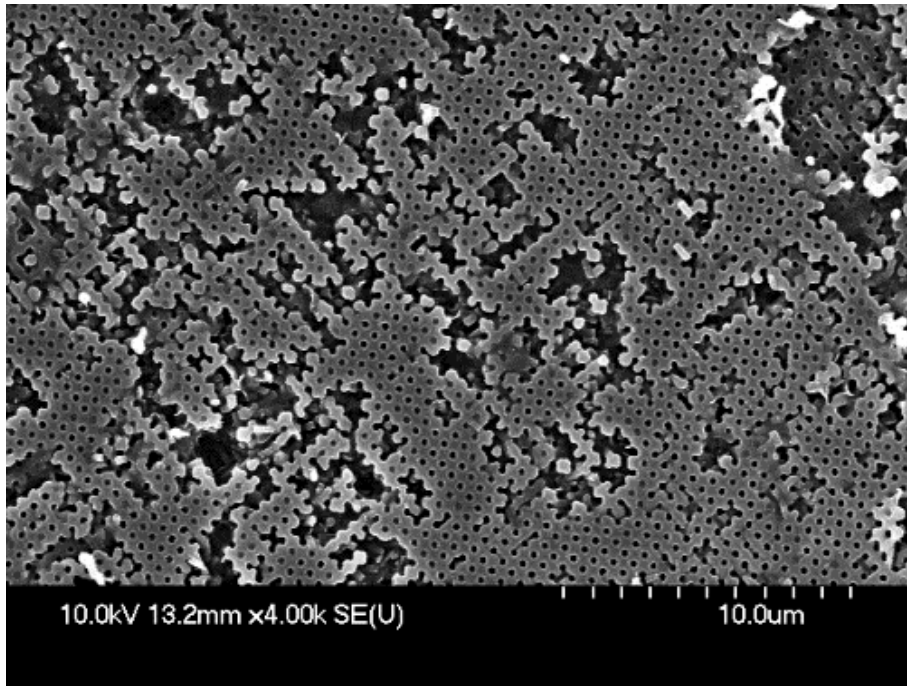


Figure 2-44 – An SEM image of the 'flowers' formed by PMMA climbing up the hydrophobic FEP pillars during imprinting at 180 °C. The thickness of the PMMA layer being less than the height of the FEP can cause this problem. Scale bar: 10 μ m.

AFM scans of the surface showed the geometric nature of the patterns, with the PMMA bridging horizontally or diagonally between pillars. When plotted in an isometric view, the defects in the PMMA film can be seen as a result of too thin imprint layer at a high temperature. The high flowability and high surface energy of the stamp result in a wicking of the molten PMMA up into the cavity of the stamp.

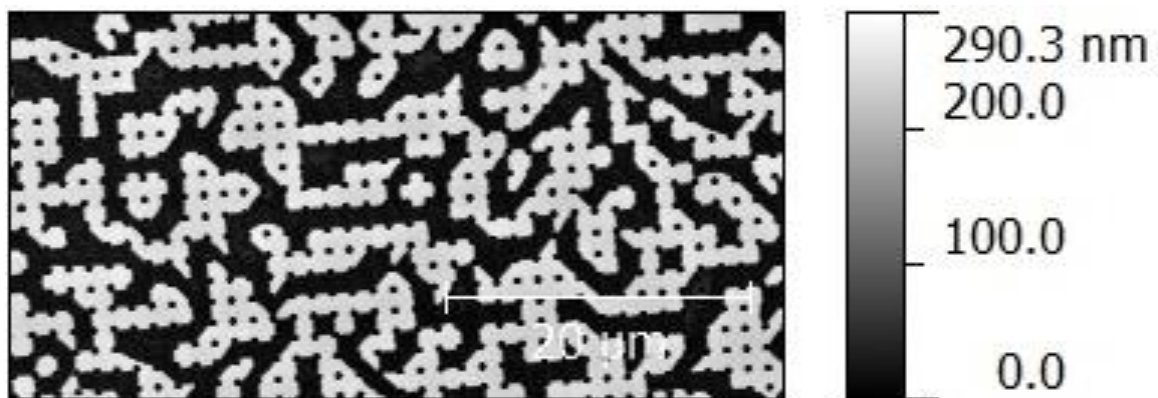


Figure 2-45- An AFM scan of the 'flower' surface illustrates the PMM bridging between individual FEP pillars. This is particularly noticeable when the PMMA film is roughly half the thickness or less than the height of the FEP features. Scale bar: 20 μ m.

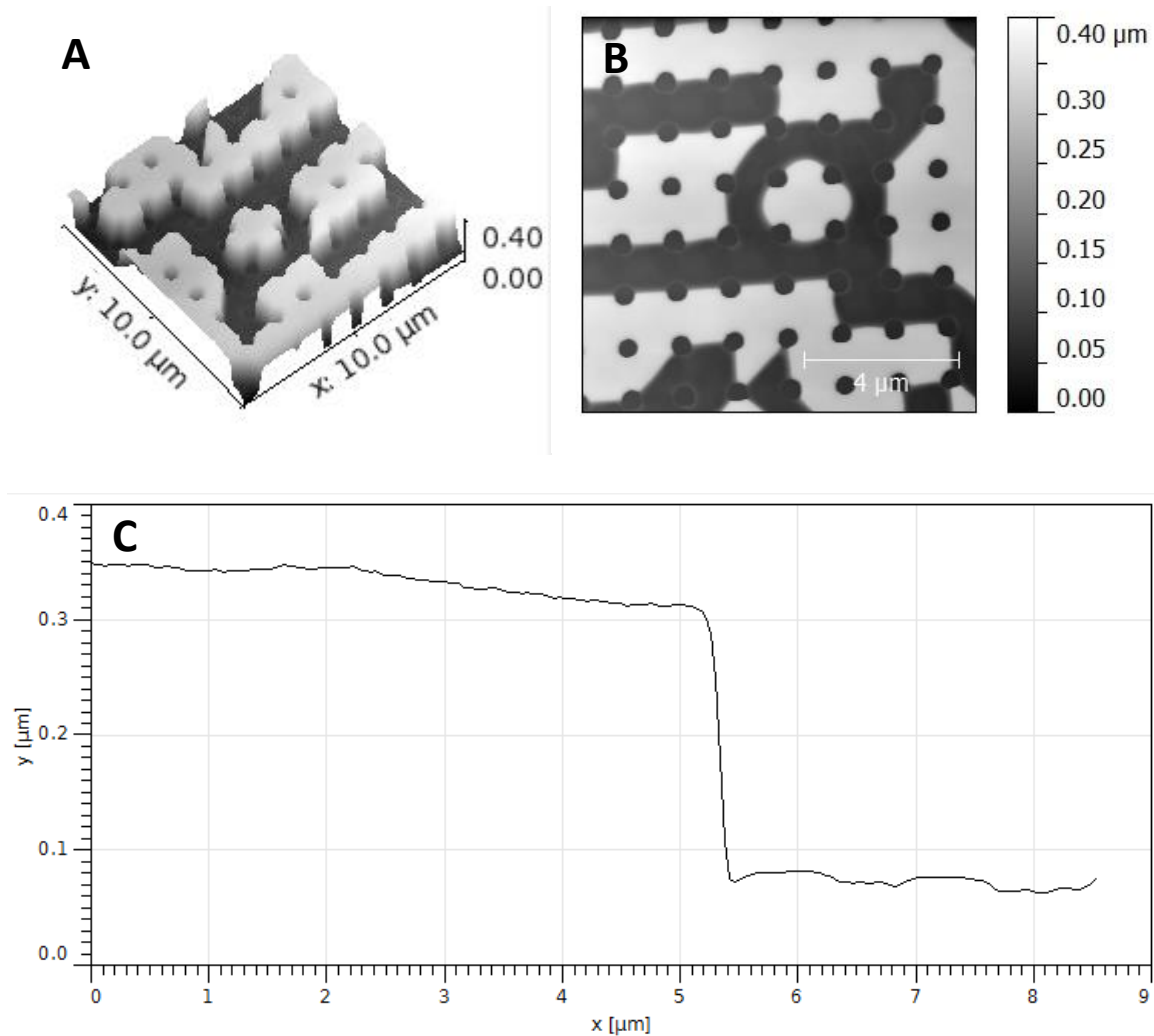


Figure 2-46 – A) 3D plot of Image of 'flower' morphology resulting from low viscosity of molten PMMA imprint layer, and a hydrophobic FEP stamp. B) The features are roughly twice as high as the spun film of PMMA, causing it to fill up the voids in the stamp by wicking up the stamp pillar features. C) A thin residual layer in the PMMA is still visible at the base of the features.

There is insufficient PMMA melt to supply the wicking when the thickness of PMMA is less than the feature height of the FEP stamp. These geometrical phenomena occurs in a less pronounced form when the melt to pillar height ratio is closer to unity, but the temperature is elevated.

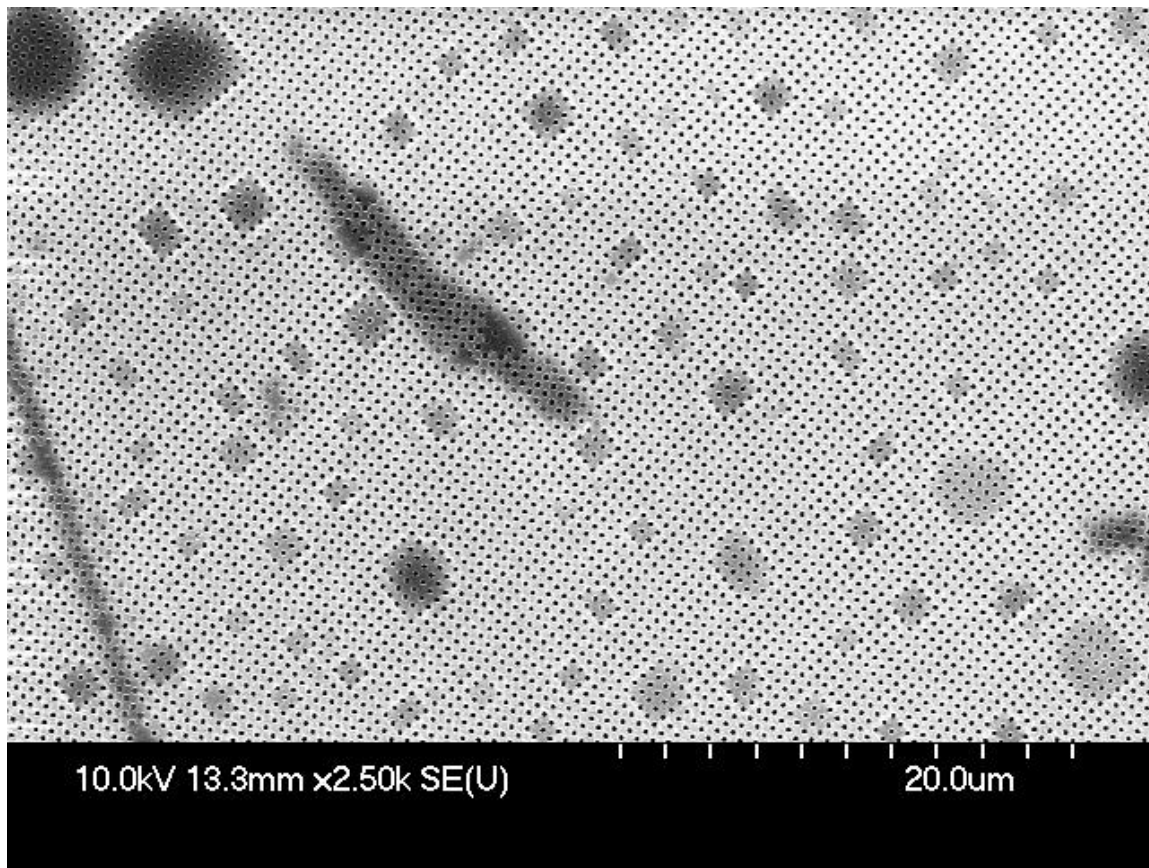


Figure 2-47 – SEM image of PMMA imprinted with a FEP pillar stamp, produced by spinning a thicker PMMA layer roughly 90 % of the height of the FEP features (500 nm). Non-uniformity can still be seen in the imprinted surface due to gas traps and the PMMA climbing up the FEP features. Marker bar: 20 μ m.

Shown in Figure 2-47 is the effect of insufficient pressure on PMMA layer imprinting with a FEP stamp during replication. It is proposed that this occurs as a result of trapped gases under the FEP film, and could be remedied by increasing pressure.

2.4.1.3 Limitations of the FEP process in master replication

Replicating pits from high aspect ratio (more than 4:1 with a 200 nm diameter) pillars has proven difficult, especially when the pitch nears half the pillar diameter. The FEP cannot be extracted, as due to the flexibility of the film, the transverse load of peeling catches on the pillars causing the film to tear. One solution for this would be to use a fixating FEP film with a cementable side etched with Fluoro Etch[®]. This would allow the film to be pulled in an exactly vertical direction from the mould, reducing the shear force on the pillars and the film.

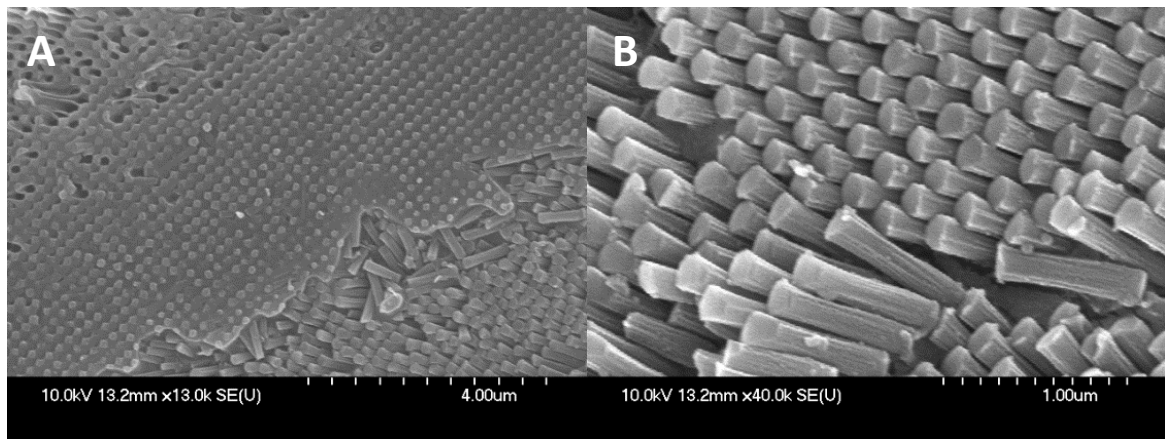


Figure 2-48 –A) SEM images of damage caused to master stamp and FEP film due to catching o the replica on the high aspect ratio (4:1 aspect 250 nm wide) pillars. The high aspect prevented the successful peeling of the FEP replica stamp. B) Peeling caused permanent damage by breaking the pillars free from the substrate on the master. Scale bars: 4 μm and 1 μm respectively.

It can also be seen that uneven feature thickness such as bulging or non-parallel feature walls can cause problems with replica separation. This is illustrated in Figure 2-48 where pillars do appear to have a thinning around the middle and a slightly expanded top, suggesting a slight undercut occurred during etching, which could cause them to stick inside the FEP, making delamination more difficult. In the absence of a purely vertical pull-off technique, and for stamps with lower aspect features; flexing the substrate could allow the sample to detach. However in the case of long and rigid pillars such as these in silicon, the result was excessive shear loading transverse to the pattern, it should be noted that all stamps were coated with evaporated silane to aid release from the imprint.

2.5 CONCLUSIONS

FEP has been shown to be a versatile, flexible and strong plastic with excellent wettability and to be chemically inert. It has been demonstrated that these plastics can play a vital in role in the manufacture of differentially patterned micro arrays, surfaces and micro-containers. While it still requires further expansion in terms of area coverage, this is a limitation in current patterning capacity and not of the FEP as a technology. Once large area patterns become available and large composite nanotopographical arrays are easily mastered, these can be quickly expanded in volume of production as FEP replicas. The process has been shown to dramatically increase the speed of this process as compared to one relying on manufacturing such features by lithographic methods. The cementability of the FEP from a regulated producer at very low cost opens the door to many possibilities, and greater freedom of experimentation. Its application to 3D curved surfaces makes this transferable to moulding and casting applications, and has sufficiently higher strength than PDMS, allowing for greater degrees of curvature without rupture.

3 HYDROGELS AND HYDROGEL ACTUATORS

3.1 INTRODUCTION

In this work, hydrogels are used as bioactive surfaces and actuators for the formation of 3D tissue engineering niches. They are a necessary step in translating the inherently 2D methods of surface pattern manufacture inherited from MEMS and electronics processing, into 3D architectures. Hydrogels offer several benefits, chief of which is their versatile chemistry, allowing the creation of different chemical sensitivities and interactions as discussed in Chapter 1. The gels can be made stealthy where they do not immobilize proteins, and thus allow controllable (by porosity) transit of intercellular chemical communication, movement of waste and nutrients [93]. Hydrogels can additionally be manufactured in layers to create environmentally responsive bilayers, by the incorporation of certain responsive pendant groups copolymers [110] and particle crosslinkers allowing for specific environmental triggers [17]. Combining tuneable hydrogel chemistry with an existing method of manufacture such as photolithography allows for the easy integration of hydrogel forming in existing photolithographic setups [1]. This provides a basis for the simple manufacture of these self-folding hydrogel geometries, which can then be scaled by other processes such as screen printing and roll-to-roll printing [67].

Hydrogels however are not without risks, as they suffer from poor actuation forces [24] and too low mechanical properties for structural applications [77]. The hydrogel often incorporates a solvent which forms the porous phase of the gel once it has been developed, thereby producing the empty space and high surface area which allows for large changes in swollen volume, depending on the amount of solvent used. This high solvent content (often water) can be incredibly difficult to apply to surfaces by spin coating, a common technique in microfabrication for applying thin polymer films by spinning the surface at high speed (Section 3.2.5). They are also difficult to maintain on the substrate surface, prevent stamp adhesion, destruction by sheer and delamination. The photolithographic process is unforgiving in this respect and requires very precise contact and demoulding between photomask and gel precursor solution. Additionally, when making structures that require lift-off from a surface in a controllable manner, hydrogels can be very difficult to anchor selectively, as their swelling can cause them to detach from many substrate surfaces. The solvent can also dissolve many lift-off layers which are not known for being chemically inert. New methods of micro fabrication and nanopatterning for the creation of hydrogel based 3D interfaces for cell culture will be demonstrated, as will the methods of fabrication available and difficulties in their implementation in the cleanroom based processes.

3.2 MATERIALS AND METHODS

3.2.1 Materials

Poly(ethylene glycol)dimethacrylate (PEGDMA) Average PEGDMA (M_n 550 g mol⁻¹), Poly(ethylene glycol) diacrylate (PEGDA) average PEGDMA (M_n 700 g mol⁻¹), Trimethylolpropane trimethacrylate (TMPTMA), Ethylene glycol dimethacrylate (EGDMA), N,N-Methylenebis(acrylamide) (MBAAm), 2-Hydroxyethyl methacrylate (HEMA), Acrylic acid (AAc), Triethylamine (TEA), N,N-Diethylaminoethyl methacrylate (DEAEMA) and Poly(N-isopropylacrylamide) (PNIPAAm) M_w 19,000-26,000 and monomer (NIPAAm) were purchased from Sigma-Aldrich, UK and used as received. Photoinitiators I819, LTPO, I2959 and D1173 were purchased as chemical analogues from Sigma-Aldrich, UK and stored in dehydrated atmosphere in the dark. Poly(acrylic acid), 25 % aqueous dilution [M_w 50,000] and, poly(hydroxyethyl methacrylate) (PHEMA) M_w 200,000 were obtained from Polysciences, USA. PAA with M_w 100,000 and 1,800 (Sigma-Aldrich, UK) were diluted with RO H₂O to produce the necessary concentration for spinning. SU8 series resists and Shipley S1818 were used as received from the distributor. Sylgard 184 poly(dimethylsiloxane) (PDMS) and curing agent for the manufacture of spacer structures was obtained from Dow Corning via Farnell, UK and mixed to manufacturers specifications. Trichloro(octadecyl)silane (Sigma-Aldrich, UK) was used as received as a release coating for stamps and photomask plates.

3.2.2 AFM and metrology for feature depth measurement

High resolution metrology was done using a Veeco Dimension 3100 Atomic Force Microscope (AFM) and profilometry was performed with Veeco Dektak 6M Height Profiler, the full procedure was previously described in section 2.2.2.1.

3.2.3 SEM imaging of nanostructures

Scanning electron microscopy (SEM) imaging was done using a Hitachi S4700 SEM. Samples were dehydrated by an ethanol series starting with 100 % RO H₂O. Samples were dried at 120 °C for one hour following further drying in a vacuum at 100 mTorr prior to sputtering with a 6 nm-9 nm iridium charge dissipating layer.

3.2.4 O₂ plasma ashing

Samples and wafers were descummed and functionalized by use of an oxygen plasma to 'ash' (etch) the surface at varied powers ranging from 60 to 200 W RF power. Deep ashing through soluble polymers was done using long ashing periods of up to 10 minutes.

3.2.5 Spin coating

The process of spinning (spin coating) involves the application of thin solution or polymer films. The process involves spinning the wafer on which further processes are to be performed, and applying a quantity of liquid material. Speeds vary between 500 rpm and 6000 rpm, with film thickness altered by adjusting the viscosity, spin speed and duration. Values are confirmed experimentally by scratching the film and measurement with surface profilometry (Dektak) or AFM.

3.2.6 Micro- and nanopattern formation on quartz and silicon

3.2.6.1 Quartz master stamp fabrication

The nanopatterned stamp used for both the pre-patterning of the sacrificial film and subsequent top-side patterning of the hydrogel films, PDMS and FEP replicas was fabricated from a 1 mm thick, square quartz sample of 25 mm length sides. The full procedure was previously described in section 2.2.3.1.

3.2.6.2 Si master stamp fabrication

The silicon stamp used for making PDMS and FEP replicas and for thermal NIL was manufactured in a similar process to those described in Section 2.2.3.2,

3.2.7 Release coating for stamps and photomasks

Release coatings were used to allow photolithographically produced devices to allow for the smooth separation of the transparent stamp from the set material underneath, this reduced the risk of stamp and feature damage during demoulding. This is also critical for making PDMS replica stamps, as the PDMS can bond very well with silicon containing substrates, by its siloxane group. To avoid these issues; prior to use in UV-NIL or manufacture of PDMS stamps the Si and qz masters were washed in acetone, methanol and isopropanol for 5 minutes each before being cleaned in an oxygen asher for 2 minutes. NiCr Photomask plates and slides were also coated with a silane release coating, to aid separation from photo-patterned resists.

Silane deposition from liquid was carried out from a 0.0001 v/v % solution of silane in heptane for 20 minutes. After the treatment was completed the master stamps were rinsed in heptane, acetone and isopropanol. Vapour deposition of silane required samples to be ashed for 1 minute at 60 W power in O₂ plasma with the stamp or mask surface facing up, and placed on a set of foil spacers inside a large glass petri dish sealed with a second glass plate. The dish had one drop of silane placed on opposite sides of the dish and was filled with nitrogen to create an inert atmosphere. The dish was placed on a hotplate heated to 150 °C for 15 minutes. The silane was allowed to evaporate and

condense onto the surface of the stamp or mask, after which the dish was cooled and flushed with nitrogen before removing the slide and testing for hydrophobicity.

3.2.8 PDMS replica stamps for NIL and UV-NIL

PDMS replica stamps were produced in a method similar to that outlined previously in section 2.2.3.3. However for tall features such as space pillars photoresist features were used. Silicon or glass was patterned with S1818 or SU8 photoresist (depending on feature height). In the case of hierarchical and spacer incorporated structures of feature size $\geq 50 \mu\text{m}$, a thin layer of SU8 3005 was first spun at 4000 rpm for 30 seconds and patterned with micro or nanofeatures by photolithography and development or thermal NIL respectively. A thick layer $>1 \text{ mm}$ of SU8 3050 was then spun on top at 1000 rpm and allowed to prebake for at least 3 hours at $90 \text{ }^\circ\text{C}$ to remove solvent. This was then photo lithographically patterned with spacer features. All non PMMA or S1818 masters were then silane treated by immersion into a heptane diluted silane, or by silane evaporation (Section 3.2.70

Release coating). Sylgard 184 PDMS (Dow Corning) was mixed at a ratio of 10:1 to curing agent, and poured onto the master pattern in a salinized glass dish. It was then sonicated for 2 minutes and de-aerated in a vacuum for 30 minutes prior to curing in an oven for 3 hours at $70 \text{ }^\circ\text{C}$. The cured PDMS slab was cut into individual patterned $15 \times 15 \text{ mm}$ squares.

3.2.9 Sacrificial layer for lift-off of patterned devices

To aid the release of photopatterned features (Figure 3-1) a sacrificial layer is needed, PAA was used in this application as a water soluble layer. PAA solutions of various M_n were spun at 4000 rpm for 30 s onto a $15 \text{ mm} \times 15 \text{ mm}$ silicon wafer of $525 \mu\text{m}$ thickness and allowed to settle at room temperature for 2 minutes. The spin speed vs. thickness were determined for varying molecular weights of PAA are shown previously in Figure 2-31. The spun film of PAA was then heated to $90 \text{ }^\circ\text{C}$ and maintained for 3 minutes to remove residual solvent [190]. The dehydrated samples were placed into an Obducat NIL 2.5 nanoimprinter, a patterned qz master was placed on top, and pattern transfer was then carried out as follows. The master and wafer stack was set to preheat to $105 \text{ }^\circ\text{C}$ under a pressure of 3bar for 5 minutes. The temperature was then raised to $115 \text{ }^\circ\text{C}$ and a pressure of 15 bar for duration of 6 minutes before dropping to 10 bar at which point the sample was air-cooled to $60 \text{ }^\circ\text{C}$ under a constant pressure. De-moulding of the master was carried out at room temperature.

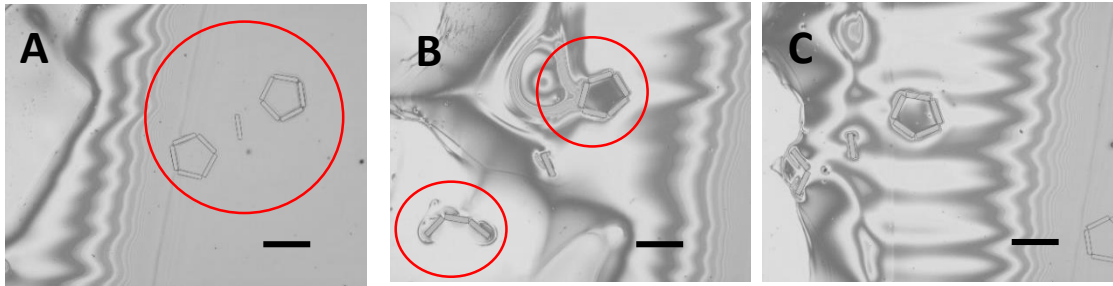


Figure 3-1 – Optical microscopy images of demonstrated lift-off of photopatterned components from a PAA sacrificial layer. One edge submerged in water causing gradual washing away of the water-soluble polymer. A) Hydrogel features on PAA being approached by a wetting front (B-C). Scale bars: 200 μm

3.2.10 Thermal nanoimprint lithography (Thermal NIL)

NIL was performed using an OBDUCAT NIL-2.5 thermal Nanoimprinter for patterning of sacrificial layers and master transfer and replication. The sample was placed facing up and the master stamp facing down on top of it, in a sandwich of two aluminium sheets, to produce an even temperature distribution within the tool, and to accommodate slight overpressures (which was problematic on every occasion). Peak temperatures for PAA thermal NIL was 105 °C at 15 bar for 6 minutes, samples were pre pressurized to 5 bar during the temperature ramp. PMMA was imprinted at 180 °C at the same pressures, but held for 8 minutes.

3.2.11 Photolithography

3.2.11.1 Photomask design

Photomasks were designed in Corel Draw Suite X3 and printed on acetate. Files were exported in vector format to preserve resolution. The files were printed by Micro Lithography Services (Chelmsford, UK) onto A4 sized acetate sheets.

3.2.11.2 Metal deposition

Metal deposition was done in a Plassys MEB 550S Electron Beam Evaporator for Au, Ti and Ni-Cr deposition up to 100 nm in thickness. These were used as charge dissipation layers for SEM imaging and EBL exposure, photomasks, selective etch masks and as etch stops.

3.2.11.3 NiCr masks

NiCr permanent masks (Figure 3-2) were made on glass slides using a modification of the standard JWNC protocol for mask preparation to replicate the Acetate master masks onto glass slides. Glass slides were washed in acetone, methanol and isopropanol for 5 minutes in each. The slides were then dried in a 120 °C oven for 15 minutes and ashed in 100 W O₂ plasma for 2 minutes prior to spin coating with Shipley Microposit S1818 Series Photo Resists, spun at 4000 rpm for 30 seconds to achieve a final thickness of 1.5 μm according to the manufacturer's guidelines [192]. The coated substrate was baked on a hotplate at 115 °C for 120 seconds. Slides were exposed under the acetate mask in the MA6 for

18 seconds to accommodate the transparent substrate. This was followed by development with MF319 for 75 seconds and an RO water wash. A post wash descum was carried out in O₂ plasma for 3 minutes under 100 W, and sputtered with 50-80 nm of nickel-chrome (NiCr) in a Plassys evaporation coating chamber. The slides were then stripped of any remaining S1818 with ethyl lactate (EC Solvent) and isopropanol. Optimum conditions were found through trial and error and minor changes to manufacturer's guidelines.

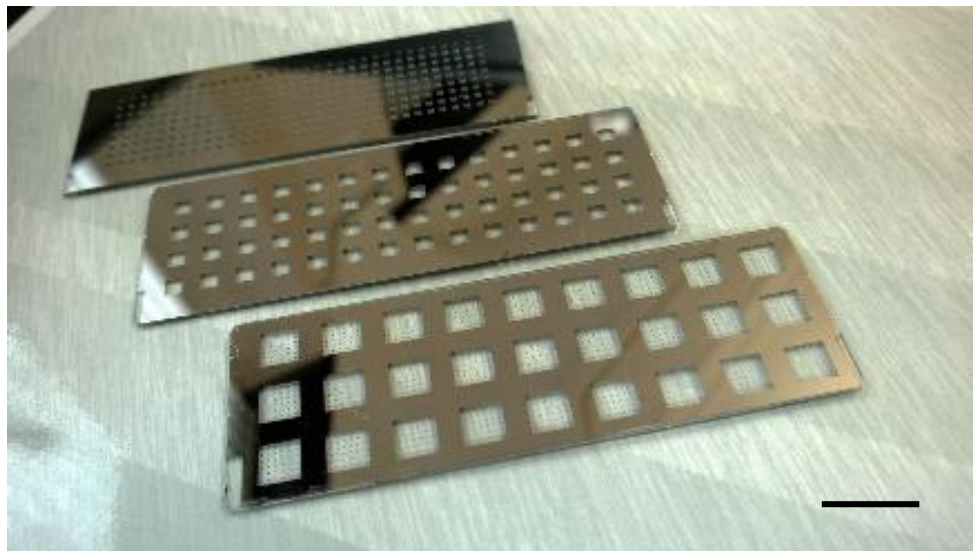


Figure 3-2 - NiCr photomasks on glass slides, scale bar 10 mm.

3.2.11.4 Mask alignment for sequential photolithography

Photolithography was performed with a SUSS MA6 Mask Aligner in top side alignment mode, operating a narrow band light source at 365 nm and intensity of 7.2 mW/cm². Photolithography is achieved by exposing a photosensitive substrate to light through a pre made mask, which isolates certain areas for the exposure the process is shown in Figure 3-3.

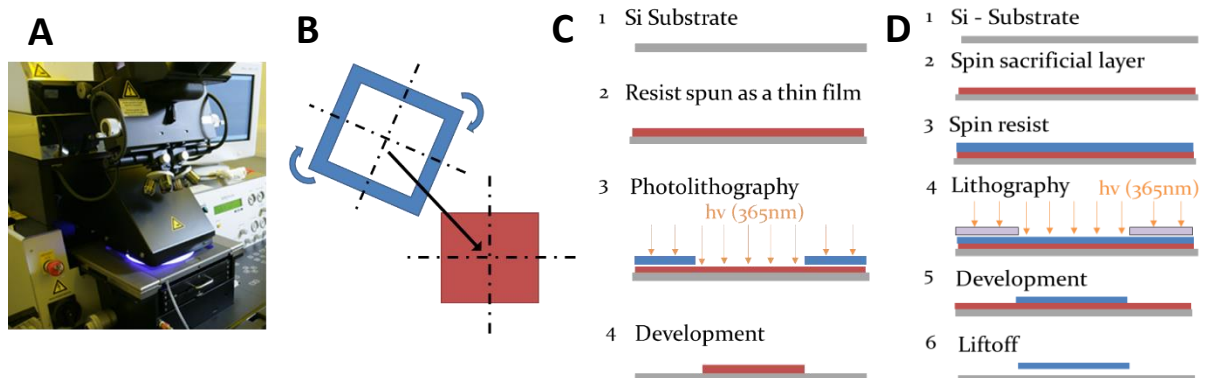


Figure 3-3 - Mask alignment process. A) MA6 mask aligner during lithography. B) Process of 'alignment' where features are positioned using microscope and x-y stage. C) Process of photolithography, and D) photolithography with lift-off process.

3.2.11.5 Hydrogel photolithography

Silicon wafers with a pre-patterned PAA sacrificial layer were placed in a Suss MA6 mask aligner with a patterned nichrome (NiCr) mask. A drop of polyethyleneglycoldimethacrylate (PEGDMA) solution was applied immediately followed by hard contact with the mask. The sample was exposed to a dose varying from 59.2 mJ/cm² to 118.4 mJ/cm² to produce sheets of varying curvature. The photo crosslinked sheets were developed in Isopropanol followed by rehydration overnight in RO water, which facilitated the dissolution of the sacrificial layer and lift-off of nanopatterned films.

3.2.12 Hydrogel synthesis

Different types of hydrogels were prepared in this thesis, ranging from 'neutral' to 'active' gels. The primary role of neutral or structural hydrogels was the structural support of photolithographically defined structures, and no environmentally triggered response. These neutral gels consisted of PEGDMA or HEMA, which is easily crosslinked by a variety of processes. PEG is known for being unresponsive to stimuli and does not readily absorb protein [93], allowing permeation of chemical signals, waste and nutrients. Active hydrogels were used to define the environmentally responsive layer of the hydrogel bilayers which came in the form of thermally and pH responsive gels based on two widely used monomers of n-isopropylacrylamide (NIPAAm) and acrylic acid (AAc). There were many possible combinations of crosslinkers, monomers and copolymers, with some that yielded far too sticky gels for the formation of homogenous solid hinges. Recipes were also fine-tuned for spin coating and photolithography under a mask aligner, as well as for use with imprinted soluble sacrificial layers.

3.2.12.1 Neutral non-responsive hydrogels

In the area of structural or neutral hydrogels, several gel formulations have been attempted, and all suffer from one drawback, which is the spinability of the pre-polymer. Spinability refers to the ease of forming a thin film by spin coating and is the most widely used method of photo resist application. With gel mixtures it was observed that while HEMA beads and flies straight off the wafer substrate, PEGDMA and PEGDA spin well initially but then segregate and form voids in the film. To prevent this, surface pre-treatment with Ti Prime (MicroChemicals GMBH, Germany) was used and seems to be a suitable solution but is not permanent and will only hold the PEG films for 5 minutes. A far more permanent treatment was found to be the deposition of a nanolayer of gold/palladium. These techniques are not necessary on PAA pre-spun surfaces due to the hydrophilicity of the OH groups present on the surface. Hydrogel films spun on polyacrylic acid sacrificial layers showed no shrinking over time due to the excellent wetting, but solvent still evaporated, limiting the amount of time available between spinning on a resist layer and having to perform the photolithography.

Table 3-1 - Neutral hydrogel recipes investigated in this work used both HEMA and EGDMA, two commonly used monomers for contact lens manufacture[47], a consumer product with significant strength and low protein absorption. Recipes resulted out of numerous trial and error experiments to achieve a reasonably stable flexible and well defined film, the PEGDMA based gel is a modification of a structural gel used by the Gracias group at Johns Hopkins [24] a different initiator (LTPO) was also used which according to BASF is less susceptible to oxygen inhibition than I2959 [115].

Pre polymer solution	0.1 –0. 5 g/ml PEGDMA + and 1-4 % initiator I2959	90-50 v/v % PEGDMA + 1 w/v % LTPO	0.5 g/ml HEMA + 1 % Crosslinker and 1 % Initiator LTPO	0.2 g/ml PHEMA+1 % Crosslinker TMPTMA + 1-4 % Initiator I 2959
Inertion	Nitrogen Purge	Nitrogen Purge	No Nitrogen	No Nitrogen
Solvent	RO water vs. 1:1 EtOH/H2O	EtOH	EtOH	EtOH
Application	Spin or Cast	Spin or Cast	Cast	Spin or Cast
Exposure	15-90 s	5-20 s	40-90 s	40-90 s
Observation	Longer exposure times due to poor I2959 absorbance at 365 nm.	Forms transparent and strong gel	Transparent Gel, but brittle if EGDMA cross linker is used	More flexible gel when made with TMPTMA.

To create the photo sensitive pre-polymer PEGDMA solution, photoinitiator was dissolved in ethanol (EtOH) at a ratio of 1:10 w/v and vortexed for 1 hour followed by 5 minutes sonication. PEGDMA was then combined with the prepared initiator solution at a ratio of 10:1 v/v resulting in an initiator concentration of 1:100 w/v. The whole solution was then agitated with nitrogen for 10 minutes, at which point the glass container was sealed and left for 18 hours before use. Photo-exposures were carried out in accordance with gelling times which varied with application. Photo-patterning was done using photolithography through a NiCr or acetate mask.

3.2.12.2 Thermo responsive hydrogels

Many hydrogel recipes exist in literature, ranging from bilayers prepared by [24] where PEGDA-NIPAAm-AAc, and NIPAAm-HEMA gels were prepared to close a ‘Venus-flytrap’ style drug device [24]. The approach in this thesis is similar, but uses different monomer combinations and less toxic solvents. One other feature is the fabrication method differs from where gels are used for encapsulation of cells such as [73] by the amount of initiator used. Gels which polymerize while in contact with living tissue need shorter exposures and less initiator to avoid compromising the cell with the radicals they generate. In this thesis the structure comes into contact with cells after fabrication, and any residual initiator can be washed away with titration prior to cell encapsulation. Lastly the gels used here focus on resolution and pattern ability as well as their actuation capacity. NIPAAm is easily crosslinked with acrylic acid, and was used to make bi-active hydrogels which shrink and expand depending on pH and temperature as mentioned before. While these pose great interest, the synthesis of a good thermo responsive hydrogel was a primary objective. The trial was

used to look at the effect of synthesis temperature on the homogeneity of the gel. Two main recipes which possessed good swelling properties, the ability to incorporate a pH responsive group and that were mechanically stable enough to handle.

3.2.12.2.1 PNIPAAm-co-PEGDMA,

Table 3-2 - Recipe for original PNIPAAm-co-PEGDMA hydrogel created for thermo responsive hinge manufacture.

Component	Concentration/mass	Function
PEGDMA (M_n 550 g mol ⁻¹)	1 ml	Polymer
IPA	0.1 ml	Solvent
LTPO	1 w/v %	Initiator
TEA	0.01 v/v %	Oxygen scavenger
NIPAAm	400 mg	Thermo responsive monomer

3.2.12.2.2 PNIPAAm-co-MBAAm

Table 3-3 - Recipe for MBAAm crosslinked PNIPAAm based gel, with the recipe adopted from the Gracias group work at Johns Hopkins Institute. Recipe for this formulation was adopted from [24].

Component	Concentration/mass	Function
NIPAAm	500 mg	Thermo responsive monomer
MBAAm	25 mg	Crosslinker
PNIPAAm	25 mg	Thermo responsive polymer
LTPO	5 mg	Initiator
1-Butanol	1.5 ml	Solvent

3.2.12.3 Cationic Hydrogels

N,N-Diethyl-amino-ethyl-methacrylate (DEAEMA) is a functional methacrylate and tertiary amine that can be used as a synergist to generate free radicals similarly to TEA, as it acts as an oxygen scavenger in photoinitiated reactions. It is water-soluble, can improve adhesion of formulations and responds to aqueous pH. The recipe using this monomer is the same as those of the two recipes in the previous section 3.2.12.2 with the NIPAAm component replaced with DEAEMA monomer in a 1:1 mol/mol ratio, giving roughly a 0.61:1 w/w substitution.

3.2.12.4 Ionic Hydrogels

PAA and AAc were dissolved in HEMA, NIPAAm and PEGDMA to make a range of pH and pH+temperature responsive gels. No successful recipe exists for making blocks of PAA-co-PEGDMA gels, and the Gracias formulation [24] was used for making bi responsive hybrid gels, in which case 0.5 ml of acrylic acid (AAc) was added to both 'Cationic' and 'Thermal' recipes shown previously, yielding gels that were sufficiently strong and stayed intact for up to 3 swelling de-swelling cycles.

3.2.13 Hydrogel bilayers

Bilayers consist of two materials with different properties being physically or chemically bound together. They are often used as cantilever actuators as the different properties on the two surfaces create asymmetric behaviour when the bilayer is stimulated in a certain way.

3.2.13.1 pH responsive bilayers

There are two ways of producing pH sensitive bilayers; the first is surface grafting and the second is bulk copolymerization such as the one used by Bassik et al [24]. The polymers and monomers which have been used to bind with the pH sensitive carboxyl groups mentioned previously are shown in Table 3-4.

Table 3-4 - Monomers and available functional and crosslinking pairs

Base (poly)mer	Co-polymer	Optional Crosslinker
HEMA and PHEMA	AA,PAA,	PEGDMA or TMPTMA
NIPAAm and PNIPAAm	AA,PAA ,MAA,P(AAm-co-AAc)	MBAAm or EGDMA
PEG based polymers	PAA,PMAA	EGDMA

PAA is a superabsorbent polymer with a 3D network filled with hydrophilic (COOH) groups at low pH. Any absorbed H₂O is therefore hard to release. By binding these groups to a surface of similarly acrylated hydrogel leads to a bilayer bi-functional film. This method of manufacture can offer a different response from a normal bulk gel network. They can be made very thin, by the novel method of “proximity graft polymerization”.

When the pH is below the pKa of the acidic carboxyl pendant groups of the polymer, they are in their protonated state (COOH). As the pH increases above the pKa, the (COOH) pendant groups dissociate to their deprotonated (COO⁻) state [95]. This causes an interaction with the polar charge of water binding H₂O molecules to the chain and propagating a swelling reaction. PAA (50000 Mw, 25 % Aq) was purchased from PolySciences. PAA (1800 Da, 63 w/v %, and 100000 Da 12 w/v % aqueous) PMAA (100000 Da) along with AA monomer were obtained from Sigma Aldrich, UK.

3.2.14 Hydrogel actuator triggering

After development in isopropanol and rehydration in RO water the samples of free floating gel would then be triggered to roll and unroll by applying aqueous pH 7 and pH 4 buffer respectively. pH values above the critical pKa of the acid groups bound to the gel, undergo a deprotonation causing them to absorb or ‘bind’ water. This leads to a triggered osmotic differential across the thickness of the gel, and leads to subsequent rolling or folding of the gel films. Thermally responsive gels have

the additional contraction of thermo-responsive groups further increasing the differential between the bilayer surfaces [108].

3.2.15 Hydrogel analysis

Correlational factors attributed to hydrogel behaviour were analysed by the methods listed in the previous section. These included contact angle measurement to record hydrophobic-to-hydrophilic switching of responsive gels. Swelling ratios and behaviour were recorded for various gels to identify the actuation of different compositions. Finally rheological and mechanical testing of cured gels was carried out to identify synthesis techniques with a beneficial effect on hydrogel mechanical properties.

3.2.15.1 Hydrogel swelling ratio

Gels were cast into 500 μl caps in a polystyrene mould, they were then exposed to UV light on an MA6 mask aligner under 365 nm UV light for a pre-set time between 6 and 120 seconds. The crosslinked gels were then allowed to dry and shrink for 24 hours before being removed from the casting mould, this is done to avoid damaging the puck. They were then rehydrated in RO water for 48 hours prior to weighing and drying out to obtain fully swollen and dry weights.

The rehydrated gels were removed from aqueous solution and gently swabbed to remove any surface liquid. These were then weighed and dehydrated in a vacuum for 24 hours. The dehydrated gel slabs were weighed again to determine their dry mass. In the case of stimuli responsive gels, an additional ‘actuated’ measurement was taken in the fully shrunken state, and in the fully hydrated state (pH 7 and 4 for ionic and cationic gels inversely, 22 °C and 40 °C for thermo-responsive gels.) Q is the equilibrium volume swelling ratio or gel fraction and q is the equilibrium mass swelling ratio [109].

$$Q = \frac{V_s}{V_d} = 1 + \frac{\rho_p}{\rho_s}(q - 1) \quad \text{Eq. 3-1}$$

Where ρ_p is the density of the polymer and ρ_s is the density of the solvent. Thus q gives a more useful equation (Eq. 3-2) where a differential measurement of the equilibrium swollen mass (M_s) and the dry polymer mass

$$q = \frac{M_s}{M_d} \quad \text{Eq. 3-2}$$

Where q is a function of the crosslinking density and the polymer–solvent interaction parameters, which can be converted to porosity using the Flory-Rehner equation for a swollen hydrogel [193]:

$$\frac{1}{M_c} = \frac{1}{\bar{M}_n} - \frac{\bar{v}}{\bar{V}_1} \cdot \frac{[\ln(1 - \varphi_{2,s}) + \varphi_{2,s} + \chi\varphi_{2,s}^2]}{\varphi_{2,s}^{\frac{1}{3}} - \frac{\varphi_{2,s}}{2}} \quad \text{Eq. 3-3}$$

Where M_c is the molecular weight of the average crosslink [97], \bar{M}_n is the number average molecular weight in the absence of crosslinking, \bar{v} is the specific volume of polymer, \bar{V}_1 the molar volume of solvent, $\varphi_{2,s}$ is the equilibrium polymer volume fraction of the swollen matrix and χ is the solvent interaction parameter.

From this the gel crosslink mesh size ξ can be expressed as [97]:

$$\xi = \varphi_{2,s}^{\frac{1}{3}} \cdot l \cdot \left(\frac{2C_n \bar{M}_c}{M_r} \right) \quad \text{Eq. 3-4}$$

$$\text{or simply: } \varphi_{2,s}^{-\frac{1}{3}} \sqrt{C_v \cdot l \cdot n} \quad \text{Eq. 3-5}$$

Where C_n is the Flory characteristic ratio (4 for PEG), M_r is the average molar mass of the repeat unit of the polymer [97], l is the length of the intermolecular bonds (0.154 nm for C-C bonds) and n is the number of bonds between crosslinks. This relation is used to estimate the mesh size or porosity of homogenous gels based on the volume fraction of monomer used in synthesis by correlating the swelling ratio of that gel. This porosity directly correlates to the transport or ease of diffusion of species through a gel. The diffusivity (D_s) of any given solute through the hydrogel matrix can then be estimated from:

$$\frac{D_s}{D_0} = \left(1 - \frac{r_s}{\xi} \right) e^{-Y \frac{\varphi_{2,s}}{1 - \varphi_{2,s}}} \quad \text{Eq. 3-6}$$

$$\text{and, } D_0 = \frac{k_B T}{6\pi\eta r_s} \quad \text{Eq. 3-7}$$

Where D_0 is the diffusivity of the solute in water and Y is a ratio of critical volume required for a successful translational movement of the solute molecule to the average free volume per molecule of liquid, and is in this case assumed to be unity, ξ is the distance between crosslinks. Finally k_B is the Boltzmann constant, T is absolute temperature, η is the viscosity (of water) at temperature T and r_s is the Stokes-Einstein hydrodynamic radius of the solute.

3.2.15.2 Rheological analysis of hydrogels

Rheology was performed using an Anton Paar MCR 301 Rheometer, a thin layer of gel was placed between a flat circular rheology probe and a 10 cm petri dish. The rheometer performed sweeps of rotational frequency, temperature by stage heating (to 42 °C) and displacement.

Rheology was used to replace dynamic mechanical analysis to determine the dynamic material properties of the soft hydrogel films. The defining principle of the parallel plate method is the application of a dynamic shear stress on a film of known thickness. In this setup a disk of 20 mm in diameter oscillates in contact with the thin sample film, which is held on the stage by a pre applied normal load of 0.5 N. The hydrogel samples were first synthesized in a Corning 10 cm petri dish, of measured thickness. If the engineering stress on a material is defined as the force F acting per initial unit area and will produce a deformation or strain, in viscoelastic materials this is represented by the shear storage and loss moduli (G' and G'' respectively), where purely elastic shear G is defined as:

$$G = \tau / \gamma$$

Eq. 3-8

and the complex modulus $G^* = G' + jG''$

Where γ is the shear strain, and τ the shear stress and j is an imaginary unit. To determine the viscoelastic shear moduli, a parallel plate setup was used where the sample is placed in a petri dish to allow it to stay hydrated as illustrated in Figure 3-4. The stress was first calibrated by performing a sweep to find the possible range of loading which does not exceed the yield stress of the gel. A torsional frequency sweep was applied and the strain was measured as a change in dimensions or a displacement. Ideal gels have an almost purely elastic response where the elastic modulus is much higher than the viscous modulus and is independent of frequency [194]. In gel networks with imperfections, the response of the polymer gel will depend on frequency with both shear moduli increasing with frequency. To correct for the presence of the dish, the measured modulus is adjusted for the measured height, subtracting the depth of the dish to find the real vertical distance of the gel over which the shear is applied.

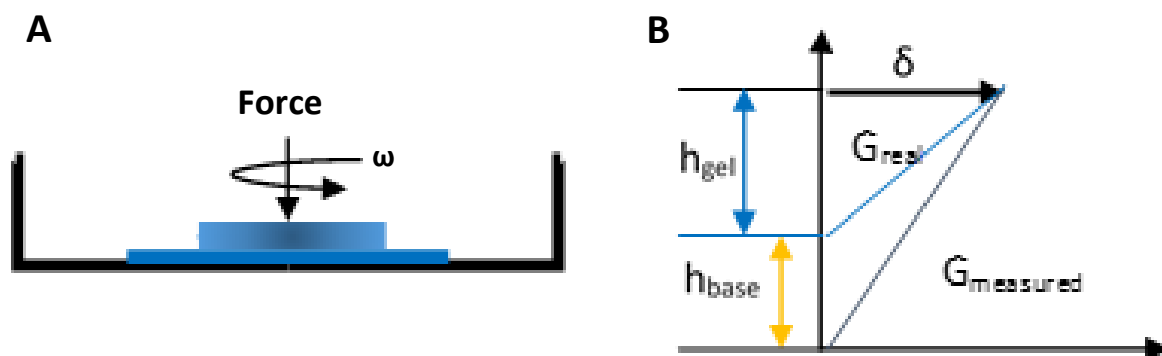


Figure 3-4 – A) Illustration of a parallel plate rheometer setup, the application of load and rotation rate used by the rheometer when the gel specimen is in a petri dish. B) The correction necessary to remove the thickness of the petri dish from the shear modulus calculation and obtain the true modulus of the material being tested.

The correction factor used to adjust the measured modulus for the true thickness of gel is based on a ratio between real and measured thickness of the sample:

$$G_{real} = G_{observed} \left(\frac{h_{measured} - h_{holder}}{h_{measured}} \right) \quad Eq. 3-9$$

Where G_{real} is the shear modulus of the sample and, $G_{observed}$ is the measured modulus based on a combination of the sample and holder thickness, $h_{measured}$ is the overall thickness and h_{holder} is the thickness of the sample holding dish. Flat plate rheology can be used to investigate various length scales by adjusting the frequency of the applied oscillation to probe relaxation dependent viscous parameters [194]. At low frequencies (0.1-1 rad/s); the polymeric chains making up the gel are undergoing Brownian motion so the measured properties reflect the elastic deformation of the gel network, where physical entanglements are created and broken quickly compared to the rate of deformation; so they do not store elastic energy. At high frequencies the polymer does not have time to rearrange, so physical entanglements persist longer than the oscillation frequency so they physically constrain or pin the polymers, thus storing elastic energy and contribute to viscous dissipation produced by the gel [195]. Amorphous polymers have different glass transition temperatures, above which the material will have rubbery instead of glassy behaviour and the stiffness of the material will drop dramatically with a more viscous-dominated response. At the glass transition, the storage modulus decreases dramatically and the loss modulus reaches a maximum. Temperature-sweeping DMA is often used to characterize the glass transition temperature of a material. In this thesis temperature sweep was used to determine the lower critical solution temperature (LCST) of NIPAAm above which it switches to a hydrophobic insoluble state.

3.2.15.3 Tensile testing of hydrogels

Tensile tests were performed on gels using a Zwick-Roell mechanical tensile machine with a 2kN load cell. Hydrogel dumbbell specimens were manufactured in a PDMS mould to size specifications given in ASTM D412 type A [196]. A half size specimen mould was cut from 3mm thick Perspex® from which a PDMS replica was made by casting. Samples were 59 x 12 x 30 mm gauge length (Figure 3-5), the PDMS mould was filled with a pre-gel solution and illuminated under the MA6 mask aligner for a pre-set duration of time from 5 seconds to 2 minutes to polymerize the gel into the sample shape.

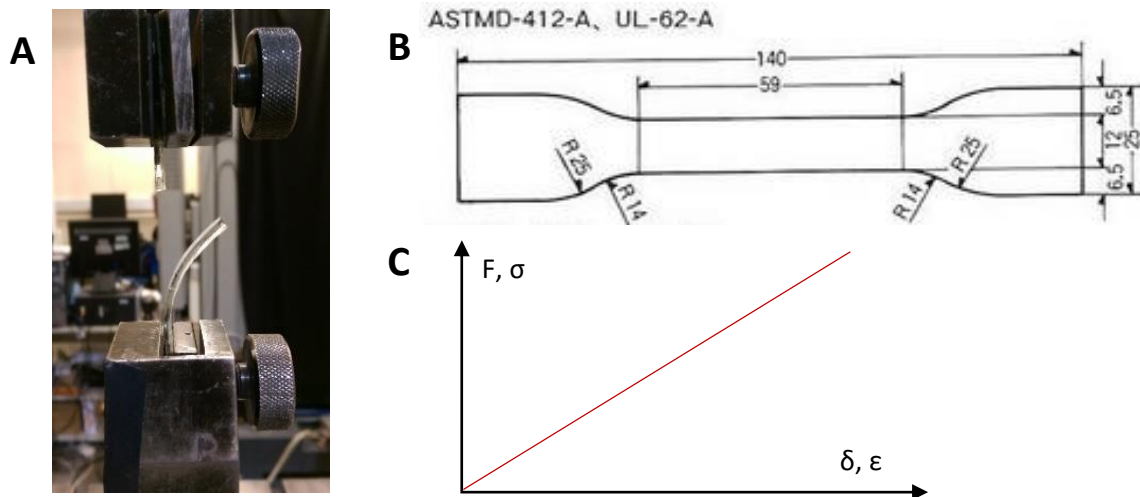


Figure 3-5 – A) Gel tensile specimen after rupture, B) The standard ASTM D412 type A sample schematic. C) The expected relationship from a perfectly linear sample as a force-displacement or stress-strain plot. It should be noted that with hydrogels a perfectly elastic response is highly unlikely given the multi-phase porous structure.

The finished tensile specimens were washed in IPA and ethanol, and air dried for 24 hours to remove residual solvent. The as-cast specimens were tested under tension in a Zwick-Roell mechanical tensile machine with a 2 kN load cell and clamp grips in displacement controlled loading at 0.5 mm/min. Prior to each test the grip opening displacement was recorded and load cell set to zero to remove preload, as only the gradient of the loading curve during the elastic regime was of interest. The force displacement curve was converted to a stress strain curve to obtain elastic modulus (assumed to be very low), as the gradient of the stress plotted against elastic strain [197].

$$\text{Engineering Stress : } \sigma = F/A \quad \text{Eq. 3- 10}$$

Where the tensile force (F) is adjusted for sample cross sectional area (A) and strain is represented as the unitless measure of change in length against the original length of the sample [197].

$$\text{Strain : } \epsilon = \frac{\Delta l}{l_0} = \frac{l-l_0}{l_0} \quad \text{Eq. 3- 11}$$

Plotting the stress and strain results in a linear segment at the start of the loading arc which is elastic. As hydrogels typically exhibit several modes of convoluted viscoelastic, poroelastic and hyperelastic behaviour later in the loading curve, only the initial elastic segment will be compared to determine the effects of formulation on the mechanical properties of a gel sheet to verify material behavioural changes.

3.2.15.4 Fourier transform infrared spectroscopy

Fourier transform infrared spectroscopy attenuated total reflection (FTIR-ATR) was performed using a PerkinElmer Universal ATR sampling accessory thin films were compressed prior to a spectrum from 400 to 4000 cm^{-1} being sampled over 12 scans per sample. Samples were compressed under

the optical crystal element usually in thin film form after dehydration, a background measurement was performed between tests. Hydrogels were analysed by FTIR-ATR to confirm crosslinking extents, presence of functional groups and effects of additives for free radical polymerization and oxygen scavenging. While the presence of PAA in the hydrogel films can be confirmed visually by placing hydrated sheets in a 0.1 w/v % toluidine blue O 1 w/v % borax solution where staining of PAA carboxyl groups was confirmed. Films with and without a PAA sacrificial layer present during manufacture were also dried and examined with FTIR-ATR to investigate the changes in hydrogel composition.

3.2.15.5 Ultraviolet-Visible spectrophotometry

Photoinitiator properties were quantified by dilution assays in a Nanodrop UV-VIS spectrophotometer. Solutions of varying concentration (w/v %) were placed as 2 μ l drops (in RO H₂O) onto the spectrometer after calibration to a baseline standard of embryo transfer water (Sigma). Concentrations were used to plot absorbance vs. aqueous concentration of various photoinitiators. Ethanol was sometimes used as a substitute depending on photoinitiator solubility, in these cases an ethanol baseline was used. To confirm the functionality of the various photoinitiators used, solutions of each were analysed by Ultraviolet-Visible (UV-Vis) spectrophotometry to identify the key absorption spectra and absorptivity, and also to test the susceptibility to photo-bleaching of the various peaks present.

3.2.15.6 Contact angle measurement and wettability

Contact angles were measured with an Attension (Biolin Scientific) Theta series Optical Tensiometer. The method is similar to that described in section 2.2.2.7. A 5 μ l droplet was applied to the substrate and allowed to equilibrate until the contact angle ceased to decrease rapidly. On highly porous surfaces such as hydrogels the measurement had to be taken more quickly to accommodate the rapid absorption of the contact angle droplet.

3.3 RESULTS

3.3.1 Photo initiator efficiency and suitability

UV-Vis spectrophotometry of photoinitiators showed absorption peaks and molar extinction coefficients of various commercial photoinitiators, providing an indication of which was most suitable for fast photolithography in the MA6 system. The measured molar absorption spectra and absorbance with concentration are shown in Table 3-5, these are then used to determine the initiator molar extinction coefficient, a measure of initiator light attenuation. A peak and high absorbance near 365 nm is key for effective use with the MA-6 mask aligner system.

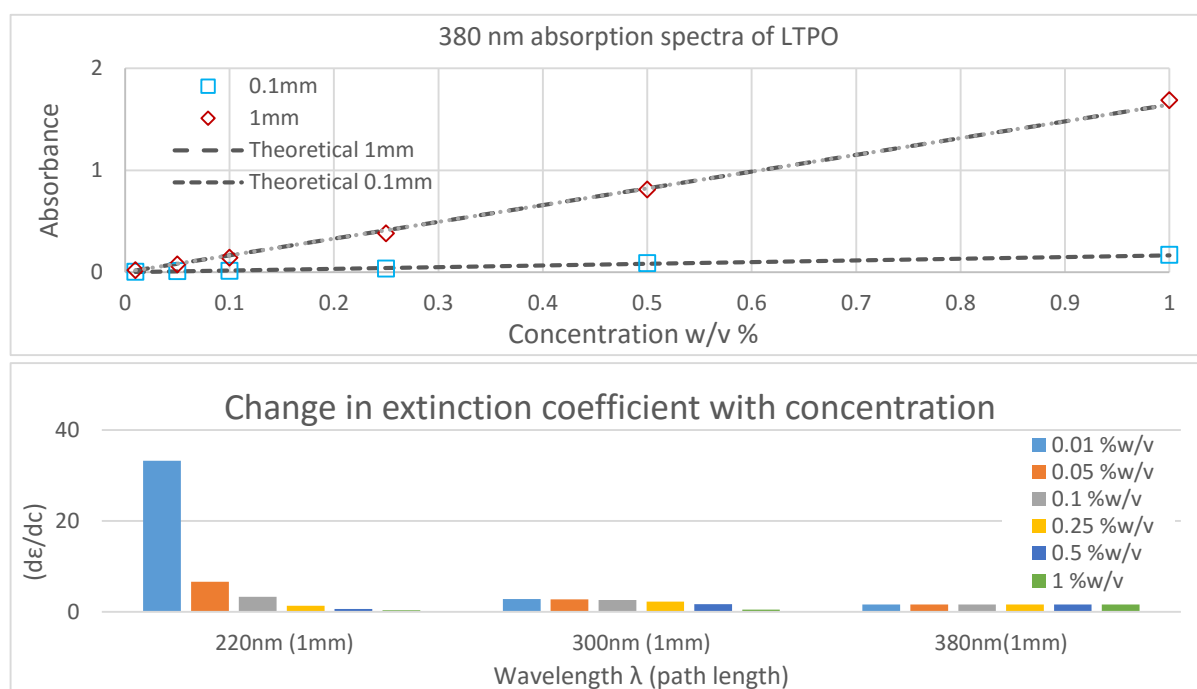


Figure 3-6- Absorption with concentration at various absorption peaks for LTPO photoinitiator. Distances in mm are the working distance of the UV-Vis spectrophotometer. Outside of the 380 nm peak for LTPO, curves show molar absorption coefficient decreases nonlinearly with concentration at the other prominent absorption peaks.

The results indicate that Lucirin LTPO and the other phenyl based photoinitiator Irgacure I819 had absorption spectra centered between 300-368 nm with distinct peak at 368 nm adjacent to that emitted by the MA6 mask aligner. Phenyl based photo initiators also showed the highest molar extinction coefficients, indicating efficient absorption compared to other alternatives (Table 3-5).

Table 3-5 - Absorption peaks, and molar extinction coefficients of implemented photoinitiators as measured by UV-VIS spectroscopy.

Initiator	Main absorption peak (nm)	Molar extinction coefficient ϵ ($M^{-1} cm^{-1}$)
Lucirin TPO	380	532.4
Irgacure 819	368	566.49
Irgacure 2959	280	110
Darocur 1173	330	121.433

It was found that LTPO and I819 are the most suitable for quick lithography at 365 nm UV wavelengths. The measured absorbance closely matched the theoretical data from the extinction coefficient (Figure 3-5).

3.3.2 Hydrogel properties

3.3.2.1 Hydrogel swelling behaviour

Swelling behaviour dictates the actuation of gel hinges, and stronger swelling extent, in combination with an overall crosslinked and stable gel are key to a robust gel scaffold.

3.3.2.1.1 Conventional Hydrogels

The swelling behaviour and permeability to nutrients of the conventional hydrogels were determined by their swelling ratio, and observed structural stability. The Flory-Rehner parameters used to estimate gel crosslink mesh size, and thereby diffusivity [109]. The swelling ratio obtained for a range of exposure doses for structurally stable gels is shown in Figure 3-7. An increase in swelling is seen with reduced exposure dose and decrease in initial monomer concentration. This increase in swollen weight is attributed to longer distances between the crosslinks within the gel due to the high solvent fraction. In addition to a weaker gel, the large mesh size and long chains between crosslinks shift the swelling to elasticity equilibrium as the crosslinking density is reduced thereby reducing the resistance to swelling. The swelling alone does not determine the quality of a gel, especially in the case of structural materials, therefore the mechanical properties of the gels are investigated later in Section 3.3.2.2.

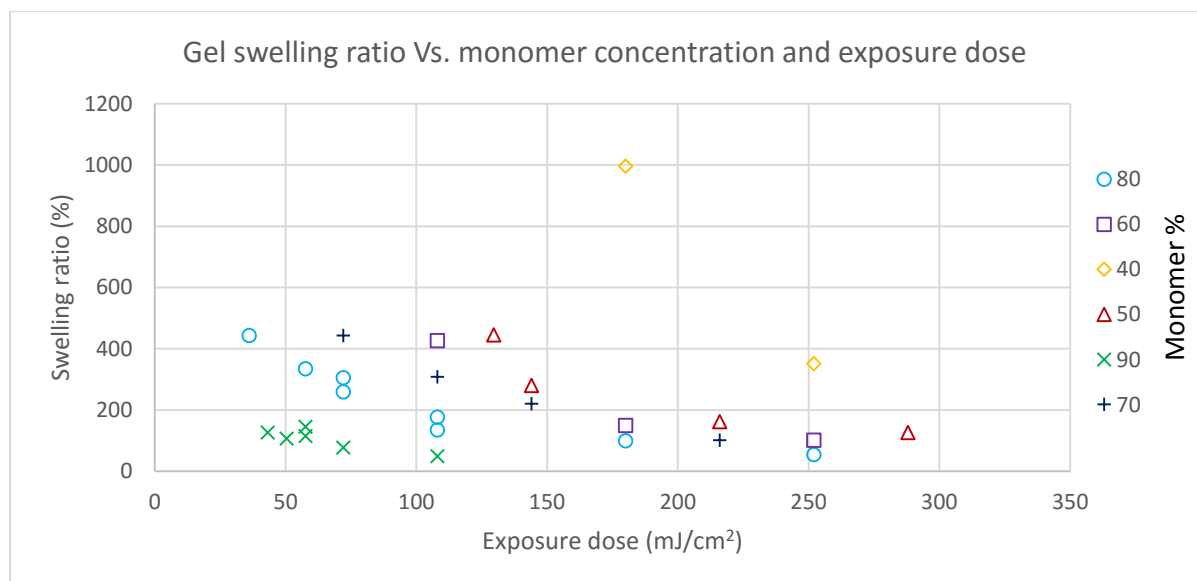


Figure 3-7 - Swelling ratios of PEGDMA based hydrogels with exposure dose and monomer concentration. Values measured by weighing swollen samples incubated for 24 hours in RO H₂O for 24 hours after synthesis, and after dehydration by drying in a 120 °C oven, followed by placing in a 100 mTorr vacuum for 12 hours.

The estimation yielded an expected pore size variation between 6-350 nm in PEGDMA hydrogels (Figure 3-8) with between 10 % and 90 % monomer content, suggesting permeability for larger dissolved species could be a problem for the less solvent laden gels. The Flory-Rehner constants for PEGDMA based gels for this calculation were obtained from the paper by Zustiak et al. [97] and Bush et al. [198] are listed in table Table 3-6 and have been used to estimate the expected nutrient permeability of PEGDMA structural gels after various exposure doses and monomer concentrations.

Table 3-6 - Variable or Flory-Rehner equations for estimating hydrogel mesh size from swelling ratios. Values found from previous work by Zustiak et al. [97] and Bush et al. [198].

Description	Variable	Value
Molar volume of the solvent	$V_1 (H_2O)$	18.018 cm ³ /mol
Polymer-solvent interaction parameter PEG-H ₂ O	χ_1	0.426
Characteristic ratio of the polymer (PEG)	C_n	4
Chain bond length (PEG)	l	0.146 nm
Molecular weight of the repeat unit (PEG)	M_r	44 g mol ⁻¹
Polymer-solvent density ratio (PEG)	ρ_p / ρ_s	1.12
Polymer average molecular weight	M_n	550 g mol ⁻¹

Using equation 2-6 and the constants for a hydrogel network constructed out of PEGDMA ($M_n = 550$ g mol⁻¹) repeat units obtained from the volume fraction of the gel are related to the porosity of the gel by the Flory-Rehner relationship described in Section 1.3.4.

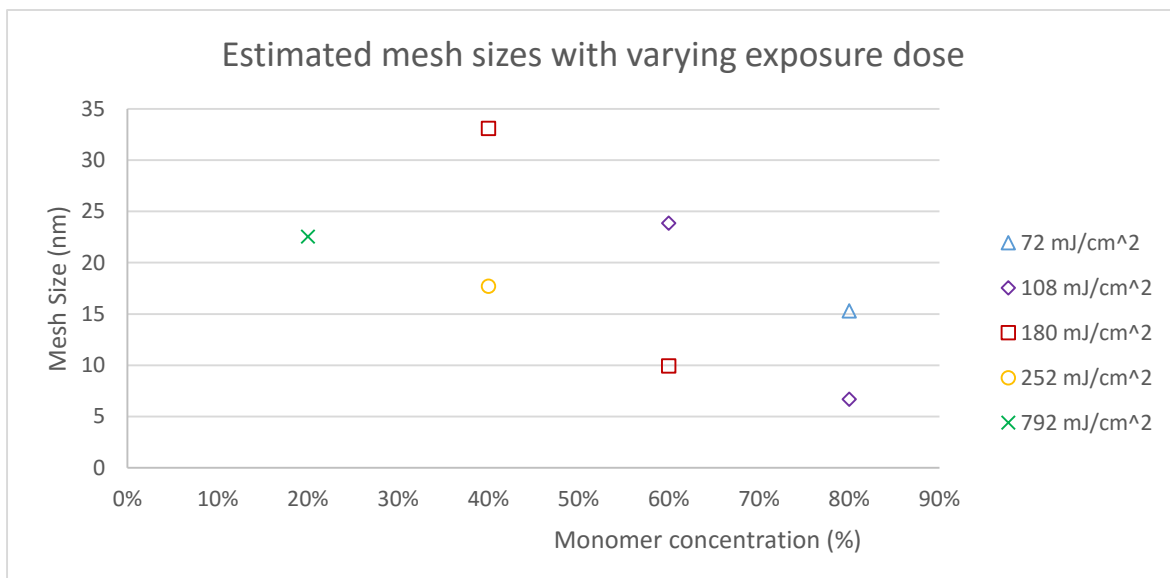


Figure 3-8 - Mesh size correlation to monomer volume fraction for PEGDMA hydrogels synthesized in EtOH solvent.

To convert mesh sizes into relative diffusion coefficients of cell culture specific media components and metabolites, the diffusion coefficients in water of several ions and metabolites were used, these are shown in Figure 3-9.

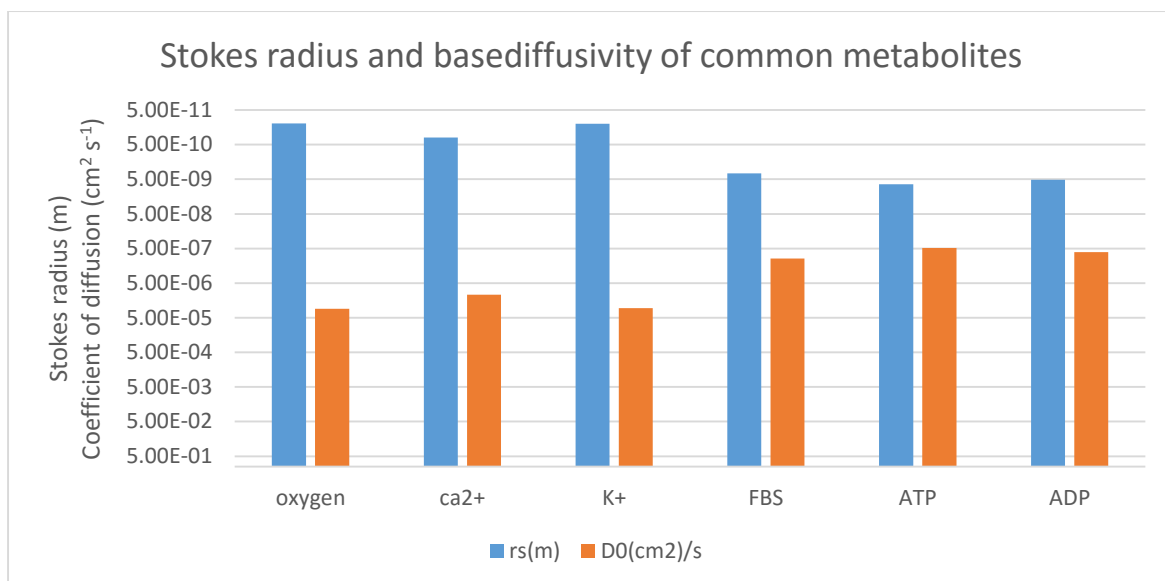


Figure 3-9- Adapted values for Stokes radii and baseline diffusion coefficients (D_0) at tissue culture temperatures for dissolved species in water at in vitro temperature (37 °C, $nu=0.682$) [199, 200]

The resulting species diffusion coefficients were correlated with the predicted pore (mesh) size with monomer concentration are shown in Figure 3-10.

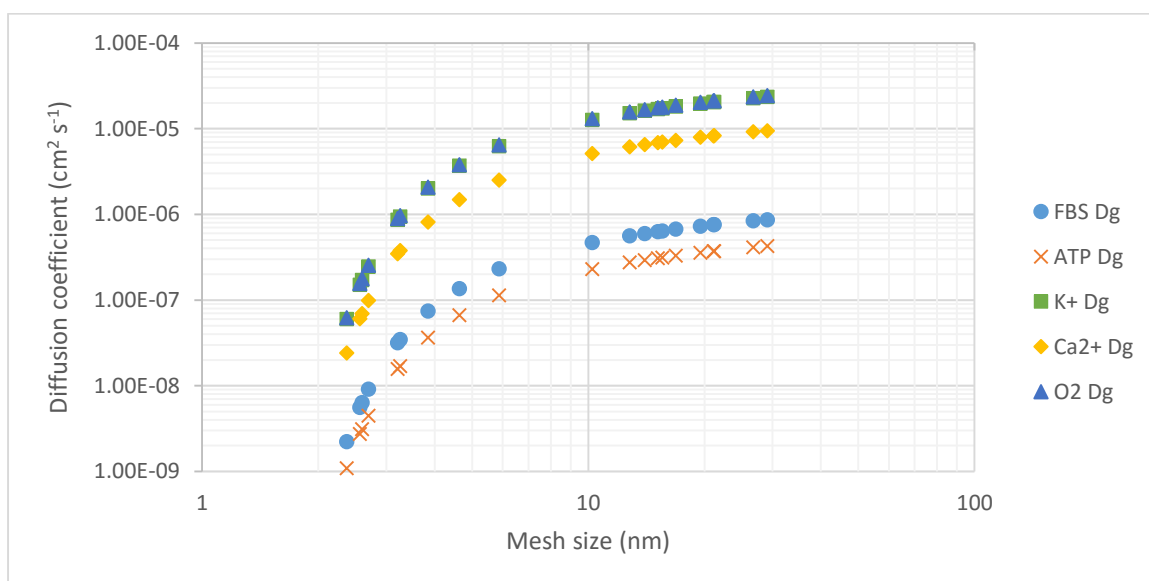


Figure 3-10 - Diffusion correlation to hydrogel mesh size for PEGDMA gels synthesized at various exposure doses and monomer concentrations as illustrated in Figure 3-7.

3.3.2.1.2 Thermo-responsive Hydrogels

Thermo-responsive and bi-responsive hybrids of NIPAAm and AAc were synthesized by photolithography early in this work. To identify key factors for the behaviour of the responsive gels a number of controlled variables were changed using a randomized Taguchi analysis [201].

Table 3-7 - NIPAAm with Acrylic Acid copolymerization with I2959 acting as photo Initiator. Mixtures were prepared in water with exposure of 5 minutes under a 300 W broad spectrum UV bulb.

No	Synthesis Temperature (°C)	NIPAAm concentration (mol/l)	Initiator 2959 concentration (w/v %)	Acrylic Acid concentration (w/v %)	Polymerized Condition	Temp induced swelling time (s) ¹	pH induced swelling time (s) ¹
1	25	1	1%	2%	Stable	3	18
2	25	1	2%	4%	Stable	6	15
3	60	1	3 %	6 %	Dense	15	8
4	60	1	4 %	8 %	Dense	25	15
5	25	1.5	1 %	8 %	Low gelation	30	15
6	25	1.5	2 %	6 %	Dense	26	15
7	60	1.5	3 %	4 %	Heterogeneous	8	10
8	60	1.5	4 %	2 %	Heterogeneous	7	4

This initial study narrowed the range of factors to be excluded, such as temperature which cannot readily be controlled in the MA6, also seeming impractical as more homogeneous gels formed at room temperature (optical transparency is a beneficial factor as subsequent processing is involved or monitoring from inside containers is necessary). Overly high AAc concentrations were also excluded as these contributed to heterogeneity while not offering sufficient boost to swelling response. A second Taguchi analysis used levels of each factor to look for the most influential parameter as a function of gel swelling.

Table 3-8 – levels for Taguchi study into synthesis factors for a NIPAAm based gel prepared under a 300 W broad spectrum UV bulb.

Factor	Level 1	Level 2
Monomer (NIPAAm)	35 w/v %	50 w/v %
Photoinitiator (I2959)	2 w/v %	4 w/v %
Crosslinker (MBAAm)	1 w/v %	2 w/v %
UV Dose	5 minutes	7 minutes
Solvent	1-Butanol	EtOH
Nitrogen atmospher	on	off
Volume during polymerization	200 µl	400 µl

¹ Times measured by visual opacity change of gels in response to stimulus, gels placed in aqueous container and allowed to equilibrate, they were then shrunken by exposure to acidic environment or temperature, and allowed to re-swallow by immersion in swelling medium.

Table 3-9 - Synthesis parameters for Taguchi study into synthesis factors for NIPAAm based gels. 1 and 2 indicate levels of that particular variable shown previously. When a change in level of a particular variable has a strong effect on the output variable (swelling) this is considered to have a strong effect on the overall system.

Mix	Monomer	Crosslinker	Initiator	UV dose	Solvent	Nitrogen	Volume	Swelling (q)
1	1	1	1	1	1	1	2	8.08
2	1	1	1	2	2	2	1	6.99
3	1	2	2	1	1	2	1	5.66
4	1	2	2	2	2	1	2	5.19
5	2	1	2	1	2	1	1	5.21
6	2	1	2	2	1	2	2	5.50
7	2	2	1	1	2	2	2	4.41
8	2	2	1	2	1	1	1	4.11

The array was quantified to swelling ratio determined by weight of swollen, actuated and dry gels. This allowed the use of ANOVA to eliminate non-contributing factors, as those with a low degree of variance caused by up or down regulation of the controlled factors could be eliminated as non-critical.

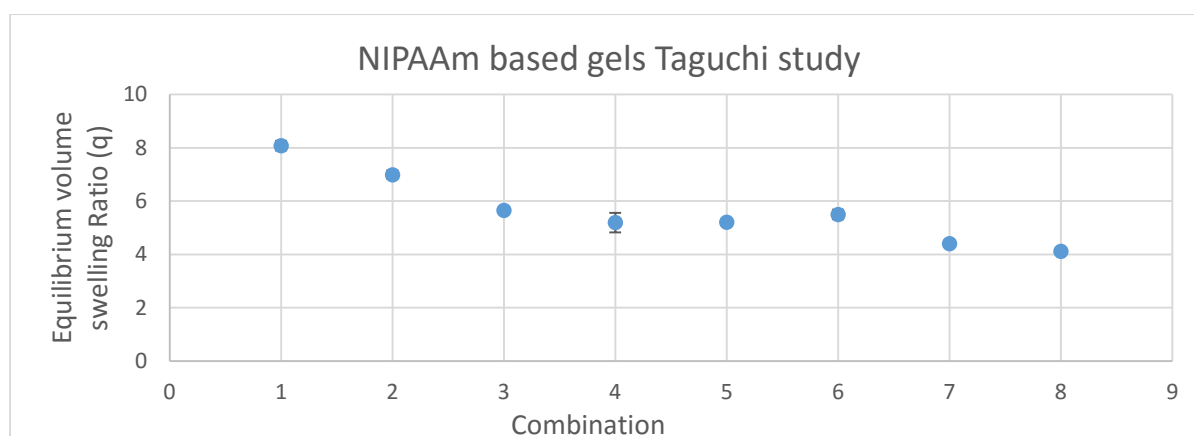


Figure 3-11 - Swelling ratio with recipe for NIPAAm based gels, Correlation of levels at each swelling ratio used to interpret effect on gel network. Error bars: 1SD from 2 measurements.

Although swelling is only one gel characteristic, if a gel is intact, and can withstand manufacture and lift-off and also offers a good swelling ratio, it has the opportunity of being a good actuator, these values are not critical they provided an indication of the critical parameters to control. The most favourable mixtures were then optimized for photolithography and compatibility with the lift-off surfaces by changing photoinitiator type to the most effective from the previous study, and adjusting the solvent to avoid dissolution of the sacrificial layer prematurely. In the end the pure NIPAAm based gels did not make it to hinge applications due to crystallization after spinning due to solvent evaporation.

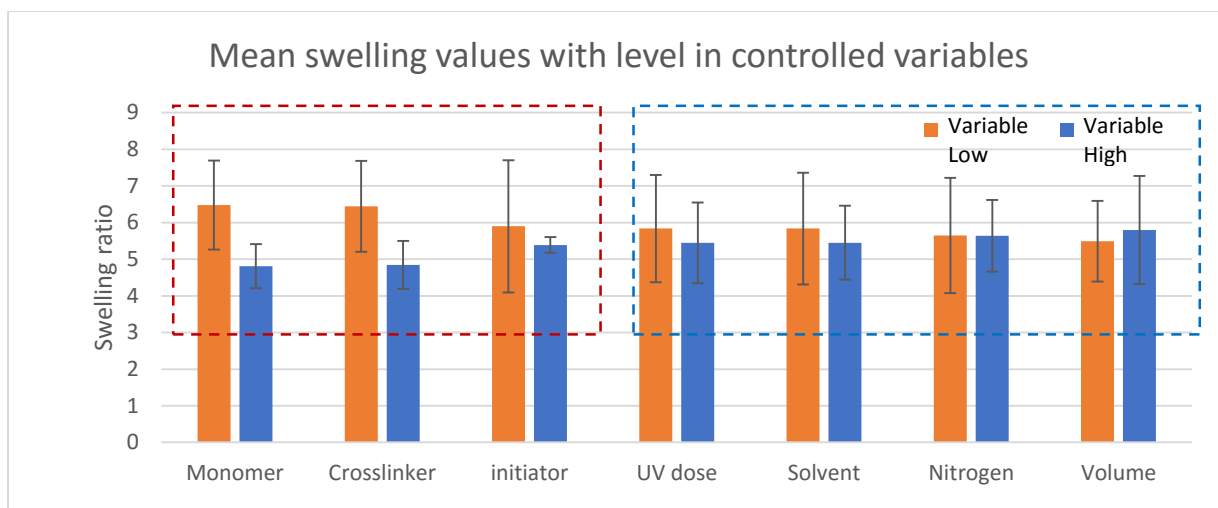


Figure 3-12 - Taguchi plot of mean value and associated variance for up and down regulation of certain synthesis parameters. (Red): variable at low level 1, (Blue) variable at high level 2. Error bars: 1SD from n=4 values.

A drastic reduction of swelling ratio is visible (Figure 3-12) in cases of increased monomer concentration, crosslinker concentration and initiator concentration, with four other factors serving a synergistic role, and while having an effect do not produce as high a deviation, although solvent type does appear to play a role in the conversion of free chains to crosslinked network. These combinations were reattempted with varied solvents ranging from EtOH to MtOH and acetone, a 50/50 blend of EtOH and water or pure EtOH gave the most homogenous gels, especially at lower temperatures of synthesis near 20 °C (Figure 3-12). However due to the incompatibility of water with the sacrificial layers, isopropanol, 1-butanol and ethanol were chosen, to avoid dissolution of the sacrificial layer by the resist.

For the manufacture of a fully transparent and strong thermal hydrogel actuator, NIPAAm monomer was crosslinked with PEGDMA to form a partially interpenetrating polymer network similar to those of Peerani et al [202]. The performance was later compared to a MBAAm crosslinked all PNIPAAm hydrogel recipe obtained and was modified for my process from [24] to see the effect this would have on the swelling (Figure 3-14). The results showed a strong correlation in the swelling of different gel recipes and processes, the major factor as expected was monomer concentration in the solvent, which in turn defines how much empty space exists in the crosslinked network and thus how much water it can hold. This tendency shows the volume ratio of swollen gel to initial casting nearing unity as exposure dose increases, suggesting density of crosslinking is so high that it resists the ingress of water into the mesh. Differences were also seen when comparing actuation in gels primary composed of NIPAAm and its polymer, and NIPAAm copolymerized with PEGDMA shown in Figure 3-15 (PEGDMA preferable as it evaporates slowly keeping NIPAAm from crystalizing).

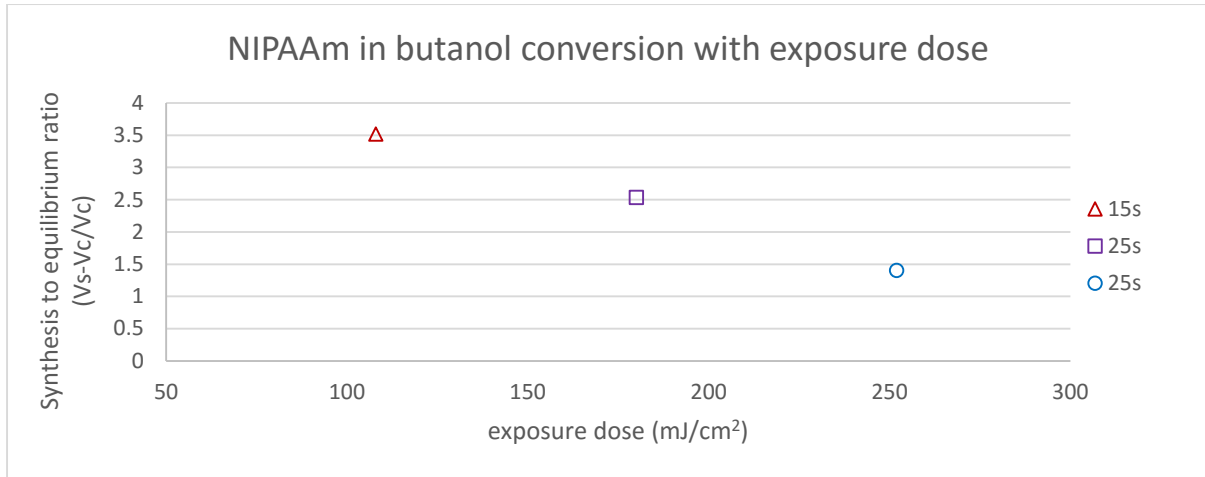


Figure 3-13 – Conversion ratio with exposure dose of MBAAm crosslinked PNIPAAm gels with LTPO as initiator, cast weight prior to development against fully swollen state, shows correlation between overexposure and loss of swelling potential as gel network is so rigid it barely accommodates any liquid other than that replacing unreacted monomer and solvent used in synthesis ($n=1$).

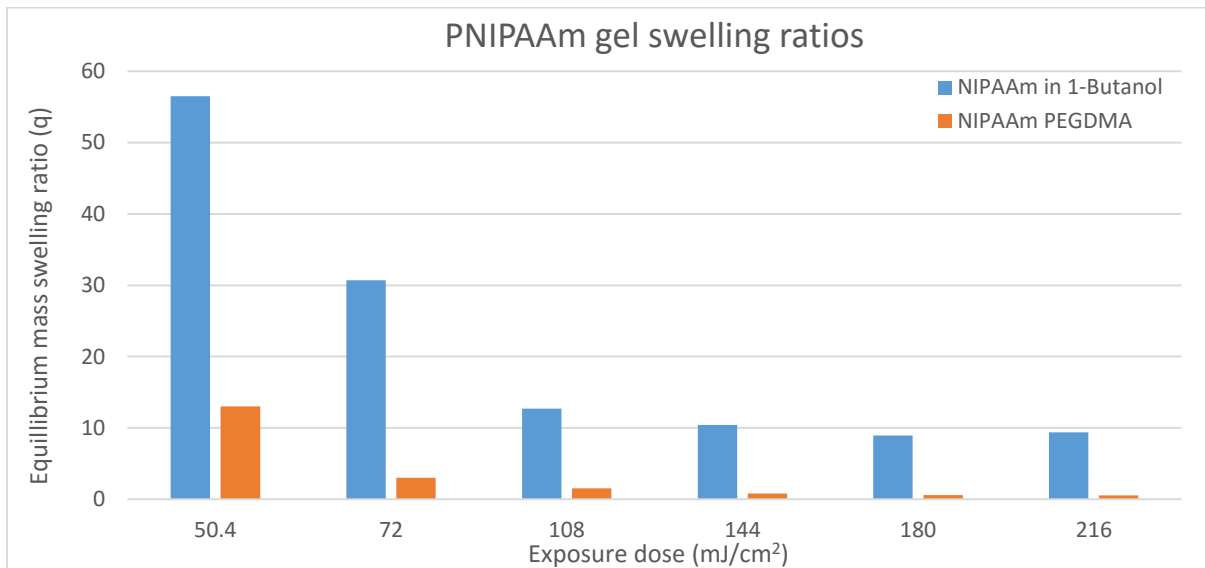


Figure 3-14- Swelling ratio of MBAAm crosslinked PNIPAAm gels compared with PNIPAAm-co-PEGDMA gels ($n=1$).

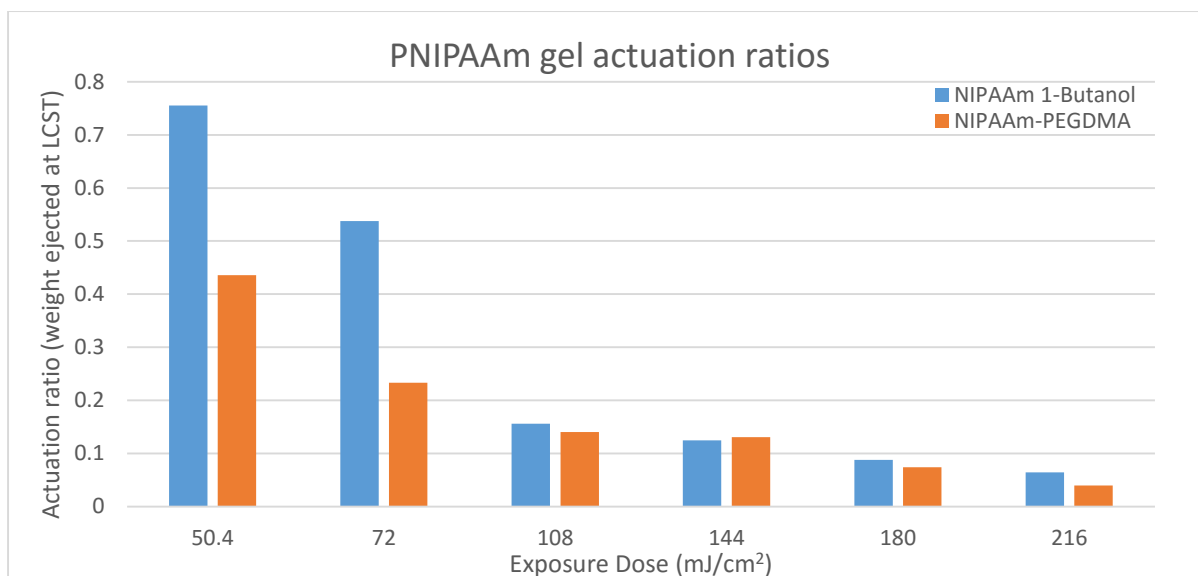


Figure 3-15 – PNIPAAm gel actuation ratios (weight fraction of water displaced above the hydrogel LCST) of the two thermo-responsive PNIPAAm hydrogel recipes ($n=1$).

The gels were dehydrated at 120 °C for 24 hours to expel all the trapped water after being equilibrated in RO water for 48 hours. While this is a good measure of hydrogel network density it does not give much information on how much water the network can expel on its own, and a second test needs to be done to measure water ejected upon heating to 36 °C. One issue which is prevalent when working with crystalline monomers like NIPAAm is that they revert back to an ordered structure when a critical portion of the solvent evaporates. This means that the time taken to get a pre-spun substrate in to do photolithography is in the range of 5 minutes.

3.3.2.1.3 Ionic and cationic gels

Ionic and cationic gels were synthesized by the addition of functional groups to the standard gels. The intention was to use them as active layers in bilayer folding or as a locking mechanism by ionic-cationic attraction. PAA ionic gels were used as described previously in a lift-off layer method. The cationic gels based on N,N-Diethylaminoethyl methacrylate (DEAEMA) were made by substitution into the NIPAAm 1-butanol recipe as a direct replacement for NIPAAm. DEAEMA based cationic gels were found to undergo a hydrophobic to hydrophilic switch (Figure 3-16) in acidic environments causing a swelling at low pH and ejection of fluid at elevated pH. This is due to the presence of amine groups in the DEAEMA monomer, in contrast to carboxyl groups in the PAA ionic gels as confirmed by FTIR.

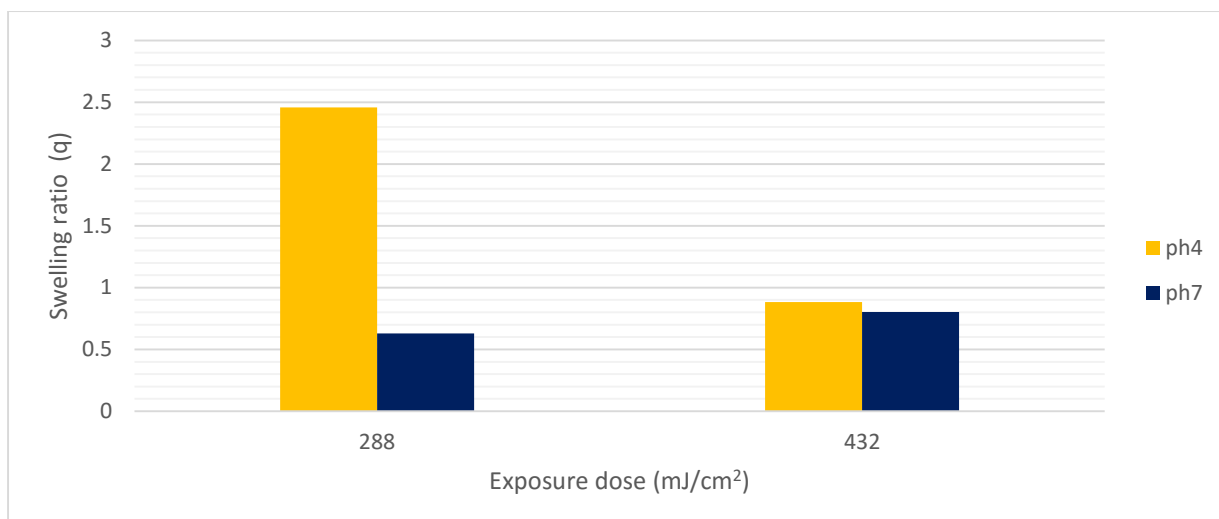


Figure 3-16- *N,N*-Diethylaminoethyl methacrylate (DEAEMA) cationic gel swelling as it varies with exposure dose ($n=1$).

Gels which had undergone a shorter exposure had a less ‘mature’ network and thus absorbed more water, they also showed increasing opacity in their collapsed state as shown in Figure 3-17.

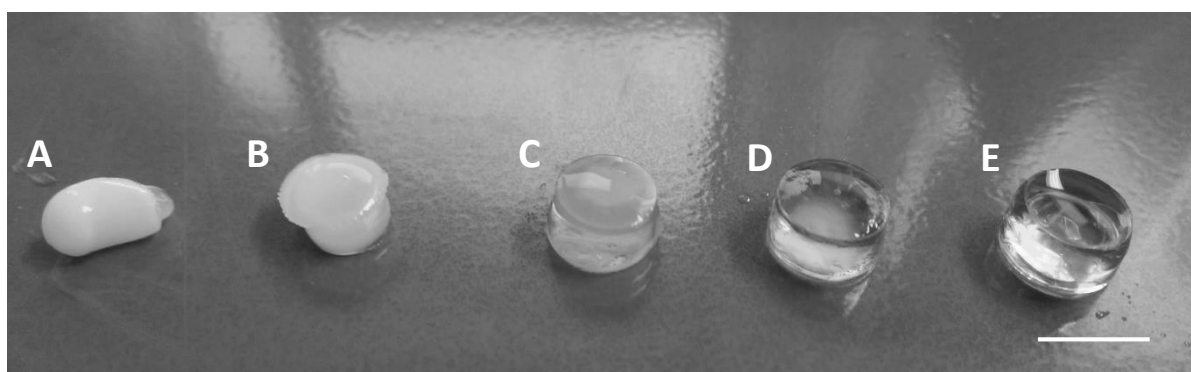


Figure 3-17 - Transition in Cationic gel homogeneity. Left to right: doses of exposure varying from A) 15 seconds, B) 30 seconds, C) 45 seconds, D) 60 seconds and E) 75 seconds at 7.2 mW/cm^2 , scale bar 10 mm.

The immersion of cationic gels into RO H₂O showed the actuation potential dropping with increasing exposure dose, highly shrunken gels were formed at lower doses, with homogeneity retained above 650 mJ/cm^2 . The gels also lost their swelling ability as a result of extended UV exposure (Figure 3-18) as had been seen in neutral gels (Figure 3-7).

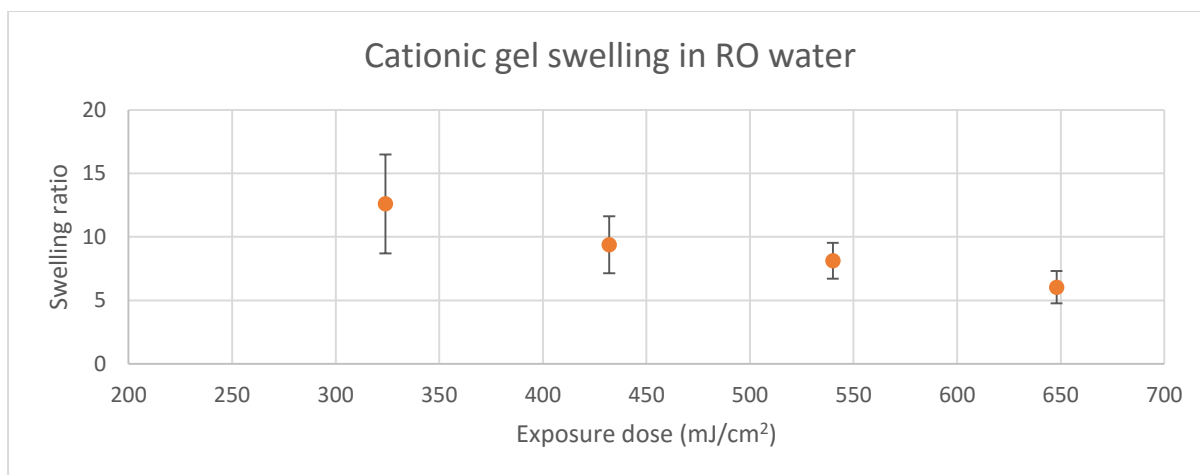


Figure 3-18 - The swelling ratios of DEAEMA and 1-butanol solvent gel, as a result of changes in exposure dose under the MA6 mask aligner. Error bars 1 SD from (n=3) measurements.

3.3.2.2 Rheology

Hydrogels when operating as an actuator in their swollen state are soft, swollen and have non-linear mechanical properties. Traditional tensile test therefore cannot be performed, other than on fully dry samples. Results were limited to one sample in this short investigation due to time constraints and limited access.

3.3.2.2.1 Neutral gel rheology

Hydrated mechanical properties were found by parallel plate rheology as described in 3.2.15.2. Initially the operating torque was found to be in the range of 1-90 μNm for hydrogel samples which showed linearity at constant angular frequency $\omega = 10 \text{ rad/s}$ (where frequency $\nu = \omega/2\pi$). Torque values above 90 μNm tore the thin gel films, strain amplitude sweep from 0.05 % to 5 % was performed with the lowest value 0.05 % used in subsequent tests (Figure 3-19).

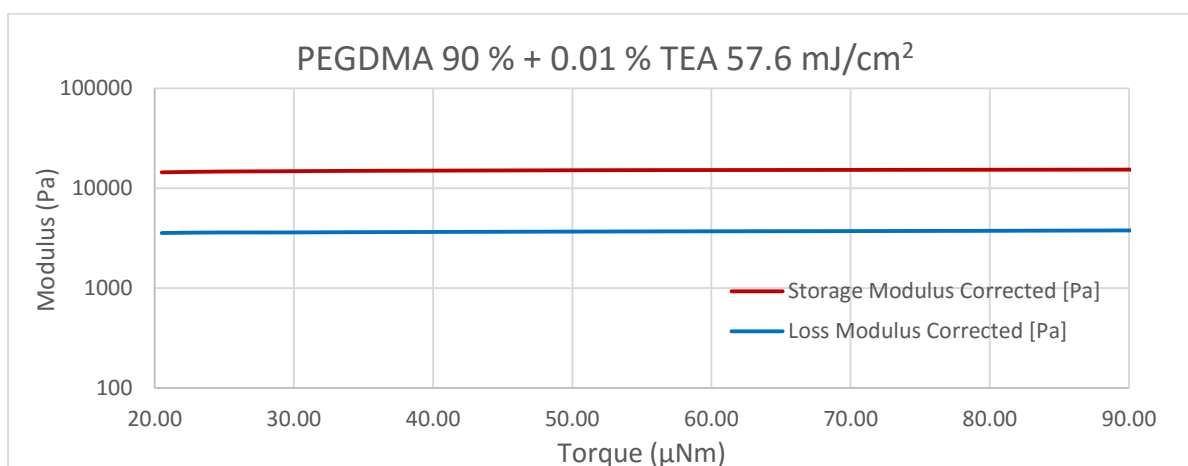


Figure 3-19 - Torque sweep of PEGDMA (90 % monomer concentration in EtOH with added 0.01 % TEA synergist) hydrogel thin film at angular frequency 10 rad/s. Storage and loss moduli corrected for the extra thickness of the sample holding plate. ($T = 21 \text{ }^\circ\text{C}$).

The sensitivity to loss of solvent was also apparent as both storage and loss moduli increased over the course of 5 minutes as solvent evaporated from the matrix (Figure 3-20). An increase in modulus is seen as the gel begins to dry, in agreement with tensile tests on dry specimens. This is likely due to the reduction of chain mobility due to the absence of the liquid interface between chains, increasing chain pinning. Subsequent tests were performed with RO H₂O applied to the edges of the hydrogel disk after compression in the rheometer.

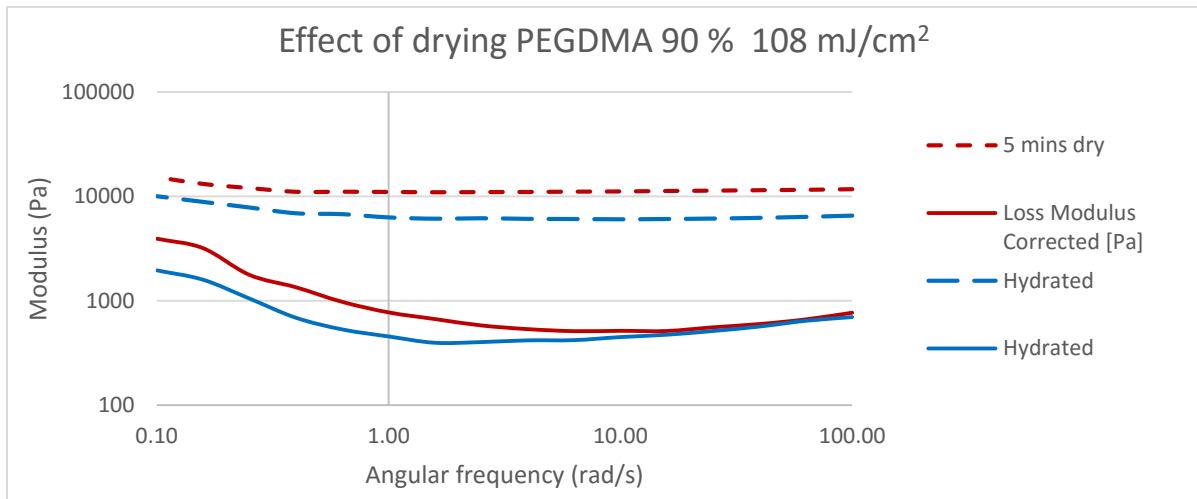


Figure 3-20 - Effect of drying as seen in the storage and loss moduli of the same gel sample- PEGDMA (90 % monomer concentration in EtOH) at 108 mJ/cm² exposure. (T = 21 °C)

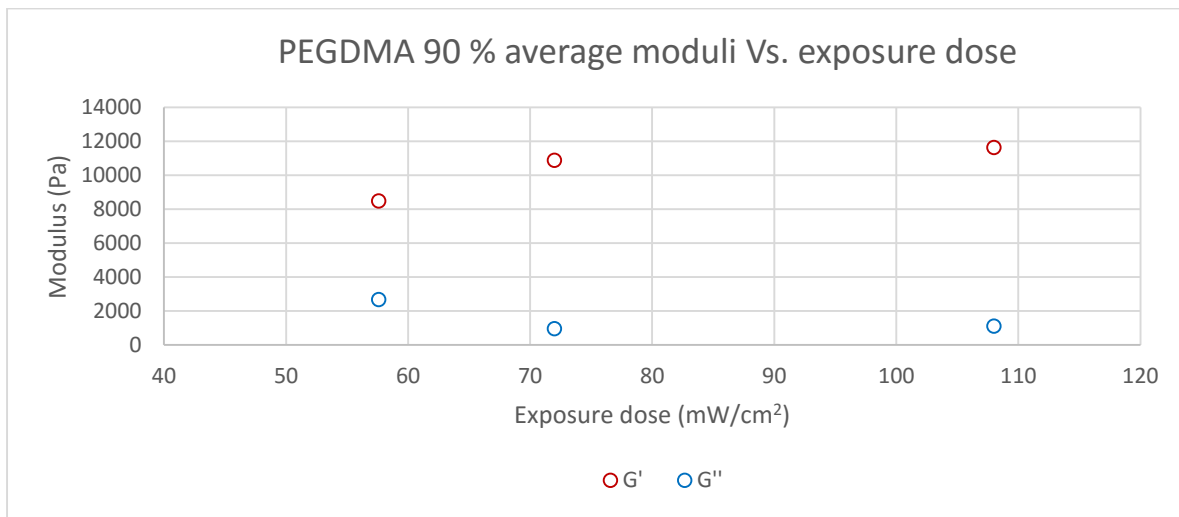


Figure 3-21 - Averaged storage and loss moduli of polymerized 90 v/v % PEGDMA films, a drop off in storage modulus is seen with reducing exposure dose, with an inverse relationship seen for the loss modulus (T = 21 °C, 1-100 rad/s). This was a short investigation, with repeat experiments were not conducted due to time constraints and limited access.

Looking at several doses for the most frequently used 90 % PEGDMA² in Ethanol showed a drop in G' and slight increase in G'' near the ideal exposure dose of 55 mJ/cm². Comparing this dose with and without a chain propagating agent yielded a very similar non-linear response. This is attributed to the relatively low conversion at this exposure dose, with the partially polymerized network showing more viscoelastic behaviour.

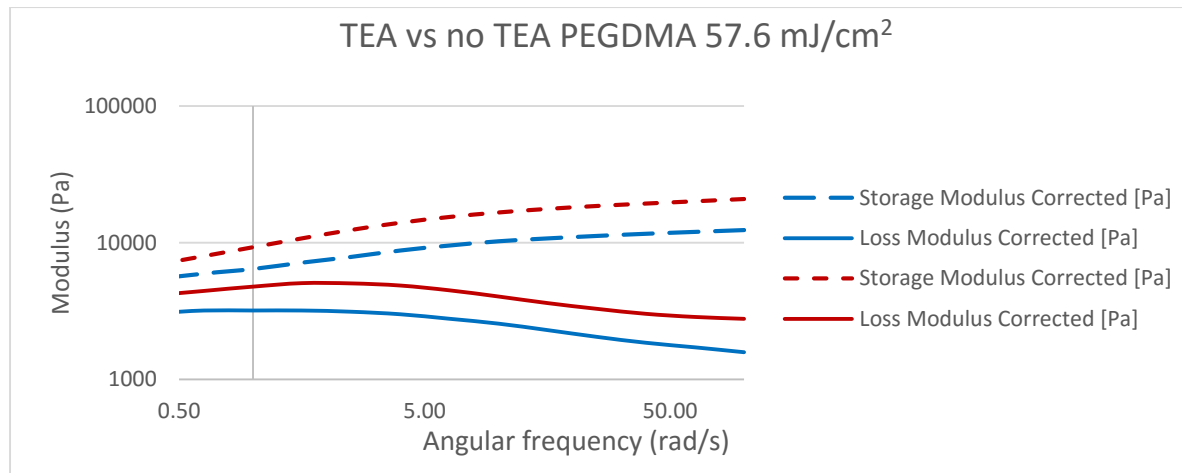


Figure 3-22 - Comparison of PEGDMA 90 v/v % with (red) and without 0.01 v/v % TEA (blue) polymerization chain transfer agent.

Presence of TEA increases the modulus slightly due to oxygen scavenging during polymerization and acting as a chain transfer agent, producing longer lengths between crosslinks and a potentially stronger and more elastic gel. However the relationship is still non-linear suggesting beneficial folding properties are maintained with the addition with such synergists.

3.3.2.2.2 Thermoresponsive gels.

NIPAAm based gels with MBAAm crosslinker were analysed in a temperature sweep, to identify the location of the formulation LCST and identify the change in mechanical properties above the LCST of NIPAAm.

² 90% PEGDMA refers to the monomer concentration, the remaining % are taken up by solvent (in this case ethanol) and some minute quantities of synergist and photoinitiator as specified.

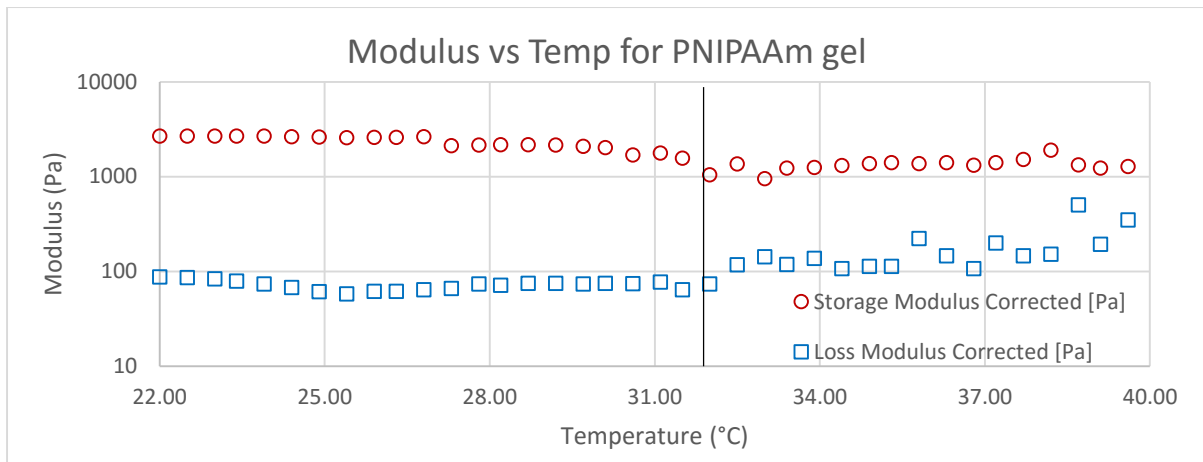


Figure 3-23 - Changes in PNIPAAm based gel storage and loss moduli during a temperature sweep. As the gel passes the LCST an increase in Loss modulus is visible due to the expulsion of fluid from the gel network. Values are corrected for the sample holder thickness. Only one sample was tested due to time constraints.

In Figure 3-23 distinct changes were seen to occur leading up to and immediately after the LCST, including a drop off of complex viscosity, similar to that predicted for determining the glass transition temperature of polymers and is adjacent to the LCST values seen in literature [103]. This LCST dependent transition is also seen in the drop of the complex (frequency dependent) viscosity η^* (Figure 3-24) at 32 °C. A gradual increase in damping factor can be seen to occur around 32 °C indicating the gel is transitioning through its LCST and ejecting water from the network³ as shown in Figure 3-25. The damping factor is recorded from feedback to the torsional load applied across the gel.

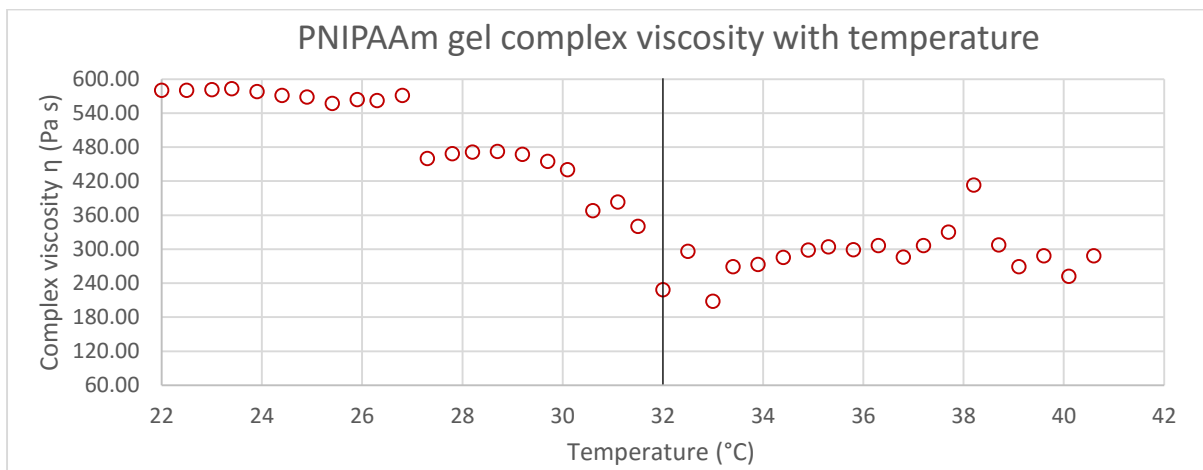


Figure 3-24- Complex viscosity dropping as a result of temperature sweep through PNIPAAm hydrogel LCST.

³ Ejected water refers to the free water filling the hydrogel network, which is released as the hydrophilic groups on the NIPAAm molecule undergo a hydrophobic transition.

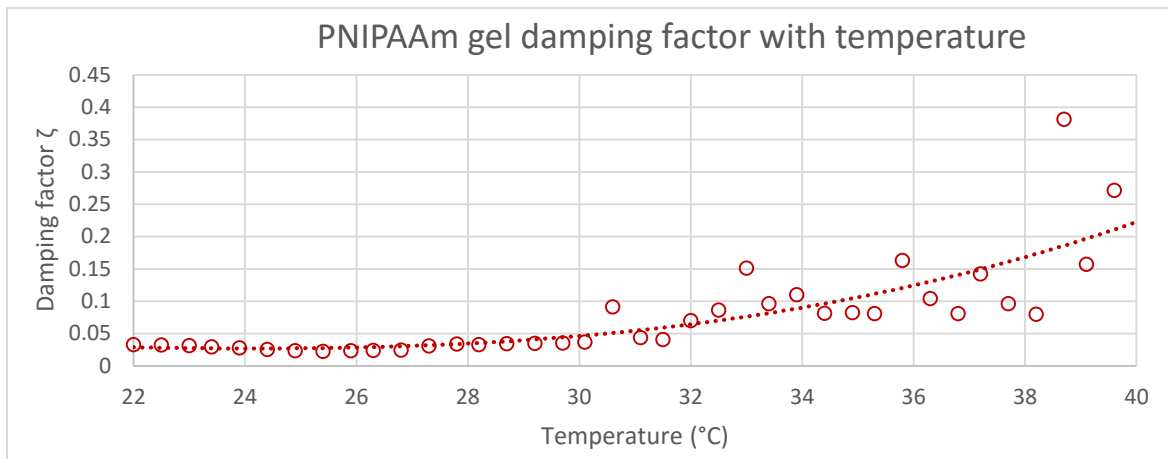


Figure 3-25 - Increase in damping factor of the NIPAAm hydrogel as it passes the LCST at 32 °C.

Looking at the NIPAAm based hydrogel before and after the hydrophobic to hydrophilic transition at constant temperatures of 22 °C and 40 °C shows a perceivable increase in modulus and a more uniform incline in line with a pure gel.

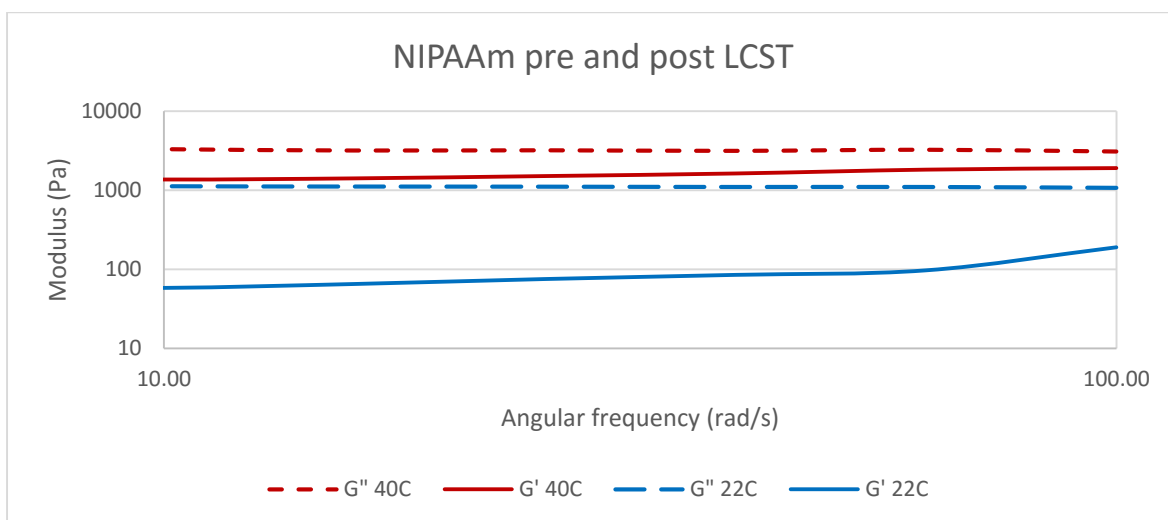


Figure 3-26 - A distinct difference can be seen between a hydrated cool NIPAAm gel sheet and one which has equilibrated at a point above the LCST. Above the LCST water is absent from the matrix, resulting in a higher modulus in the 40 °C gel.

The result gives further evidence that PEGDMA and NIPAAm hydrogels are physical gels. In addition to increasing G' and G'' after the LCST, there are no observed crossover points between storage and loss moduli indicating that the gels do not undergo a sol-gel transition.

3.3.2.3 Contact Angle

Contact angle measurements were performed to investigate the hydrophilic to hydrophobic switch of the NIPAAm laden gels. Passing the LCST causes the surface to become more hydrophobic, it is the shrunken state that the surface can immobilize cells, with the swollen state causing detachment [70].

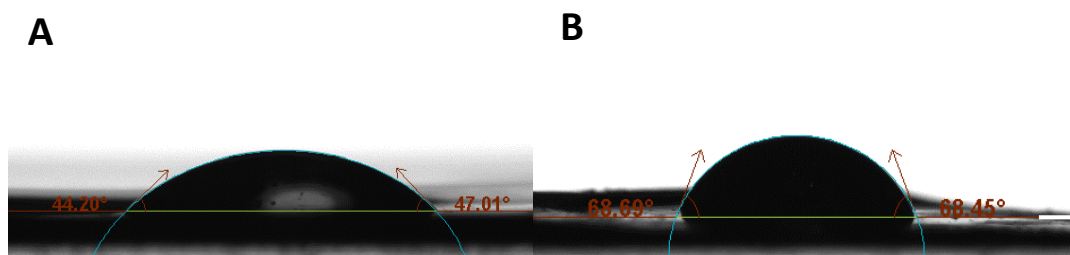


Figure 3-27 - Contact angle image capture at A) 22 °C, and B) 40 °C PNIPAAm films.

The transition in contact angle measurements with temperature for different thermally responsive gel surfaces that had been synthesised is shown in Table 3-10 and represents the availability in that gel of functional NIPAAm groups, although this is not as a comparative measure, as the quantity of NIPAAm monomer used in the synthesis of each is not equal in the pre-polymer mixture, thus conclusions on which is more functionalised cannot be drawn from this. The result does confirm temperature response in both gel recipes that had been produced, and a lack thereof in the all PEGDMA hydrogels.

Table 3-10 - Contact angles on NIPAAm and PEGDMA based gels as well as hybrid with response to temperature ($n=1$).

Hydrogel	Temperature (°C)	Contact angle (°)
PNIPAAm-co-MBAAm	20	40.6
	40	65.9
PNIPAAm-co-PEGDMA	20	36.0
	40	61.0

The measurements show the hydrophobic switch is present both in both gels where NIPAAm is copolymerized, this behaviour is the one that leads to the contraction of the gels in response to elevated temperatures, as polymer-to-polymer interactions dominate above the LCST.

3.3.2.4 Tensile tests

Tensile tests performed on cast and dry gel specimens as these were sufficiently strong enough to register a measurable reading on the 2 kN load cell of the Zwick-Roell. The force-displacement output was converted into stress and strain by taking the cross sectional area of the samples along with the initial gauge length and displacement until failure. This produced a comparative analysis of the Young's modulus of gels (Figure 3-28) with certain modifications, such as TEA addition (Figure 3-29) and monomer concentration (Figure 3-30).

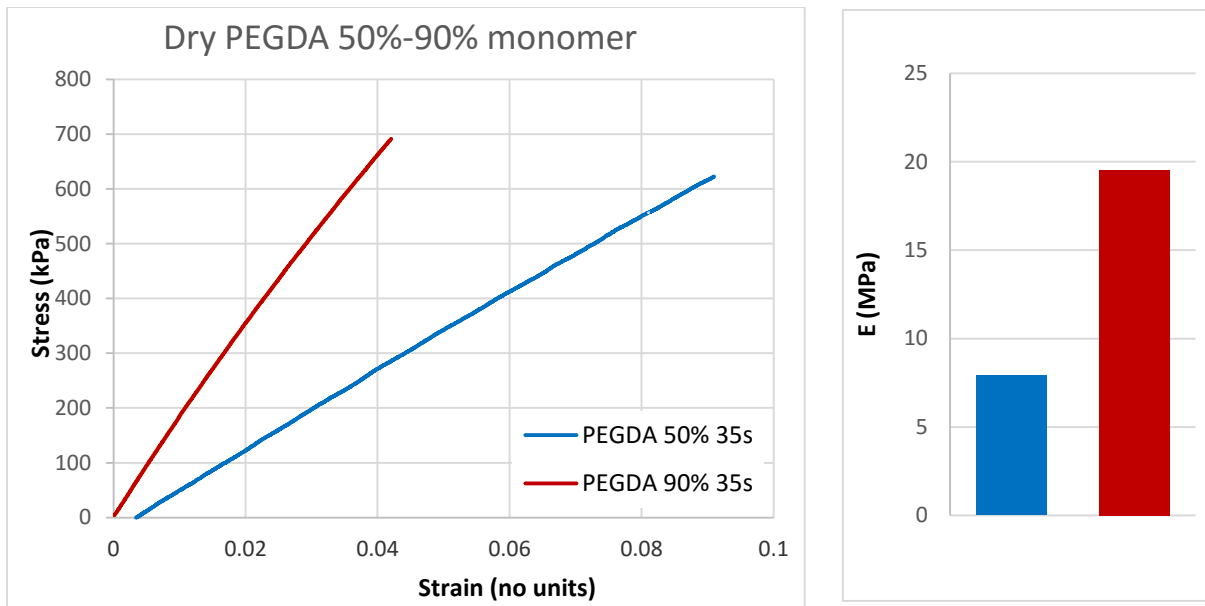


Figure 3-28- Effect of monomer concentration on two samples of PEGDMA gel under tensile load. A lower gradient for the 50 % monomer concentration gel, shows a lower elastic modulus with a reduction in monomer concentration, possibly due to the reduced density of the gel network, longer distances between crosslinks and higher fluid portion resulting in less resistance to elastic deformation.

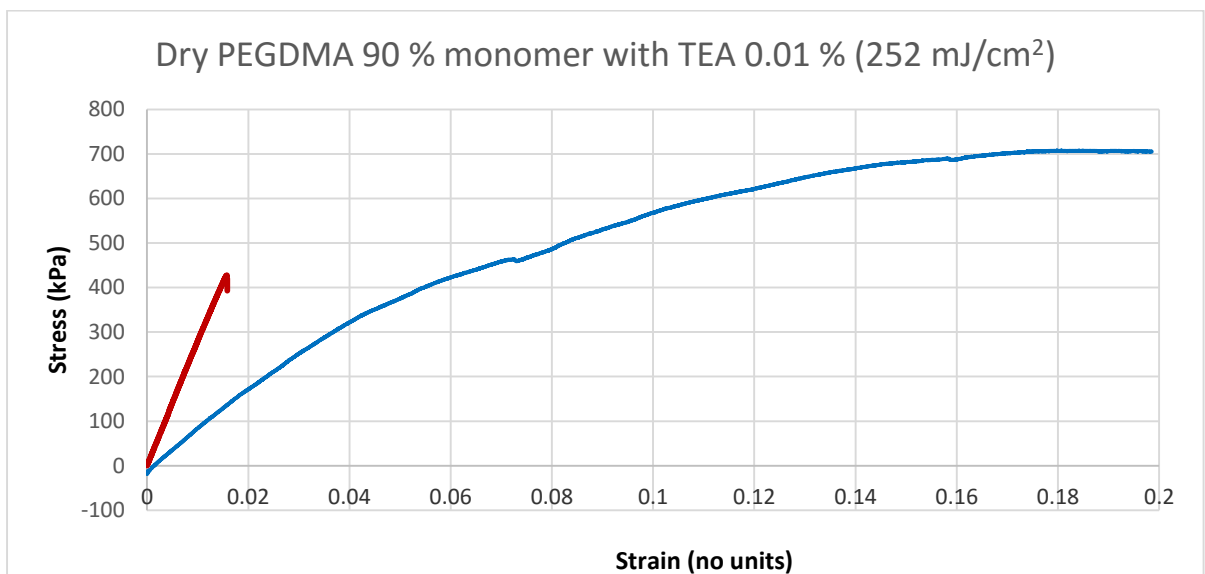


Figure 3-29 - The addition of TEA as an oxygen scavenger and copolymer even at very low concentration shows an increased elasticity of the gel (blue), with samples contracting rather than breaking and eventually sliding out from the tensometer grips, while the sample numbers are low it is assumed to give an indication of the modifications oxygen scavengers give to the gel structure, with a potentially more mature network with fewer oxygen terminated connections.

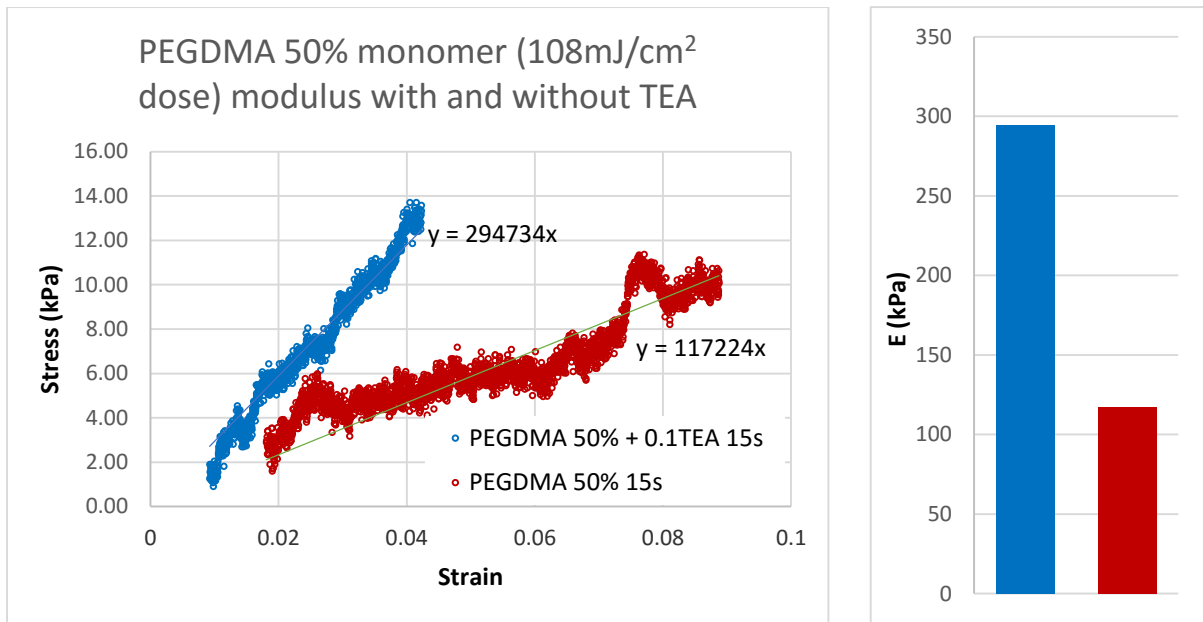


Figure 3-30- Effect of TEA polymerization chain transfer agent on low monomer content gels shows a somewhat different characteristic of the oxygen scavenger. In these very soft gels the addition appears to increase the modulus, again this is suggested to be due to a more mature network structure, with fewer oxygen terminated connections. Signal noise due to load cell sensitivity.

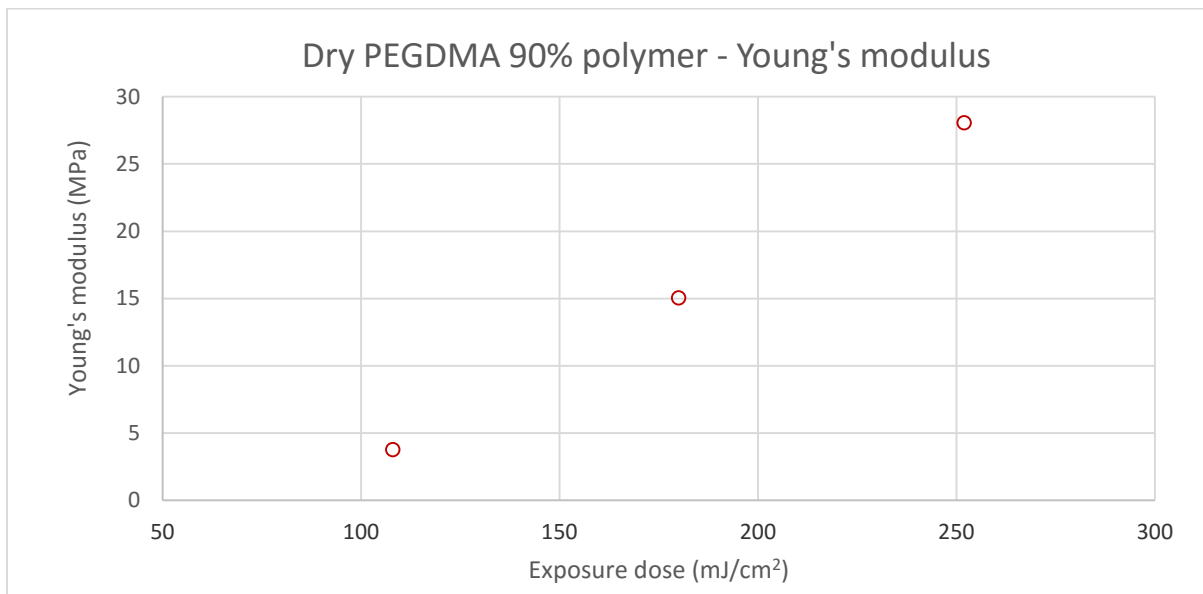


Figure 3-31 – Figure shows the effect of UV exposure dose on PEGDMA hydrogel Young's modulus, with an increase directly correlated to exposure dose. All samples were dried prior to testing to facilitate the ability to be gripped in the crosshead.

Comparing the Young's modulus of PEGDMA gels subjected to three exposure doses (Figure 3-31) yields the confirmation that exposure dose dictates the stiffness of the material, and produces the rigidity which counteracts the folding action of the bilayer swelling. The testing also highlighted the transition from mechanically weak to brittle of the hydrogels with exposure dose, as the hydrogel network continues to crosslink chain mobility is reduced and the overall structure becomes brittle and loses its significant ductility obtained at the intermediate exposure doses.

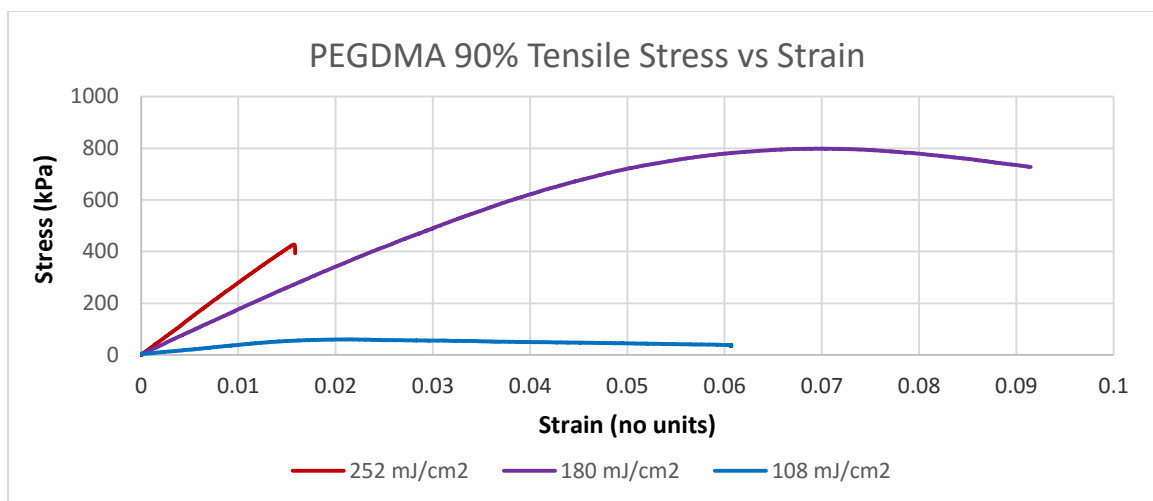


Figure 3-32- Figure shows the effect of exposure dose on Yield stress and elongation at failure of 90 v/v % PEGDMA hydrogels. There is a large shift from the softer weaker gels to a strong but brittle state, and a middle dose at which the network appears to have the most beneficial properties of both.

3.3.3 Fourier transform infrared spectroscopy

Fourier transform infrared spectroscopy – attenuated total reflection (FTIR-ATR) was performed on photolithographically defined hydrogel films and bilayers. The key functional groups and quantification of crosslinking density are derived from the intensity and any shift in specific absorption peaks.

3.3.3.1 DEAEMA cationic gel FTIR analysis

The FTIR spectrum of cationic DEAEMA hydrogels (shrink in elevated pH) is shown in Figure 3-33. The analysis was performed to confirm the presence of cationic N-H groups but also crosslinking state of the DEAEMA monomer. The spectrum shows a peak of acryl stretch at 1719 cm^{-1} is attributed to (C=O) absorption from the acryl group, additionally a peak at $2865\text{-}2979\text{ cm}^{-1}$ (saturated C-H stretching vibration). The large peak at 1103 cm^{-1} is in close proximity to the (C-C) stretching vibrations, but the large absorption is attributed to (C-N) vibrations due to the large polarity on the tertiary amine present in DEAEMA [203]. These gels were later used in attempted locking mechanisms relying on ion interaction between anionic and cationic gels, therefore making the pendant group presence an important confirmation prior to undertaking their integration in a photolithographic process.

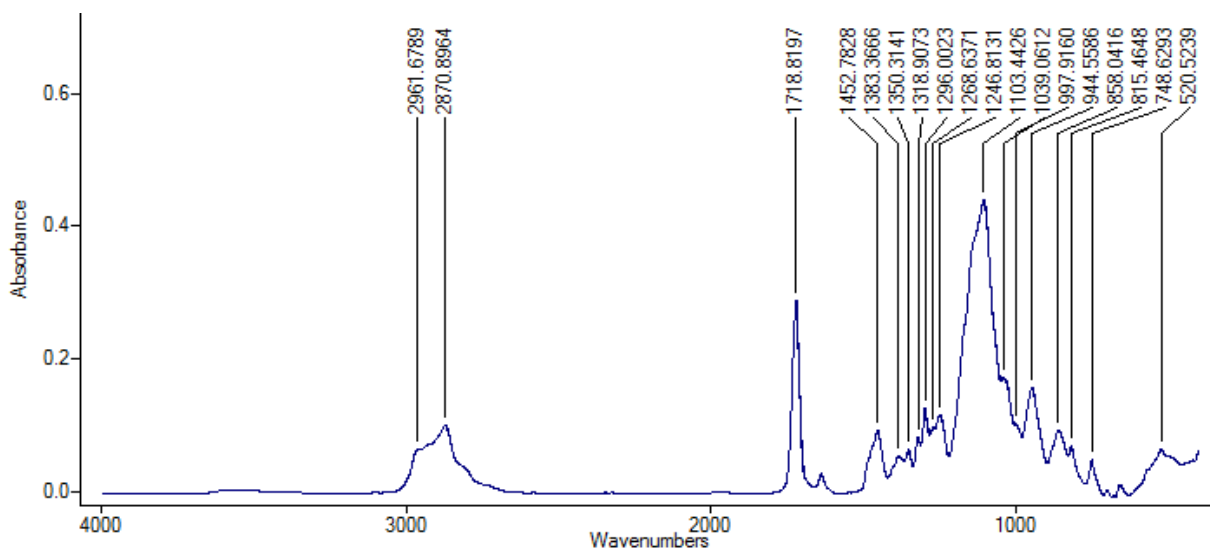


Figure 3-33- FTIR spectrum of cationic gel containing *N,N*-diethylaminoethylmethacrylate (DEAEMA).

3.3.3.2 NIPAAm thermoresponsive gel FTIR analysis

Thermo-responsive NIPAAm hydrogels were analysed using FTIR to confirm the crosslinking of the NIPAAm monomer into the MBAAm and PEGDMA copolymer hydrogel matrix, and being responsible for the LCST phase transitions. The presence of NIPAAm and its polymer in these gels was compared.

In the poly(MBAAm-co-NIPAAm) MBAAm crosslinked gels seen in Figure 3-34, there is a more typical amide carbonyl (C=O) vibration at 1640 cm^{-1} [110]. There is also more prominent (N-H) bending at 1535 cm^{-1} and a sharp peak of (N-H) stretch at 3286 cm^{-1} , in addition to the broad plateau starting at 3400 cm^{-1} [203]. The overall presence of NIPAAm monomer is much higher as a solid fraction of the gel, so the prominence of these peaks is attributed to the higher concentration of active pendant groups responsible for the LCST transition in these gels.

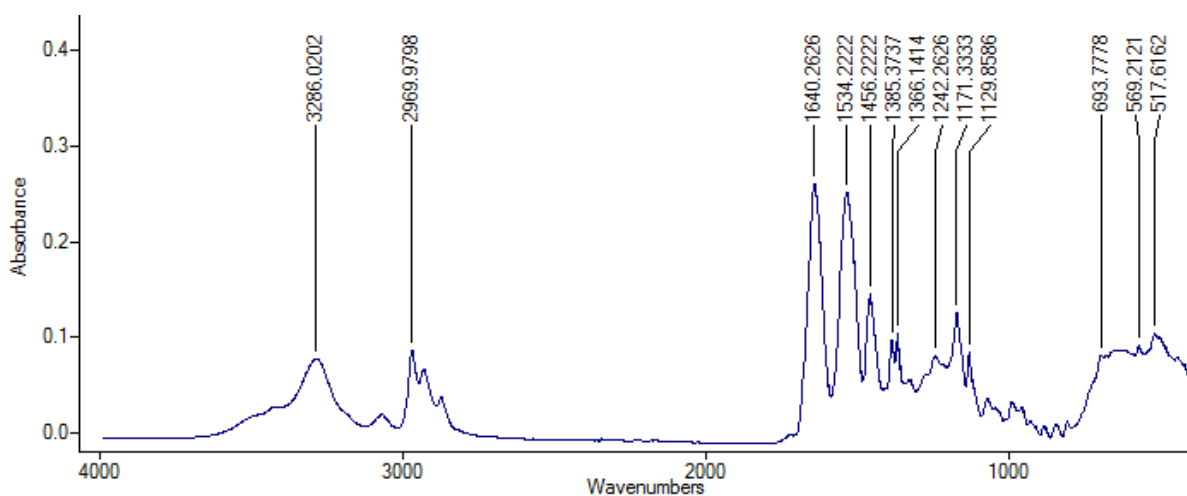


Figure 3-34- FTIR Transmittance spectrum of PNIPAAm co MBAA hydrogel when dry.

NIPAAm presence in the pNIPAAm-co-PEGDMA copolymer gels is confirmed in FTIR spectra shown in Figure 3-35. There is a main carbonyl (C=O) stretching vibration at 1717 cm^{-1} , and barely noticeable amide I band stretching as a shoulder of the same peak roughly by 1680 cm^{-1} [203]. N–H stretching vibration of the NIPAAm repeat units represented as a broad plateau at 3402 cm^{-1} , and a double peak of symmetric and asymmetric C–H vibration of the $-\text{CH}(\text{CH}_3)_2$ alkyl group at 1388 cm^{-1} and 1452 cm^{-1} is also confirmed in accordance with literature [110, 203].

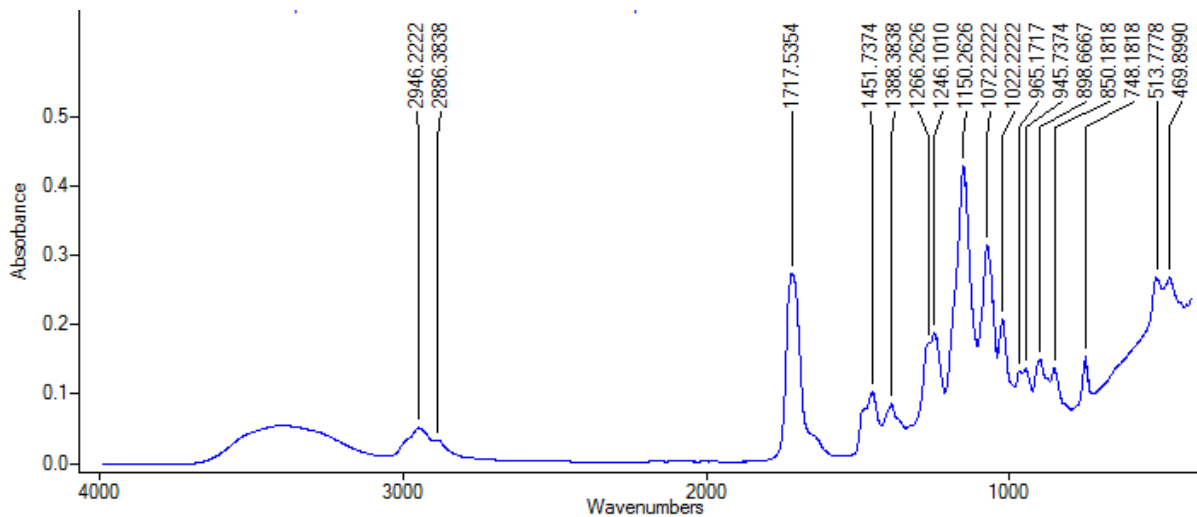


Figure 3-35 - FTIR Transmittance spectrum of *n*-isopropylacrylamide (NIPAAm) co PEGDMA hydrogel

3.3.3.3 FTIR analysis of PEGDMA gels produced with and without PAA lift-off

The presence of PAA copolymer graft on the underside of PEGDMA hydrogel sheets was confirmed with FTIR spectroscopy by comparing lift-off layers from polyacrylic acid (PAA) sacrificial surfaces and clean silicon. All sheets had received the same UV exposure dose. Absorption spectra were considered for all PAA layers (lift-off from 100,000, 50,000, and 1800 Da sacrificial films) against a pure PEGDMA hydrogel film seen in Figure 3-36. The extent of polymerization is also identifiable by looking at C-C groups present due to the long chains of PAA in comparison with the 700 Mn PEGDMA bulk gel.

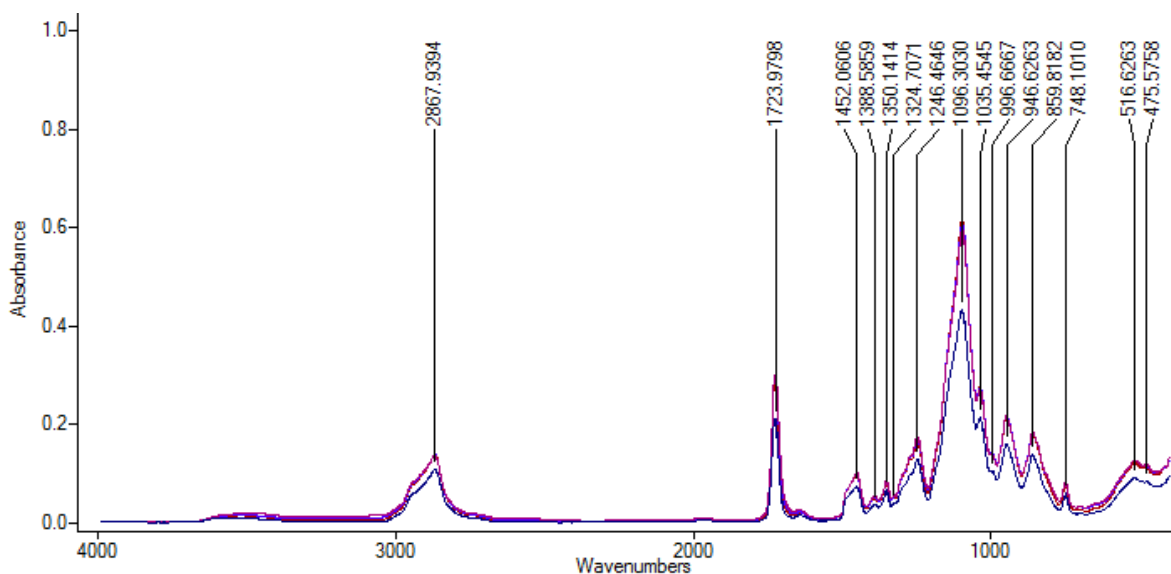


Figure 3-36- FTIR absorbance spectrum of PAA modified and unmodified films. Blue- Unmodified, with the Light Blue-PAA Mw 1800, Purple PAA Mw 50,000, Red PAA Mw 100,000 all coinciding in the elevated trace.

An increased absorbance at 1720 cm^{-1} could suggest presence of the C=C-COOH groups of PAA. No carboxylate peak is visible due to the gel sheet being in the flat protonated form during FTIR. A jump in (C-C) bending at 500 cm^{-1} and (C-C) stretch at 1095 cm^{-1} [203] is visible. This is likely corresponding to the significantly longer chain lengths of PAA compared to the 700 repeat unit PEGDMA, as this also increases with PAA M_w .

3.3.3.4 FTIR analysis of PEGDMA polymerization with TEA synergist

The spectrum obtained from polymerized hydrogels containing a TEA polymerization chain transfer agent/ oxygen scavenger is shown in Figure 3-37. An increase in crosslinking is seen by the relative increase in absorption for the C-C bond at 1096 cm^{-1} an increase is confirmed by higher absorption at the 520 cm^{-1} corresponding to C-C bending vibration. The increase is due to higher crosslink maturity and average chain length caused by the dual effect of TEA as a radical initiation synergist.

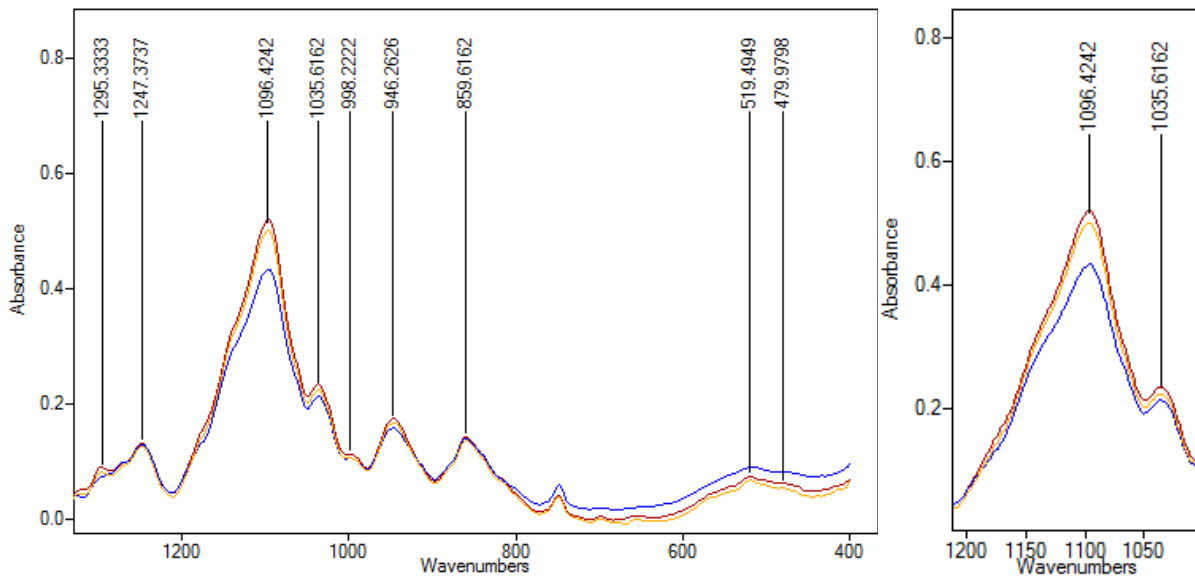


Figure 3-37- FTIR spectrum of PEGDMA hydrogels (blue) with addition of 0.25 w/w % TEA (yellow) and 1 w/v % TEA (red).

3.3.3.5 FTIR analysis of PEGDMA Polymerisation at different UV-exposure doses

Gels were found to have a peak shift in the C=O group from 1716.5 to 1730.1 cm^{-1} between 6 s and 80 s exposure time where almost full conversion is expected as the local conditions change surrounding the DMA C=O bonds. A sharp increase in peak shift is seen in Figure 3-38a between a 6 and 8 second exposure dose, with the peak starting to settle at longer exposures, this continues the observed trend that lightly exposed gel bilayers (6 seconds to 8 seconds at 7.2 mW/cm^2) have very different properties from their fully crosslinked counterparts, this is in agreement with the observed changes in rheological properties of gels at lower exposure doses as seen in sub-section 3.3.2.2.1.

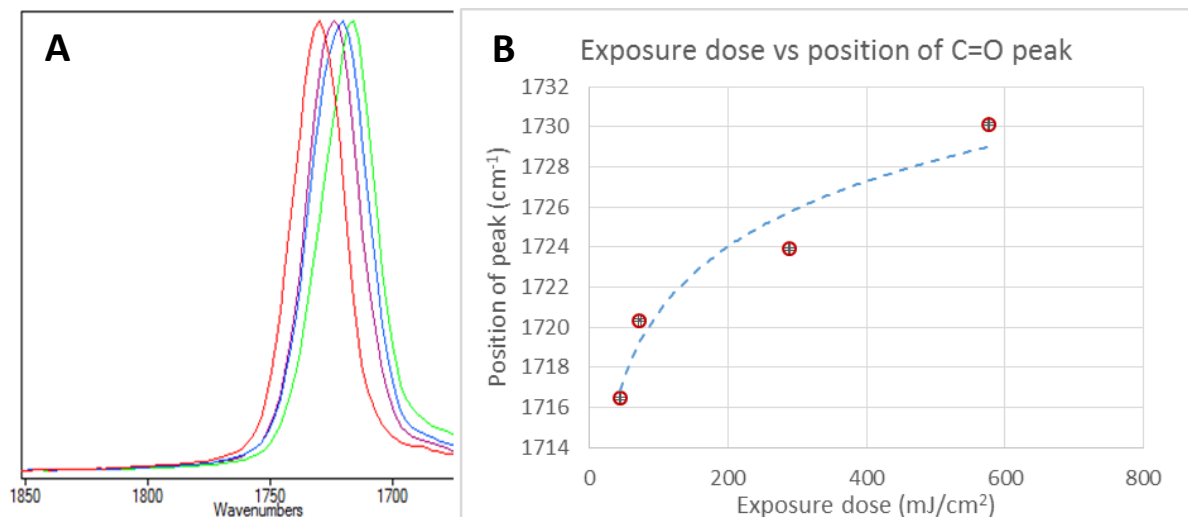


Figure 3-38 - Polymerization extent with exposure dose A) W shift in C=O peak in methacrylated PEG polymer (red = 6 s, purple = 8 s, blue = 40 s, green = 80 s). B) The shift in peak is thought to occur due to increasing crosslink density changing local conditions and thus harmonics of the pendant group by the proximity of local chains.

3.3.4 Bilayer actuation and predicted ideal conditions

The combinational process of patterning and functionalization created very thin bilayers, tuneable in their folding actuation by the exposure dose, as demonstrated by increasing the modulus of the material, in relation to the swelling potential of the functionalized surface. The grafting or interpenetrating network of PAA on one side of the gel surface, results in unequal osmotic pressure at the two interfaces as the pH rises above its pKa value. PAA is hydrophilic resulting in less hydrodynamic resistance. If the PAA layer is thick enough as the pH rises it will swell and absorb water faster than the PEG layer to which it is bound. Figure 3-39 shows the minimum measured radius of curvature of dissected hydrogel bilayer rolls as determined by SEM imaging. Rolls were fractured in liquid nitrogen after vacuum drying, radius is that from the roll centroid to the nearest internal roll edge. The variation in hydrogel bilayer curvature can be used to increase or decrease the central roll capillary diameter, as well as adjust the substrate stiffness for tissue culture applications where cell proliferation depends on substrate stiffness (Chapter 5).

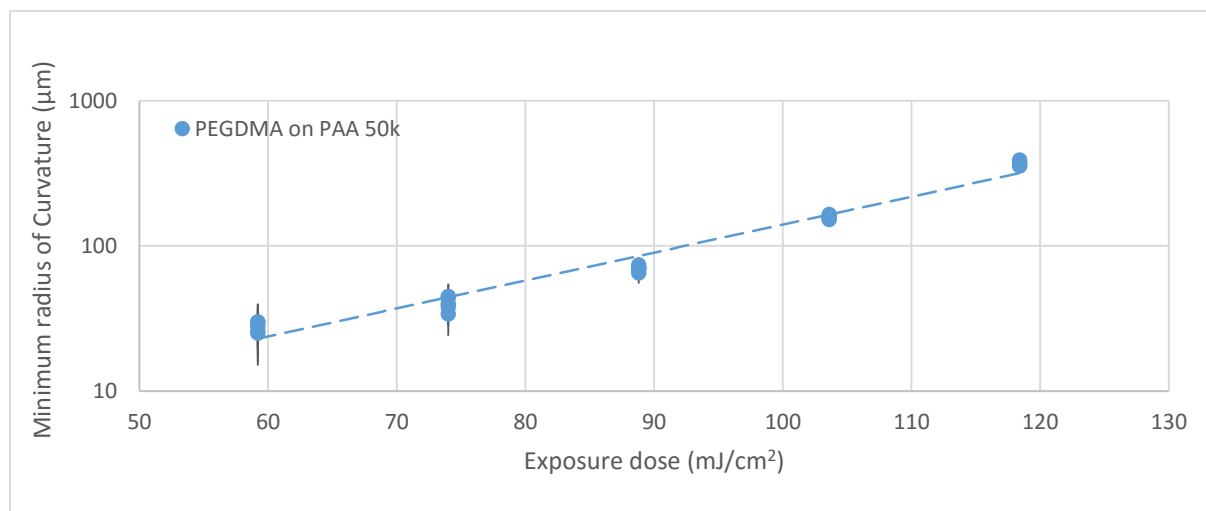


Figure 3-39 - PEGDMA 550 hydrogel film roll radius of curvature after scaffold lift-off from PAA 50,000 Da spun at 4000 rpm for 30 s and buffered at pH 7 at different UV exposure doses. Error bars = 1SD from n=5 measurements of minimum curvature radius in the centre of SEM cross-section of gel rolls. Reproduced from Vasiev et al. [1].

Hydrogel bilayer rolling can be predicted with the Timoshenko equation. The equation stems from metal bilayer applications [132] but has been modified for predicting hydrogel curvature relates the curving tendency of the hydrogel bilayer actuator [129], where:

$$Curvature (\mathcal{K}) = \frac{1}{R} = \frac{6(\varepsilon_2 - \varepsilon_1)(1 + m)^2}{t \left[3(1 + m)^2 + (1 + mn) \left(m^2 + \frac{1}{mn} \right) \right]} \quad Eq. 3-12$$

$$Where: m = \frac{h_1}{h_2} \text{ and } n = \frac{E_1}{E_2}$$

And E_1, E_2 are Young's modulus, h_1, h_2 are the layer thicknesses, t is the total thickness of the bilayer, and $\epsilon_{1,2}$ are the actuation strains of the two layers, and R is the radius of curvature[132].

A prediction of ideal conditions for folding emerges giving the required bilayer thickness ratio between actuating and passive layers shown in Figure 3-40. In the case of PAA-co-PEGDMA diffusion based hydrogel bilayers, this ratio is very small due to the slow diffusion of PAA in PEGDMA[45]. As the distance of diffusion could not be established by staining and optical microscopy, it is assumed to be under 500 nm in depth, which is the size of nanofeatures that can be achieved by PAA layer embossing, it is thought that if the diffusion exceeded this the feature quality would be degraded due to the absorption and migration of the sacrificial PAA layer into the PEGDMA resist. From the Timoshenko equation the optimum thickness ratio of active to passive bilayer layers is shown to be in the region of 1:2 irrespective of the overall difference in layer swelling and thereby strain ($d\epsilon$).

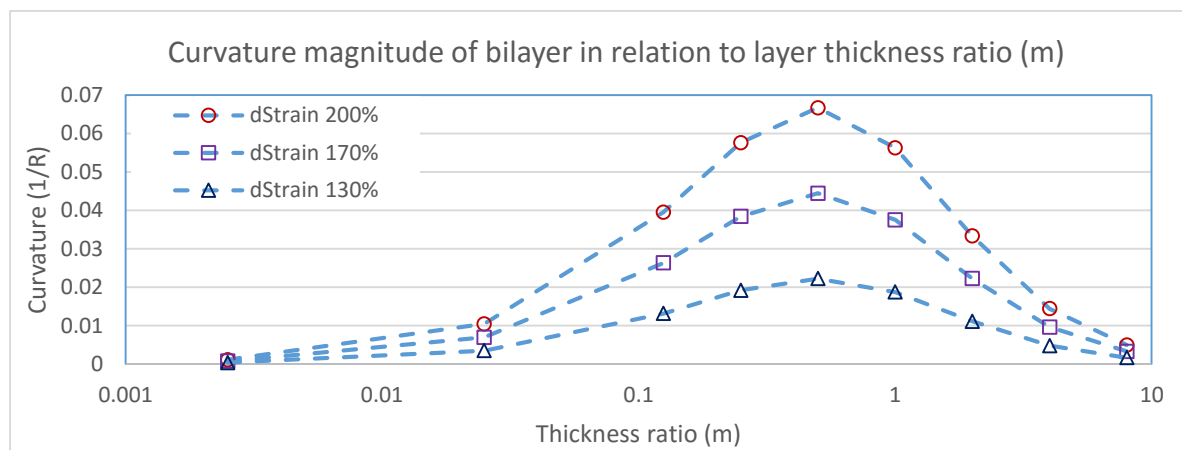


Figure 3-40 – Effect of bilayer thickness ratio (active/passive) as well as active gel actuation ratio on relative curvature. Young's modulus and base swelling kept constant (8 kPa, 0.3 ϵ respectively), only actuator thickness and actuation strain varied, resulting in most efficient curvature achieved at thickness ratio of 0.125-1, peak at 0.375.

There is difficulty in the fitting of this model to the hydrogel films due to coupling between hydrogel crosslinking density, modulus and swelling ratio. This coupling means that the actuation strain is inversely proportional to the Young's modulus of the material, both of which change at different rates depending on exposure dose. It is this reason and the additional lack of information on the diffusive PAA bilayer thickness distribution which means no real data comparison is made to the Timoshenko model. Predictions can however be made based on this model to determine the factors which play a dominant role in bilayer folding such as the effect of gel modulus (Figure 3-41) and total bilayer thickness (Figure 3-42).

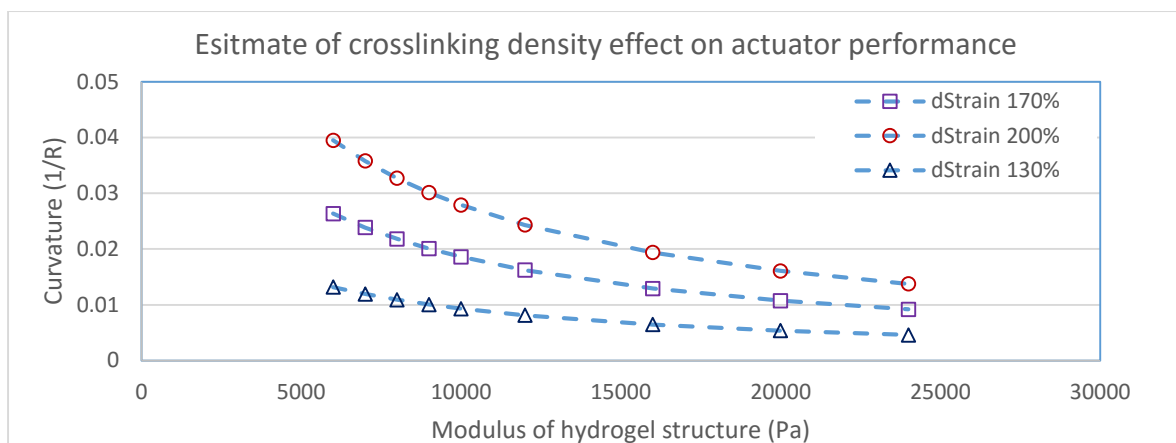


Figure 3-41 - Effect of bilayer actuation strain differential (dstrain) on the curvature (K) and modulus relationship for an idealized gel bilayer at constant thickness ratio ($m=8$)

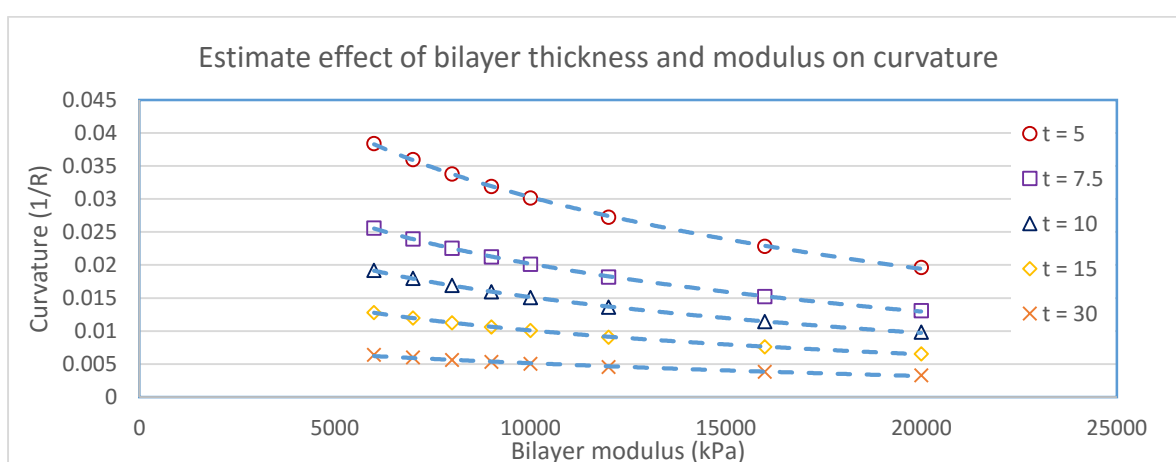


Figure 3-42 - Effect of bilayer thickness (microns) on curvature $K=1/R$ (μm) for bilayers of varying Young's modulus E .

The gel films resulting from this fabrication method possess a sensitivity to environmental pH and will roll when exposed to pH 7 solution. The rolling of these structures as a result of changes in aqueous pH is caused by a differential swelling. The swelling differential is a product of differences in water absorption between the PAA and PEGDMA layers due to protonation or deprotonation of the PAA pendant carboxyl groups when exposed to pH 7 solution. PAA is an anionic polymer at pH values above the polymers pKa value of 5.5-6.5 and is fully ionized at pH > 9.5 and fully de-ionized at pH 4 [204], thus the side chains of PAA will deprotonate and acquire a negative charge resulting in rapid swelling and water absorption at which point hydrogen bonding interaction become dominated by polymer interactions with the polar aqueous environment. As PEGDMA is neutral it does not experience a change in swelling when exposed to pH 7 buffer.

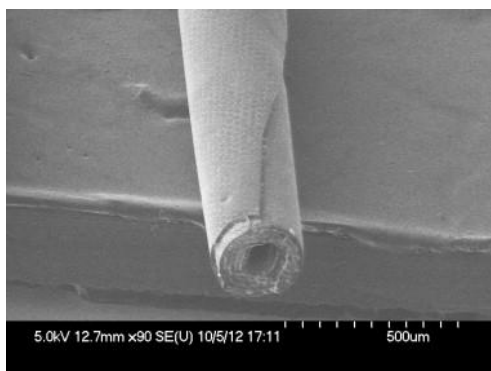


Figure 3-43 - SEM image of hydrogel film roll after actuation in pH7 buffer and drying at room temperature.

The rolled sheet of 5mm square can create spiral tubes of varying thickness with a varied inter-sheet spacing, reducing further when the scaffold was dried. The rolled sheet can be unrolled on exposure to pH 4 buffer with some agitation as the layers tend to stick in acidic pH due to preferential polymer-to-polymer molecular interaction. The sheets were subsequently rolled and unrolled over many cycles by switching the aqueous pH from 4 to 7. This behaviour was still observable in sheets which had been stored in RO water for 7 days.

3.4 CONCLUSIONS

This chapter is intended to lay out the framework for producing hydrogel actuators, capable of assembling 2D patterned components into 3D micro containers. Initially a qualitative approach was used to find gel recipes that showed promise by forming well defined flexible films. During this phase numerous recipes were tested, with some of the most practical combinations listed in Table 3-1. While listing every possible recipe and combination of crosslinked monomer and initiator is equally impractical, the most dominant variables in gel formulation were found by a Taguchi study of thermoresponsive/pH responsive PNIPAAm-co-AAc gels. This sensitivity study (Figure 3-12) showed that monomer, crosslinker and initiator concentration affect overall gel swelling capability the most. The same applies to non-actuating gels, as it is those components which create the structural crosslinking connections responsible for the strength and flexibility of a given gel.

Initiators were chosen based on efficiency, determined by UV-visual spectrophotometry, and by their ability to dissolve in ethanol and IPA. Solubility was a factor because they had to be soluble in the gel pre-mixture, but also have a solvent other than water to avoid dissolving the sacrificial layer prematurely. Lucirin TPO was chosen as a candidate initiator in part due to its efficiency at the 365 nm wavelength produced by the MA6 maskaligner (photolithography tool), and due to its resistance to oxygen inhibition.

Structural gels were streamlined to use PEGDMA, which offered a wide variety of commercially available molecular weights, low protein absorption, good mechanical properties and acrylate chemistry suitable for crosslinking by photoinitiated free radical polymerisation. The PEGDMA gels were analysed by weighing, thereby determining their swelling ratios, these would give an indication of mesh size, and thereby gas and nutrient diffusion rates. High diffusion rates would be beneficial for cell survival, while large pores would allow the chemical microclimate to escape. It was found

that PEGDMA gels with a monomer concentration of 80-90 % should have a mesh size of under 10 nm (Figure 3-8), providing a good compromise between permeability and patternability of the gel. Significant amounts of time went into trying to make thermoresponsive bilayers work, these were intended to use NIPAAm monomer with various copolymers. The gels were analysed by rheology, contact angle and swelling ratios to determine their transition temperature, where the gel begins to collapse and expel free water. While gels could be produced which were photopatternable and thermoresponsive, we were unable to produce a thin film of this gel, and producing a functioning bilayer was only possible at cumulative thicknesses near 200 μm . These surfaces remain useful and could be used within the scaffold or as a grafted layer on the surface (polymer brushes) to selectively attach and detach cells as seen in Tsuda et al [70]

A successful gel-bilayer was obtained in the form of a pH responsive thin film of PEGDMA-co-PAA, produced by photolithographically patterning PEGDMA gels on a PAA sacrificial layer. It is proposed by this author that partial diffusion of the PAA chains into the gel above, and diffusion of initiators into the PAA layer below result in a tethering and partial crosslinking of this polyacid to the PEGDMA chains. This diffusion should be short in time scale and may extend to the top surface of the gel. It is therefore likely a resulting gradient of polymerisation formed during short exposures which creates a gradient of swelling ability through the gel thickness. This bilayer formation resulting in pH responsive thin films which roll on exposure to elevated pH (above pKa of PAA) as seen in Figure 2-37. The presence of PAA pendant groups were confirmed by FTIR-ATR (Figure 3-38) with an increase in peaks corresponding to the PAA chain backbone when the PAA molecule Mw was increased, slight increases in carboxylic O-H bending was also observed, while FTIR could confirm the presence of certain groups (within reason) the thickness of the diffuse PAA layer could not be determined by this or by optical methods.

Tensile tests performed on thin hydrogel tensile specimens produced by solvent casting into a laser cut PDMS mould, were used to determine optimum formulations for improving the robustness and mechanical properties of these PEGDMA bilayers. One key issue was thought to be oxygen, as much of the patterning procedure resulted in the gel thin spun film being exposed to atmosphere. In order to scavenge the dissolved oxygen in the resist layer, TEA (an oxygen scavenger) was added to the solution, this markedly improved the toughness of the gels thought to be due to an improved chain completion rate, by reducing the number of chains ending disconnected by oxygen termination. The addition of TEA leads to an increase in crosslinking extent (Figure 3-29), with the gel eventually becoming more brittle, but undergoing a favourable toughening and improved strain at break at lower concentrations of added TEA synergist.

The optimum exposure dose for actuation was found to be 8 s or 57.6 mJ/cm², values below this yielded sticky films which were too soft to retain shape, crosslinking density increased, but at intermediate values facilitated suitable curvature rates for use as hydrogel hinges discussed further in Chapter 4.

It was estimated from a modified Timoshenko equation for a bilayer folding mechanism shown in Figure 3-40, that peak folding potential would be obtained when the active layer constitutes 1/3rd of the overall gel sheet thickness, irrespective of the modulus of the overall film. Because the gels change constantly during exposure, parameters were not controllable to the extent where this model could be validated, it is used rather as an indicator of the ideal film folding conditions.

Additionally cationic gels were trialled, and were thought to be a means of locking containers by attaching ionic and cationic gels to one another, these gels could be patterned in structurally intact blocks, but the logistics of integrating them into a 3D container, and as a photolithographic stage proved to be difficult. The details of this are discussed in Chapter 4.

4 DESIGN AND MANUFACTURE OF 3D STRUCTURES

4.1 INTRODUCTION

This chapter covers my attempts made to combine hydrogel synthesis with micro- and nanoscale manufacture. The established and novel 2D patterning methods outlined in Chapter 2 where epoxy and polymeric films were patterned by NIL and UV-NIL and combined with gel chemistry from Chapter 3. The end result is nanopatterned micro features linked together by photolithographically defined hydrogel hinges, which fold these layers up into 3D structures, thereby creating nanopatterned, self-folding niches. While any cell work and demonstration thereof is in Chapter 5 the resulting containers are really the culmination of this work, and where the title “cell origami” ultimately originates.

Many 3D containers exist in literature such as those created by the Gracias group at Johns Hopkins University [23, 24, 27], who are leaders in the field of self-assembly, and many others [22, 124, 126, 128-130]. However, they are yet to demonstrate nanoscale patternability and actuation methods which are compatible with cell culture. Quite often thermo-responsive hinges will work by swelling in cool conditions, these then while possibly suitable for yeast culture cannot be used with cells, at least not in the longer term. Others which are pH responsive require high ionic concentrations or highly elevated pH [71].

This work rather than focusing on the maximum folding potential of these gel hinges, focus on their geometric arrangement and utilization at cell friendly pH neutral conditions. It is a primary objective for these devices to close in milder pH conditions such as cell culture media, and one means of doing this is to lengthen the hinge size, and use the more conservative folding at lower ionic concentrations and less extreme pH to best utilise the minute degrees of curvature available, thus producing a folded structure.

Optimum folding geometries using platonic polyhedral will be manufactured, to find a best balance of hinge number, and hinge folding angle necessary to fold the structure. The number of faces ultimately leads to uncertainty, with more potential areas to fail, however by increasing the number of faces, the overall radius of curvature at each hinge decreases. The design of hinge arrangements that has been opted for follows the idea that “less is more” with the most simple constructions expected to cause the least issues in assembly, this is in agreement for the optimum folding geometries found by Pandey et al. [26], where containers that have a central axis of symmetry are expected to be optimal at folding into 3D structures.

In addition to folding, one aspect which is novel in this work is the incorporation of nanopatterns to the folded container faces, such as those seen in Chapter 2. This is something which to the author's knowledge has not previously been done, and certainly has not been combined with self-folding hydrogel hinges. Nanopatterns used for contact guidance, to aid cell proliferation as shown by Seunarine et al. [148], and potentially stem cell differentiation, as shown to be the case with MSCs in Dalby et al. [39], will be incorporated into the structures with the ambition of using these to topographically control cell behaviour in a specifically tailored 3D environment. NIL and UV-NIL techniques will be utilised to create nanopatterned surfaces in commercially used photoresists such as SU8 and a number of potentially useful thermoplastic films of polymethylmethacrylate (PMMA), polycaprolactone (PCL) and poly-L-lactide (PLLA), these materials are selected due to their biocompatibility [56] and in the case of PMMA for its known use in nanotechnology manufacturing as an electron beam resist. These polymers (with exception of PCL which can be semi-crystalline) are amorphous thermoplastics and should retain their imprinted shape and pattern on solidification and result in less residual stress after forming.

Nanopatterned stamps, and replica stamps reproduced in PDMS and FEP will be utilised as detailed in Chapter 2, to imprint these polymeric surfaces in between subsequent, photopatterning, etching and development steps to produce nanopatterned containers, to be folded by defined hydrogel hinges. The PAA sacrificial films will be used as detailed in Chapters 2 and 3, to aid in the lift-off of final devices prior to actuation, as this would involve much more toxic chemicals, and more laborious processes if these sacrificial films are to be done without [190]. It is also an amorphous thermoplastic and retains its imprinted shape as it cools after imprinting. This chapter will outline the difficulties encountered in the combination of these two streams of work, primarily in material-material interactions, incompatibility of processes and solvents, and various artefacts of the manufacturing process.

Novel methods of etching and fixating containers to the solid substrate underneath the sacrificial film will also be discussed, as these would allow the containers to be localised to a precise point and potentially be used in lab-on-a-chip type applications, where an array could be produced that had specific patterns and stimuli in a traceable location. I will aim to demonstrate successfully actuating containers, and several design aspects found during this work which aid the manufacture and application of nanopatterned self-folding 3D cellular niches.

4.2 MATERIALS AND METHODS

In this chapter methods of combining previously covered surface nanopatterning with the swelling nature of hydrogels to create self-folding 3D architectures were used. The manufacturing, triggering

and release mechanisms for creating these 3D self-folding micro scaffolds will be covered. This section of the work is a pilot study into various fabrication techniques, device usability and compatibility with cell culture techniques.

4.2.1 Materials

SU8 Negative Epoxy Series Resists (SU8 – 3005, 3010 and 3050) were obtained from Micro Chem and used as received. Shippley microposit S1818 was obtained from the manufacturer and used as received. Polyacrylic acid (PAA) (1800, 15000 (neutralized), 50000 and 100000 Da) were obtained from Sigma Aldrich and Polysciences (50000 Da) respectively. Polymethylmethacrylate (PMMA) 84,000 Da was received from DuPont (Elvacitate 2010) and diluted in o-xylene (8 % and 2.5 %). Poly-L-lactic acid (PLLA) PURASORB PL 18 (1.8 dl/g) was obtained from Corbion-Purac and washed twice with heptane, before oven drying and full dissolution in chloroform at 7.5 w/v %. PCL 65,000 Da was also dissolved in chloroform obtained from Sigma-Aldrich. All solvents and developers (acetone, methanol, acetone, ethyl lactate (EC-SOLVENT), tetramethylammonium hydroxide 2.2 % Aq. (MF 319), N-methyl-2-pyrrolidone (NMP) were obtained from Farnell and used as received.

4.2.2 Software

4.2.2.1 Mask design

Photomasks for producing the containers were designed using Corel Draw X3 and ordered and obtained from Microlithography services Ltd as acetate masks, which were subsequently transferred to Glass be photolithography and Ni-Cr evaporation, this process is outlined in Chapters 2 and 3.

4.2.2.2 Computer aided modelling.

Models of diffusion in closed containers was done using COMSOL Multiphysics V4.2, and the results of this are shown in Appendix A.

4.2.3 Methods

4.2.3.1 Photolithography

Photolithography was done using a SÜSS MA6 mask aligner photolithographic system at 365 nm and 350 W lamp. An array of nickel-chrome (NiCr) masks on glass, quartz and acetate flexible masks were used (Chapter 3).

4.2.3.2 Nanoimprint Lithography

Nano imprint lithography was performed in an Obducat NIL 2.5 Nanoimprinter. Section 4.2.3.5 provides the details, and Chapter 2 gives a full overview of the process.

4.2.3.3 Metal deposition

Sputtering of gold, titanium and palladium coatings was done in a Plassys MEB 550S Electron Beam Evaporator. A crucible of the desired metal was sputtered in a vacuum at the sample target on a rotating stage to produce a uniform film.

4.2.3.4 Surface metrology

Depth measurements were obtained by scanning profilometry on a Veeco Dektak 6M Height Profiler, for smaller features, and patterned surface profiles were scanned using an atomic force microscope (AFM), in tapping mode with a silicon nitride tip. Samples were placed with pattern facing upwards, in scanning profilometry, a tip was drawn across the surface recording irregularities in surface height, detected by a laser reflecting on the stylus cantilever arm, resulting in timing shifts in this reflection as the stylus traversed up and down. The AFM was used in scanning mode, with a conical cantilever tip, operating in a similar manner, however it instead taps out the surface at a pre-set frequency, with any attenuation recorded by a laser reflected from the cantilever tip. The reflected laser beam strikes a photo-detector consisting of four-segment array. The differences between the signals indicate the position of the laser spot on the detector and thus the angular deflections of the cantilever scanning the surface.

4.2.3.5 Nanoimprint lithography (NIL)

Devices were constructed in layers by standard MEMS processes. The layers started with lift-off layer, boundary layer, solid surface layer and finally a hydrogel actuator film, although a case is discussed where this was performed in reverse order with hydrogel applied first, the pitfalls of this method are discussed in Section 4.4.5.

4.2.3.6 Sacrificial film application

PAA sacrificial layers were created by spinning solutions of varying Mw (1800, 50000, and 100000) at different dissolutions (63 %, 25 % and 25 % in H₂O, respectively). The sacrificial films were embossed by the use of a PDMS, FEP or qz stamp at 105 °C. (Details of the manufacture of PDMS, FEP and qz stamps, as well as PAA spin thickness are given in Chapter 3). The process of transferring nanopatterns into sacrificial PAA films is shown in Figure 4-1.

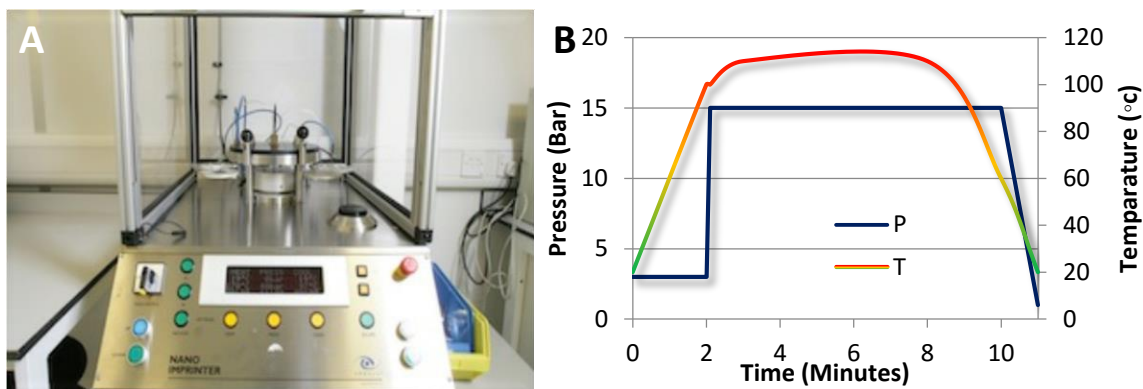


Figure 4-1 – A) Obducat nano-imprint lithography (NIL) tool, and B) the imprinting routine for PAA patterning. Colour spectrum line shows heating cycle, blue line illustrates the variation of pressure through the imprinting cycle.

The process chain for nanopattern transfer by embossing in the Obducat NIL tool is as follows:

1. Pre-heat step: 100 °C preheat ramp over 2 minute duration at 3 bar.
2. Imprint step: 15 bar at 110 °C for a 6 minute duration.
3. Cool down step: Maintained pressure of 15 bar until temperature drops to 60 °C

4.2.3.7 SU8 structures

SU8 features were applied by spinning onto a 500 µm thick silicon wafer or glass slide pre-coated with a PAA layer as described previously. Subsequently two methods existed for patterning the film, either a post exposure emboss instead of post bake, which created features in the SU8 surface, or the modular mastering approach outlined in Chapter 3 using FEP masters in both cases.

Two thinner spinning SU8 resists were used the SU8 3005 series and SU8 3010 series due to lack of supply and short expiration time of the resist.

Table 4-1 – Photolithographic processes for two low thickness SU8 formulations, the 3005 and 3010 series resists. The 10 is a more viscous formulation of the 3005, and spins a thicker film. Both resists were used as received.

Resist:	SU8 3005	SU8 3010
Thickness	5 µm (3000 rpm)	5.5 µm (6000 rpm)
Soft bake	2 minutes at 95 °C	3 minutes at 95 °C
Exposure dose	24s on Glass and Au 15s on uncoated Si	30s on Glass and Au 21s on uncoated Si
Post bake (Thermal NIL)	Stage 1: 1min at 65 °C Stage 2: 2minutes at 95 °C	Stage 1: 1min at 65 °C Stage 2: 3 minutes at 95 °C
Development	3 min	3.5 min

4.2.3.8 Boundary layer films

SU8 was found to require a boundary layer film applied in either gold or PMMA. Gold was sputtered to a depth of 50 nm prior to SU8 Spinning. This was etched after SU8 development with a 4:1 potassium iodide and Iodine solution in IPA:MeOH (50:50). PMMA was applied by spinning at 5000 rpm for 60 seconds of a 2.5 % solution of 84,000 Da PMMA in o-xylene followed by a 30 second bake at 95 °C. The films were developed by the same ethyl lactate developer used for SU8. Samples were ashed after normal SU8 development to remove any PMMA film remaining, this method is considerably cheaper, but the gold boundary layer stays on the containers after lift-off, which has merits in terms of surface chemistry and the possibility of integrating circuitry.

4.2.3.9 PLLA application and patterning.

PLLA was spun onto the sacrificial film from chloroform, a solvent with which PAA does not react [205]. The spun film PLLA film was covered in a layer of S1818 in which the photo-patterns were defined, and the subsequent layer was ashed in O₂ Plasma for up to 20 minutes to define the necessary microfeatures. O₂ ashing unlike wet or dry etching is a relatively slow process preventing the PAA film underneath from getting damaged by more caustic etchants. Patterning was performed in a similar fashion just above the PLLA melting temperature of 160 °C and 15 bar [206].

4.2.3.10 Hydrogel hinge application.

Thin films of hydrogel could be spun onto substrates in the case of PEGDMA and PEGDA preparations (Chapter 2) NIPAAm and DEAEMA formulations showed issues with crystallization due to solvent evaporation, unless dissolved in PEGDMA. There was some substrate dissolution due to a small concentration of water present in the PAAc and AAc solutions (including HEMA-co-AAc). Hinges would operate on the principle covered in Chapter 1 and illustrated in Figure 4-2.

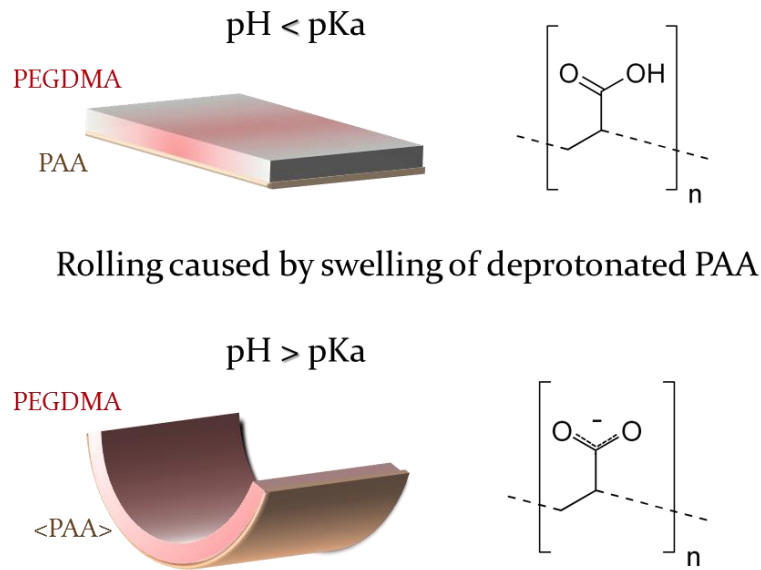


Figure 4-2 - Illustration of ionic hydrogel bilayer swelling in elevated pH, resulting in film rolling by an uneven swelling differential between top and bottom surfaces. Reproduced from Vasiev et al. [1].

The issue with spinning is the difficulty it poses for repeatability due to waiting time between spin and exposure, as well as causing oxygen diffusion problems, solvent evaporation problems and issues with substrate dissolution. It also makes it difficult to perform proper mask alignment, as the mask spears the solution after making working distance contact measurements. It was therefore replaced with a solvent solution applied by pipette at 25 μl per square cm of substrate, allowing a film of roughly 250 μm in height before hard contact mode, which was allowed to further displace the fluid for 5 seconds prior to exposure. The SU8 features act as a limiting spacer in the gel thickness, which would have to be at least higher than the existing features on the substrate. Initially the mask aligner base was coated with a sticky vinyl wrap film to cover the vacuum ports and prevent the hydrogel solution from fouling the machine. Secondly a carbon cement tab used for SEM sample adhesion was placed in the middle of the vinyl film on the sample holder chuck, and the sample was placed on top, to hold it during alignment. Once applied to the cement tab, alignment was performed as usual, with the drop of hydrogel applied prior to exposure during an unload cycle, carefully without shifting sample position. A second quick adjustment was performed just before exposure to check the feature positions.

4.2.3.11 TPM modification for hydrogel anchoring

For permanent hydrogel bonding to glass or silicon surfaces, a methacrylated monomer based coating of 3-(trimethoxydsilyl)propyl methactylate (TPM) was utilized. The coating can be applied to surfaces containing silicon (Si) atoms at their surface. Two methods of applying this coating were used.

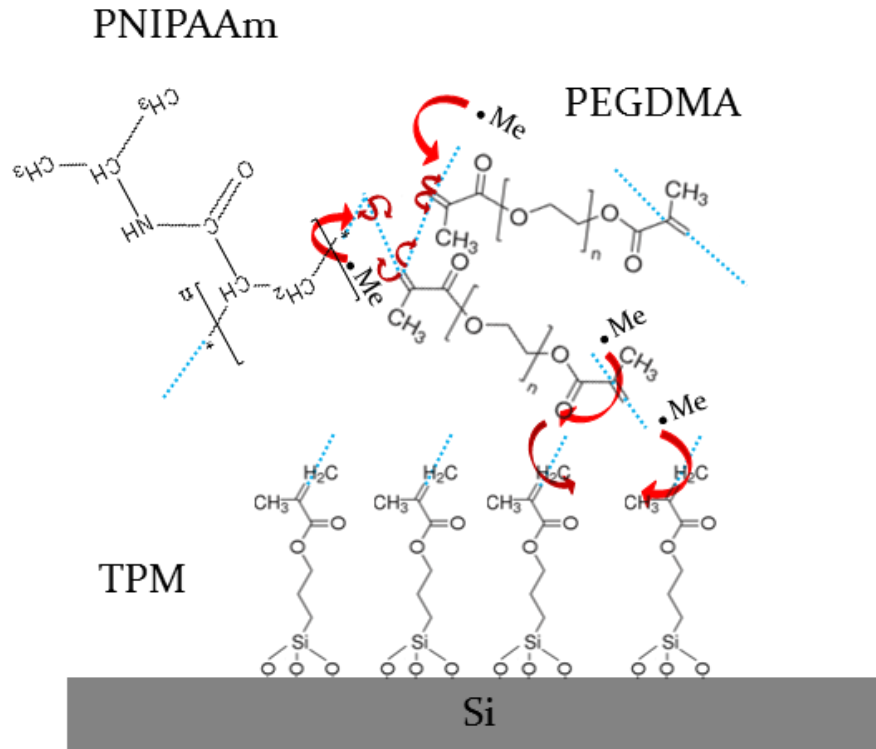


Figure 4-3 - Illustration of hydrogel anchoring to methacrylate groups of TPM coated surface. Attachment works for acrylic monomers and polymers, and can be used to semi-permanently bond the hydrogel photopatterns or structures to a glass slide or silicon wafer.

4.2.3.12 Liquid application of TPM

In the first process, silicon or glass substrates were treated for 5 min, at room temperature, in a 1 mM heptane solution of TPM, followed by washing with heptane, acetone, methanol, IPA and water each for 3 minutes in that order. The surface showed a hydrophobic tendency after the coating had been applied.

4.2.3.13 TPM deposition by evaporation.

Substrates (glass or silicon) were first ashed in O₂ plasma for 3 minutes at 80 W. They were then placed in an inert N₂ atmosphere (a glass petri dish with glass cover plate) with a drop of TPM (liquid, as obtained) applied to opposite corners of the volume. The sealed and inert container containing the samples was then placed on a hotplate at 150 °C for 15 minutes. After this time the volume was flushed with nitrogen and allowed to cool, a drop test with RO water would show a hydrophobic surface if the coating had been successfully applied.

4.3 DESIGN OF CONTAINERS

4.3.1 Hinge design

Hinges were designed using the hydrogel formulations available for the sacrificial layer technique, as this was quick to manufacture, thin and tested for photolithographic manufacture. Initially the hinge actuating radius was checked for thickness effects, with gels spun to different film thicknesses and exposed to two of the most promising energy levels, to test/measure the radius of curvature. This added to the previous knowledge that curvature of PEGDMA-co-PAA bilayer film depends on the exposure dose (Chapter 3) due to increasing modulus. The thickness of these gels can be further controlled to augment folding potential as shown by the spin thickness curve in Figure 4-4.

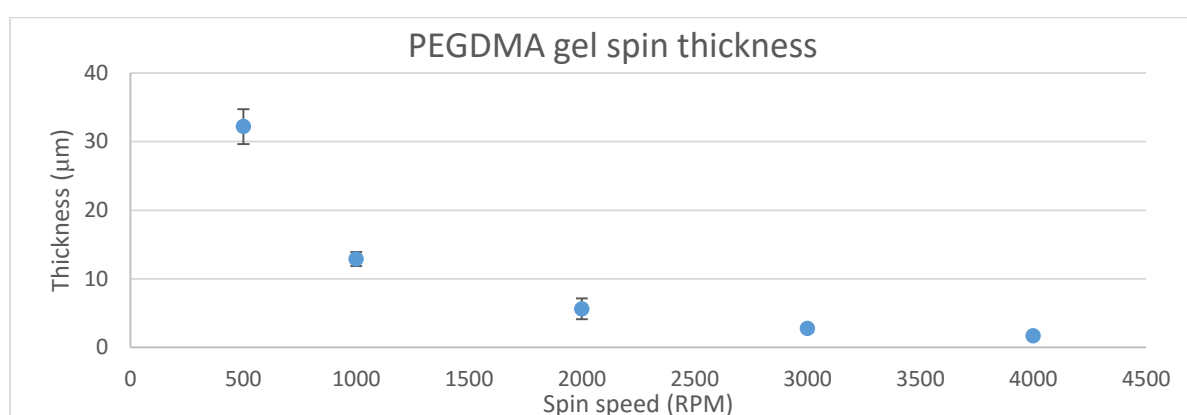


Figure 4-4 - PEGDMA plot of thickness against spin speed for 90 % PEGDMA in EtOH resist. Spin durations: 10s. Layers were exposed in proximity mode with 25 µm Teflon spacer between mask and gel surface. Thickness measured by profilometry on developed gels after development in IPA, while the gels were still adhered to the glass surface. Error bars: 1SD from 3 measurements.

The resulting thickness has an effect on hinge actuation, complying with the assumptions of Timoshenko equation, as the thickness reduces the bilayer proportion of active and passive layer thickness reaches closer to the key folding at thickness ratios at approximately 0.5, as the diffusive layer of PAA is very low, and thinning of the overall PEGDMA film increases its overall proportion in the bilayer film. Thickness was measured by profilometry of the developed gels prior to lift-off, with the resulting curl radius for a given layer thickness shown in Figure 4-5.

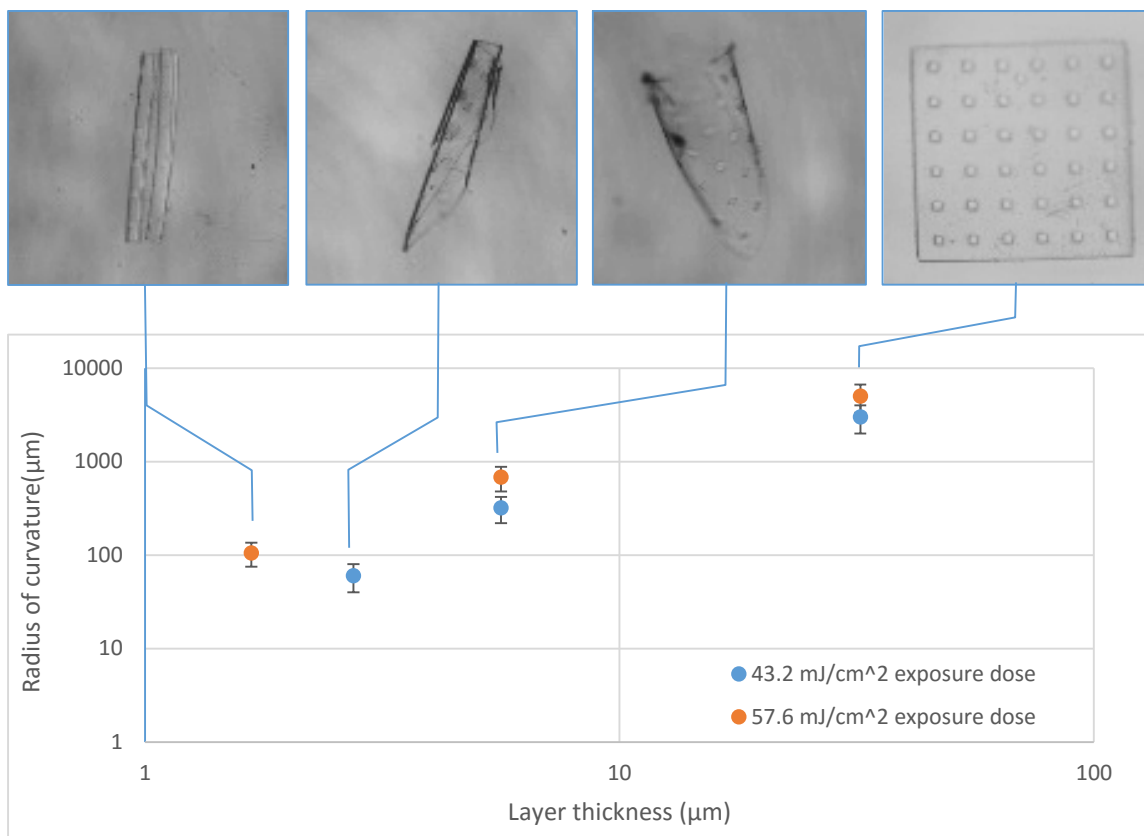


Figure 4-5 - Gel thickness and radius of curvature for PEGDMA hydrogel films with grafted PAA from the lift off layer. Thickness was measured by profilometry immediately after development of hydrogel squares. Radius of curvature was measured from minimum cross-sectional diameter in optical microscopy images. Two exposure doses of 8s and 6s at 7.2mW/cm². Gel thickness modified by spin speed. Error bars: 1SD from 3 measurements of each representative sample.

Breaking apart an idealised arc created by each hydrogel roll to suggests that the diameter of the polyhedral was well within reach for gels under 10 μm in thickness, at which point it was predicted that the roll curvature radius will exceed the 1 mm threshold for micro container diameter set at the beginning of the project to allow them to be transported through a syringe needle. This was produced mainly in the 6-8 second exposure time (43.2-57.6 mJ/cm²), above this little actuation was visible. The first stage in implementing a design which would work was finding a hinge size which provides sufficient curvature to mate adjoining faces on the polyhedral containers. Geometric constraints for various polyhedrons dictate the hinge dimensions, as the inter-face angle varies between geometries.

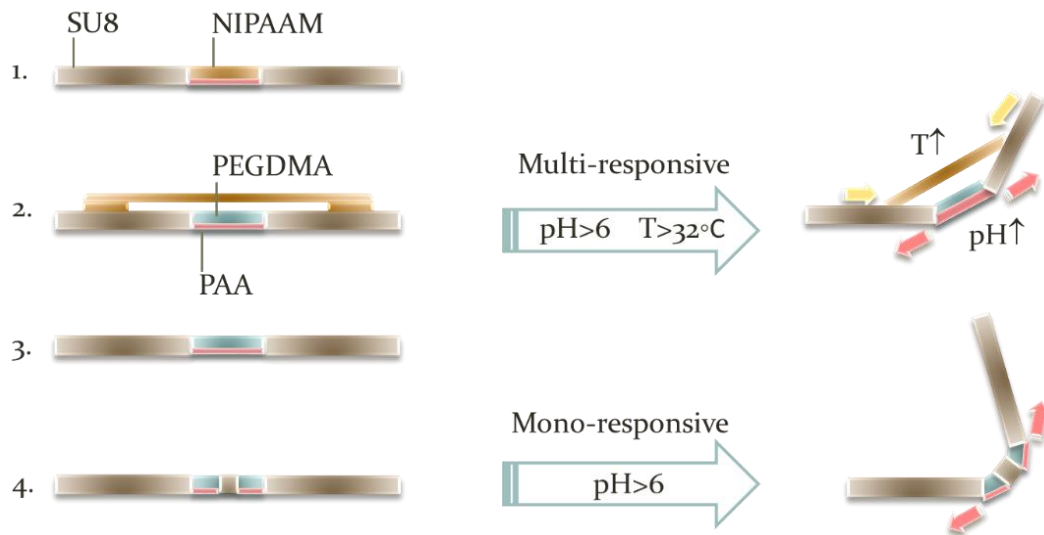


Figure 4-6- Possible uses of hydrogels as hinges in folding solid structure. Solid material is indicated in this case as the photo-crosslinkable epoxy SU8. Version 1) a thermally constricting gel based on PEGDMA-Co-PNIPAAm with a PAA activated base. 2) A similar design but with elongated thermal 'pulling' actuator to give it more actuating leverage. 3) PEGDMA hinge with PAA activated base, and 4) Double hinge design where two layers of gel are separated by a rigid block.

4.3.2 Box design

The various 3D devices and manufacturing methods in this work can be broken down into several subsets, depending on their level of manufacturing complexity, robustness and characteristics which can be incorporated within them. The use of hybrid construction where the function of each component is modular, i.e. hydrogel hinges for folding and solid elements for patterning and cell interaction, offer an advantage because each aspect can be changed without necessarily impacting the quality of the others. The use of more complex structures also offers a larger toolset for possible material and pattern selection. During the course of this work the apparent advantages and disadvantages of each method of construction, application and versatility of the various devices will be outlined. The breakdown of design criteria is shown in Figure 4-7.

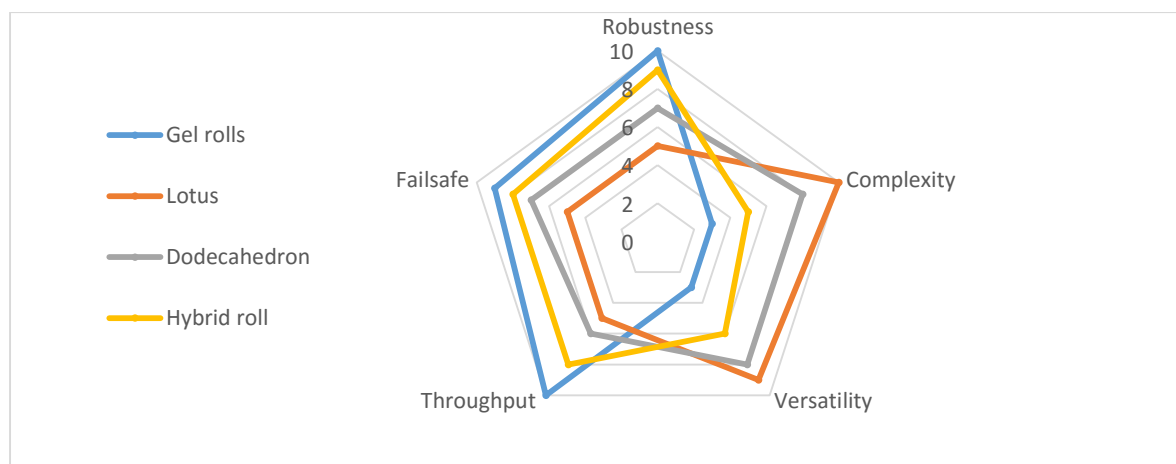


Figure 4-7 - Radial plot of various container designs, shows the effect of falling versatility and complexity with rising robustness, or the susceptibility of a structure to fail when in use.

The various container designs are shown in Figure 4-8 moving from most to least ‘complex’ in terms of the relative ease with which they can be manufactured. The hinge sizes were estimated from the roll curvature for hydrogel rolls made in the previous chapter. A hinge width for the desired radius of curvature is shown in Section 4.3.2.1 along with the angle of actuation. Those highlighted in red show hinge sizes which qualify for the desired geometry. The Idea was to separate them into two beneficial streams, the dodecahedral boxes utilized a smaller radius of curvature to achieve the desired angle of bend between adjacent faces. The radius of curvature required from the dodecahedron gel hinges was significantly lower than would be the case for simpler geometries such as triangular tetrahedrons, which would have wasted internal area on hinge and adhesive overlap space. In terms of robustness the tetrahedrons were ideal because they contained only 3 moving hinges making alignment potentially easier with less components to fail.

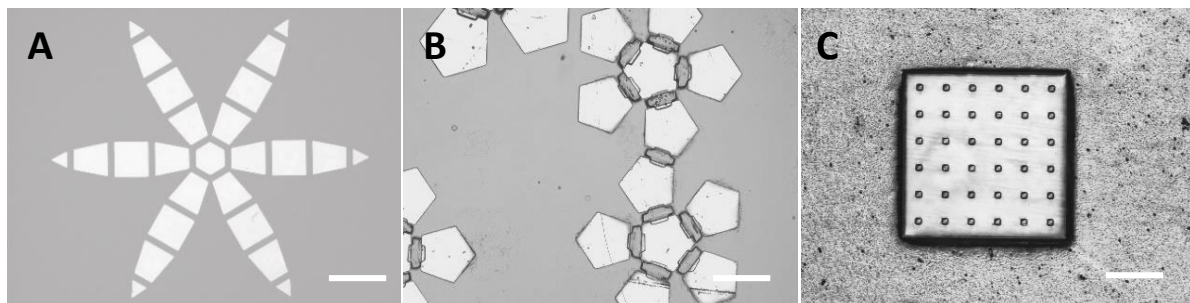


Figure 4-8 - Various container designs, left to right: 'Lotus' multi-symmetry containers, 'Dodecahedron' type containers and finally hydrogel rolls, showing square windows for cell movement and oxygen permeability. Scale bars: 500 μ m.

A lotus multi petal design was finally implemented allowing control over the number of faces, the folding angle and more importantly symmetry which was lacking in the dodecahedrons, while retaining the low curling angle required for closure by having many dissections through the shape of an ideal sphere.

4.3.2.1 Shape and hinge optimization

The required hinge curvature that would work for given polyhedron shapes was found analytically from roll curvatures in the previous chapter (Figure 3-39), the swollen radius was later confirmed with optically measured actuated rolls. The triangular, square and pentagonal polyhedral conditions are shown in this subsection with the optimum condition outlined for each. An arc angle of 360° indicates a full roll, with arc angles greater than this indicating a rolling up or coiling of the hinge. Coiling is however not necessary and it is the more minute actuation arc angles that are of interest.

4.3.2.1.1 Triangular Polyhedron required angle between faces = 120°

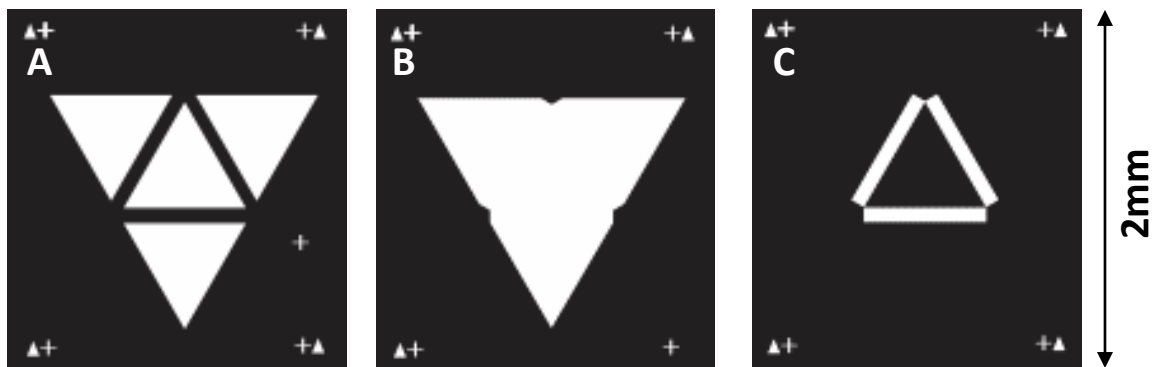


Figure 4-9 - Triangular polyhedron mask design stack. (A) The SU8 solid elements comprising the faces of the finished structure, which are non-flexible. (B) A potential all over coating with hydrogel for improved SU8/ hydrogel interface and bonding strength. (C) The lighter hydrogel hinge alternative.

The optimum hinge dimensions for the triangular polyhedron are shown in Table 4-2, with the dimensions of the hinge affecting triangle spacing in Layer 1 and the hinge thickness in layer 2b. In the case of the overlapping hydrogel layer, this would be adjusted for an increased triangle spacing.

Table 4-2- . Ideal hinge dimensions for triangular polyhedron, red indicates the ideal hinge angles, with yellow being acceptable in the case of some extra adhesive force before closing the faces.

Hinge Length (μm)	Hinge radius of curvature (μm)				
	30	45	70	150	360
50	95.49	63.66	40.93	19.10	7.96
60	114.59	76.39	49.11	22.92	9.55
70	133.69	89.13	57.30	26.74	11.14
80	152.79	101.86	65.48	30.56	12.73
90	171.89	114.59	73.67	34.38	14.32
100	190.99	127.32	81.85	38.20	15.92
110	210.08	140.06	90.04	42.02	17.51
120	229.18	152.79	98.22	45.84	19.10
130	248.28	165.52	106.41	49.66	20.69
140	267.38	178.25	114.59	53.48	22.28
150	286.48	190.99	122.78	57.30	23.87
160	305.58	203.72	130.96	61.12	25.46
170	324.68	216.45	139.15	64.94	27.06
180	343.77	229.18	147.33	68.75	28.65
190	362.87	241.92	155.52	72.57	30.24
200	381.97	254.65	163.70	76.39	31.83
210	401.07	267.38	171.89	80.21	33.42
220	420.17	280.11	180.07	84.03	35.01
230	439.27	292.85	188.26	87.85	36.61
240	458.37	305.58	196.44	91.67	38.20
250	477.46	318.31	204.63	95.49	39.79

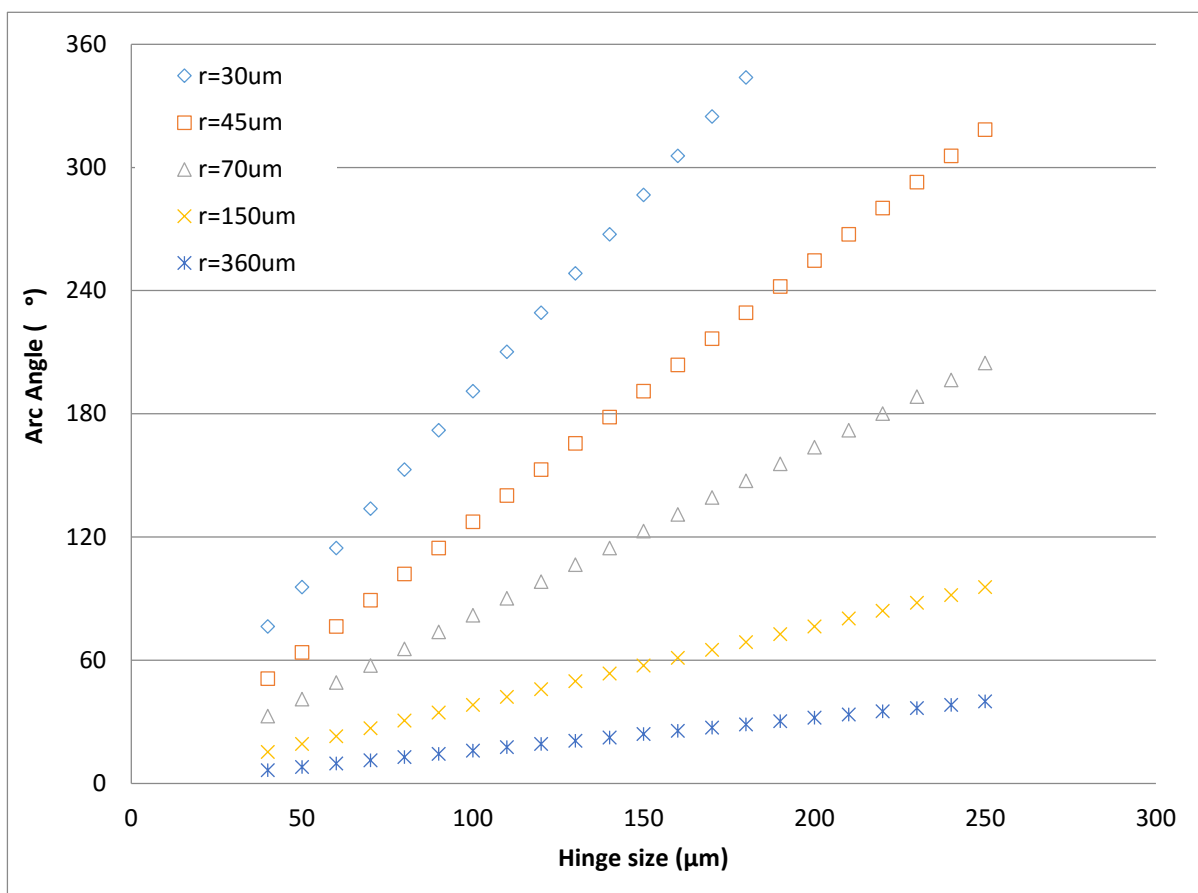


Figure 4-10 Hinge dimensions - triangular polyhedral container. Plots indicate the expected hinge angle of hydrogel hinges given a set hinge size and radius of curvature (Chapter 3). 360 degree arc angle indicates full rolling (tube).

As the closure of the container depends on the hinges displacing the solid faces through a sufficient fold angle, Figure 4-10 illustrates the ideal fold angle of curvature and possible hinge dimensions to achieve the necessary angle for a closed container configuration. 60 -90 μm were found to be the range of possible hinge size attainable with the current hinge material. Overexposure of the film and subsequently larger radii of curvature would mean a box that failed to close fully.

4.3.2.1.2 Square Polyhedron required angle between faces = 90°

The square container was thought to be structurally unstable due to the relatively large folding angles and parallel faces which would be easy to topple in shear. A mask for this box set was thus never attempted, but potential hinge designs were manufactured and are shown in and Figure 4-11. Plotting ideal hinge angle shows the possible choices, with 50 μm being the smallest possible size of hinge to attain a closed cube container.

Table 4-3 – Ideal hinge dimensions for box polyhedron. Red indicates the ideal hinge angle, with yellow being acceptable in the case of some extra adhesive force then closing the faces.

Hinge length (μm)	Hinge radius of curvature (μm)				
	R=30	45	70	150	360
50	95.49	63.66	40.93	19.10	7.96
60	114.59	76.39	49.11	22.92	9.55
70	133.69	89.13	57.30	26.74	11.14
80	152.79	101.86	65.48	30.56	12.73
90	171.89	114.59	73.67	34.38	14.32
100	190.99	127.32	81.85	38.20	15.92
110	210.08	140.06	90.04	42.02	17.51
120	229.18	152.79	98.22	45.84	19.10
130	248.28	165.52	106.41	49.66	20.69
140	267.38	178.25	114.59	53.48	22.28
150	286.48	190.99	122.78	57.30	23.87
160	305.58	203.72	130.96	61.12	25.46
170	324.68	216.45	139.15	64.94	27.06
180	343.77	229.18	147.33	68.75	28.65
190	362.87	241.92	155.52	72.57	30.24
200	381.97	254.65	163.70	76.39	31.83
210	401.07	267.38	171.89	80.21	33.42
220	420.17	280.11	180.07	84.03	35.01
230	439.27	292.85	188.26	87.85	36.61
240	458.37	305.58	196.44	91.67	38.20
250	477.46	318.31	204.63	95.49	39.79

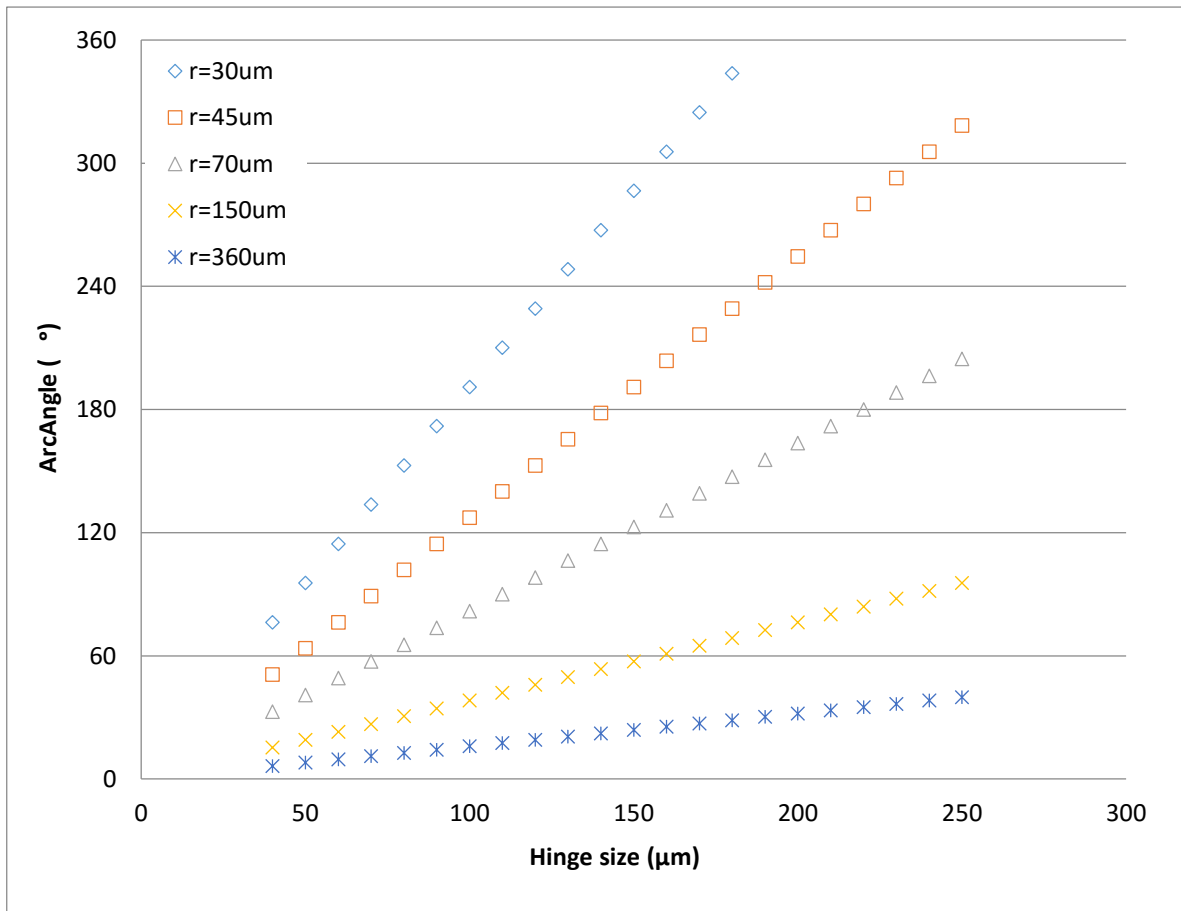


Figure 4-11 - Hinge dimensions - box polyhedral container. Plots indicate the expected hinge angle of hydrogel hinges given a set hinge size and radius of curvature (Chapter 3). 360 degree arc angle indicates full rolling (tube).

While the square polyhedron lies between the triangular polyhedron and the dodecahedron in terms of complexity, it has an asymmetric folding profile, having 6 sides, the sixth is always affixed to one of the other faces, which says that if each hinge has the same folding potential, one of the four walls will have a 100 % increase in surface area, this imbalance suggests a potential cause for error. The triangular polyhedron pyramid meanwhile has three symmetric faces which move from the base, however the angle of curvature required by the triangular polyhedron is significantly higher and would mean it has to have a longer hinge length, wasting cell adhesive space. The optimum hinge dimensions for these pentagonal polyhedrons are shown in Table 4-4.

4.3.2.1.3 Pentagonal Polyhedron required angle between faces = 72°

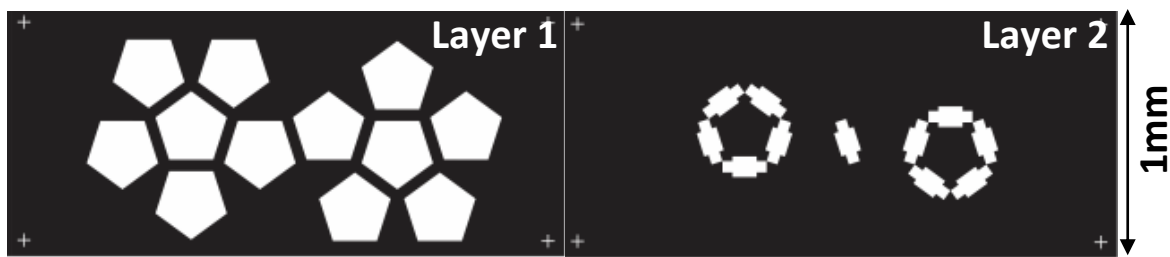


Figure 4-12 - Mask design of a single pentagonal polyhedron container. The container involves two stages, the creation of rigid elements with the first mask (left) and the addition of slightly overlapping hinges (right) for better adhesion. This is fabricated on a sacrificial PAA film for lift-off.

Table 4-4 – Ideal dimensions for pentagonal polyhedron Red indicates the ideal hinge angle, with yellow being acceptable in the case of some extra adhesive force then closing the faces

Hinge length (μm)	Hinge radius of curvature (μm)				
	R= 30	45	70	150	360
50	95.49	63.66	40.93	19.10	7.96
60	114.59	76.39	49.11	22.92	9.55
70	133.69	89.13	57.30	26.74	11.14
80	152.79	101.86	65.48	30.56	12.73
90	171.89	114.59	73.67	34.38	14.32
100	190.99	127.32	81.85	38.20	15.92
110	210.08	140.06	90.04	42.02	17.51
120	229.18	152.79	98.22	45.84	19.10
130	248.28	165.52	106.41	49.66	20.69
140	267.38	178.25	114.59	53.48	22.28
150	286.48	190.99	122.78	57.30	23.87
160	305.58	203.72	130.96	61.12	25.46
170	324.68	216.45	139.15	64.94	27.06
180	343.77	229.18	147.33	68.75	28.65
190	362.87	241.92	155.52	72.57	30.24
200	381.97	254.65	163.70	76.39	31.83
210	401.07	267.38	171.89	80.21	33.42
220	420.17	280.11	180.07	84.03	35.01
230	439.27	292.85	188.26	87.85	36.61
240	458.37	305.58	196.44	91.67	38.20
250	477.46	318.31	204.63	95.49	39.79

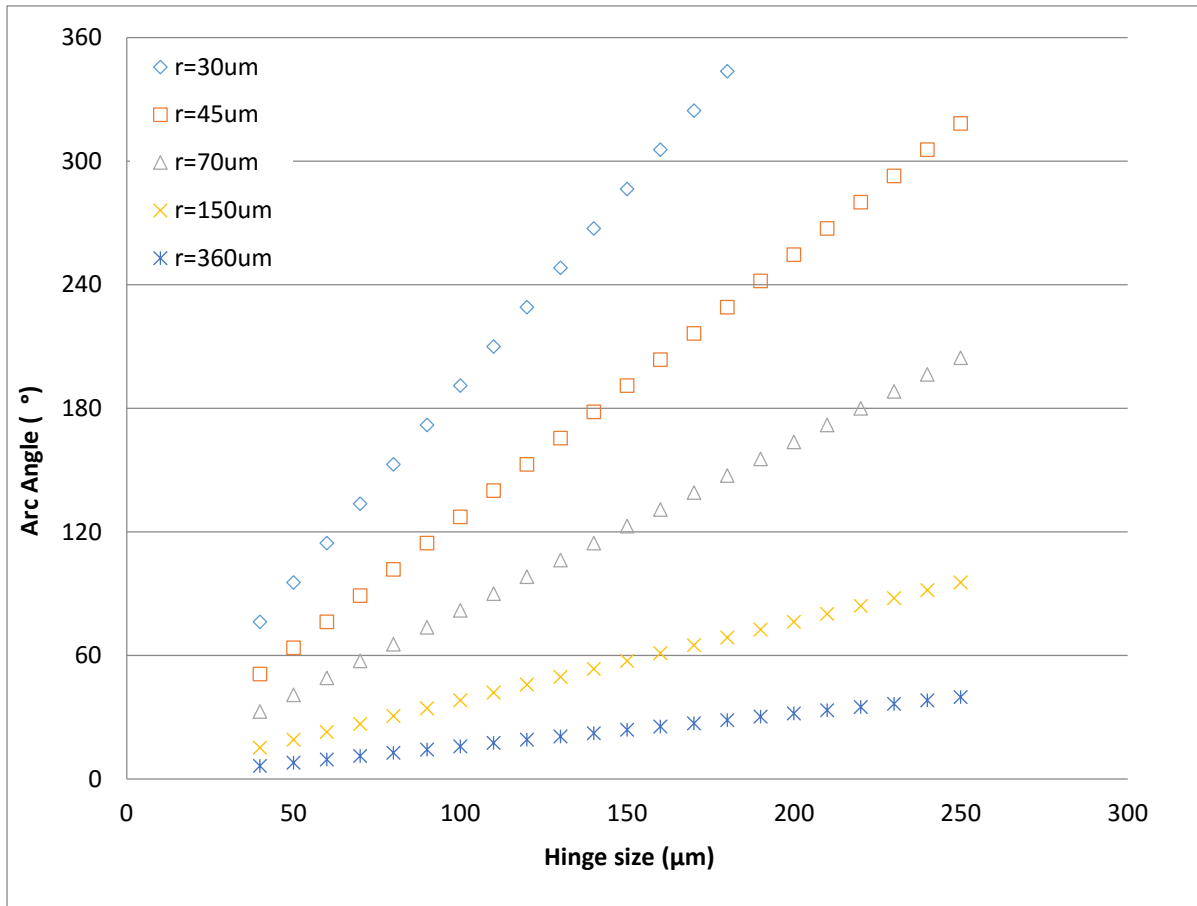


Figure 4-13 - Ideal hinge dimensions for pentagonal polyhedron. Plots indicate the expected hinge angle of hydrogel hinges given a set hinge size and radius of curvature (Chapter 3). 360 degree arc angle indicates full rolling (tube).

In this extrapolation of useful area and low angle of folding necessary to attain a fully closed container: the dodecahedron requires the least actuating hinge curvature to fold and has two symmetric hemispheres which then rely on a single hinge as a source of symmetry, while also prone to failure due to an imbalance of loads, it is thought that this could be designed around by placing a longer and stronger hinge between the two domes if it were an issue. Plotting the hinge angles shows a hinge size of 40 μm can be used. A range of hinge sizes were created on one mask to investigate the optimum hinge dimensions for device closure.

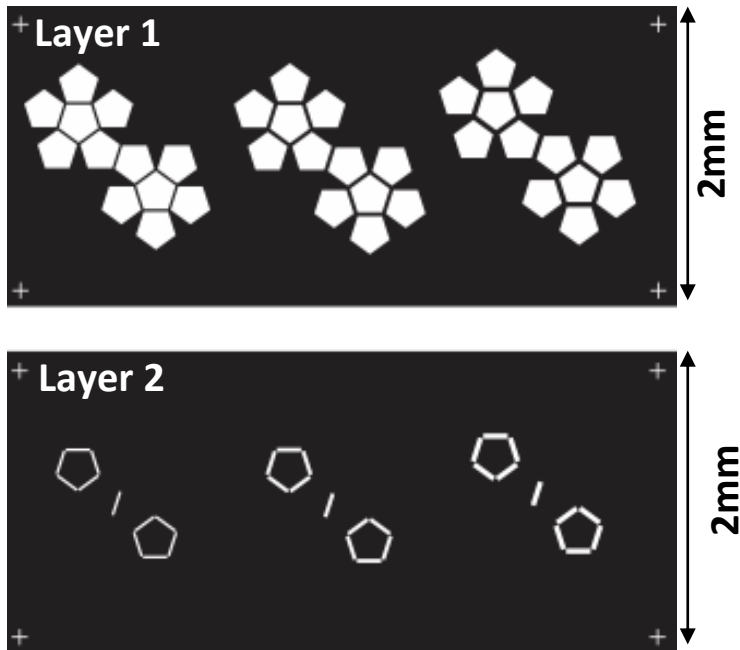


Figure 4-14 - Pentagonal polyhedrons in their two stages with the design incorporating three hinge thicknesses of (left to right) $20\ \mu\text{m}$, $40\ \mu\text{m}$ and $60\ \mu\text{m}$ respectively. Several box dimensions were also designed, ranging from $200\ \mu\text{m}$ faces up to $600\ \mu\text{m}$ to cover possible future applications.

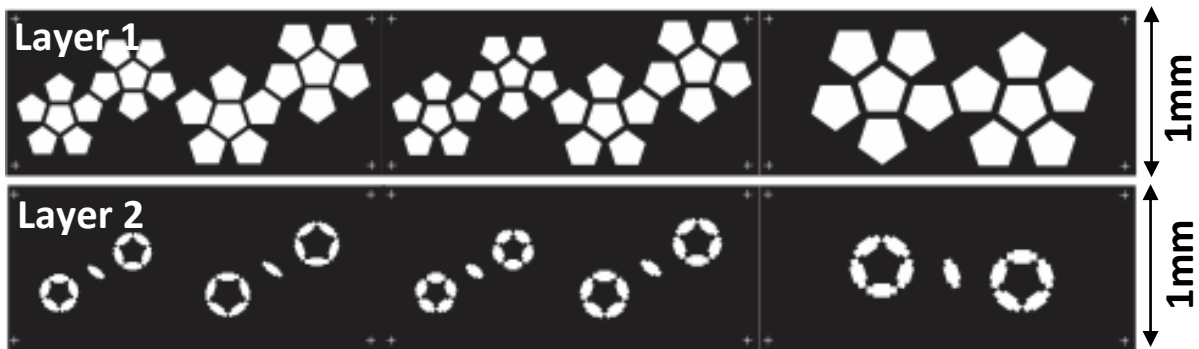


Figure 4-15 - Left to right: two smaller container sizes with two hinge widths of 20 and $40\ \mu\text{m}$. Far right: largest container with hinge dimension of $80\ \mu\text{m}$.

In addition to the classic polyhedral shapes a more symmetric flower or ‘lotus’ design was made, where the design is symmetric around one central point, and the subsequent faces are arranged in a flower like arrangement, curling up toward the central axis. The idea was to maximize symmetry to produce evenly distributed loads between adjacent faces. These loads limit over closure, where one face is obstructing the others from closing, and in these symmetric system faces limit their neighbours.

4.3.2.2 Lotus polyhedral containers

To combine the benefits of the dodecahedron, and the triangular prism, a 'lotus' shaped container design was made (Figure 4-16), which uses the symmetry of the triangular prism, but also the increased number of facets of the dodecahedron to reduce the required angle of curvature at each hinge. These 'lotus' style boxes have equidistant hinges and less critical dependents for each hinge, so the box can come together as planned even if one branch folds before the others.

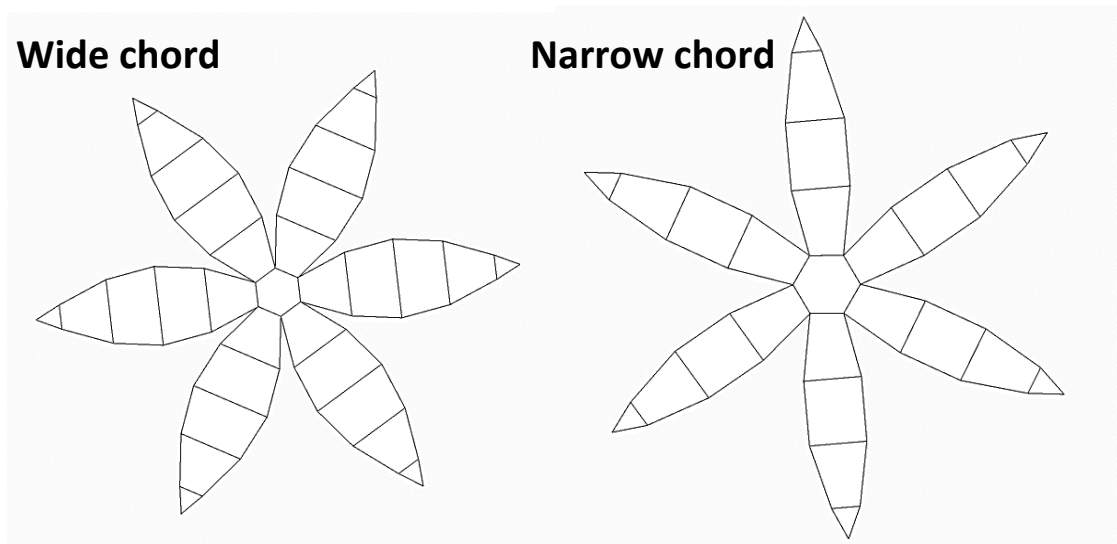


Figure 4-16 - New 'lotus' containers with varying hinge numbers, both have six folding surfaces but one consists of the decagonal arrangement with 5 hinges per extremity while on the right is an octagonal arrangement with four hinges per extremity. The decagonal arrangement benefits from lower required hinge angles, while the octagonal structure benefits from fewer hinges and thus fewer things to fail should an alignment or exposure deviate from that required.

The design of these containers was based on selection of the number of petals to dissect a sphere with, and also to choose the correct number of hinges to produce the curvature of each petal. In the end the minimal arrangement of 6 petals and 4 hinges was chosen to increase the overall surface area of the box, improve circularity and limit the number of hinges which potentially could go wrong compared to the 8 petal, 5 hinge designs (Table 4-5).

Table 4-5 - Petal chord widths for a 1mm diameter “lotus” container, allowing the selection of the number and arrangement of petals to optimize the folding of these containers into a sphere of relevant size.

Petals number:	5	6	8
Hinge lengths in Hexagonal cross-section (numbered from center)			
Hinge 1 length (μm):	293.89	250	191.34
Hinge 2 length (μm):	587.78	500	382.68
Hinge 3 length (μm):	293.89	250	191.34
Hinge lengths in Octagonal cross-section (numbered from center)			
Hinge 1 length (μm):	224.94	191.34	146.45
Hinge 2 length (μm):	363.95	331.41	270.60
Hinge 3 length (μm):	363.95	331.41	270.60
Hinge 4 length (μm):	224.94	191.34	146.45
Hinge lengths in Decagonal cross-section (numbered from center)			
Hinge 1 length (μm):	181.64	154.51	118.26
Hinge 2 length (μm):	475.53	404.51	309.60
Hinge 3 length (μm):	587.79	500	382.68
Hinge 4 length (μm):	475.53	404.51	309.60
Hinge 5 length (μm):	181.64	154.51	118.26

Calculation of the petal sizes was done using Excel, and the required face widths and heights for boxes of 1 mm, 500 μm and 300 μm are shown in Figure 4-17 and Figure 4-18 respectively. The shape refers to the number of hinges present in one curvature. Whether a sphere is cut as a hexagon, octagon or decagon will dictate the number of hinges, being 6, 8 and 10 respectively. While having the minimum moving hinges reduces the risk of the box not closing correctly, having more requires a smaller angle of curl, and makes the box less sensitive to hinge exposure dose and variations in thickness. A 1 mm diameter box was chosen in this table as this is the maximum size of box to fit into a large diameter syringe needle (under Gauge 17).

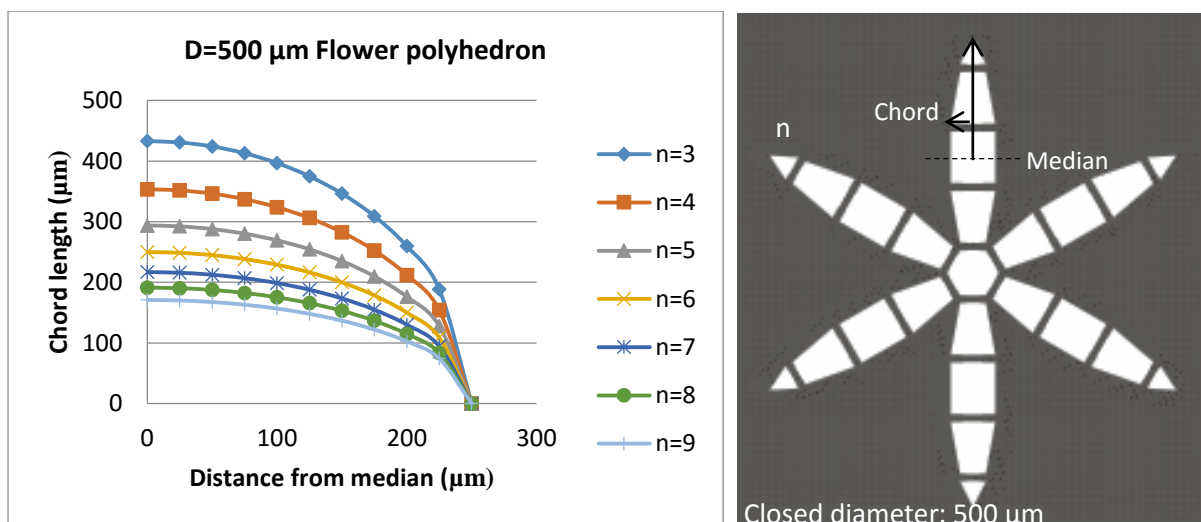


Figure 4-17 - Comparing leaf dimensions over length from tip to median for different numbers of petals on 'lotus' form.

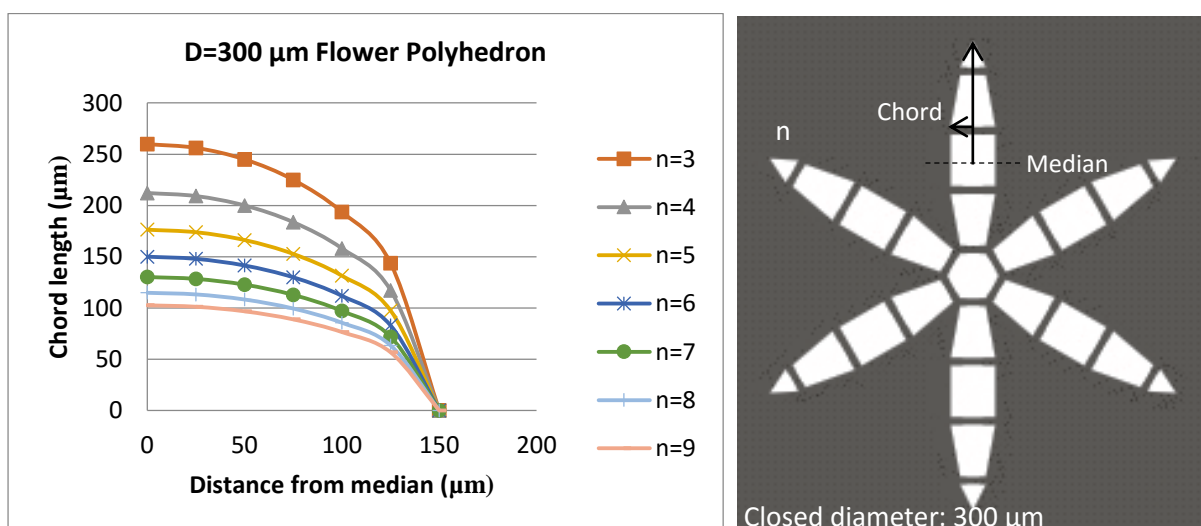


Figure 4-18 - Comparing leaf dimensions over length from tip to median for different numbers of petals on 'lotus' form.

4.3.2.3 Locking mechanisms

It was found through trials, that the main issue with folding a container in aqueous media is the density and shear forces of the fluid greatly overpower the weak swelling forces and low modulus of the hydrogel hinges. Similar to an anemone or seaweed at the bottom of the ocean, these structures will roll, and flex if any fluid turbulence is present. A locking mechanism is therefore required to lock up the box and allow it to sustain these forces as a 3D structure, where faces provide support to one another and stabilise the structure. One attempted locking mechanism was the addition of positive (+ve) and negative (-ve) polarity gel elements to the inner faces of the box. These elements or 'dots' were composed of anionic or cationic gel using AA and DEAEMA gels respectively. To achieve this a sub mask was needed to pattern the locking features after the main box features had been defined

(Figure 4-19). The resulting mask designs for the locking elements or ionic ‘dots’ are shown below, with the pictures in order showing faces, hinges and locking supports added respectively.

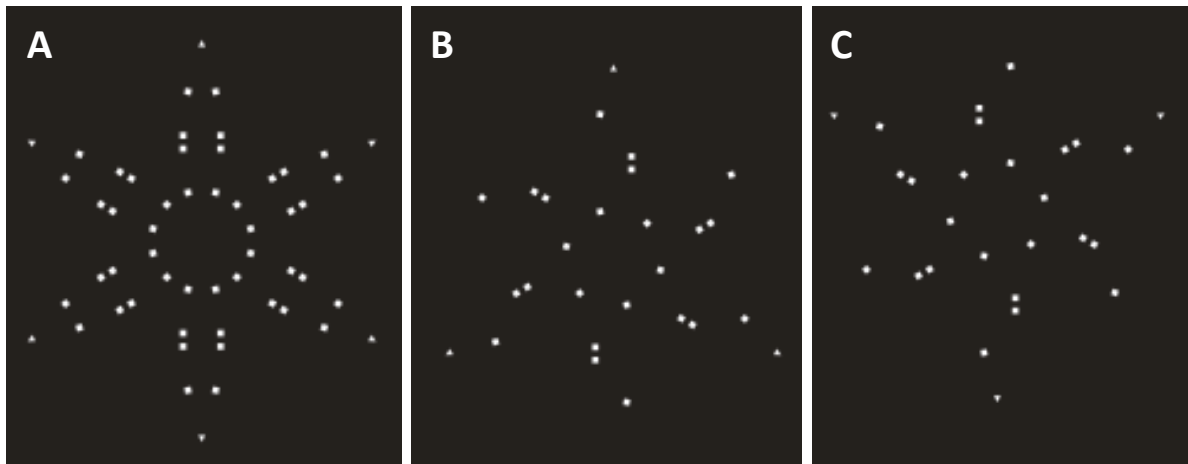


Figure 4-19 Mask split to create negative and positive polarity hydrogel elements. (A) The full array of locking points to be patterned in magnetic resist or self-adhesive hydrogel. (B) Half of an negative to positive locking mechanism, with half the array to be made of an ionic hydrogel and the other half of a cationic one respectively.

In the case of locks which lack sufficient force to connect based on ionic charge alone, overlapping locks were also designed as illustrated in Figure 4-20c. These would jam adjoining faces together, to transfer loads between the various faces and prohibit individual relative motions, in what is believed by the author to make the structure stronger.

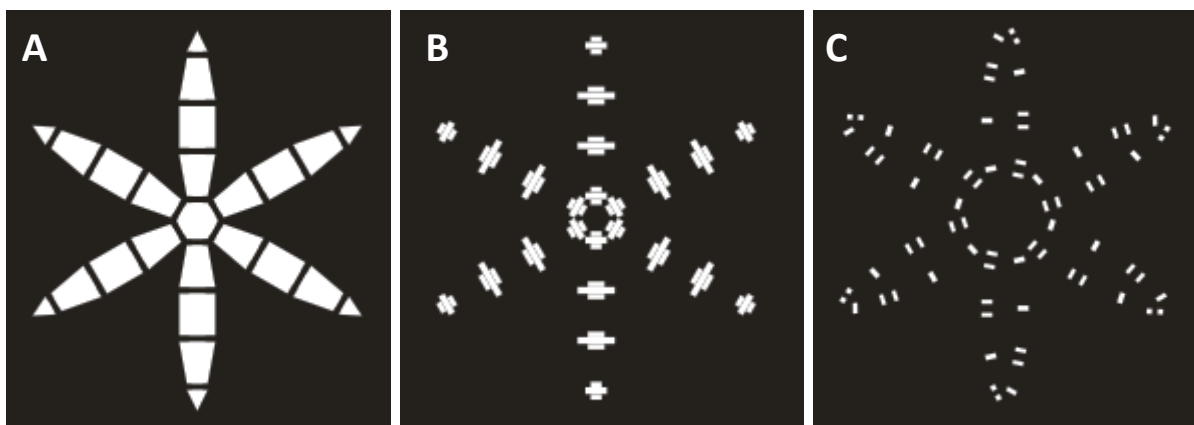


Figure 4-20 - Photomask design for new ‘lotus’ containers. (A) faces of container to be patterned in SU8 or other ‘structural’ material. (B) Hydrogel hinges to be patterned during a second stage of photolithography. (C) The locking mechanism to be patterned out of another layer of structural material, or a self-adhesive hydrogel.

4.4 RESULTS

4.4.1 Roughness of PAA

To achieve good patterning of the sacrificial film, film uniformity is crucial, although rougher surfaces adhere subsequent layers better, a uniform film makes more uniform contact with an imprinting stamp, and reduces contact stress concentrations. PAA becomes rougher with O₂ plasma ashing (Figure 4-21), this roughness which is also independent of spin speed (Figure 4-22) is not ideal for patterned surfaces, it does however, increase surface area of the sacrificial layer. Larger surface area improves adhesion in subsequent layers minimizing feature detachment. An increased surface roughness also means a larger area of functionalised PAA is available for gel interaction.

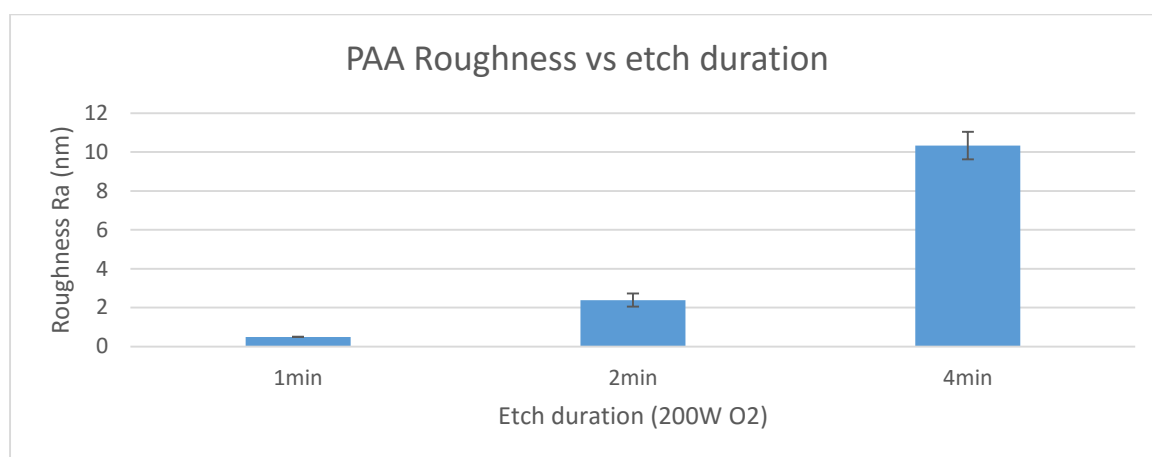


Figure 4-21 – Surface roughness plotted for increasing doses of oxygen plasma ashing of the PAA sacrificial films. It can be seen that the surface roughness increases at a non-linear rate with increasing exposure to O₂ plasma. AFM profilometry performed on three random locations on ashed samples. PAA Mw 1800 spun at 4000 rpm. Error bars: 1SD from n=5 AFM measurements of n=5 separate 20 x 20 μm square areas.

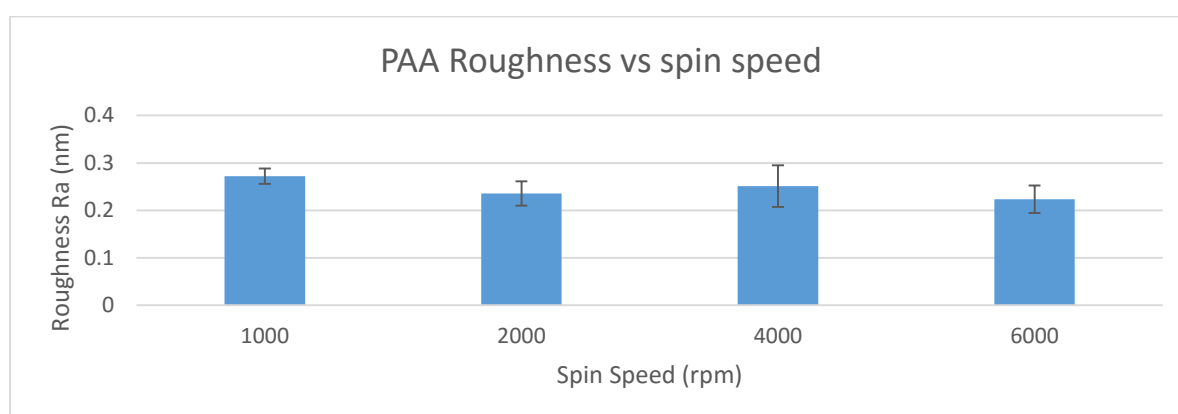


Figure 4-22 - Surface roughness Ra plotted against spin speed for PAA Mw 1800 spun at increasing RPM. It can be seen that the roughness of the surface does not vary greatly with increasing spin speed. Error bars: 1SD from n=5 measurements of 20 x 20 μm AFM scans.

The measured surface roughness of PAA was found to be in line with data from the Whitesides group covering the water soluble sacrificial layer process [190].

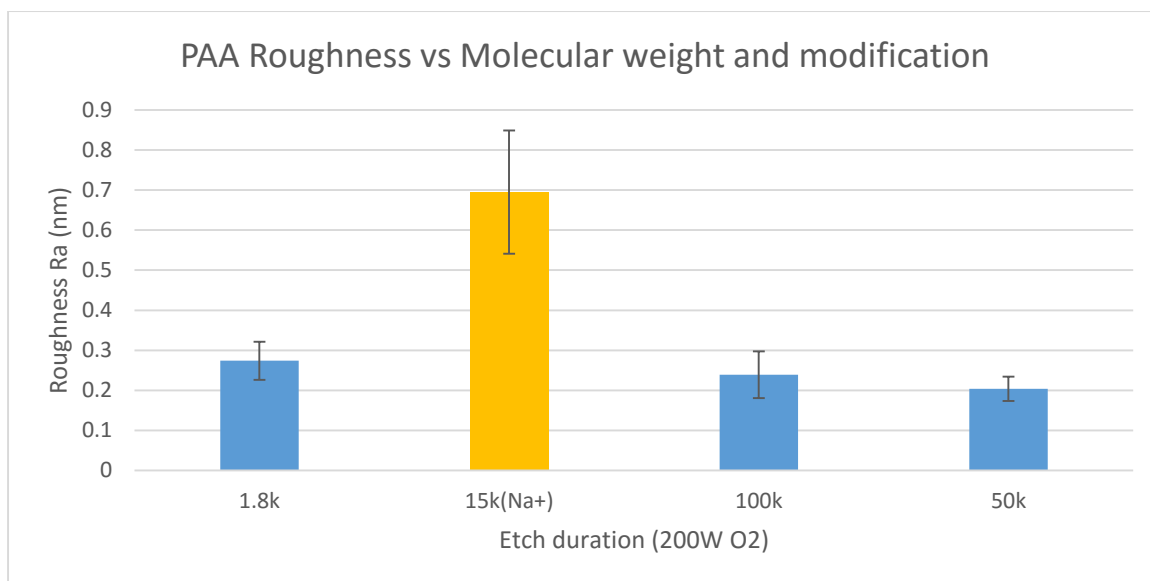


Figure 4-23 - Surface roughness of four different molecular weights of PAA. All surfaces dried on a hotplate at 90 °C for 5 minutes prior to measurement by AFM. It can be seen that while the roughness is fairly consistent between different molecular weights, it does increase dramatically when the PAA is in its neutralised state (buffered with NaOH). Error bars: 1SD of n=5 measurements of 20 x 20 μm square AFM scan.

To see the effect of neutralization on the PAA and if this procedure affected its characteristics for nanopatterning; PAA of Mw 15,000 which had been neutralized to pH 7 by the addition of NaOH (as obtained from Sigma-Aldrich) was spun onto a clean silicon surface as stated in the previously outlined processes (section 4.2.3.6). The roughness was found to be considerably higher than that of normal non-neutralized PAA (Figure 4-23). This PAA additionally exhibited lower wetting of the Si substrate causing ruptured and beading, oxygen plasma ashing of the silicon wafer prior to application the deprotonated PAA resolved this issue, but poor adhesion to the substrate and no visible actuation in gels lifted off from this surface deemed it incompatible with the desired stream of processing.

4.4.1.1 Material Application

Several structural materials were tested in the construction of the patternable solid facets and act as the solid reinforcing structure in the self-folding devices. The first was SU8 the commercial epoxy based negative photo resist. The spinability and patternability of two biocompatible materials was also tested: Poly-L-lactide (PLLA) and polycaprolactone (PCL). While both polymers spun had similar thicknesses to SU8 3005 (Figure 4-24) the uniformity was a key factor in patterning requirements, PCL in this case showed a film uniformity an order of magnitude lower than PLLA and SU8 (Figure 4-25), this was confirmed in literature for other diluting solvents [207].

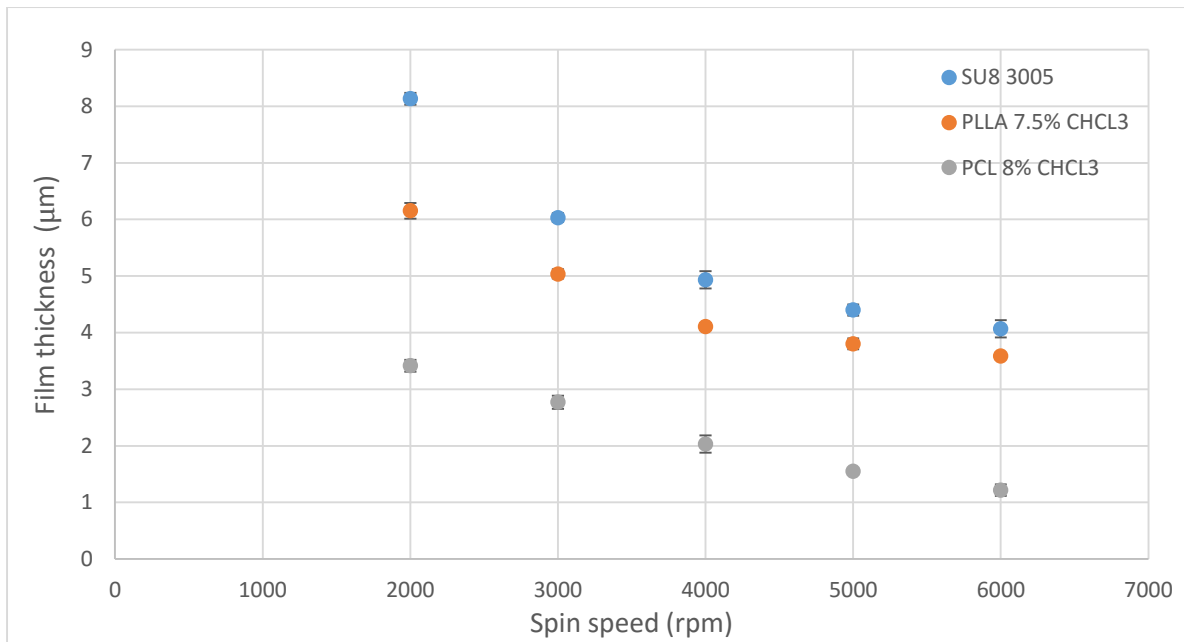


Figure 4-24 - Spin curves for SU8, PLLA 7% w/v in CHCL₃ and PCL 8% w/v in CHCL₃ films measured by profilometry. Error bars 1SD from 5 measurements.

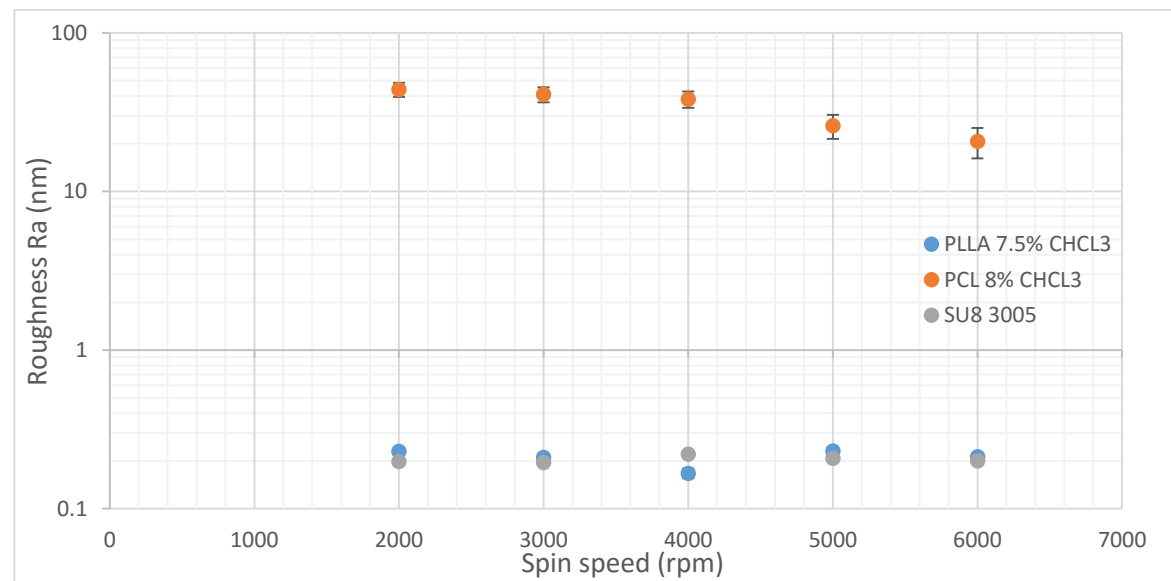


Figure 4-25 – Mean values for film uniformity in spun polymer films, Roughness Ra value collected from 20 x 20 µm AFM surface topography scans. Error bars: 1SD from n=5 measurements.

PCL was ruled out due to film non-uniformity (3 orders of magnitude higher Ra, PCL: 34nm, PLLA: 0.21 and SU: 8: 0.204) for further patterning (Figure 4-25), PCL also exhibited peeling from PAA films, making it unfavourable for layered fabrication. Surface AFM scans of PLLA and PCL in chloroform spun at 4000 rpm and 6000 rpm are shown in Figure 4-26.

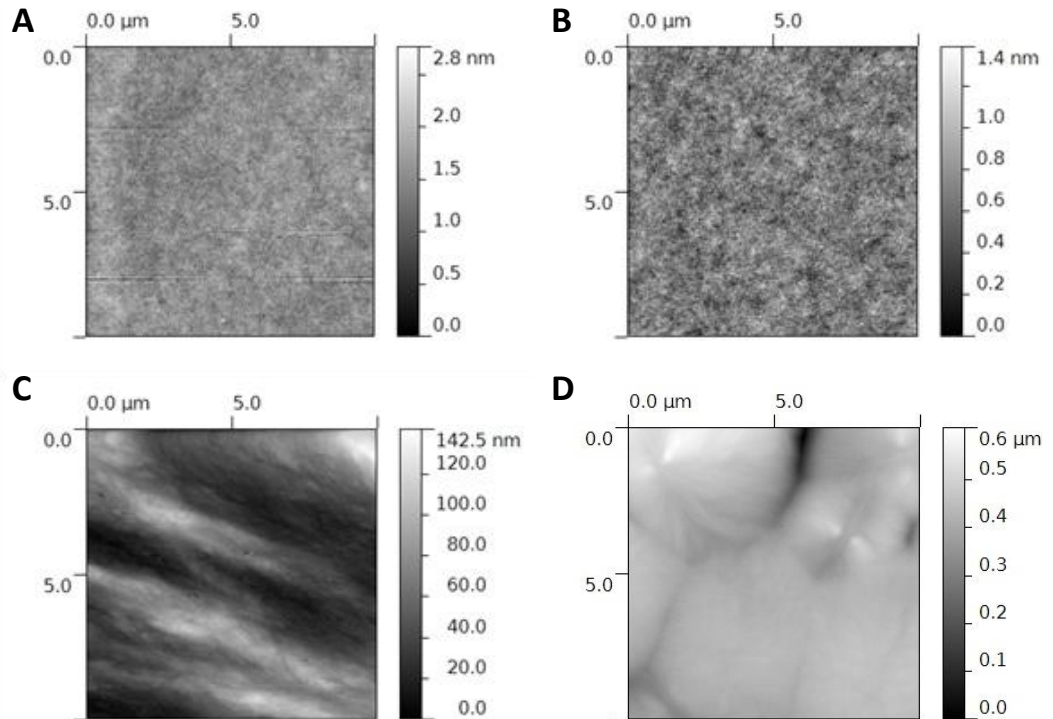


Figure 4-26 - Spun polymer films considered as an alternative to traditional SU8 photoresist. A: PLLA spun at 6000 rpm, B: PLLA spun at 2000 rpm (both solutions 8 w/v % solution in chloroform). C: PCL spun at 4000 rpm D: PCL spun at 2000 rpm (both solutions 6 w/v % in chloroform)

4.4.2 Patterning of SU8 surfaces

SU8 is an epoxy resin which returns to a flowing state upon heating (only prior to crosslinking), it is during this phase of heating that the photo acid crosslinking groups generated during exposure can migrate and crosslink the resin into a solid. Double sided nanopatterning of SU8 was achieved by hot embossing of PAA sacrificial layers at 15 bar and 110 °C and subsequent hot post exposure hot embossing of the SU8, by a novel method. A variety of stamps ranging from PDMS to quartz and silicon have been used with varying degrees of success. The images below show a hexagonal honeycomb structure reproduced with a PDMS stamp onto the top surface of a dodecahedral container patterned out of SU8 (Section 4.4.2). Post exposure bake-embossing (PEBE) is to the author's knowledge a novel way of introducing nano- and micropatterns into SU8 without the need for complicated UV-Nil setups. If a stamp is introduced to a pre exposed layer of SU8 during post baking the SU8 will flow into the stamp features and solidify within those constraints, reproducing the pattern. The unexposed areas can be washed away after development to create micro patterned features on nanopatterned surfaces. A hierarchical pattern can also be introduced by the method outlined in Chapter 3.

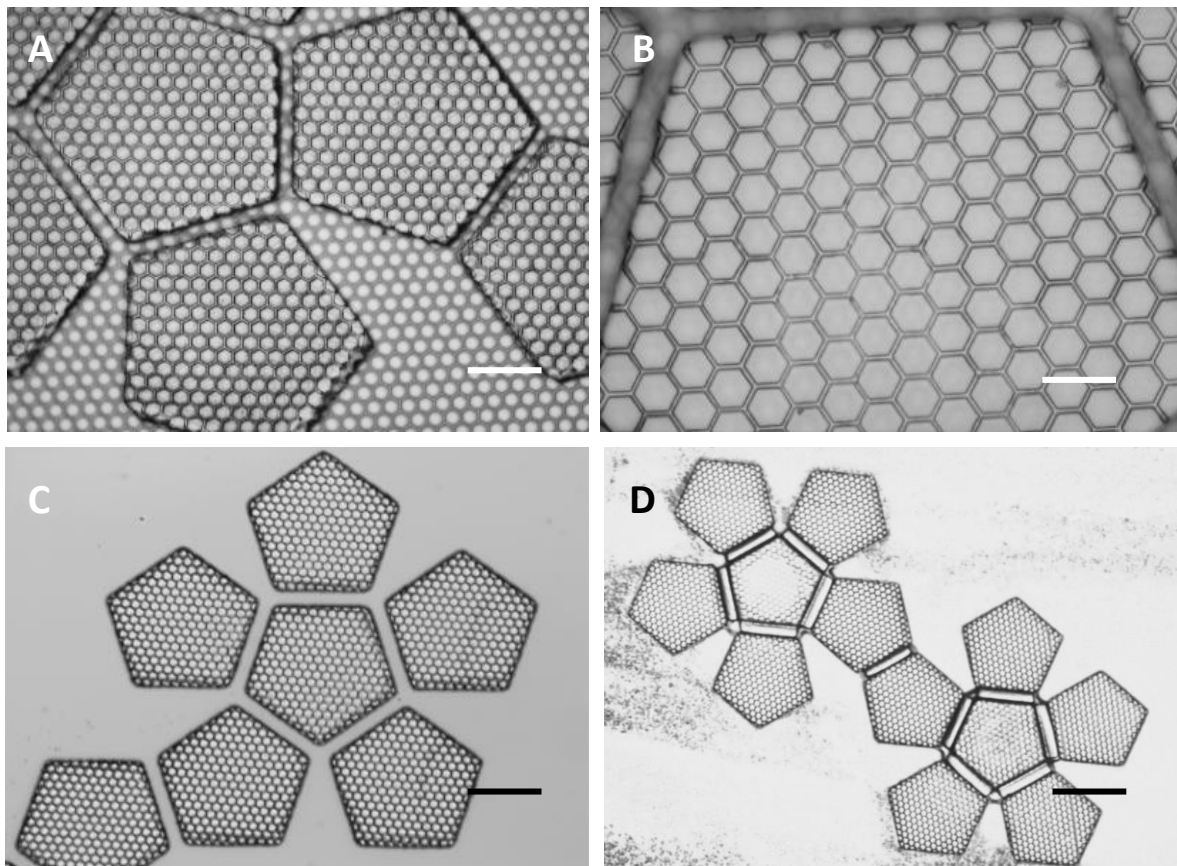


Figure 4-27 – Top left to right: 24 μm hexagonal pattern embossed into SU8 Dodecahedral container surface with a pre-embossed PAA layer creating double sided patterning. Bottom left to right: Devices with and without hinges after PAA dissolution. Scale bars: 100 μm , 50 μm , 200 μm and 300 μm respectively.

4.4.3 Patterning of PLLA surfaces

One alternative to using SU8 which shows promise as a biodegradable alternative is PLLA (Poly-L-lactide). This natural polymer is degradable by hydrolysis with varying degrees depending on chain length and crosslinking groups. Work was carried out to investigate the ease of patterning the material, and the results were very promising (Figure 4-28). Above its T_g of 65 $^{\circ}\text{C}$ the polymer flows well and holds patterns well upon cooling. Fabrication is extremely compatible with PAA lift-off, the PLLA ligands dissolve in chloroform in which PAA is insoluble, and so any subsequent spinning steps will not affect a pre patterned PAA sacrificial layer. Additionally the temperature at which PLLA can be shaped and formed is far below that necessary to damage or crosslink the PAA underneath. The two chemicals are similar and no complexation should be seen as with SU8, so there is less risk of a boundary film forming and affecting the hinge closing dynamics. This method however requires shaping into container faces by dry etching rather than lithography alone.

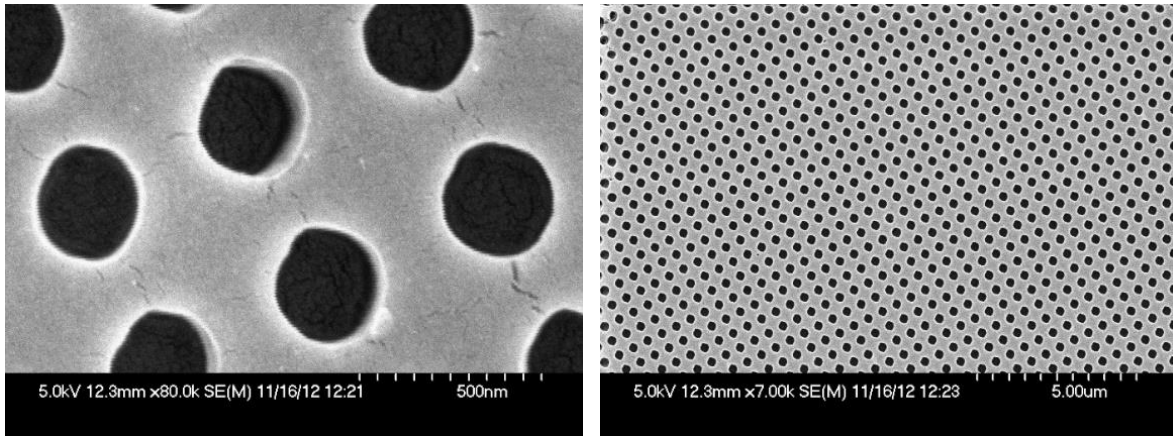


Figure 4-28 – SEM images of nanopatterned PLLA film with 2500nm diameter 1:1 aspect pits on 200 nm pitch. Left to right decreasing magnification. Scale bars 500 nm and 5 μm respectively.

To form the nanopatterned PLLA film into the individual faces of the microcontainers it has to be cut, as the film is a thermoplastic and not a cross linkable epoxy like SU8. Dry etching by oxygen plasma was tested on PAA and PLLA films spun on silicon substrates. The etch rates are outlined in Figure 4-29 the PLLA etches significantly faster, allowing for some selectivity in the process, so that damage to PAA features can be avoided.

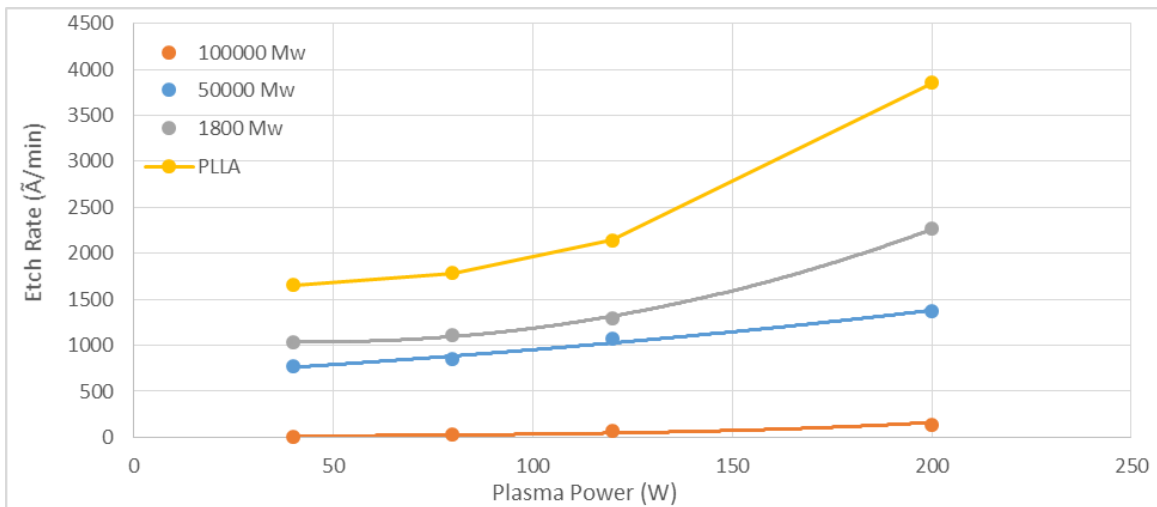


Figure 4-29 - Shown are the dry etch rates for PLLA and PAA thin films. The data shows a dry etching selectivity ratio in oxygen plasma of almost 2:1 between PLLA and PAA Mw 50,000. Point mean of n=3 profile scans.

A thin layer of S1818 is applied to the PLLA and can either be used as an etch-stop directly with a selectivity of roughly 2:1 [208] or by applying an Au mask over the S1818 and then removing it with MF-319, the Au can be used with the potassium iodide in IPA based etch which does not damage the underlying PAA sacrificial layer. The process is more time consuming compared to SU8, but as PLLA can be blended with PLGA to adjust dissolution rate [209] it is a useful component in a potential toolbox. When fabricated these PLLA boxes will degrade by hydrolysis in aqueous environment, allowing for safe disposal within the body and no need for manual scaffold removal or monitoring.

Additionally the PLLA is significantly cheaper than SU8 photoresist, and would be more economically viable in a scaled process.

4.4.4 Manufacture of all-hydrogel 3D microcontainers

Using a number of photolithographic approaches it is possible to create all hydrogel microcontainers in a single or double lithographic step, with articulating faces rather than the rolling motion demonstrated in chapter 3. An all hydrogel container with the appropriate immobilized ECM proteins for cell adhesion would be capable of immobilizing cells while providing a permeable and non-fouling membrane for oxygen and nutrients as well as waste to migrate through. This should avoid common problems such as starvation and hypoxic conditions within the micro-container.

The 'double exposure' method, where a scaffold structure is created out of self-folding hydrogel film, but then through a second mask certain areas are over exposed to make them rigid, this creates structures with different extents of curvature to produce a folded round shape. Spinning of resist was attempted to limit thickness variation, the resulting quick spun gel mixture was then exposed through a photo mask.

In the 'double exposure method' micro containers are created as one sheet with faces defined in the second photolithography Figure 4-30. The result of the first lithography is shown in Figure 4-31 where the container takes an unrestricted form upon folding and is too uniformly flexible to fold into the desired shape. For the box to work certain parts need to be made rigid by a second exposure, while leaving the hinge areas masked off to remain flexible.

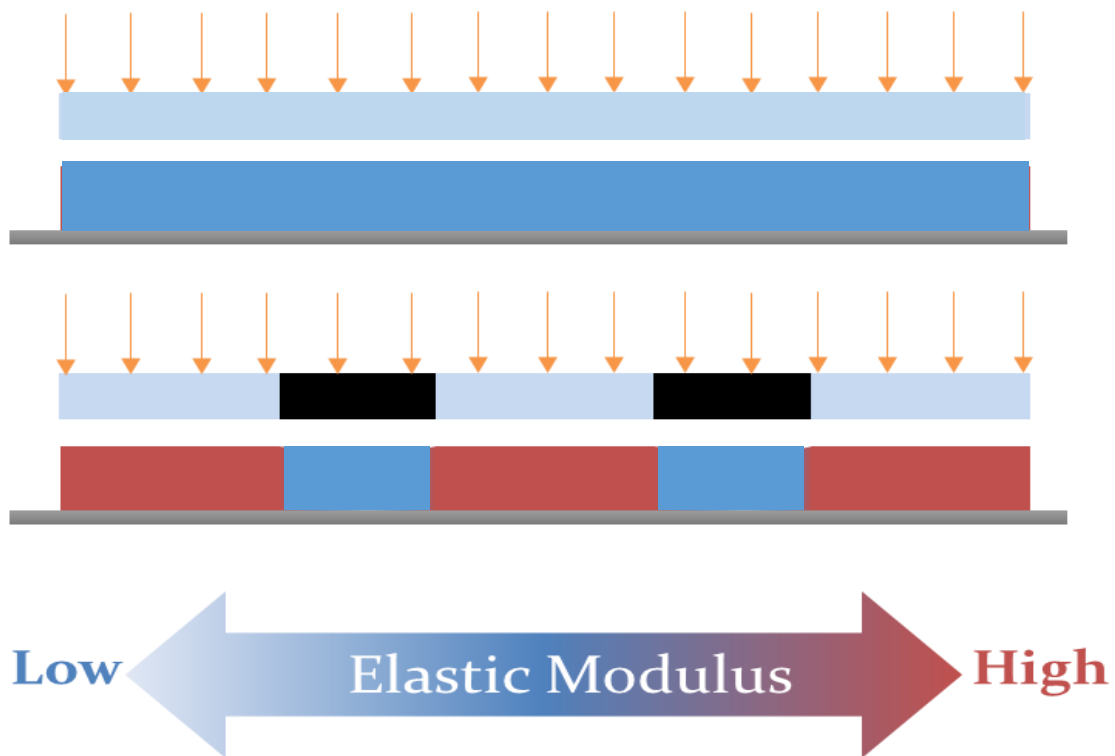


Figure 4-30 - Dual exposure patterning method. The hydrogel film is exposed once to take it to the initial gelling state, it is then sequentially exposed to light through a different mask to further crosslink some sections, but leave others under-exposed. This heterogeneous exposure produces differential swelling effects across the film causing it to fold.

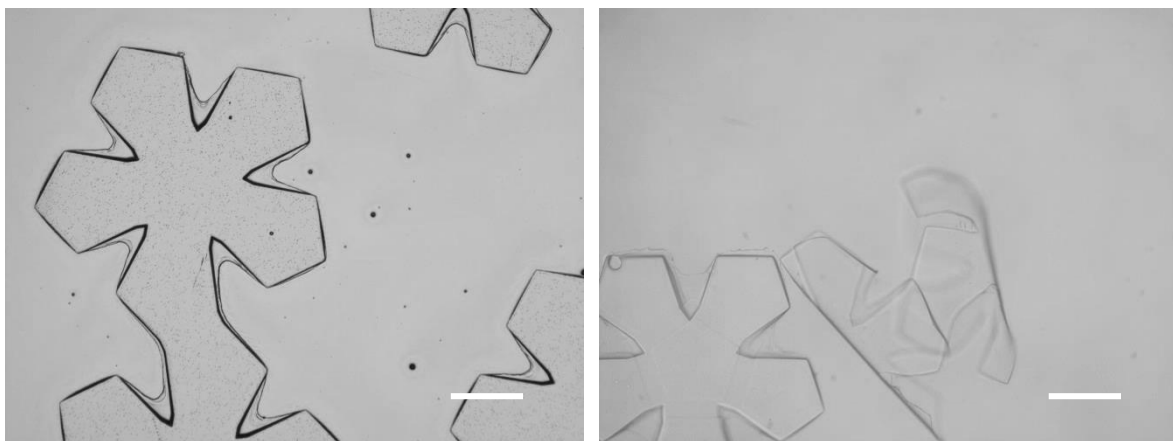


Figure 4-31 - A, Double exposure pentagonal polyhedrons prior to lift-off. B, Post lift-off but without second exposure the films roll up in a unrestricted way. Note that the second exposure was not effective at creating solid sections, as the active components Scale bars: 300 μm.

The overexposure method is slightly different in that the hinge is made by indirect crosslinking. The faces of the box are exposed through a mask but the gaps in between form as a result of the reaction pouring out during the crosslinking stage, and adjoining neighbouring faces producing a flexible actuating hinge connection as shown in Figure 4-32 it is not limited to gels as it occurs in SU8 also, but the result with hydrogel photo curable resist is far more pronounced. This secondary crosslinking is caused by the diffusion of radicals unlike that directly in the path of UV light (Figure 4-33), creating a differentially flexible structure capable of folding at these under-exposed regions. The product of this type of hinge is shown below in **Error! Reference source not found..**

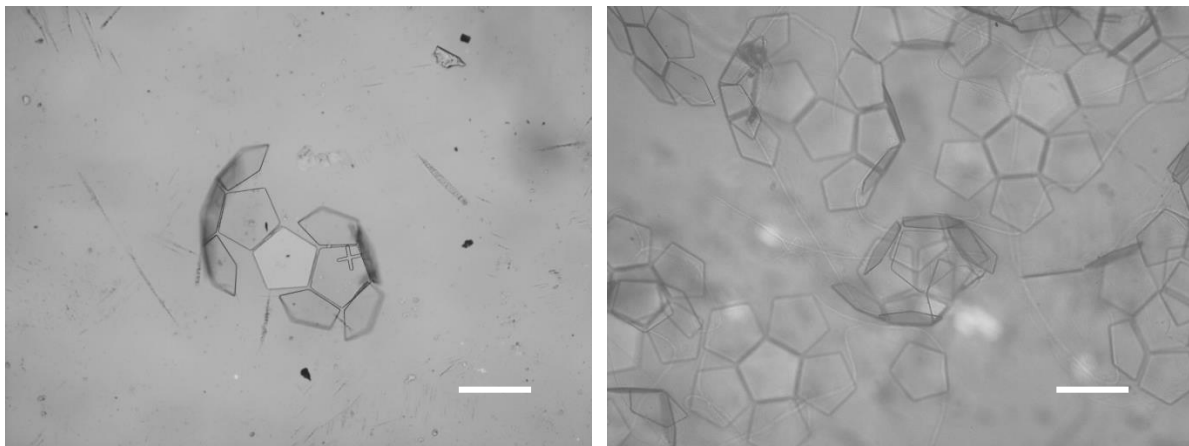


Figure 4-32 - SU8 micro containers attempting to close by PAA immobilized SU8 epoxy at the hinges. Scale bars: 500 μm

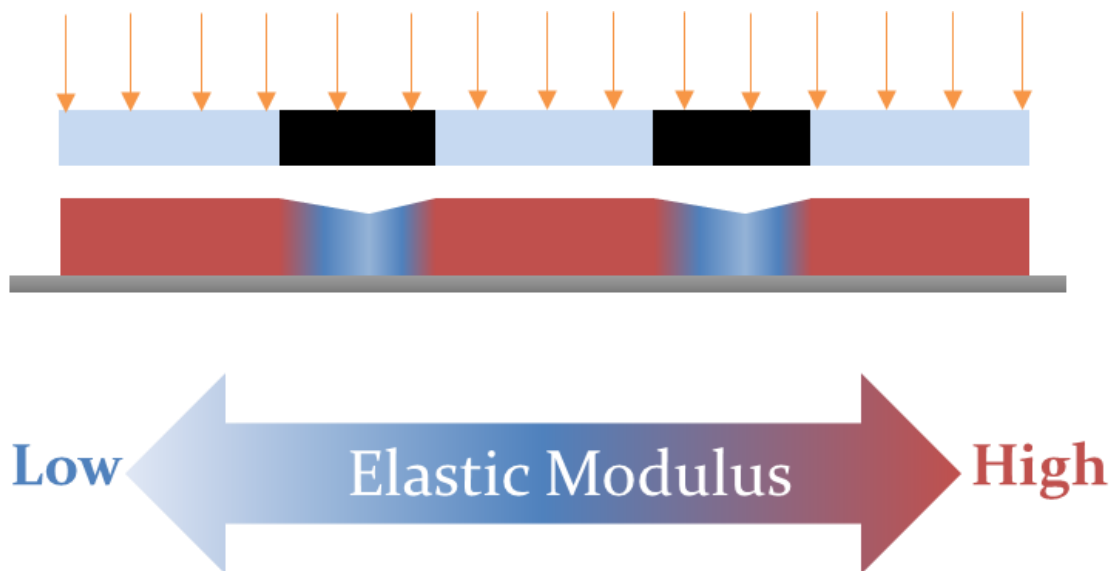


Figure 4-33 - The over-exposure method for producing self-folding hydrogel containers. The exposure undercuts the mask by way of diffusion, and produces a crosslinking gradient underneath the mask feature. If correctly spaced, these under-exposed undercuts meet to produce a hinge which folds by differentia swelling.

The process of optimizing the hydrogel container folding methods is time consuming and batch specific (yield of successful all-gel containers estimated as 20-30 %). It depends on hinge spacing, solvent concentration and polymerisation rate, as too little initiator in the solution and the reaction is killed off by oxygen dissolved in the solution acting as a radical scavenger.

Several iterations were used to determine the containers which fold more often (Figure 4-35). When the reaction rate is too high, the faces do not have time to become rigid before the structure merges together creating an inflexible webbed sheet. If the reaction is too slow the gel is too weak and the hinges have problems holding faces together, creating boxes which are too weak to stand up to the fluid shear forces. Two hinge widths of 20 and 40 μm were attempted with the ideal hinge polymerisations occurring at 6-8 seconds for the 200 μm hinges and 10 and 12 seconds for 400 μm hinges. The designs fluctuated between insufficient and excessive angle of curvature with little control over the interfacial angle, yield of successfully actuating all-gel containers in a batch is typically in the region of 20-30 %.

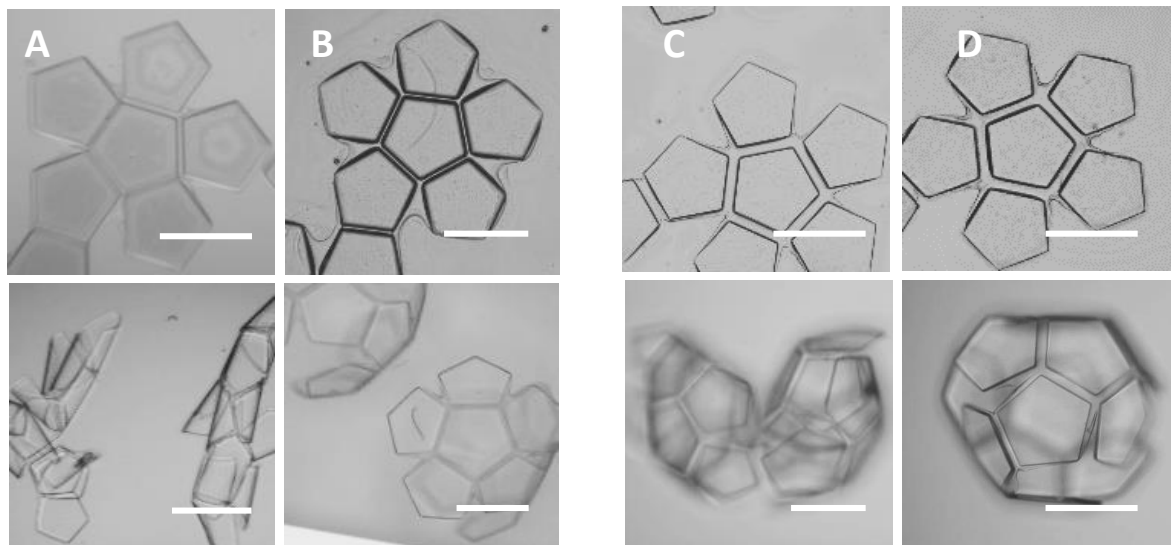


Figure 4-34 – Over-folded boxes made by overexposure method for the 20 μm length hinges, faces exposed for (A) 43.2 mJ/cm^2 and (B) 57.6 mJ/cm^2 . And 40 μm length hinges exposed to: (C) 72 mJ/cm^2 and (D) 86.4 mJ/cm^2 . This folding results due to underexposure of the PEGDMA hydrogel in the container faces, making the whole structure flexible and unable to hold the shape properly. In instances where the structure is solid enough, the hinges are too rigid to attain the necessary folding angle. Scale bars: 500 μm .

4.4.5 Manufacture of hybrid containers

Boundary layers between the PAA and SU8 layer interfered with early attempts to make SU8 and hydrogel hybrid containers shown in Figure 4-37 below. The interaction of SU8 with the sacrificial PAA films occurred when attempting to bind hydrogel hinges to the PAA below the SU8 faces, as it was crosslinked and contaminated with a less flexible and reactive film. The crosslinked film is thin, flexible and sticks to faces and stops them from moving freely, it also acts as a boundary between the gel and the PAA OH- groups which are needed to make the bilayer function correctly. Several methods were trialed in an attempt to resolve the issue, and expose the active PAA layer underneath, involving the use of stronger solvents, over development, the use of oxygen plasma, under baking and applying a barrier layer.

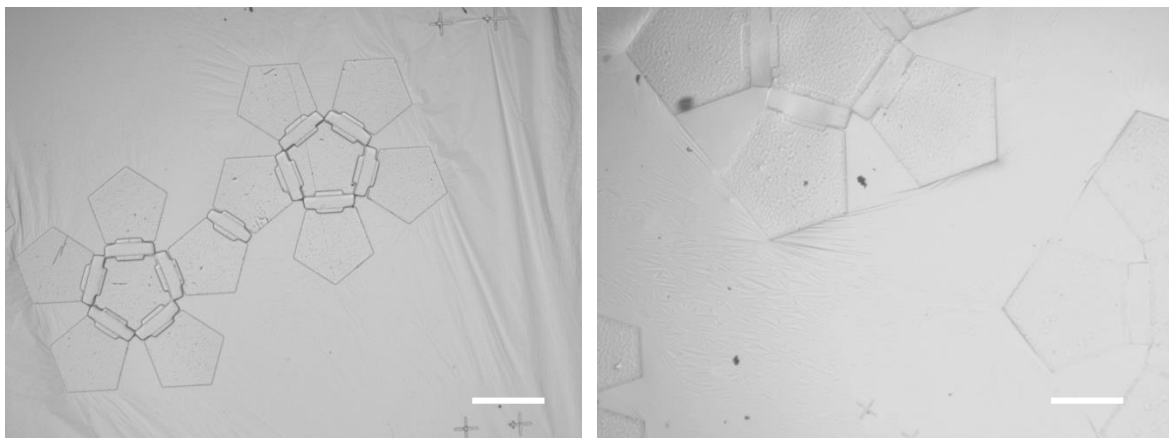


Figure 4-36 - SU8 and Hydrogel hybrid containers affected by a thick boundary film, stress marks are visible after dissolution of PAA. Scale bars: 300 μm .

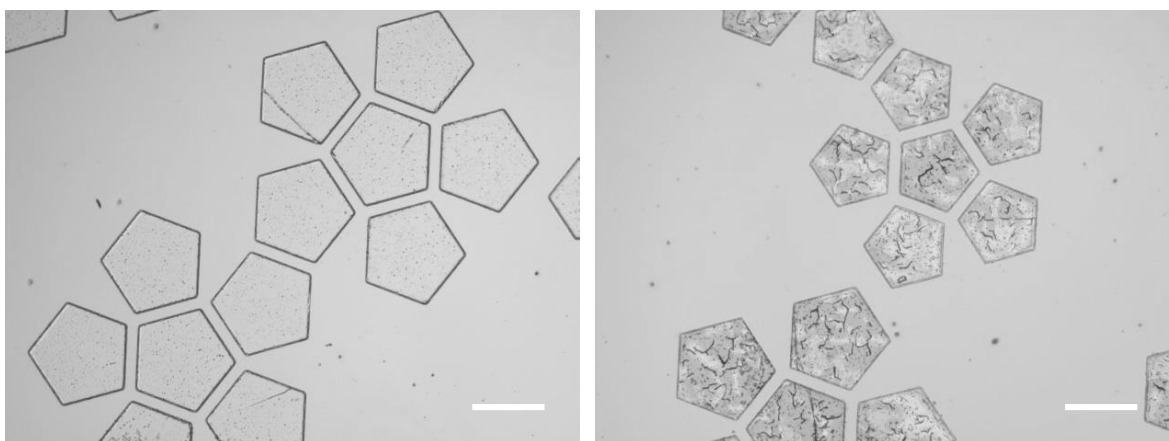


Figure 4-35 - SU8 micro-container layer before (left) and after wet etching with NMP (right) to remove the inter-facial film that had been affecting the performance of the subsequent hydrogel hinges. Excessive cracking can be seen after overdevelopment in NMP. Scale bars: 300 μm

Acetone or N-Methyl-2-pyrrolidone (NMP) solvents were used, but while these removed much of the film they also severely damaged the surfaces of the SU8 structures, creating residual stress fractures and pitting after a 40second etch (Figure 4-36). This was not acceptable if the prime objective is to have well defined nanopatterns on these surfaces, as these would be stripped from

the surface. Based on these results, a gentler or more selective process was considered to get through the films but limit the damage to the top surface of the SU8.

Over development in EC Solvent (ethyl lactate) developer for SU8 was not observed to break the films, suggested to be caused by the PAA chains being insoluble in ethyl lactate. The result again was damage to the SU8 structures with no visible effect on the film problem resulting in pitting and excess surface roughness (Figure 4-37) without fully removing the film.

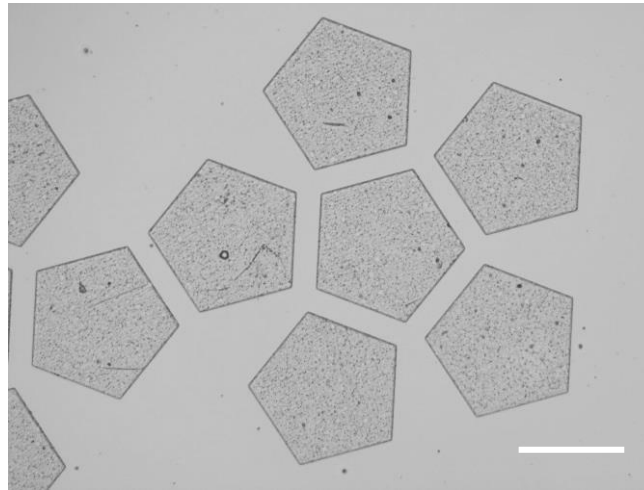


Figure 4-37 - SU8 showing the effects of overdevelopment after 6 minutes in EC solvent. Scale bar: 300 μ m.

The use of oxygen plasma was attempted as a less damaging alternative. Samples were ashed in O₂ plasma for 2-3 minutes at 200 W. This setting appeared to get rid of the film at times, but as the PAA is ashed more easily than the SU8 hybrid, thinner lift-off layers were prone to be etched too deep by the time the rest of the interface film was degraded, resulting in uneven surfaces and hence variability in bending after the hinges were manufactured. To see if the process is linear and predictable various durations of dry etch time were tested (Figure 4-38). The etch rate of PAA is seen to be linear, suggesting sample heating at elevated ash durations (>10mins) did not drastically change the etch rate with only a noticeable rise after 20 minutes.

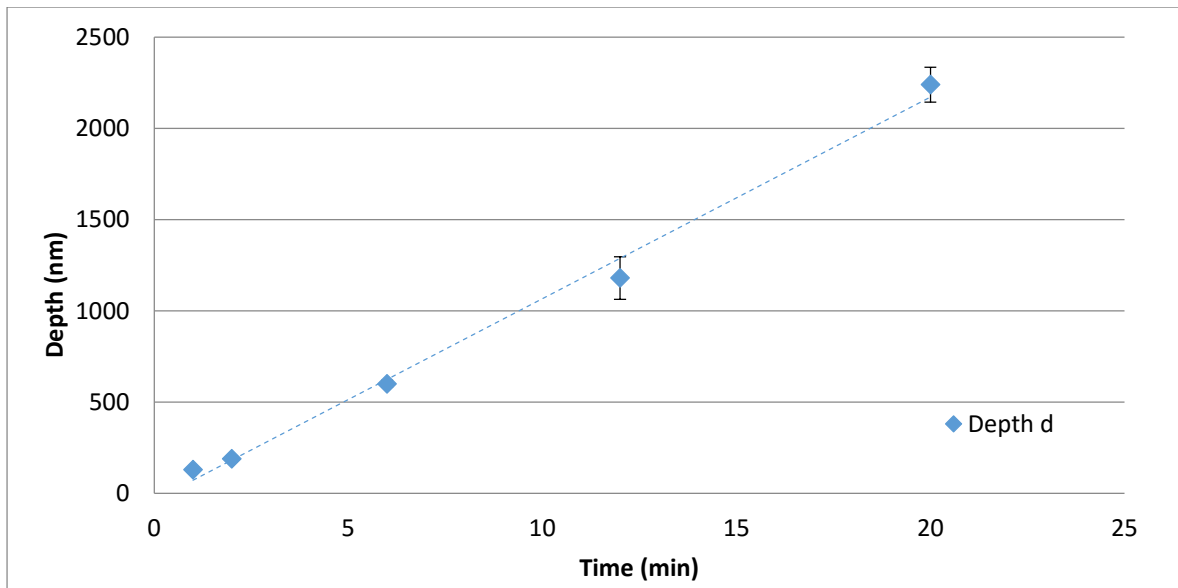


Figure 4-38 - PAA oxygen plasma dry etch depth with time, process was very time consuming with practical etch depths in the region of a micron taking approximately 15 minutes. . Depths measured by profilometry. Error bars: 1SD (n=3).

Another approach to avoid the film is to avoid long baking of the SU8. This yielded better results with limited film formation. The reason for the result is it limits the diffusion and reaction between the SU8 and the underlying PAA. Post exposure baking was limited to 2 minutes at 90 °C for 5 μm SU8 films, this is half of the recommended bake time. This rapid process is harder to achieve in a non-commercial clean-room environment as booking schedules between the different stages of the process meant the film would spend uncontrolled periods of time idle, making it hard to achieve repeatable results.

To investigate the occurrence of films features were washed away straight after development using the standard recipe performed within 2 hours. A lapse of feature lift off in Figure 4-40 shows the release of structures from PAA which were manufactured by this rapid processing, while they generally are clean of overall film, areas close to one another stick and move as a chain rather than individual objects.

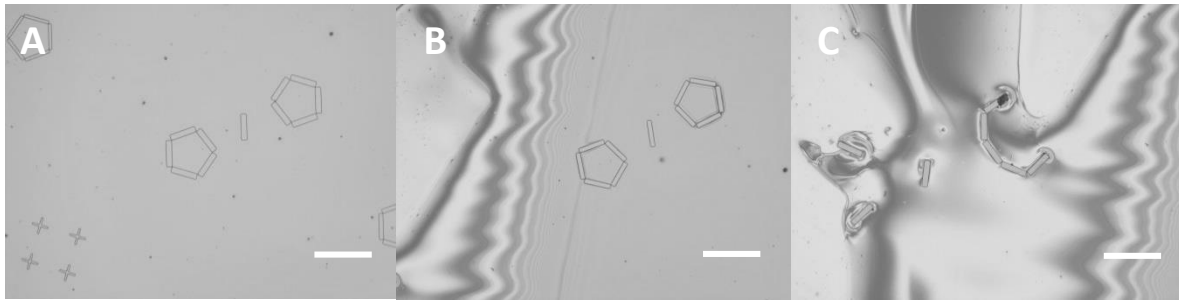


Figure 4-39 - Release of structures from PAA which were manufactured by this rapid processing Scale bars: 400 μm

One method of avoiding this issue was to combine a rapid method for SU8 with an upside-down approach, where the hydrogel hinges were made in the beginning, to allow them to be functionalised by the untainted PAA surface. This method yielded good closure (Figure 4-40), but the flexibility of the hydrogel made it easy for hinges to blow away during SU8 spinning, or be damaged during processing and solvent washing, the resulting losses would be too high for any reasonable yields. The resulting containers show good closure demonstrating the potential for hybrid structures, but a new method of separating the SU8 and hydrogel processes would have to be found. A good candidate was using a boundary layer to prevent contact between the two until completely necessary.

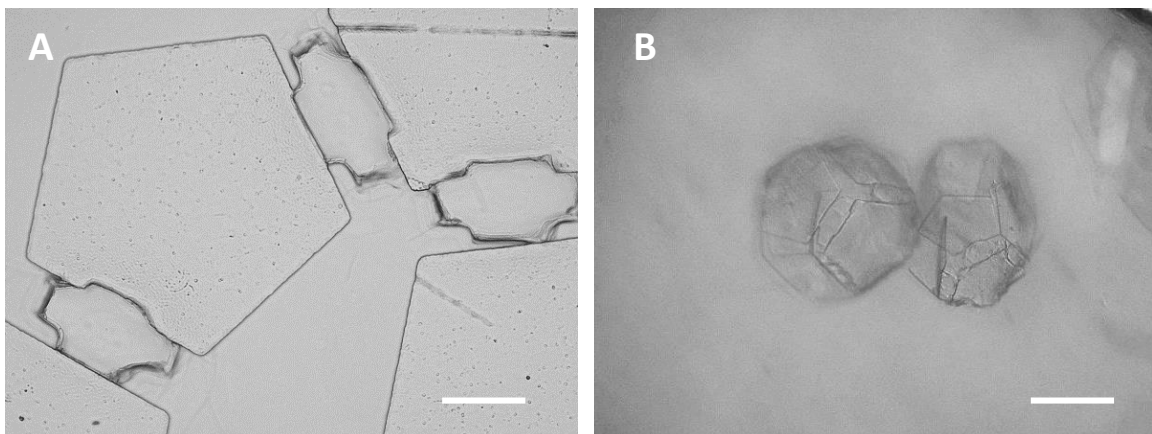


Figure 4-40 - Containers made by the reverse process. A) The hinge integration into the SU8 face, and B) the closed containers in pH 7 solution. Scale bars: 50 μm and 300 μm respectively.

4.4.6 Boundary layers

One way of avoiding contact between acidic polymer groups in the PAA and the photo-acid mediated crosslinking epoxy that SU8 consists of, is to introduce a boundary layer such as PMMA, which is fully compatible with both processes. There is however an issue with an undercut forming in the PMMA film when it is thick (>500 nm), as it etches in EC solvent (ethyl lactate) at the same time as the SU8. This visible undercut occurs very rapidly beneath the structures (Figure 4-41), causing problems for consistency and also pattern transfer from the PAA, as the layer on the outside of the boxes is damaged. It is shown to be remedied by reducing PMMA layer thickness to under 200 nm.

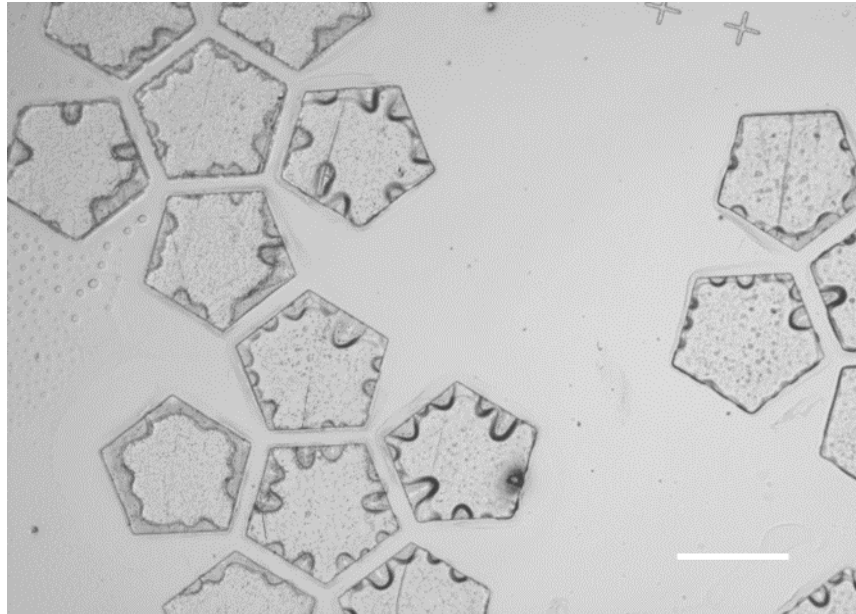


Figure 4-41 - SU8 structures patterned onto a 1 μm thick PMMA layer. The PMMA is undercut by EC solvent development, creating voids at the patterned edges, thinner layers do not suffer from the same issues, and 80 nm films spun from *o*-xylene proved to be a suitable candidate for this method of fabrication. Scale bar: 300 μm .

An alternative would be a different thin film which can be processed by several dry and wet means, such as metals and oxides. Gold is a good candidate although it is highly expensive, costing orders of magnitude more than PMMA or some other boundary layer polymeric film. Overall this would be a disproportionate part of the overall container cost, but does offer the potential for integrated circuits, sensors and gold specific surface modifications such as cell repelling surfaces. Gold is also biocompatible and etched by a number of very specific wet and dry processes. There are several technical issues with gold the first is the available wet etches for gold, which consists of water and either acids or dissolved iodine salt and ions, as water attacks PAA and would make it impossible to achieve bilayer hydrogel hinges afterwards. A novel modified gold etch was made using methanol as the carrier solvent (Figure 4-43).

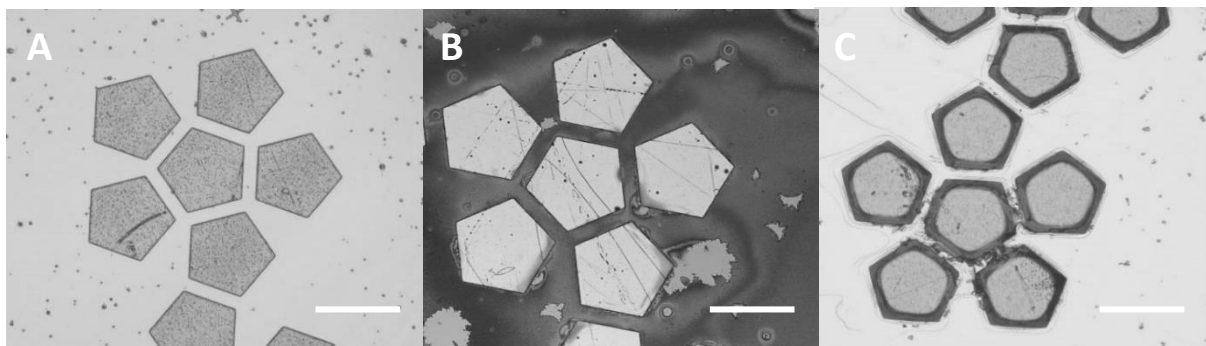


Figure 4-42- Gold etch with time A) 10, B) 30 and C) 60 seconds with 30 nm gold barrier film a slight undercut below the SU8 features is visible. Ratio of potassium iodide to iodine is 2:1 with 4 g and 2 g in every 80 μl of MeOH:IPA 1:1 mix. Scale bars: 300 μm .

As the concentrations of potassium iodide and iodine that this solvent can carry was significantly reduced, it resulted in a slower etch rate, useful for precision etching of a 50 nm thick layer. 4 g of potassium iodide and 1 g of iodine were dissolved in 40-80 ml of Isopropanol and stirred for half an hour before use. The first resulting and subsequent etches are shown in As the concentrations of potassium iodide and iodine that this solvent can carry was significantly reduced, it resulted in a slower etch rate, useful for precision etching of a 50 nm thick layer. 4 g of potassium iodide and 1 g

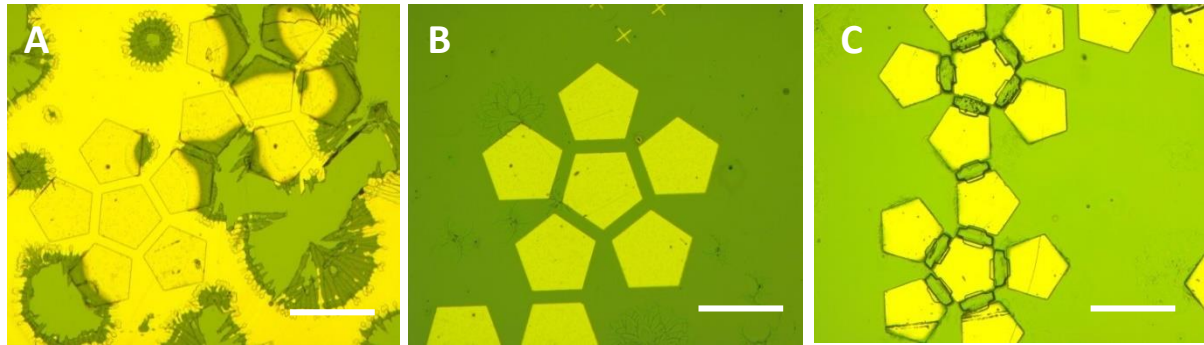


Figure 4-43 - Containers made by the gold boundary layer process. A) etch attempt prior to cleaning with O_2 plasma. B) etch with pre-clean. C) Hinges applied. Scale bars: 500 μm .

of iodine were dissolved in 40-80 ml of Isopropanol and stirred for half an hour before use.. Ashing the SU8 after development was noted to be critical to get rid of fouling which can block the wet etch process and result in 'snowflake' style defects.

The recipe was sensitive to iodine concentration with the etch rate reducing sharply as this was reduced to a 1:1 ratio and 1 gram of iodine in 80ml of IPA:MEOH as shown in Table 4-6.

Table 4-6 - Modified gold etch rates with different concentrations of potassium iodide and iodine, shown are the respective etch rates as determined by the duration necessary to strip through a 50 nm and 80 nm gold layer. Rates are measured by profilometry of etch depth at single time points over 5 discrete areas, overall etch depth then divided by etch duration.

Potassium iodide (g)	Iodine (g)	Solvent IPA:MEOH (1:1) (ml)	Etch rate (nm/s)
4	2	80	1.34
4	1	80	2.67
2	2	80	0.90
2	1	80	0.62
1	1	80	N/A

(Figure 4-44c) and resulted in successful actuation of containers in pH 7 buffer solution. The resulting free-floating gold coated dodecahedrons were allowed to fold fully before imaging with optical microscopy.

The containers made by this method were far more visible and may result in improved capture of these devices. Some difficulty was seen in the container pivoting around the central hinge connecting the two domes of the dodecahedron. It is thought that this occurred due to a proportionally greater load on this hinge, extra time to swell resolved this initial issue. While the containers did not capture cells in this experiment, it was a successful proof of concept, and a step forward as a repeatable solution to the thin film issues had been found. The ability to assemble layers shown in Figure 4-45 into a functional device allowed more complex geometries to be trialed in future experiments. This led to the design of a 'lotus' design mask, which had more axes of symmetry and was expected to be a more robust and reliable alternative to the dodecahedrons.

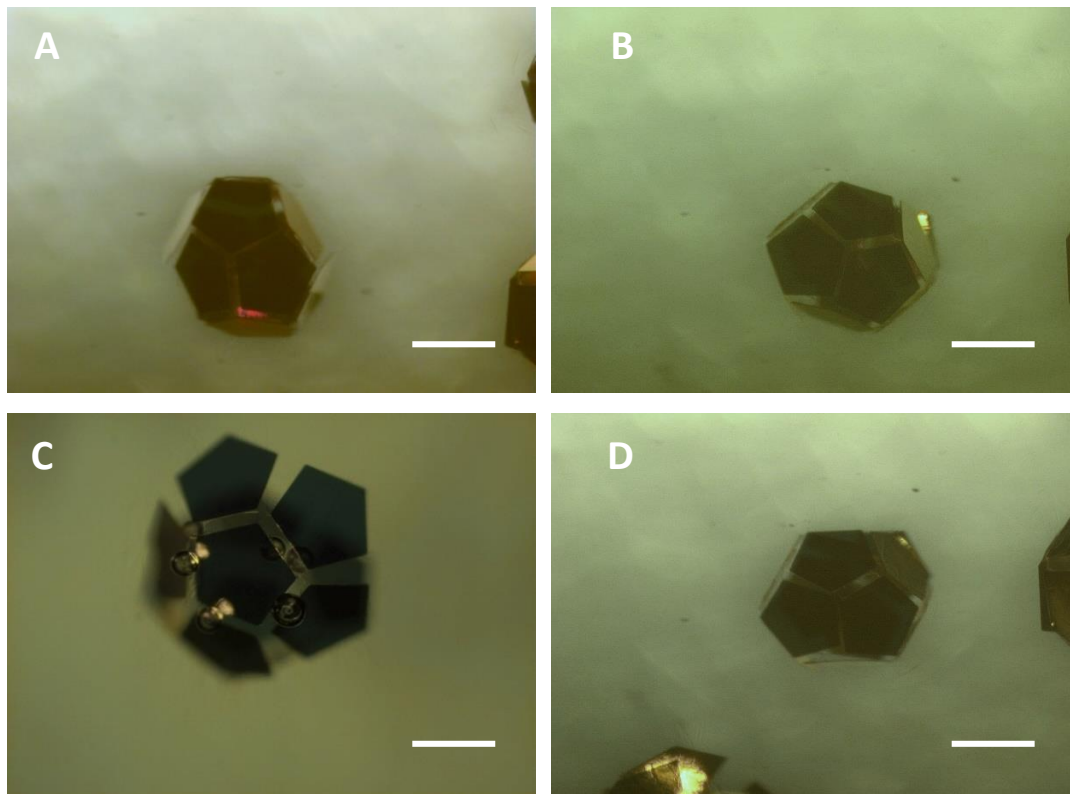


Figure 4-44 - Containers made by the gold boundary layer process. A,B,D) closed containers, C) container in the process of folding. Scale bars: 500 μm .

Functional dodecahedron containers at an estimated yield of 10-30 % were obtained in the following process:

1. Spinning of PAA at 4000 rpm followed by drying at 90 °C for 2 minutes,
2. Sputtering of gold onto the PAA to a 50 nm thickness
3. SU8 3005 spun at 4000 rpm followed by a 5 minute pre-bake at 90 °C by hotplate, followed by a 45 second UV exposure, 3 minute post-bake and finally 3 minute development in EC solvent followed by a 20 second O₂ plasma ash .
4. Gold etched in 4:2 w/w I/PI iodine etch in 1:1 v/v IPA/MeOH for 40 seconds
5. Sample ashed in O₂
6. PEGDMA 90 v/v % in IPA applied as hinges in a 6 second UV exposure.

Detailed process optimisation and improved controls as part of future work may improve yields further. No distinct pattern in the location of defective containers was seen on the wafer, however from 50-70 % of containers which were undamaged and began to actuate, only 10-30 % achieved near full closure. One area of weakness appeared to be the central hinge which had to hold two domes of this dodecahedron together, resulting in more noticeable deformities than if a petal hinge were to fail.

Variation is thought to occur due to film non-uniformity, variation in exposure, oxygen concentration within the gel, and possibly due to damage during mask separation from the gel resist. This could be improved by:

- Processing the gel and gel thin film in an inert atmosphere prior to and during exposure.
- An automated method of applying the gel precursor solution immediately prior to exposure would also improve film uniformity.
- Mask-substrate vertical tilt alignment during contact and disengagement from the gel would improve uniformity and limit damage to the gel during mask removal
- Flushing of the substrate prior to mask removal to reduce hydrostatic forces from unexposed gel precursor solution.
- Limiting edge bead formation by spinning in a vacuum or laminar flow spinner would also help reduce photomask pivoting on substrate irregularities.

Many of these features can be implemented in a commercial photolithographic system.

4.4.7 Lotus structures

4.4.7.1 Assembly

Lotus structures were attempted to be manufactured utilizing PMMA and Au boundary layers during SU8 manufacture. The stages of assembly shown in Figure 4-46. PMMA was easier to use as a boundary layer, but prone to early lift-off if the ethyl lactate was allowed to etch an undercut beneath the SU8 faces. Sputtered Au was first etched with the modified gold etch outlined previously in Table 4-6 in the highest concentration 4:2g of PI:I in 80ml of IPA:MeOH gold etch. Hinges were subsequently applied in a second photolithography stage using PEGDMA 90 % monomer in IPA with 1 w/v % LTPO as photoinitiator.

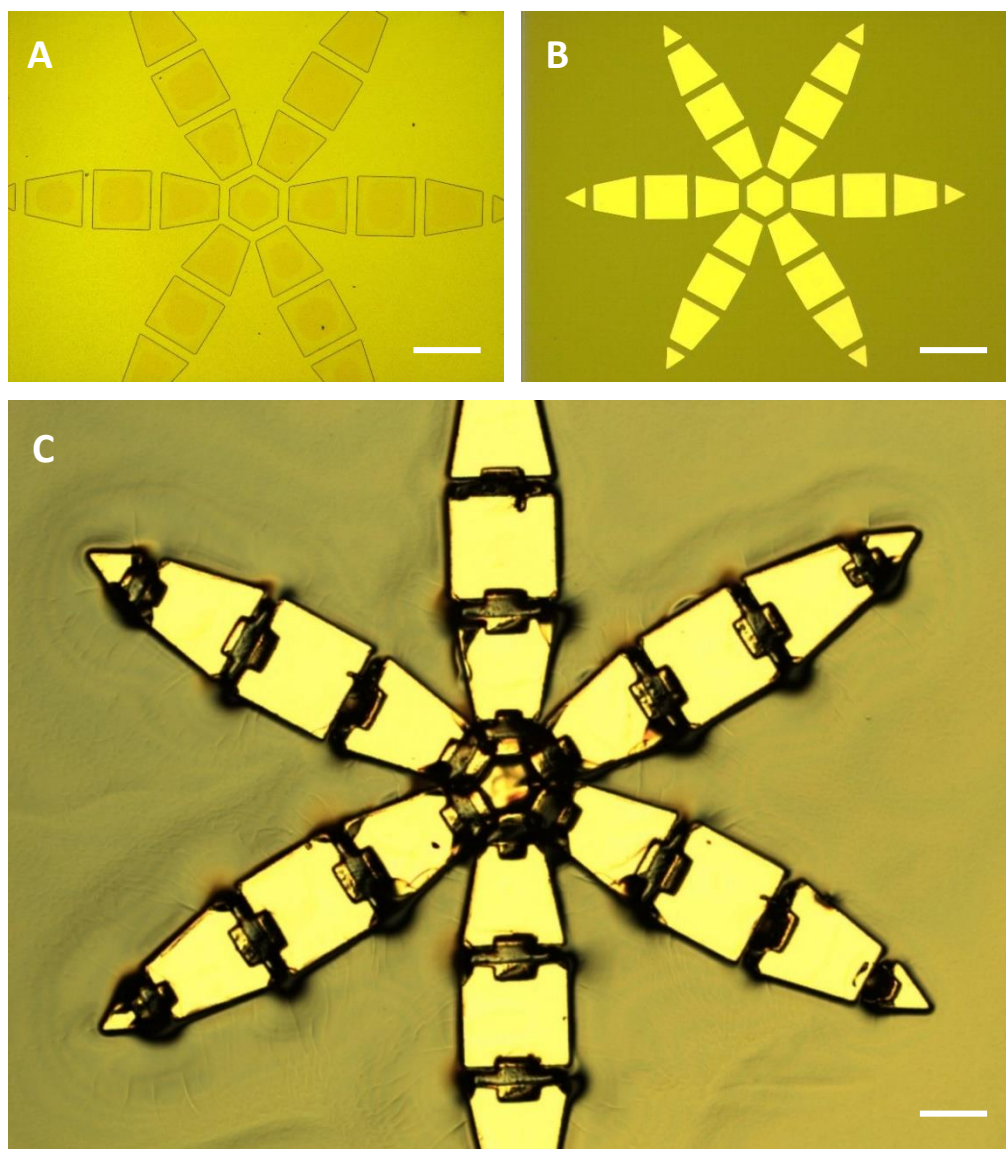


Figure 4-45 - Lotus container made with the gold boundary layer method. (A) SU8 features of the lotus are created on a gold coated PAA surface. (B) The gold is etched in areas where it is not covered with SU8 features, exposing the PAA surface underneath, in preparation for hinge addition. Scale bars: a) 200 μm , b) 400 μm and c) 100 μm respectively.

This process can also be achieved by a 200 nm PMMA based boundary layer process using o-xylene dissolved polymer described in 4.2.3.6 which is identical to that of the gold except the PMMA is spun on and automatically removed by EC-Solvent during the SU8 development (accommodated by extra 15 s of development time) shown in Figure 4-46. With the actuating container shown in Chapter 5 - Figure 5-45. After dissolution of the surrounding PAA in H₂O samples were ready for cell seeding.

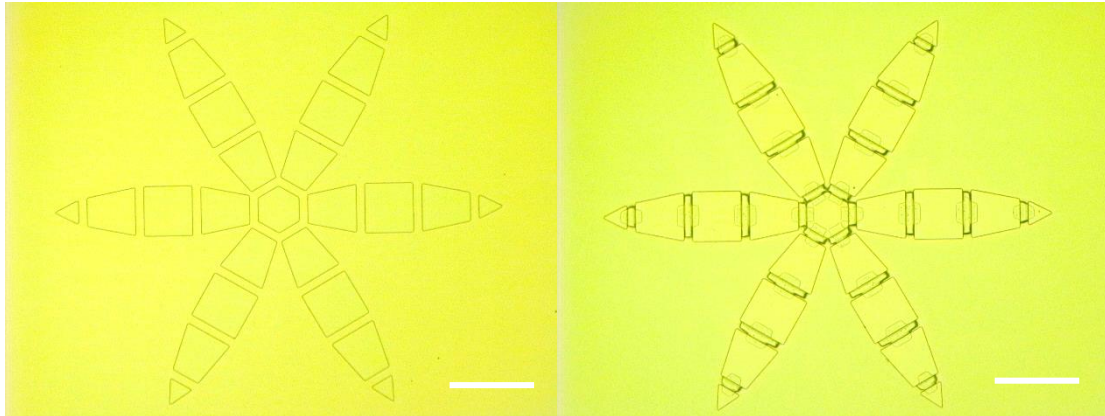


Figure 4-46 – PMMA boundary layer formed 'lotus' containers manufactured from SU8 before (left) and after (right) the application of hydrogel hinges. Scale bars = 500 μ m.

4.4.7.2 Actuation

As previously polyhedral were triggered by the addition of pH 7 buffer, DMEM or PBS. The actuation process was tracked in successfully formed devices by using the time points on the images captured.

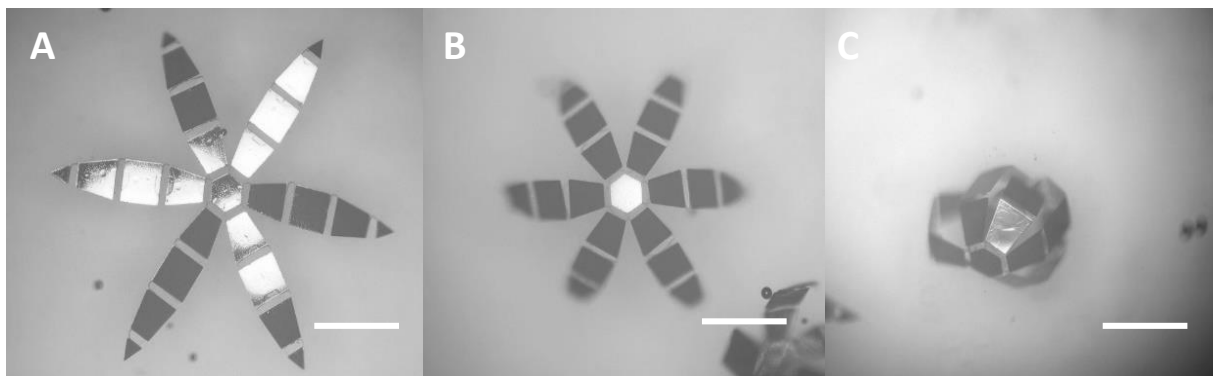


Figure 4-47 - A gold covered 'lotus' container undergoing folding in pH 7 buffered solution. The position of the tips relative to the box centroid can be tracked in consecutive images to record container folding dynamics. Showing A) t=0, B) t=4 minutes C) t=10 minutes. Scale bars: all 500 μ m.

The petal tip to centre distance was calculated from optical microscopy in ImageJ software and plotted against the registered time stamp to track the extent of container closure over time as shown in Figure 4-48. The time in seconds after the addition of pH 7 buffer to containers lifted off in RO H₂O.

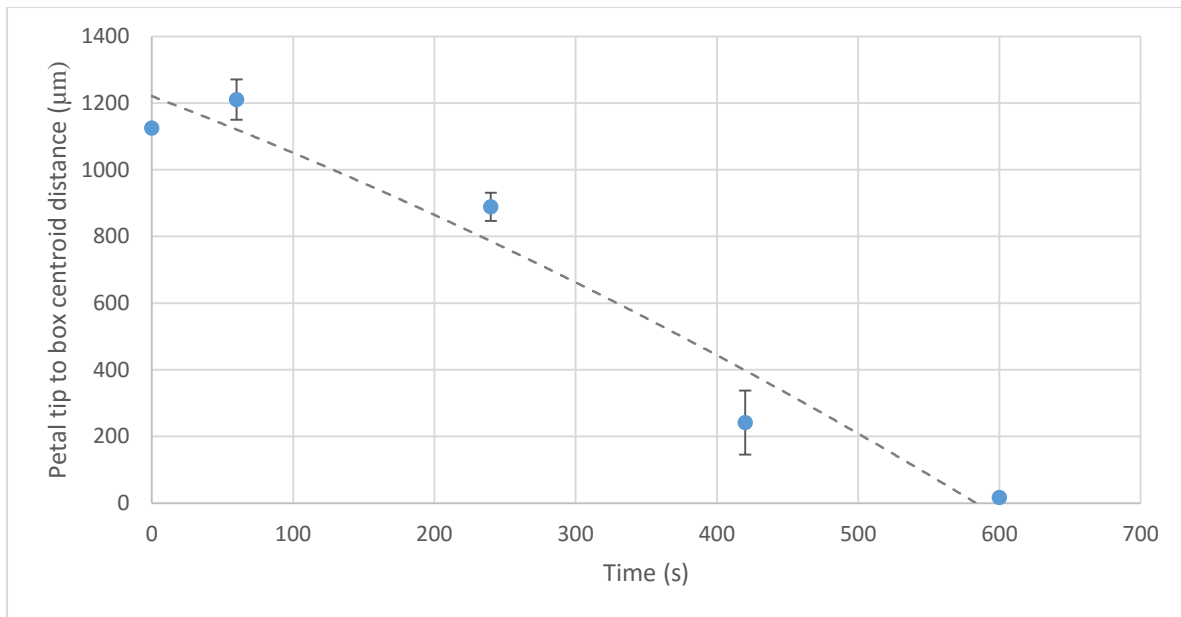


Figure 4-48 - Distance between the petal tip and the centroid of 'lotus' containers with time (centroid is axis in z-axis through central hexagonal face on x-y plane, where petals lie in the x-y plane), the transitional folding can be seen as the tip is folded and curled inwards to meet at the centroid of the container mask (the central hexagon to which all the petals attach). Error bars: 1SD from n=3 measurements.

The fully folded container would reach an equilibrium state when the hinges became fully hydrated.

The swelling rates of PEGDMA based hydrogels were measured by looking at the weight at discrete time intervals in RO H₂O. Equilibrium was found to occur at about 30 minutes (Figure 4-49).

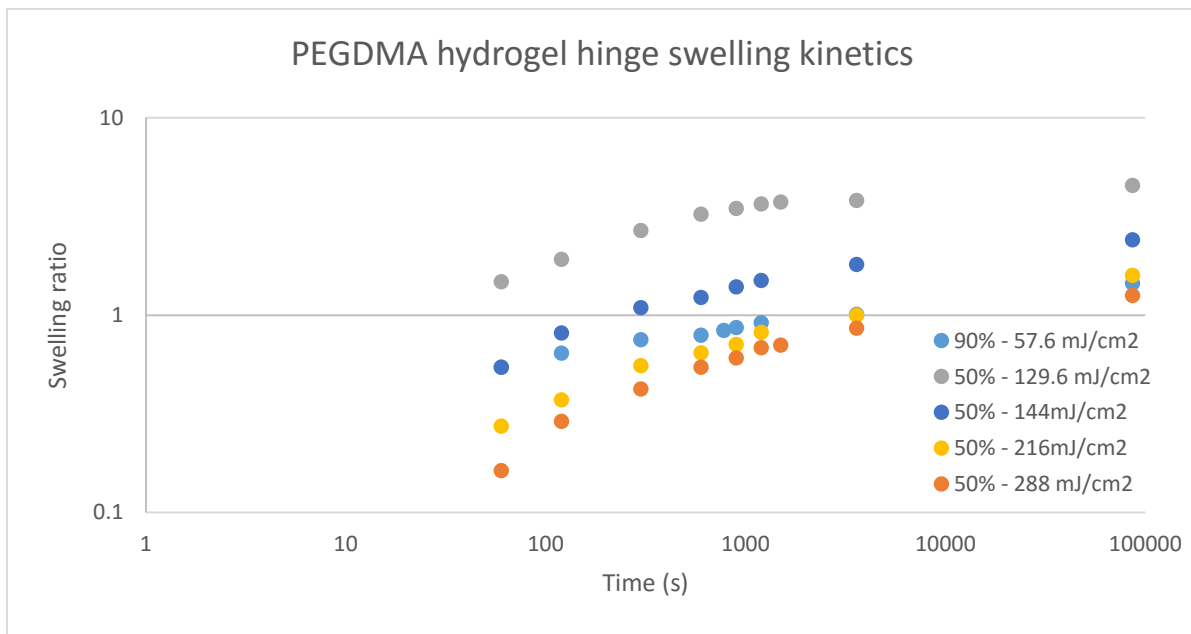


Figure 4-49 - Swelling kinetics of PEGDMA hydrogels for various monomer concentrations and exposure doses. , n=1 per sample.

4.4.7.3 Locking Mechanism

Interweaving elements were used as a comb type structure which catch each other when they are in close proximity by ionic interaction. Ionic locking elements use oppositely charged ionic and cationic gels to attract neighbouring faces to each other and hold them in place in the operational pH range. The cationic locking side was produced by photolithography similar to the recipe for NIPAAm hinges mentioned in previous reports, however a cationic NH_2 bond containing monomer was added to the pre-polymer mixture to create gels with an inverted swelling response at elevated pH and created a positively charged surface. This positive charge allows them to stick to negatively charged gels such as those made with acrylic acid and poly acrylamide. The gel constituent responsible for cationic swelling was DEAEMA. The DEAEMA component making the bulk of the gel swells in pH 4 and shrinks in pH 6 and above. This swelling is accompanied by a surface chemistry transition where the gel becomes positively charged. After several attempts it was found that the gel was difficult to apply in such small elements and no visible bonding was seen between the cationic and ionic gels elements. Mechanically Interweaving elements were intended instead to be used as a comb type structure which catch each other when they are in close proximity (Figure 4-51),

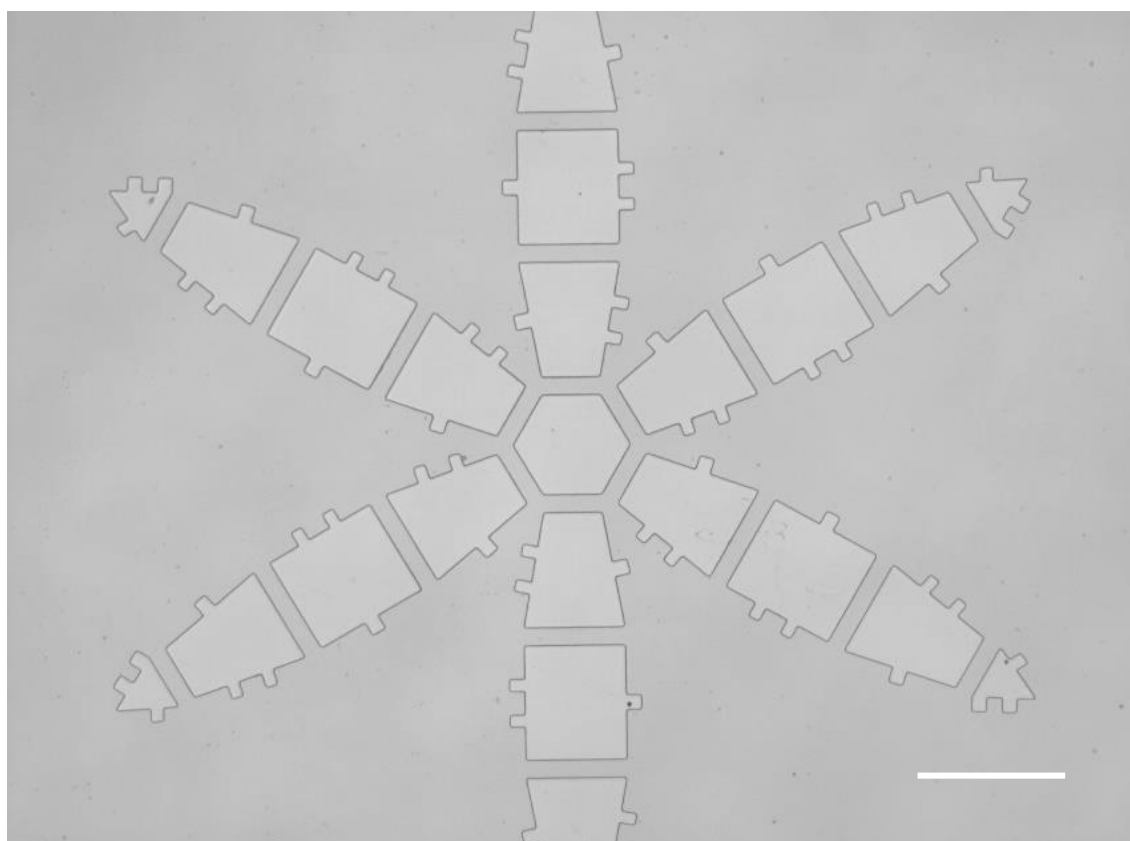


Figure 4-50 - Interlocking mechanism design as applied to a 'lotus' container. The protrusions are created to overlap and thus reinforce adjoining faces, and limiting over-closure, where one face moves further inward than its neighbours, blocking them in the process. Scale bar: 300 μm .

4.4.8 Device immobilization

Various methods were tested to create voids in the sacrificial film, thereby anchoring the structures to the substrate underneath via a small window. Wet etching of PAA through a photopatterned port was attempted, but yielded a large undercut which was not ideal as the areas immediately next to this port were no longer of equal thickness.

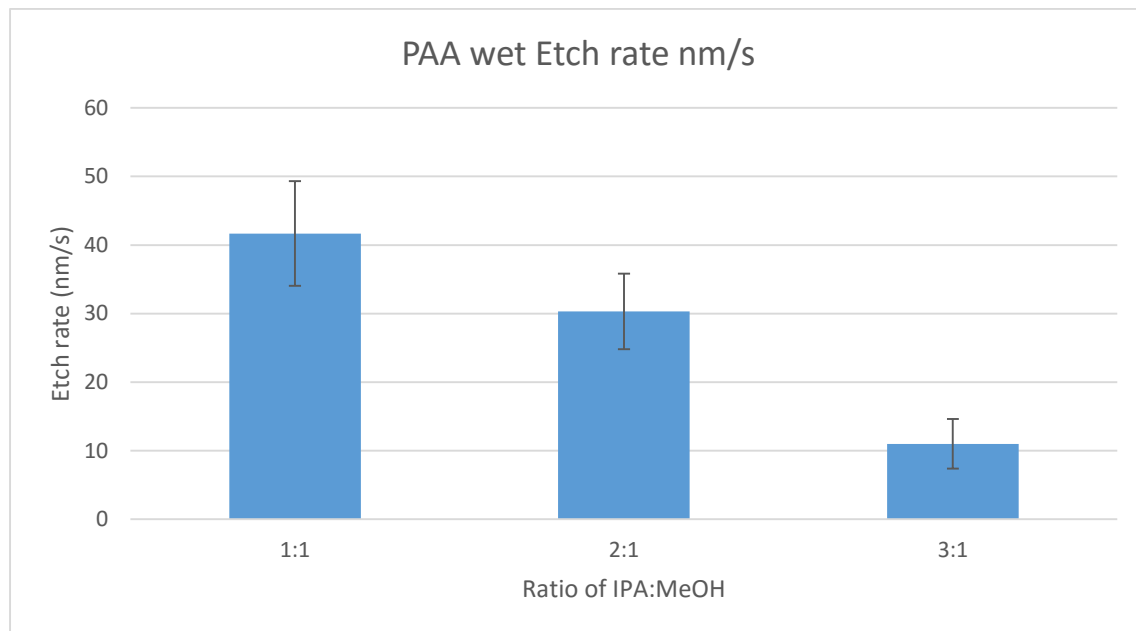


Figure 4-51 - Etch rate of PAA in different concentrations of methanol diluted with isopropanol. Methanol was found to dissolve PAA readily, but did so in a more controlled manner when diluted by an unreactive solvent such as IPA or EtOH. Depths measured by profilometry. Error bars: 1SD from n=5 measurements.

Anchoring of lotus and dodecahedron containers was done by the prior patterning of the substrate with S1818 features, which were spun over with a layer of PAA. The PAA was ashed to expose the S1818 corners underneath, followed by development and lift-off of the S1818 in ethyl lactate over 1 minute, etch rate was found to be roughly 1.9 $\mu\text{m}/\text{min}$. Following lift-off substrates were ashed again to descum and a layer of TPM was applied to the surface to immobilize the gels and or SU8 faces positioned above.

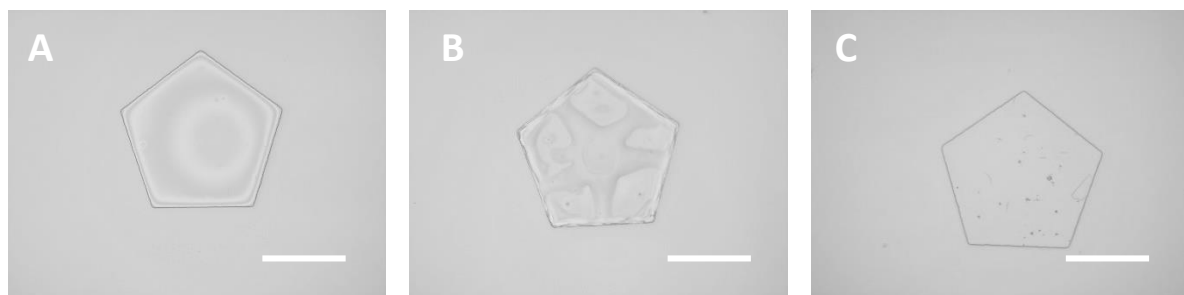


Figure 4-52 - Lift-off of S1818 from under PAA to provide an adhesive point to anchor devices. Showing the development of S1818 with etch duration in Ethyl lactate. A) Non-etched surface, B) 45 seconds etch, C) 2 minutes etch. Scale bars: 100 μm .

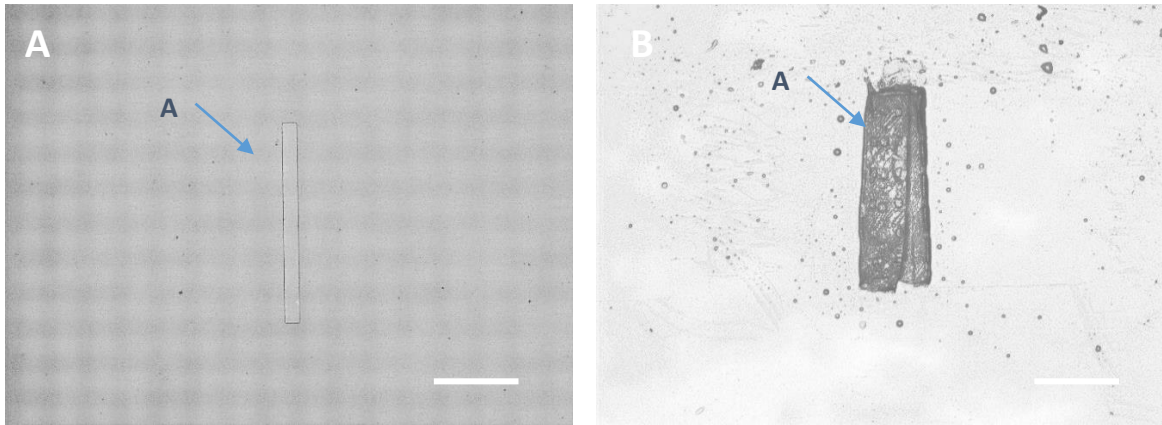


Figure 4-53- A) TPM anchoring agent evaporated to slot dissolved through PAA by a S1818 mask coating glass underneath) hydrogel roll patterned above this slot is permanently anchored to the glass surface. Scale bars: 400 μm .

This technique is also used for the immobilization of NIPAAm based smart gel, cell capture and release surfaces. The same process can be used for polyhedron manufacture. To look at the optimum coating conditions, contact angle measurements were taken of silicon substrates exposed to TPM vapour in an inert N_2 environment at discrete time points. A plateau can be seen after 10 minutes at 150 °C. The standard protocol used which gave good coverage was 15 minutes evaporation in an enclosed nitrogen rich atmosphere at 150 °C followed by an N_2 gas flush, to displace the toxic silane vapour.

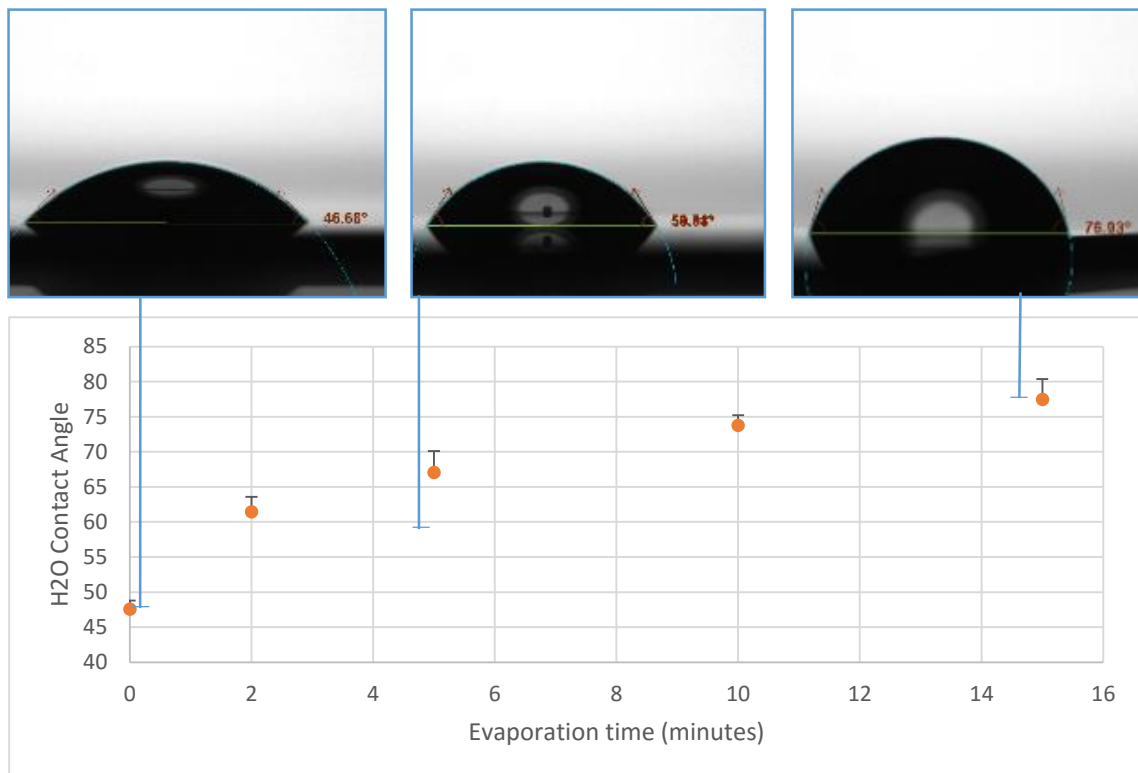


Figure 4-54 - Contact angles of Si treated with evaporated TPM. Measurements taken at discrete time points during coating in a sealed and inert container filled with N_2 heated to 150 °C. . Error bars: 1SD from $n=5$ measurements.

The results show an optimum coating time of 15 minutes, after which no extra hydrophobicity was produced. It was noted that after long periods in silane TPM vapour, substrates became opaque and patchy, this is considered to be due to deposition of secondary and tertiary layers of TPM, which subsequently polymerise.

4.5 CONCLUSIONS

This chapter successfully demonstrates that it is possible to create self-folding containers out of hydrogel hinges and nanopatterned polymeric structure. Several different kinds of structure have been demonstrated, ranging from the all polymeric container, comprised of differentially swelling zones of PEGDMA hydrogel, as well as those which are novel hybrid constructions.

Of the available materials, PCL was found to not spin smoothly enough to be compatible with nanopatterning (Figure 4-25), as film uniformity is key. Of the remaining polymers, SU8 and PMMA remained the most compatible with PAA processing due to their lower temperatures during patterning. Of these SU8 was the simplest to use due to the ease of photopatterning, while PMMA required etching to define the microfeatures.

Of the sacrificial film polymers used, it was found that PAA was much rougher if using neutralised PAA as suggested in the pioneering paper by Linder et al. [190]. Where deprotonated or 'neutralised' PAA allows for more selective dissolution using calcium salts, non-neutralised PAA was used, which created issues with subsequent SU8 patterning and lift-off as the SU8 sets as a result of a photo-acid generated during exposure to UV light. The acidity of the PAA substrate caused problems with insoluble films forming at the interface with PAA.

These interface issues were successfully resolved by the use of PMMA and Au boundary layers, etched away prior to the addition of box hinges. A novel Au etch was developed to remove the Au boundary layer, and relied on a solution of iodine and potassium iodide in an isopropanol solution, unlike the traditional and much faster water based iodine etch.

Containers were also successfully immobilised on the substrate surface by a single joining connection, allowing them to fold but stay in a predefined point on the substrate, done by etching through the sacrificial layer at a finite spot, prior to patterning the container above. For hydrogel containers this was achieved by using TPM to selectively bind them to the silicon underneath the etched sacrificial layer.

While some problems remain, and gaps can occasionally be seen in the container walls, this proof of concept can be used as a platform for future development and complexity. Both the dodecahedral

and lotus containers showed promise in this respect, and can be used for similar or different applications, such as the gripper made by the Gracias research group, which utilises a dissected sphere claw for attaching to bio-tissue in the intestines for drug delivery [29].

Additional issues still remain with yield, as many devices still suffer from incorrect folding and problems with structural integrity. It was also noted that the cationic locking mechanism, containing gels of different charge, did not photo polymerise successfully on the devices, and soon fell apart. It also failed to provide sufficient force to lock adjacent faces together, this could be resolved in the future by attempting to integrate DNA based adhesive regions [210] on the container edges, which have shown great promise as a means of selective adhesion and assembly. However the equipment and facilities were not available during the time of the current work being carried out.

5 CELL CULTURE IN 2D AND 3D

5.1 INTRODUCTION

This chapter covers the cell culture work undertaken in part at the University of Glasgow with hTERT immortalised fibroblasts, seeded onto nanopatterned 2D surfaces, and the work performed during one month secondment to the University of Oslo School of Medicine, using hESCs seeded on feeder free nanopatterned 2D surfaces and the 3D nanopatterned containers discussed in Chapter 4. The intent of the work in this chapter was to take a step ahead and investigate what patterns could be applied to the internal surfaces of the self-folding containers to aid them in the formation of a specific cell type. This is particularly important if we consider that stem cells were intended to be used in this organelle formation using topographical cues. It was a proof of principle pilot study, and aimed to push ahead with a very ambitious aim of stem cell differentiation on nanopatterns in 3D within a very short period of time.

Initially hTERT fibroblasts were used to determine any cytotoxic effects, resulting from the microfabrication processes involved in making the 3D cellular niches. The fibroblasts, which multiply quickly and are relatively cheap compared to human stem cells, were used to look at cell-surface attachment, and check that modifications made to hydrogel containers, composed of PEGDMA and certain ECM constituents (vitronectin, collagen and Matrigel®) were effective in improving cell attachment on these hydrogel surfaces. PEG is known to not immobilise proteins, and thereby non-biocompatible as a culture surface [27] unless modified with RGD or somehow incorporating binding sites. For the hTERT fibroblast studies, cells were seeded on nanopatterned surfaces developed during previous work by the Bio Interfaces Group (BIG) at the University of Glasgow, and the work by Dalby and Gadegaard et al. [39]. These surfaces (square, near-square 50, planar and random configurations of nanopits) were reproduced in SU8, the material chosen as a means of manufacturing 3D containers in Chapter 4. The nanopatterned SU8 surfaces were seeded with hTERTs to see if cells began to proliferate after 24 hours, or if mass apoptosis followed the initial seeding. This pilot study aimed to identify any issues before the container materials and design moved forward. Hydrogels (PEGDMA) were also tested for cell attachment, by adding collagen to the PEGDMA hydrogel pre-polymer solution which was then photo polymerised onto TPM coated glass slides, to keep the hydrogel films adhered to the surface of the glass. hTERT fibroblasts were passaged onto the gel pads. The cells were counted at the 24 hour time point after washing with PBS, and immune stained with rhodamine phalloidin and DAPI (4', 6-diamidino-2-phenylindole) to

see if any cells were adhering to the hydrogel pads as the collagen concentration within the gels increased.

In Oslo the same collagen treated gels were tested on a human H2 ESC line (WiCell Inc., Detroit USA), with and without further treatment with ECM proteins (vitronectin and Matrigel®). The 3D patterned containers were then seeded with H2 hESCs to confirm the cells could adhere to the faces of the containers successfully, and ultimately to attempt to release the container and fold it into a 3D conformation with hESCs contained inside. The final stages of this chapter look at a proof of concept pilot study into what kind of topographical stimuli could in principle be applied to the inside walls of these 3D cellular niches, with the objective of differentiating the hESCs *in vitro*. Several established nanotopographies from the group including the NSQ, SQ and planar injection moulded surfaces from a previous study by Dalby et al. [39] on MSC differentiation into bone were tested. In addition to nanopit covered inserts, pillar arrays, comprising gradients of pillars with variable height, were used to investigate hESC affinity and colony size as a function of substrate feature height (Figure 5-1). These gradient arrays had previously been used to segregate cells by their respective type, based on cellular preferences on topographical cues [211].

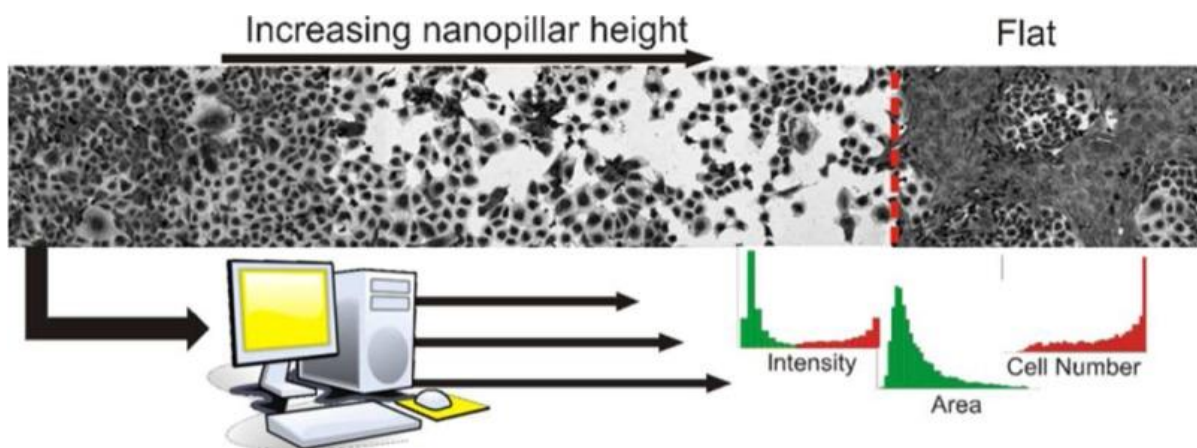


Figure 5-1 - A nanopillar gradient, where pillars increase in height along one axis of the 1cmx1cm pattern area. As a result of this topographical gradient cells selectively adhere to certain areas. This topographical preference was used to distinguish different cell types that would otherwise be difficult to identify. Images were analysed with cell profiler which output cell concentration, increases in a certain fluorescence probe over a region of pattern and overall cell number on particular areas of the gradient. Reproduced from Reynolds et al. [211].

Similarly to the gradient arrays, some ultra-high aspect ratio (UHAR) pillar arrays which simulated substrates with varying stiffness were also tested on hESCs to look for conformation changes as a function of substrate stiffness (as opposed to feature height previously). The relative stiffness at the pillar tips decreased with their overall height and thickness, which changed four times on one substrate (from tall and short pillars of 100 nm and 150 nm diameter), providing cells with four different substrate stiffness. The resulting cell attachment was quantified with cell profiler to give cell density and cluster size information, and thereby determine preferences amongst the

undifferentiated hESCs. The objective was to find clues as to what kind of stimuli dominated the differentiation processes of hESCs, as this had not been studied in this way previously. Should any successful topographical controls be found, these could then be incorporated into the walls of self-folding 3D cellular niches, provided these could release and fold in cell culture media at the correct time.

5.2 MATERIALS AND METHODS

5.2.1 Materials

All hESCs used in this study were H2 hESCs (WiCell Inc., Detroit USA) which were maintained at 37°C and 5 % CO₂ in feeder-free conditions in E8 culture Medium, with routine passaging performed at a 1:3 ratio using 0.5 mM EDTA or Acutase and ROCK-inhibitor (all Life Technologies, Oslo, Norway) in the case of cultures referred to as “single cell” seeded. qPCR markers for OCT4, SOX2 and NANOG FOXA2, MIXL, T, GSC and ACTB (Life Technologies, Norway) were used as received with TaqMan fast universal PCR master mix (Thermo Fisher Scientific, Oslo, Norway). DMSO 99.9 % (Sigma-Aldrich, Norway) was used in 1 v/v % working concentration in media. For differentiation of hESCs RPMI 1640 and B27 supplement, GlutaMAX, 2-mercaptoethanol, and MEM non-essential amino acids (all from Life Technologies, Oslo, Norway) were used with CHIR99021 (Stemgent, USA). hTERT fibroblasts (ATCC, UK) were obtained in P5 with a routine passage of 1:10 using Trypsin-Versene[®] solution with 500 mg/L litre Trypsin 1:250 and 200 mg/L Versene (EDTA) in PBS. hTERTs were cultured in DMEM complete media (all Life Technologies, UK) with added 100 µg/mL Penicillin and 100 µg/mL of Streptomycin. For fluorescence microscopy VECTASHIELD anti-fade mounting medium with DAPI (Vectorlabs, UK) and rhodamine phalloidin (Life Technologies, UK) were used. Sulfo-SANPAH crosslinker (Thermo Fisher Scientific, Oslo, Norway)

5.2.2 Cell freezing and defrosting

To facilitate continuity of the cell lines utilized during these experiments, early passages were stored at -80 °C in 10 % DMSO, in E8 or DMEM (depending on cell line, stem cells and fibroblasts respectively) and defrosted in their relevant media (E8 or DMEM complete) with frequent media changes, first three changes every 6 hours, followed by 12 hours followed by 24 hours as normal to remove residual DMSO.

5.2.3 Nano patterned insert preparation

To create surfaces for testing cellular responses to topographical cues, a high volume of nanopatterned surfaces was necessary for the relevant proliferation and phenotype studies. To achieve this high volume and consistency between samples nanopatterned surface substrates were

produced by injection moulding in polycarbonate (NSQ, FSQ and Planar) and (UHAR (polystyrene) and pillar gradient arrays (polycarbonate)) of which the specific pitch and feature size of the pattern arrays is described in previous publications by the BIG research group of the University of Glasgow [162, 185]. Samples were prepared by Paul Reynolds and Johnny Stormonth-Darling of the BIG research group.

Prior to use, nanopatterned inserts were placed in a 6-well Corning cell culture tray. The tray was illuminated with UV for 10 minutes for sterilization, Inserts were then coated with vitronectin or Matrigel® (section 5.2.6). The rhVTN or Matrigel plating was then aspirated and the surface was seeded with cells using a dry-plating technique (Cells applied in a drop seated on the patterned region, the well was only fully filled with media 12 hours after cell seeding to aid attachment to the substrate) which limits cell attachment outside the patterned insert. Various dilution concentrations and surfaces were tested with both to identify both minimum plating requirements for future box constituent materials, but also the stem cell morphological behaviour when seeded on various surfaces. Matrigel is a blend of ECM proteins and does not have a precisely ordered or controllable ligand type, but offers a versatile base for attaching stem cells to a variety of substrates without the use of a feeder layer. It offers a wide variety of ECM proteins for the attachment of cells which are known to be difficult to adhere, and have a specific or unknown preference for certain ECM binding sites. However inevitable batch variation and uncertainty as to proportional quantities of select binding proteins means that repeatability and full environmental control are difficult. Vitronectin is a key ECM binding protein and has the advantage of being known and quantifiable so the amount of binding sites and coating density can be more precisely controlled.

5.2.4 Contact angle

Contact angle analysis of polycarbonate inserts with and without nanotopographical patterning was carried out in the same manner as outlined in Chapter 3. It was postulated that contact angle could have an effect on plated vitronectin density which is necessary for cell adhesion. For each pattern type 3 copies of each substrate were measured four times to obtain a mean contact angle value for NSQ, SQ and flat surface topographies.

5.2.5 Matrigel coating

The presence of ECM proteins is necessary for cellular attachment to surfaces, and would certainly be necessary if cells were to adhere to the patterned surfaces of the aforementioned 2D inserts and 3D container walls. Matrigel is a mix of ECM proteins which offers a convenient but non-specific cover-all of possible ECM binding sites. The plating procedure for Matrigel was done in media at reduced temperatures to avoid a sol-gel transition of the Matrigel: plates were coated with a 1:48

dilution in Advanced DMEM-F12 (Life Technologies) and incubated at 37 °C and 5 % CO₂ for 1 hour prior to use [172], the full protocol was as follows:

1. Matrigel (Geltrex - Life Technologies) was kept cool at 4 °C and separated into 1 ml aliquots.
2. Each 1 ml aliquot was combined with 23 ml of Gibco DMEM Advanced F12 (Life Technologies, Oslo, Norway) to make a working plating solution.
3. Samples were separated to well trays to which plating media was applied (The plating volumes are outlined in the method for vitronectin plating above in Section 5.2.6).
4. The wells were incubated at 37 °C for 45 minutes.
5. Cells were passaged and 'dry-plated' directly onto the Matrigel[®] coated inserts and incubated for 1 hour at 37 °C with further media added to fill the well once the cells had adhered to the insert surface. This is done to prevent cells being swept off the patterned inserts.

In the case of fast swelling gel scaffolds on glass, the gel sheet was first immobilized by the application of a stainless steel ring to pin it down, the ring was present until plating and seeding were complete, at which point the ring could be removed and the cell sheet allowed to roll into its 3D conformation.

5.2.6 Vitronectin coating

Vitronectin was one of the ECM proteins tested for hESC adhesion to nanopatterned surfaces, it offers an advantage to Matrigel by being of known composition, and was a standard ECM coating used in the culture of hESCs on tissue culture plastic at the lab at the University of Oslo. The truncated recombinant human vitronectin (rhVTN-N) purified from inclusion bodies and refolded for use as a substrate for the feeder free culture was obtained from Life Technologies, UK. The vitronectin thawed at room temperature and was split into 60 µL aliquots, then frozen at -80°C. For plating, 60 µL of thawed rhVTN was diluted into a 15 mL conical tube containing 6 mL of sterile DPBS at room temperature and re-suspended by pipetting. This results a concentration of 5 µg/mL which is split further to create a dilution series. 0.5 mL of the diluted rhVTN solution is then gently pipetted to the centre of each insert (Inserts seated in individual wells of a 6-well plate), covering the nanopattern and producing a droplet of roughly 18 mm in diameter and a coating area of 2.54 cm².

1. Coated plates incubated at room temperature for 1 hour.
2. Vitronectin solution aspirated and discarded.
3. Cells passaged directly onto the vitronectin-coated substrates.

For hydrogel samples (process the same for Matrigel plating, section **Error! Reference source not found.**); when coating vitronectin, anchoring of the scaffold is necessary to prevent premature separation from their glass carrier slide, as the plating takes place in PBS solution which is well above the pK_a of poly(acrylic acid) and poly(methacrylic acid), resulting in rapid swelling and folding. The anchoring was done by placing an autoclave sterilized titanium washer (ID: 4mm) over the corners of the hydrogel sheet, to pin it down for plating and subsequent cell seeding. The optimal working concentration of vitronectin is more critical for ESCs than other cells, as mentioned in Chapter 1, and has to be adjusted depending on surface area being coated. A median concentration of 0.5 µg/cm² was used as a baseline for TCP as suggested by Life Technologies, UK. Where for nanopatterned surfaces the dilutions are adjusted based on the stock concentration and the area needing plated, where:

$$C_w = C_p \times \frac{A}{V} \quad \text{and} \quad F_D = \frac{C_S}{C_w} \quad \text{Eq. 5-1}$$

C_w , C_C , C_S are the working, plating and stock concentrations respectively, F_D is the dilution factor, A is the surface area to be coated and V the required volume of plating solution. The optimal working concentration of vitronectin is cell line and substrate dependent, ranging from concentration of 1 µg/cm² on TCP surfaces and dropping to 0.01 µg/cm² on nanopatterned substrates as will be shown further in this chapter (section 5.3.4.3). A working concentration of vitronectin was made using the formula below to dilute the stock into subsequent aliquots (Table 5-1). Adjusting this for the droplet volume used to cover an injection moulded nanopatterned insert:

$$\text{Working Concentration} = \text{Coating Concentration(Insert)} \times \frac{2.54 \text{ cm}^2}{0.5 \text{ ml}} \quad \text{Eq. 5-2}$$

Table 5-1 - Vitronectin dissolved concentration with concentration per unit area and effective dilution ratio from working stock.

Working Concentration µg/ml	Coating Concentration µg/cm ²	Dilution Factor
5	1	100x
2.5	0.5	200x
1	0.2	500x
0.5	0.1	1000x
0.25	0.05	2000x
0.1	0.02	5000x
0.05	0.01	10000x

The dilution series was used to reduce the plating quantities necessary on nanopatterned topographies when compared with planar surfaces as will be demonstrated later. This is in part due to the smaller surface area of the insert requiring less media, but even at similar dispensations nanopatterned inserts appear to show better cell attachment.

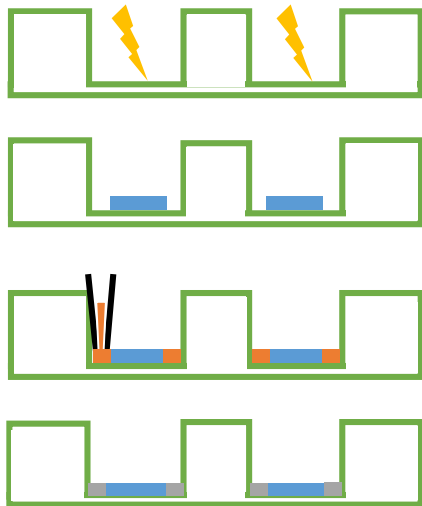
5.2.7 Sulfo-SANPAH modification of hydrogel rolls

Due to a concern that the ECM proteins would adhere poorly to both the polymer inserts and especially the protein non-binding PEG the use of a commercial crosslinker for ECM attachment was trialled in the hope that this would improve cell attachment. Sulfo-SANPAH crosslinker (Thermo Fisher Scientific, Oslo, Norway) is capable of tethering ECM proteins to a number of surfaces [212], and was tested as a means of attaching pendant ECM proteins to the surface of otherwise unadhesive PEGDMA hydrogel scaffolds, or improving plating ECM coverage and adhesion on injection moulded samples at lower concentrations of ECM protein. The method of using sulfo-SANPAH was [213]:

1. PEGDMA gel roll scaffolds in 6 well plates were soaked in HEPES or PBS for 24 hours prior to coating with 0.2 mg/ml of Sulfo-SANPAH which was dissolved in 50 nM HEPES buffer pH 8.5.
2. Roughly 0.5 ml of solution applied per well (6 well) or enough to cover the gel rolls in sulfo-SANPAH solution.
3. Well plate illuminated by UV source for 10 minutes to crosslink followed by rinsing with 1ml of 50 mM HEPES to eliminate unreacted S-SANPAH.
4. rhVTN or Matrigel dissolved in HEPES buffer or PBS was added to the wells and incubated overnight at 37 °C.
5. The wells were then washed with 1 ml of PBS twice and sterilized under UV hood for 10-20 minutes. Seeding of cells was done by the standard process described in section 5.2.9.

5.2.8 Anchoring inserts in 6-well trays with a cell repelling hydrogel

Injection moulded substrates were immobilized in a PEGDMA hydrogel cast within the wells of a 6 well TCP tray (Figure 5-2). This was done to limit wasted volume and prohibit cells from adhering outside the main patterned area, thus interfering with the qPCR markers, collected from insert and cells sitting on the planar TCP plastic underneath.



1. Polycarbonate 6 well exposed to Plasma (80 W – 20 sec) or exposed to 365 nm UV 180 W bulb (5-10 minutes)
2. Injection moulded inserts placed in wells.
3. Edges filled with 600 μ l of 90 % PEGDMA + 9 % EtOH + 1 % LTPO photoinitiator.
4. UV Cure for 10 minutes at 90 W (6 x 15 W tubes) – from High power trans-illuminator
5. Soak for 48 hours in PBS to remove unreacted initiator LTPO is toxic to cells. Cell friendly initiator I2959 can be substituted but may not bind styrene as LTPO, advised concentration is 2-3 w/v %.

Figure 5-2- Process tree for immobilizing injection moulded inserts in PEGDMA gel to limit wasted volume and create a cell repellent surface on periphery of injection moulded slides. Refer to Chapter 2 for ael formulations.

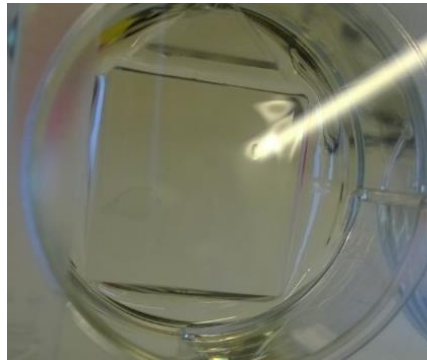


Figure 5-3 - PEGDMA fixated nanopatterned insert after 24 hours soaking in PBS, gel ends at edges of upper nanopatterned surface.

Well coating brings base of well to same level as sample height or more if excess is carefully added to well liquid onto sample. PEGDMA should not bind with Matrigel or vitronectin plating, preventing cell attachment. Optical clarity is improved for microscopy removing sample base/ media/ styrene well interference. Sample is fixed in place and cushioned, reducing movement (Figure 5-3). Less media is used in covering samples.

5.2.9 Cell seeding procedure

Cells were seeded in 4 quantities to find the optimum size of colonies for a two to three day culture period. Sufficient size is judged on the premise that a critical mass of cells is required for differentiation, which is short of confluence, but robust enough to undergo differentiation into definitive endoderm at later steps. This stage is hard to quantify and depends largely on the cell viability, and experienced judgment, typically a working concentration $\geq 200,000$ cells/ml is sufficient to get sustainable hESC colonies on Matrigel coated TCP 6 well plates. A conversion for the reduced seeding area of the injection moulded inserts is shown in Table 5-2.

Table 5-2 - Cells per unit area were adjusted for a standard 500ml drop of media covering an approximate area of 2.55 square centimetres based on observed average droplet diameter on injection moulded inserts.

Seeding solution concentration cells/ml	Seeded cells/cm ² when seeding on injection moulded slides
500,000	100,000
400,000	80,000
200,000	40,000
100,000	20,000

Seeding densities were adjusted to accommodate lack of attachment on poorly coated surfaces (Section 5.3.4.1). Two different passaging protocols were carried out to obtain these cell numbers, one after detachment of cells from substrate with EDTA and subsequent washing and re-suspension in media to then be seeded in clumps. The second protocol lifted the cells with Acutase and re-suspended after filtration and subsequent washing to separate colonies out into single cells. All passages were done in a 3:1 ratio, with one well of a 6 well plate providing sufficient cells to cover a further 3 well plates.

5.2.10 Initial screening with hTERT immortalized cell lines

Due to the expense of human embryonic stem cells (hESCs) and more so induced pluripotent stem cells (iPSCs), screening of the nanopatterned cell culture surfaces and hydrogels discussed in Chapter 1 was done using an easy to maintain and cheaper immortalized hTERT fibroblast cell line. hTERT fibroblasts were initially seeded on hydrogel rolls to test the hydrogel biocompatibility, by counting adhered cells after a 24 hour culture period. Counting was done manually with the substrate split into 1mm² hydrogel islands, the cell count was then averaged per island over the four gel types tested. In this proof of concept investigation; devices were immobilized in 2D on a glass slide to test doping of the hydrogel scaffolds with collagen (Rat tail – Sigma Aldrich, UK) to aid further ECM immobilization (Figure 5-4). Subsequent tests were performed using hESCs, which as described in Chapter 1. The preliminary attachment of hTERTs was used as a pilot study to judge the surface biocompatibility and look for markers of cytotoxicity prior to switching to the stem cell line.

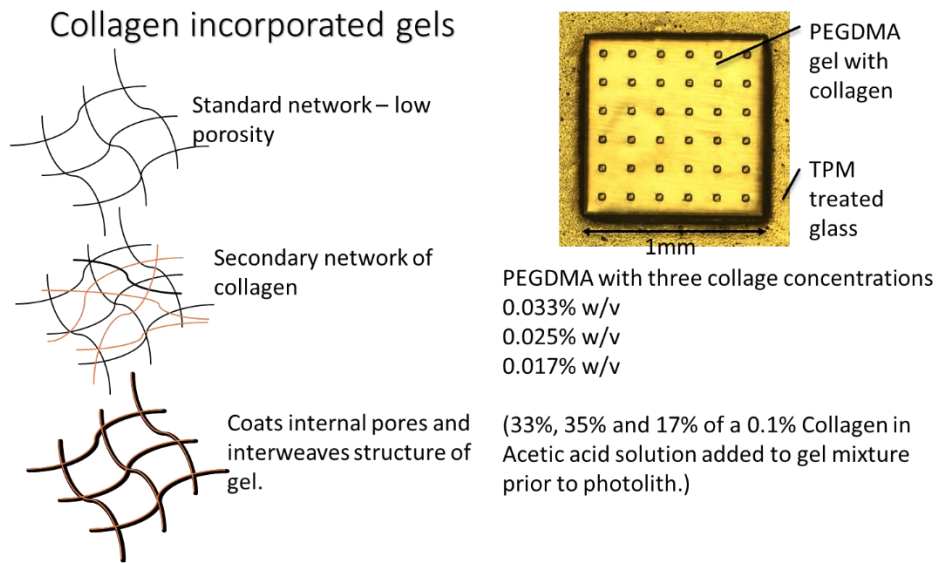


Figure 5-4 - Structure of hydrogel sheet with added dissolved collagen at three concentrations. Acetic acid solution contains 0.1 M acetic acid and collagen added to stated concentration. Gel mixtures had to be kept cool prior to photolithography to limit clumping and polymerization of collagen mixture.

To test cell adhesion to pure PEGDMA and collagen laden hydrogel scaffolds, sheets were fixed to glass substrates by a 3-(trichlorosilyl)propyl methacrylate (TPM) methacrylated silane based binding agent[113]. The resulting sheets were permanently bound to the surface of the glass allowing for cell seeding and long term proliferation studies.

5.2.11 hESC small molecules initiated differentiation into hepatocytes

Cells were seeded at between 80,000 and 40,000 cells/cm² onto the relevant substrate coated in vitronectin or Matrigel® inside a 6-well plate. This was done in E8 medium as before in a 1:3 split ratio and allowed to adhere for 24 hr at 37 °C and 5 % CO₂ prior to changing the media. An optimum cell density for each line needed to be established (up to 72 hours). Prior to changing to media containing small molecules in the form of the GSK-3 inhibitor CHIR99021 (Stemgent, USA), cells were washed three times with PBS before being treated with differentiation media in a well-established process adjusted for small molecules use and outlined in a recent paper by Siller et al.[172]. Differentiation of hESCs required media was swaps in three phases, of which two were attempted. For Phase 1 of differentiation RPMI 1640 GlutaMAX + B27 supplement, both from Life Technologies, Oslo, Norway plus 3–4 µM CHIR99021 (Stemgent, USA) were applied for a 24 hour period followed by RPMI-B27 alone for a further 24 hours to push the cells towards definitive endoderm. Phase 2 or the hepatic specification had a 5 day duration with DMEM containing 20 % knockout serum replacement, 2 mM GlutaMAX, 100 µM 2-mercaptoethanol, 1× MEM non-essential amino acids (Life Technologies, Oslo, Norway), and 1 % DMSO as the small molecule (Sigma-Aldrich, Norway). The small molecules stimulate the cells into a state of differentiation, only the initial two

stages of the three stages could be attempted during the limited time frame. The process is lengthy and in its full duration requires three stages over a longer time frame than could be attempted during the visit to Oslo. This approach and the subsequent results are a proof of concept to see how the process can be used with nanopatterned inserts and furthermore with nanopatterned self-folding 3D scaffolds.

5.2.12 cDNA preparation for Real Time - qPCR

To quantify cell gene expression with preliminary Real Time-qPCR cDNA was prepared using the High Capacity Reverse Transcription kit (Life Technologies, Oslo, Norway) and PCR thermo-cycler from collected RNA samples. RNA was first isolated from cells using TRIzol according to the manufacturer's instructions and quantified using a spectrophotometer (NanoDrop, Oslo, Norway). RNA was extracted as follows:

1. Cells were scraped into PBS and pelleted by centrifugation in a 1.5ml Eppendorf tube, with the supernatant removed manually by careful pipetting.
2. 1 ml of TRIzol[®] reagent was added to lyse the cells, which were re-suspended by pipetting.
3. The samples were incubated for 5 minutes at room temperature.
4. 0.2 mL of chloroform was added to the 1 mL of TRIzol[®] used for homogenization for 15s.
5. 3 minutes at room temperature incubation.
6. Samples were then centrifuged at 12000 × g for 15 minutes at 4°C.
7. The aqueous transparent phase of the sample was pipetted and moved to a new Eppendorf.
8. To precipitate the RNA, 0.5 mL of 100 % isopropanol was added to the aqueous phase and incubated at room temperature for 10 minutes.
9. The mixture was again centrifuged at 12000 × g for 10 minutes at 4°C.
10. The supernatant from the centrifugation step was removed by pipetting.
11. The RNA pellet that remained was washed with 1 mL of 75 % ethanol for every 1 mL of TRIzol[®] used in the initial homogenization step.
12. The sample was centrifuged at 7500 × g for 5 minutes at 4 °C and the supernatant discarded.
13. The RNA pellet was air dried for 5–10 minutes.
14. The washed RNA pellet was re-suspended in RNase-free water (20–50 µL depending on volume and quality) by pipetting followed by a vortex prior to testing, and after every subsequent defrost (to homogenize the solution).
15. The yield of RNA was determined using absorbance at 260 nm and 280 nm in a UV-VIS spectrophotometer (NanoDrop, Oslo Norway), with the absorbance was correlated to concentration.

cDNA was reverse-transcribed from RNA using a High Capacity Reverse Transcription kit and thermal cycler (Life Technologies, Oslo, Norway).

5.2.13 Real-time quantitative PCR

To determine cell gene expression and indications of cell phenotype after exposure to nanopatterned surfaces, real-time quantitative PCR (RT-qPCR) was performed using RNA reverse-transcribed to cDNA with a TaqMan VIIA 7 Real Time PCR system using Taqman Fast reagents and TaqMan Gene Expression Master Mix (Life Technologies, Oslo, Norway). The cDNA was diluted to a standardized concentration (Section 5.2.12). TaqMan assays were used to assess markers of interest with three replicates per normalized against an *ACTB* Actin endogenous control (i.e. three cell culture samples being studied for *OCT4* levels would require 9 wells total with *OCT4* hybridization reagents and fluorescent probes). The diluted cDNA was mixed in a 96 well with a polymerase and fluorescent probe marker, as the 96 well tray cycled through ramping temperature cycles, a polymerase chain-reaction took place, increasing the fluorescent signal in each well, the cycle at which the reaction begins to accelerate indicates the concentration of the target mRNA expression amongst the cells harvested in that sample (**Error! Reference source not found.**). *ACTB* Actin was used as the endogenous control in all tests, with data normalized against H2 seeded undifferentiated cells on tissue culture plastic (TCP). The expression levels were calculated using the $\Delta\Delta C_T$ method for relative quantification, output from the VIIA 7 software. The melt curves for the TaqMan primers and gels are not available to verify product sizes. Primer efficiency was determined for each primer (found to be in the range of 95-100 %) and accounted for in the determination of RQ.

5.2.14 Estimating substrate stiffness of tall pillar arrays

An injection moulded array of ultra-high aspect ratio pillars (UHAR) were manufactured by injection moulding [185] to perform cell substrate interaction studies on substrates with effectively varying stiffness. The inlays were 2cm² with 4mm² arrays of four pillar sets with varied height and thickness (Figure 5-5). The adjustment of the pillar aspect ratio allows for a fine tuning of the deflection at the pillar tip when it is subject to a load, thus emulating a bulk material substantially less stiff than that of the injection moulding material (polystyrene).

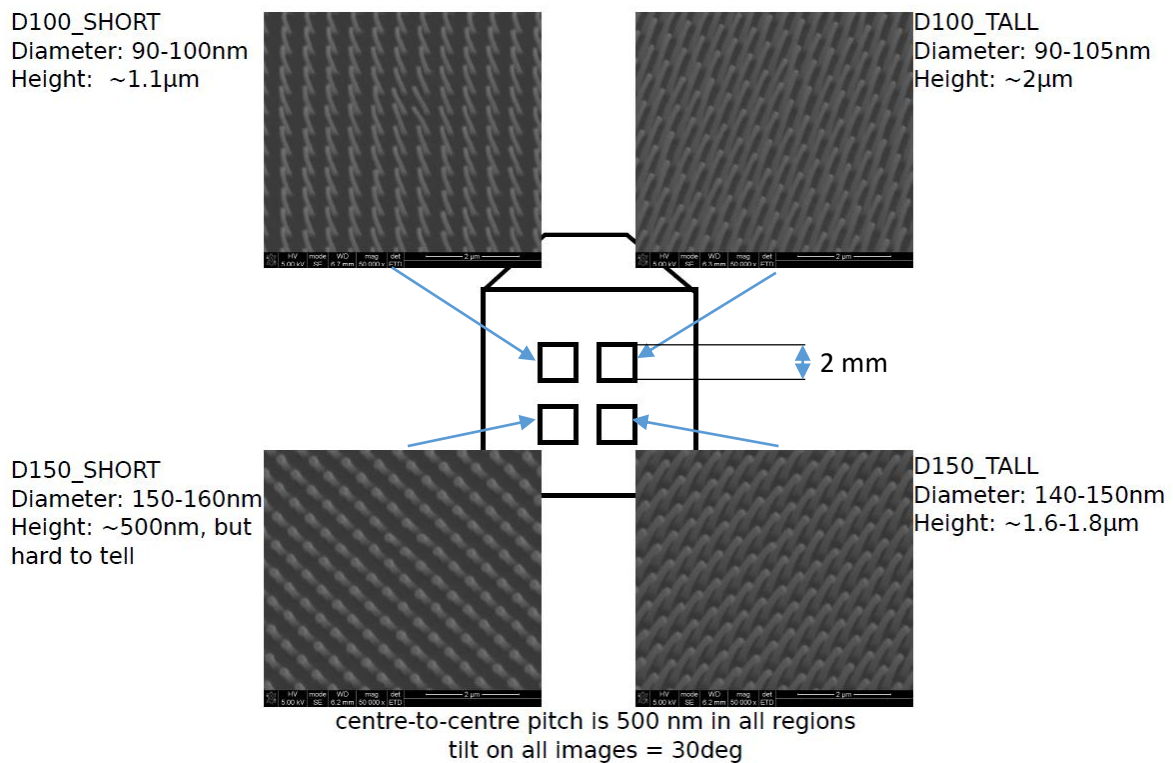


Figure 5-5 – UHAR Pillars and insert arrangement produced by injection moulding in polystyrene (PS) using the technique of Stormonth-Darling et al. [185].

The pillar compliance was estimated using the standard cantilever beam deflection equations [197]. Assuming small deflections and linear elasticity the displacement at the UHAR pillar tip can be defined as:

$$\delta = \frac{FL^2}{2EI} \quad \text{Eq. 5- 3}$$

Where F is the force, L is the length of the beam, E is the Young's modulus and I is the second moment of area. The deflection angle of the pillar tip:

$$\theta = \frac{FL^3}{3EI} \quad \text{Eq. 5- 4}$$

Polystyrene has a Young's modulus E of 3.25 GPa, and Poisson's ratio of 0.35 [214] with the other factors derived for the pillar geometry. The area moment of inertia for a circular cross section is [197]:

$$I_x = \frac{\pi}{4} r^4 \quad \text{Eq. 5- 5}$$

Table 5-3 - UHAR pillar array dimensions from SEM imaging measurements.

Pillar type	Height (m)	Diameter (m)	Area moment of inertia (m ⁴)
D150 Short	5×10^{-7}	1.5×10^{-7}	2.485×10^{-29}
D100 Short	1.1×10^{-6}	1×10^{-7}	4.909×10^{-30}
D150 Tall	1.7×10^{-6}	1.5×10^{-7}	2.485×10^{-29}
D100 Tall	2×10^{-6}	1×10^{-7}	4.909×10^{-30}

Assuming that $F = k \cdot \delta$ where δ is the displacement of the pillar top and k is the equivalent stiffness if the cantilever were to be represented as tension spring. This only takes into account the bending at the pillar base [215] with k_{bend} for a bottom fixed elastic cantilever of circular cross-section in pure bending defined as:

$$k_{bend} = \frac{3\pi E D^4}{64 L^3} \quad \text{Eq. 5- 6}$$

However according to Schoen et al.[215]; accounting for shear, tilt and base displacement yields more accurate results for soft substrates:

$$\delta = \delta_{bend} + \delta_{tilt} + \delta_{shear} + \delta_{base} \quad \text{Eq. 5- 7}$$

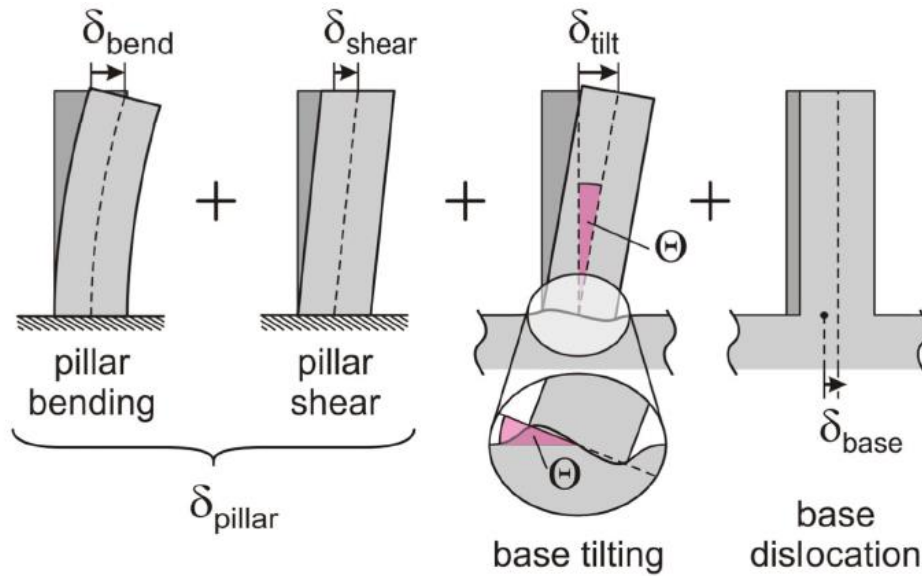


Figure 5-6- Different components responsible for overall deflection of anchored pillars. Reproduced from Schoen et al. [215]

Inserting the notation produced by Schoen et al.[215] separates the total tip deflection into its components (Figure 5-6). The effective spring constant k_t of an elastically founded pillar is then found from the constant of pure bending k_{bend} multiplied by a geometric correction factor $Corr$ [215] defined as:

$$Corr = \frac{\frac{16}{3} \left(\frac{L}{\varnothing}\right)^3}{\frac{16}{3} \left(\frac{L}{\varnothing}\right)^3 + \frac{7+6\nu}{3} \left(\frac{L}{\varnothing}\right) + 8T_{tilt}(\nu) \left(\frac{L}{\varnothing}\right)^2} \quad Eq. 5-8$$

Where the tilting coefficient T corrects for the amount of substrate tilt when a force is applied to the pillar tip.

$$T_{tilt}(\nu) = \theta \cdot \frac{E}{\sigma_{max}} = a \frac{(1-\nu)}{2\pi} \left\{ 2(1-\nu) + \left(1 - \frac{1}{4(1-\nu)} \right) \right\} \quad Eq. 5-9$$

A plot of the dependence of substrate Poisson's ratio to the tilt component of pillar deflection is shown in Figure 5-7.

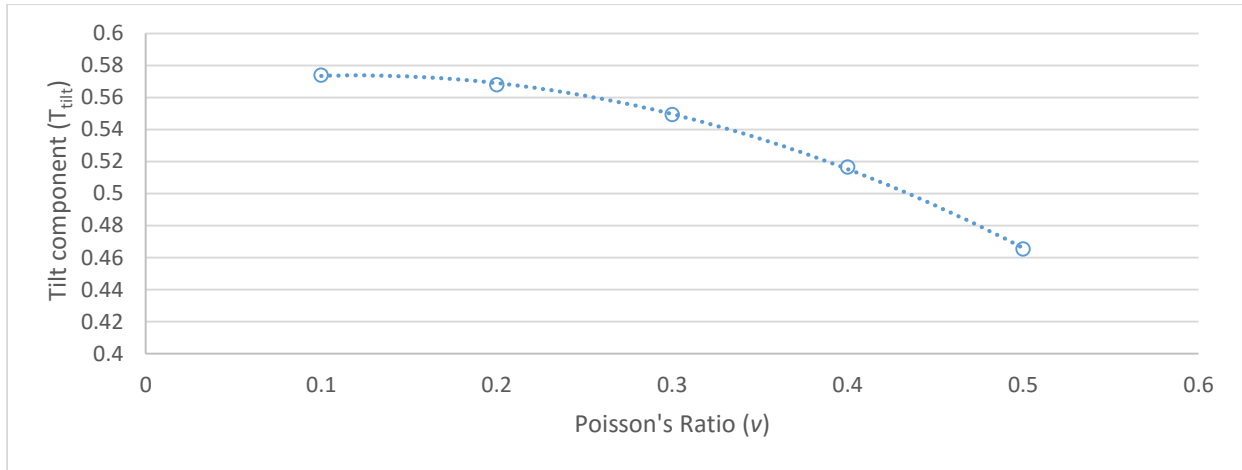


Figure 5-7 - Tilt correction factor with respect to substrate Poisson's ratio. Tilt significantly reduced in rubbery materials (where ν tends to 0.5).

The fitting parameter is specified as $a = 1.3$ for the pillar geometry [215] although the pillars are substantially thinner than those analysed by Schoen et al. [215], the parameter is consistent given the aspect ratio similarity between their work and those pillars used in the UHAR study in this work. Incorporating these terms provides a corrective factor for pillar deflection [215] to account for substrate interaction with true stiffness k_t :

$$k_t = \text{corr} \cdot k_{\text{bend}} \quad \text{Eq. 5- 10}$$

The pillar stiffness equation then becomes the combined notation, incorporating a tilt and shear component of the pillar deflection:

$$F = k_t \cdot \delta \quad \text{Eq. 5- 11}$$

The resulting plots of stiffness as well as extrapolations of the stiffness with pillar height and diameter are given in the next section.

5.2.14.1 Estimating pillar array stiffness using COMSOL® multiphysics simulation

Pillars were modelled in COMSOL® 4.2a a finite element multi-physics package to confirm empirically derived stiffness values. The pillars were represented in a static loading study. Output was recorded as a linear elastic deformation for load step of 10nN applied to the pillar tips while the base was considered an encasté boundary as substrate tilt is not expected in stiffer materials such as polystyrene with the results shown in Table 5-5 (page 257).

5.2.15 Quantifying cell colony size and area coverage with Cell profiler™

H2 hESC colonies, and overall cell coverage were analysed with Cell Profiler™ for trends in cluster size in relation to the substrate topography, as well as to quantify cell attachment and proliferation. A pipeline was used to sort images (Figure 5-8), pre-set with the relevant background correction and

threshold to identify cell covered areas. This information was then output as either cluster size with centroid location, or for confluent topographies, as percentage area coverage (Figure 5-9). The confluence and size of colonies was stipulated to correlate to how easy it was for hESCs to thrive on a given surface at a discrete time interval after passage.

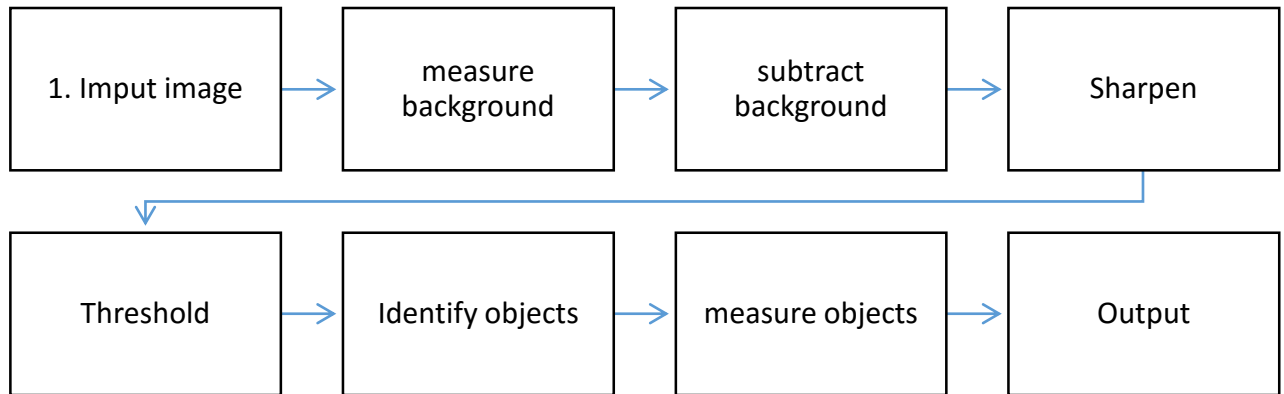


Figure 5-8 - Cell profiler pipeline tree for hESCs colony cluster analysis, and cell area coverage analysis.

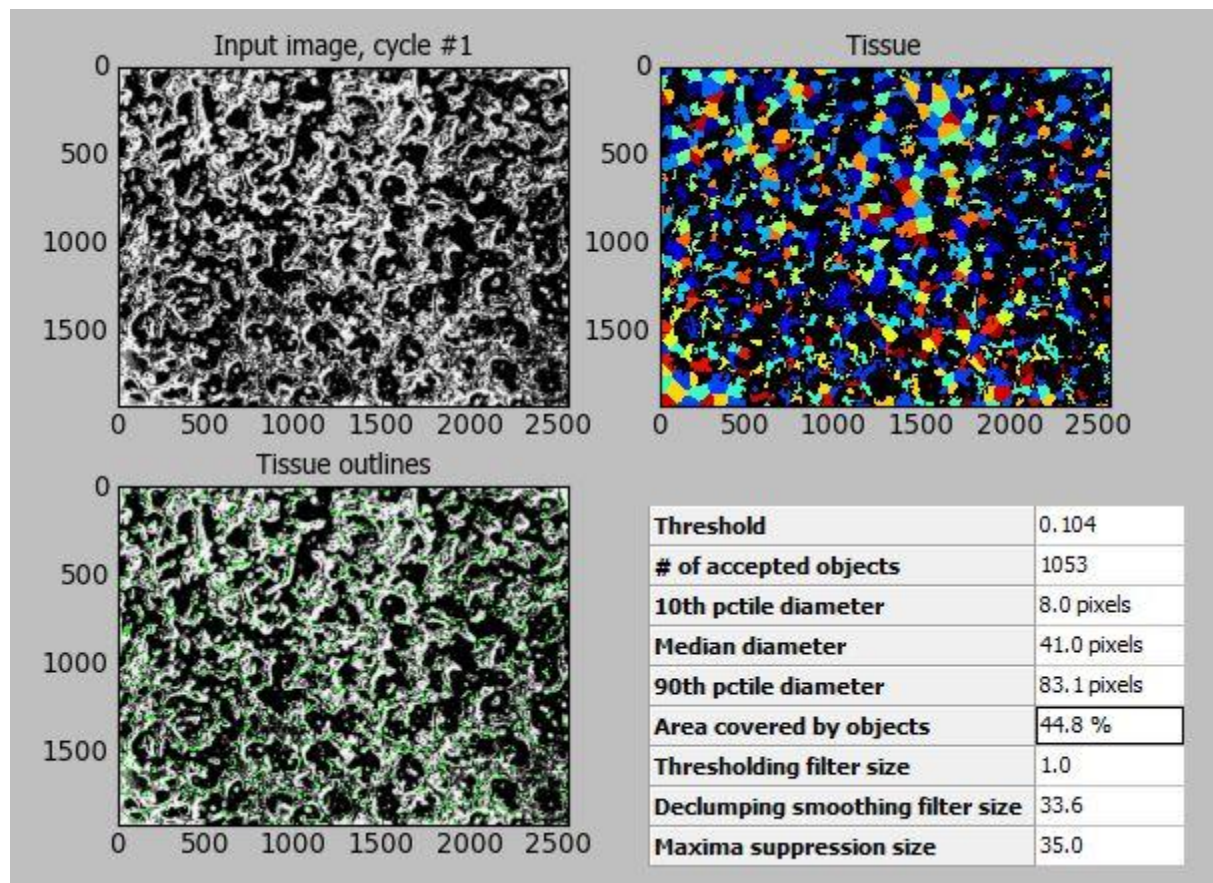


Figure 5-9 - Area coverage output and the threshold mask image after background subtraction and the subsequent edge identification and area segregation to calculate the total area covered by hESC colonies. Field of view is 1800x2200 μm , area coverage worked out as contrast between occupied and empty pixels.

To optimize the cell seeding and ECM plating densities area coverage data was then correlated to vitronectin coating concentration for those particular substrates (NSQ, FSQ and Planar). In the case of the nanopillar gradient arrays, due to their relatively large area in relation to the microscope field of view; an aggregate was made of 12 sets of low magnification 4x images taken across the gradient pattern and analysed with Cell Profiler™ to identify correlations in cell coverage shown in Figure 5-10.

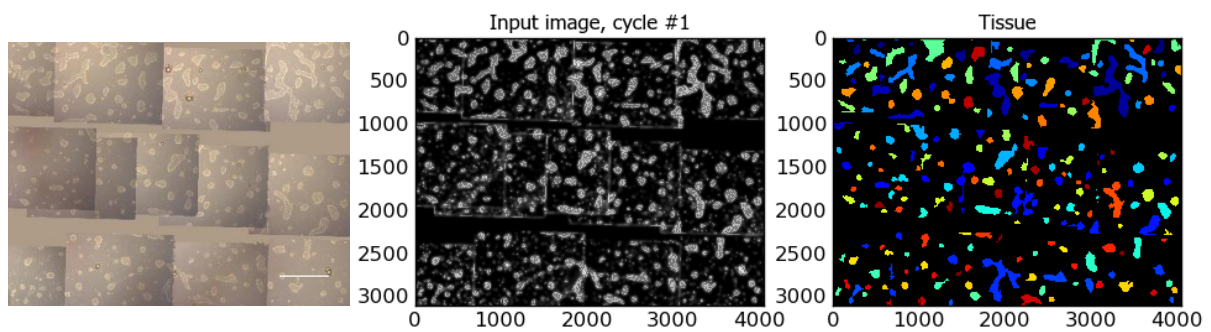


Figure 5-10 - Left to right: Original microscopy montage of images spanning the nanopillar gradient (bottom to top, from highest to lowest), Centre: Threshold applied to identify cell clusters, Right: Individual cell colony clusters identified. Scale in pixels, x axis distance 9mm. Scale bar: 1mm

5.3 RESULTS

5.3.1 Contact angle

Topographies were analysed by water contact angle measurement to identify changes in surface wetting as an indicator of their suitability for cell and protein adhesion. The polycarbonate inserts used in all the subsequent cell studies showed an increased contact angle on nanopatterned substrates when compared to planar surfaces, as would be expected for the reduced wetted area on patterned surfaces (Figure 5-11).

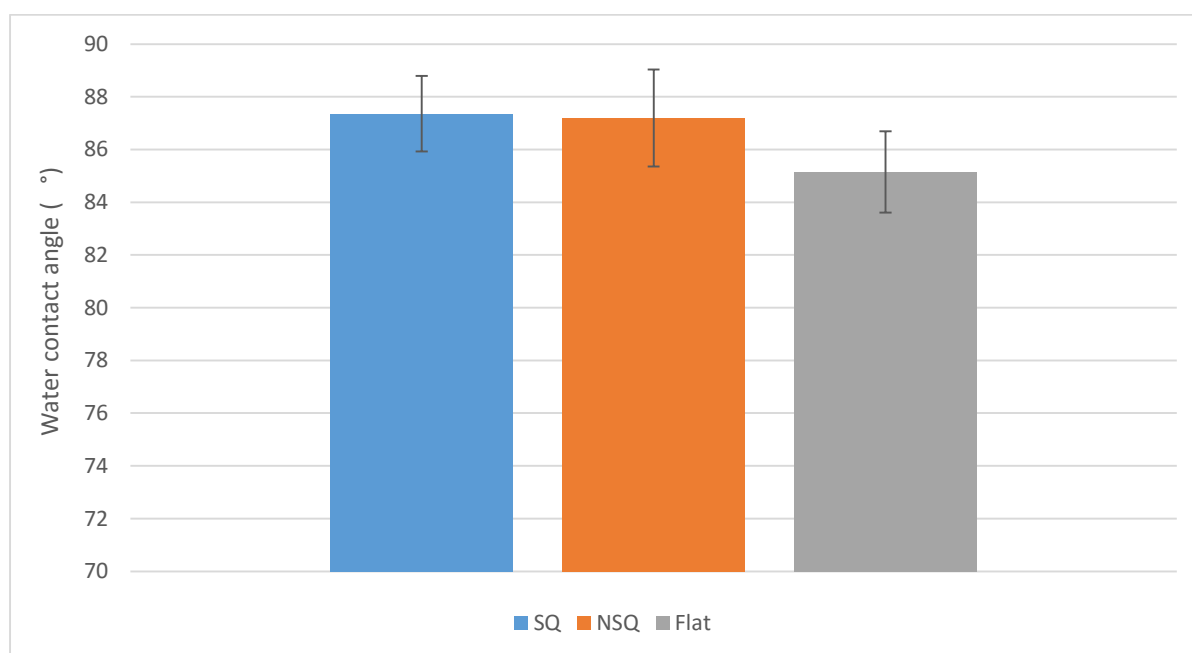


Figure 5-11 - Contact angles of injection moulded (IM) nanopatterned polycarbonate substrates covered with Full Square (FSQ), Near-Square (NSQ 50) topographies and planar control. Error bars SD from 15 measurements.

The wetting of the substrates was to ascertain the ability for hESCs to settle on the fabricated self-folding tissue scaffolds outlined in Chapter 4, as both FSQ, NSQ would later be applied to the container surfaces. The wettability of SU8 was found to improve drastically after ashing and retained this for a prolonged period depending on the ash extent (Table 5-4).

Table 5-4 – Water contact angles on SU8 before and after plasma ashing for 20 s at 80 W (n=12).

Material	Contact angle (°)
SU8 Planar	87.55 ± 18.35
SU8 Planar 24 hours post ash	7.06 ± 5.16
SU8 Planar 48 hours post ash	18.37 ± 8.98

5.3.2 Fibroblast attachment to hydrogel surfaces

Before the devices are used on more expensive and difficult to culture cell types, the adhesion and materials they incorporate were tested using human fibroblast hTERT cells. These cells are immortalized, grow quickly and adhere to many surfaces, making them a good test subject to determine the adhesion and cytotoxic effects of the hydrogel and structural materials comprising the 3D self-folding containers, it is assumed that while hESCs are known to be much more difficult to culture that the fibroblast hTERTs were a good starting point for initial testing.

To enable the adhesion of embryonic stem cells, the surfaces of any scaffold need to be treated with ECM like proteins or peptides to allow for cell attachment. ESCs are known to not stick easily to substrates and usually require Matrigel® coatings or feeder layers [172]. The problem of adhesion with PEG and HEMA hydrogels only exacerbates this issue as these gels are known for being cell repellent by not immobilizing the native ECM. A collagen treatment of PEGDMA gels was attempted by mixing a 0.1 v/v % collagen/acetic acid solution into the pre-polymer at various levels, to both increase porosity and permeability, but also to line the gel with something into which the cell can be immobilized. The concentrations were 33, 25 and 17 % (0.1 v/v % collagen in acetic acid) in the pre-polymer mixture prior to photolithography, this is slightly higher than that used for coating cell culture dishes. Gels were patterned into individual 1mm square islands with 100 µm pits to see if cells landed simply by fluid entrapment or actual attachment onto the island surface. While being a significantly cheaper method to make gels cell adhesive than RGD immobilization by pegylation, or by the use of SULFO-SANPAH, the dilution of collagen offers a workable modification to peg based hydrogels to immobilize fibroblasts. The culture of cells on hydrogels showed a contrast to cells grown on solid substrates however, with cells in a much tighter conformation and in much lower numbers, this could be due to the mechanical properties of the gel, compounded by the normal difficulty of adhering to PEGDMA and HEMA based gels.

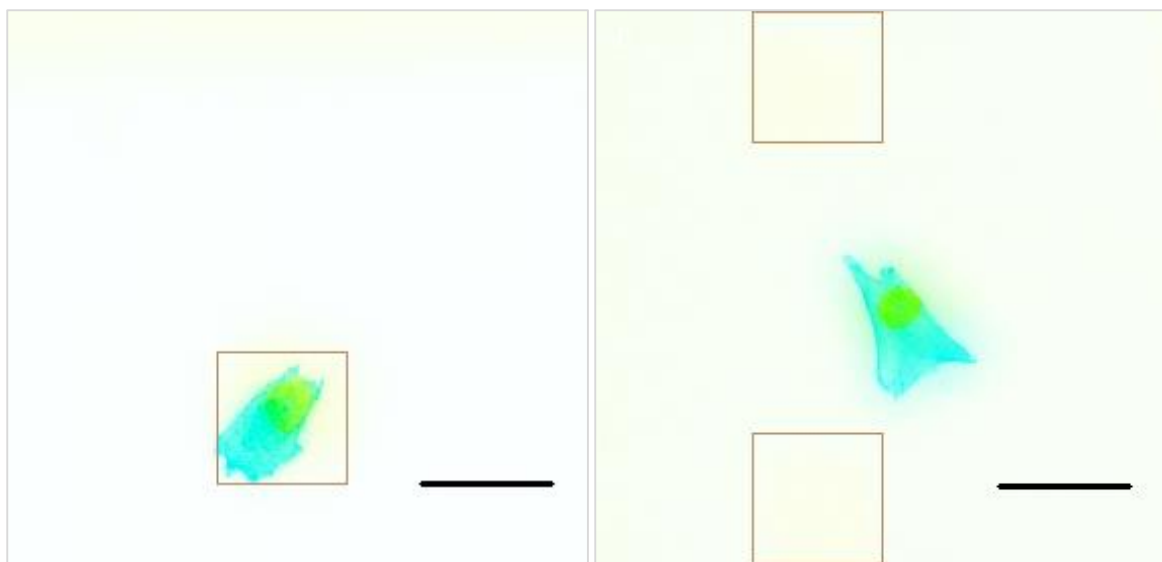


Figure 5-12 - Cells stained with DAPI and phalloidin, attached to a collagen modified PEGDMA hydrogel sheet. (A): Cell has fallen into window of hydrogel sheet appearing more compacted, (B) Cell spreading on solid hydrogel section. Cells seeded at 10,000 cells/cm². Boxes are photolithographically defined windows in the hydrogel sheet. Scale bars 100 μm.

hTERT fibroblasts cultured on hydrogels showed similar levels of elongation across all collagen treatments but the number of viable cells attached on the hydrogel islands showed a trend of improvement with collagen concentration (Figure 5-13), suggesting that this method could work to modify the surfaces for cell attachment. Future modifications used Matrigel® and vitronectin plating based surface modification. hTERT fibroblasts cultured on gels showed a significant increase in cell attachment when collagen is applied to the pre-polymer, expressed mostly in a jump in the numbers of successfully attached cells.

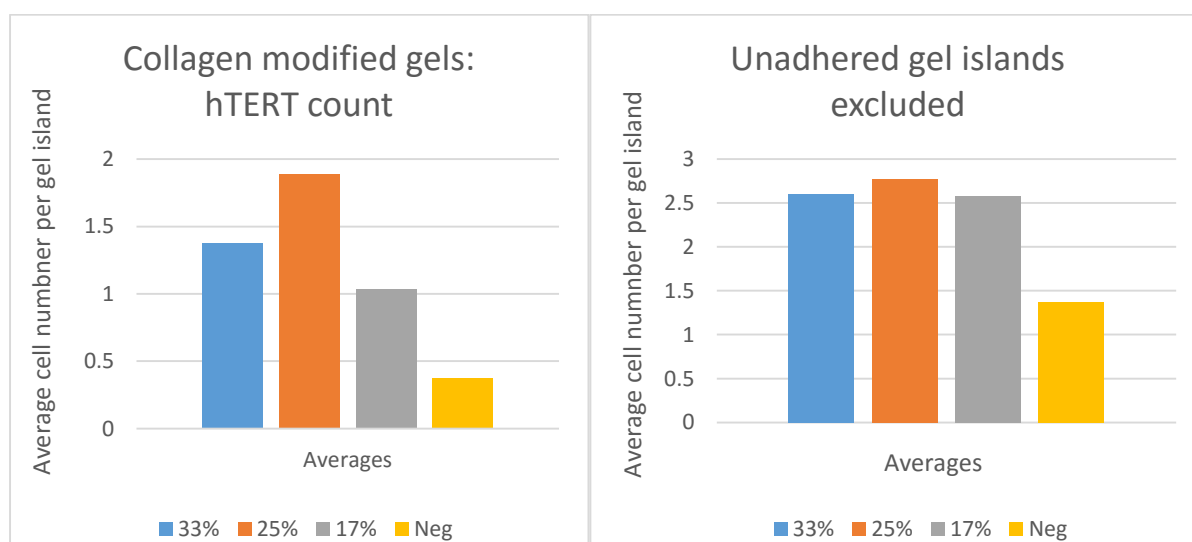


Figure 5-13 - Average hTERT fibroblast count per hydrogel square on 100 square array, with various degrees of collagen modification in the pre-polymer. Fibroblasts seeded at 10,000 cells/cm² and counted manually after 24 hours of incubation in DMEM media. All hydrogel surfaces were soaked for 24 hours in PBS and 12 hours in DMEM prior to seeding of cells. Unmodified PEGDMA gel used as negative control. Only one replicate was run as a pilot study.

5.3.3 Fibroblast attachment to SU8 epoxy surfaces

Unlike the hydrogel surfaces where increasing the concentration of collagen in the hydrogel films improved the visible cell adhesion, the SU8 epoxy surfaces showed an overwhelming improvement in attachment and proliferation of hTERT fibroblasts simply by ashing (Figure 5-14). Cell adhesion was improved by a post ash of SU8 surfaces for 20 seconds at 80 W resulting in reduced contact angle (Table 5-4) This is thought to be due to increased surface roughness according to work by Vernekar et al. [216].

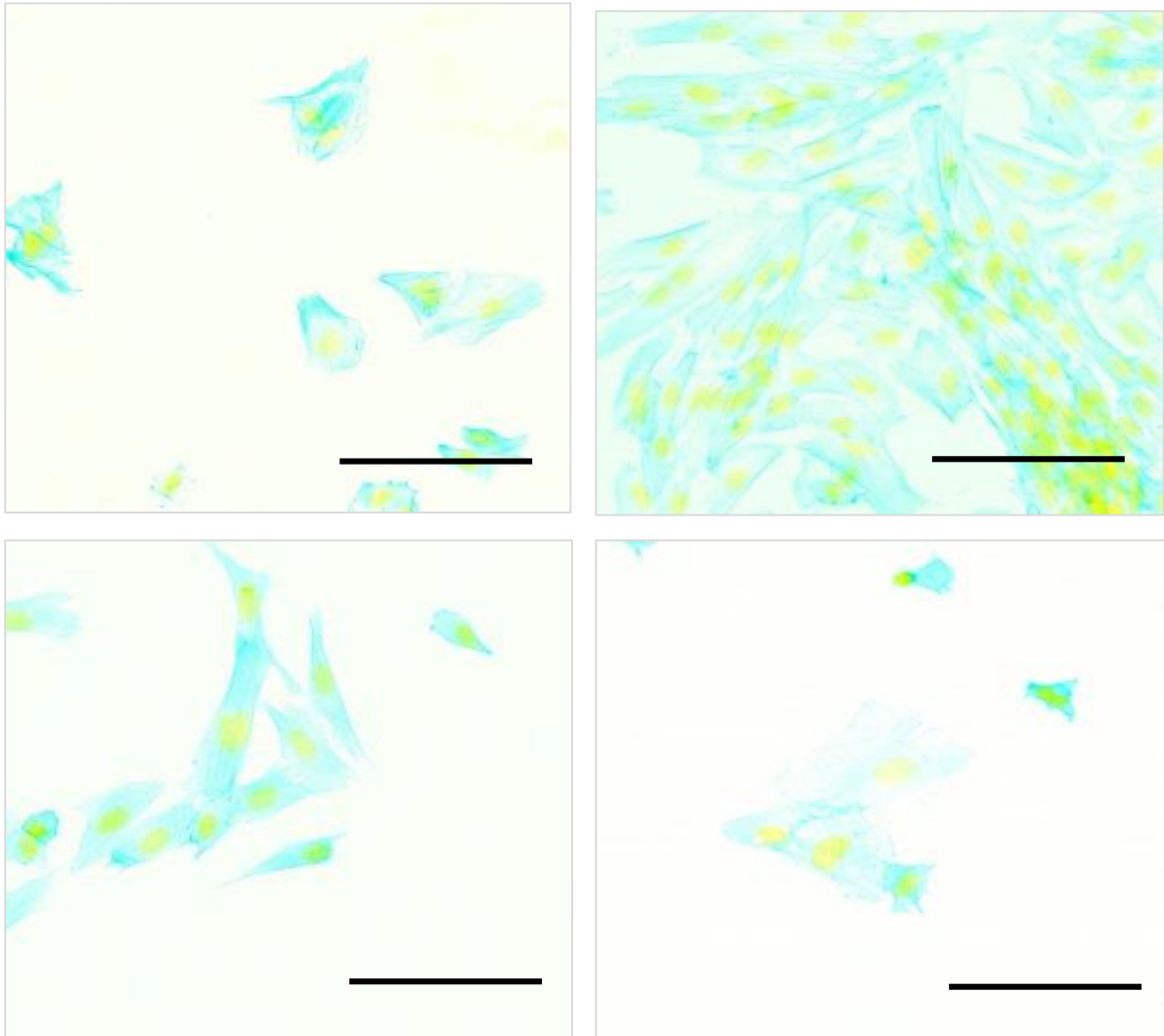


Figure 5-14 – hTERT fibroblasts stained with DAPI (green) and phalloidin (teal) attached to (A) SU8 surfaces patterned with NSQ50 patterned nanopits, (B) SU8 simply ashed for 30 seconds at 80W in O₂ plasma, (C) SU8 patterned with FSQ nanopits and (D) SU8 patterned with a randomized series of nanopits. Untreated SU8 without patterns showed very poor cell attachment after 24 hours. Scale bars: 200 μ m.

5.3.4 hESC proliferation on patterned surfaces

5.3.4.1 Effect of Rock inhibitor on hESC survival and proliferation

The hESCs used (H2 cell line) preferentially form clusters in absence of Rho-associated protein kinase inhibitor (ROCK-i) with size playing large role in 48 hour viability, smaller clusters and individual cells quickly undergo apoptosis [9, 172]. The behaviour was irrespective of substrate pattern and was consistent on all substrates used including polycarbonate culture plastic and planar injection moulded polycarbonate. Comparisons of normal seeding protocol was carried out, where tissue was passaged and redistributed without ROCK-i, resulting in cell proximity and colony size as the key factor for cell survival.

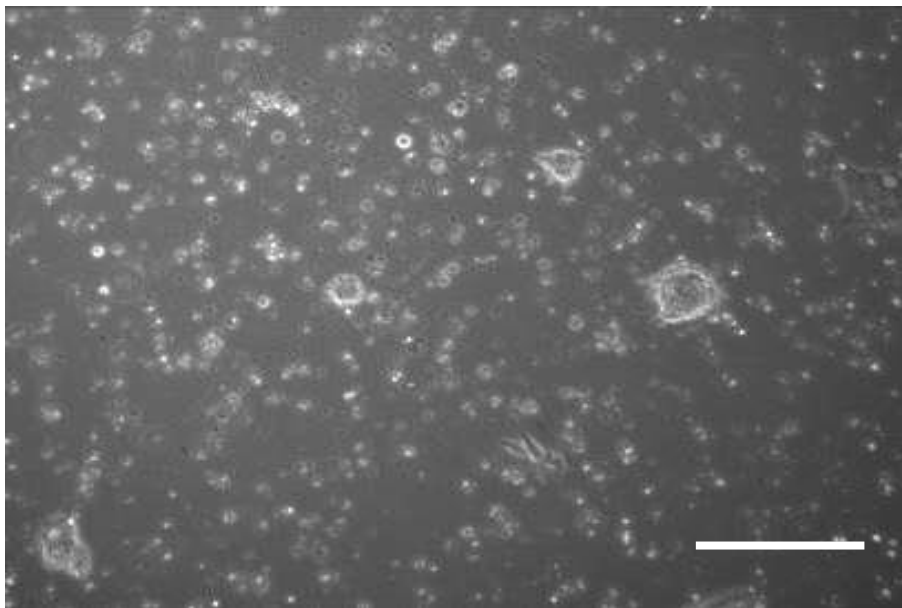


Figure 5-15 – H2 hESCs seeded as clumps on Matrigel coated FSQ surface. Cells seeded at roughly 20,000 cells/cm² and cultured in Advanced DMEM. Phase contrast microscopy. Scale bars 600 μ m

5.3.4.2 hESC morphology changes with ECM density

To identify the minimum possible ECM concentration on nanopatterned substrates, a factorial concentration series was used. The comparison of single-cell and clump seeding protocols demonstrated morphological and coverage differences between hESCs seeded on Matrigel[®] and Vitronectin coated surfaces at the maximum of 20,000 cells/cm². Cell distribution was more uniform when seeding ‘single cells’, and allowed for a more controlled coverage of the nanopatterned substrates. Minor differences were seen in subsequent cell density on the different topographies but this can be attributed to differences in cell concentration, fluid flow artefacts and sample defects, as well as a lack of data points for quantifying full substrate coverage. However a distinct difference was observed between ‘planar’ non-patterned inserts and those with a nanopit array, this is attributed to lower ECM conformation to planar surfaces, and discussed in the subsequent sections.

The difference in cell viability lead to the later study of minimum ECM concentration on patterned and non-patterned surfaces, with a hundred-fold improvement in ECM adhesion on artificially roughened surfaces.

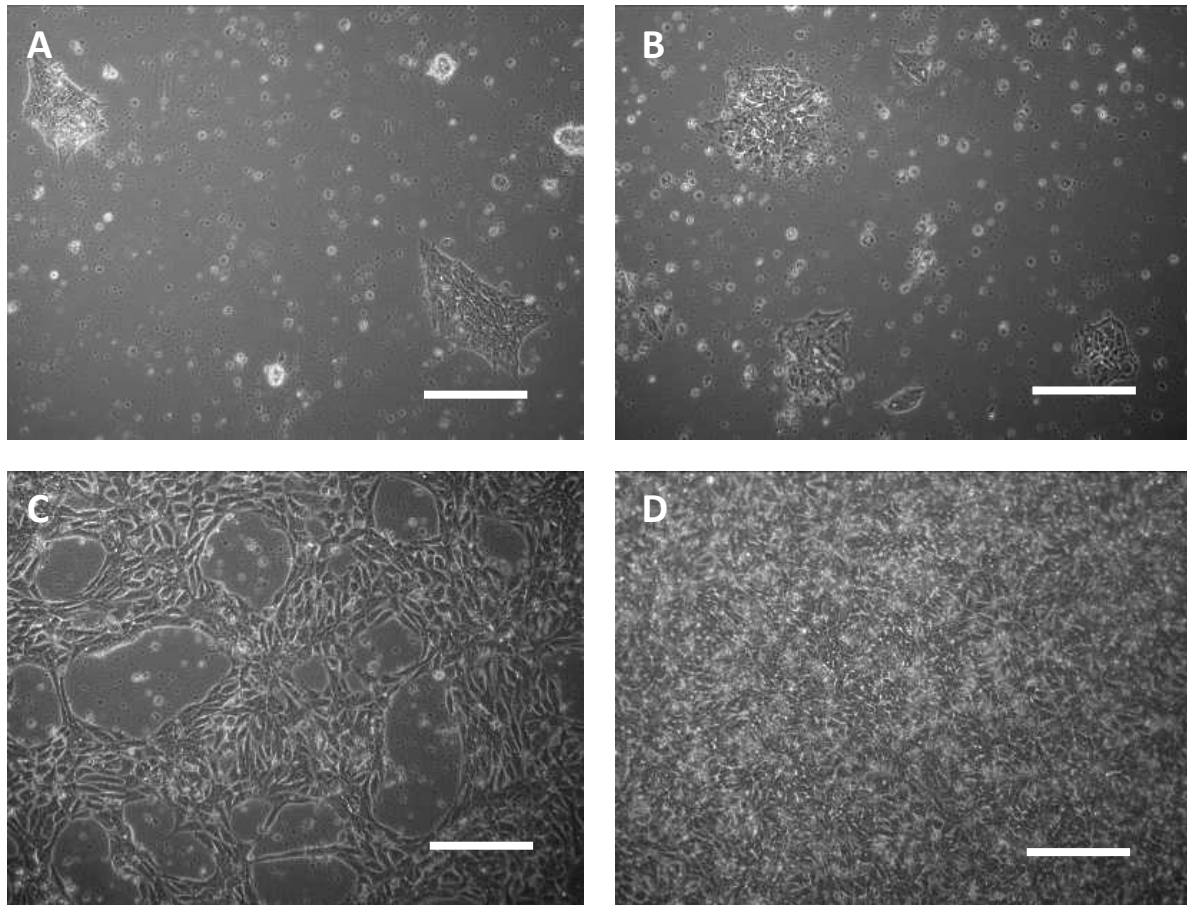


Figure 5-16 - H2 hESCs on NSQ patterned inserts. A) Matrigel (standard protocol – 23ml DMEM+1ml Matrigel Aliquot) 24hrs - Adherence of H2 hESCs to planar substrates was visibly reduced, perhaps due to poorer Matrigel® coating of the non-patterned surface. In relation to this result vitronectin coating of the polymer inserts showed significantly improved promise and greater cell attachment on all surfaces shown below. B) Vitronectin (0.5 $\mu\text{g}/\text{cm}^2$ – Standard) 24 hrs. C) Standard matrigel coatings 24hrs on three injection moulded topographies 24hrs after seeding at 40,000 cells/ cm^2 . D) Standard Vitronectin coatings on an identical set of injection moulded topographies 24hrs after seeding shows high density layer of cells in all samples. Phase contrast microscopy. Scale bars: 300 μm .

The morphology at 48 hours varied but the formation of colonies became more distinct between ROCK inhibited and clump seeded hESCs. A sharp drop off was especially visible on Matrigel coated planar surfaces. Inhibition significantly improved the adhesion in all cases, with little difference seen between the three topographies.

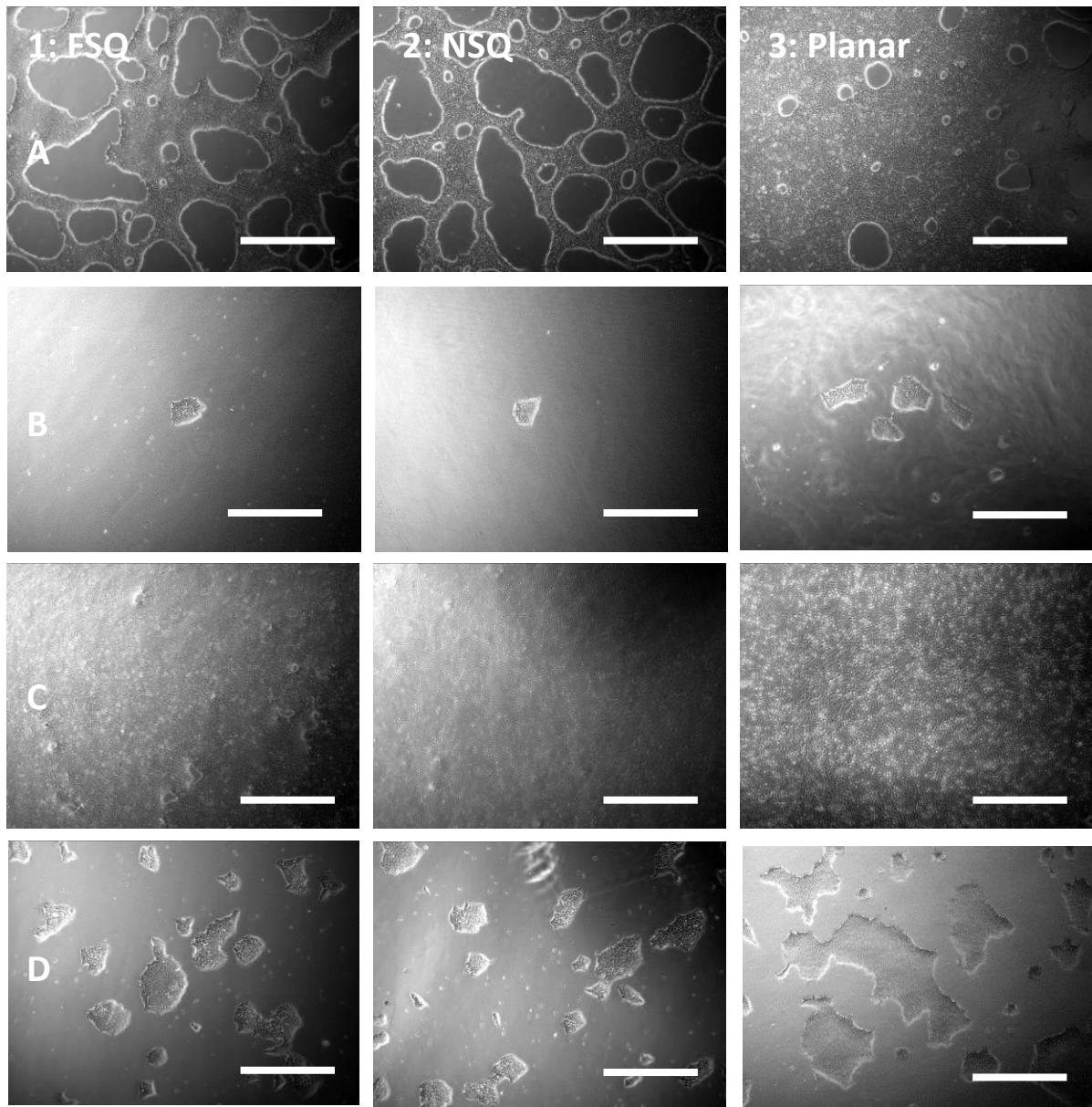


Figure 5-17 - A1-3: The morphology of single cell seeded H2 hESCs onto a Matrigel coated surface with rock inhibitor. B1-3 Cells seeded in 'clumps' after separation in EDTH onto Matrigel surface and shows distinct lack of cell viability In contrast to vitronectin where coverage was higher on average. C1-3: Show samples covered in vitronectin and seeded with single ROCK inhibited cells. D1-3: Clump seeded cells on vitronectin. Scale bar: 600 μ m.

Seeded cell clumps showed little or no visible changes in cell morphology, with colony size also practically invariant. Long term cell attachment may however, be dependent on more than critical colony size as large colonies on the planar surface later underwent apoptosis or delaminated. Patterned surfaces showed better colony viability, reaching confluence at 4-5 days after seeding.

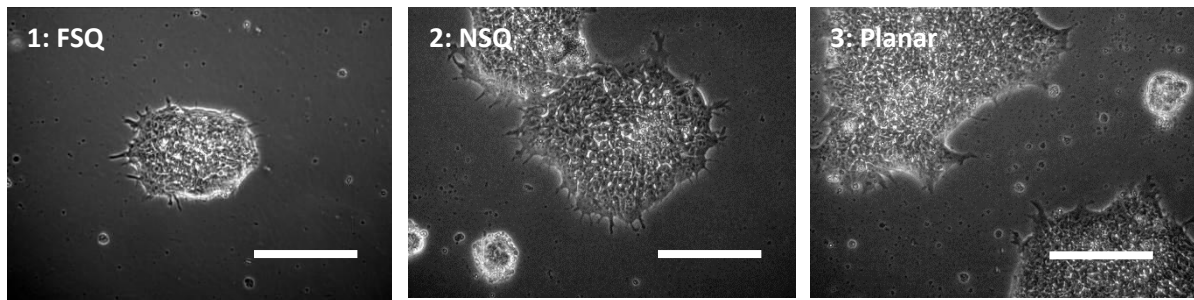


Figure 5-18 - Phase contrast microscopy of H2 hESCs clustering 24 hours after seeding in clumps on vitronectin coated FSQ, NSQ and Planar injection moulded insert respectively, little change in morphology is visible at 20x magnification. Scale bars: 300 μm .

qPCR collected from single cells 72 hours after seeding on various surfaces was compared for pluripotency and lineage markers (Figure 5-19) RQ is the relative quantification in relation to actin as a reference sample. The chosen markers *OCT-4*, *SOX-2* and *NANOG* all shown to positively regulate transcription of all pluripotency circuitry proteins in the LIF pathway[217], and all interact and form complexes with *NPM-1* a transcriptional regulator involved in cell proliferation[218]. *SOX-2* and *OCT-4* show an amplified joint expression and are shown to act together in relation to regulating pluripotency[172]. A significant spike in *NANOG* was seen in all cases compared with TCP controls. A slight but not statistically significant under expression of *SOX-2* was also seen.

As *NANOG* is a proliferation and self-renewal factor in undifferentiated stem cells[172], it can be assumed that this indicated a maintained pluripotency and continued cell proliferation on the inserts. This could be attributed to factors such as initial wettability, surface chemistry, oxygen concentration, as the inserts tend to maintain cells slightly closer to the surface of the fluid in the well, this factor also appears in cycles, and it could be that cells were harvested during a peak in its expression. In the case of *SOX-2* the difference is considered negligible at this stage, both due to possible errors, and the apparent ability of *OCT-4* to continue its function in situations of under expressed *SOX-2* [219].

Cofactors which can in concert with *NANOG* expression play a role in differentiation of H2 hESCs into the three germ layers during embryonic development were not analysed on this occasion as no morphological changes were yet observed in culture, the extent of maintenance of pluripotency is described in section 5.3.4.5. A slight up-regulation of *NANOG* can be seen on insert surfaces primarily on Matrigel® in relation to the planar control (Figure 5-19).

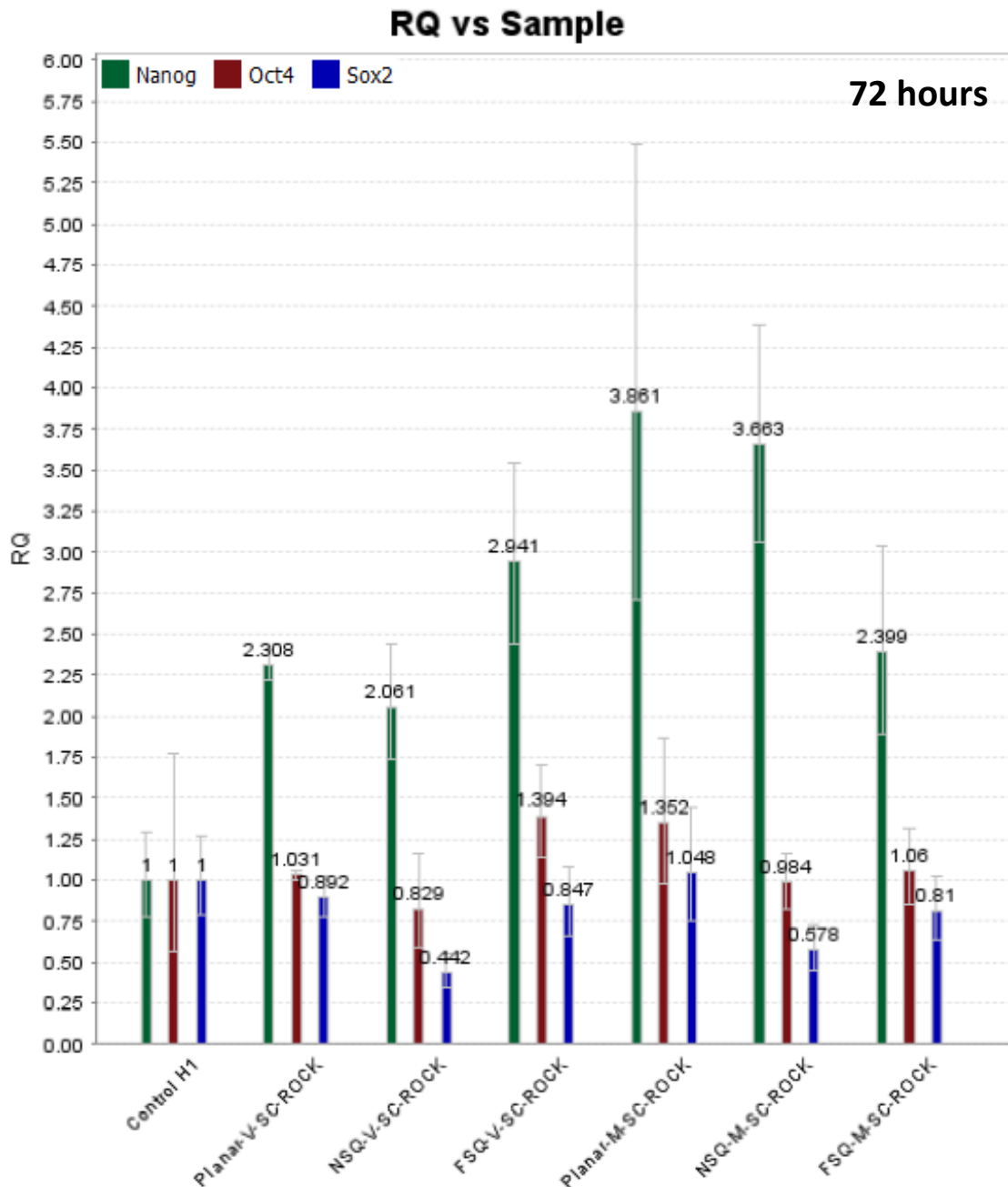


Figure 5-19 - H2 hESC gene expression study with cells seeded as single cells from Acutase passage onto vitronectin (VTN) and Matrigel® coated nanopatterned inserts with NSQ50, FSQ patterned, with both planar polycarbonate and TCP controls. Cells collected after 72 hours in culture, after seeding at an initial concentration of 40,000 cells/cm². RQ is the relative quantification to Actin ACTB endogenous control, all normalized to H2 undifferentiated TCP control. Error bars: 1SD.

This expression is in contrast to clumped cells collected at 120 hours after seeding (Figure 5-20). At 120 hours the larger colonies reached confluence and showed an opposite relationship, where SOX2 appears to be significantly upregulated. A slight but not statistically significant down-regulation of SOX2 can be seen on patterned surfaces primarily on NSQ. This down-regulation could be attributed to normal fluctuations and potentially an artefact of minor changes in cell density between samples.

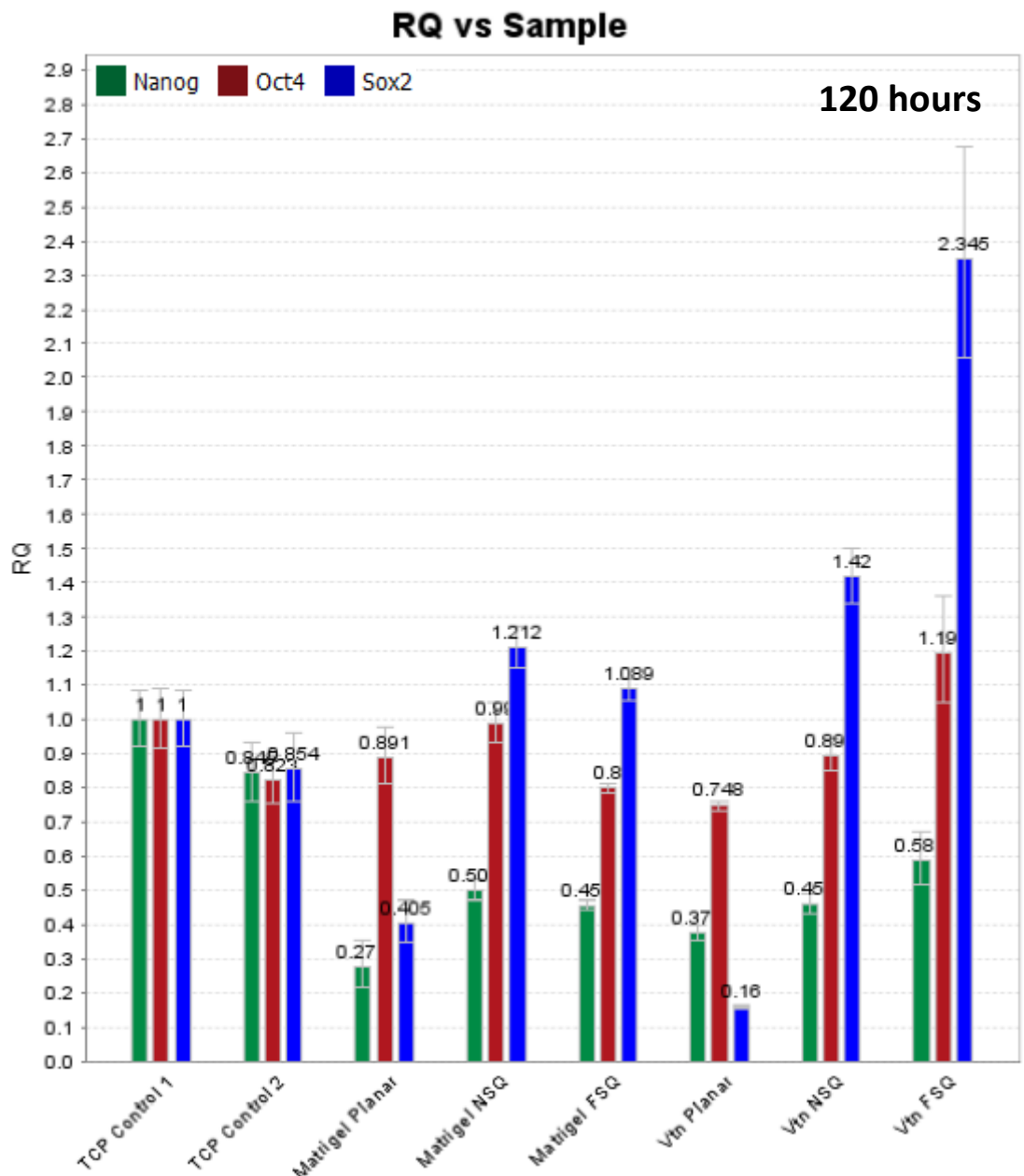


Figure 5-20 – H2 hESC gene expression study with cells seeded as clumps from EDTA passage onto vitronectin (VTN) and Matrigel® coated nanopatterned inserts with NSQ50, FSQ patterned, with both polycarbonate planar controls and TCP controls. Cells collected after 120 hours in culture, after seeding at an initial concentration of 40,000 cells/cm². RQ is the relative quantification to Actin ACTB endogenous control, all normalized to H2 undifferentiated TCP control. Error bars: 1SD.

5.3.4.3 hESC morphology changes with seeding density.

Optical microscopy looked at cell attachment at lower concentrations of both cells and ECM coating media. The 24hour cell proliferation on NSQ, FSQ, Planar and PS control samples is shown in Figure 5-21 and Figure 5-22. Injection moulded substrates With NSQ and FSQ pattern morphologies were compared at similar rhVTN plating concentrations. Little observable difference was visible on all substrates, which was anticipated due to the similar contact angle and surface area coverage of nanopits. No visible changes in this relationship were seen, even when vitronectin concentrations were reduced to a minimum concentration of $0.25 \mu\text{g}/\text{cm}^2$. Cell coverage only improved with cell plating concentrations ($\geq 80,000 \text{ cells}/\text{cm}^2$) but did not show improvement as the vitronectin concentration was increased from 0.25 to $1 \mu\text{g}/\text{cm}^2$ (Figure 5-21). Nanopatterned inserts showed significantly better cell coverage at both low and high cell seeding densities (Figure 5-22).

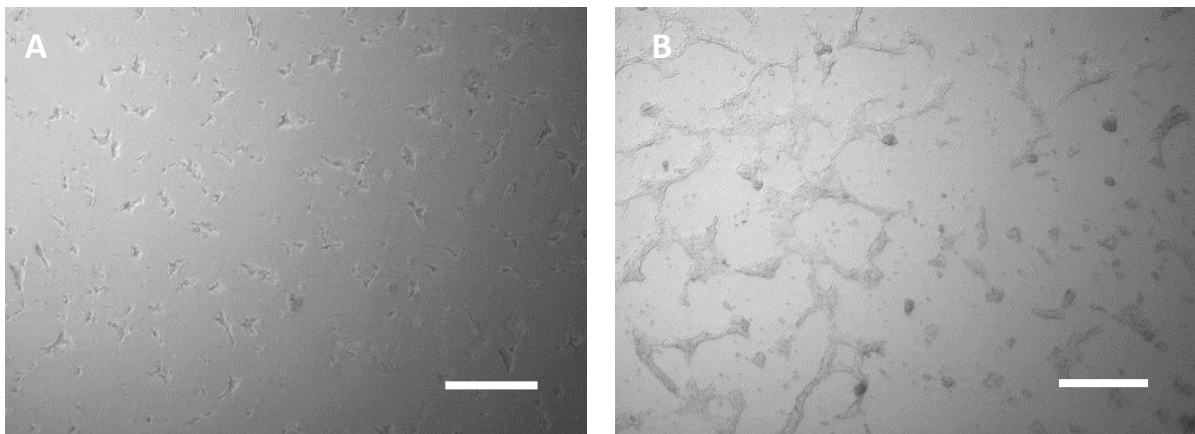


Figure 5-21 – H2 hESCs 24 hrs after seeding. Cells cultured on TCP controls (polycarbonate) coated at progressively lower concentrations of vitronectin. A) Cells seeded at $40,000 \text{ cells}/\text{cm}^2$. B) Cells seeded at $80,000 \text{ cells}/\text{cm}^2$. Similar behaviour was seen at 0.5 and $1 \mu\text{g}/\text{cm}^2$ rhVTN concentration. Scale bars: $500 \mu\text{m}$.

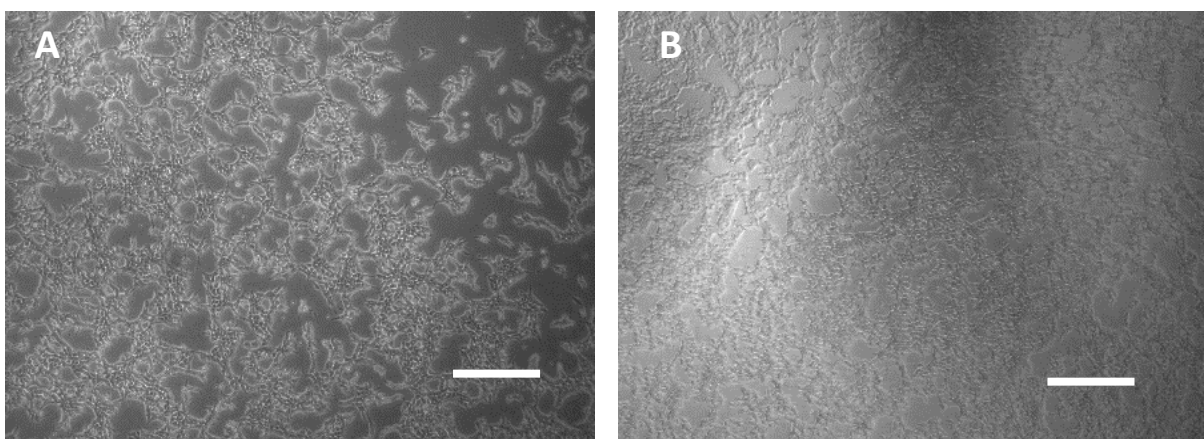


Figure 5-22 – H2 hESCs 24hrs after seeding on vitronectin coated NSQ substrates at various seeding densities and rhVTN concentrations. A: NSQ at $40,000 \text{ cells}/\text{cm}^2$. B: NSQ at $80,000 \text{ cells}/\text{cm}^2$. Similar behaviour was seen on FSQ substrates and at 0.5 and $1 \mu\text{g}/\text{cm}^2$ rhVTN concentrations. Scale bars: $500 \mu\text{m}$.

At 48 hours post seeding changes in colony size and distribution became apparent (Figure 5-23). The dominant effect of seeding with ROCK-I diminished after the first media change, resulting in substantial cell death as cell-to-cell interaction began to mediate cell survival leading to far more 3D aggregations of hESCs.

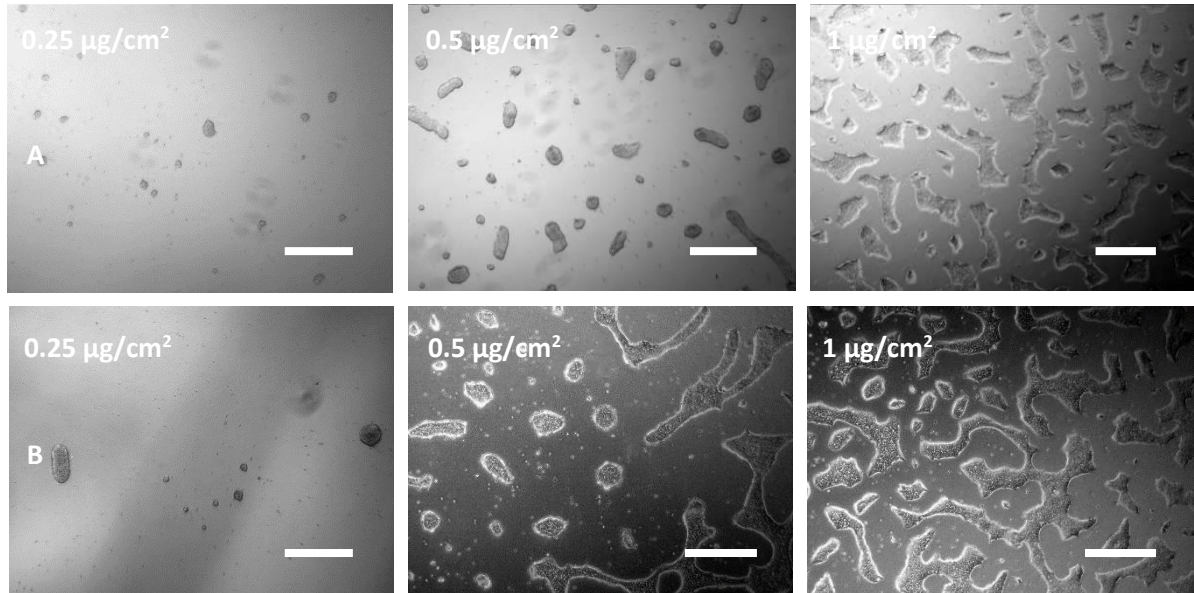


Figure 5-23 – H2 hESCs on PS TCP controls at 48hrs after seeding: A) Seeding done at 40,000 cells/cm². B) Seeding done at 80,000 cells/cm². Scale bars: 500 µm

Unlike TCP controls showed a sharp drop off in cell coverage at the 48 hour time point, even after successful aggregation into colonies over the previous 24 hour period (1st 24 hours after seeding). Critical vitronectin concentration was found to be near 0.25 µg/cm² at which cells had difficulty adhering to TCP.

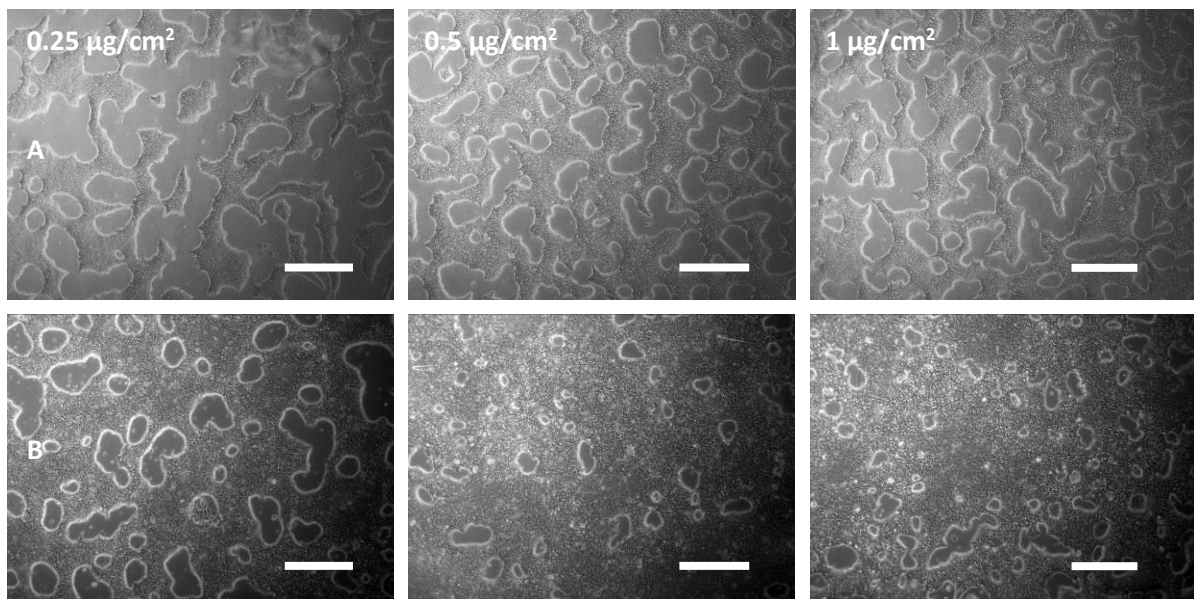


Figure 5-24 - H2 hESCs on rhVTN coated NSQ injection moulded substrates at 48hrs after seeding at various plating and seeding densities. A) NSQ 40,000 cells/cm². B) NSQ 80,000 cells/cm². Similar behaviour was seen on FSQ substrates in these conditions. Scale bars: 500 µm.

Planar samples at 48 hours had no living cell colonies remaining and could not be documented, suggesting the ECM concentration or adhesion was too low and lead to subsequent colony detachment.

The qPCR from the 96 hours culture on the rhVTN dilution gradient for cells seeded at 400,000 cells/ml (80,000 cells/cm²) and 200,000 cells/ml (40,000 cells/cm²) is shown in Figure 5-25. Substrates were coated in the standard concentration of rhVTN at 5, 2.5, and 1.25 µg/ml (1, 0.5 and 0.25 µg/cm²) Variations in seeding density and VTN concentration were split across the two reference genes showing the slight up-regulation in *SOX-2*, although up-regulation in *OCT-4* tended to follow. The difference is not large enough to gauge and significant changes, but can be used to confirm pluripotency at this stage in the culture process, with the highest levels seen in the more densely coated substrates in both NSQ and FSQ.

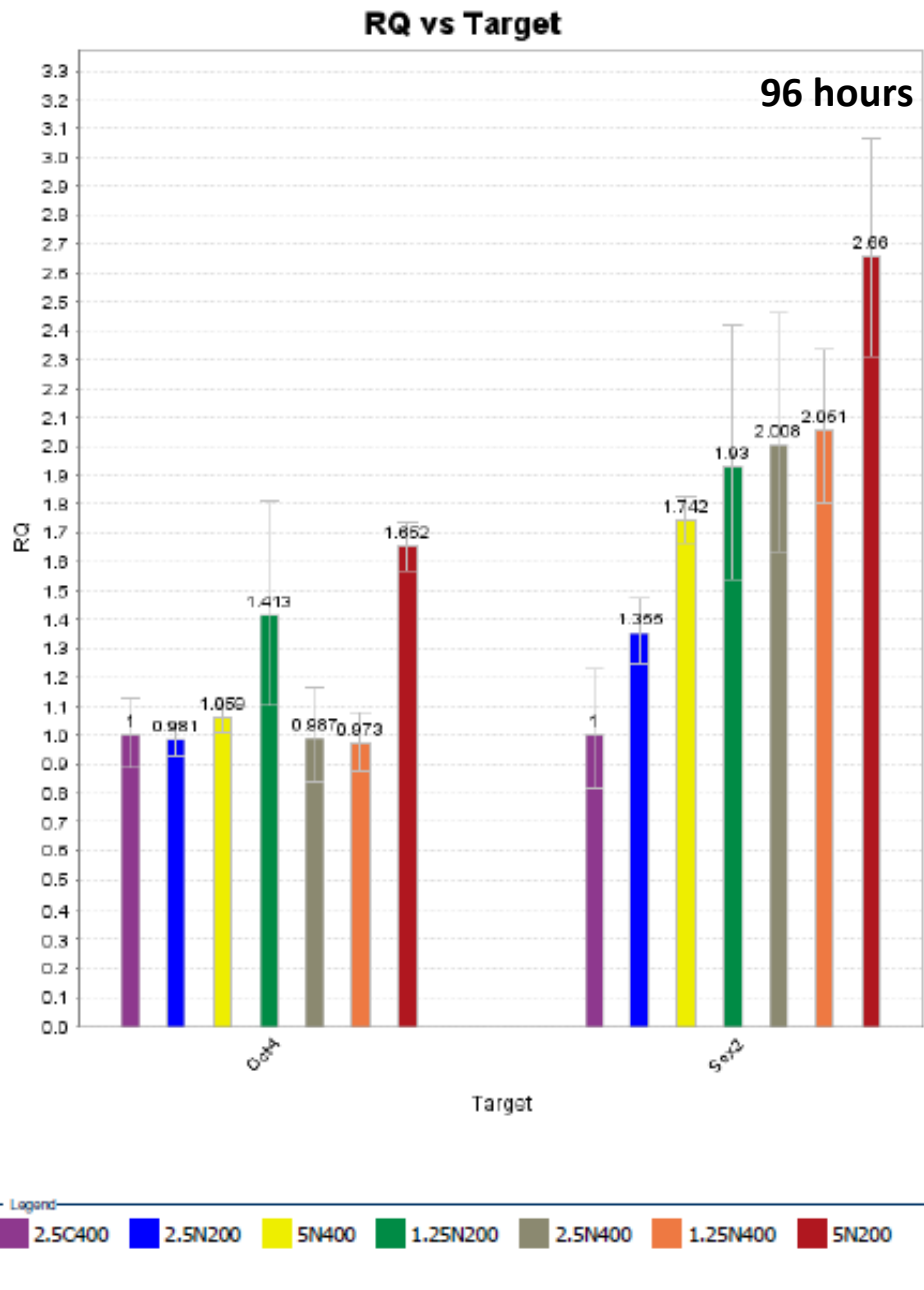


Figure 5-25 – H2 hESC gene expression study with varying vitronectin concentration and cell seeding density. Cells collected after 96 hours in culture. 1.25, 2.5 and 5 represent plating density in $\mu\text{g/ml}$. 200 and 400 represent seeding density of 200k and 400k cells/ml. C represents TCP controls and N represents NSQ nanopatterned surfaces. Results are split by expression of Oct-4 and Sox-2 respectively which are common pluripotency markers for hESCs. RQ is the relative quantification to Actin ACTB endogenous control, all normalized to H2 undifferentiated TCP control. Error bars: 1SD.

Subsequent broader spectrum analysis was conducted to investigate peculiar morphological patterns in cell culture. The qPCR data showed slight but significant down-regulation of *MIXL1* and *T* with slight up-regulation of *FOXA2* (Figure 5-26)

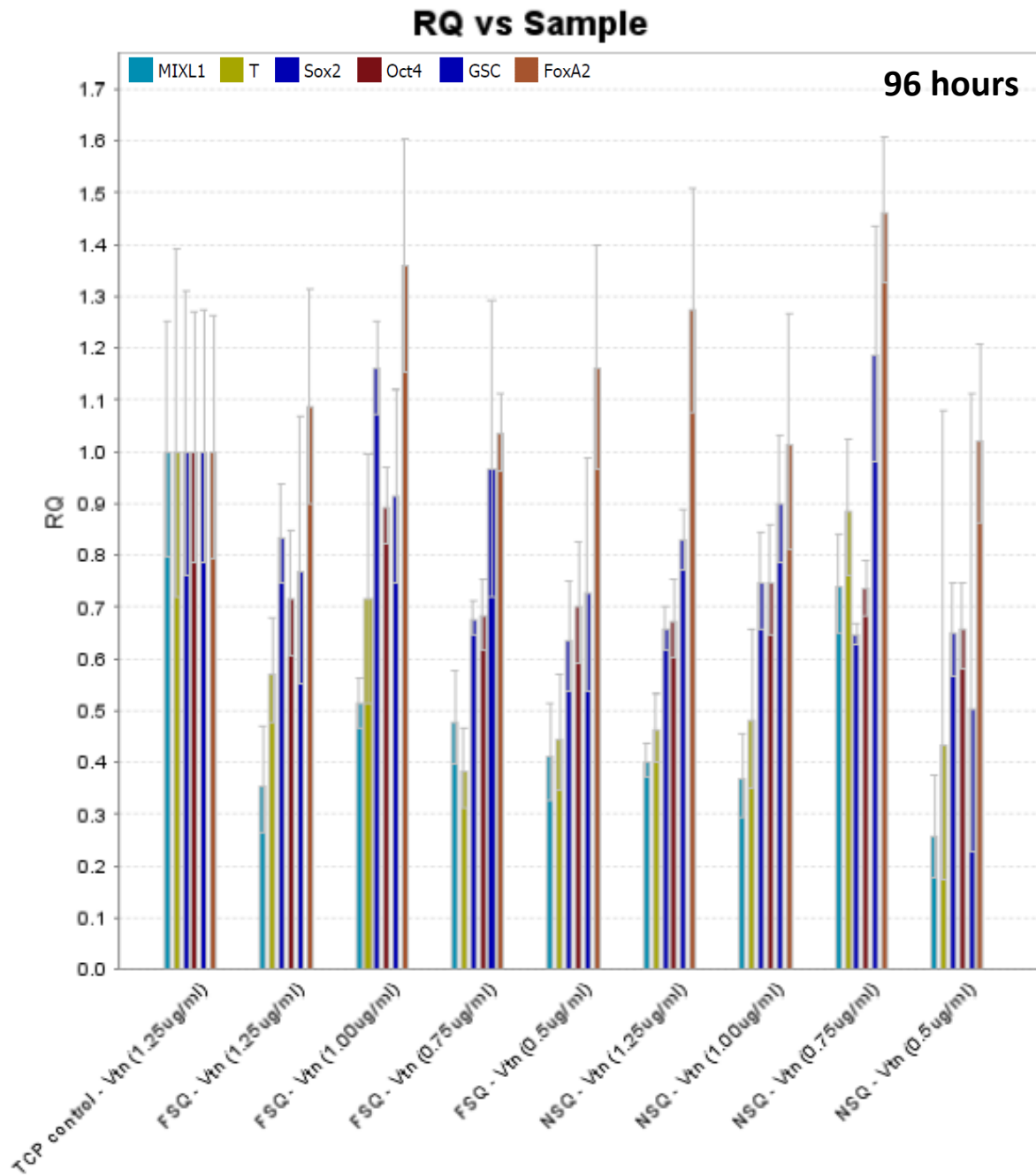


Figure 5-26 – H2 hESC gene expression study combining 3x96 well plates containing triplicates of cDNA from 9 culture wells and endogenous control. Substrates with varying plating concentration of vitronectin and seeding density. Cells collected after 96 hours in culture, after seeding at an initial concentration of 200,000 cells/cm². The results are showing common pluripotency and lineage markers for H2 hESCs RQ is the relative quantification to Actin ACTB endogenous control, normalized to undifferentiated H2 TCP control. Up-regulation of FoxA2 can be seen on all patterned substrates, with a down-regulation of T and MIXL1. The cells had been imaged showing nodular 3D architecture after 84 hours of incubation (a day prior). All cells kept in E8 culture medium. Error bars 1SD.

5.3.4.4 hECS morphology at extreme vitronectin concentrations

Cells were seeded at constant cell density (40,000 cells/cm²) with vitronectin concentrations reduced further and varied between 0.25 and 0.1 µg/cm² or roughly 10 times less than the recommended concentration by Life Technologies Figure 5-27.

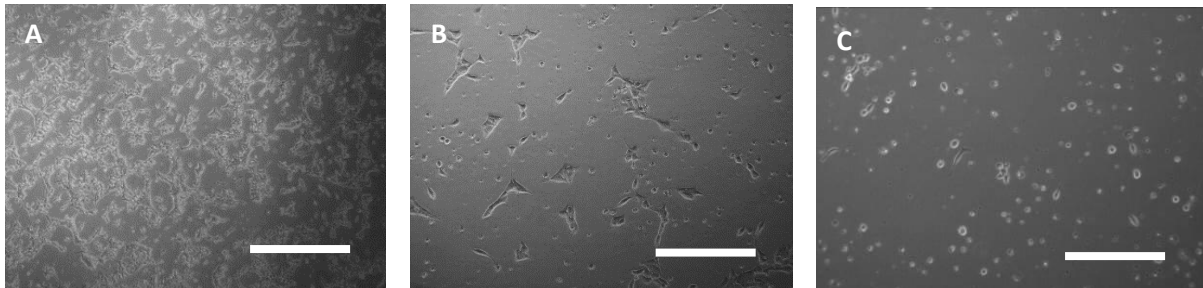


Figure 5-27 - H2 hECSs 12 hours post seeding on A) NSQ B) TCP controls coated with 0.1 µg/cm² rhVTN and C) uncoated TCP. All seeded with 40,000 cells/cm². Images taken using phase contrast microscopy. Similar correlation was seen in the range of 0.25 and 0.1 µg/cm² rhVTN in increments of 0.05. All scale bars: 300 µm.

Compared to TCP controls treated with extremely low dilutions of vitronectin, the injection moulded substrates showed significantly improved in cell adhesion down to concentrations of 0.01 µg/cm². In contrast at this cell dilution non-patterned surfaces showed no cell attachment.

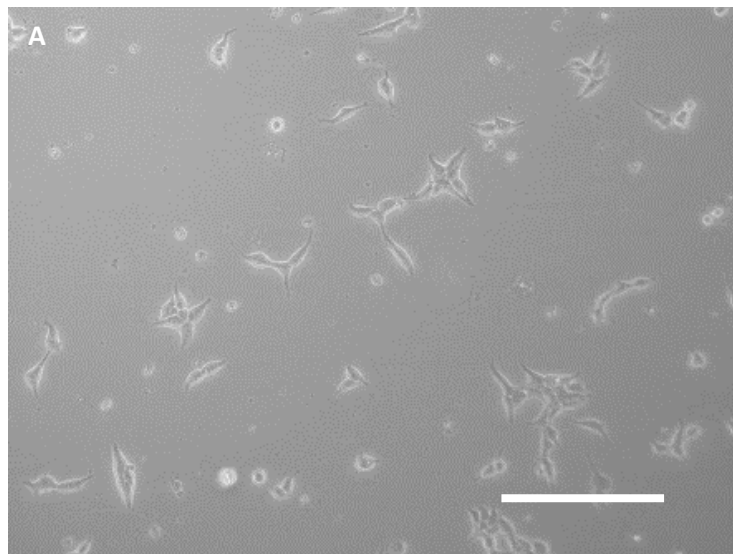


Figure 5-28 - H2 hECSs seeded on 0.01 µg/cm² rhVTN plated FSQ after 24 hrs 40,000 cells/cm². Similar results were seen on NSQ substrates at this concentration regardless of cell seeding density. Scale bar: 300 µm.

Quantification of area coverage was done by cell profiler analysis. A threshold was applied to phase contrast images for data from the 24 hour culture, individual cell colonies labelled, and total cell area coverage extracted (Figure 5-29). A sharp decline in cell are coverage is seen as rhVTN is reduced to a critical concentration of 0.01 µg/cm². This suggests that the use of nanopatterned surfaces can improve the yield of rhVTN coatings for hESC culture, reducing the necessary amount of rhVTN to 100x dilution compared to planar surfaces.

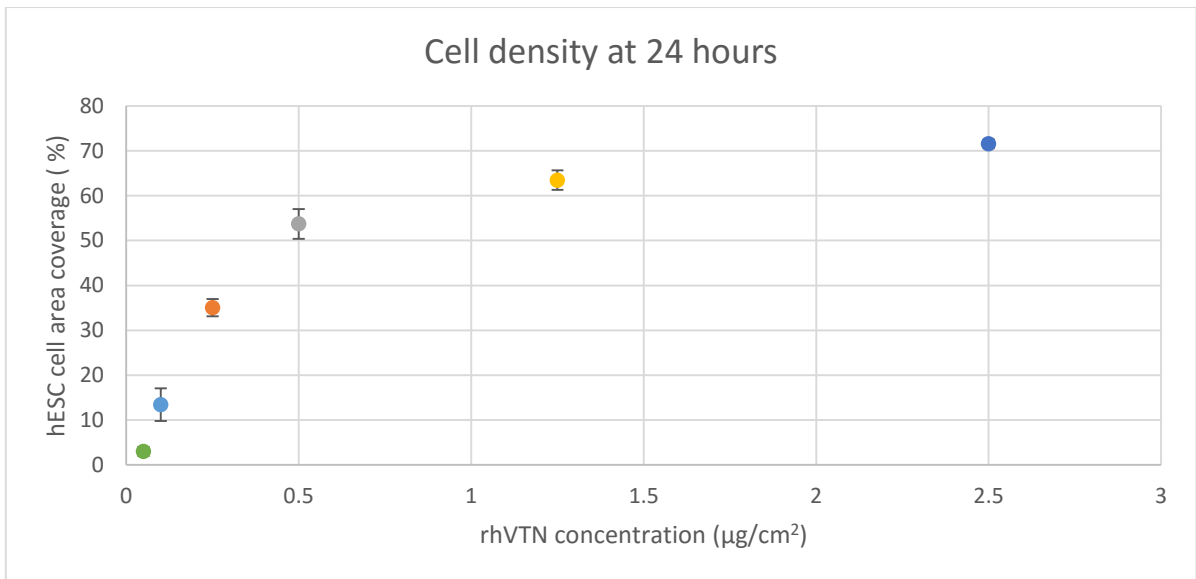


Figure 5-29 - Cell area coverage with vitronectin coating concentration. Error bars: 1SD from n=5 measurements

5.3.4.5 Forced and random differentiation of hESCs on nanopatterned surfaces

The effect of topography and coating density on random and directed differentiation of H2 hESCs was also evaluated. Conditions were changed after 48 hours of normal culture when colonies had grown to a sufficient size (50-60 % area coverage).

Several cases were studied with relevant TCP controls with and without induced differentiation:

- 1.) hESCs differentiated by a standard small molecule protocol [172] on TCP.
- 2.) hESCs differentiated by a standard small molecule protocol [172] on nanopatterned inserts.
- 3.) hESCs left on nanopatterned inserts for random differentiation in RPMI B27.
- 4.) hESCs left on TCP surfaces for random differentiation in RPMI B27.
- 5.) Some of the samples from 3) and 4) progressed to phase 2 in DMSO.

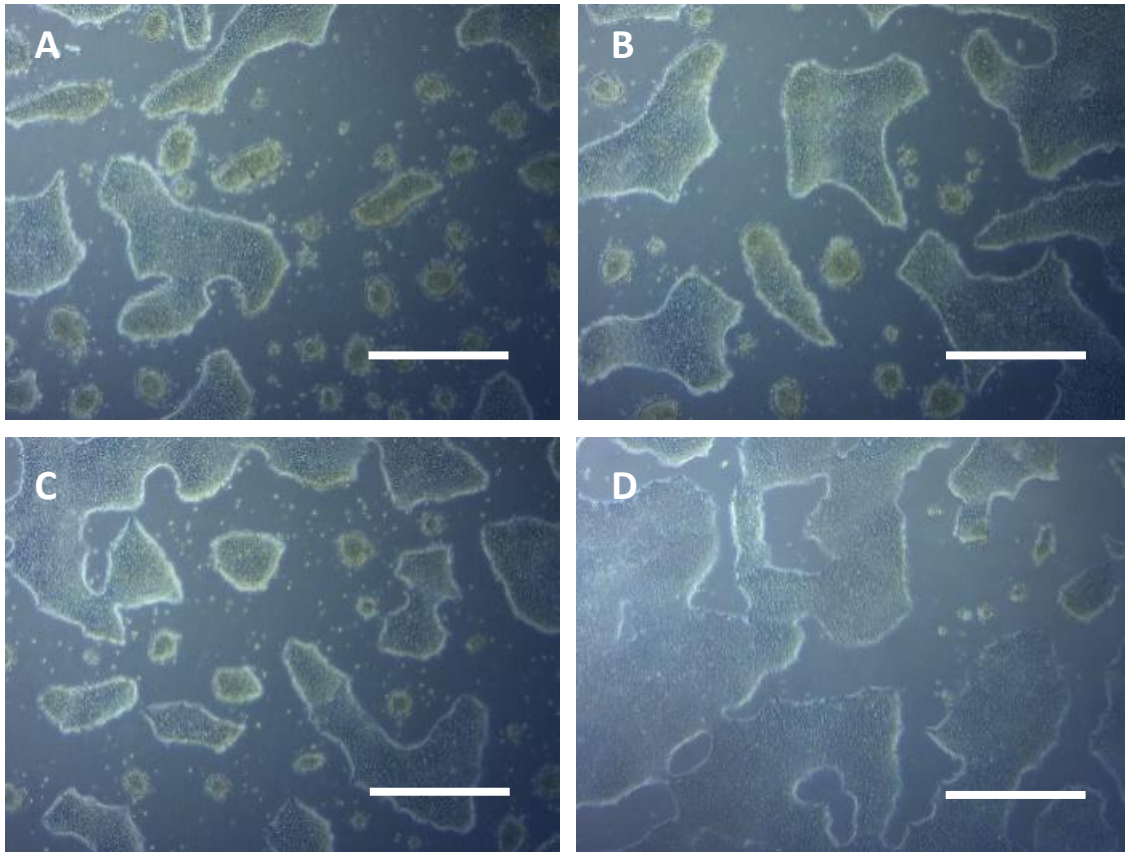


Figure 5-30 - Phase contrast imaging at 24 hours after start of random differentiation of H2 hESCs on F5Q at A) 0.02, B) 0.05, C) 0.1 and D) 0.25 $\mu\text{g}/\text{cm}^2$ of vitronectin respectively. NSQ showed a similar trend and 3D morphology. All scale bars: 600 μm .

Random differentiation on nanopatterned inserts in the same 24 hour period showed a distinctly more 3D structure (Figure 5-30). This 3D heterogeneous clustering was reminiscent of the behaviour seen in the small molecules differentiation procedure in RPMI+B27[172] (Figure 3-31), except for one key difference: the small molecule cell cultures on both TCP controls and the patterned surfaces show closely packed 3D colonies of cells with a new and slightly coarser cell type emanating out from the clusters, thought to be primitive streak given the short duration after swapping out the pluripotency maintaining E8 media. The primitive streak emanating out is a transitional state before a differentiation pathway is fixed. Controls on TCP undergoing random differentiation appeared to be highly 2D and homogenous (Figure 5-32). This homogeneous structure is indicative of sustained pluripotency, and is thought to be the result of the hESCs conditioning the media, even in the absence of E8 media [172]. The self-conditioning of the media is also apparent in random differentiation of hESCs on nanopatterned surfaces when large cell densities are present (Figure 5-33). The sustained pluripotency persisted well into differentiation, with high densities of cells undergoing phase 2 of differentiation in DMSO also showing a largely planar and homogeneous structure (Figure 5-34).

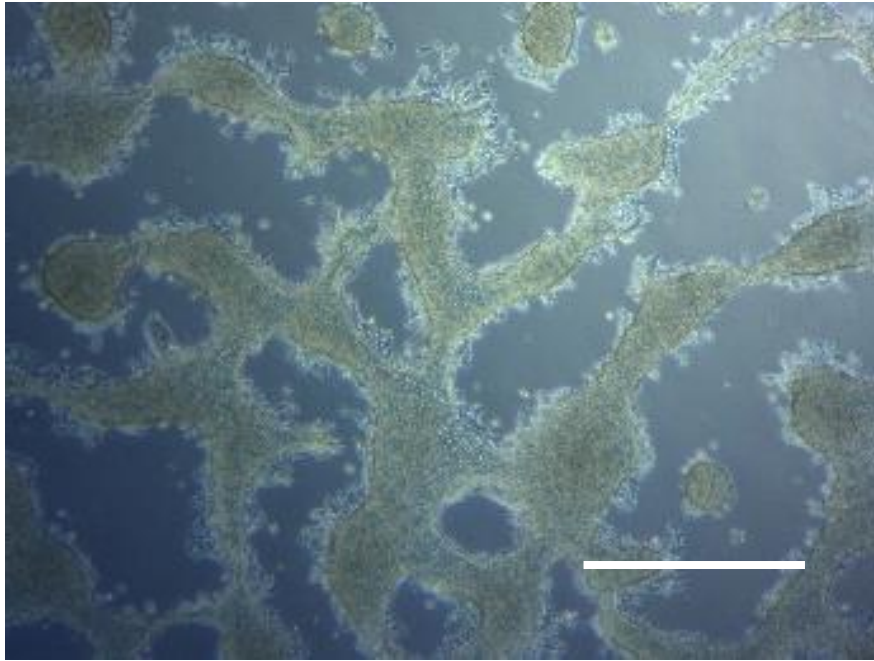


Figure 5-31- Phase contrast imaging of induced differentiation of H2 hESCs in small molecules 24 hours post media swap, 72 hours total culture duration. $0.1 \mu\text{g}/\text{cm}^2$ rhVTN. Cells seeded at $40,000 \text{ cells}/\text{cm}^2$. Similar heterogeneous morphology was seen at concentrations of 0.02 to $0.5 \mu\text{g}/\text{cm}^2$ rhVTN on both FSQ and NSQ. Scale bar: $600 \mu\text{m}$.

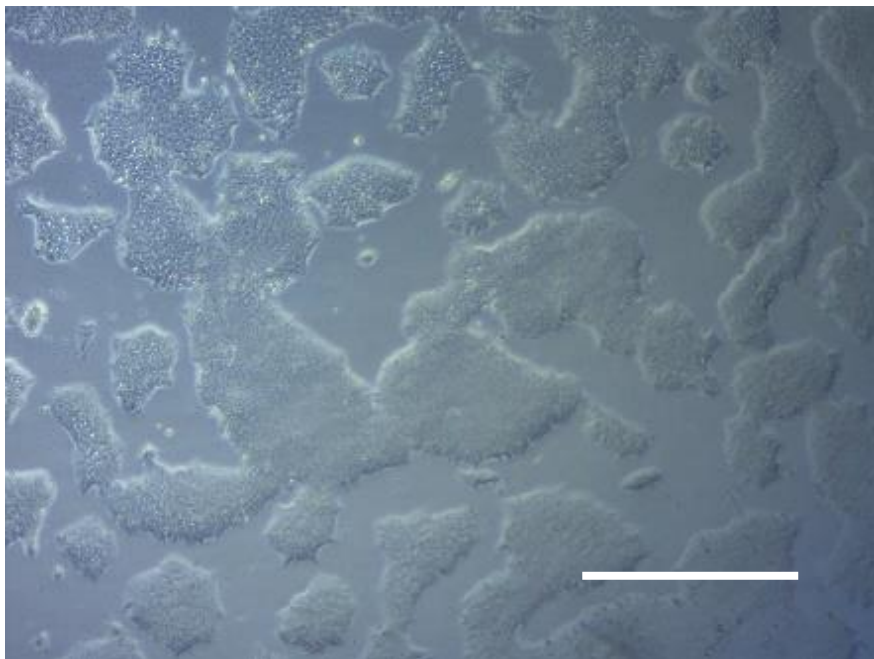


Figure 5-32 - Phase contrast imaging of H2 hESCs in E8 media on TCP coated with $0.5 \mu\text{g}/\text{cm}^2$ rhVTN at 72 hours total, 24 hours after the differentiation of all sample sets started. Similar 2D flat and homogenous morphology was seen on $1 \mu\text{g}/\text{cm}^2$ TCP controls in the same conditions. All cells seeded at $40,000 \text{ cells}/\text{cm}^2$. Scale bar: $600 \mu\text{m}$.

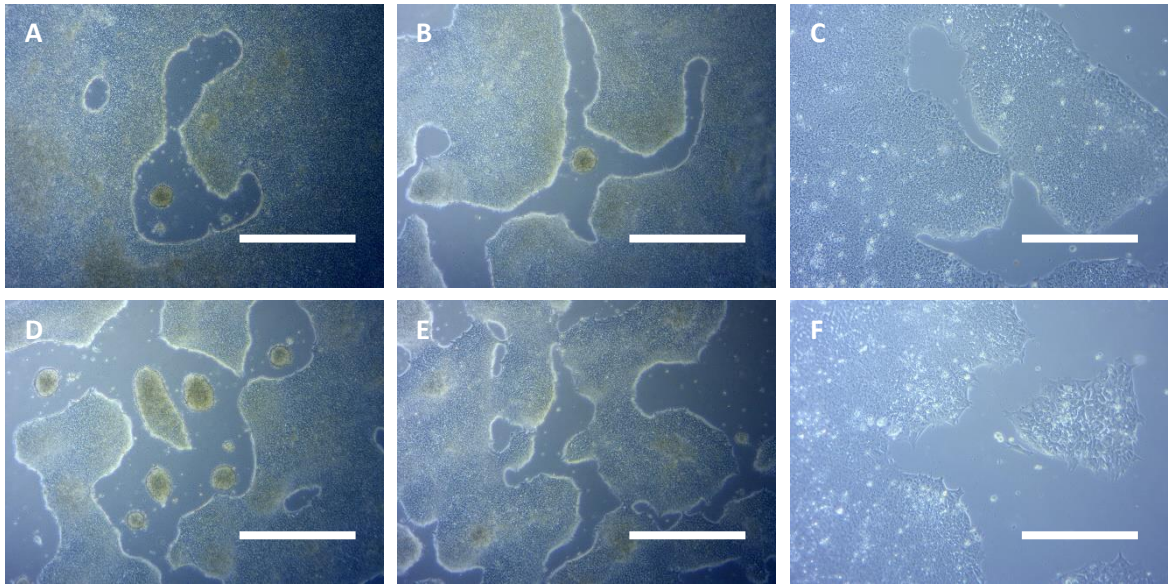


Figure 5-33 - H2 hESCs in E8 media on: A) FSK 0.05 $\mu\text{g}/\text{cm}^2$, B:) FSK 0.1 $\mu\text{g}/\text{cm}^2$, C) FSK 0.25 $\mu\text{g}/\text{cm}^2$. D) NSQ 0.05 $\mu\text{g}/\text{cm}^2$ E): NSQ 0.1 $\mu\text{g}/\text{cm}^2$, F) NSQ 0.5 $\mu\text{g}/\text{cm}^2$ rhVTN. Cells seeded at 40,000 cells/ cm^2 . All scale bars: 750 μm :

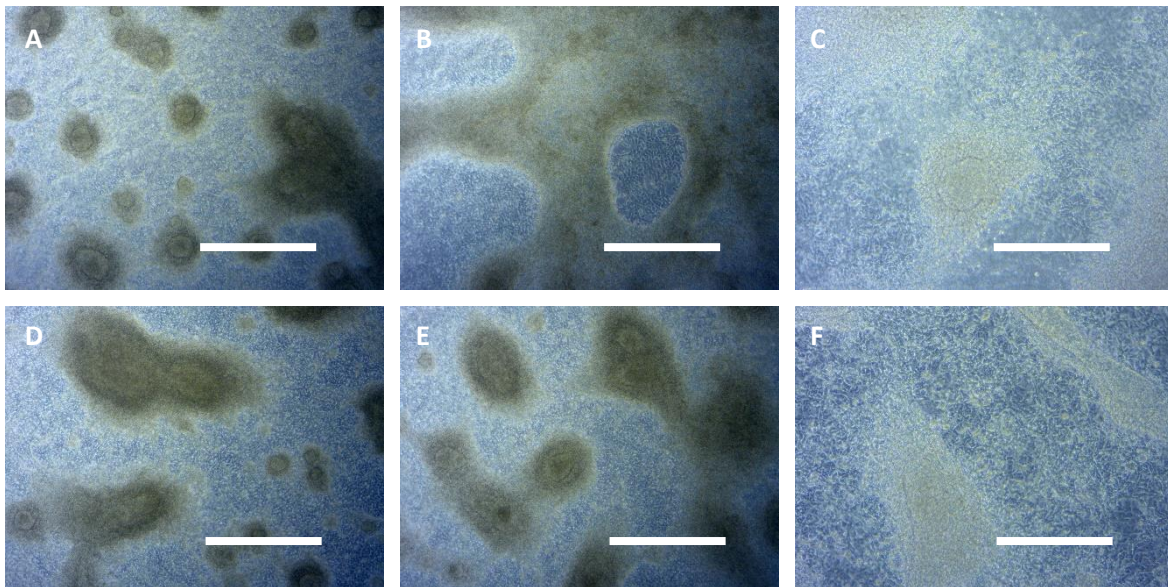


Figure 5-34 - Phase contrast imaging of H2 hESCs after differentiation in RPMI+B27 with small molecules, 48hrs after media swap: H2 hESCs in E8 media on: A) FSK 0.05 $\mu\text{g}/\text{cm}^2$, B:) FSK 0.1 $\mu\text{g}/\text{cm}^2$, C) FSK 0.25 $\mu\text{g}/\text{cm}^2$. D) NSQ 0.05 $\mu\text{g}/\text{cm}^2$ E): NSQ 0.1 $\mu\text{g}/\text{cm}^2$, F) NSQ 0.5 $\mu\text{g}/\text{cm}^2$ rhVTN. Cells seeded at 40,000 cells/ cm^2 . All scale bars: 750 μm .

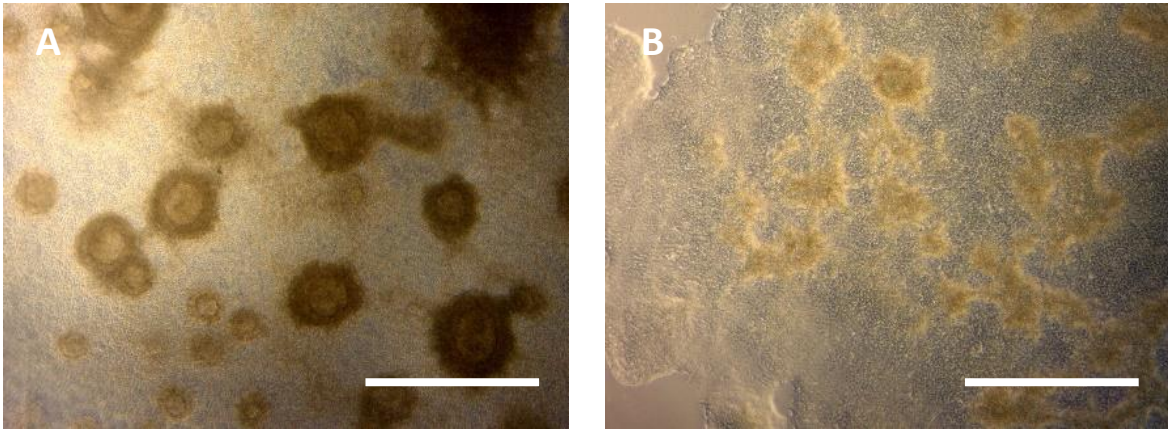


Figure 5-35 - Phase contrast imaging of H2 hESCs on immersion in SRDMSO media after the small molecules procedure, 24 hours after this second media swap. Samples died due to contamination at 48 hours. A) Small molecules induced differentiation on NSQ with $0.1 \mu\text{g}/\text{cm}^2$ rhVTN coating. B) Random differentiation on NSQ with $0.1 \mu\text{g}/\text{cm}^2$ rhVTN coating. Similar results were seen on higher density rhVTN up to $0.25 \mu\text{g}/\text{cm}^2$. All cells seeded $40,000 \text{ cells}/\text{cm}^2$. Scale bars: $600 \mu\text{m}$.

The presence of nanopatterned surfaces appeared to influence hESC pluripotency, with cells showing increasingly heterogeneous structure even without the use of forced ‘small molecule’ differentiation (Figure 5-35). Similar 3D behaviour with a distinctly different second phenotype was noticed on nanopatterned substrates after 84 hours.

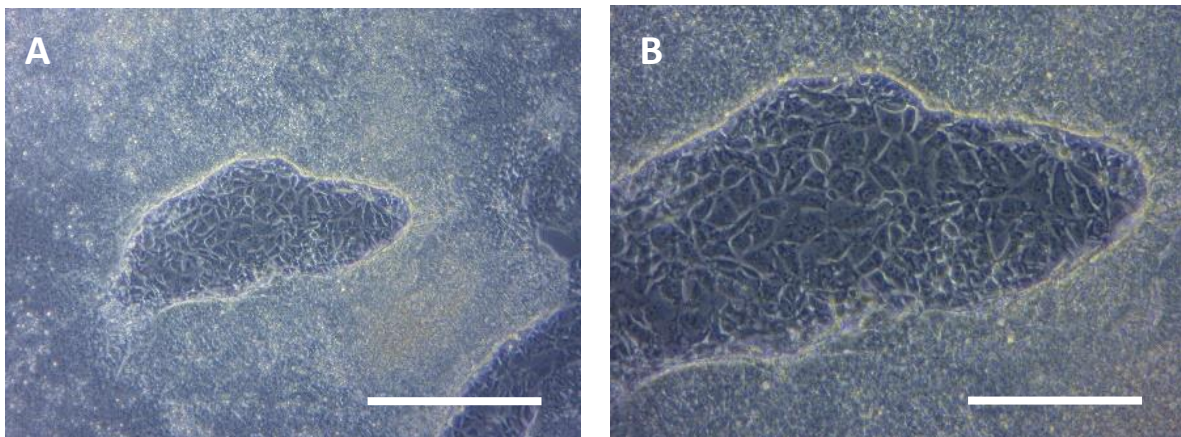


Figure 5-36 - Differentiation seen in H2 hESCs on nanopatterned insert substrates after 84 hours in E8 media. The pattern morphology, highly 3d structure and what appears as a changed cell phenotype is reminiscent of the behaviour seen in small molecule induced differentiation. All cells seeded at $40,000 \text{ cells}/\text{cm}^2$. Scale bars: A) $400 \mu\text{m}$ B) $300 \mu\text{m}$.

5.3.4.6 hESC behaviour on UHAR pillar arrays

Cells cultured on the Ultra-high aspect ratio (UHAR) pillars [185] showed distinct changes in adhesion depending on pillar height and aspect ratio (Figure 5-37). This modulation of cell adhesion is thought to be caused by changes in mechanical properties and equivalent surface stiffness.

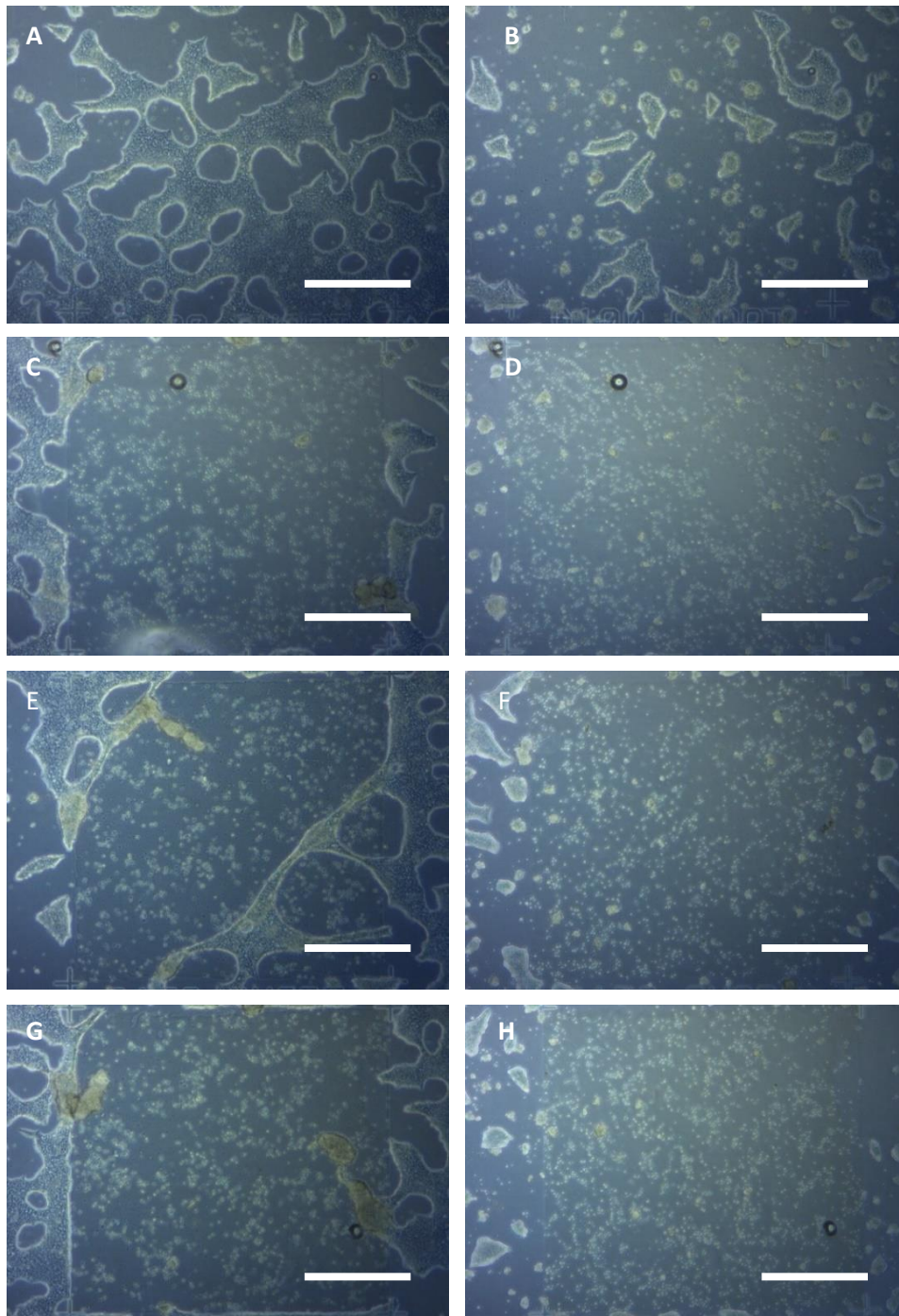


Figure 5-37 – Images taken of H2 hESCs 48 hours after seeding with Rock-, all cells seeded at 25,000 cells/cm². Right untreated, Left 0.1 µg/cm² VTN coating A, B) D100 Short, C, D) D100 Tall, E, F) D150 Short, G, H) D150 Tall. It can be seen that cells attach to the D100 short surface even without coating. All scale bars: 300 µm.

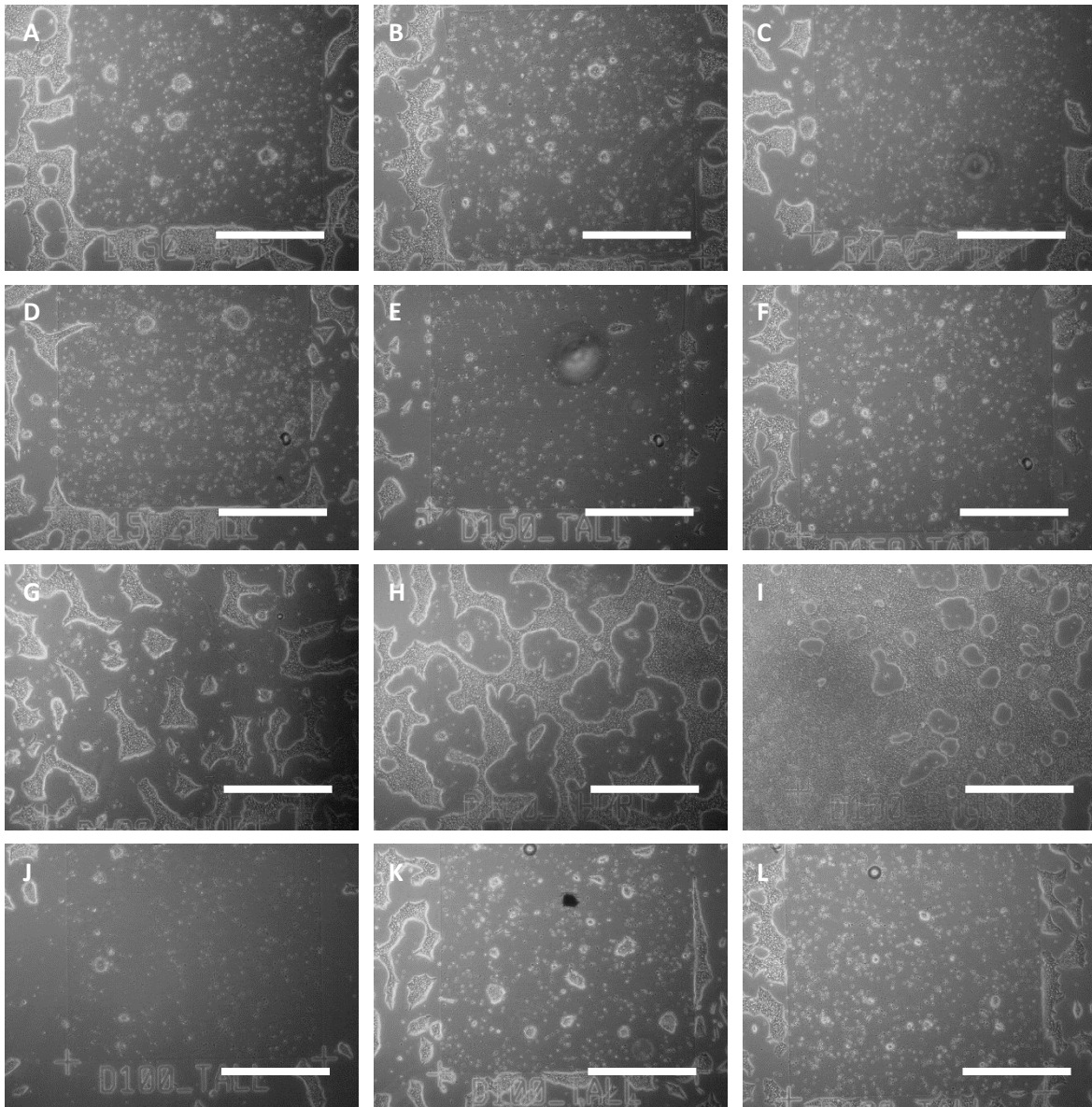


Figure 5-38 - A-C: D150 Short at 0.05, 0.25 and 0.5 $\mu\text{g}/\text{cm}^2$ rhVTN at 24 hours. D-F: D150 Tall at 0.05, 0.25 and 0.5 $\mu\text{g}/\text{cm}^2$ rhVTN at 24 hours. G-I: D100 Short at 0.05, 0.25 and 0.5 $\mu\text{g}/\text{cm}^2$ rhVTN at 24 hours. J-L: D100 Tall at 0.05, 0.25 and 0.5 $\mu\text{g}/\text{cm}^2$ rhVTN at 24 hours. All scale bars: 300 μm .

Results suggest cells prefer the intermediate stiffness D100 tall pillars (Figure 5-38), with cell concentration falling off sharply at both higher and lower stiffness surfaces. Higher could be due to height effect, whereas lower due to softness (Figure 5-39).

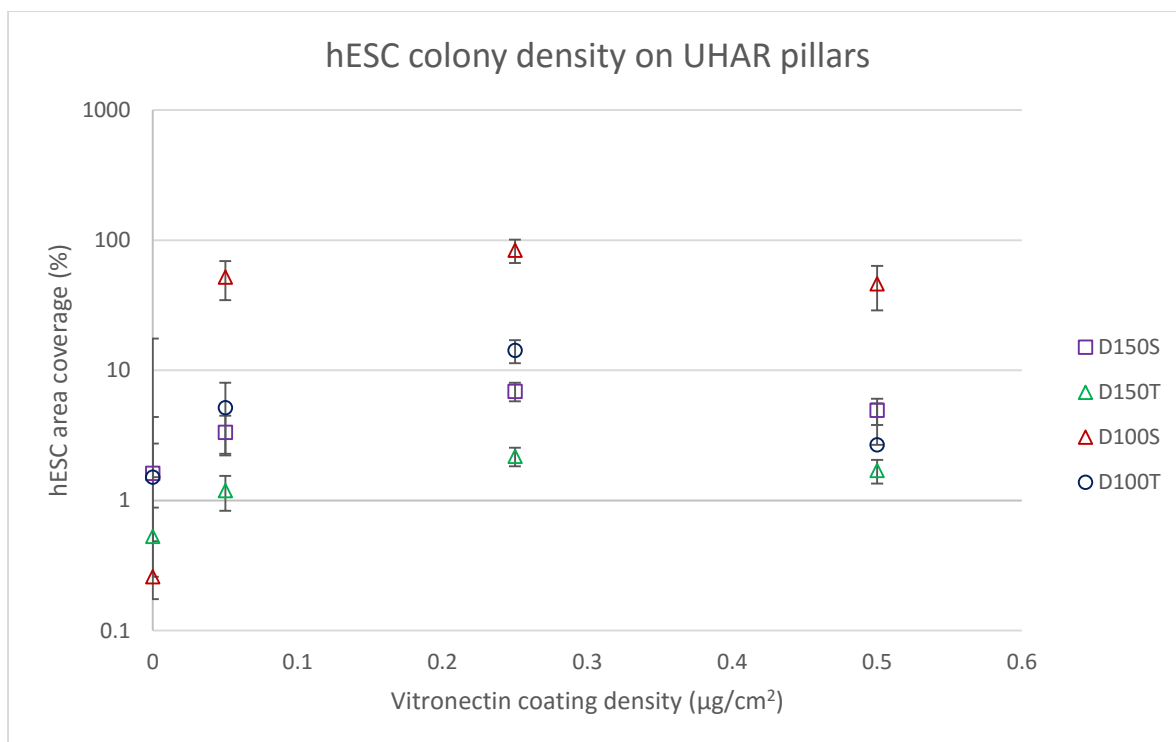


Figure 5-39 – hESC colony area coverage with pillar type and coating density at 24 hours. D100T, D150T, D100S and D150S refer to the Diameter 100 nm tall, 150 nm tall, 100 nm short and 150 nm short respectively. Error bars: SE.

As stated earlier the UHAR arrays offer a programmable surface flexibility, the result of which have been calculated using $\nu = 0.35$ and $E = 3.25$ GPa (values for polystyrene) [220] to give the deflection plots for the 4 pillar arrays found on the UHAR slides (Figure 5-40).

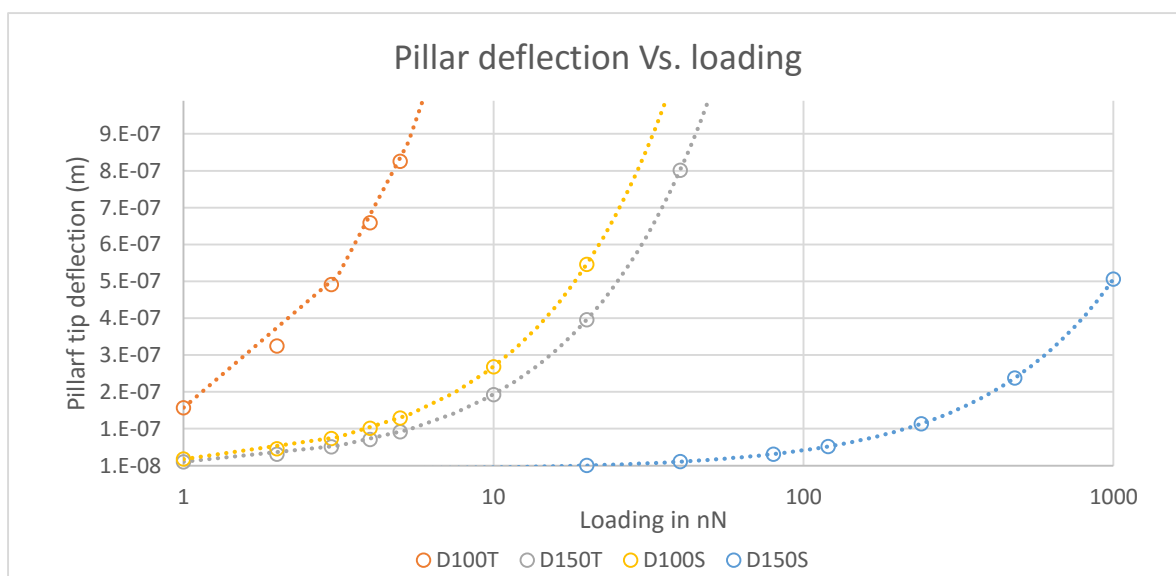


Figure 5-40 - Correlation of loading plotted against deflection for the four UHAR pillar geometries as determined from calculations. D100T, D150T, D100S and D150S refer to the Diameter 100 nm tall, 150 nm tall, 100 nm short and 150 nm short respectively.

Additionally the pillar angle of deflection under load was extrapolated for different geometric combinations (Figure 5-41).

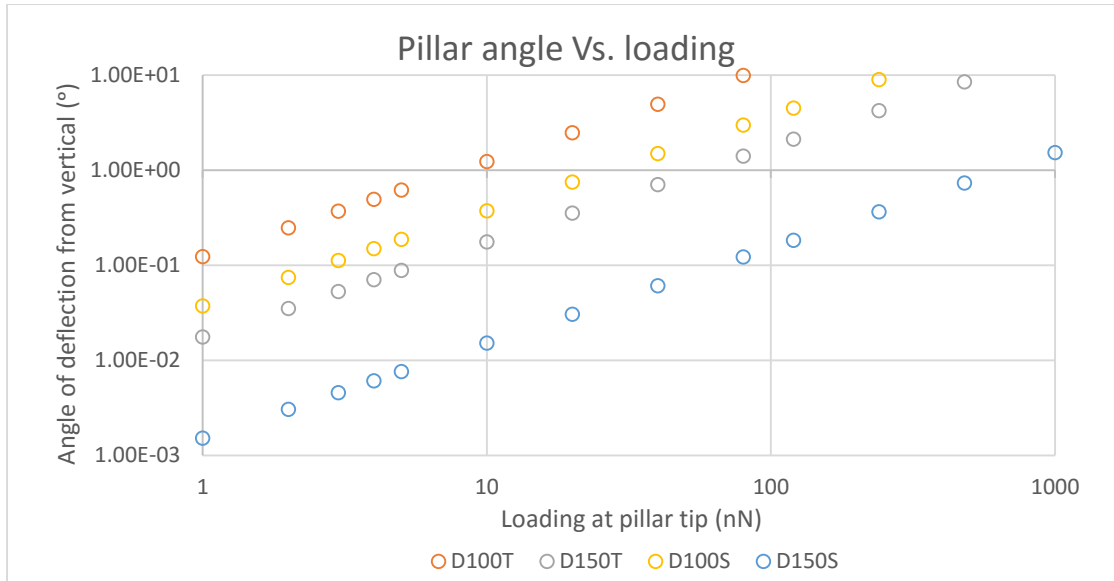


Figure 5-41 - Angle of inclination at pillar tip in relation to the non-deformed axis with varied tip loading compared for the four UHAR pillar geometries as determined from calculations with decreasing accuracy above 5° pillar deflection. D100T, D150T, D100S and D150S refer to the Diameter 100 nm tall, 150 nm tall, 100 nm short and 150 nm short respectively.

Optimum pillar dimensions were found by extrapolating the pillar height and diameter, to provide possible combinations of input parameters to provide the desired stiffness value (Figure 5-42). This confirms that the UHAR pillars used in this work do cover a range of stiffness values commonly seen in the work of Trichet et al. [158] of between 1 and 100 nN/μm where ‘Stiff’ > 30. These values were then correlated to equivalent substrate stiffness to identify what modulus of a bulk material the pillars were capable of simulating.

$$E_{eff} = \frac{9k}{4\pi a} \quad \text{Eq. 5- 12}$$

Where k is the pillar stiffness and a is a scaling constant dependent on pillar radius or FA area as the pillar radius was significantly larger in the calculation of the pillars used in the source paper, we assume that unlike the large pillars used in the work of Ghibaudo et al. [221], the 100 and 150 nm diameter UHAR pillars respectively will not be holding all the force of a 1 μm diameter focal adhesion, but rather be sharing the loading from one attachment. In this case it is easier to use the linear extrapolation to roughly estimate the equivalent stiffness under a shared predicted loading.

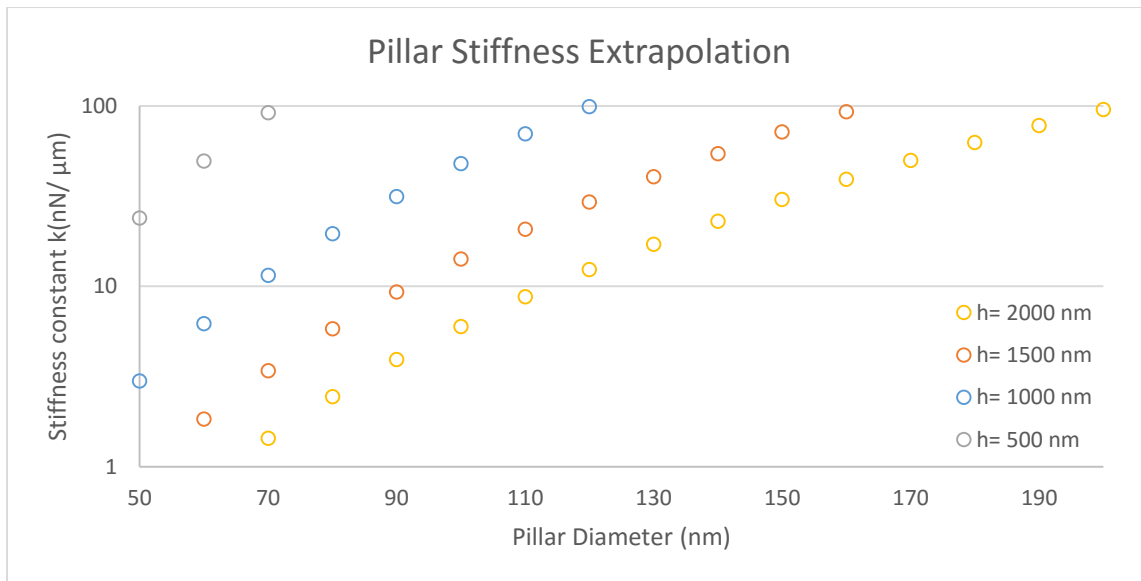
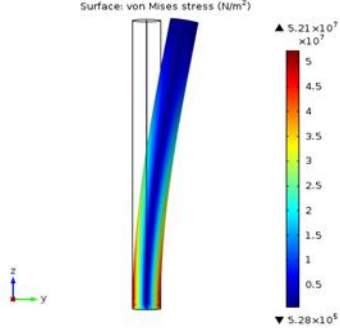
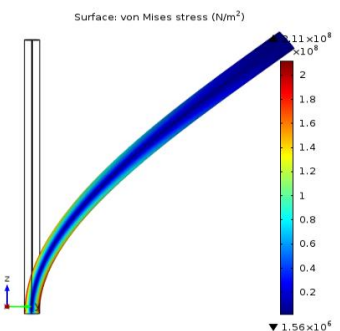
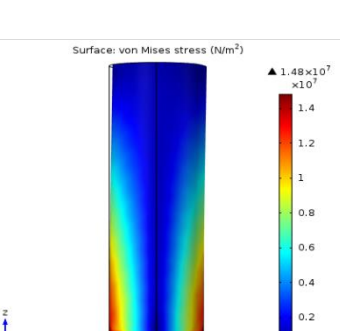
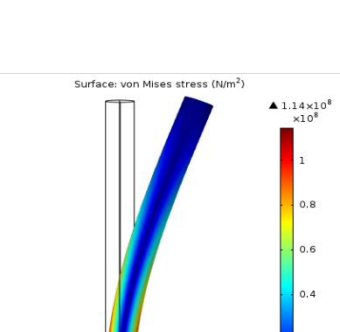


Figure 5-42 - Pillar stiffness's of interest between 5 and 100 $\text{nN}/\mu\text{m}$ for pillars of 500 nm, 1000 nm, 1500 nm and 2000 nm in height (h), as a way of tuning substrate stiffness for cell attachment. 1000-2000 have the largest useful range for cell culture applications.

The bending simulations of pillars used in the study are shown in Table 5-5 (p 257), along with an extrapolation to effective Young's modulus as seen in Ghibaudo et al. [221].

Table 5-5 - UHAR Pillar type with corresponding cantilever stiffness as linear material, corrected, linear FEA model and equivalent stiffness for a flexible flat substrate. Load applied in model 10 nN. Effective modulus determined from approximations by Trichet et al. [158].

FEA Model image output	Pillar type	Radius (μm)	k_{corr} (nN/ μm)	k (nN/ μm)	k_{FEA} (nN/ μm)	$E_{\text{effective}}$ (kPa)
	D150 Tall	0.075	45.85	49.32	51.15	35.3
	D100 Tall	0.050	5.74	5.98	6.03	4.28
	D150 Short	0.075	1499.06	1938.34	1855.30	1390.00
	D100 Short	0.050	33.35	35.96	36.10	25.80

The equivalent and actual stiffness of the pillar arrays is given in Table 5-5. This variety of stiffness highlights the variation in hESC attachment on the substrates of varying stiffness and height. A drop off is seen above and below a substrate stiffness roughly equal to 25.8 kPa.

5.3.4.7 Adhesion of hESCs on hydrogel scaffold surfaces

H2 hESCs seeded at 400,000 cells/ml as single cells from a 3:1 passage with Acutase showed very low adhesion on the hydrogel roll surfaces, with cells initially spreading over the surface of the gel in the first 24 hours in the presence of ROCK inhibitor (see Chapter 4) but subsequently underwent apoptosis before 48 hours. Those that stayed alive formed large colonies, as the cell-to-cell interaction became preferable to the surface of the gel (Figure 5-43).

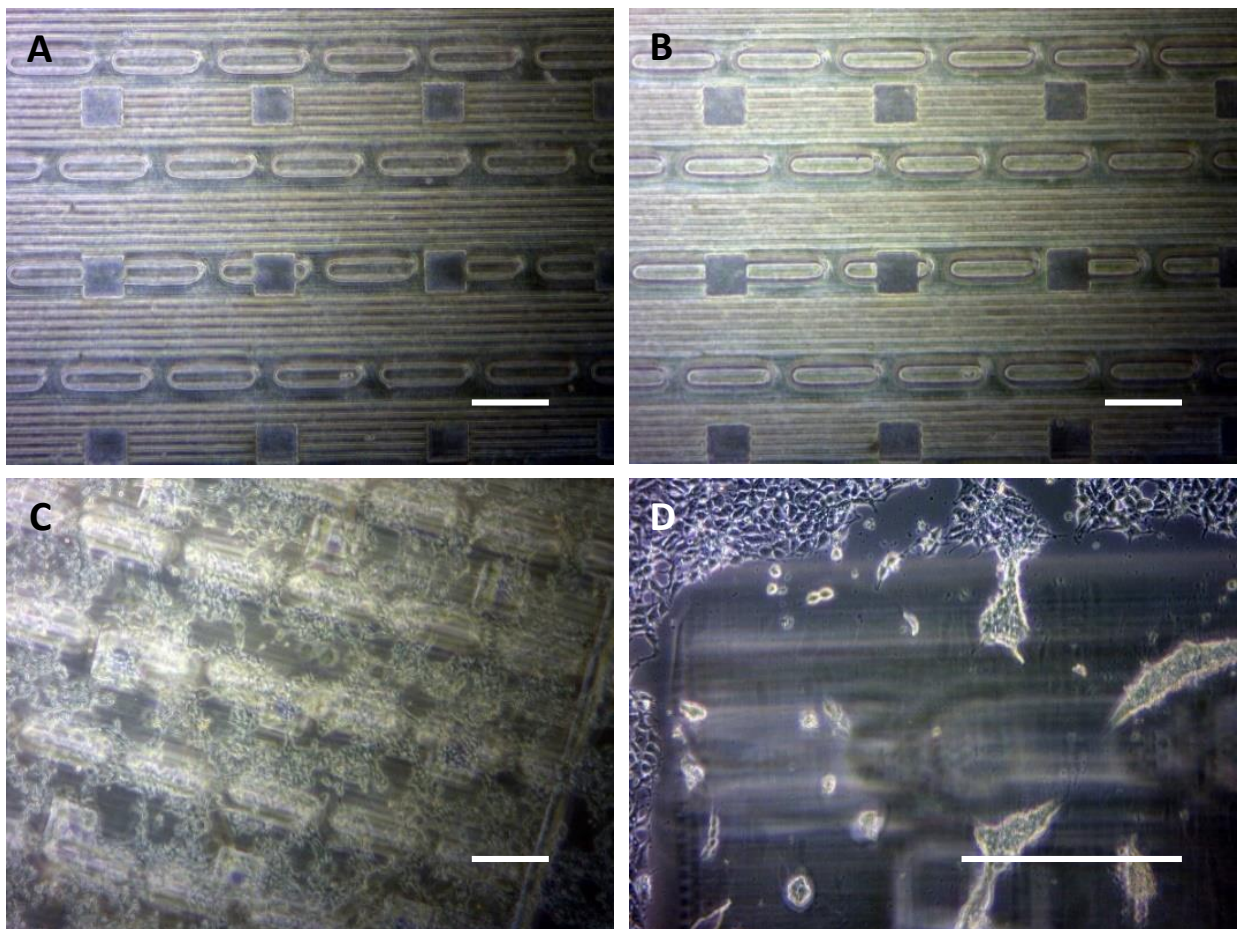


Figure 5-43 - A.B.) PEGDMA-Collagen (33 %) hydrogel rolls unfolded by pinning with thin PAA layer on Glass. Scale bars 400 μm C.) Cells at 24 hours Scale bar 400 μm and D.) 48 hours forming cell colonies to escape gel sheet Scale bars 400 μm .

The cause of this is thought to be that the aforementioned surface modulus was too low to maintain viable cell attachment. While encapsulation with the rolls was possible, the large colonies detached during the rolling process, and those stained with live-dead stain showed some signs of life but cannot be called a proliferating colony.

5.3.4.8 Adhesion of hESCs on hard scaffold surfaces

Adhesion was very good on the hard epoxy scaffold structures (Figure 5-44), similar to the injection moulded inserts. This provides the justification for the hybrid containers, as an all hydrogel roll lacks the structural support necessary to adhere hESCs and allow them to proliferate so that a downstream differentiation can be attempted in 3D.

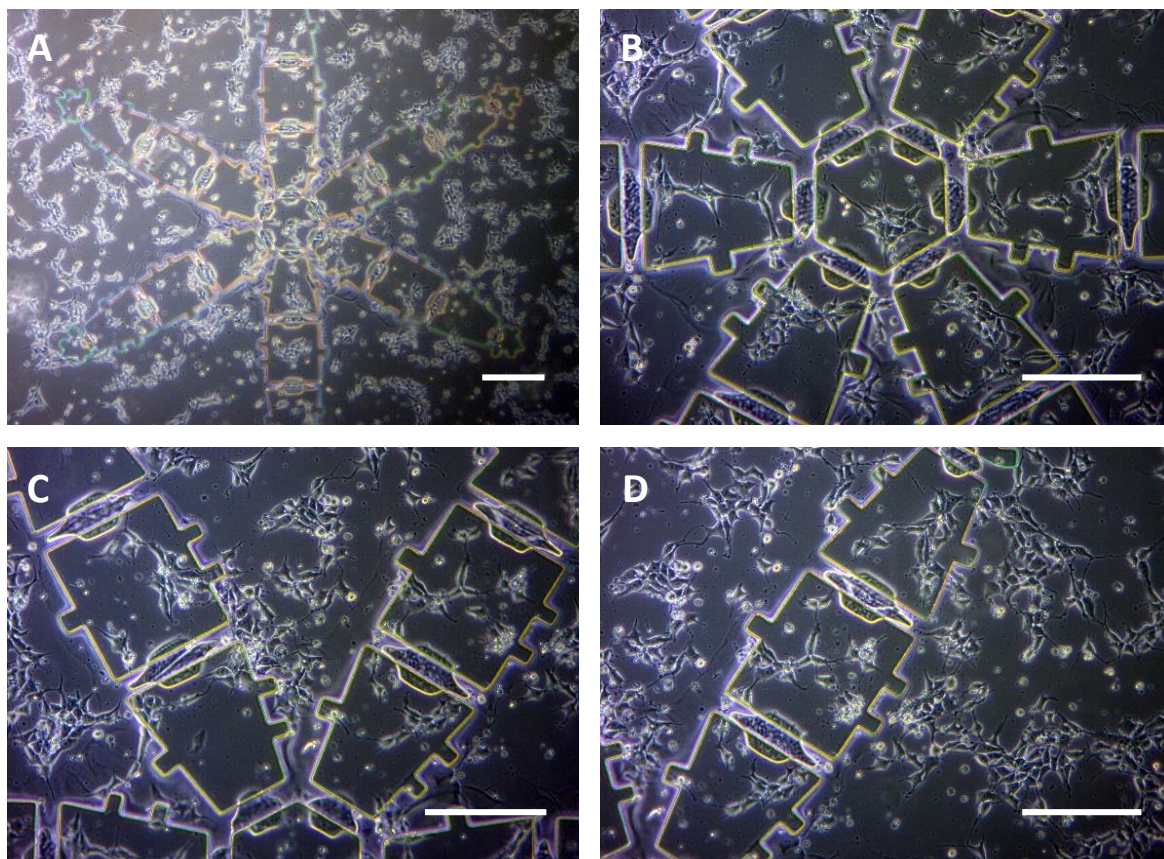


Figure 5-44 - '6 petal octagonal Lotus' folding scaffolds with overlapping lock mechanism (see Chapter 4). Device seeded on 250 nm PAA lift-off layer, slowing down release rate long enough to seed H2 hESCs. Lift-off time confirmed as 5 days post seeding. hESCs seeded as single cells after Acutase 3:1 passage in a 200,000 cell/cm² concentration. Cells were "dry-plated" onto containers immobilized on glass slide. Slide and containers previously washed in EtOH and irradiated with UV for 10 minutes, they were then soaked for 12 hours in PBS and 12 hours in E8 media. Prior to cell seeding the slide was plated with vitronectin in a 1 μ l/cm² concentration for 30 minutes at room temperature. All scale bars: 250 μ m

Capturing cells in these containers was a partial success during a proof of concept seeding, but was only successful while working with hTERT fibroblasts (Figure 5-45) after the hESC experiments were complete. Regrettably the containers failed to work, or when they did the cells had started to die due to infection or other reasons. The low maintenance schedule of the hTERTs meant more attempts could be made until one proved to be fruitful.

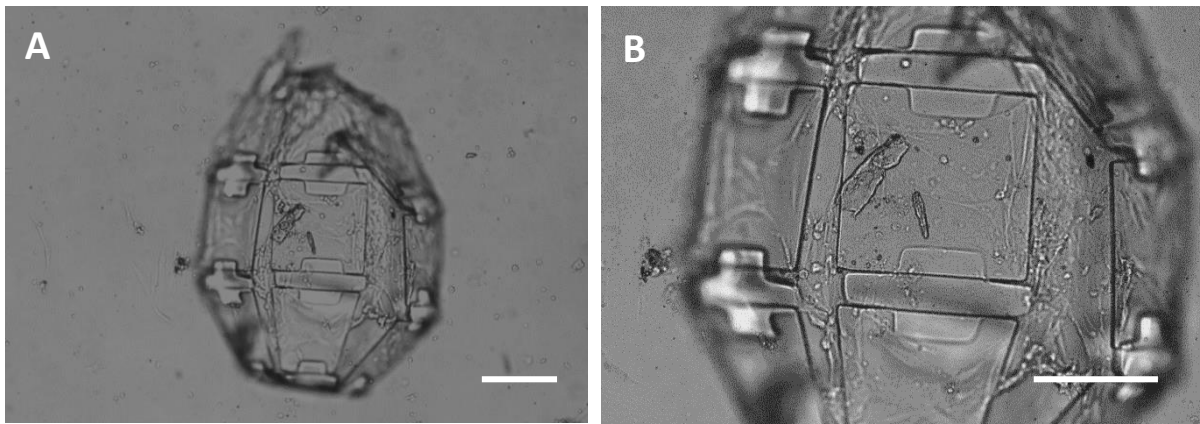


Figure 5-45 - Optical microscopy image of a closed 'lotus' container with hTERT fibroblast cells visible on the inside surface, cells visibly stressed however by lack of feeding schedule to allow container to fully detach and fold without being torn apart by frequent fluid changes. hTERTS seeded at 20,000 cells/cm². Image taken 72 hours after seeding of cells on glass slide bound tetrahedrons on 400 nm thick PAA sacrificial layer. '6 petal octagonal Lotus' containers manufactured by PMMA lift-off process from Chapter 3-4 with container design outlined in Chapter 4. Scale bars: 250 μm

5.3.5 hESC colony formation on Pillar Gradient Array

Patterning hard surfaces was looked into as a means of controlling hESC colony size and location within the 3D scaffolds by adjusting their ability to attach in certain areas. Calculation of the pillars on the gradient array slides, showed that the range of pillars all fall well within the range of 'stiff' pillars and substrate stiffness likely plays little role in cell behaviour on these patterns. The composite manually produced from optical microscopy over the 9 x 9 mm array square is shown in Figure 5-46.

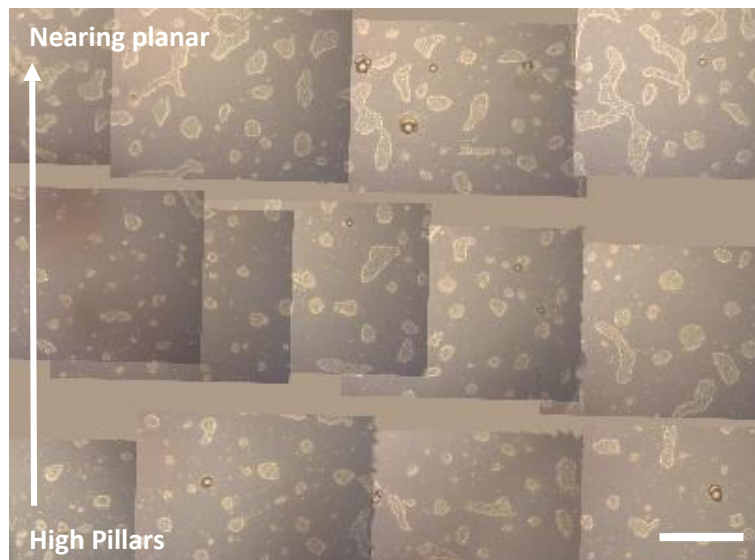


Figure 5-46 - Compiled manual scan of the 9 x 9 mm square containing the nanopillar array. Some areas not imaged, however each strip is representative of a range of the array showing increasing colony size in each section. Scale bar: 1mm.

Following a prolonged incubation with no change in media from the Advanced DMEM E8 standard the pillar gradient at 94 hours showing highly 3D morphology (Figure 5-47), all substrates were covered in a $0.5 \mu\text{g}/\text{cm}^2$ vitronectin coating.

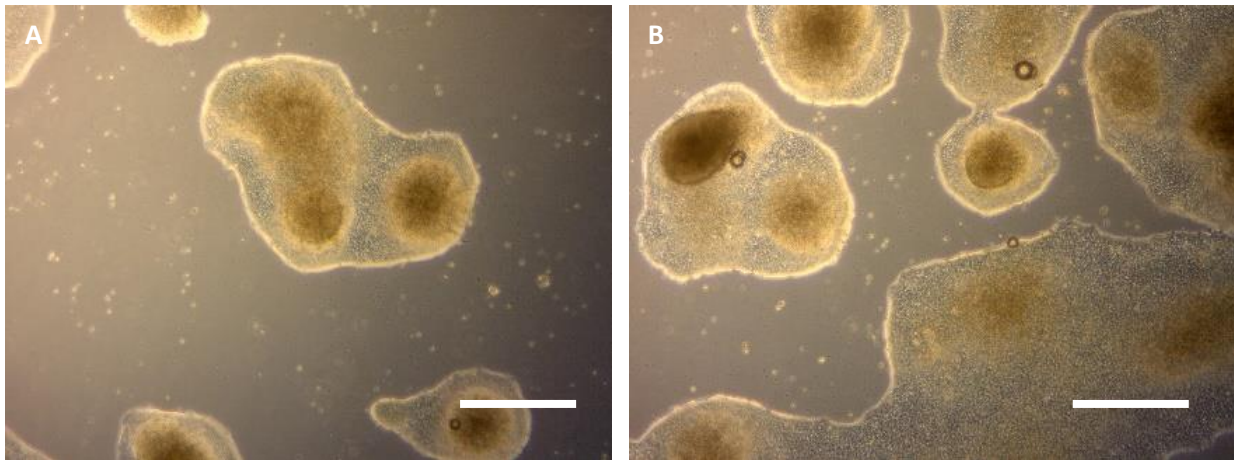


Figure 5-47 Phase contrast microscopy 10x magnification. Images showing H2 hESC forming highly 3D colonies on pillar gradient array. These were found to occur in random differentiation conditions, with no induced differentiation (Small molecules), cells incubated in E8 media. Scale bars: $250 \mu\text{m}$.

The occurrence of these 3D colonies is a good indicator for being able to control colony size, and fine tune the critical density at which selective differentiation pathways are chosen. A 3D colony is also crucial in achieving the critical mass necessary to differentiate into mesoderm[172].

5.3.5.1 Pillar stiffness gradient calculation

The gradient arrays had pillars of varying height from flat to 250 nm tall, but this height change did not significantly alter their flexibility, due to their low aspect ratio (Figure 5-48). Thus all the pillars on the array could be considered 'stiff', with changes in cell attachment assumed to correlate with the height of features rather than emulating a changing substrate stiffness, as was the case with the UHAR arrays covered previously. The variation in pillar stiffness (1×10^9 to 1×10^3) from one side of the array to the other is shown in Figure 5-48, calculated using equations 5.3-5.11.

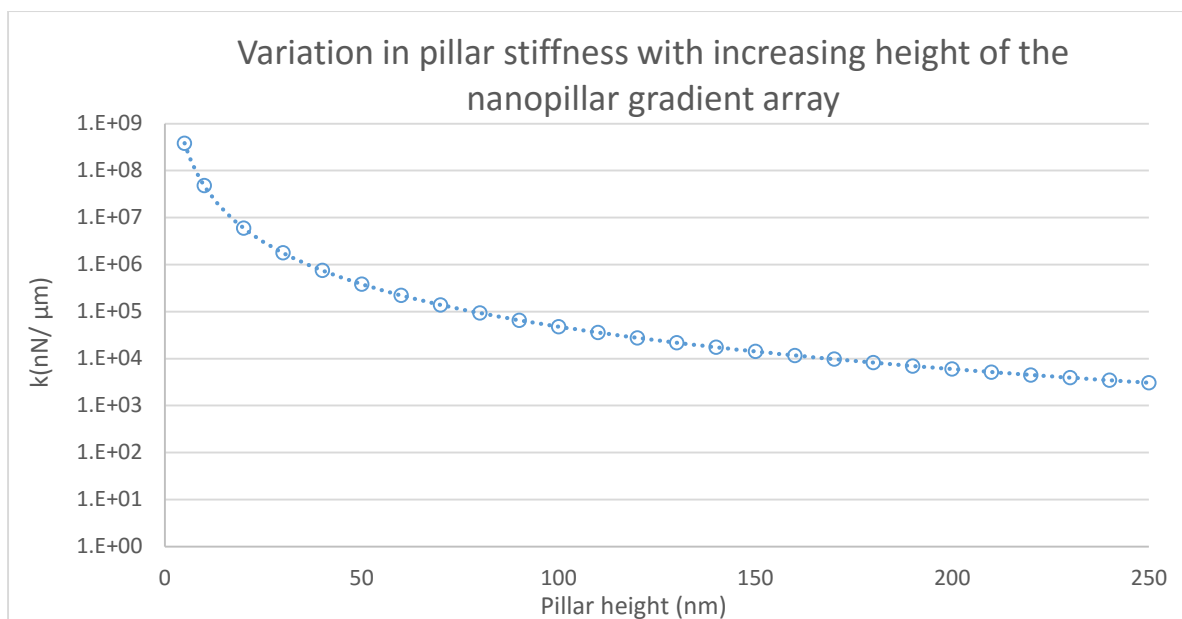


Figure 5-48 - Pillar stiffness with varying height over the nanopillar gradient array.

The variation in pillar height (and corresponding stiffness) decreases on the Y-axis of Figure 5-49 below. Pillar gradients showed repeated correlations in cell coverage at various ECM coating concentrations. Substrates were coated in $0.25 \mu\text{g}/\text{cm}^2$ and $0.5 \mu\text{g}/\text{cm}^2$ of vitronectin and seeded with a cell density of $40,000 \text{ cells}/\text{cm}^2$.

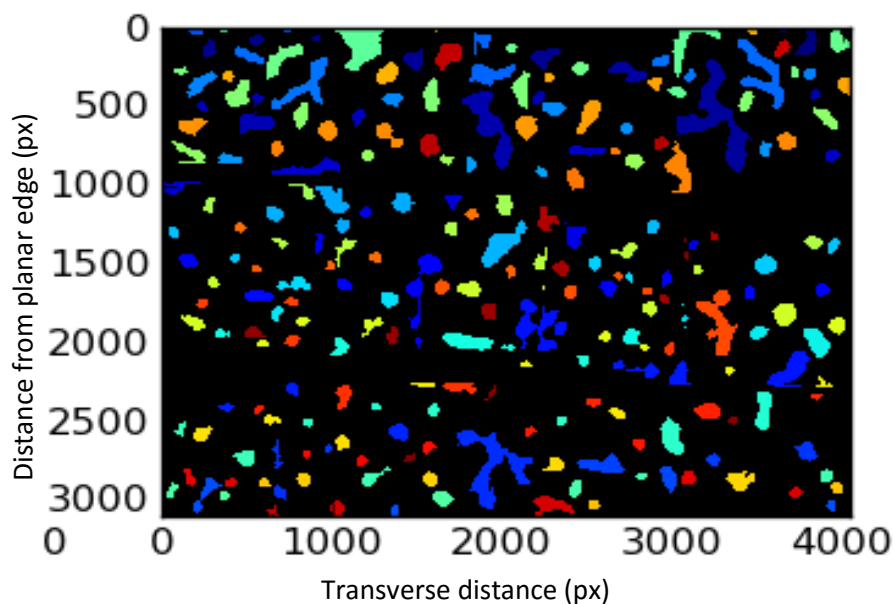


Figure 5-49 - Cell profiler labelled colonies shown as different coloured blobs, colony size and position plotted in Matlab script, correlating colony position and overall size in pixels (px)

Correlating cell colony position with their relative size (as represented by the amount of pixels from the centre of the colony to its outermost edge) a scatter plot is shown in Figure 5-52.

Most cell clusters fell in the range of being under 150 μm in diameter, a colony size histogram is shown in Figure 5-50.

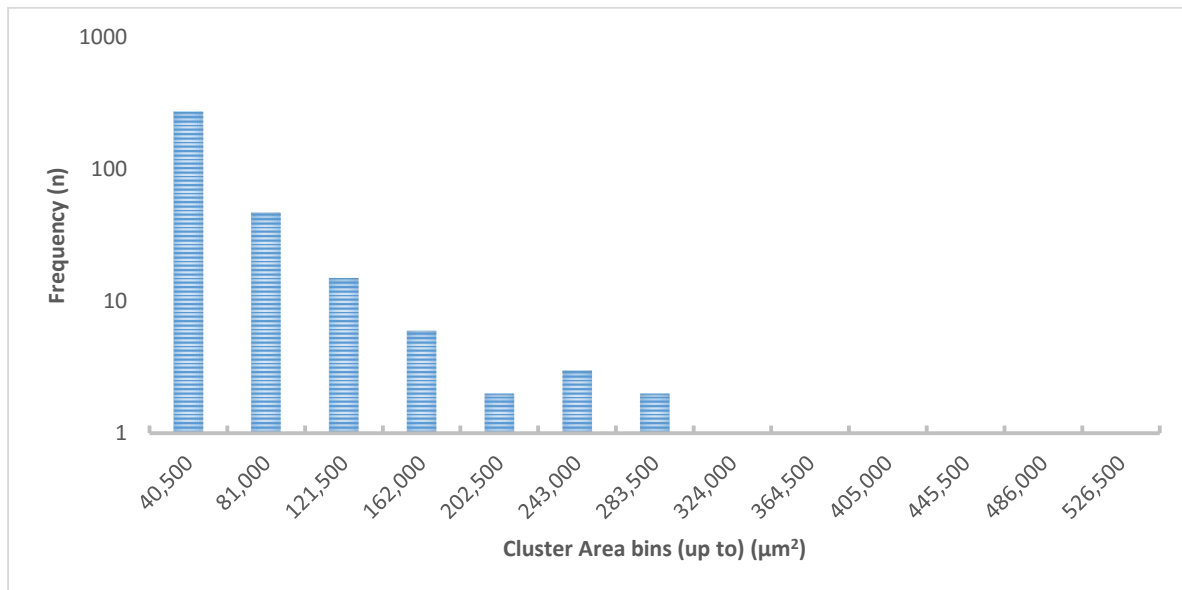


Figure 5-50 – hESC cluster area histogram, showing the tally of cell colonies by their area of coverage, data post-processed from Cell Profiler® colony labelling.

With the colonies being oddly shaped their radius was correlated to the overall cell cluster area and showed an almost linear relationship between the two as shown by the heat-map (Figure 5-51).

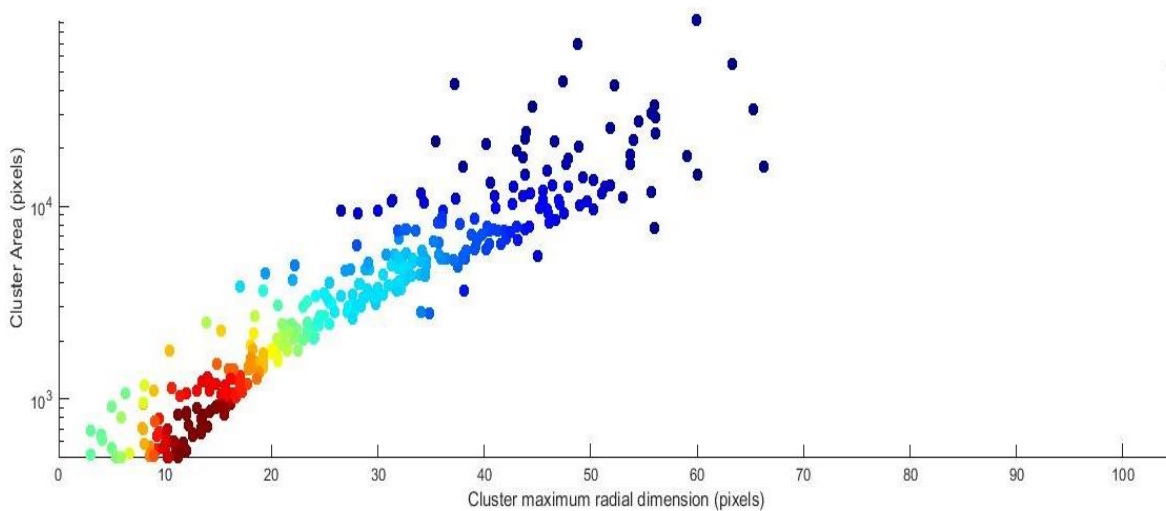


Figure 5-51 - Plot of cluster area against maximum radius from centroid as analysed by cell profiler and post-processed in Matlab. A linear relationship can be seen between the two.

The cell colony area was therefore used to map the level of cell-to-cell interaction and aggregation with increasing pillar height. This trend is better represented by producing a heat map of the cell cluster area and distribution, obtained from processing image data in Matlab, the resulting trend of cell cluster size and position is shown where yet again the distance x-axis represents the y-axis of the

labeled colony image in Figure 5-49. The colour represents concentration of adjacent points. Section lines between images show large concentrations of small colonies as these were cut by the image border, however a trend of increasing peak colony area can be seen moving to the origin. Generally the nanopillar gradients showed visible changes in hESC proliferation over the pillar range at all ECM concentrations. FEA and mechanical calculations show that pillars would be rigid enough to exclude substrate stiffness as the reason for these variations. The changes in distribution are rather likely the result of the changes in height of the pillars and the ability for the cell to interact with the underlying surface.

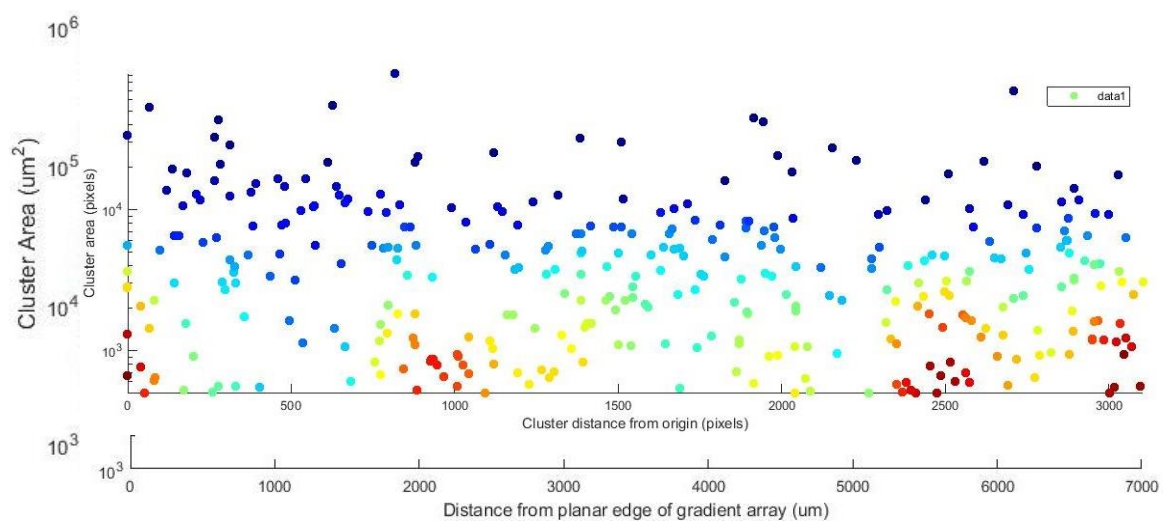


Figure 5-52 – Joined heat map scatter plot, where intensity (red) indicated several data points overlapping one another. The key trend to note is the average cluster area is higher where distance $\rightarrow 0$ with it dropping off on average moving along the x-axis. The converted location and cluster area in μm is shown in the lower plot.

5.4 CONCLUSIONS

A partial success in achieving cell encapsulation in a self-folding nanopatterned cellular niche has been demonstrated. Initially cell seeding on collagen modified hydrogel inserts showed a trend of improvements in cell attachment, when compared to the pure PEGDMA negative control. It was a time sensitive pilot study, and succeeded in answering the question regarding PEGDMA gel modification with co cast collagen in the pre polymer solution, as evident from Figure 5-3. SU8 surfaces showed successful cell attachment as seen in Figure 5-14 and Figure 5-44. The one dominant factor was not so much the type of nanotopography but oxygen plasma ashing of the surface, which is thought to be caused by surface chemistry modification, and partial roughening of the surface after etching, as evident in Chapter 4.

Following seemingly successful attachment of hTERT fibroblasts in a trial prior to beginning work with hESCs, several sets of nanopatterned inserts manufactured by injection moulding were taken to Oslo for experimentation with human embryonic stem cells (hESCs). The use of injection moulded substrates aimed at minimising the cost during this pilot study, as nanopatterned container samples were still in the low batch manufacturing stage, and took substantial resources and time to manufacture, when compared to the hundreds of samples that can be injection moulded in one afternoon.

Testing of hESC seeding began by calibrating the necessary ECM coating concentration, seeding density, ECM type and procedure for coating and culturing cells on these substrates. It was found that vitronectin maintained prolonged attachment of hESCs to the substrates when compared to the commercially available Matrigel® as evident in sub section 5.3.4.2. It was also found that cells remained attached to the surfaces even at very low concentrations of vitronectin (up to 100 times dilution) (Figure 5-29) when compared to TCP controls.

Cells cultured on hydrogel sheets showed poor long term attachment, and formed larger colonies, in what is believed to be a survival tactic. These large colonies broke off from the substrate, and when compared to the rhVTN coated glass in the images (Figure 5-43), the soft hydrogel surfaces are not favoured by the hESCs. This issue is circumnavigated by the hybrid faced containers which did successfully immobilise cells and remain anchored to the surface long enough to seed (achieved by using a very thin PAA release coating), the immobilised cells are shown in Figure 5-44. Sadly the seeded containers suffered from infection before lift-off of the containers could be achieved, and those that did had the hinges damaged by successive media changes. Successful capture of cells from culture by the gradual release of containers after cell seeding was only successfully achieved at the end of this work with hTERT fibroblasts in the University of Glasgow lab, as seen in optical microscopy of closed containers containing fibroblast layers (Figure 5-45).

The lack of hESC attachment to hydrogel containers was confirmed by their poor adhesion on the softer UHAR pillar arrays as seen in Figure 5-48, this is in agreement with literature, where softer substrates were not favoured by human embryonic and induced pluripotent stem cells [173]. Further work is necessary to see if pillar height and thereby substrate stiffness changes gene expression in hESCs, and can be used as a means of selective substrate induced differentiation, as has been demonstrated on MSCs by the past work of Dalby et al.[39] for bone formation. The gradient pillar array meanwhile showed a decrease in hESC attachment as the pillar height increased as demonstrated by the FEA analysis shown in Table 5-5 (p 257). It was observed that smaller colonies formed on the high pillar region as shown in the cell coverage densities in Figure 5-52. This

correlates in cell profiler analyses of cell proliferation (as colony size) on the various regions of the gradient pillar array in Figure 5-50. These gradients can potentially be used in the future as a means of controlling cell colony size on different faces of the 3D nanopatterned containers in Chapter 4.

This was a pilot study to assess if it would be possible to seed hESCs on 3D nanopatterned containers and influence their behaviour by changes in substrate topography. It has demonstrated that this technique could be possible, with the colony formation of hESCs successfully controlled, and even signs of spontaneous differentiation observed in the 3D clustering behaviour seen in Figure 5-30.

While no hESCs could be transitioned successfully in a closed 3D container due to issues with infection and problems with manufacturing, hTERT fibroblasts could be captured in cell media by slow lift-off of these self-assembling containers. Had more time been available, with the newly learned techniques and lessons from subsequent failures it is entirely possible that hESCs could be captured within these containers, although this would have required more time in Oslo. There were also difficulties in that the manufacturing of the boxes took place in another country, limiting the available stocks that could be accessed and accounted for. Whether they could be maintained in this configuration, and even influenced down a certain differentiation pathway remains to be seen, and would be an excellent candidate for future work on this subject. However the tool box and approach to creating these niches has now been established.

6 OVERALL DISCUSSION AND CONCLUSIONS

The desire to design and construct micro- and nanoscale systems for tissue engineering originates from the need for sustained and precise control over cellular proliferation, function and differentiation. This task is a vital milestone in moving from materials which are “observed to function”, to those which are “made to function”. This ‘design’ process reflects the main factors controlling cell function *in vivo*, such as: architecture, chemical and mechanical stimuli, gradients and cross talk between diverse cell types. A multi-stimuli and multi-dimensional environment is therefore desirable if we are to emulate the complex biological systems.

The aim of this work was to create 3D structures using traditional 2D nanopatterning techniques which could be used in cell culture to create tailored and nanopatterned niches. This has been demonstrated as a proof of concept work. While the differentiation of stem cells or prolonged culture of cells in the 3D containers has not been achieved, the tool box and the ability to apply it have been demonstrated. However given sufficient time, with the new understanding of the process and nuances of cell culture that this task would be possible by building on this work.

The success of the project in creating the self-folding containers, is achieved by the use of a number of novel manufacturing techniques listed in Chapter 2 which aim to limit the difficulties in throughput, created by brittle and costly imprint stamps, and coping with the occasional film non uniformity which is an inevitable by-product of spinning multiple layers to produce complex structures. The first of these novel fabrication methods is the hierarchical patterning using FEP two tier stamps shown in Figure 2-21, which can be used to add an extra level of adjustable and tailored complexity to the surfaces cells interact with inside the scaffolds, and secondly to the patterning of a 3D curved surface seen in Figure 2-26, as the increased toughness of the FEP films allows them to conform to more complex geometries. This flexibility in turn allows the application of patterns traditionally produced by stamping using qz and Si stamps on planar 2D surfaces to 3D, curved and non-planar, non-uniform surfaces, providing greater throughput, easier replication and significant cost reductions when compared to lithographically manufactured stamps. For medium sized nanotopographies in the region of 500 nm, it has been shown that the FEP films can be combined with traditional EBL resists and metal evaporation to recreate low aspect master stamps on Si surfaces, (Section 2.3.3). The ability to pattern non planar surfaces with FEP stamps, leads into the proposed novel technique of modular NIL (Section 2.2.3.6). Combinational mastering provides a tool for creating any combination of nano- and micropatterned hierarchical structures on surfaces by UV-NIL to have greater control of cell segregating patterns as shown in Figure 2-25, and thereby

controlled contact guidance of cells in culture. Although this final claim has not been demonstrated experimentally due to a lack of time, it is worthy of future study.

A key achievement has been the hybrid containers described in Chapter 4, in the form of dodecahedral containers, and the flower shaped “lotus containers” shown in Figure 4-48. These containers combine hydrogel synthesis by photolithography, with a number of nanofabrication techniques including NIL and UV-NIL described in Chapter 2 to create self-folding nanopatterned structures by a simple and quick method. The containers created during this work differ from those seen in literature, such as those from created by Bassik et al. [24] and in the work Py et al. [222] on capillary folding, in that they can be nanopatterned by conventional means, and fold in cell culture media as shown in Figure 5-45. These advantages do not stem from novel hydrogel chemistry but the way the devices are manufactured and used.

The container construction hinges on the creation of the bilayer as a by-product of lift-off from a pH responsive PAA sacrificial layer underneath, as shown in Figure 4-2 [1]. This method of creating hydrogel bilayers has two distinct advantages compared to serial lithography as seen in the bilayers produced by Bassik et al. [24] in their greater simplicity and faster production speed and in the exposure gradient hydrogels produced by Jamal et al [27], in that these bilayers can incorporate patterning in the same step by the novel method of sacrificial layer embossing shown in Chapter 2 - Figure 2-32.

These novel bilayer films are much thinner, suggesting better permeability to dissolved species, they have also been demonstrated as a stand-alone self-rolling scaffold, much like a Swiss-roll, which can incorporate spacer pillars, patterns and photopatterned windows to aid cell migration and reinforce the roll structure. The patterned rolls while easily foldable in cell culture media and pH buffer solution had to be modified to allow for cell attachment, by the incorporation of collagen in the pre-polymer mixture which was markedly improved by the dissolution of collagen, and then further coated by dry plating vitronectin for the attachment of hESCs. While the all hydrogel scaffolds were not ideal in their present form, they were the justification for the use of hybrid containers composed of solid patterned faces, and flexible hydrogel hinged as a “best of both worlds” approach. The issues with cell attachment to the hydrogels could potentially be improved by modification with RGD or by tethering a ECM protein to the gel [36], this could be attempted in future work to improve the usability of the all hydrogel rolls.

In the hybrid container construction it was demonstrated that these hydrogel bilayer films can be utilized as photolithographically defined thin hinges in a process almost identical to photolithography and UV-NIL performed on conventional micro fabrication photoresists. They also

require less preparation [23], and are not sensitive to atmospheric oxygen due to the incorporation of minute amounts of TEA as an oxygen scavenger. This allows for the hinges to be applied in a conventional photolithographic setup, provide the potential to be scaled up to roll-to-roll printing and screen printing manufacturing, where keeping a deoxygenated polymer mixture over large areas does not have practical merit.

The hybrid container designs limited the necessary folding angle, by increasing the number of faces of which the spheroid was constructed, as seen in Chapter 4. By doing this, the gel chemistry was less of an issue, as the containers would form semi-confluent and confluent containers even at modest hinge deflections. By limiting the required gel swelling, the overall strength of the hinges could be improved thus reducing the fragility of the 3D containers, as the swelling ability of the gel is inversely proportional to its strength due to the crosslinking network being sparser as seen in rheological data in section 3.3.2.2.1. In creating mechanically stronger hinges there is therefore a trade-off of actuation potential as demonstrated by the Timoshenko relation (Figure 3-41).

While many designs were proposed in Chapter 4 not all were achieved, the key demonstrators became the dodecahedral container and that of the symmetrical lotus. Key difficulties that had to be overcome were interactions between various layers. For instance the sacrificial nanopatterned PAA lift-off layer could not be combined with solvents that could dissolve it, limiting all gel hinge formulations to those using ethanol (EtOH) as a solvent. There were also artefacts in the form of insoluble films (Figure 4-37). These were eventually overcome by introducing a boundary layer, that is removed in the hinge areas by development or etching prior to hydrogel hinge application, to give it a clear path to the pH responsive PAA layer underneath. It was assumed that this insoluble film that affected manufacture was a result of a reaction between the acidic underlying PAA layer, and the SU8 photoresist above, as the SU8 is crosslinked by a photo-acid generated during photo exposure. The assumption was that the acidic shorter chains in the PAA partially crosslinked the interface, or were somehow bound by ionic bonding to the SU8 epoxy chains. The introduction of a PMMA boundary layer which was later removed by ethyl-lactate during SU8 development solved this issue, as did a more costly Au boundary layer, removed by a novel slow iodine etch using isopropanol instead of water, to avoid damaging the PAA layer below.

The containers were tested on hTERT fibroblasts cultured in complete DMEM and also in Oslo on hESCs obtained from the Oslo Centre for Stem Cell Research. The cell encapsulation and behaviour on nanopatterned surfaces was intended to follow on from Siller et al. [172] where hESC differentiation was directed towards endoderm and subsequent hepatic tissue formation by the use of a proprietary small molecules technique. The inspiration was to attempt to recreate the

topography induced differentiation seen in MSCs in Dalby et al. [39], however in this case it would be done with hESCs and hepatic tissue rather than bone.

It was noted that the use of nanopatterned surfaces significantly reduced the amount of ECM necessary for substrate coating, thereby reducing overall cost of cell culture (Section 5.3.4.4). The hESCs also showed the spontaneous formation of much more 3D structures, similar to those seen in small molecule induced differentiation but perhaps not as pronounced. This was done in the absence of any differentiation inducing media (Section 5.3.4.5).

A foundation for discovering desirable nanopatterns for hESC proliferation control has been established, as have the means of producing these patterns on the surfaces of foldable containers, produced by simple photolithographic methods. These containers have been shown to be able to fold in the native cell culture environment, by the use of permeable hydrogel hinges. The folding of these containers is controlled by the thickness of lift-off sacrificial layer, which is also responsible for the folding of the containers, and when patterned produces a nanopattern on both internal and external surfaces of the container, something entirely novel.

The 3D containers produced within this work, have been shown to be able to capture cells and transfer them from a 2D culture surface to a 3D environment. While the merit of this, and any possible effect on cell differentiation, proliferation and organelle metabolism remains to be determined, this pilot study and proof of concept design provide the tool box for it to be attempted in future work.

7 FUTURE WORK

A number of ways exist which could add to and broaden the existing understanding of these 3D cellular niches and patterning techniques. While a proof-of-principle tool-box has been created and demonstrated, many areas require additional statistical verification through repeat studies. In addition to expanding the existing knowledge, a number of additional investigations would be of great interest:

- A structural investigation of 3D container triggering and release could help improve their versatility. While the hinges close the boxes successfully, it was found that it is the anchoring duration to the substrate (before the box detaches and floats away) that would play a key role in cell survival, premature detachment is detrimental to cell survival while late detachment is inefficient and potentially costly. A sacrificial layer which dissolves as a result of cell released metabolites could be a key to their autonomous operation, once sufficient cell density and attachment is achieved the colony would begin to dissolve the sacrificial film, releasing the container and causing it to fold automatically.
- Having shown that these containers can in principle capture cells from culture media, and potentially keep them alive in the long term, more work is necessary to understand the survivability of cells in containers of different sizes and the metabolomics of IPS and ESC cells on various nanotopographical patterns in 2D and in the 3D containers. This could lead into a full differentiation from embryonic state through to definitive endoderm liver and ultimately hepatic tissue in a 3D patterned cellular niche.
- Having relied on photo patternable epoxies, photo resists and touched on some biodegradable polymers such as PLLA and their patternability by embossing, creating a polymer blend with tunable degradation rate could introduce biodegradability into the containers, to allow them to dissolve and leave a cell cluster behind after the cells have formed a confluent colony. This degradation would allow applications *in vivo* and the potential for cell therapies where a container remaining indefinitely is not desirable.
- It has been shown that containers can be made incorporating conductive layers such as gold on one or both surfaces, introducing sensory circuitry into the surface of the container and a miniaturized gel power supply to allow for their use as internal sensors and grippers, or for stimulation of cardiac and/or neuronal tissue.

REFERENCES

1. Vasiev, I., Greer, A.I.M., Khokhar, A.Z., Stormonth-Darling, J.M., Tanner, K.E., and Gadegaard, N., *Self-folding nano- and micropatterned hydrogel scaffolds by single step photolithographic process*. *Microelectronic Engineering*, 2013. **109**: p. 76-81.
2. Hagino, K., Onuma, R., Kawachi, M., and Horiguchi, T., *Discovery of an Endosymbiotic Nitrogen-Fixing Cyanobacterium UCYN-A in Braarudosphaera bigelowii (Prymnesiophyceae)*. *PLOS-One*, 2013. **8**(12): p. e81749.
3. Katifori, E., Alben, S., and Cerda, E., *Foldable structures and the natural design of pollen grains*. *Proceedings of the National Academy of Sciences*, 2010. **107**(17): p. 7635-9.
4. Hales, T.C., *Cannonballs and Honeycombs*. *Notices of the American Mathematical Society*, 2000. **47**(4): p. 440-449.
5. Bakker, B.S., Jong, K.H., Hagoort, J., Oostra, R.-J., and Moorman, A.F.M., *Towards a 3-dimensional atlas of the developing human embryo: The Amsterdam experience*. *Reproductive Toxicology*, 2012. **34**(2): p. 225–236.
6. Alvarez, S., *Polyhedra in (inorganic) chemistry*. *Dalton Transactions*, 2005(13): p. 2209-2233.
7. Mohty, M., Malard, F., Abecassis, M., Aerts, E., Alaskar, A.S., Aljurf, M., Arat, M., Bader, P., Baron, F., Bazarbachi, A., Blaise, D., Ciceri, F., Corbacioglu, S., Dalle, J.H., Duarte, R.F., Fukuda, T., Huynh, A., Masszi, T., Michallet, M., Nagler, A., NiChonghaile, M., Pagluica, T., Peters, C., Petersen, F.B., Richardson, P.G., Ruutu, T., Savani, B.N., Wallhult, E., Yakoub-Agha, I., and Carreras, E., *Sinusoidal obstruction syndrome/veno-occlusive disease: current situation and perspectives[mdash]a position statement from the European Society for Blood and Marrow Transplantation (EBMT)*. *Bone Marrow Transplant*, 2015. **50**(6): p. 781-789.
8. Van de Kerkhove, M.P., Hoekstra, R., Chamuleau, R.A.F.M., and Van Gulik, T.M., *Clinical application of bioartificial liver support systems*. *Annals of Surgery*, 2004. **240**(2): p. 216–230.
9. Shan, J., Schwartz, R.E., Ross, N.T., Logan, D.J., Thomas, D., Duncan, S.A., North, T.E., Goessling, W., Carpenter, A.E., and Bhatia, S.N., *Identification of small molecules for human hepatocyte expansion and iPS differentiation*. *Nature Chemical Biology*, 2013. **9**(8): p. 514–520.
10. Gjorevski, N., Ranga, A., and Lutolf, M.P., *Bioengineering approaches to guide stem cell-based organogenesis*. *Development*, 2014. **141**(9): p. 1794-1804.
11. Schiff, E.R., Sorrell, M.F., and Maddrey, W.C., *Schiff's Diseases of the Liver*. 10 ed. 2006: Lippincott Williams & Wilkins.
12. Desmet, V.J., *The amazing universe of hepatic microstructure*. *Hepatology*, 2009. **50**(2): p. 333-344.
13. Khetani, S.R. and Bhatia, S.N., *Microscale culture of human liver cells for drug development*. *Nature Biotech*, 2008. **26**(1): p. 120-126.
14. Zhang, D., Luo, G., Ding, X., and Lu, a.C., *Preclinical experimental models of drug metabolism and disposition in drug discovery and development*. *Acta Pharmaceutica Sinica B*, 2012. **2**(6): p. 549–561.
15. Perel, P., Roberts, I., Sena, E., Wheble, P., Briscoe, C., Sandercock, P., Macleod, M., Mignini, L.E., Jayaram, P., and Khan, K.S., *Comparison of treatment effects between animal experiments and clinical trials: systematic review*. *BMJ : British Medical Journal*, 2007. **334**(7586): p. 197-197.
16. Freier, T., *Advances in Polymer Science - Polymers for Regenerative Medicine*, ed. C. Werner. Vol. 203. 2006: Springer.
17. Zhang, X., Pint, C.L., Lee, M.H., Schubert, B.E., Jamshidi, A., Takei, K., Ko, H., Gillies, A., Bardhan, R., Urban, J.J., Wu, M., Fearing, R., and Javey, A., *Optically- and thermally-responsive programmable materials based on carbon nanotube-hydrogel polymer composites*. *Nano Letters*, 2011. **11**(8): p. 3239-3244.

18. Zhang, L.G., Fisher, J.P., and Kam, L., *3D Bioprinting and Nanotechnology in Tissue Engineering and Regenerative Medicine*. 2015: Elsevier - Academic Press.
19. Weiß, T., Schade, R., Laube, T., Berg, A., Hildebrand, G., Wyrwa, R., Schnabelrauch, M., and Liefelth, K., *Two-photon polymerization of biocompatible photopolymers for microstructured 3D biointerfaces*. *Advanced Engineering Materials*, 2011. **13**(9): p. B264–B273.
20. McCullen, S.D., Miller, P.R., Gittard, S.D., Gorga, R.E., Pourdeyhimi, B., Narayan, R.J., and Lobo, E.G., *In situ collagen polymerization of layered cell-seeded electrospun scaffolds for bone tissue engineering applications*. *Tissue Engineering Part C: Methods*, 2010. **16**(5): p. 1095-105.
21. Fioretta, E.S., Fledderus, J.O., Burakowska-Meise, E.A., Baaijens, F.P., Verhaar, M.C., and Bouten, C.V., *Polymer-based scaffold designs for in situ vascular tissue engineering: controlling recruitment and differentiation behavior of endothelial colony forming cells*. *Macromolecular Bioscience*, 2012. **12**(5): p. 577-90.
22. Legrain, A., Janson, T.G., Berenschot, J.W., Abelmann, L., and Tas, N.R., *Controllable elastocapillary folding of three-dimensional micro-objects by through-wafer filling*. *Journal of Applied Physics*, 2014. **115**(21): p. 214905.
23. Yoon, C., Xiao, R., Park, J., Cha, J., Nguyen, T.D., and Gracias, D.H., *Functional stimuli responsive hydrogel devices by self-folding*. *Smart Materials and Structures*, 2014. **23**(9): p. 094008.
24. Bassik, N., Abebe, B.T., Laflin, K.E., and Gracias, D.H., *Photolithographically patterned smart hydrogel based bilayer actuators*. *Polymer*, 2010. **51**(26): p. 6093-6098.
25. Guan, J., He, H., Hansford, D.J., and Lee, L.J., *Self-folding of three-dimensional hydrogel microstructures*. *The Journal of Physical Chemistry B*, 2005. **109**(49): p. 23134-7.
26. Pandey, S., Ewing, M., Kunasc, A., Nguyend, N., Gracias, D.H., and Menon, G., *Algorithmic design of self-folding polyhedra*. *Proceedings of the National Academy of Sciences*, 2011. **108**(50): p. 19885–19890.
27. Jamal, M., Kadam, S.S., Xiao, R., Jivan, F., Onn, T.-M., Fernandes, R., Nguyen, T.D., and Gracias, D.H., *Bio-origami hydrogel scaffolds composed of photocrosslinked PEG bilayers*. *Advanced Healthcare Materials*, 2013. **2**(8): p. 1142–1150.
28. Fusco, S., Sakar, M.S., Kennedy, S., Peters, C., Bottani, R., Starsich, F., Mao, A., Sotiriou, G.A., Pané, S., Pratsinis, S.E., Mooney, D., and Nelson, B.J., *An integrated microrobotic platform for on-demand, targeted therapeutic interventions*. *Advanced Materials*, 2014. **26**(6): p. 952–957.
29. Leong, T.G., Randall, C.L., Benson, B.R., Bassik, N., Stern, G.M., and Gracias, D.H., *Tetherless thermobiochemically actuated microgrippers*. *Proceedings of the National Academy of Sciences*, 2009: p. 703–708.
30. Boncheva, M. and Whitesides, G.M., *Making things by self-assembly*. *Materials Research Society Bulletin*, 2005. **30**(10): p. 736-742.
31. Deligkaris, K., Tadele, T.S., Olthuis, W., and van den Berg, A., *Hydrogel-based devices for biomedical applications*. *Sensors and Actuators B: Chemical*, 2010. **147**(2): p. 765-774.
32. Klein, Y., Efrati, E., and Sharon, E., *Shaping of Elastic Sheets by Prescription of Non-Euclidean Metrics*. *Science*, 2007. **315**(5815): p. 1116-1120.
33. Holmes, D.P., Ursinya, M., and Crosby, A.J., *Crumpled surface structures*. *Soft Matter*, 2008. **4**(1): p. 82-85.
34. Khetan, S. and Burdick, J.A., *Patterning hydrogels in three dimensions towards controlling cellular interactions*. *Soft Matter*, 2011. **7**(3): p. 830-838.
35. Liu, V.A. and Bhatia, S.N., *Three-dimensional photopatterning of hydrogels containing living cells*. *Biomedical Microdevices*, 2002. **4**(4): p. 257-266.
36. Huang, J., Grater, S.V., Corbellini, F., Rinck, S., Bock, E., Kemkemer, R., Kessler, H., Ding, J., and Spatz, J.P., *Impact of Order and Disorder in RGD Nanopatterns on Cell Adhesion*. *Nano Letters*, 2009. **9**(3): p. 1111-1116.

37. Chung, B.G., Flanagan, L.A., Rhee, S.W., Schwartz, P.H., Lee, A.P., Monuki, E.S., and Jeon, N.L., *Human neural stem cell growth and differentiation in a gradient-generating microfluidic device*. Lab on a Chip, 2005. **5**(4): p. 401-6.
38. Kim, D.-H., Lee, H., Lee, Y.K., Nam, J.-M., and Levchenko, A., *Biomimetic nanopatterns as enabling tools for analysis and control of live cells*. Advanced Materials, 2010. **22**(41): p. 4551-66.
39. Dalby, M.J., Gadegaard, N., and Oreffo, R.O.C., *Harnessing nanotopography and integrin-matrix interactions to influence stem cell fate*. Nature Materials, 2014. **13**(6): p. 558-569.
40. Bettinger, C.J., Langer, R., and Borenstein, J.T., *Engineering substrate topography at the micro- and nanoscale to control cell function*. Angewandte Chemie International Edition, 2009. **48**(30): p. 5406-5415.
41. Hwang, N.S., Varghese, S., and Elisseeff, J., *Cartilage tissue engineering: Directed differentiation of embryonic stem cells in three-dimensional hydrogel culture.*, in *Stem Cell Assays*, M.C. Vemuri, Editor. 2007, Humana Press. p. 351-73.
42. Powell, C.A., Smiley, B.L., Mills, J., and Vandenberg, H.H., *Mechanical stimulation improves tissue-engineered human skeletal muscle*. American Journal of Physiology - Cell Physiology, 2002. **283**(5): p. 1557-65.
43. Jawad, H., Ali, N.N., Lyon, A.R., Chen, Q.Z., Harding, S.E., and Boccaccini, A.R., *Myocardial tissue engineering : a review*. Tissue Engineering, 2007. **1**(5): p. 327-342.
44. Langer, R. and Peppas, N., *Advances in biomaterials, drug delivery, and bionanotechnology*. Bioengineering, Food, and Natural Products, 2003. **49**(12): p. 2990-3006.
45. Bae, Y.H. and Kim, S.W., *Hydrogel delivery systems based on polymer blends , block copolymers or interpenetrating networks*. Advanced Drug Delivery Reviews, 1993. **11**(1-2): p. 109-135.
46. Bikram, M., Gobin, A.M., Whitmire, R.E., and West, J.L., *Temperature-sensitive hydrogels with SiO₂-Au nanoshells for controlled drug delivery*. Journal of Controlled Release, 2007. **123**(3): p. 219-227.
47. Nicolson, P.C. and Vogt, J., *Soft contact lens polymers: an evolution*. Biomaterials, 2001. **22**(24): p. 3273-3283.
48. Choi, D., Lee, W.-J., Lee, Y., Kim, D.-N., Park, J., and Koh, W.-G., *Fabrication of macroporous hydrogel membranes using photolithography for enzyme immobilization*. Journal of Chemical Technology & Biotechnology, 2008. **83**(3): p. 252-259.
49. Kitsara, M., Beltsios, K., Goustouridis, D., Chatzandroulis, S., and Raptis, I., *Sequential polymer lithography for chemical sensor arrays*. European Polymer Journal, 2007. **43**(11): p. 4602-4612.
50. Chen, C.Y. and Chen, C.T., *A PNIPAM-based fluorescent nanothermometer with ratiometric readout*. Chemical Communications, 2011. **47**(3): p. 994-996.
51. Kim, P. and Zarzar, L.D., *Hydrogel-actuated integrated responsive systems (HAIRS): Moving towards adaptive materials*. Current Opinions in Solid State and Materials Science, 2011. **15**(6): p. 236-245.
52. Castellanos, A., DuPont, S.J., Heim, A.J., 2nd, Matthews, G., Stroot, P.G., Moreno, W., and Toomey, R.G., *Size-Exclusion "capture and release" separations using surface-patterned poly(N-isopropylacrylamide) hydrogels*. Langmuir, 2007. **23**(11): p. 6391-5.
53. Maharjan, P., Woonton, B.W., Bennett, L., Smithers, G.W., DeSilva, K., and Hearn, M.T.W., *Novel chromatographic separation — The potential of smart polymers*. Innovative Food Science & Emerging Technologies, 2008. **9**(2): p. 232-242.
54. Harmon, M.E., Tang, M., and Frank, C.W., *A microfluidic actuator based on thermoresponsive hydrogels*. Polymer, 2003. **44**(16): p. 4547-4556.
55. Li, A., Khosla, A., Drewbrook, C., and Gray, B.L., *Fabrication and testing of thermally responsive hydrogel-based actuators using polymer heater elements for flexible microvalves*. SPIE Proceeding: Microfluidics, BioMEMS, and Medical Microsystems IX, 2011. **7929**.

56. Park, J.B. and Lakes, R.S., *Chapter 7 - Polymeric implant materials.*, in *Biomaterials: An Introduction*. 2007, Springer Science & Business Media. p. 173-205.
57. Liu, B., Liu, Y., Lewis, A.K., and Shen, W., *Modularly assembled porous cell-laden hydrogels*. *Biomaterials*, 2010. **31**(18): p. 4918-25.
58. Martina, M., Subramanyam, G., Weaver, J.C., Hutmacher, D.W., Morse, D.E., and Valiyaveetil, S., *Developing macroporous bicontinuous materials as scaffolds for tissue engineering*. *Biomaterials*, 2005. **26**(28): p. 5609-16.
59. Sachlos, E. and Czernuszka, J.T., *Making tissue engineering scaffolds work. Review: the application of solid freeform fabrication technology to the production of tissue engineering scaffolds*. *European Cells & Materials*, 2003. **5**: p. 29-40.
60. Slaughter, B.V., Khurshid, S.S., Fisher, O.Z., Khademhosseini, A., and Peppas, N.A., *Hydrogels in Regenerative Medicine*. *Advanced Materials*, 2009. **21**(32-33): p. 3307–3329.
61. Brown, R.A., Wiseman, M., Chuo, C.B., Cheema, U., and Nazhat, S.N., *Ultraprapid engineering of biomimetic materials and tissues: fabrication of nano- and microstructures by plastic compression*. *Advanced Functional Materials*, 2005. **15**(11): p. 1762-1770.
62. Dai, X., Chen, X., Yang, L., Foster, S., Coury, A.J., and Jozefiak, T.H., *Free radical polymerization of poly(ethylene glycol) diacrylate macromers: Impact of macromer hydrophobicity and initiator chemistry on polymerization efficiency*. *Acta Biomaterialia*, 2011. **7**(5): p. 1965-1972.
63. Decker, C., *Kinetic study and new applications of UV radiation curing*. *Macromolecular Rapid Communications*, 2003. **23**(18): p. 1067–1093.
64. Starly, B., Chang, R., and Sun, W. *Fabrication of hepatocyte encapsulated poly-ethyleneglycol hydrogels using UV-photolithography*. in *17th Solid Freeform Fabrication Symposium*. 2006. Austin, TX, USA.
65. Xiao, W., He, J., Nichol, J.W., Wang, L., Hutson, C.B., Wang, B., Du, Y., Fan, H., and Khademhosseini, A., *Synthesis and characterization of photocrosslinkable gelatin and silk fibroin interpenetrating polymer network hydrogels*. *Acta Biomaterialia*, 2011. **7**(6): p. 2384-93.
66. Gaston, A., Khokhar, A.Z., Bilbao, L., Sáez-Martínez, V., Corres, A., Obieta, I., and Gadegaard, N., *Nanopatterned UV curable hydrogels for biomedical applications*. *Microelectronic Engineering*, 2010. **87**(5-8): p. 1057-1061.
67. Subramani, K. and Ahmed, W., *Soft-photolithography of hydrogel micropatterns*, in *Emerging Nanotechnologies in Dentistry*, K. Subramani and W. Ahmed, Editors. 2011, Elsevier. p. 175-182.
68. Pasparakis, G. and Vamvakaki, M., *Multiresponsive polymers: nano-sized assemblies, stimuli-sensitive gels and smart surfaces*. *Polymer Chemistry*, 2011. **2**(6): p. 1234.
69. Tirumala, V.R., Divan, R., Mancini, D.C., and Caneba, G.T., *Fabrication of high-aspect-ratio hydrogel microstructures*. *Journal of Applied Polymer Science*, 2005. **11**(4-5): p. 347-352.
70. Tsuda, Y., Kikuchi, A., Yamato, M., Nakao, A., Sakurai, Y., Umezumi, M., and Okano, T., *The use of patterned dual thermoresponsive surfaces for the collective recovery as co-cultured cell sheets*. *Biomaterials*, 2005. **26**(14): p. 1885-93.
71. Ionov, L. and Diez, S., *Environment-friendly photolithography using poly(N-isopropylacrylamide)-based thermoresponsive photoresists*. *Journal of the American Chemical Society*, 2009. **131**(37): p. 13315-9.
72. Yamato, M., Akiyama, Y., Kobayashi, J., Yang, J., Kikuchi, A., and Okano, T., *Temperature-responsive cell culture surfaces for regenerative medicine with cell sheet engineering*. *Progress in Polymer Science*, 2007. **32**(8-9): p. 1123-1133.
73. Koh, W.-G., Revzin, A., and Pishko, M.V., *Poly(ethylene glycol) hydrogel microstructures encapsulating living cells*. *Langmuir*, 2002. **18**(7): p. 2459-2462.
74. Moon, S., Hasan, S.K., Song, Y.S., Xu, F., Keles, H.O., Manzur, F., Mikkilineni, S., Hong, J.W., Nagatomi, J., Haeggstrom, E., Khademhosseini, A., and Demirci, U., *Layer by layer three-*

- dimensional tissue epitaxy by cell-laden hydrogel droplets*. Tissue Engineering. Part C, Methods, 2010. **16**(1): p. 157-66.
75. Ahearne, M., Yang, Y., and Liu, K., *Chapter 12 - Mechanical characterisation of hydrogels for tissue engineering applications.*, in *Topics in Tissue Engineering, Vol. 4.*, R.R. N Ashammakhi, & F Chiellini, Editor. 2008, Oulu University Finland: ebook.
 76. Zhang, J. and Wang, A., *pH- and thermo-responsive dispersion of single-walled carbon nanotubes modified with poly(N-isopropylacrylamide-co-acrylic acid)*. Journal of Colloid and Interface Science, 2009. **334**(2): p. 212-216.
 77. Haroguchi, K. and Takehise, T., *Nanocomposite hydrogels: A unique organic-linorganic network structure with extraordinary mechanical, optical and swelling/de-swelling properties*. Advanced Materials, 2002. **14**(16): p. 1120–1124
 78. Haraguchi, K., *Nanocomposite hydrogels*. Current Opinion in Solid State and Materials Science, 2007. **11**(3-4): p. 47-54.
 79. Chiang, E.N., Dong, R., Ober, C.K., and Baird, B.A., *Cellular responses to patterned poly(acrylic acid) brushes*. Langmuir, 2011. **27**(11): p. 7016-7023.
 80. Madden, P.G.A., *Development and modeling of conducting polymer actuators and the fabrication of a conducting polymer based feedback loop.*, in *Mechanical Engineering*. 2003, Massachusetts Institute of Technology: Massachusetts.
 81. Ulijn, R.V., Bibi, N., Jayawarna, V., Thornton, P.D., Todd, S.J., Mart, R.J., Smith, A.M., and Gough, J., *Bioresponsive hydrogels*. Materials Today, 2007. **10**(4): p. 40-48.
 82. Chong, S., Lee, J., Zelikin, A.N., and Caruso, F., *Tuning the permeability of polymer hydrogel capsules: an investigation of cross-linking density, membrane thickness, and cross-linkers*. Langmuir, 2011. **27**(5): p. 1724-1730.
 83. Chou, A.I., Akintoye, S.O., and Nicoll, S.B., *Photo-crosslinked alginate hydrogels support enhanced matrix accumulation by nucleus pulposus cells in vivo*. Osteoarthritis Cartilage, 2009. **17**(10): p. 1377-84.
 84. Ito, Y., Chen, G., Guan, Y., and Imanishi, Y., *Patterned immobilization of thermoresponsive polymer*. Langmuir, 1997. **13**(10): p. 2756-59.
 85. Bettencourt, A.F., Neves, C.B., de Almeida, M.S., Pinheiro, L.M., Oliveira, S.A., Lopes, L.P., and Castro, M.F., *Biodegradation of acrylic based resins: A review*. Dental Materials, 2010. **26**(5): p. e171-e180.
 86. Kloxin, A.M., Kasko, A.M., Salinas, C.N., and Anseth, K.S., *Photodegradable hydrogels for dynamic tuning of physical and chemical properties*. Science (New York, N.Y.), 2009. **324**(5923): p. 59-63.
 87. Ebrahimi, R., Tarhande, G., and Rafiei, S., *Ultrasonic degradation of poly(acrylic acid-co-acrylamide) hydrogels in aqueous solutions*. Organic Chemistry International, 2012. **2012**: p. 1-16.
 88. Schwalm, R., *Chapter 7: Tackling the Drawbacks of UV Systems, in UV Coatings: Basics, Recent Developments and New Applications*. 2006, Elsevier. p. 179-194.
 89. Studer, K., Decker, C., Beck, E., and Schwalm, R., *Overcoming oxygen inhibition in UV-curing of acrylate coatings by carbon dioxide inerting: Part II*. Progress in Organic Coatings, 2003. **48**(1): p. 101-111.
 90. Gibas, I. and Janik, H., *Review: Synthetic polymer hydrogels for biomedical applications*. Chemistry & Chemical Technology, 2010. **4**(4): p. 297-304.
 91. Bose, R.K. and Lau, K.K.S., *Mechanical properties of ultrahigh molecular weight PHEMA hydrogels synthesized using initiated chemical vapor deposition*. Biomacromolecules, 2010. **11**(8): p. 2116–2122.
 92. Hoffman, A.S., *Hydrogels for biomedical applications*. Advanced Drug Delivery Reviews, 2002. **54**(1): p. 3-12.
 93. Lin, C.-C. and Anseth, K.S., *PEG Hydrogels for the controlled release of biomolecules in regenerative medicine*. Pharmaceutical Research, 2009. **26**(3): p. 631-643.

94. Pelton, R.H. and Chibante, P., *Preparation of aqueous latices with N-isopropylacrylamide*. Colloids and Surfaces, 1986. **20**(3): p. 247–256.
95. Lee, W., Lee, T.G., and Koh, W.-G., *Grafting of poly(acrylic acid) on the poly(ethylene glycol) hydrogel using surface-initiated photopolymerization for covalent immobilization of collagen*. Journal of Industrial and Engineering Chemistry, 2007. **13**(7): p. 1195-1200.
96. Pomogailo, A.D., *Chapter 2 – Monomeric and Polymeric Carboxylic Acids*, in *Springer Series - Macromolecular Metal Carboxylates and their Nanocomposites*. 2010, Springer-Verlag Berlin Heidelberg.
97. Zustiak, S.P. and Leach, J.B., *Hydrolytically degradable poly(ethylene glycol) hydrogel scaffolds with tunable degradation and mechanical properties*. Biomacromolecules, 2010. **11**(5): p. 1348-1357.
98. Shriver, D.F. and Atkins, P.W., *Chapter 5: Acids and Bases*, in *Inorganic Chemistry*. 1999, Oxford University Press: Oxford.
99. Lu, Y., Sun, J., and Shen, J., *Cell adhesion properties of patterned poly(acrylic acid)/poly(allylamine hydrochloride) multilayer films created by room-temperature imprinting technique*. Langmuir, 2008. **24**(15): p. 8050–8055.
100. Naficy, S., Razal, J.M., Whitten, P.G., Wallace, G.G., and Spinks, G.M., *A pH-sensitive, strong double-network hydrogel: Poly(ethylene glycol) methyl ether methacrylates–poly(acrylic acid)*. Journal of Polymer Science Part B: Polymer Physics, 2012. **50**(6): p. 423-430.
101. Westbrook, K.K. and Qi, H.J., *Actuator designs using environmentally responsive hydrogels*. Journal of Intelligent Material Systems and Structures, 2008. **19**(5): p. 597-607.
102. Uchida, K., Tamura, A., and Yajima, H., *Effect of the polymer chain length of poly(N-isopropylacrylamide) on the temperature-responsive phase transition behavior of its conjugates with [60]fullerene*. Biointerphases, 2010. **5**(1): p. 17-21.
103. Makino, K., *Thermosensitive Gels*, in *Encyclopedia of Surface and Colloid Science, Volume 2*, P. Somasundaran, Editor. 2006, CRC Press. p. 6283-6284.
104. Ahir, S.V. and Terentjev, E.M., *Photomechanical actuation in polymer-nanotube composites*. Nature materials, 2005. **4**(6): p. 491-495.
105. Fujigaya, T. and Nakashima, N., *Chapter 19: Single-Walled Carbon Nanotubes as a Molecular Heater for Thermoresponsive Polymer Gel Composite*, in *Carbon Nanotubes - Polymer Nanocomposites*, S. Yellampalli, Editor. 2011, INTECH.
106. Liang, J., Huang, Y., Oh, J., Kozlov, M., Sui, D., Fang, S., Baughman, R.H., Ma, Y.F., and Chen, Y.S., *Electromechanical actuators based on graphene and graphene/Fe₃O₄ hybrid paper*. Advanced Functional Materials, 2011. **21**(19): p. 3778-3784.
107. Pal, K., Banthia, A.K., and Majumdar, D.K., *Polymeric Hydrogels : Characterization and biomedical applications – A mini review*. Designed Monomers and Polymers, 2009. **12**: p. 197-220.
108. Richter, A., *Chapter 4: Hydrogels for Actuators*, in *Hydrogel Sensors and Actuators: Engineering and Technology* G. Gerlach and K.-F. Arndt, Editors. 2009. p. 221-248.
109. Kuckling, D., Arndt, K.-F., and Richter, S., *Chapter 2: Synthesis of Hydrogels*, in *Springer Series on Chemical Sensors and Biosensors - Vol. 6: Hydrogel Sensors and Actuators*, A.K.-F. Gerlach G., Editor. 2009, Springer: Heidelberg. p. 15-68.
110. Craciunescu, I., Nan, A., Kacso, I., Bratu, I., Leostean, C., and Vekas, L., *Synthesis, characterization and drug delivery application of the temperature responsive pNIPA hydrogel*. J. Phys.: Conf. Ser. Processes in Isotopes and Molecules, 2009. **182**.
111. Bryant, S.J., Nuttelman, C.R., and Anseth, K.S., *The effects of crosslinking density on cartilage formation in photocrosslinkable hydrogels*. Biomedical Sciences Instrumentation, 1999. **35**: p. 309-14.
112. CIBA, *CIBA Products Guide - Photoinitiators for UV Curing*. 2003.

113. Revzin, A., Russell, R.J., Yadavalli, V.K., Koh, W.G., Deister, C., Hile, D.D., Mellott, M.B., and Pishko, M.V., *Fabrication of poly(ethylene glycol) hydrogel microstructures using photolithography*. *Langmuir*, 2001. **7**(18): p. 5440-7.
114. Xiao, X.C., *Effect of the initiator on thermosensitive rate of poly(N-isopropylacrylamide) hydrogels*. *eXPRESS Polymer Letters*, 2007. **1**(4): p. 232–235.
115. Green, W.A., *Industrial Photoinitiators: A Technical Guide*. 2010, CRC Press. p. 99-109.
116. Studer, K., Decker, C., Beck, E., and Schwalm, R., *Overcoming oxygen inhibition in UV-curing of acrylate coatings by carbon dioxide inerting , Part I*. *Progress in Organic Coatings*, 2003. **48**(1): p. 92-100.
117. Florio, J.J. and Miller, D.J., *Handbook of Coating Additives*. Vol. 2. 2004: CRC Press.
118. Allen, N.S., Segurolo, J., Edge, M., Santamari, E., McMahon, A., and Wilson, S., *A comparative kinetic study of commercial photoinitiators for UV/visible curable acrylate clear coating*. *Surface Coatings International*, 1999. **82**(2): p. 67-76.
119. Neumann, M.G., Schmitt, C.C., Ferreira, G.C., and Corrêa, I.C., *The initiating radical yields and the efficiency of polymerization for various dental photoinitiators excited by different light curing units*. *Dental Materials*, 2006. **22**(6): p. 576–584.
120. Biswal, D. and Hilt, J.Z., *Analysis of oxygen inhibition in photopolymerizations of hydrogel micropatterns using FTIR imaging*. *Macromolecules*, 2009. **42**(4): p. 973-979.
121. Seunarine, K., Meredith, D.O., Riehle, M.O., Wilkinson, C.D.W., and Gadegaard, N., *Biodegradable polymer tubes with lithographically controlled 3D micro- and nanotopography*. *Microelectronic Engineering*, 2008. **85**(5-6): p. 1350-1354.
122. Gadegaard, N., Dalby, M.J., Riehle, M.O., Curtis, A.S.G., and Affrossman, S., *Tubes with Controllable Internal Nanotopography*. *Advanced Materials*, 2004. **16**(20): p. 1857–1860.
123. Seunarine, K., Gadegaard, N., Tormen, M., Meredith, D.O., Riehle, M.O., and Wilkinson, C.D.W., *3D polymer scaffolds for tissue engineering*. *Nanomedicine*, 2006. **1**(3): p. 281-296.
124. Azam, A., Laflin, K.E., Jamal, M., Fernandes, R., and Gracias, D.H., *Self-folding micropatterned polymeric containers*. *Biomedical Microdevices*, 2011. **13**(1): p. 51-58.
125. Zhu, A.P., Chan-Park, M.B., and Gao, J.X., *Foldable micropatterned hydrogel film made from biocompatible PCL-b-PEG-b-PCL diacrylate by UV embossing*. *Journal of Biomedical Materials Research Part B: Applied Biomaterials*, 2006. **76b**(1): p. 76-84.
126. Randall, C.L., Gultepe, E., and Gracias, D.H., *Self-folding devices and materials for biomedical applications*. *Trends in Biotechnology*, 2012. **30**(3): p. 138-146.
127. Liu, Y.-Q., Tu, W.-T., Yang, D., and Wang, T.-Y., *Fabrication of long-period fiber gratings by CO2 laser in fiber under tension*. *Journal of Shanghai University*, 2011. **15**(1): p. 1-6.
128. Shim, T.S., Kim, S.-H., Heo, C.-J., Jeon, H.C., and Yang, S.-M., *Controlled origami folding of hydrogel bilayers with sustained reversibility for robust microcarriers*. *Angewandte Chemie - International Edition*, 2012. **51**(6): p. 1420-1423.
129. Ionov, L., *Soft microorigami: Self-folding polymer films*. *Soft Matter*, 2011. **7**(15): p. 6786-6791.
130. Zakharchenko, S., Sperling, E., and Ionov, L., *Fully biodegradable self-rolled polymer tubes: A candidate for tissue engineering scaffolds*. *Biomacromolecules*, 2011. **12**(6): p. 2211-2215.
131. Xia, Y. and Whitesides, G.M., *Soft lithography*. *Annual Review of Materials Science*, 1998. **28**(1): p. 153-184.
132. Timoshenko, S., *Analysis of bi-metal thermostats* *J. Opt. Soc. Am.*, 1925. **11**: p. 233-256.
133. Ionov, L., *Biomimetic 3D self-assembling biomicroconstructs by spontaneous deformation of thin polymer films*. *J. Mater. Chem.*, 2012. **22**(37): p. 19366–19375.
134. Qin, D., Xia, Y., and Whitesides, G.M., *Soft lithography for micro- and nanoscale patterning*. *Nature Protocols*, 2010. **5**(3): p. 491-502.
135. Ren, K., Dai, W., Zhou, J., Su, J., and Wu, H., *Whole-Teflon microfluidic chips*. *PNAS - Physical Sciences - Engineering*, 2011. **108**(20): p. 8162-8166.

136. NaPANIL, *NaPANIL Library of Processes*. 2004–2008, Paul Scherrer Institut (PSI), Switzerland: Jouni Ahopelto.
137. Dupont, *DuPont Teflon FEP Film Tech-Bulletin*. 2013.
138. Schiff, H. and Kristensen, A., *Nanoimprint lithography – Patterning of resists using molding*, in *Springer Handbook of Nanotechnology*, P.B. Bhushan, Editor. 2010, Springer: (Online). p. 279-282.
139. Lee, J.N., Jiang, X., Ryan, D., and Whitesides, G.M., *Compatibility of mammalian cells on surfaces of poly(dimethylsiloxane)*. *Langmuir*, 2004. **20**(26): p. 11684-11691.
140. Goff, J., Arkles, B., Olenick, L., and Kimble, E., *Silicone elastomers by step-growth polymerization of monodisperse dual functional silicones*. *Polymer Preprints*, 2012. **53**(1): p. 486-7.
141. Honda, K., Morita, M., and Takahara, A., *Room-temperature fabrication of nanotexture in crystalline poly(fluoroalkyl acrylate) thin film* *Soft matter*, 2008. **4**(7): p. 1400-1402.
142. Dolbier, W.R., *Fluorine chemistry at the millennium*. *Journal of Fluorine Chemistry*, 2005. **126**(2): p. 157-163.
143. Smith, D.W., Iacono, S.T., and Iyer, S.S., *11.5 Possible Applications*, in *Handbook of Fluoropolymer Science and Technology*, S.T.I. Dennis W. Smith, Suresh S. Iyer, Editor. 2014, John Wiley & Sons.
144. Griesser, H.J., Chatelie, R.C., Gengenbach, T.R., Vasic, Z.R., Johnson, G.J., and Steele, G.J., *Plasma surface modifications for improved biocompatibility of commercial polymers*. *Polymer International*, 1992. **27**(2): p. 109–117.
145. Ferchichi, A.K., Panabièrre, M., and Desplats, O.a.G., C., *Fabrication of superhydrophobic surfaces on flexible fluorinated foils by using dual-scale*. *Materials Research Express*, 2014. **1**(2).
146. Neinhuis, C. and Barthlott, A.W., *Characterization and distribution of water-repellent, self-cleaning plant surfaces*. *Annals of Botany*, 1997. **79**(6): p. 667.
147. Autumn, K., Liang, Y.A., Hsieh, S.T., Zesch, W., Chan, W.P., Kenny, T.W., Fearing, R., and Full, R.J., *Adhesive force of a single gecko foot-hair*. *Nature*, 2000. **405**(6787): p. 681-685.
148. Seunarine, K., Curtis, A.S.G., Meredith, D.O., Wilkinson, C.D.W., Riehle, M.O., and Gadegaard, N., *A Hierarchical Response of Cells to Perpendicular Micro- and Nanometric Textural Cues*. *NanoBioscience, IEEE Transact.*, 2009. **8**(3): p. 219-225.
149. Cao, C., Chan, H.F., Zang, J., Leong, K.W., and Zhao, X., *Harnessing localized ridges for high-aspect-ratio hierarchical patterns with dynamic tunability and multifunctionality*. *Advanced Materials*, 2014. **26**(11): p. 1763-1770.
150. Radha, B., Lim, S.H., Saifullah, M.S.M., and Kulkarni, G.U., *Metal hierarchical patterning by direct nanoimprint lithography*. *Scientific Reports*, 2012. **3**: p. 1078.
151. Cho, W.K. and Choi, I.S., *Fabrication of hairy polymeric films inspired by geckos: wetting and high adhesion properties*. *Advanced Functional Materials*, 2008. **18**(7): p. 1089-1096.
152. Toepke, M.W. and Beebe, D.J., *PDMS absorption of small molecules and consequences in microfluidic applications*. *Lab Chip*, 2006. **6**(12): p. 1484–1486.
153. Dumond, J.J., Low, H.Y., and Rodriguez, I., *Isolated, sealed nanofluidic channels formed by combinatorial-mould nanoimprint lithography*. *Nanotechnology*, 2006. **17**(8): p. 1975–1980.
154. Hu, H., Yeom, J., Mensing, G., Chen, Y., Shannon, M.A., and King, W.P., *Nano-fabrication with a flexible array of nano-apertures*. *Nanotechnology*, 2012. **23**(17): p. e175303.
155. Ge, H., Wu, W., Li, Z., Zhang, J., Shen, Y., Yuan, C., and Chen, Y., *Nanopatterning highly curved surfaces using hybrid nanoimprint lithography*, in *SPIE Newsroom: Micro/Nano Lithography*. 2013.
156. Bhawalkar, S.P., Qian, J., Heiber, M.C., and Jia, L., *Development of a colloidal lithography method for patterning nonplanar surfaces*. *Langmuir*, 2010. **26**(22): p. 16662–16666.
157. Anselme, K. and Bigerelle, M., *Role of materials surface topography on mammalian cell response*. *International Materials Reviews*, 2011. **56**(4): p. 243-266.

158. Trichet, L., Digabel, J.L., Hawkins, R.J., Vedula, S.R.K., Mukund, G., Ribault, C., Hersen, P., Voituriez, R., and Ladoux, B., *Evidence of a large-scale mechanosensing mechanism*. PNAS, 2011. **109**(18): p. 6935.
159. McMurray, R., Dalby, M.J., and Gadegaard, N., *Nanopatterned Surfaces for Biomedical Applications*, in *Biomedical Engineering, Trends in Materials Science*, A. Laskovski, Editor. 2011, InTech Open.
160. Mahlstedt, M.M., Anderson, D., Sharp, J.S., McGilvray, R., Muñoz, M.B., BATTERY, L.D., Alexander, M.R., Rose, F.R.A.J., and Denning, C., *Maintenance of pluripotency in human embryonic stem cells cultured on a synthetic substrate in conditioned medium*. Biotechnology and Bioengineering, 2010. **105**(1): p. 130–140.
161. Lamshead, J.W., Meagher, L., O'Brien, C., and Laslett, A.L., *Defining synthetic surfaces for human pluripotent stem cell culture*. Cell Regeneration, 2013. **2**(7): p. 1-15.
162. McMurray, R.J., Gadegaard, N., Tsimbouri, P.M., Burgess, K.V., McNamara, L.E., Tare, R., Murawski, K., Kingham, E., Oreffo, R.O.C., and Dalby, M.J., *Nanoscale surfaces for the long-term maintenance of mesenchymal stem cell phenotype and multipotency*. Nature Materials, 2011. **10**(8): p. 637-644.
163. Thomson, J.A., Itskovitz-Eldor, J., Shapiro, S.S., Waknitz, M.A., Swiergiel, J.J., Marshall, V.S., and Jones, J.M., *Embryonic Stem Cell Lines Derived from Human Blastocysts*. Science, 1998. **282**(5391): p. 1145-1147.
164. Xu, C., Inokuma, M.S., Denham, J., Golds, K., Kundu, P., Gold, J.D., and Carpenter, M.K., *Feeder-free growth of undifferentiated human embryonic stem cells*. Nature Biotechnology, 2001. **19**(10): p. 971–974.
165. Mardilovich, A., Craig, J.A., McCammon, M.Q., Garg, A., and Kokkoli, E., *Design of a novel fibronectin-mimetic peptide–amphiphile for functionalized biomaterials*. Langmuir, 2006. **22**(7): p. 3259–3264.
166. Kima, H.-T., Leea, K.-I., Kimb, D.-W., and Hwang, D.-Y., *An ECM-based culture system for the generation and maintenance of xeno-free human iPS cells*. Biomaterials, 2013. **34**(4): p. 1041–1050.
167. Adjaye, J., Huntriss, J., Herwig, R., Benkahla, A., Brink, T.C., Wierling, C., Hultschig, C., Groth, D., and Yaspo, M.L., *Primary Differentiation in the human blastocyst: comparative molecular portraits of inner cell mass and trophectoderm cells*. Stem Cells, 2005. **23**(10): p. 1514–1525.
168. Hughes, C.S., Radan, L., Betts, D., Postovit, L.M., and Lajoie, G.A., *Proteomic analysis of extracellular matrices used*. Proteomics, 2011. **11**(20): p. 3983–3991.
169. Suzuki, S., Oldberg, A., Hayman, E.G., Pierschbacher, M.D., and Ruoslahti, E., *Complete amino acid sequence of human vitronectin deduced from cDNA. Similarity of cell attachment sites in vitronectin and fibronectin*. The EMBO Journal, 1985. **4**(10): p. 2519–2524.
170. Lee, B.P., Messersmith, P.B., Israelachvili, J.N., and Waite, J.H., *Mussel-Inspired Adhesives and Coatings*. Annual Review of Materials Research, 2011. **41**: p. 99-132.
171. Nakayama, M., Okano, T., and Winnik, F.M., *Poly(N-isopropylacrylamide)-based Smart Surfaces for Cell Sheet Tissue Engineering*. Material Matters, 2010. **5.3**(56).
172. Siller, R., Greenhough, S., Naumovska, E., and Sullivan, G.J., *Small-molecule-driven hepatocyte differentiation of human pluripotent stem cells*. Stem Cell Reports, 2015. **4**(5): p. 939 - 952.
173. Guerra, N.B., González-García, C., Llopis, V., Rodríguez-Hernández, J.C., Moratal, D., Rico, P., and Salmerón-Sánchez, M., *Subtle variations in polymer chemistry modulate substrate stiffness and fibronectin activity*. Soft Matter, 2010. **6**(19): p. 4748-4755.
174. Akhar, R., Sherratt, M.J., Cruickshank, J.K., and Derby, B., *Characterizing the elastic properties of tissues*. Materials Today, 2011. **14**(3): p. 96-105.
175. Zuidema, J.M., Rivet, C.J., Gilbert, R.J., and Morrison, F.A., *A protocol for rheological characterization of hydrogels for tissue engineering strategies*. J Biomed Mater Res B Appl Biomater, 2014. **102**(5): p. 1063-1073.

176. Ohgushi, M., Matsumura, M., Eiraku, M., Murakami, K., Aramaki, T., Nishiyama, A., Muguruma, K., Nakano, T., Suga, H., and Ueno, M., *Molecular pathway and cell state responsible for dissociation-induced apoptosis in human pluripotent stem cells*. *Cell Stem Cell*, 2010. **7**(2): p. 225-239.
177. Barbaric, I., Biga, V., Gokhale, P.J., Jones, M., Stavish, D., Glen, A., Coca, D., and Andrews, P.W., *Time-lapse analysis of human embryonic stem cells reveals multiple bottlenecks restricting colony formation and their relief upon culture adaptation*. *Stem Cell Reports*, 2014. **3**(1): p. 142–155.
178. Olariu, V., Harrison, N.J., Coca, D., Gokhale, P.J., Baker, D., Billings, S., Kadirkamanathan, V., and Andrews, P.W., *Modeling the evolution of culture-adapted human embryonic stem cells*. *Stem Cell Research*, 2010. **4**(1): p. 50-56.
179. Peerani, R., Rao, B.M., Bauwens, C., Yin, T., Wood, G.A., Nagy, A., and Zandstra, P.W., *Niche-mediated control of human embryonic stem cell self-renewal and differentiation*. *The EMBO Journal*, 2007. **26**(22): p. 4744–4755.
180. Bauwens, C.L., Peerani, R., Niebruegge, S., Woodhouse, K.A., Kumacheva, E., Husain, M., and Zandstra, P.W., *Control of human embryonic stem cell colony and aggregate size heterogeneity influences differentiation trajectories*. *Stem Cells*, 2008. **26**(9): p. 2300–2310.
181. Gennes, P.G., Brochard-Wyart, F., and Quere, D., *Capillarity and wetting phenomena. Drops, Bubbles, Pearls, Waves*. 2004: Springer New York.
182. Wenzel, R.N., *Resistance of solid surfaces to wetting by water*. *Industrial & Engineering Chemistry*, 1936. **28**(8): p. 988-994.
183. Cassie, A.B.D. and Baxter, S., *Wettability of porous surfaces*. *Transactions of the Faraday Society*, 1944. **40**(0): p. 546-551.
184. Greer, A.I.M. and Moran, D.A.J., *Charge dissipation layer optimisation for nano-scale electron-beam lithography pattern definition onto diamond*. *Diamond and Related Materials*, 2012. **29**: p. 13-17.
185. Stormonth-Darling, J.M., Pedersen, R.H., How, C., and Gadegaard, N., *Injection moulding of ultra high aspect ratio nanostructures using coated polymer tooling*. *Journal of Micromechanics and Microengineering*, 2014. **24**(7): p. 075019.
186. Mohamed, K. and Alkaisi, M.M., *Investigation of a nanofabrication process to achieve high aspect-ratio nanostructures on a quartz substrate*. *Nanotechnology*, 2013. **24**(1): p. 015302.
187. Yunkin, V.A., Fischer, D., and Voges, E., *Reactive ion etching of silicon submicron-sized trenches in SF₆/C₂Cl₃F₃ plasma*. *Microelectronic Engineering*, 1995. **27**(1-4): p. 463-466.
188. Andrew I. M. Greer, I.V., Benoit Della-Rosa and Nikolaj Gadegaard, *Fluorinated Ethylene-Propylene: The Better Alternative to PDMS for Nanoimprint Stamps*, *Fluorinated Ethylene-Propylene: The Better Alternative to PDMS for Nanoimprint Stamps*. *Nanotechnology*, 2015. **In press**.
189. Palacios-Cuesta, M., Vasiev, I., Gadegaard, N., Rodríguez-Hernández, J., and García, O., *Direct micrometer patterning and functionalization of polymer blend surfaces by using hot embossing*. *European Polymer Journal*, 2014. **59**: p. 333-340.
190. Linder, V., Gates, B.D., Ryan, D., Parviz, B.A., and Whitesides, G.M., *Water-soluble sacrificial layers for surface micromachining*. *Small*, 2005. **1**(7): p. 730-736.
191. Winkleman, A., Perez-Castillejos, R., Lahav, M., Narovlyansky, M., Rodriguez, L.N.J., and Whitesides, G.M., *Patterning micron-sized features in a cross-linked poly(acrylic acid) film by a wet etching process* *Soft matter*, 2007. **3**(1): p. 108-116.
192. Dow, *Microposit S1800 series photo resists*. <http://micromaterialstech.com>.
193. Flory, P.J. and Rehner, J., *Statistical mechanics of cross-linked polymer networks II. Swelling*. *J. Chem. Phys.*, 1943. **11**(521).
194. Grillet, A.M., Wyatt, N.B., and Gloe, L.M., *Polymer Gel Rheology and Adhesion*, in *Rheology*, J.D. Vicente, Editor. 2012, InTech.

195. Patel, S.K., Malone, S., Cohen, C., Gillmor, J.R., and Colby, R.H., *Elastic modulus and equilibrium swelling of poly(dimethylsiloxane) networks*. *Macromolecules*, 1992. **25**(20): p. 5241–5251.
196. International, A., *ASTM D412 - 06a - Standard test methods for vulcanized rubber and thermoplastic elastomers—tension*. 2013, American Society for Testing and Materials: West Conshohocken, PA.
197. Timoshenko, S., *Strength of Materials, Parts I & II*. 2 ed. 1947, Lancaster: Lancaster Press.
198. Bush, B.G., Shapiro, J.M., DelRio, F.W., Cook, R.F., and Oyen, M.L., *Mechanical measurements of heterogeneity and length scale effects in PEG-based hydrogels*. *Soft Matter*, 2015. **11**(36): p. 7191-7200.
199. Althaus, F.R. and Richter, C., *ADP-ribosylation of proteins: enzymology and biological significance*. *Mol Biol Biochem Biophys*, 1987. **37**: p. 1-237.
200. Millot, G., *Geology of Clays: Weathering · Sedimentology · Geochemistry*. 2013: Springer Science & Business Media.
201. Pourjavadi, A., Ayari, M., and Amini-Fazl, M.S., *Taguchi optimized synthesis of collagen-g-poly(acrylic acid)/kaolin composite superabsorbent hydrogel*. *European Polymer Journal*, 2008. **44**(4): p. 1209-1216.
202. Kim, S.J., Lee, C.K., Lee, Y.M., and Kim, S.I., *Preparation and characterization of thermosensitive poly(N-isopropylacrylamide)/poly(ethylene oxide) semi-interpenetrating polymer networks*. *Journal of Applied Polymer Science*, 2003. **90**(11): p. 3032-3036.
203. Kōji, N., *Infrared absorption spectroscopy, practical*. 1963, San Francisco: Holden-Day.
204. Choi, J. and Rubner, M.F., *Influence of the degree of ionization on weak polyelectrolyte multilayer assembly*. *Macromolecules*, 2005. **38**(1): p. 116-124.
205. PolymerSource, *PolymerSource.com*. 2012.
206. Nakafuku, C. and Takehisa, S.-Y., *Glass transition and mechanical properties of PLLA and PDLLA-PGA copolymer blends*. *Journal of Applied Polymer Science*, 2004. **93**(5): p. 2164 – 2173.
207. Simon, D., Holland, A., and Shanks, R., *Poly(caprolactone) thin film preparation, morphology, and surface texture*. *Journal of Applied Polymer Science*, 2007. **103**(2): p. 1287–1294.
208. Lucibello, A., Proietti, E., Marcelli, R., and Bartolucci, G., *Smoothing and surface planarization of sacrificial layers in MEMS technology*. *Microsystem Technologies*, 2013. **19**(6): p. 22 - 26.
209. Tan, H.Y., Widjaja, E., Boey, F., and Loo, S.C., *Spectroscopy techniques for analyzing the hydrolysis of PLGA and PLLA*. *J Biomed Mater Res B Appl Biomater*, 2009. **91**(1): p. 433-40.
210. Qi, H., Ghodousi, M., Du, Y., Grun, C., Bae, H., Yin, P., and Khademhosseini, A., *DNA-directed self-assembly of shape-controlled hydrogels*. *Nature Communications*, 2013. **4**.
211. Reynolds, P.M., Pedersen, R.H., Stormonth-Darling, J., Dalby, M.J., Riehle, M.O., and Gadegaard, N., *Label-Free Segmentation of Co-cultured Cells on a Nanotopographical Gradient*. *Nano Letters*, 2013. **13**(2): p. 570-576.
212. Gaudet, C., Marganski, W.A., Kim, S., Brown, C.T., Gunderia, V., Dembo, M., and Wong, J.Y., *Influence of Type I Collagen Surface Density on Fibroblast Spreading, Motility, and Contractility*. *Biophysical Journal*. **85**(5): p. 3329-3335.
213. Pierce-Biotechnology, *Instructions - NHS/Nitrophenyl Azide Crosslinkers* T.-F.-S. Inc., Editor. 2008.
214. Mark, J.E., *Physical Properties of Polymers Handbook*. 2007: Springer Science & Business Media.
215. Schoen, I., Hu, W., Klotzsch, E., and Vogel, V., *Probing cellular traction forces by micropillar arrays: contribution of substrate warping to pillar deflection*. *Nano Letters*, 2010. **10**(5): p. 1823–1830.

216. Vernekar, V.N., Cullen, D.K., Fogleman, N., Choi, Y., García, A.J., Allen, M.G., Brewer, G.J., and LaPlaca, M.C., *SU-8 2000 rendered cytocompatible for neuronal bioMEMS applications*. Journal of Biomedical Materials Research Part A, 2009. **89A**(1): p. 138-151.
217. Niwa, H., Ogawa, K., Shimasato, D., and Adachi, K., *A parallel circuit of LIF signalling pathways maintains pluripotency of mouse ES cells*. Nature, 2009. **460**(7251): p. 118-122.
218. Johansson, H. and Simonsson, S., *Core transcription factors, Oct4, Sox2 and Nanog, individually form complexes with nucleophosmin (Npm1) to control embryonic stem (ES) cell fate determination*. Aging, 2010. **2**(11): p. 815-822.
219. Masui, S., Nakatake, Y., Toyooka, Y., Shimosato, D., Yagi, R., Takahashi, K., Okochi, H., Okuda, A., Matoba, R., Sharov, A.A., Ko, M.S., and Niwa, H., *Pluripotency governed by Sox2 via regulation of Oct3/4 expression in mouse embryonic stem cells*. Nat Cell Biol, 2007. **9**(6): p. 625-35.
220. Goodfellow, *Polystyrene*. 2015, Goodfellow: <http://www.goodfellow.com/E/Polystyrene.html>.
221. Ghibaudo, M., Saez, A., Trichet, L., Xayaphoummine, A., Browaeys, J., Silberzan, P., Buguin, A., and Ladoux, B., *Traction forces and rigidity sensing regulate cell functions*. Soft Matter, 2008. **4**(9): p. 1836-1843.
222. Py, C., Reverdy, P., Doppler, L., Bico, J., Roman, B., and Baroud, C.N., *Capillary origami: spontaneous wrapping of a droplet with an elastic sheet*. Physical Review Letters, 2007. **98**(156103).
223. Buchwald, P., *FEM-based oxygen consumption and cell viability models for avascular pancreatic islets*. Theoretical Biology and Medical Modelling, 2009. **6**: p. 5.
224. Prado-Lopez, S., Conesa, A., Armiñán, A., Martínez-Losa, M., Escobedo-Lucea, C., Gandia, C., Tarazona, S., Melguizo, D., Blesa, D., Montaner, D., Sanz-González, S., Sepúlveda, P., Götz, S., O'Connor, J.E., Moreno, R., Dopazo, J., Burks, D.J., and Stojkovic, M., *Hypoxia Promotes Efficient Differentiation of Human Embryonic Stem Cells to Functional Endothelium*. STEM CELLS, 2010. **28**(3): p. 407-418.

APPENDIX A – SIMULATION OF OXYGEN CONCENTRATION IN CELL CULTURE MICROCONTAINERS

To investigate the oxygen consumption of cells in an enclosed container, and ultimately to see if they were likely to undergo rapid cell death; COMSOL models were created to look at the rate of diffusion into a container with permeable slots or hinges, and solid faces. The model is based on a simulation by Buchwald [223] for the simulation of pancreatic islets. Here the geometry is adjusted to that of an enclosed container. Hinge lengths were 40 μm with box faces varying between 125, 250 and 500 μm . The cell layer was 20 μm thick and 10 μm clear of the box face edges. The model (Appendix figure 2) is a 2D representation of a 3D container. While the cells used in literature are different from those hESCa, the dynamics of cells being in enclosed architectures was a pilot study to gain insight into how cultures in these niches would operate and survive. While diffusion and consumptions rates may differ, the overall combination of these and the laws governing the oxygen concentration remain the same, experimental consumption rates and dissolved gas concentrations can be fed into the model in the future, as can diffusion coefficients. To simulate the problem COMSOL physics used were the time dependent diffusion relationship:

$$\frac{\partial c}{\partial t} + \nabla \cdot (-D\nabla c) = R - u \cdot \nabla c$$

Where, c denotes the concentration in $\text{mol}\cdot\text{m}^{-3}$ of oxygen and D the diffusion coefficient $\text{m}^2\cdot\text{s}^{-1}$ thereof. R the reaction rate in $\text{mol}\cdot\text{m}^{-3}\cdot\text{s}^{-1}$, and u is the diffusion velocity field in $\text{m}\cdot\text{s}^{-1}$, where ∇ is the standard *del* operator [223].

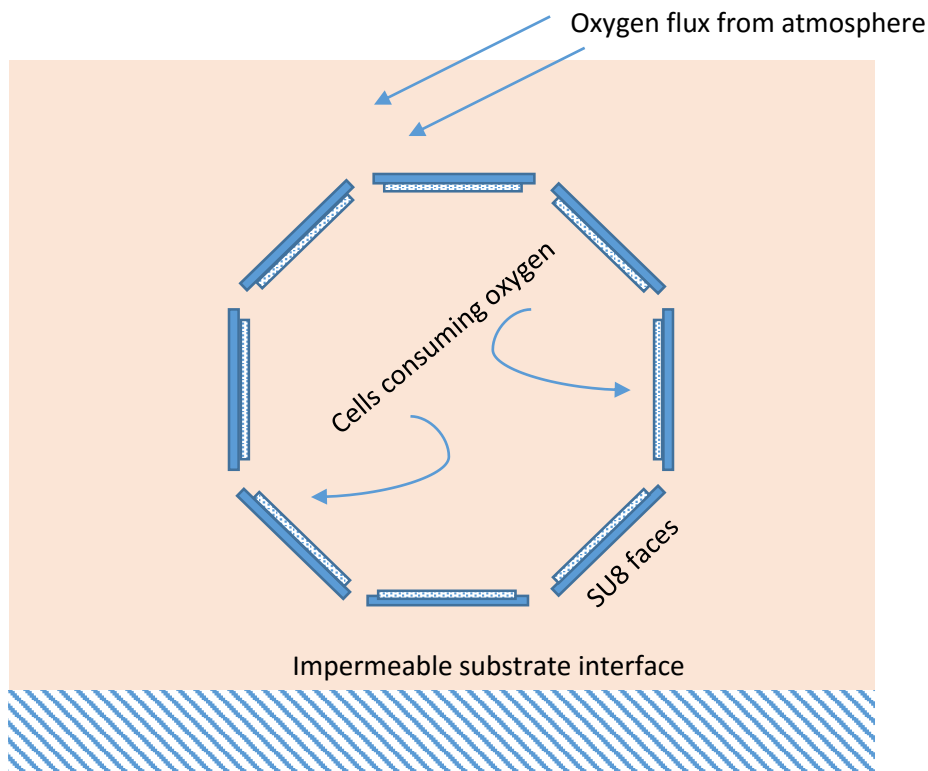
For oxygen consumption, Buchwald [223] assumes a Michaelis-Menten-type consumption rate ($R < 0$) where a step-down function decreases the oxygen consumption rate when a critical concentration is reached, this simulates hypoxic conditions where the cell metabolism is slowed down to limit consumption is reduced in the face of a dwindling oxygen supply. While Butchwald [223] used this in applications for pancreatic islets with relatively large cellular mass, we are applying this to thin cell films on the walls of an inert container, the step function is useful though as the species transport into these containers is limited by the faces of the box, and only the hydrogel hinge and closure areas openly allow gas diffusion to occur. The governing equation of cell oxygen consumption from Butchwald [223]:

$$R_{O_2} = R_{max,O_2} \left(\frac{C_{O_2}}{C_{O_2} + C_{MM,O_2}} \right) \cdot \delta(C_{O_2} > C_{cr})$$

Where, R_{\max} is the maximum oxygen consumption rate, C_{MM,O_2} the Michaelis-Menten concentration constant at which O_2 consumption rate drops by 50 % of its maximum, C_{cr} is the critical oxygen concentration below which necrosis is assumed to occur after a sufficiently long exposure, these areas are highlighted in the output as hypoxic zones. Here δ is the step-down function to account for the reduced O_2 consumption rate in those cells where the oxygen concentration fell below the critical levels. To define the reduced oxygen consumption in hypoxic conditions the COMSOL's inbuilt smoothed Heaviside function *flc1hs* was used, in the same way as with Butchwald's islet simulation [223]:

$$\delta(c) = \text{flc1hs}(c - 1.0 \times 10^{-4}, 0.5 \times 10^{-4}).$$

The other parameters used are shown in Appendix Table 1. A schematic of the model is shown in Appendix Figure 2. The construction remains the same for the three sizes, with a hexagonal construction also attempted. In this model influx oxygen diffusion occurs only from the atmosphere into cell media solution, with the oxygen sink in the model remaining within the containers in the form of thin cell sheets adhered to the container walls.

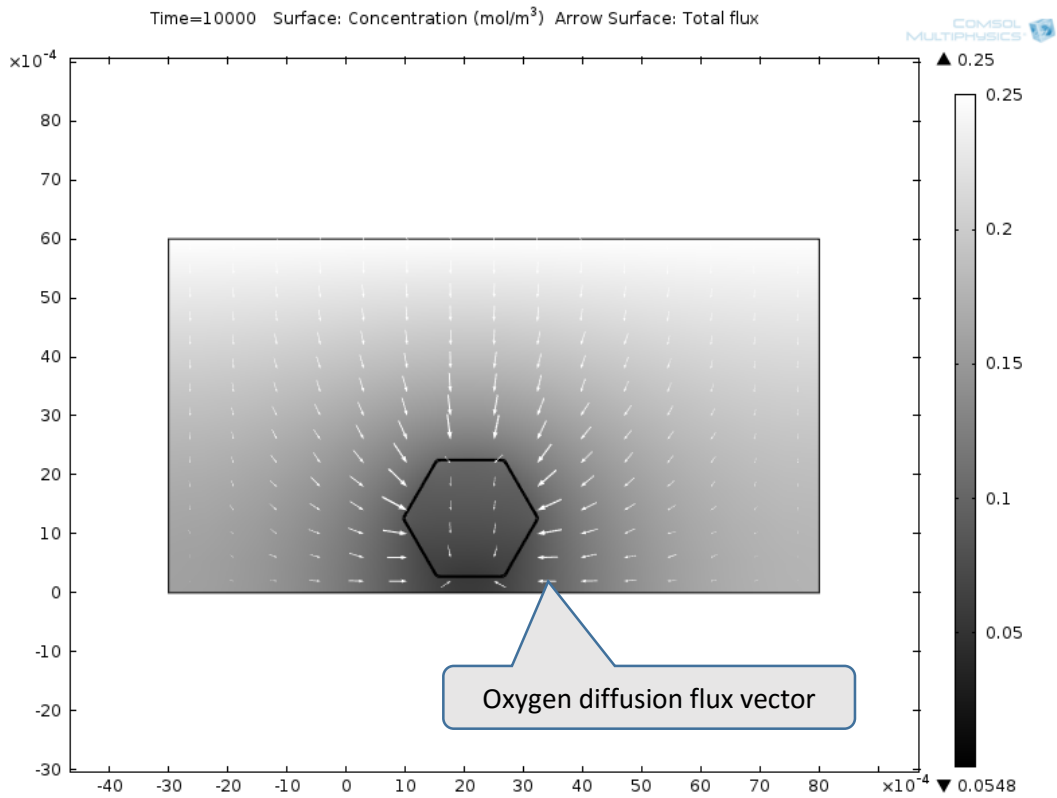


Appendix Figure 1 - Schematic of COMSOL model for looking at oxygen consumption by cells in an enclosed space.

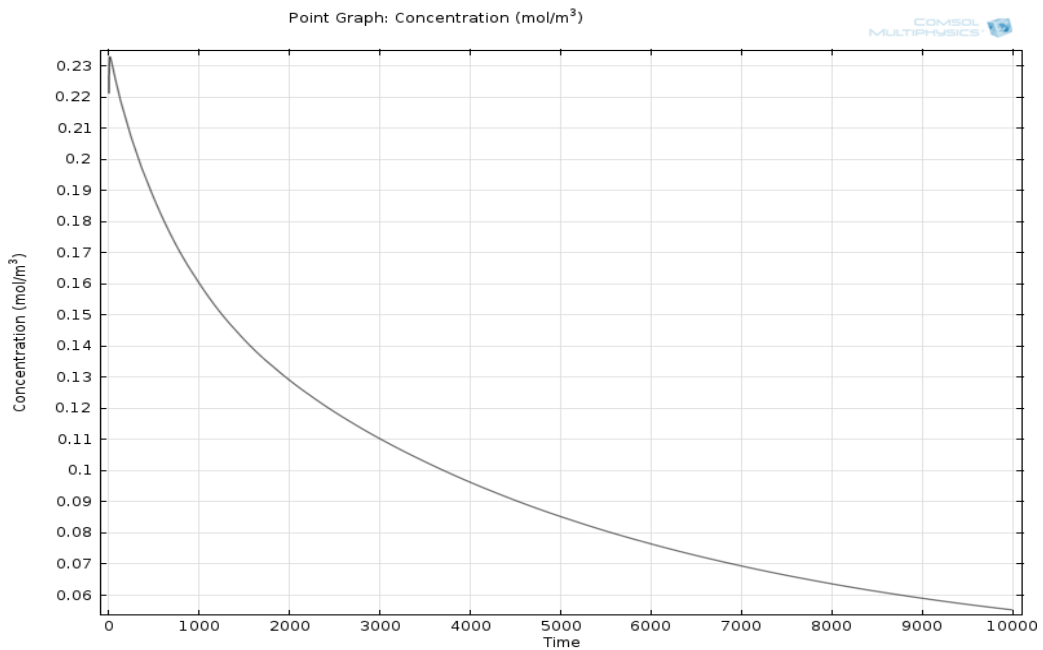
Appendix Table 1 – Variable definitions assigned to the model and assumptions made. Values were adapted from Buchwald paper on pancreatic islets[223]. Definitions were added to model the hydrogel containers, and islets replaced with thin cell layers lining the walls of the container. [223]

Variable	Description	COMSOL variable	Value
C_{MM,O_2}	Cut-off concentration of O_2	CMM_O2	$1E-3 \text{ mol/m}^3$ (1 μM)
P_{MM,O_2}	Partial pressure O_2	PMM_O2	0.7 mm/Hg
C_{cr}	Concentration limit O_2	C_cr	$1E-4 \text{ mol/m}^3$ (1 μM)
Rmax	Rate consumed O_2 max	Rmax	0.034 mol/s/m^3
D_{O_2}	Diffusion of O_2 in water	DO2	$3E-9 \text{ m}^2/\text{s}$
D_{cells}	Diffusion of O_2 in cell layer	Dc	$2E-9 \text{ m}^2/\text{s}$
D_g	Diffusion of O_2 in gel hinge	Dg	$2E-9 \text{ m}^2/\text{s}$
C_{atm}	Atmospheric O_2 concentration	C_atm	0.23 mol/m^3
C_{cells}	Concentration in cell layer	C_cell	0.16 mol/m^3

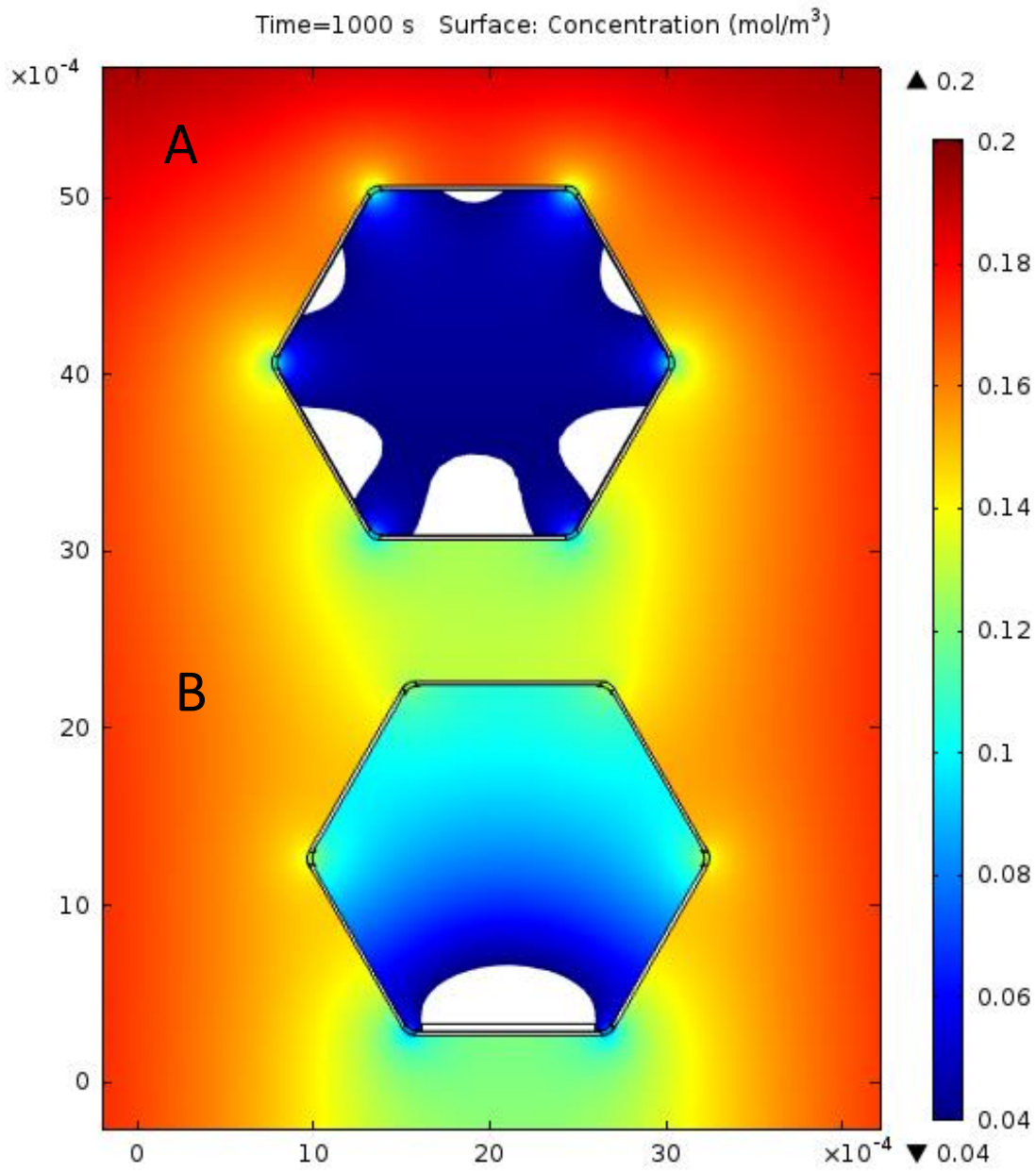
Two models are shown one for a hexagonal container (Appendix figure 2) showing the oxygen diffusion flux and the steady state oxygen level within the container (Appendix Figure 4). The resulting areas of hypoxia are shown as white regions in Appendix Figure 5, and show the result when the cells are evenly distributed (A) and if a single colony of cells 5 layers thick forms on the container floor (B).



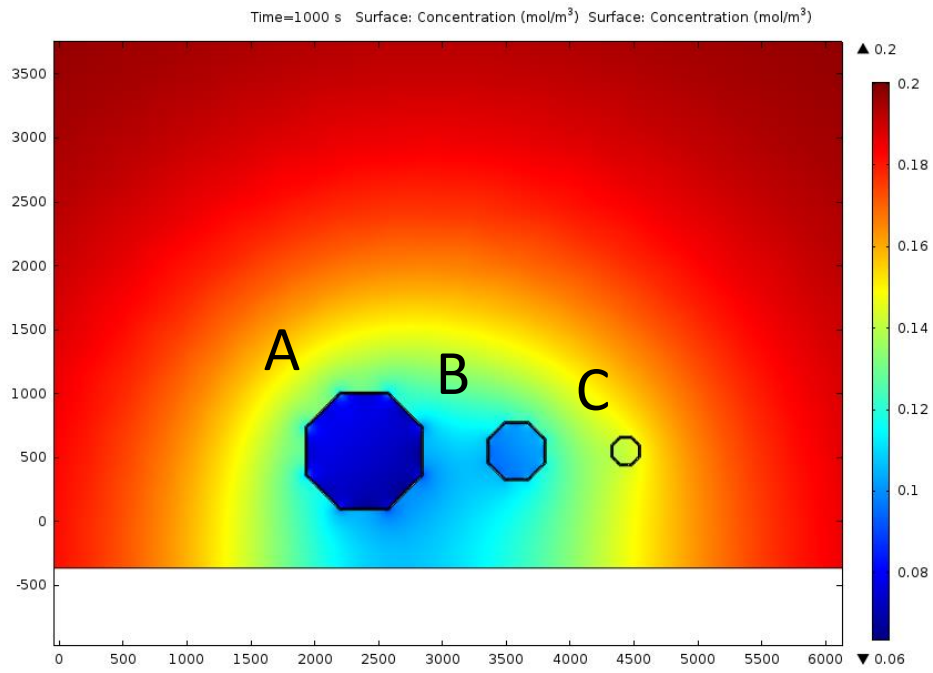
Appendix Figure 2 - Model as seen in COMSOL interface, hexagonal container with cells modelled on the inside surfaces consuming oxygen which is diffusing into the culture medium from the above atmosphere. Contour lines indicate direction of oxygen flux in system.



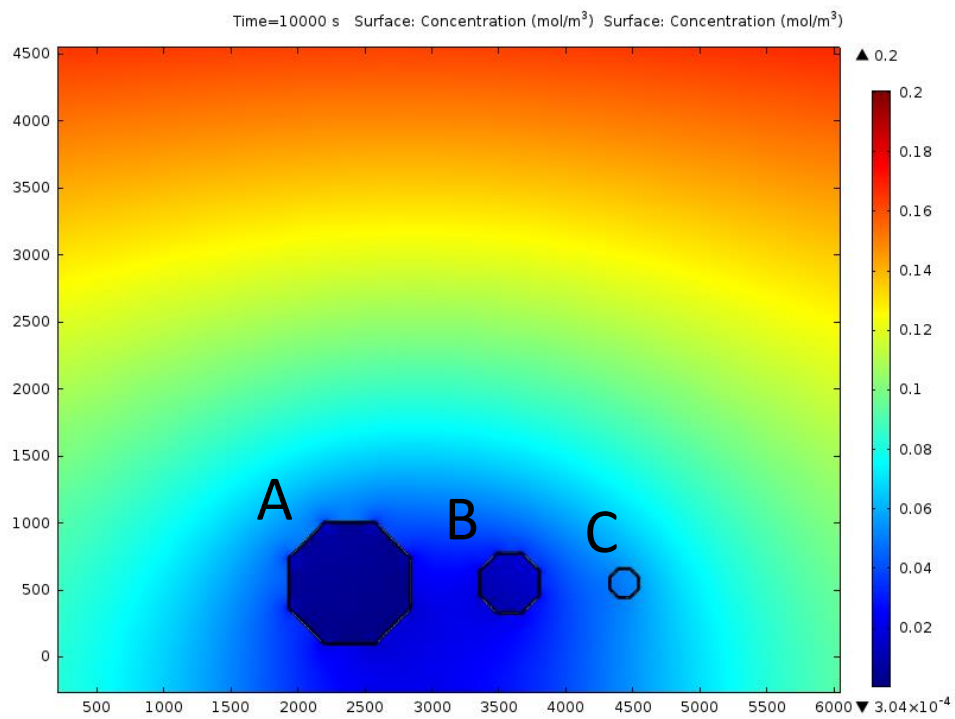
Appendix Figure 3 - Oxygen concentration minimum value within the container over time, a steady state is reached near 10000 seconds.



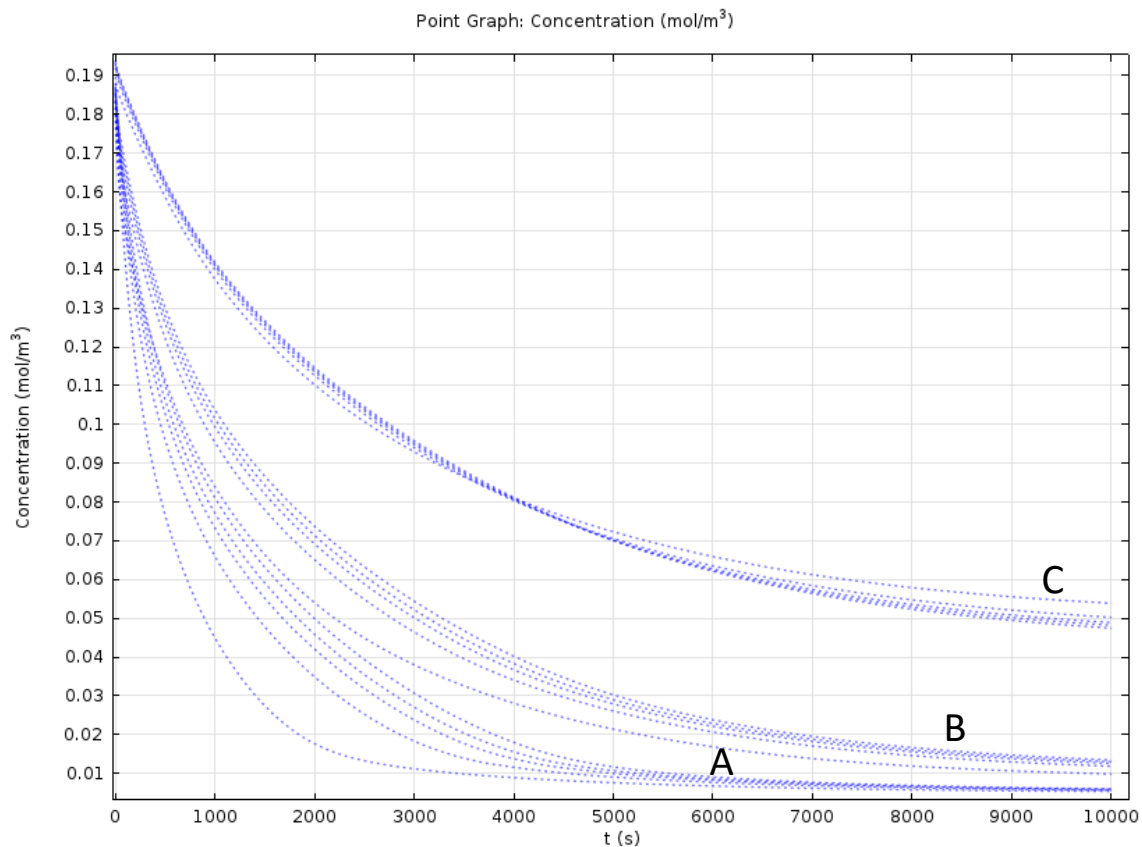
Appendix Figure 4 - Simulation of two containers positioned adjacent, the top container has a 20 μm thick layer of cells spread over every face, the bottom container has one cell block 80 μm thick placed on the bottom face. White zones indicate what can be called hypoxic conditions. This illustrates that the containers could generate a similar nutrient gradient as seen in hepatic lobules, discussed in Chapter 1.



Appendix Figure 5 - Time = 1000 s when the oxygen concentration has not yet reached a steady state. For a cell sheet two layers thick (3000 cells per surface) in containers of three different sizes ranging from 1000 to 500 to 250 μm respectively.



Appendix Figure 6 – Oxygen concentration at $t=10000$ seconds when steady state has been reached.



Appendix Figure 7 - Steady state oxygen levels achieved with changing container size, as the diameter of the container drops from 1000 to 500 and 250 μm . As the size of the container drops the hinge is proportionally a larger part of the container surface area, while the area populated by cells is decreasing. Smaller containers therefore have a benefit in providing greater oxygen permeability.

This simulation shows (Appendix Figure 5) that with oxygen diffusing at the 3D container hinges and face edges, each face, seeded with cells effectively reproduces a nutrient and oxygen concentration gradient, it also suggest that larger hinges are needed on larger containers to maintain sufficient oxygen diffusion into the container.

One other suggested benefit of these hypoxic conditions may be the *in situ* effects on differentiation of human embryonic stem cells (hESCs) with Prado-Lopez et al. [224] suggesting that hypoxia promotes endothelial differentiation. Keeping containers with different sizes and conditions in co-culture could create different lineages depending on oxygen saturation, forming a co culture in solution.

Conference abstracts and awards

1. Keynote speaker: *Cell Origami – 3D Self-Folding Nanopatterned Scaffolds for Tissue Engineering*
Iskandar Vasiev, Elizabeth Tanner and Nikolaj Gadegaard
Annual Stem Cell Symposium 2014 – The Norwegian Center for Stem Cell Research, Oslo.
2. Oral: *Cell Origami – 3D Self-Folding Nanopatterned Scaffolds for Tissue Engineering*
Iskandar Vasiev, Elizabeth Tanner and Nikolaj Gadegaard
The European Society for Biomaterials 25th Annual Conference 2013 – Madrid
3. Poster: *Cell Origami – 3D Self-Folding Nanopatterned Scaffolds for Tissue Engineering*
Iskandar Vasiev, Elizabeth Tanner and Nikolaj Gadegaard
The European Society for Biomaterials 25th Annual Conference 2013 – Madrid
4. Oral: *Environmentally Actuated 3D Hydrogel Scaffolds for Cell Capture and Delivery*
Iskandar Vasiev, Elizabeth Tanner and Nikolaj Gadegaard
The UK Society for Biomaterials Annual Conference 2012 - Nottingham
5. Poster: *Cell Origami – 3D Self-Folding Nanopatterned Scaffolds for Tissue Engineering*
Iskandar Vasiev, Elizabeth Tanner and Nikolaj Gadegaard
Award: Best Poster Presentation (Biomedical) Global Circus 2013 - Niigata, Japan
6. Poster: *Self-folding 3D patterned hydrogel scaffolds for cell culture*
Iskandar Vasiev, Andrew Greer, Elizabeth Tanner and Nikolaj Gadegaard
MNE 2013 – London
Award: Best Poster Presentation (Life and Systems)
7. Oral: *Self-folding 3D patterned hydrogel scaffolds for cell culture*
Iskandar Vasiev, Andrew Greer, Elizabeth Tanner and Nikolaj Gadegaard
MNE 2013 – London
8. Poster: *Self-folding 3D patterned hydrogel scaffolds for cell culture*
Iskandar Vasiev, Andrew Greer, Elizabeth Tanner and Nikolaj Gadegaard
Cell and Proteomic Technologies Symposium 2013 Glasgow
Award: Best Poster Presentation - British Society for Proteome Research

Publications

1. Iskandar Vasiev, Andrew I.M. Greer, Ali Z. Khokhar, John Stormonth-Darling, K. Elizabeth Tanner, Nikolaj Gadegaard, Self-folding nano- and micropatterned hydrogel tissue engineering scaffolds by single step photolithographic process, *Microelectronic Engineering*, Volume 108, August 2013, Pages 76-81, ISSN 0167-9317, <http://dx.doi.org/10.1016/j.mee.2013.04.003>.
2. Marta Palacios-Cuesta, Iskandar Vasiev, Nikolaj Gadegaard, Juan Rodríguez-Hernández, Olga García, Direct micrometre patterning and functionalization of polymer blend surfaces by using hot embossing, *European Polymer Journal*, Volume 59, October 2014, Pages 333-340, ISSN 0014-3057, <http://dx.doi.org/10.1016/j.eurpolymj.2014.07.020>.
3. Andrew Greer, Iskandar Vasiev, Benoit Della-Rosa and Nikolaj Gadegaard "Fluorinated Ethylene-Propylene: The Better Alternative to PDMS for Nanoimprint Stamps" (In press - nanotechnology 2015)